Ahad Kh. Janahmadov
Maksim Y. Javadov

Synergetics and Fractals in Tribology

Materials Forming, Machining and Tribology

Series editor

J. Paulo Davim, Aveiro, Portugal

More information about this series at http://www.springer.com/series/11181

Ahad Kh. Janahmadov · Maksim Y. Javadov

Synergetics and Fractals in Tribology

Springer

Ahad Kh. Janahmadov
National Aviation Academy
Baku
Azerbaijan

Maksim Y. Javadov
ASNAF Industrial Company
Baku
Azerbaijan

Preface

The last decade is characterized by an increased interest in all industrialized countries to the problems of tribology, such as friction, lubrication, and wear. As a result of friction and wear, the surfaces of the solid frictional units undergo significant changes of their initial physical and mechanical properties. Therefore, the tribology of fracture faces a more challenging tasks than the usual problems of strength, it requires a consideration of wide range of factors, both in the study and the calculation of the processes of friction, wear, and lubrication, and in creating a reliable, durable economically and environmentally effective frictional units for machines, appliances, and apparatuses of technological processes.

The engineering science entered into the twenty-first century with a clear understanding of the importance of friction and need for its consideration in processes of development and design of various machine units.

In the first half of the twentieth century, the engineers approached friction with certain pragmatism, reducing the problem mainly to determining the coefficients of friction for specific practical conditions. It can be said that the theory of friction did not play any significant role for a long period of time. The second half of the twentieth century can be deservedly called the golden age of the tribological science; there was a significant interest to the theory of friction. The intensive development of nanotechnologies and the technologies of surface hardening, the emergence of new composites and nanomaterials could explain such interest to the theory of friction. Starting from the 1980s, a fundamentally new mathematical and physical methods were developed, which made possible to study the frictional contacts at the microscopic and atomic levels. Physical meso-mechanics, non-equilibrium thermodynamics, synergetics, fractals, nonlinear dynamics, and others—it is not even a complete list of new horizons in tribology. An integrated approach in finding correlations between tribological and strength properties of materials and their characteristics of the interatomic interaction can be the basis for an adequate description of the contact mechanism and also a prediction of tribological properties.

The development of mentioned scientific fields and their practical implementation will expand the application area of human intelligence and energy. Specialists and engineers will be able to calculate, diagnose, predict, and select appropriate materials for frictional pairs, and also assign the optimal operation regime for tribocoupling.

Baku   Ahad Kh. Janahmadov
2014

Contents

Introduction

Prior to the beginning of the twentieth century, tribology had a long and interesting path, even it did solved some practical problems which arisen with the technological progress, it merely had any effect on process itself. Since then, the engineering science have a more clear understanding of tribology and its place in design and development of machines, equipment, and various frictional units. The theoretical solutions to the problems of the external friction provided a ground to develop new construction materials, and the surface hardening technologies gave a progress in macroelectronics and created micro- and nanotechnologies.

The big achievements of applied sciences and technology in last few decades are owing to new results and methods developed by fundamental and applied physics and mathematics. Tribology is no exception; the science of friction, wear, and lubrication has made significant progress as well.

At the end of 1960s the German scientist Hermann Haken introduced a new terminology "synergetics," which translates as "joint action" from Greek, to emphasize the role of a collective in the formation of dissipative structures. Today, synergetics, as the theory of self-organization, is one of the most popular and promising interdisciplinary approaches.

The offered monograph is written based on works of those exceptional authors and explains tribology as the physical phenomena using synergetics and fractals. This new direction in research aims to explore the general principles of evolution and self-organization of complex systems in the different fields of knowledge on the basis of the construction and the examination of nonlinear dynamic systems. It has been determined by now that the resistance of metals and alloys to fatigue is defined by the dynamic structure and requires the analysis of a deformable material as an open system that exchanges energy and matter with medium. In tribology, both the external layers and all internal boundary layers should be studied as independent nonlinear planar subsystems, which are the leading functional subsystems of deformable solids, with broken transmission invariants. The bulk of stresses caused by friction are concentrated in close to the surface external layers of the frictional elements. The restructuring of the external layer under the influence of external thermal stresses precisely takes place during the formation of thermal field, and by

the moment when the temperature reaches certain stability, it is already affected by various residual stresses. Generally, there is a hierarchy within the levels of the structural elements of the deformation in the form of Cayley tree. This hierarchy is defined as the initial structure of medium, as the formation of dissipative structures caused by the deformation defects.

The self-organizing in open systems dissipative structures are fractal that dictates the necessity to combine theories of synergetics and fractals in the study of physical and mechanical nature of fracture of materials. Synergetics has expanded the notion of structure, giving it the versatility, and the theory of fractals has enabled the introduction of new quantitative measure for structures in the form of the fractal dimension. The founder of the theory of fractals, B. Mandelbrot, formed the technical term "fractal" from the Latin word "fractus" meaning "broken," i.e., to create fragments of arbitrary shapes. The self-similarity, as the main characteristic of fractals, means that it is more or less uniformly arranged in a wide range of scales. Sometimes the scale invariance is referred to as self-similarity or auto-modeling. Thus, the concept of fractals, as the quantitative measure of the dissipative structure of the predestruction zone, creates a link between the fractal dimension and the mechanical properties, as well as the critical deformation states of metals and alloys.

Any real physical objects and signals, even possessing of self-similarity features, quite rarely can be described by only one measure of the fractal dimension. That is why the theory of multifractals, inhomogeneous fractal objects, has received a wide spread analysis. The infinite spectrum of such dimensions, generally called the fractal dimension or Rényi entropy, is required to characterize the multifractal dimension. So by combining the principles of the self-organization of condensed mediums and the theory of fractals for the hierarchically coordinated systems, we get a possibility of the systemic analysis of the restructuring process of the defective crystal lattice in solids and that combination also allows us to calculate the generalized fractal dimension of the fatigue fracturing by using the properties of the super-stable bifurcation cycles during the transition from order to chaos, the Feigenbaum scenario.

In monograph, the authors are trying to give a clear picture of a quite complex topic, and they are well aware of all obstacles and difficulties that have to face, especially when the terminology in the studied field is still evolving. The monograph findings have a great importance for tribology itself and it opens possibilities to develop new branches such as tribophysics, materials, mechanics, diagnostics, and monitoring. The book is intended for a wide range of scientists, engineers who specialize in the field of tribology, who face challenging problems in development and operation of various types of machines and equipment.

The authors will be grateful for any comments on the content of the monograph.

Chapter 1
Key Features and Operating Conditions of Tribocoupling

1.1 Friction, Wear, and Lubrication. Concepts Development

The improvement of the machine reliability and durability is one of the most challenging tasks of modern engineering. In most cases, the equipment longevity is limited to the surface wear of individual friction parts, but the growing productivity exposes machines to extreme stresses, heavy loading, fast speeds, and high temperatures. So the wear resistance becomes highly dependent on mechanical, physical, and chemical processes that take place in friction contacts. All that comprise the foundation of modern tribology studying.

The economic losses due to the mechanical wear make 5.4 % of the national income of developed countries. The friction resistance consumes 30–40 % of the worldwide energy generated within a year. So energy generated by friction does not just disappear, it gets converted into heat, which in its turn heats up mechanisms and all related machine units. The excessive heat leads to failure and accidents. Studies show that approximately 80–90 % of mechanical failures are caused by wear of mechanical units and machine parts.

The behavior of materials, their frictional, and wear properties are largely explained by the set of complex physical and chemical, mechanical, and electrical and magnetic processes that take place in near-surface layers at friction.

According to I.V. Kragelsky, when studying and analyzing the friction process, it is important to examine the surface contact between interacting bodies as a three-stage process: the interaction on the friction surface—the changes taking place in the friction surfaces—the destruction of surfaces. For these parameters, the change in direction is defined by the Le Chatelier–Braun principle, according to which any system, when it is subjected to external changes, evolve in way that to maximally reduce those effects (i.e., to increase entropy). As a result of the tribosystem readjustment to such loading conditions, microstructures, microrelieves, and submicrorelieves are formed in the near-surface layers of the interacting bodies,

which along with the deformation of the secondary structures of various origin on the frictional surfaces provide the minimization of the energy loss on friction and the localization of the friction failure zone in the thin surface layer. Besides, during the friction of solids, a "third" body is formed in the contacting surface layers due to the thermo-mechanical loading with certain properties. The "third" body exists only within the contacting time and has very "special properties". In reality, a new material is formed in the contact zone, which resists to failure at friction.

The theoretical development of tribology can be divided into distinctive stages. The first stage covers the period from ancient times till the beginning of twentieth century. It is the stage when the human civilization began to accumulate the knowledge and made great discoveries. This includes the discovery of fire through friction, the creation of wheel, the first ball bearings, the first transmission through friction, and the lubrication of frictional units. The second stage covers a period from the beginning of twentieth century until 1970, and the third stage is everything from middle of 1970s till present times. The last period is characterized by the interdisciplinary interest from physicists, mechanical engineers, material specialists, chemists, and tribologists to study and find correlations between atomic and tribological properties and examine the interacting materials on nano-, micro-, and mesoscopic structural levels.

In his fundamental monograph, the famous English scientist D. Dawson thoroughly detailed the history of tribology from ancient times to the end of the nineteenth century and where he also expressed his views on its further development. He noted that during the early civilizations, tribology had a positive impact on the technological progress. The advantage of the rolling process over sliding while moving heavy freight contributed to the invention of wheel and some primitive carts. The first wheeled cart was discovered in the Kura-Araks valley (the present territory of Azerbaijan), and it dated back to 4–3 millennium BC.

The history of tribology is enriched with famous scientists such as Leonardo da Vinci, G. Amontons, Ch.O. deCoulomb, O. Reynolds, W.B. Hardy, N.P. Petrov, P.A. Rebinder, B.V. Deryagin, F.P. Bowden, I.V. Kragelsky, M.M. Khrushchev, A.V. Chichinadze, and many others, who made brilliant scientific and technological discoveries. The Amontons–Coulomb law is the main achievement of tribology as the science of friction, and it shows the dependence of the friction force on the normal load. In subsequent studies, there were many attempts to experimentally verify and theoretically justify that law. Owing to such great mathematicians as L. Euler, G. Leibniz, J. Leslie, L. Gumbel, and others, the tribology laws were taking shape as from the standpoint of mechanics as from engineering practice. The elementary friction model is given in Fig. 1.1.

The scientists, such as J.T. Desaguliers, L.N. Brillouin, W.B. Hardy, and G.A. Tomlinson, established the foundations of the molecular interaction for the contacting surfaces of friction pairs.

Fig. 1.1 The elementary
friction model
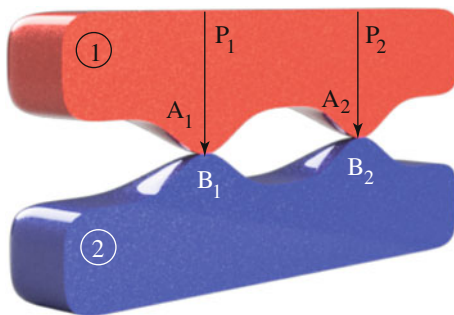
B.V. Deryagin developed the theoretical aspects of the molecular friction theory and the binomial friction law. His concept is based on the notion of the discrete atomic and molecular structures of material and additive properties of friction forces for crystalline and amorphous solids. The Deryagin's theoretical diagram is based on the contact model of two sliding, ideal and identically oriented monocrystals (Fig. 1.2). The contacting surfaces of friction pairs act as two rough surfaces with protrusions and hollows due to their atomic structures. Friction, according to Deryagin, is caused by the action of repulsive forces formed when the electron shells of atoms approach each other.

V.D. Kuznetsov proposed the physical friction theory. And it was first time, when friction was considered from the energy prospective. He indicates that when assessing the friction material properties, the surface energy becomes the determining factor. He connects the coefficients of friction with the structural properties of interacting bodies. In other words, every energy loss is assessed through the sound phenomena that accompany the friction process, the electrification of friction bodies, their heating, the abrasion, and the fragmentation of abrasive particles.

Tross and Fleischer developed the energy theory of friction and wear founded on the energy conservation principle. Based on the energy theory of strength developed by Tross, Fleischer got his formulas for the energy relationships and he also derived the energy balance equation. According to Fleischer, the energy density is

Fig. 1.2 The diagram of the
atom contacts and sliding that
forms the surface of two
monocrystals by Deryagin
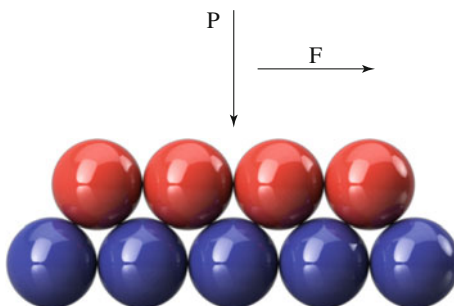
the ratio of the work required to overcome friction, to the volume of material that receives the mechanical loading during friction.

The energy approach developed by Rabinovich states that if the energy accumulated in particles much distant from the surface due to the elastic deformation is greater than the energy stored in particles much closer to the surface due to adhesive forces, then the free particles of wear are formed.

G.M. Bartnev proposed another physical theory of friction—the molecular kinetic, applicable to the polymer amorphous materials.

The deformation theories of friction that based on the interaction of the contact surfaces with respect to sliding, shear, cut, ousting of metal, formation of plastic wave, plowing, grasping, etc., are explained by I.V. Kragelsky, F.P. Bowden, B.I. Kostetsky, G.I. Epifanov, and many others.

I.V. Kragelsky in the form of molecular-mechanical theory developed the adhesion–deformation theory of friction. I.V. Kragelsky was first to put forward the model of the discrete contact of solid bodies at friction and the hypothesis of the dual nature of the friction contacts of solid bodies, which were further developed by his students N.B. Demkin, N.M. Mikhin, N.M. Dobychin, V.S. Kombalov, and Y.F. Nepomnyaschiy.

It should be noted that the two most well-known adhesion–deformation theories were almost simultaneously developed in the former USSR by I.V. Kragelsky and in Great Britain by F.P. Bowden and D. Tabor. I.V. Kragelsky gave a special attention to the deformation component, while F.P. Bowden gave a special attention to the adhesive component of the coefficient of friction.

The great influence on the tribological processes has the heat emission in the friction contact. The creation of calculation methods for assessing the heating due to friction is associated with such name as H. Block, D. Eger, R. Holm, M.V. Korovchinsky, A.V. Chichinadze, and others.

In the former USSR, A.V. Chichinadze and his students have created and developed new scientific branch of tribology: thermal dynamics of friction and wear of friction pairs with respect to dry friction and boundary lubrication. This new theory has created modern methods for calculation and modeling of the friction process, wear, and heat formation in the friction contact, by taking into account the relationship between the dynamic processes in machines with heat formation in the friction pairs.

Studies on one of the most dangerous types of wear—the abrasive, conducted by M.M. Khruschev, M.M. Tanenbaum, G.M. Sorokin, and others, allowed to link the process characteristics with the physical and mechanical properties of worn materials. Other types of wear have been studied by A.P. Semenov, S.B. Ratner, L.I. Pogodaev, S.P. Kozyrev, S.G. Chulkin, A.M. Gafarov, and others.

Thyssen and Rebinder, in their works, raised a special attention to the chemical and tribochemical processes occurring friction in the metal bodies. In the phenomenon of the selective transfer, discovered by I.V. Kragelsky D.N. Garkunov, it turned out that the important role belongs to the chemical and electrochemical

processes. Many studies are dedicated to the problems of the tribochemistry of friction contact.

The significant progress in tribology was made when the fatigue and the thermo-mechanical theory of wear were developed. The creation of these theories associated with the names of I.V. Kragelsky, E.F. Nepomnyaschiy, G.M. Kharacha, A.Kh. Janahmadov, and others. The basic concept of these theories is in necessity of the multiple impacts on the frictional surfaces in order to weck them, where the number of these impacts is quantitatively expressed and is dependent on the thermo-stressed condition of the frictional contact.

Even the electrical and electromagnetic phenomena in tribology have been known for while, however, no attempts were made to provide the theoretical explanation. So the electro-thermo-mechanical theory developed by A.Kh. Janahmadov and A.I. Volcheko is successfully developed and implemented by their students.

The substantial contribution into theory of lubrication was made by G.A. Khirn, N.A. Petrov, B. Tower, O. Reynolds, A.I. Zommerfeld, N.E. Zhukovsky, R. Stribeck, M. Ghersi, A.S. Ahmatov, M.V. Korobchinsky, R.M. Matveevsky, G.I. Fux, I.A. Buyanovsky, A.M. Ertel, A.I. Petrusevich, D. Dawson, S.D. Kodnir, A.N. Grudin, and others.

Refinement of the electro-hydro-dynamic lubrication theory and its distribution on the non-isothermal conditions of lubricant flow, the non-Newtonian behavior of lubricants, and the consideration of friction surface roughness can be found in the works of Yu.N. Drozdov, M.A. Galakhov, A.I. Petrusevich, D.S. Kondir, etc.

Since mid-1960s, the method of physical modeling of friction and wear is developed under the guidance of E.D. Brown and A.V. Chichinadze.

The theory and practice of modeling of friction and wear were considerably presented in the works of Yu.A. Evdokimov, A.Kh. Janahmadov, A.Yu. Albagachiev, Yu.Ya. Izakson, and others.

The problem of seizure (jamming) in various friction units is covered in the papers of B.I. Kostetsky, H. Block, A.P. Semenov, Yu.N. Drozdova, N.A. Boucher, N.M. Alekseev, S.M. Zakharov, H. Winter, D. Buckley, etc.

A major contribution into the field of the tribotechnical materials science, polymers, and into the development of effective methods of hardening surfaces of machine parts are made by the works V.A. Belov, D.N. Garkunov, I.A. Gribovoy, V.E. Panin, A.P. Semenov, W.V. Ignatev, V.Ya. Kerschenbaum, L.I. Kuksenov, I.M. Lyubarsky, V.I. Kolesnikov, A.D. Kuritsyn, E.D. Brown, N.A. Boucher, A.I. Sviridenek, etc.

The well-known scientists and engineer designers such as M.P. Aleksandrov, G.M. Shahmaliev, A.V. Chichinadze, V.I. Kolesnikov, Yu.N. Drozdov, A.Kh. Janahmedov, S.S. Kokonin, Yu.A. Evdokimov, A.I. Volchenko, M.M. Borodulin, V.G. Inozemtsev, and others were working on problems of optimizing the design of the frictional brakes and clutches, creating new composite materials for frictional units that provide high friction.

N.K. Myshkin, L.V. Markov, O.K. Kvoun, N. Kona, and others with their original researches made enormous contribution in the field of tribodiagnostics and monitoring.

The development of nanotechnology and the emergence of a new class of devices with micro- and nanoelectromechanical systems made it necessary to control tribological processes in micro- and nanoscales. This technique along with a computer modeling and with the solutions to a number of specific nanotribology problems provided a major breakthrough in friction, lubrication, and wear. The rapid growth in the number of scientific publications indicates the exceptional interest to the problems of nanotribology.

As mentioned above, tribology has the status of the interdisciplinary field of knowledge by virtue of their specific relationships with other disciplines. The behavior of friction materials and their wear–friction properties are largely driven by a complex of physical, mechanical, electro-thermo-mechanical and physical–chemical processes in the surface and near-surface layers of the frictional units. This complex approach, on the one hand, makes professionals to analyze the physical foundations of their science and formulate the problem at the junction of the molecular and stochastic physics, and on the other hand, they scrutinize the fundamental problems of tribology, such as the relationship between adhesion and deformation mechanisms of friction. We consider the discussing trends as the main factors with various roles in the friction processes. Figure 1.3 provides the overview of the contact interaction at friction, and it also shows a diagram of mutually interacting various factors, depending on the current scale (macro, micro, nano) of reviewing process.

If we analyze the known types of wear, it can be concluded that they are all related with the components of the friction force. Thus, the fatigue wear manifests itself mainly as the material deformation in friction, while the surface forces cause the adhesive wear during the material destruction and its transfer between the friction bodies. Furthermore, friction always occurs in a specific environment, which affects the contacting pair through chemical reactions. These reactions change the rate of the material deformation and also affect on the intensity of the surface interactions.

In recent years, the publications on nanotribology contain significant information not only about nanobiomechanics of joints, but also about the results of the specific studies on the joint lubrication and the role of the synovial fluid and articular cartilage in its existence.

The joints of the human body as a part of biological friction system can carry out various kinds of motion (sliding, rotation, angular, and circular motions).

At present, there are liquid crystal formations of various fluids and tissues of living beings and the fundamental role that state plays in the biointerface. With regard to the role of the liquid crystalline state in the biological tribosystems, it is not confined to the data that we do have at the moment. Further studies on the role of the lyotropic lisomorphism not only provides new theoretical understanding of liquid crystals, but also helps to explain many physiological processes in nano-bio-tribological systems.

(a)

Range	Scale	Models	Characteristics and components

I 10^{-3} Macro

II 10^{-6} Micro

III 10^{-9} Nano

- Models of tribological systems with subsystems of tribokinetic processes and phenomena at various hierarchial levels
- Mechanical, physical and chemical properties of friction pair materials
- Topology of surface and contact-impulse interaction of friction pairs in vrious environments
- Compliance of structural elements of friction components and their joints
- Stress-strain state of contacting surfaces and their bodies at interaction of friction pairs
- Electro-thermo-stimulated polarization and depolarization of contacting surfaces of friction pairs
- Formation of microcapacitors in interacting microprotrusions, connected through various circuits and attached to cylinrical macrocapacitor
- Electrical field induced by currents arising due to: electrification of sliding and contacting; motion of charged particles of friction masstransfer; thermal conditions; sorption-desorption processes in near-surface contact layers; reverse charge

(b)

Range	Scale	Models	Characteristics and components	Frictional model

I 10^{-3} Macro

II 10^{-6} Micro

III 10^{-9} Nano

- Operation of micro-thermo-electric batteries in the regimes of: micro-thermo-electric generators; refrigerators
- Formation of contour chains of micro-thermo-batteries of types: RC; RCL
- Magnetic field caused by electric currents accompanying friction process
- Thermal field, temperatures, temperature gradients in closed and open states of friction pairs
- Wear-friction properties of friction pairs at their interaction
- Tribophysics and tribochemistry of surface and near-surface layers of friction pairs at their interaction
- Unified field of interaction of surface and near-surface layers of friction pairs

deformation

adhesion

Fig. 1.3 The general diagram of the contact interaction at friction

The knowledge gained in this direction will undoubtedly contribute to the creation of new methods of treatment and prevention of pathological conditions of human being.

In recent years, the tribological system is considered as a self-organizing system with provisions of non-equilibrium thermodynamics, synergetics, fractals, and multifractals. Kinetics of fatigue cracks and formation of contact in details, similarity and self-similarity of self-organizing processes, fractal geometry of fatigue cracks formation, and many others were studied from this perspective.

It should be noted that the findings of non-equilibrium thermodynamics do not contradict to the classical thermodynamics, since the reduction of entropy only refers to the local system, being offset by the increase in entropy of the external media, which is in interaction with that system. Bifurcation, i.e., split, is normal for non-equilibrium systems.

The authors believe that synergetics and fractals in tribology will have a great influence on the development of fracture mechanics and, in particular, on tribo-materials science. Generalizing the accumulated large number of theoretical and experimental materials at a new level will contribute to the development of new technologies that will allow managing the structure of materials and obtaining set of pre-defined properties. The authors hope that this project will help attracting researchers to study new laws of the tribological processes at elastic, elastic–plastic, plastic deformations, and fracture (wear) of materials using synergetic approaches and fractals.

1.2   Performance Analysis of Oil Field Equipment in Terms of Mechanical–Chemical Defectiveness

The distinctive feature of the equipment operating in the hostile environment, leading to its malfunction, is the intensity of damages caused by the combined action of the mechanical failures and the corrosive medium. The mechanical–chemical damage of material (MCDM) has an impact on the equipment performance and that is due to specifics of kinetics of the chemical reactions taking place on the surfaces of the strained structural elements. This problem becomes more exacerbated with increase in the level of the material strain and the corrosive activity, and it is among of the less studied, complex, and topical problems.

The majorities of oil and gas machinery are made of the metal and are weight loaded, and they also have a constant surface contact with the operating medium. Examples of such kind of equipment are the downhole equipment, columns, apparatus, and pipelines. Based on their middle surface geometry and stress state, they belong to the general group of the hull-type equipment.

The monograph provides the analysis of methods for assessing the performance of these types of equipment, taking into account the kinetics of MCDM, while the efficiency of equipment is interpreted as the combination of material components and the structural elements, ensuring the ability to perform specific functions under the simultaneous influence of external loads and corrosively active medium.

1.2.1 Assessment of the Level of Corrosive Mechanical Fracture in Equipment

The operational damage is conventionally divided into three groups [1]: the initiation of shallow cracks; the formation of cracks through unsealing; and the brittle fracturing. The stress concentrators in the material and the non-stationary loading usually initiate the first two groups of damages. The brittle fracturing usually forms under the high strain constraint, the availability of the triple-axis residual stresses, and low temperatures that are favorable to the material brittleness. The damages caused by the corrosive media and the non-stationary loading are usually associated with the corrosion mechanics fatigue.

The corrosion mechanics fatigue (CMF) is a major cause of failures (40 %) in oil and gas equipment. The vast majority of the oil pipeline destructions are associated with corrosion. The level of exposure to the aggressive media increases for pipelines and equipment when the oil gathering and processing in refineries go under the high temperatures. That is when corrosion becomes more active. The destruction of the oil field equipment is associated [2] with the CMF phenomena, which is part of the oil tribology studying.

The stress corrosion cracking (SCC) is particularly a dangerous type of the corrosion mechanics fatigue (CMF); it is realized in the solutions of hydrogen sulfide, acids, ammonia, chlorides, as well as hydrogen gas and other media [3–5]. The stress corrosion cracking is characterized by the absence of the significant macro-plastic strains in fractures, which indicates the high-speed (avalanche) nature of destruction.

SCC is formed under both the static and cyclic loading. It should be noted that cracking is possible even in the absence of mechanical stresses—the intercrystalline corrosion of some stainless steels and alloys [6–8]. Naturally, the intercrystalline corrosion increases with the external loading.

Depending on the mechanism of the stress corrosion cracking, it should be distinguished [9] between those caused by the brittleness (adsorption or hydrogen) and those caused by the mechanical–chemical dissolution. Such a division has somewhat an arbitrary character, since most of the stress corrosion cracking happens due to the simultaneous action of both mechanisms (brittleness and dissolution). Nevertheless, it becomes useful in the development of computational methods for assessing the effects of the stress corrosion cracking.

The corrosive destruction should be considered in conjunction with kinetics of the general corrosion, resulting in an increase of the nominal stress and a danger of the stress corrosion cracking.

The phenomenon of strengthening of the metal corrosion under the influence of mechanical stresses is called [9] the mechanical–chemical effect (MCE). MCE is most strongly manifested itself in the dynamic plastic flow, which is observed in the metal with overstrain at the cyclic–static loading.

The main provisions of the mechanical and chemical theory of metals are given in [10]. The local chemical potential at the point of the crystal structure is

determined by the spherical tensor σ_a, wherein the amount of the chemical potential of atoms of the deformed metal does not depends on the sign of applied stresses. It is proven [10] that the anode current of dissolution exponentially increases with the growth of the absolute hydrostatic pressure Δp in the solid phase

$$I = i_a \cdot \exp\frac{\Delta p \gamma}{RT} - i_k, \qquad (1.1)$$

where i_a—the anode current of undeformed metal; i_k—the cathode current; γ—the molar volume of metal; and R and T—the universal gas constant and the absolute temperature. Moreover, the cathode current does not depend on the degree of the metal stress.

The impact of stress on the metal corrosion penetration in the laboratory and real operating conditions is reflected in Fig. 1.4.
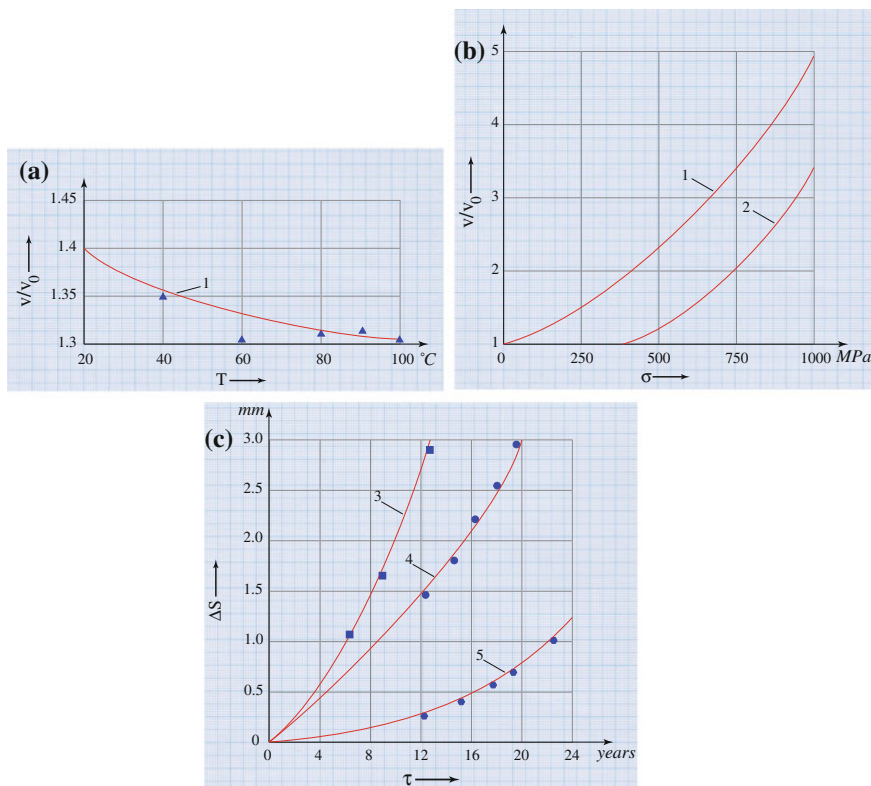
Fig. 1.4 The impact of stress on the corrosion penetration of metal specimens and oil tanks: *1* the steel "D" in the carbon dioxide; *2* the cable steel in 3 % NaCl; *3* the oil tank; *4* the petrol tank; *5* the diesel tank. v_0 and v_a—the rate of corrosion in strained and unstrained metal; ΔS—the change in the wall thickness

On the basis of formula (1.1), the stress and durability analysis of structural elements under uniaxial state are performed in work [10]. It is shown that the durability of the elastically strained structural elements essentially depends on the initial strength properties of metal, the coefficient of efficiency of loading capacity, and others.

The analyses of kinetic stresses and durability for the various hull-type constructions, operating under the strain and changeable loads, are given in work [11]. The results of those analyses are set as the basis for the strength calculation of various structural elements of equipment operating in corrosion [12].

MCE intensifies during the plastic deformation as result of the initiation and annihilation of dislocations. The greater the degree of the plastic deformation ε, the higher the density of mobile dislocations N, wherein

$$N = \bar{a} \cdot (\Delta\varepsilon)^m, \tag{1.2}$$

where $a = 10^9 \ldots 10^{11}$ disl/cm^3, $m = 1 \pm 0.5$.

The chemical potential of the metal atoms μ_M is determined by the excessive enthalpy due to dislocations. The difference between the chemical potential of the metal atoms and the various densities of dislocations (N_0 and N) makes

$$\Delta\mu_M = RT \ln \frac{N}{N_0} - \Delta pT. \tag{1.3}$$

Therefore, the hardening is equivalent to the additional excess pressure Δp at the plastic deformation:

$$A\tau = \Delta pR \frac{R}{\bar{a}R'v}, \tag{1.4}$$

where $R' = kN_{max}$; k—the Boltzmann constant; and N_{max}—the maximum possible number of dislocations per unit of volume. The factor $R/\bar{a}R'v$—a constant value for material (for iron it is close to one).

Equation (1.4) shows the uniform distribution of dislocations per unit of volume. Actually, the dislocations form the flat clusters from n' coplanar dislocations trapped in the areas of the planar aggregation which results in an increase of the resistance to the plastic flow. The hardening during the plastic deformation makes the excess pressure n' times higher. Therefore, the increase of the chemical potential of dislocations is equivalent to the increase of stress n' times during the formation of the coplanar clusters.

Kinetics of the mechanical activation of the corrosion process at the plastic deformation is descried by the equation [10]:

$$I = i_a \cdot \exp \frac{n'\Delta\tau}{\bar{a}RT} - i_k. \tag{1.5}$$

In the mode of the dynamic plastic flow, the deformation increment of the dissolution current is linearly dependent on the rate of deformation [10]:

$$\Delta i_a = i_a \left(\frac{\dot{\varepsilon}}{\dot{\varepsilon}_0} - 1 \right). \tag{1.6}$$

where $\dot{\varepsilon}$—the rate of deformation at static loading.

Given the kinetic equations of the mechanical–chemical dissolution (MCD) of metals form the basis of methods that determines the strength and the durability of the structural elements of the oil field equipment and pipelines with the different structural and technological stress concentrators at the different modes of the static and cyclic loading.

Thus, under the simultaneous influence of the external loads and corrosive environments, the metal structural elements, as a result of MCD, undergo a most intensive stress corrosion cracking. The MCD degree exponentially depends on the spherical tensor and proportionally depends on the growth rate of the plastic deformation.

1.2.2   Mathematical Modeling of Mechanical–Chemical Defectiveness and Calculations on Durability

Phenomenologically, the destruction is interpreted as the kinetic process of the gradual damage accumulation. The dimensionless parameter Π is introduced as the measure of damage being equal to zero at the initial stage and one at the limit [13, 14].

The complexity of the corrosive mechanical destruction is explained by the variety of the operating environments with specific properties, as well as the damage mechanisms in relation to the particular material.

Based on the provisions of the mechanics-chemistry of metal [10], as well as the results on the mechanical activation of the corrosion processes, the mathematical model of the mechanical chemical damage of material (MCDM) can be represented through the components of the deformation tensor in the form [9]:

$$\frac{d\Pi}{dt} = V = \frac{d\Pi_0}{dt} (K_{CT} \cdot \varepsilon_i - 1) \cdot \left(\frac{\dot{\varepsilon}_i}{\dot{\varepsilon}_{i_0}} \right)^{K_g} \exp[K_H \psi_\sigma \varepsilon_i(\sigma_i)], \tag{1.7}$$

where $\dot{\varepsilon}_i = {d\varepsilon_i}/{dt}$—the rate of plastic deformation intensity ε_i; $\dot{\varepsilon}_{i_0}$—the rate of plastic deformation intensity at the short-term static stretching; σ_i—the stress intensity; $\psi_\sigma = {\sigma_a}/{\sigma_i}$, σ_a—the spherical tensor; Π_0—the measurement of damage of the unstressed material; and K_{CT}, K_g, and K_H—constants, which depend on the parameters and properties of material and environment.

At the stage of the deformation (parabolic) hardening of material, as it is shown in [9], the MCDM rate increases proportionally along with the preliminary plastic deformation intensity. The coefficient K_{CT} in Eq. (1.7) represents a tangent to the experimental curve $\mathrm{d}\Pi/\mathrm{d}t = f(\varepsilon_i)$, and it characterizes the sensitivity of the pre-deformed material to mechanical and chemical damages. The coefficient K_g, according to E.M. Gutman, J. Bockris, etc., can be equal to one for the carbon steel. The experimental studies of mechanical and chemical deformations of carbon and low-alloy steels at the elastic deformation show that values of K_H for the purpose of engineering calculations can be determined from Gutman's formula

$$K_H = \frac{V}{RT},$$

where V—the metal molar volume; R—the universal gas constant.

The special MCDM estimates are followed from Eq. (1.7) for the elastic and the elastic–plastic deformations [10, 11], as well as for the dynamic deformation [13, 14].

Integrating the expression (1.7), and taking into account the equation of mechanics for the deformed solid body and strength, it yields the function for the measurement of damage $\Pi = \varphi(t, \ldots)$, for which at $\Pi = 1.0$ the time is set before the occurrence of one or another critical (durability) state of the constructional element. The von Mises yield criterion is accepted as the critical condition of the elastic deformation. The maximum durability is determined using the criteria of mechanics of fracture. In general, the range of variables of the function $\varphi(t, \ldots)$ includes the tensor components such as stress T_σ, deformation T_ε, speed $\dot{T}_\varepsilon$, temperature T, and others.

The obtained model of the mechanical–chemical damage of material allows us to analyze the kinetics of stress changes and the destruction rate of elements at all stages of loading, including failure, and analyze the various temperature–time impact conditions of corrosively active environments.

1.3   Performance Analysis of Oil Field Equipment in Terms of Non-stationary Loading

One of the main tasks of the modern machine building is to increase the longevity of machine elements and aggregate while improving the strength and reducing the metal consumption.

What matters most is the correct assessment of the ultimate stresses based on the viscous, brittle, low-cycle, and high-cycle fatigue failures at stages of the crack formation and development.

The strength calculations at low-cycle loading are carried out on the basis of the low-cycle failure curves in the strains (or the conditional elastic stresses) taking into account the mechanical properties of the employed construction materials (strength,

ductility, the degree of hardening in the inelastic region with the single and non-stationary loading), as well as the cycle asymmetries on stresses and deformations.

Let us analyze the efficiency of oil field equipment under non-stationary loading and study the mechanisms of the accumulation of damages in the materials of machine parts.

The non-stationary loading leads to the accumulation of damages in metal and then to fatigue failure. The low-cycle fatigue is more relevant to the oil field equipment [1–12, 15] and is also accelerated in the corrosive environments [16].

The majority of the proposed low-cycle fatigue equations relate the number of cycles before failure N with the amplitude of plastic deformations ε_{pl} and ultimate strain ε_u. These are the equations

$$\text{Orowan}: N \cdot \varepsilon_{pl} = \text{const}; \tag{1.8}$$

$$\text{Coffin} - \text{Manson}: N^{m_c} \cdot \varepsilon_u = C_c \tag{1.9}$$

where mc and C_c—constants. The constant C_c is associated with the ultimate ductility of metal: $C_c = 0.5\varepsilon_u = 0.5 \ln\frac{1}{1-\psi}$, where ψ—the relative necking at the breakage of specimen.

Langer and Gross [17] proposed to place into Eq. (1.9) the total strain amplitude $\varepsilon_a = \varepsilon_{pl} + \varepsilon_e$, where ε_e—the amplitude of elastic deformation. In this case, the equation of durability takes the form

$$\varepsilon_a = 0.25 \sqrt[-m_c]{N}\varepsilon_u + \frac{\sigma_{-1}}{E}, \tag{1.10}$$

where σ_{-1}—the ultimate fatigue; E—Young's modulus.

Sometimes, this equation is represented in the conditional stresses:

$$\sigma_a^* = \varepsilon_a \cdot E = 0.25 \cdot E \sqrt[-m_c]{N}\varepsilon_u + \sigma_{-1}, \tag{1.11}$$

The exponent m_c in these equations depends on the mechanical characteristics of metal. The steels with high m_c are characterized by the low ratio of the ultimate strength to the yield strength. The parameter m_c is correlated with the coefficient of hardening m. At $m < 0.15$, $m_c = 0.2$; at $m > 0.15$, $m_c = 0.2 + 2.4(m - 0.125)$ [18].

Manson suggested a more general equation of the low-cycle fatigue at the amplitudes of the full deformations based on the deformation and the force criteria:

$$\varepsilon_a = SN^{-s} + TN^t, \tag{1.12}$$

where S, s, T, and t—the material constants, and for many materials, $s = 0.12$; $S = \frac{3.5\sigma_t}{E}$; $t = 0.6$; $T = \ln\frac{1}{1-\psi}$.

Obviously, the differences in the strength properties of metals lead to the fact that in Eqs. (1.10)–(1.12), the durability curves for various steels must intersect at the

certain amplitude of strain ($\varepsilon_a \approx 0.75\ \%$) and durability ($N = 10,000\ldots15,000$). This allows, on the one hand, the simplification in construction of the fatigue curves and, on the other hand, the assessment in application of steels with the various mechanical properties. Naturally, the steels with the high strength properties and the lower plastic properties lose their advantage when are employed in the areas with the high amplitudes of strain (at the high levels of stress concentrations).

Coffin–Manson equation reflects the kinetics of the damage accumulation in the metal at the hard symmetric (alternating) loading. In terms of the soft symmetric (alternating) loading, the kinetic equation for damage is similar in its form to the equation of hard loading:

$$\varepsilon_a = mN^{-m_1} + \frac{\sigma_{-1}}{E}, \tag{1.13}$$

where $m = \ln\frac{1}{1-\psi_t}$ —the strain coefficient of hardening; ψ_t—the uniform component of total relative narrowing of specimen at breakage.

The exponent m_1 depends on the ratio of the yield strength to the ultimate strength K_m, for the symmetric loading $m_1 = 1.2K_m - 0.35$ [19]. Sometimes, at the soft loading, the fatigue curve is presented as the power function [19]

$$\sigma N^\gamma = \sigma_t N_t^\gamma, \tag{1.14}$$

where $N_t = 10$—the number of cycles before failure at ultimate strength; γ—the material constant ($\gamma \approx 0.08$).

The equations like Coffin–Manson reflect the kinetics of fatigue failure under the uniaxial stress. The walls of hull-type equipment and pipelines are subjected more to the planar stress rather than the volumetric stress. And the ratio of the main stresses $m_\sigma \left(m_\sigma = \sigma_z / \sigma_\theta\right)$ varies over the wide range of values: $0 < m_\sigma < 1$.

The durability especially depends on the stress diagram at the low-cycle fatigue failure. Under the pressure, the durability decreases by up to 30 % during the transition from the uniaxial stress to the biaxial stress [20].

The paper [21] shows the substantial differences of the metal fatigue curves under the uniaxial stress and torsion. The low-cycle durability at the alternating torsion, expressed through the amplitude of the equivalent plastic deformation, is several times (more than two) greater than one occurring at the uniaxial stress. The difference of the metal cycling failure at the different types of the cyclic deformation is due to the fact that the ultimate plasticity depends on the voluminosity (stiffness) of the stressed state, characterized by the ratio of the spherical tensor to the strain deviator.

This factor can be included if the method developed by V.L. Kolmogorov is applied [22]. It postulates that the metal failure occurs if the shear deformation λ exceeds some ultimate value λ_p: $\psi = \lambda / \lambda_p \geq 1.0$, where ψ is interpreted as the usage of reserved plasticity. The shear deformation is different from the deformation intensity ε_i by the constant factor $\sqrt{3}\left(T = \sqrt{3}\varepsilon_i\right)$. The parameter λ depends on the

temperature–velocity factors as well as the rigidity stress factor ψ_σ estimated by the ratio of spherical tensor to deviator. In case of the pure shear, $\psi_\sigma = 0$, and at the axial tension, $\psi_\sigma = 1/3$. The maximum value $\psi_\sigma \left(\psi_\sigma = 2/3 \right)$ takes place at the biaxial tension with the equal stress components $m_\sigma = 1.0$.

The impact of the rigidity stress factor ψ_σ on the index of plasticity is estimated by the following formula [9]

$$\varepsilon_{i_u} = k_\varepsilon \cdot \varepsilon_u^{(0)}, \tag{1.15}$$

where k_ε—the coefficient which depends on the parameter ψ_σ; $\varepsilon_u^{(0)}$—the ultimate plasticity at the uniaxial tension.

The experiments show [23] that the value k_ε exponentially depends on the parameter ψ_σ

$$k_\varepsilon = \exp C_\varepsilon \left(\psi_\sigma - \frac{1}{3} \right), \tag{1.16}$$

where C_ε—the constant.

Thus, the ultimate plasticity of metal exponentially decreases with an increase of the rigidity stress factor. The assessment of the fatigue curve should be done taking into account the stress diagram by substituting the value ε_u in the fatigue equation (1.10) with the ultimate plasticity ε_{i_u}, found in the formula (1.9).

Some environments cause much stronger changes in the plasticity properties of metals. Figure 1.5 shows the results of the mechanical experiments on specimens from the low-carbon (20ЮЧ) and the low-alloy (16ГС) steels after exposing them to the saturated solution of hydrogen sulfide.
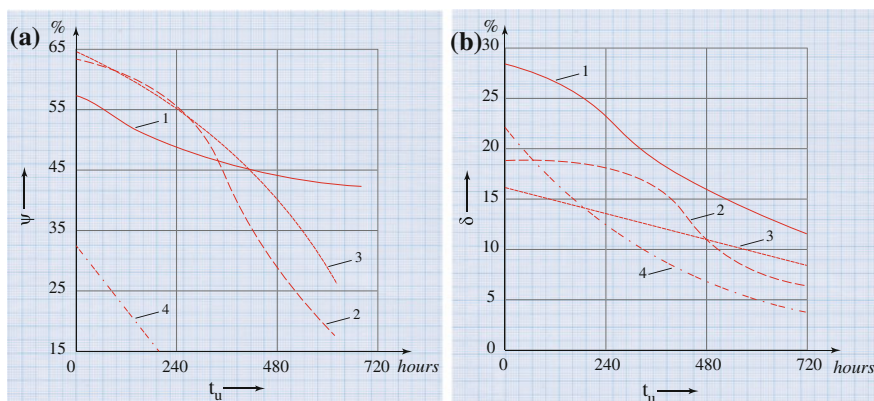
Fig. 1.5 Reduction in metal plasticity after exposure to a saturated solution of hydrogen sulfide: 1 20ЮЧ thermal; 2 16ГС hardening; 3 20ЮЧ annealing; 4 ГС

There are significant decreases in the mechanical properties of specimens after soaking them in corrosive medium, especially in the elongation δ and necking ψ. The data in Fig. 1.5 suggest that in assessing the ultimate plasticity of metal, besides the stressed state, it is also necessary to consider the impact of medium on brittleness.

The influence of medium on the metal plasticity is estimated [9] by a coefficient $k_{kc}\left(k_{kc} = \psi_{kc}/\psi\right)$, where ψ_{kc}—the specimen necking in the corrosive medium.

Then,

$$\varepsilon_{i_u} = k_{kc} \cdot k_\varepsilon \cdot \varepsilon_{i_u}^{(0)}. \tag{1.17}$$

Substituting the value of ε_{i_u} in the formula (1.15) into the equation of fatigue (1.10), we obtain

$$\varepsilon_a = 0.25 \sqrt[-m_c]{N} \cdot k_{kc} \cdot k_\varepsilon \cdot \varepsilon_{i_u}^{(0)} + \frac{\sigma_{-1}}{E}. \tag{1.18}$$

In the corrosive medium, at the short-term tension just before failure (e.g., sodium chloride), many grades of steel do not change their mechanical properties, although the low-cycle fatigue curves pass much lower than values tested in air. This demonstrates that when tested in the corrosive medium, the exponent of power m_c in Eq. (1.10) must be much greater than when tested in air (for most of low-carbon and low-alloy steels $m_c = 0.5$). After the long maintenance in the produced water, the mechanically tested pipe steels showed the basic mechanical properties not lower than the original ones. This suggests that corrosive embrittlement does not take place in such mediums.

Hence, the drop in durability for such corrosive mediums should be attributed to the kinetics of corrosive dissolution of metal. Besides, if as the low-cycle durability criteria we accept the number of cycles before the cracks initiation, then the fatigue curves in mediums, that do not cause the metal embrittlement, should not be much different than those in air. The impact of medium on durability becomes much noticeable at the stage of the cracks spreading [16].

Thus, the low-cycle durability in such corrosive mediums can be estimated on the basis of formula (1.10) by substituting the m_c values in it with the value m_{cc} obtained through the cyclic tests in the corrosive medium. However, the diversity of corrosive mediums and the variability of steels make it almost impossible to find the experimental values of m_{cc}.

In the presence of data on the steel resistance to the low-cycle fatigue, it is advisable to build the low-cycle durability curves according to the following technique [9].

For the given grade of steel, the boundary of endurance limit σ_{-1} is set at $N_0\left(N_0 = 10^6\right)$, for example, based on the concept of the coefficient of effective stress concentration k_e:

$$k_e = \frac{\sigma_{-1}}{\sigma_{-1}^{(g)}} = 1 - q(\alpha_\sigma - 1),$$

where σ_{-1} and $\sigma_{-1}^{(g)}$—the fatigue strength of smooth specimen and specimen with concentrator; g—the metal sensitivity to concentrators.

The cyclic failure depends not only on the theoretical stress concentration α_σ, but also on the stress gradient $\bar{G}\left(\bar{G} = G/\sigma_{max}\right)$, where $G = dy/dx$—the gradient of the first main stress in the dangerous section of the viewed specimen; σ_{max}—the maximum value of that stress. Parameters k_e, G, and α_σ are related by the relationship [24, 25]:

$$k_e = \frac{\alpha_\sigma}{1 + \sqrt{G} \cdot 10^{-(0.33 + \sigma_T/712)}}. \tag{1.19}$$

Next, the assessment of the impact of the corrosive medium on the fatigue strength: $\sigma_{-1k} = k_{\sigma_{-1}} \cdot \sigma_{-1}$, $k_{\sigma_{-1}}$—the level of reduction in the fatigue strength as result of the impact of medium $\left(k_{\sigma_{-1}} = \sigma_{-1k}/\sigma_{-1}\right)$. The number of cycles before failure at the ultimate stress level N_t may be equal to 10 [24]. Parameters σ_{-1k}, N_0 and σ_t, N_t are the reference points for the construction of the durability line in logarithmic coordinates $(\log\sigma, \log N)$ (Fig. 1.6a).

Here, the equation of the fatigue curve is defined by formula (1.14). It shall be noted that sometimes the value of N_t is significantly different from 10 (Fig. 1.6b). The stress values corresponding to the intersection point on the durability curves (σ_c) for the low-carbon and low-alloy steels are approximately 80 % of the ultimate strength σ_u of metal. There are the durability curves possibly different from the described ones (Fig. 1.6c, d).

Table 1.1 shows the properties of the fatigue curves for the low-carbon, low-alloy, and stainless steels in the chloride solutions that are specific to the oil field equipment.

The fatigue curves for carbon steels and the produced water are compared on Fig. 1.6e.

As it is already known, the phenomenological fracture is divided into three stages [9]: the cracks initiation; the distribution of major cracks; and fracture (spontaneous distribution). The last two stages are evaluated by the methods of fracture mechanics. Briefly concentrate on the assessment methods of the construction elements durability (longevity) based on the distribution of major cracks.

Subjected to the conditions of self-similarity, the range of stress intensity factor (SIF) K_1 controls the crack distribution process: $dl/dN = V_{cl} = f(\Delta K_1)$, where l—the length (depth) of crack. When the function $f(\Delta K_1)$ is known, then the integration of this function allows determining the durability of construction element N_d. The middle section of the fracture strength diagram is approximated by the Paris–Erdogan exponential function
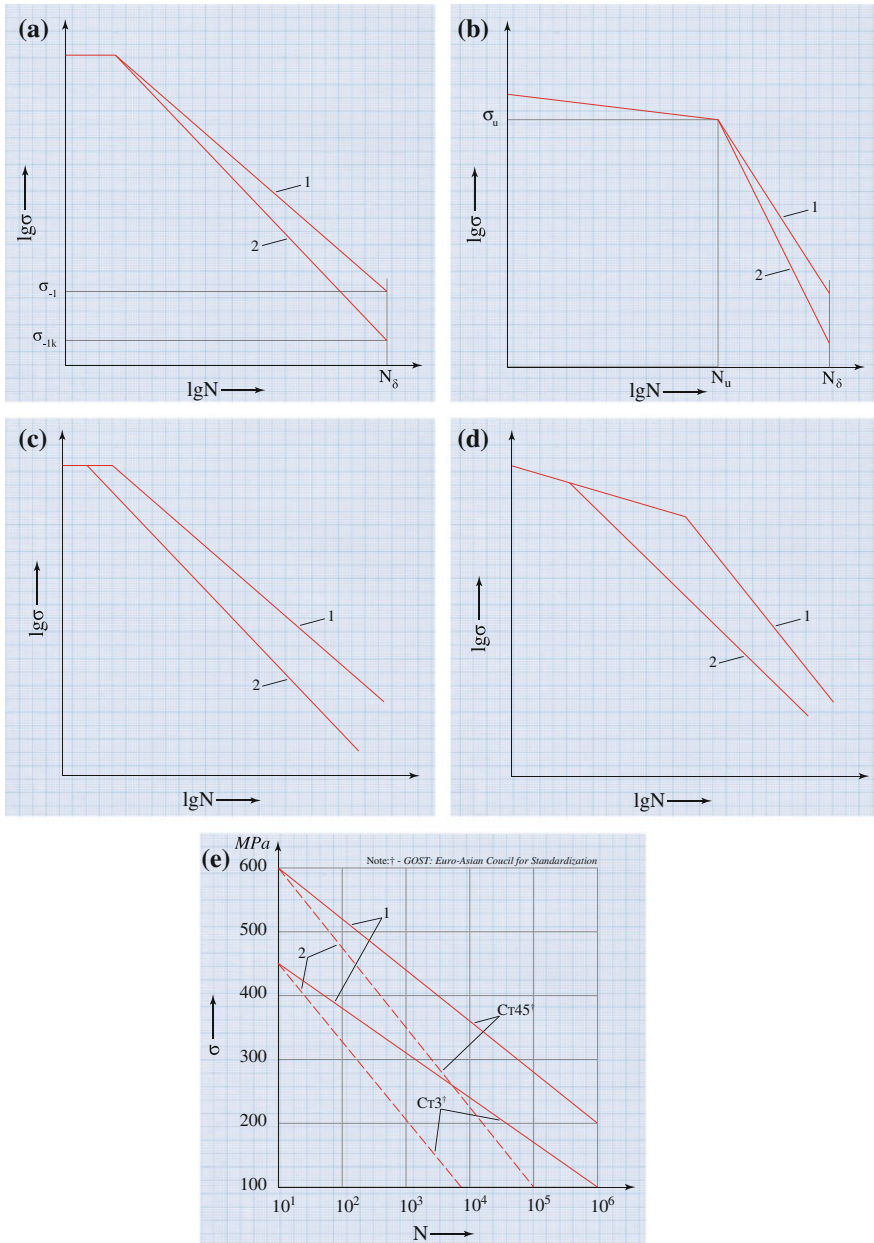
Fig. 1.6 The stress corrosion fracture curves: *1* in the air; *2* in the corrosive medium

Table 1.1 The properties of the low-cycle corrosion fatigue for the carbon, low-alloy, and stainless steels

Steel	σ_t, MPa	σ_{-1}, MPa	$\frac{\sigma_{-1}}{\sigma_t}$	σ_{-1k}		$k_{\sigma_{-1}}$		γ	$\gamma^{(k)}$	
				Prod. water	3 % NaCl	Prod. water	3 % NaCl		Prod. water	3 % NaCl
10	340	180	0.53	115	–	0.65	0.28	0.055	0.095	–
20	420	190	0.45	115	50	0.60	–	0.07	0.11	0.185
Ст.3	450	200	0.44	112	48	0.56	0.24	0.07	0.12	0.194
Ст.35	580	275	0.47	–	70	–	–	0.065	–	0.183
Ст.45	590	240	0.40	165	–	0.68	–	0.078	0.11	–
16ГС	504	196	0.39	137	69	0.70	0.35	–	–	–
17ГС	550	209	0.38	149	–	0.71	–	–	–	–
17Г1С	560	218	0.39	160	81	0.73	0.37	–	–	–
09Г2С	500	200	0.40	138	–	0.69	–	–	–	–
15 × 5 M	540	200	0.37	162	–	0.81	–	–	–	–
12 × 18H10T	660	265	0.40	150	130	0.57	0.50	0.08	0.13	–

$$V_{cl} = C_\sigma \cdot \Delta K_1^{n_\sigma}, \tag{1.20}$$

where C_σ and n_σ—the material constants.

At the range of crack growth with the low rates $V_c < 10^{-8}$ m/cycles, the durability curve cuts a section with the length K_{th}, also called the SIF threshold. When $K_{max} < K'_{th}$ the crack does not develop during the test. At the range of the crack growth with the high rates $V_c > 10^{-8}$ m/cycles, the durability curve asymptotically approaches the line $K_{max} = K_{fc}$. The fracture of the construction element begins at $K_{max} > K_{fc}$. The critical values of SSC K_c and K_{fc} are ambiguous, but for the tentative calculations, we take $K_c \approx K_{fc}$. The value of K_{th} is of the great practical importance, since it allows setting the safety properties for the cyclic loading and the crack dimensions. The parameter K_{th} depends on the initial mechanical properties of material, medium, and others. At the zero cycle (pulsed) of loading, the value of K_{th} is linked to the yield stress σ_{-1} through the following empirical relationship [25]:

$$K_{th} = 12.7 - 0.006 \cdot \sigma_T, \tag{1.21}$$

where σ_T is measured in *MPa*. The diagram parameters C_σ and n_σ are linked with the specific work of failure W_c [26]:

$$C_\sigma = 0.000103 \cdot 861; \quad n_\sigma = (5.065 \pm 0.1168) - (0.00168 \pm 0.0001)W_c, \tag{1.22}$$

where W_c is measured in MJ/m³. The specific work of failure W_c is defined from the stress–strain diagrams of the smooth specimens, in particular by formula [26]:

$$W_c = (\sigma_T - S_k) \cdot \ln \frac{1}{1 - \psi}, \tag{1.23}$$

where S_k—the true fracture strength; ψ—the relative necking. According to M.P. Markov:

$$S_k = \sigma_t(1 + 1.4\psi). \tag{1.24}$$

For the elastic–plastic models, the middle section of the cyclic fracture strength diagram is described by N.A. Makhmutov's equation:

$$V_c = C_\sigma \cdot \Delta K_{1\varepsilon}^{n_\sigma}, \tag{1.25}$$

where $K_{1\varepsilon}$—the elastic–plastic stress intensity factor; constants C_σ and n_σ are equal to in (1.25):

$$C_\sigma = (2\pi\bar{\varepsilon}_{i_u})^{-1}, n_\sigma = 2.0, \tag{1.26}$$

where $\bar{\varepsilon}_{i_u} = \ln {}^1\!/_{1-\psi} \cdot \varepsilon_T^{-1}$; ε_T—the yield strain.

The definition of parameters of the cyclic fracture strength diagram in the corrosive active mediums is performed under special conditions, particularly at the constant value pH of medium during the specimen testing [27]. Sometimes, the cyclic fracture strength diagrams are built in V_c and J—interval coordinates [28].

The mechanism of the damage accumulation in the material of oil field equipment is studied and their influence on performance of that equipment at the non-stationary loading is analyzed.

Literatures

1. G.P. Karzov, V.P. Leonov, B.T. Timofeev, *Svarnye sosudy vysogo davleniia* (Leningrad, Mashinostroenie, 1982), p. 287
2. A.Kh Janahmadov, *Neftianaia tribologiia* (Baku, Elm, 2003), p. 326
3. P. Bastien, H. Veron, C. Roques, Special steels resistant to stress corrosion by hydrogen sulfide. Revue de Metallurgies Memoires, **55**, 310–312 (1958)
4. M.Y. Bartz, C.E. Ruwlins, Effects of hydrogen generated by corrosion of steel. NACE, Urrual Meeting Corrosion, №5, April, 187–206 (1948)
5. A.V. Shreider, Zashchita metallov ot korrozii v neftepererabatyvaiushchei i neftekhimicheskoi promyshlennosti. Bor'ba s korroziei neftekhimicheskogo oborudovaniia. (CNIITEneftemash, Moscow, 1969), pp. 3–12
6. V.A. Vinokurov, Svarochnye deformatsii i naprjazheniia. Metody ikh ustraneniia. (Mashinostroenie, Moscow, 1968), p. 236
7. V.V. Gerasimov, V.V. Gerasimova, *Korrozionnoe rastreskivanie austenitnykh nerzhaveyushchikh staley* (Moscow, Metallurgiya, 1976), p. 176

 8. V.S. Girenko, V.P. Diadin, Zavisimosti mezhdu udarnoi viazkost'iu i kriteriiami mekhaniki razrusheniia konstruktsionnykh staley i ikh svarnykh soedinenii. Avtomaticheskaia svarka **9**, 13–20 (1985)
 9. R.S. Zajnullin, Obespechenie rabotosposobnosti oborudovaniia v usloviiah mekhanokhimicheskoi povrezhdaemosti (Ufa, 1997), p. 426
10. E.M. Gutman, *Mekhanokhimiia metallov i zashchita ot korrozii* (Moscow, Metallurgiia, 1981), p. 271
11. E.M. Gutman, R.S. Zainullin, A.T. Shatalov, R.A. Zaripov, *Prochnost' gazo-promyslovykh trub v usloviiakh korrozionnogo iznosa* (Nedra, Moscow, 1984), p. 75
12. Metodika rascheta shleifovykh truboprovodov na prochnost' i ustoichivost' v usloviiah obshchej korrozii, (UNI, Ufa, 1980), p. 35
13. L.M. Kachanov, *Osnovy mekhaniki razrusheniia* (Nauka, Moscow, 1974), p. 311
14. Y.N. Rabotnov, *Mekhanika deformiruemogo tverdogo tela* (Nauka, Moscow, 1979), p. 744
15. V.V. Nezhdanov, V.N. Permakov, K analizu nagruzhennosti magistral'nykh nefteprovodov raionov Zapadnoi Sibiri. Ekspress-informacija VNIIOENG. Ser. Transport i khranenie nefti i nefteproduktov. Otechestvennyi opyt. VNIIOENG Vyp. 2, (Moscow, 1986), pp. 12–15
16. G.V. Karpenko, K.B. Katsev, N.V. Kakotailo i dr., Malotsiklovaia ustalost' stali v rabochikh sredah. (Naukova dumka, Kiev, 1977), p. 110
17. R.S. Zajnullin, M.S. Tulumguzin, Issledovanie parametrov gidravlicheskoi opressovki truboprovodov i sosudov. Nauchno-tehnicheskie dostizheniia i effektivnost' proizvodstva, Tezisy dokl., Resp. konf., (Sterlitamak, 1979), p. 130
18. V.M. Finkel', Fizicheskie osnovy tormozheniia razrusheniia (Metallurgiia, Moscow, 1977), p. 360
19. S.V. Serensen, V.P. Kogaev, R.M. Shneiderovich, *Nesushchaja sposobnost' i raschety detalei mashin na prochnost'* (Moscow, Mashinostroenie, 1975), p. 438
20. D. Forazassi, Medlennoe ustalostnoe razrushenie pri dvuhosnom napriazhennom sostoianii. (Ricerca Scientifica, №C-11247), №69, 81–119 (1970)
21. M. Kikukava i dr. Sravnenie malotsiklovoi ustalostnoi prochnosti riada konstruktsionnykh materialov v usloviiakh tsiklicheskogo osevogo deformirovaniia i tsiklicheskogo znakoperemennogo kruchenija. Bulletin of the ISME, VCP(C-162 07a) **15**(86), 889–898 (1972)
22. V.L. Kolmogorov, A.A. Bogatov, B.A. Migachev i dr., Plastichnost' i razrushenie. (Metallurgiia, Moscow, 1977), p. 336
23. A.V. Puiko, Razrabotka raschetnykh i eksperimental'nykh metodik ocenki mehanicheskikh svoistv kol'tsevykh stykov magistral'nykh truboprovodov. (Avtoreferat diss. na soisk. uchen. stepeni kand. tekh. nauk: 05.03.86), (Cheliabinsk, 1986), p.18
24. V.P. Kogaev, N.A. Makhutov, A.P. Gusenkov, Raschety detalei mashin i konstruktsii na prochnost' i dolgovechnost'. Spravochnik (Mashinostroenie, Moscow, 1985), p. 224
25. V.P. Kogaev, *Raschety na prochnost' pri napriazheniiakh, peremennykh vo vremeni* (Moscow, Mashinostroenie, 1977), p. 232
26. L. Tot, Romavari, Primenenie koncepcii udel'noi raboty razrusheniia dlia otsenki tsiklicheskoi treshchinostoikosti stalei. Problemy prochnosti **1**, 11–17 (1986)
27. V.I. Pokhmurskii, *Korrozionnaia ustalost' metallov* (Moscow, Metallurgija, 1985), p. 207
28. P. Rabba, Primenenie mekhaniki razrushenija dlia izucheniia rasprostraneniia ustalostnykh treshchin. (Circulaire d' information's techniques, №C-11234), Vol 28(1), pp. 229–256 (1971)
29. A.Kh. Janahmadov, Tribotekhnicheskie problemy v neftegazovom oborudovanii. – (Elm, Moscow, 1998), p 216

Chapter 2
Scientific Foundations of Stochastic Tribomodeling

Modeling (simulation) is one of the most effective methods of knowledge. The effectiveness of modeling (simulation) as a tool for learning is determined, above all, by the ability to highlight the main (essential) and to abstract the minor (inconsequential).

The solution of the adequate mathematical models in the complex technical problems, such as tribotechnical, is the qualitative analysis primarily based on the one of the main classification systems. Therefore, in the modeling (simulation), we should progress from the object to the model. The current research provides a systematic approach to the study of tribological applications. The importance of that approach rises especially when the probabilistic–statistic methods are applied.

The objects, their properties, and relationships between those two define the system. According to N.P. Fedorchenko, the part of the system objects are the purpose, input, the process, output, the boundaries and the inverse connection. The purpose of such a system is the achievement of optimal functioning of the tribotechnical system and its further maintainability at the level of maximum stability. This goal has to be achieved by complying at least two restrictions: The quantity of materials required for the manufacture of friction units should not exceed the predetermined level, and the operational cost of the entire system must not exceed the certain values.

Through the system analysis, we can determine the system class: deterministic or stochastic (probabilistic). V.P. Trofimov defined that "the system is the rigidly deterministic if under those initial conditions it transfers itself in a single state. Accordingly, the system is stochastic (probabilistic) if under the same initial conditions it can transfer itself into different states, with different probabilities."

The division of system into the rigidly deterministic and stochastic (probabilistic) is very objective. B.V. Gnedenko wrote that "the deterministic systems are quite rare. Moreover, there is an established view in the modern physics that in nature there is no purely deterministic laws, and all laws are of probabilistic nature." This statement is consistent with the fundamental research of V.V. Bolotin for designing the structures using methods of theory of probability and reliability.

The issues of practical application of statistical modeling (simulation) in various fields of scientific and technical research are well documented in numerous literatures.

2.1 Probability Analysis of Generalized Variables Based on Stochastic Nature of Parameters

Studying the failure of friction bodies using the conventional methods makes the task almost impossible. Therefore, the applications of new mathematical methods such as physical–statistical and probabilistic methods are required for tribology. The significant progress has recently been achieved in the related problems [1–5].

The conventional mathematical methods applied in solving problems for even simple friction processes are virtually ineffective, because besides the complexity of analyzed process, there is also the stochastic nature of its functionality. So the negligence of even a large number of random factors usually leads to the inaccurate test results of the assessed process, even when there is a perfect mathematical model.

At the present time, there is a wide range of literatures that analyze ideas and practical implementation of probabilistic methods [6–9], which can be used to solve many actual problems. The method of statistical test (Monte Carlo) in this sense is of particular importance.

The evaluations of various loading conditions of friction devices and the methods of stochastic description have received a lot of attention currently. The evaluation of real load of friction devices is associated with both solving the problem through theory of reliability and predicting its actual durability and founding the optimal test modes [10].

The statistical characteristics of the loading indicators of machine usually vary significantly for the different operation modes, so it is advisable to consider not the impact of the individual values, but the complex values, called the generalized variables (GV) (the similarity criteria). In reality, the technical systems are mainly stochastically defined, and their parameters are subject to the random changes. The GV, combining those system parameters, will also be subjected to the random variations. The considerable interest is of studying the probability distribution of GV and the definition of probability characteristics. Generally, the GV can be represented as follows [11]:

$$\pi_k = \prod_{i=1}^{n} P_i^{\pm \alpha_i}, \qquad (2.1)$$

where P_i—the parameters included in the GV and α_i—the exponent parameters.

The parameters included in the GV are the random variables with their own distributions, and the GV is the function of those random variables. It should be

noted that the probability distribution of the P_i parameters is mainly known as a result of the test or a priori data. To study the probability distribution of π_k, we have to analyze the dependence of the form:

$$\pi_k = \varphi\left(P_1^{\pm \alpha_1}, P_2^{\pm \alpha_2}, \ldots, P_n^{\pm \alpha_n}\right). \tag{2.2}$$

Due to the complexity of analytical solution, it is advisable to investigate the problem through the method of statistical tests on a computer or by the analytical approximation [12, 13].

The essence of statistical test for solving the problem is that parameters included in GV are modelled through the specified distribution, and the array of data is formed for the random values π_k. On the basis of this array, the GV distribution is determined and its statistical characteristics are calculated.

To analyze the expression (2.2), we represent the initial GV as a function of two random variables—X_1 and X_2 and denote the GV by $y{:}y = \varphi(x_1, x_2)$.

Given the probability density of random variables (X_1, X_2). Then, the distribution function of the random variable $Y = $ GV can be determined based on the probability density function of the individual random variables X_1 and X_2 [14].

$$F(y) = \iint_D f(x_1, x_2) \mathrm{d}x_1 \, \mathrm{d}x_2,$$

where D—the region in the plane $X_1 O X_2$ for which $Y < y$.

The probability density is:

$$f(y) = \frac{\mathrm{d}}{\mathrm{d}y} F(y).$$

Consider some typical for GV (consisting of two parameters), the expressions of the density distribution functions of the continuous random variables:

1. $Y = X_1 X_2$; $f(y) = \int \left|\frac{1}{x_1}\right| f_1(x_1) f_2\left(\frac{y}{x_1}\right) \mathrm{d}x_1 = \int \left|\frac{1}{x_2}\right| f_1\left(\frac{y}{x_1}\right) f_2(x_1) \mathrm{d}x_2$;

2. $Y = \frac{X_1}{X_2}$; $f(y) = \int |x_2| f_1(y x_2) f_2(x_2) \mathrm{d}x_2 = \int \left|\frac{x_1}{y^2}\right| f_1(x_1) f_2\left(\frac{x_1}{y}\right) \mathrm{d}x_1$.

(1) When the allocation of X_1 and X_2 follows the normal law, the density distribution of Y for product [15] is:

$$f(y) = \frac{1}{\pi \sigma_{x_1} \sigma_{x_2}} K_0 \frac{y}{\sigma_{x_1} \sigma_{x_2}},$$

where K_0—the Macdonald function.

(2) When the allocation of X_1 and X_2 follows the uniform law within the interval (a, b), the density distribution for product will be:

$$f(y) = \begin{cases} \frac{1}{(b-a)^2} \ln \frac{y}{a^2}, & a^2 \le y \le ab; \\ \frac{1}{(b-a)^2} \ln \frac{a^2}{y}, & ab \le y \le b^2. \end{cases}$$

(3) When the allocation of X_1 and X_2 follows the normal law, the density distri-
bution of Y for the individual case is:

$$f(y) = \frac{1}{\pi \left[y^2 + (\sigma_{x_1}/\sigma_{x_2})^2 \right]} \cdot \frac{\sigma_{x_1}}{\sigma_{x_2}}$$

which complies with the Cauchy distribution.

If the function depends on many random variables, there is the determinant of
Ostrogradski–Jacobi for the transformation of random variables $(X_1, X_2, \ldots, X_n)$
into the random variables $(Y_1, Y_2, \ldots, Y_n)$.

$$f(y) = \frac{\partial(x_1, x_2, \ldots, x_n)}{\partial(y_1, y_2, \ldots, y_n)} = \begin{vmatrix} \frac{\partial x_1}{\partial y_1} & \frac{\partial x_1}{\partial y_2} & \cdots & \frac{\partial x_1}{\partial y_n} \\ \frac{\partial x_2}{\partial y_1} & \frac{\partial x_2}{\partial y_2} & \cdots & \frac{\partial x_2}{\partial y_n} \\ \vdots & \vdots & & \vdots \\ \frac{\partial x_n}{\partial y_1} & \frac{\partial x_n}{\partial y_2} & \cdots & \frac{\partial x_n}{\partial y_n} \end{vmatrix}$$

and if this transformation is bijective, then

$$f_y(y_1, y_2, \ldots, y_n) = |D| f_x(x_1, x_2, \ldots, x_n)$$

where the quantities of $x_1, x_2, \ldots, x_n$ are expressed through $y_1, y_2, \ldots, y_n$.

The task becomes more complex, when we deal with the multidimensional
system of random variables and with the calculation of multiple integrals.

Because of the complexity of determining the density distribution $f(y)$, in some
cases we can restrict the finding of numerical values. In this case, we assume that
the distribution of arguments or their numerical characteristics are given. Then, to
find the expectation and the variance of the functions of random variables, the
following expression is applied [14].

$$m_\varphi = M[\varphi(X_1, X_2, \ldots, X_n)] = \int\limits_{-\infty}^{+\infty} \cdots \int\limits_{-\infty}^{+\infty} \varphi(x_1, x_2, \ldots, x_n) \times f(x_1, x_2, \ldots, x_n) dx_1, dx_2, \ldots, dx_n$$

$$D[\varphi(X_1, X_2, \ldots, X_n)] = \int\limits_{-\infty}^{+\infty} \cdots \int\limits_{-\infty}^{+\infty} [\varphi(x_1, x_2, \ldots, x_n) - m_\varphi]^2 \times f(x_1, x_2, \ldots, x_n) dx_1, dx_2, \ldots, dx_n.$$

$$(2.3)$$

Due to the necessity of studying the distribution of GV, it is of considerable
interest to determine the distribution of π_k. In this paper, when the number of
variables is more than three, the most appropriate method for solving the problem

should be the Monte Carlo method [16]. For the study, the GV of friction was taken from the tribological nodes of oil equipment, obtained in [17].

Figure 2.1 shows the GV and the probability distribution histograms for normal and uniformly distributed parameters. The parameter tolerance values are given within ±(5–15) % of its baseline values. The calculations were performed on PC. The algorithm for the GV probability distributions using the Monte Carlo method is shown in Fig. 2.2. Tables 2.1 and 2.2 show the numerical characteristics of these distributions and the normal and uniform distributions of P_i, respectively, where $\overline{\pi}$—the average value, σ—the dispersion, S_{π}—the skewness ($S_{\pi} = \mu_3/\sigma_3$; μ_3—the central point of the third order), E_{π}—the excess ($E_{\pi} = \mu_4/\sigma_4$; and μ_4—the fourth-order central moment) for the random variable π.

To calculate the n-dimensional integrals, appearing in the second line of the expressions (2.3), for the expectation and variance of the random variable functions $\varphi(X_1, \ldots, X_n)$, we apply the Monte Carlo method [18, 19], which is used for the approximation of integral

$$I = \int_G f(x_1, \ldots, x_2)p(x_1, \ldots, x_2)dx_1 \ldots dx_n, \tag{2.4}$$

where $p(x_1, \ldots, x_n)$—the joint probability density function of the random variables $X_1, \ldots, X_n$, defined in G so that

$$\int_G p(x_1, \ldots, x_2)dx_1 \ldots dx_n = 1. \tag{2.5}$$

Here, G—the limited range of variation values $X_1, \ldots, X_n$, since the variables P_i, included in that we consider the GV of the form (2.1), are limited by their physical meaning: $0 < P_i < c_i$.

In (2.3), x_i—the GV P_i, as $f(x_1, \ldots, x_n)$ we adopt the function $\varphi(x_1, \ldots, x_n)$, and the probability density function $p(x_1, \ldots, x_n)$ is denoted by $f(x_1, \ldots, x_n)$.

To evaluate the integral (2.4) through the Monte Carlo method, we consider the random point $Q \in G$ with the density $p(x)$, where $x = (x_1, \ldots, x_n)$—the n-dimensional random variable $X = (X_1, \ldots, X_n)$ and we introduce the random scalar variable $Z = f(Q)$, the mathematical expectation of which is equal to the desired integral (2.4)

$$MZ = \int f(x)p(x)dx = I, \tag{2.6}$$

M the mathematical expectation. Recall that, by definition, the expectation MZ exists if and only if there is $M|Z|$.

Item №	Generalized variables	Expression	Formal representation	Properties of probability distribution	
				When π has a normal distribution	When π has a uniform distribution
1.	Hardness	$\pi_1 = \dfrac{HB_1 \cdot HB_2 \cdot K_{r_1}^{2/3} \cdot K_{r_2}^{2/3}}{P^2}$	$\pi_1 = \dfrac{P_1 \cdot P_2 \cdot P_3^{2/3} \cdot P_4^{2/3}}{P_5^2}$		
2.	Density	$\pi_2 = \dfrac{P_1 \cdot P_2 \cdot P_3 \cdot \vartheta^6 \cdot K_{r_1} \cdot K_{r_2}}{P^3}$	$\pi_2 = \dfrac{P_6 \cdot P_7 \cdot P_8 \cdot P_9^6 \cdot P_3 \cdot P_4}{P_5^3}$		
3.	Dynamic viscosity	$\pi_3 = \dfrac{\eta_1 \cdot \eta_2 \cdot \eta_3 \cdot \vartheta^2 \cdot K_{r_1}^{1/3} \cdot K_{r_2}^{1/3}}{P^2}$	$\pi_3 = \dfrac{P_{10} \cdot P_{11} \cdot P_{12} \cdot P_9^2 \cdot P_3^{1/3} \cdot P_4^{1/3}}{P_5^2}$		
4.	Macro-geometry	$\pi_4 = \dfrac{A_{a_1} \cdot A_{a_2}}{K_{r_1}^{2/3} \cdot K_{r_2}^{2/3}}$	$\pi_4 = \dfrac{P_{13} \cdot P_{14}}{P_3^{2/3} \cdot P_4^{2/3}}$		
5.	Single asperities	$\pi_5 = \dfrac{r_1 \cdot r_2}{K_{r_1}^{1/3} \cdot K_{r_2}^{1/3}}$	$\pi_5 = \dfrac{P_{15} \cdot P_{16}}{P_3^{1/3} \cdot P_4^{1/3}}$		
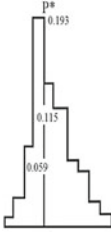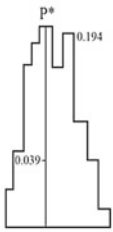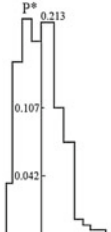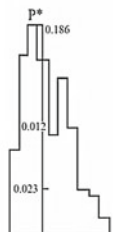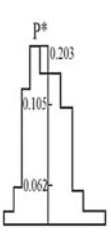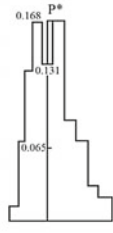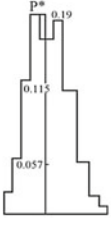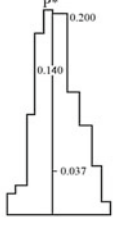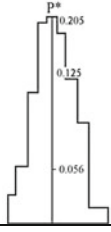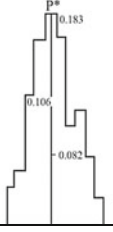
Fig. 2.1 The GV and the probability distribution histograms for normal and uniformly distributed parameters

Item №	Generalized variables	Expression	Formal representation	Properties of probability distribution	
				When π has a normal distribution	When π has a uniform distribution
6.	Maximum height of asperity of rough surface	$\pi_6 = \dfrac{h_1 \cdot h_2}{K_{r_1}^{1/3} \cdot K_{r_2}^{1/3}}$	$\pi_6 = \dfrac{P_{17} \cdot P_{18}}{P_3^{1/3} \cdot P_4^{1/3}}$		
7.	Modulus of elasticity	$\pi_7 = \dfrac{E_1 \cdot E_2 \cdot K_{r_1}^{2/3} \cdot K_{r_2}^{2/3}}{p^2}$	$\pi_7 = \dfrac{P_{19} \cdot P_{20} \cdot P_3^{2/3} \cdot P_4^{2/3}}{P_5^2}$		
8.	Shear strain of films on surface of friction	$\pi_8 = \dfrac{\tau_{\text{пл}_1} \cdot \tau_{\text{пл}_2} \cdot K_{r_1}^{2/3} \cdot K_{r_2}^{2/3}}{p^2}$	$\pi_8 = \dfrac{P_{21} \cdot P_{22} \cdot P_3^{2/3} \cdot P_4^{2/3}}{P_5^2}$		
9.	Friction duration	$\pi_9 = \dfrac{t \cdot v}{K_{r_1}^{1/6} \cdot K_{r_2}^{1/6}}$	$\pi_9 = \dfrac{P_{23} \cdot P_3}{P_3^{1/6} \cdot P_4^{1/6}}$		
10.	Thermal conductivity	$\pi_{10} = \dfrac{\lambda_1 \cdot \lambda_2 \cdot \lambda_3 \cdot \vartheta_1^{3/2} \cdot \vartheta_2^{3/2}}{p^3 \cdot v^3 \cdot K_{r_1}^{1/2} \cdot K_{r_2}^{1/2}}$	$\pi_{10} = \dfrac{P_{24} \cdot P_{25} \cdot P_{26} \cdot P_{27}^{3/2} \cdot P_{28}^{3/2}}{P_5^3 \cdot P_9^3 \cdot P_3^{1/2} \cdot P_4^{1/2}}$		

Fig. 2.1 (continued)

Item №	Generalized variables	Expression	Formal representation	Properties of probability distribution	
				When π has a normal distribution	When π has a uniform distribution
11.	Coefficient of specific heat	$\pi_{11} = \dfrac{C_1 \cdot C_2 \cdot C_3 \cdot \vartheta_1^{3/2} \cdot \vartheta_2^{3/2}}{\upsilon_6^5}$	$\pi_{11} = \dfrac{P_{29} \cdot P_{30} \cdot P_{31} \cdot P_{27}^{3/2} \cdot p_{28}^{3/2}}{P_9^6}$		
12.	Coefficient of linear expansion	$\pi_{12} = \alpha_1 \cdot \alpha_2 \cdot \vartheta_1 \cdot \vartheta_2$	$\pi_{12} = P_{32} \cdot P_{33} \cdot P_{27} \cdot P_{28}$		
13.	Acceleration	$\pi_{13} = \dfrac{\omega \cdot K_{r_1} \cdot K_{r_2}}{\upsilon^3}$	$\pi_{19} = \dfrac{P_{34} \cdot P_3 \cdot P_4}{P_9^2}$		
14.	Coefficient of heat transfer	$\pi_{14} = \dfrac{\sigma_1 \cdot \sigma_2 \cdot K_{r_1}^{2/3} \cdot K_{r_2}^{2/3} \cdot \vartheta_1 \cdot \vartheta_3}{P^2 \cdot \upsilon^3}$	$\pi_{14} = \dfrac{P_{35} \cdot P_{36} \cdot P_3^{2/3} \cdot p_4^{2/3} \cdot P_{27} \cdot P_{28}}{P_5^2 \cdot P_9^2}$		
15.	Work under breaking	$\pi_{15} = \dfrac{W_{т.п.}}{P \cdot K_{r_1}^{1/6} \cdot K_{r_2}^{1/6}}$	$\pi_{15} = \dfrac{P_{37}}{P_5 \cdot P_3^{1/6} \cdot P_4^{1/6}}$		

P* - the value of empirical function of density
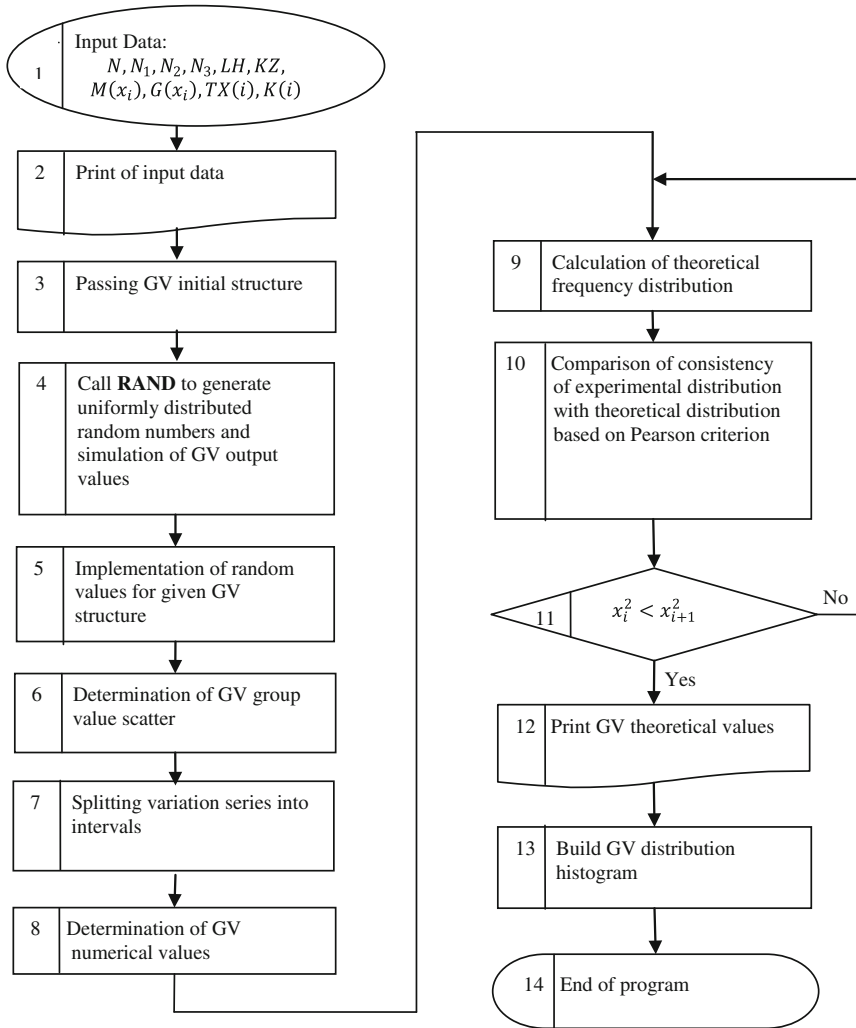
Fig. 2.2 The program algorithm for the GV probability distributions using the Monte Carlo method

Table 2.1 The first 10 values of $p_3(i)$

i	1	2	3	4	5	6	7	8	9	10
i triple	1	2	10	11	12	20	21	22	100	101
$p_3(i)$ triple	0.1	0.2	0.01	0.11	0.21	0.02	0.12	0.22	0.001	0.101
$p_3(i)$	1/3	2/3	1/9	4/9	7/9	2/9	5/9	8/9	1/27	10/27

Table 2.2 Numerators V_j^s ($j = 1, \ldots, n$)

l \ s	1	2	3	4	5	6	7	8	9	10	11	12	13	14	15	16	17	18	19	20
1	1	1	1	1	1	1	1	1	1	1	1	1	1	1	1	1	1	1	1	1
2	1	3	5	15	17	51	85	255	257	771	1285	3855	4369	13,107	21,845	65,535	65537	196,611	327,685	983,055
3	1	1	7	11	13	61	67	79	465	721	823	4091	4125	4141	28,723	45,311	53,505	250,113	276,231	326,411
4	1	3	1	5	31	29	81	147	433	149	719	3693	3841	11,523	16,641	49,925	16,671	83,229	515,921	482,707
5	1	1	5	3	15	51	125	141	177	759	267	1839	6929	16,241	16,565	17,139	82,207	50,979	252,717	851,901
6	1	3	7	7	9	11	79	63	193	707	1351	1479	6857	1227	32,527	36,863	102,401	241,667	258,055	323,591
7	1	1	3	11	7	31	13	161	309	901	2007	1311	6235	2915	27,745	35,885	34,225	112,177	378,387	246,491
8	1	3	3	13	23	57	11	219	101	687	449	579	3779	717	17,751	20,473	23,627	261,147	140,453	658,927
9	1	1	1	15	11	29	13	85	475	63	1233	337	6577	16,383	24,859	24,845	110,365	175,013	97,387	453,871
10	1	3	5	1	29	61	79	169	293	177	689	2259	2197	6225	22,861	64,589	15,455	107,641	103,861	247,585
11	1	1	7	5	5	3	127	97	47	819	765	3341	3379	15,217	21,513	19,463	15,387	50,237	130,435	790,151
12	1	3	1	11	25	15	9	191	417	631	789	1327	2885	4295	29,021	37,603	62,509	248,899	87,493	716,363
13	1	1	5	7	19	51	51	151	157	141	389	901	5889	16,131	12,039	11,055	90,495	123,227	49,489	574,417

To find the value of I, we choose N independent and identically distributed (i.i. d.) values of $Z_i = f(Q^{(i)}) (i = 1, \ldots, N) \left(Q^{(i)} = \left(Q_1^{(i)}, \ldots, Q_n^{(i)} \right) \right)$—$i$th value of the n-dimensional random quantity $Q = (Q_1, \ldots, Q_n)$ and we calculate the arithmetic mean

$$\overline{Z}_N = \frac{1}{N} \sum_{i=1}^{N} Z_i, \qquad (2.7)$$

Since the sequence of independent identically distributed random variables $\{Z_i\}_{i=\overline{1,N}}$, with the mathematical expectation, follows the law of large numbers (theorem of A.Y. Khinchin [20]), the arithmetic mean of these values converges with the expectation $MZ = I$ when $N \to \infty$, i.e., for any $\varepsilon > 0$

$$P\{|\overline{Z}_N - I| \geq \varepsilon\} \to 0. \qquad (2.8)$$

Briefly, this is written as

$$\overline{Z}_n \xrightarrow{P} I. \qquad (2.9)$$

Thus, for large N, the value of $\overline{Z}_n \approx I$ and the evaluation (2.7) can be used in all cases when there is $MZ = I$, for which, as indicated above, it is necessary and sufficient that the integral

$$M|Z| = \int_G |f|x||p(x)\mathrm{d}x. \qquad (2.10)$$

The existence of the integral (2.10) follows from restrictions

$$0 < f(x) \leq c, \qquad (2.11)$$

which comes from the definition of GV considered by us $\Pi_k (k = 1, \ldots, 15)$ (see Fig. 2.1).

Let us say that there is the Monte Carlo method for calculating some scalar value a, if there is a random variable η, where its expectation is equal to a:

$$M\eta = a, \qquad (2.12)$$

and the estimate for a is the arithmetic mean

$$a \approx \frac{1}{N} \sum_{i=1}^{N} \eta_i, \qquad (2.13)$$

Here $\eta_1, \ldots, \eta_N$—the independent values of η. With respect to the integral (2.4), we have: $a = I$, $\eta = Z$, $\eta_i = Z_i$, $Z_i = f(Q_i)(i = 1, \ldots, N)$.

Let us say that there is the *Monte Carlo algorithm* for calculating the value of a, if, besides the formula (2.13), there is formula

$$\eta = \Phi(\gamma_1, \ldots, \gamma_{n,\ldots}), \tag{2.14}$$

which expresses the desired value of a through the independent uniformly distributed random numbers $\gamma_1, \ldots, \gamma_n, \ldots$.

Definition 1 [19]. If the function Φ depends on n arguments

$$\Phi = \Phi(\gamma_1, \ldots, \gamma_n),$$

then we say that the constructive dimension (c.d.) of the algorithm (2.13)–(2.14) is equal to n.

In this case, for the ith implementation of "test," it is sufficient to choose the n random numbers $\gamma_1^{(i)}, \ldots, \gamma_n^{(i)}$ and based on them to calculate the values of $\eta_i = \Phi\left(\gamma_1^{(i)}, \ldots, \gamma_n^{(i)}\right)$. The constructive dimension of n is the maximum number of random values that may be required to implement a test.

By condition, since each of the independent variables $\gamma_1, \ldots, \gamma_n$ is uniformly distributed in the interval (0; 1), the function $\Phi(\gamma_1, \ldots, \gamma_n)$ is defined in the unit n-dimensional cube

$$K^n = \{0 < y_1 < 1, \ldots, 0 < y_n < 1\}, \tag{2.15}$$

and the random n-dimensional value of $Q = \{\gamma_1, \ldots, \gamma_n\}$ is uniformly distributed in the K^n: Its density is $p_Q(y_1, \ldots, y_n) = 1$ for $(y_1, \ldots, y_n) \in K^n$. Therefore, the desired value of a can be written in the form of the n-dimensional integral over K^n:

$$a = M\eta = M\Phi(Q) = \int_0^1 \int_0^1 \Phi(y_1, \ldots, y_n) \mathrm{d}y_1 \ldots \mathrm{d}y_n. \tag{2.16}$$

Thus, the common interpretation of the Monte Carlo algorithm is as follows: If the structural dimension of the algorithm is n (c.d. = n), then the algorithm is the approximation method for calculating the n-dimensional integral (2.16) with random points $Q^{(i)} = \left(\gamma_1^{(i)}, \ldots, \gamma_n^{(i)}\right)$, evenly distributed in the K^n

$$\int_{K^n} \Phi(Q) \mathrm{d}Q \approx \frac{1}{N} \sum_{i=1}^N \Phi\left(Q^{(i)}\right). \tag{2.17}$$

Here and below, for brevity, we use the notation

$$\int\limits_{K^n} \Phi(Q)\mathrm{d}Q \equiv \int\limits_0^1 \ldots \int\limits_0^1 \Phi(y_1, \ldots, y_n)\mathrm{d}y_1 \ldots \mathrm{d}y_n. \tag{2.18}$$

Formula (2.17) is equivalent to (2.13) and (2.14).

We assume that the domain G in (2.4) is the n-dimensional parallelepiped $\Pi^n = \{a_j \le x_j \le b_j, j = 1, \ldots, n\}$, which can be easily reduced to the n-dimensional cube (2.15) through the linear transformations

$$y_j = \frac{x_j - a_j}{b_j - a_j} (j = 1, \ldots, n).$$

In the case of the integral (2.14) (with the proviso that n-dimensional random quantity $Q = (\gamma_1, \ldots, \gamma_n)$ is evenly distributed in the cube K^n), we have $\Phi(Q) = f(Q)$ and the formula (2.16) can be written in the form of

$$I = \int\limits_0^1 \ldots \int\limits_0^1 f(y_1, \ldots, y_n)\mathrm{d}y_1 \ldots \mathrm{d}y_n, \tag{2.19}$$

where $(y_1, \ldots, y_n)$—the value of n-dimensional random variable Q.

The question naturally arises: Is it possible to specify a non-random sequence of points $P^{(1)}, \ldots, P^{(i)}, \ldots$ of K^n such that

$$\int\limits_{K^n} \Phi(Q)\mathrm{d}Q = \lim_{N \to \infty} \frac{1}{N} \sum_{i=1}^N \Phi\left(Q^{(i)}\right). \tag{2.20}$$

Definition 2 [19]. The sequence of points $P^{(1)}, \ldots, P^{(i)}, \ldots$ is uniformly distributed in the K^n, if (2.20) holds for any function $\Phi(y_1, \ldots, y_n)$, integrable in K^n according to Riemann.

Weyl introduced this notion in 1916 [21], and also produced examples of the uniformly distributed sequences. Therefore, the sequence $\{P^{(i)}\}$, uniformly distributed by the Definition 2, is also called the *Weyl equidistributed*.

Recall that the Riemann integral is defined only for limited functions.

The comparison of the formulas (2.20) and (2.17) shows that for the implementation of Monte Carlo algorithms with c.d. = n, we can try to use instead of the random points $Q^{(i)}$ the points of sequence $\{P^{(i)}\}$, which are Weyl equidistributed. To do this, at the i-th step of "test" instead of random numbers $\left(\gamma_1^{(i)}, \ldots, \gamma_n^{(i)}\right)$ we use the Cartesian coordinates $y_{i1}, \ldots, y_{in}$ of the point $P^{(i)}$. The relation (2.20) guarantees the convergence of this calculation method for the majority, occurring in practice, of the Monte Carlo algorithms.

The equality (2.20) is not violated if we change any finite number of points in the sequence $\{P^{(i)}\}$. However, the convergence of arithmetic means toward the limit

and, in this case, can become very slow. Therefore, in practice, not every the Weyl equidistributed sequence is reasonable to use as pseudorandom points. Among all uniformly distributed sequences, we should select "good" ones in some sense. Such sequences are the sequence of Holton $P^{*(i)}$ and the ЛП$_\tau$ sequence of $Q^{*(i)}$, which will be described below.

Let G denote an arbitrary n-dimensional domain that belongs to K^n and through V_G—its volume (n-dimensional). Next, let $S_N(G)$ be the number of points with numbers $1 \leq i \leq N$, belonging to G.

Theorem 1 (Weyl) *For the sequence of points $P^{(1)}, \ldots, P^{(i)}, \ldots$ to be uniformly distributed in the K^n (by Definition 2), it is necessary and sufficient that for every $G \subset K^n$*

$$\lim_{N \to \infty} \left[\frac{S_N(G)}{N} \right] = V_G. \tag{2.21}$$

This shows that for the large values of N, the number of points belonging to G, among points $P^{(1)}, \ldots, P^{(N)}$, is approximately proportional to the volume of V_G.

Let us consider a random point $\Gamma = (\gamma_1, \ldots, \gamma_n)$, uniformly distributed in the K^n, and N of its independent realizations $\Gamma^{(1)}, \ldots, \Gamma^{(N)}$. Since the probability is $P(\Gamma \in G) = V_G$, the convergence of the hitting rate for these implementations in G to the probability of hitting G means that

$$\left[\frac{S_N(G)}{N} \right] \xrightarrow{P} V_G.$$

The comparison of this formula with (2.21) shows once again that the points $Q^{(i)} = \left(Q_1^{(i)}, \ldots, Q_n^{(i)} \right)$ of the non-random Weyl equidistributed sequence $\{Q^{(i)}\}$ are the analogues of independent realizations $\Gamma^{(i)}$ of the uniformly distributed random point $\Gamma = (\gamma_1, \ldots, \gamma_n)$.

The "uniformity" of distribution of the non-random sequences can be evaluated using the value called the deviation. To determine it, we choose in K^n some arbitrary point P and it is denoted by Π_P parallelepiped with the diagonal OP and sides parallel to the coordinate axes (Fig. 2.3).

The deviation of the group of points $P^{(1)}, \ldots, P^{(N)}$ is defined by

$$D_N = \sup |S_N(\Pi_P) - N \cdot V_{\Pi_P}|, \quad P \in K^n. \tag{2.22}$$

Theorem 2 [19]. *For the sequence of points $P^{(1)}, \ldots, P^{(N)}, \ldots$ to be uniformly distributed in the K^n (in the sense of Weyl), it is necessary and sufficient that*

$$\lim_{N \to \infty} \left[\frac{D_N}{N} \right] = 0.$$

Fig. 2.3 Parallelepiped with the diagonal *OP* and sides parallel to the coordinate axes
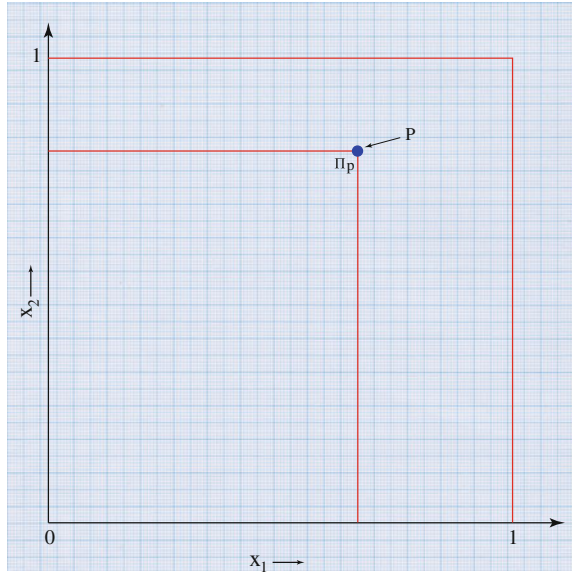
It is obvious that the faster the ratio D_N/N decreases, the more evenly the sequence is distributed. In the literature, the ratio D_N/N is often referred to as a deviation, as this is the upper bound of deviations of the empirical distribution function $S_N(\Pi_P)/N$ for points $P^{(1)}, \ldots, P^{(N)}$ from the theoretical distribution function of random point Γ in K^n, in which the point P is equal to V_{Π_P}.

We can prove that $\frac{1}{2} \le D_N \le N$, but it is unclear which is the best order growth of D_N at $N \to \infty$. At the present time, there are only two known classes of sequences of points in K^n, such that for all N

$$D_N = O(\ln^n N). \tag{2.23}$$

This sequence of Holton [22] and the ЛП$_\tau$ sequences [23] are denoted by P_i^* and Q_i^*, respectively. Examples of such sequences are listed below. Are there any sequences for which $D_N = O(\ln^n N)$ for all N is unknown. However, for the points $Q^{*(1)}, \ldots, Q^{*(N)}$ in the ЛП$_\tau$ sequence with $N = 2^m$, the deviation is $D_N = O(\ln^{n-1} N)$.

Let us investigate in more detail the convergence of limit in (2.20). The Eq. (2.20) holds for all Riemann integral functions $\Phi(y_1, \ldots, y_n)$. If we consider the more restricted classes of functions, then there can be an estimate error of this formula. For example, the inequality

$$\left| \int_{K^n} \Phi(P)\mathrm{d}P - \frac{1}{N}\sum_{i=1}^{N} \Phi\left(P^{(i)}\right) \right| \le c(\Phi)\frac{D_N}{N}, \tag{2.24}$$

where $c(\Phi)$ does not depend on neither N, nor points $P^{(i)}$ being valid for all $P^{(1)}, \ldots, P^{(N)}$ and for all functions $\Phi(y_1, \ldots, y_n)$, which are continuous and bounded in K^n along with their partial derivatives containing not more than one differentiation with respect to each variable. All of these derivatives can be written by the formula $\partial^k \Phi / \partial y_{j_1} \ldots \partial y_{j_k}$, where $1 \leq j_1 < j_k \leq n$ and k can take the values $1, 2, \ldots, n$. The oldest among these derivatives is $\partial^n \Phi / \partial y_1 \ldots \partial y_n$.

By the way, in the integral (2.4) with $\Phi(y_1, \ldots, y_n) = f(y_1, \ldots, y_n)$, the above-mentioned conditions for the smoothness of Φ, where the inequality (2.23) holds, are fulfilled for all considered GV $\pi_k (k = 1, \ldots, 15)$, if their constituent variables P_i satisfy the condition $P_i > 0$ in the domain G.

If the sequence of Holton $P_i = P_i^*$ or ЛП$_\tau$ sequence $P_i = Q_i^*$ is substituted into (2.24), then according to (2.23) the right-hand side will be the order of $O(N^{-1} \ln^n N)$. Since for all sufficiently large N, the inequality $\ln^n N < N^\varepsilon$ (for any fixed $n \geq 1$ and $\varepsilon > 0$) is valid, we can say that the error (2.24) decreases faster than $N^{-(1-\varepsilon)}$ with any $\varepsilon > 0$. The accuracy of formula (2.20) with the "real" random points is equal to $N^{\frac{1}{2}}$, i.e., much worse.

Definition 3 [24]. The numbers $\gamma_1, \ldots, \gamma_n$, which are calculated by any given formula and resemble the random numbers with their statistical properties, are called the *pseudorandom numbers*.

The "good" pseudorandom numbers are the terms of Holton sequence P_i^* or the terms of ЛП$_\tau$ sequence Q_i^*.

Definition 4 [19]. If in the r-ary $(r \geq 2)$ system the numeration is $i = a_m a_{m-1} \ldots a_2 a_1$, then again in the r-ary system

$$p_r(i) = 0, \ \ a_1 a_2 \ldots a_{m-1} a_m.$$

The entire a_s are the r-ary digits, i.e., they are equal to one of the values 0, $1, 2, \ldots, r - 1$.

In the decimal system, the last two formulas are as follows:

$$i = \sum_{S=1}^{m} a_S r^{S-1}, \ p_r(i) = \sum_{S=1}^{m} a_S r^{-s}.$$

The first 10 values of $p_3(i)$ are listed in Table 2.1.

Let $r_1, \ldots, r_n$ be the pairwise prime numbers.

Definition 5 [19]. The sequence of Holton is a sequence of points in the unit cube K^n (2.15) with the Cartesian coordinates.

$$(p_{r_1}(i), \ldots, p_{r_n}(i)), \quad i = 1, 2, \ldots.$$

The sequences were designed by Holton [22], and he also obtained values for them (2.23). All such sequences are distributed uniformly in K^n (according to Definition 2).

Usually in practice, as $r_1, \ldots, r_n$, we choose the first n primes $r_1 = 2, r_2 = 3, r_3 = 5, \ldots$ and use the n-dimensional points

$$P_i^* = (p_2(i), p_3(i), p_5(i), \ldots, p_{r_n}(i)), \quad i = 1, 2, \ldots.$$

Definition 6 [19]. The points $Q_i = (q_{i_1}, \ldots, q_{i_1})$ of the unit n-dimensional cube are defined by the formula

$$Q_i = e_1 V_1 \cdot e_2 V_2 \cdot \ldots \cdot e_m V_m. \tag{2.25}$$

where $i = e_m e_{m-1} \ldots e_2 e_1$—the binary representation of i ($e_m \in \{0, 1\}$—the binary digits) and $V_s (s = 1, 2, 3, \ldots, m)$—the guiding points, the denominators of coordinates of which are equal to 2^s, and the numerators are defined in Table 2.2, called the points of ЛП$_\tau$ sequences studied in detail in [23].

Here, (*) denotes the bitwise addition modulo 2 in the binary system. As a rule, all computers have a dedicated function to carry out operations (*): This is the so-called function of "comparison" (in each digit, the numbers are added by the rules $0 + 0 = 1 + 1 = 0, 0 + 1 = 1 + 0 = 1$).

Here is an example of calculating the coordinates of V_s for $s = 3$ and $n = 13$

$$V_s = \left(\frac{1}{8}, \frac{5}{8}, \frac{7}{8}, \frac{1}{8}, \frac{5}{8}, \frac{7}{8}, \frac{3}{8}, \frac{3}{8}, \frac{1}{8}, \frac{5}{8}, \frac{7}{8}, \frac{1}{8}, \frac{5}{8}\right).$$

Here, the denominator is $2^3 = 8$, and the numerators for $s = 3$ are taken from the third column of Table 2.2. If there is a need in a point of lower dimension n, then it should be limited to the first n-numbers of the sth column.

Table 2.2 makes easy to calculate the points $Q_0, Q_1, \ldots, Q_{n-1}$ that for any N form, the "good" integration formula (2.20) can be written as

$$\int\limits_0^1 \ldots \int\limits_0^1 f(y_1, \ldots, y_n) dy_1 \ldots dy_n \approx \frac{1}{N} \sum_{i=1}^{N-1} f\left(Q^{(i)}\right). \tag{2.26}$$

For an explanation of the rule (2.25), let us calculate the point Q_{22} in four-dimensional cube. In the binary system, the number 22 is written as 10110. Therefore, in accordance with (2.25), we obtain $Q_{22} = V_2 \cdot V_3 \cdot V_5$.

The coordinates of point $Q_{22} = (q_{22,1}, q_{22,2}, q_{22,3}, q_{22,4})$ are as follows:

$$q_{22,1} = \frac{1}{4} \cdot \frac{1}{8} \cdot \frac{1}{32} = 0.01 \cdot 0.001 \cdot 0.00001 = 0.01101 = \frac{13}{32};$$

$$q_{22,2} = \frac{3}{4} \cdot \frac{5}{8} \cdot \frac{17}{32} = 0.11 \cdot 0.101 \cdot 0.10001 = 0.1101 = \frac{29}{32};$$

$$q_{22,3} = \frac{1}{4} \cdot \frac{7}{8} \cdot \frac{13}{32} = 0.01 \cdot 0.111 \cdot 0.01101 = 0.11001 = \frac{25}{32};$$

$$q_{22,4} = \frac{3}{4} \cdot \frac{1}{8} \cdot \frac{31}{32} = 0.11 \cdot 0.001 \cdot 0.11111 = 0.00011 = \frac{3}{32}.$$

And so,

$$Q_{22} = \left(\frac{13}{32}, \frac{29}{32}, \frac{25}{32}, \frac{3}{32} \right).$$

The number of operations made on a computer to calculate Q_i increases along with i, but slowly decreases as $\log_2 i$. It uses only the simplest (logical) operations that are performed on computer faster than arithmetic operations.

The various coordinates of point Q_i are unequal: The coordinates with lower values are better distributed. Therefore, in the integrand function $f(y_1, \ldots, y_n)$, the variables are better to be numbered so that the most significant coordinates have smaller values.

The accuracy of formula (2.26) is better estimated, if instead of points Q_i we use nodes of the Π_τ mesh or the initial parts of ЛП_τ sequence:

$$\|\delta\| \approx \frac{2^{n-1+\tau}}{N^{\frac{1}{p}}}, \tag{2.27}$$

if the function f belongs to the linear space S_p.

The order of convergence (at $N \to \infty$) in (2.27) is best. The space S_p is entered using the function represented by the series of Haar:

$$f(P) = c_1 + \widehat{\sum} \sum_{k_1 \ldots k_s} c_{k_1 \ldots k_s}^{i_1 \ldots i_s} \chi_{k_1}(x_{i_1}) \ldots \chi_{k_s}(x_{i_s}) \tag{2.28}$$

where

$$c_1 = \int_{K^n} f(P)\, dP,$$

$$c_{k_1 \ldots k_s}^{i_1 \ldots i_s} = \int_{K^n} f(P) \chi_{k_1}(x_{i_1}) \ldots \chi_{k_s}(x_{i_s})\, dP,$$

the indexes $k_1, \ldots, k_s$ vary from 2 to ∞. Each of the quantities in (2.27) located under the sign of $\widehat{\sum}$ depends only on the variables $x_{i_1}, \ldots, x_{i_s}$, and we can assume that it is given on the verge of $K_{i_1 \ldots i_s}$ of cube K^n.

The Haar function $\chi(x)$ of one variable x is defined by the formula

$$f(y) = \begin{cases} 2^{\frac{m-1}{2}} \text{ at } x \in l_{mj}^{-} \\ -2^{\frac{m-1}{2}} \text{ at } x \in l_{mj}^{+} , \\ 0 \text{ at } x \notin l_{mj} \end{cases} \tag{2.29}$$

where $l_{mj} = \left[\frac{j-1}{2^{m-1}}, \frac{j}{2^{m-1}}\right]$, $(j = 1, \ldots, 2^{m-1})$—the binary segments obtained by dividing the $[0, 1]$ interval into 2^m equal parts $(m = 1, 2, \ldots)$; l_{mj}^{-} and l_{mj}^{+}—the left and right halves of the segment l_{mj}.

Definition 7 [23]. The class $S_P(A_{i_1 \ldots i_s})$ is the set of functions $f(P)$, represented in the form of (2.28), and the coefficients of the Fourier–Haar satisfy the conditions:

$$A_p^{i_1 \ldots i_s}(f) \le A_{i_1 \ldots i_s}, \tag{2.30}$$

In any marked indexes $1 \le i_1 < i_2 < \cdots < i_s$, $1 \le s \le n$; $A_{i_1 \ldots i_s}$—constants; $1 \le p < \infty$; the value $A_p^{i_1 \ldots i_s}(f)$ is associated with each term in the series (2.28)

$$\sum_{k_1 \ldots k_s} c_{k_1 \ldots k_s}^{i_1 \ldots i_s} \chi_{k_1}(x_{i_1}) \ldots \chi_{k_s}(x_{i_s}) \tag{2.31}$$

and it is defined as

$$A_p^{i_1 \ldots i_s}(f) \le \sum_m 2^{\frac{m_1-1}{2} + \cdots + \frac{m_s-1}{2}} \left\{ \sum_j |c_k^i|^p \right\}^{\frac{1}{p}}, \tag{2.32}$$

where for short $i = (i_1, \ldots, i_s)$, $m = (m_1, \ldots, m_s)$, $j = (j_1, \ldots, j_s)$, $k = (k_1, \ldots, k_s)$.

The constants $A_{i_1 \ldots i_s}$ from (2.30) are called *defining constants* of class $S_p(A_{i_1 \ldots i_s})$.

The union of all classes $S_p(A_{i_1 \ldots i_s})$ for all possible constants $A_{i_1 \ldots i_s}$ and substitutions $i_s \ldots i_s \subset (1, 2, \ldots, n)$ will be denoted by S_p.

If $1 < p < p'$, then it follows:

$$S_1(A_{i_1 \ldots i_s}) \subset S_P(A_{i_1 \ldots i_s}) \subset S_{p^1}(A_{i_1 \ldots i_s}). \tag{2.33}$$

For any function $f(P)$ on $S_P(A_{i_1 \ldots i_s})$, the series (2.28) converges absolutely and uniformly.

As it is known, for the functions $f(x)$ of one variable x the Holder class functions H_α (in particular, the differentiable function $f(x)$ belongs to the class H_α with $\alpha = 1$) are embedded in the class S_P. This property can be generalized to the class of functions $f(x_1, \ldots, x_n)$.

Definition 8 [23]. The class of Holder functions $H_\alpha(L_{i_1 \ldots i_s})$ is the set of functions $f(P)$, which satisfy the following conditions: If $P = (x_1, \ldots, x_n) \in K^n$ and $P + Q \in K^n$, where $Q = (\xi_1, \ldots, \xi_n)$, then for any $1 \le i_1 < i_2 < \cdots < i_n \le n$, $1 \le s \le n$

$$\left|\Delta_{\xi_{i_1}}\ldots\Delta_{\xi_{i_s}}f(P)\right|\le L_{i_1\ldots i_s}\left|\xi_{i_1}\ldots\xi_{i_2}\right|^{\alpha},\tag{2.34}$$

where $\Delta_{\xi_{i_s}}f(P)=f\left(x_1,\,\ldots,x_{i_s}+\xi_{i_s},\,\ldots,x_n\right)-f(x_1,\,\ldots,x_n)$—the   increment operator of function $f(P)$ with respect to x_{i_s}. The constants $L_{i_1\ldots i_s}$ are called *defining constants* of class $H_{\alpha}(L_{i_1\ldots i_s})$; the parameter is $0<\alpha<1$.

Just as in the one-dimensional case, if $\alpha<\alpha'<1$, then

$$H_1\left(L_{i_1\ldots i_s}\right)\subset H_{\alpha'}\left(L_{i_1\ldots i_s}\right)\subset H_{\alpha}\left(L_{i_1\ldots i_s}\right).\tag{2.35}$$

The classes $H_{\alpha}(L_{i_1\ldots i_s})$ are the generalization of n-dimensional case of the class of Holder functions with one variable $H_{\alpha}(L)$. However, it should be emphasized that the condition (2.34) is different from the Holder multidimensional conditions used in the theory of differential equations [25]:

$$|f(P+Q)-f(P)|\le\sum_{i=1}^{n}L_i|\xi_i|^{\alpha},\tag{2.36}$$

For a function $f(P)$ satisfies (2.36) with $\alpha=1$, it is sufficient that all its partial derivatives $\partial f/\partial x_i$ were limited: $|\partial f/\partial x_i|\le L_i$. And to ensure that it satisfies (2.34) with $\alpha=1$, this is not enough: We must require that all partial derivatives $\partial^s f/\partial x_{i_1}\ldots\partial x_{i_s}$ were limited, as if $|\partial^s f/\partial x_{i_1}\ldots\partial x_{i_s}|\le L_{i_1\ldots i_s}$, then the equality

$$\Delta_{\xi_{i_1}}\ldots\Delta_{\xi_{i_s}}f(P)=\int\limits_0^{\xi_{i_1}}\ldots\int\limits_0^{\xi_{i_s}}\frac{\partial^s f(P+T)}{\partial x_{i_1}\ldots\partial x_{i_s}}\,dt_{i_1}\ldots dt_{i_s},$$

where $T=(0,\,\ldots,\,0,t_{i_1},\,0,\,\ldots,0,\,t_{i_2},0,\,\ldots,0,t_{i_s},\,0,\,\ldots,0)$, and it is easy to obtain (2.34) with $\alpha=1$.

Theorem 3 [23]. *If $\alpha p>1$, then $H_{\alpha}(L_{i_1\ldots i_s})\subset S_P(A_{i_1\ldots i_s})$, where*

$$A_{i_1\ldots i_s}=\left(2^{1+\alpha}-2^{1+\frac{1}{p}}\right)^{-s}L_{i_1\ldots i_s}.\tag{2.37}$$

We denote the GV $\varphi(x_1,\ldots,x_n)$ in the first of formulas (2.3) through $f(x_1,\ldots,x_n)$, and the probability density function $f(x_1,\ldots,x_n)$ through $p(x_1,\ldots,x_n)$. Assuming that the integrals in (2.3) after the above linear transformations lead to integrals over the unit cube K^n, on the basis of formula (2.19), we have

$$m_{\varphi}=\int\limits_0^1\ldots\int\limits_0^1 f(y_1,\,\ldots,\,y_n)\,dy_1\ldots dy_n.\tag{2.38}$$

besides the integral in (2.38) can be calculated from the approximate quadrature formula (2.26), where as the nodes $Q_i=\left(y_1^i,\ldots,y_n^i\right)$ of the integration grid points

are taken the points $Q_i^* = \left(y_1^i, \ldots, y_n^i\right)$ of the ЛП$_\tau$ sequence (2.25), and not the random points obtained through the random number generator.

Since the function $f(x_1, \ldots, x_n)$ for all 15 GV has the bounded partial derivatives $\partial^s f / \partial y_{i_1} \ldots \partial y_{i_s}$, these functions also satisfy the conditions (2.34) with $\alpha = 1$ and therefore belong to the class S_p, which allows to use the formula (2.27) for the error approximation formula (2.26) in the case of the integral (2.38) for m_φ and the corresponding integral for $D_\varphi = M\left[\left(\varphi - m_\varphi\right)^2\right]$.

Unfortunately, the constants $2^{n-1+\tau(n)}$ increase along with n in the error estimation (2.27). In any case, when $n = 2, 3, 4$, these constants are equal to, respectively, 2, 4, and 16 and can be considered small. Therefore, the use of non-random nodes of the quadrature formula (2.26) in the form of ЛП$_\tau$ sequences, defined by (2.25), is recommended in [23] as a good method for the computation of integrals with not too high multiplicity ($n \leq 4$) from not too smooth functions, which can be also useful if $n > 4$.

As noted in [26], the existing generators of the pseudorandom numbers, developed to model these distributions, perform this function well; however, an attempt to consider the sequences generated by the generator (e.g., RANDU), as the trajectories of a random sequence (or rather a sequence of independent identically distributed random variables with corresponding distribution), is theoretically incorrect and can lead to the false conclusions. The simulated process is obtained by applying a model through filter F to the generator of white noise $X(t)$, and at the same time, the researchers often assume the adequacy of the sequence generator of white noise or the statistical uncorrelatedness of its successive observations $X(t)$.

Generating the pseudorandom numbers of satisfactory quality is a very complicated process, since there are no algorithms that could produce sequences having all the properties of random sequences.

In this regard, the above-described methods for the approximate calculation of multidimensional integrals with the help of grid points in the unit cube forming Q_i^* points of the ЛП$_\tau$ sequences are the virtually convenient way to calculate the expectation and variance of the GV from Fig. 2.1.

If we approach the issue more closely, then it will be good to impose following requirements on of pseudorandom numbers:

1. the asymptote of D_N (2.22) is the best (or at least close to the best);
2. the constant in (2.23) is the best (or at least sufficiently small);
3. the value of D_N/N is small even for small N;
4. the algorithm for calculating these points on a computer is simple enough.

Unfortunately, it is not currently possible to check all of these requirements; as for D_N, the best order of growth is not even known. However, the points of P_i^* (terms of the Holton sequence) and the points Q_i^* (terms of the ЛП$_\tau$ sequence) fully satisfy the first condition. For small n, the points of Q_i^* satisfy the second and third requirements. Finally, the calculation time for the points Q_i^* is of the same order as the time for standard pseudorandom points Γ_i (unless there is a ready table

for $V_j^{(S)}$). To calculate the points P_i^*, we need only n primes, but in comparison with time to calculate Q_i^*, it is approximately n times greater.

In the calculations performed on the points Q_i^*, the actual error is often on the order less than the probable error

$$r_N = 0.6745\sqrt{\frac{D_\eta}{N}}. \tag{2.39}$$

where η—the random variable in (2.12).

We should not think that if the variance does not find an error, then all methods aimed at reducing the variance [19, 27] are meaningless. Firstly, the algorithms with a less variance correspond to the functions Φ in (2.14) with a little change, which, generally speaking, are better to integrate. Secondly, the algorithms with a less variance often correspond to the smooth functions Φ, satisfying the criteria (2.24).

We can expect higher convergence rate through a deterministic random number by using the Monte Carlo methods [19].

Taking into account that in practice we do not require a high precision of determination of the GV probability distribution, the evaluation approach to these issues [11] becomes obvious. For the purposes to simplify the analysis of the GV probability distribution, we represent the expression (2.1) in the form:

$$\ln \pi_k = \sum_{i=1}^{n} \alpha_i \ln P_i. \tag{2.40}$$

Therefore, the probability distribution π_k will tend to approach the lognormal view; it can be used as the statistical model for the random variables. The value of GV is obtained by multiplying a large number of small errors [28]. This premise can be taken as the basis for studying the patterns of the probability distribution of the parameters that are included in the GV. If deviations ΔP_i do not exceed (10–20) % of their nominal value P_i, then the expression (2.40) can be written as follows:

$$\ln \pi_k = \sum_{i=1}^{n} \alpha_i \ln[1 + (P_i - 1)] \approx \sum_{i=1}^{n} \alpha_i (P_i - 1), \tag{2.41}$$

i.e., to linearize the function (2.40) and take into account only the first term of the expansion (2.41). In this case, the estimate of the variance is easily defined

$$D(\ln \pi_k) = \sum_{i=1}^{n} \alpha_i^2 D(P_i).$$

Since the distribution P_i is accepted as normal, $(\ln \pi_k) \approx \sum \alpha_i (P_i - 1)$ is also distributed approximately normal.

In general, the probability density function π_k will be determined as follows (at $M(\ln \pi_k) = 0$):

$$P(\pi_k < \pi) = F(\pi) = F(\ln \pi_k < \ln \pi) = \Phi\left(\frac{\ln \pi}{\sqrt{\sum_{i=1}^{n} \alpha_i^2 D(P_i)}}\right), \qquad (2.42)$$

$$F(\pi) = \frac{dP(\pi_k < \pi)}{d\pi} \approx \frac{1}{\sqrt{2\pi \sum \alpha_i D(P_i)}} \exp + \left[\frac{1}{2} \cdot \frac{\ln \pi}{\sum_{i=1}^{n} \alpha_i D(P_i)}\right]. \qquad (2.43)$$

Let us consider the case with $\Delta P_i = \pm 20$ %, or

$$\alpha = \frac{1}{15}.$$

$$D(\ln \pi_k) = \frac{1}{225} \sum_{i=1}^{n} \alpha_i^2,$$

and substitute in (2.43) the values of the various structures π_k, shown in Fig. 2.1.

For any GV structure, we can write the corresponding expressions of the probability density function π_k.

For example, for GV 2, 12, and 13

$$F(\pi) \approx \frac{15}{\sqrt{50\pi}} \varphi\left(\frac{15 \ln \pi}{\sqrt{50}}\right); \ F(\pi) \approx \frac{15}{\sqrt{4\pi}} \varphi\left(\frac{15 \ln \pi}{\sqrt{4}}\right);$$
$$F(\pi) \approx \frac{15}{\sqrt{7\pi}} \varphi\left(\frac{15 \ln \pi}{\sqrt{7}}\right) \qquad (2.44)$$

These expressions can be used to define the GV range variation and also their probability distributions. For example, asking the value of standard deviation σ, we can find the variation limits of π_k.

For the practical purpose, we set $P = 0.95$ in most cases. The calculations showed that the value of π with probability $P = 0.95$ is in that area.

Since the results of evaluation approach are compared with the results obtained through the statistical tests, we need also to examine the probability distribution of GV depending on the particular set of random numbers. It is obvious that the probability distribution of the same GV, defined by statistical tests twice with the same number of tests, will be somewhat different from each other. The conducted comparative calculations show that the error of the results does not exceed 12 %.

It should be noted that the probability distributions of GV determined by the evaluation procedure are within the range of the distributions obtained by the statistical tests. The analysis of GV probability characteristics (Tables 2.3 and 2.4) showed that the GV distribution curves are close to the lognormal distribution.

Table 2.3 The analysis of GV probability characteristics

GV #	$\bar{\pi}$	σ	S_π	E_π	$\pi_{\min}$	$\pi_{\max}$
1	4.66×10^2	3.74×10	0.44	0.027	3.76×10^2	5.76×10^2
2	2.44×10^{-2}	5.30×10^{-3}	0.47	0.075	1.37×10^{-2}	4.31×10^{-2}
3	8.62×10	8.60	0.282	0.155	6.55×10	1.12×10^2
4	2.60×10	7.08×10^2	0.074	0.327	2.52×10^4	2.90×10^4
5	2.78×10^{-6}	1.29×10^7	0.044	0.292	2.47×10^{-6}	3.14×10^{-6}
6	3.71×10^{-9}	1.71×10^{-10}	0.044	0.302	3.29×10^{-9}	4.19×10^{-9}
7	2.28×10^6	1.82×10^4	0.440	0.021	1.83×10^6	2.81×10^6
8	3.52	0.28	0.440	0.020	2.83	4.35
9	1.44×10^3	8.39×10	0.034	0.164	1.23×10^3	1.67×10^6
10	1.94×10^{-11}	3.11×10^{-12}	0.470	0.544	1.38×10^{-11}	2.76×10^{-11}
11	1.04×10^{16}	1.23×10^{15}	0.136	0.163	6.89×10^{15}	1.38×10^{16}
12	2.04×10^{-4}	7.50×10^{-5}	0.02	0.558	1.31×10^{-4}	3.99×10^{-4}
13	1.17×10^{-9}	8.21×10^{-11}	0.281	0.20	9.55×10^{-10}	1.40×10^{-9}
14	2.11×10^{-10}	2.89×10^{-11}	0.442	0.50	1.32×10^{-10}	3.04×10^{-10}
15	7.44×10^4	3.13×10^2	0.205	0.455	6.58×10^4	8.18×10^4

Table 2.4 The GV distribution curves

GV #	$\bar{\pi}$	σ	S_π	E_π	$\pi_{\min}$	$\pi_{\max}$
1	4.69×10^2	3.62×10	0.074	-0.679	3.84×10^2	5.61×10^2
2	2.41×10^{-2}	5.40×10^{-3}	0.472	-0.584	1.48×10^{-2}	3.90×10^{-2}
3	8.57×10	6.02×10^{-1}	0.296	-0.350	6.58×10	1.09×10^2
4	2.68×10^4	6.66×10^2	0.079	-0.346	2.52×10^4	2.86×10^4
5	2.77×10^{-6}	1.20×10^{-7}	0.209	-0.617	2.50×10^{-6}	3.05×10^{-6}
6	3.69×10^{-9}	1.58×10^{-10}	0.123	-0.518	3.33×10^{-9}	4.07×10^{-9}
7	2.29×10^6	1.76×10^5	0.074	-0.684	1.87×10^6	2.74×10^6
8	3.54	2.27×10^{-1}	0.074	-0.684	2.90	4.23
9	1.43×10^4	7.77×10	0.148	-0.603	1.26×10^4	1.67×10^4
10	1.97×10^{-11}	3.00×10^{-13}	0.386	-0.240	1.37×10^{-11}	2.83×10^{-11}
11	1.05×10^{16}	1.27×10^{15}	0.401	-0.287	8.16×10^{15}	1.50×10^{16}
12	1.93×10^{-4}	7.01×10^{-5}	0.047	-1.109	6.73×10^{-5}	3.54×10^{-4}
13	1.17×10^{-3}	8.90×10^{-11}	0.180	-0.642	1.0×10^{-3}	1.40×10^{-9}
14	2.09×10^{-10}	2.75×10^{-11}	0.503	-0.149	1.50×10^{-10}	2.50×10^{-10}
15	7.46×10^4	3.27×10^2	0.082		6.77×10^4	8.24×10^4

　　All distribution curves are characterized by a positive value of the asymmetry coefficient. The asymmetry of distribution curves increases when the parameter tolerance increases and the presence of higher orders in the first parameters. At the relatively lower values of tolerance, the distribution curves lie between normal and

lognormal. The distribution curves are characterized by the structure of GV and do not depend on the numerical values of parameters.

At P_i, with the normal distribution, the GV has six or more parameters, and the kurtosis of distribution curves would be somewhat larger (see Fig. 2.1, for GV 10, 14), when the uniform distribution is even less. When the product of parameters describes the GV, the distribution curves get closer to theoretical normal and uniform shapes, respectively (see Fig. 2.1, for GV 12). The GV distribution curves with similar structures can be used in studying other the physical processes. Applying the method of statistical tests or the evaluation techniques, we can find the influence characteristics of parameters included in the GV of friction processes. Based on the probability distributions of the process GV and applying the known models of failure, it is possible to calculate the reliability and predict the possible behavior of any particular friction unit.

2.2 Varying Generalized Variable When Planning Experiments

The questions on the synthesis of the similarity theory and the mathematical theory of experiment planning are highly relevant and promising [7, 12]. The application of the theory of experimental planning to the analysis of criterion correlations (of the GV) has a number of features associated with the fact that in this case there is no need to operate with separate parameters, like it is done usually, but with generalized parameters (the criterion of similarity) [11]. In those cases when the parameters are only included in one of the GV, the definition of variation pitch and the construction of the planning matrix can be carried out in accordance with [7]. The task becomes much more complicated when the same parameter is entered into the several GV.

Let us consider one of the possible ways of varying the GV and building the planning matrix. The experiment planning matrix (EPM), which contains the GV, can be successfully used for the generalized regression equations in the analysis of tribological problems.

Generally, in order to realize the full or fractional factorial experiment, we must meet the following conditions:

$$\sum_{u=1}^{N} X_{iu} = 0; \ \sum_{u=1}^{N} X_{iu}^2 = N; \ \sum_{u=1}^{N} X_{iu} X_{ju} = 0.$$

where u—the number of columns in matrix and N—the number of experiments. These conditions correspond to the symmetry, normalization, and orthogonality of the planning matrix.

The analysis of these conditions for the EPM, containing GV, shows that in the EPM building, the GV plays the role of factors, consisting of a number of parameters. Of course, while building the planning matrix in the form of GV, all the mentioned conditions are fully hold, i.e.,

$$\sum_{u=1}^{N} \pi_{iu} = 0; \; \sum_{u=1}^{N} \pi_{iu}^2 = N; \; \sum_{u=1}^{N} \pi_{iu}\pi_{ju} = 0.$$

The GV variation is achieved by varying the parameters included in it. If we analyze the matrix columns, relating to one of GV, the following is noted:

$$\sum_{u=1}^{N} X_{iu}\pi_{iu} = 0; \; \sum_{u=1}^{N} (X_{iu}\pi_{iu})^2 = N; \; \sum_{u=1}^{N} X_{iu}\pi_{iu}X_{ju}\pi_{ju} = \pm N.$$

where $X_{iu}\pi_i$—the parameter in the kth of GV, $+N$ corresponds with multiplication, and $-N$ corresponds with division. It will be seen that the EPM has the orthogonal and symmetric properties. In principle, there can be a variety of options of the GV, as by a combination of parameters and as by a combination of structures.

For the convenience of presentation, the proposed method is used as an example of variation of three GV:

$$\pi_1 = \frac{A}{BC}; \; \pi_2 = \frac{DM}{A}; \; \pi_3 = \frac{A}{NK}.$$

The GV variation limits are defined by the specific deviation parameters. The upper level is:

$$\pi_1 + \Delta\pi_1 = \frac{(A+\Delta A)}{(B+\Delta B)(C-\Delta C)};$$

$$\pi_2 + \Delta\pi_2 = \frac{(D+\Delta D)(M+\Delta M)}{(A-\Delta A)};$$

$$\pi_3 + \Delta\pi_3 = \frac{(A-\Delta A)}{(N-\Delta N)(K-\Delta K)}.$$

The lower level is:

$$\pi_1 - \Delta\pi_1 = \frac{(A-\Delta A)}{(B+\Delta B)(C+\Delta C)};$$

$$\pi_2 - \Delta\pi_2 = \frac{(D-\Delta D)(M-\Delta M)}{(A+\Delta A)};$$

$$\pi_3 + \Delta\pi_3 = \frac{(A-\Delta A)}{(N+\Delta N)(K+\Delta K)}.$$

Let us assume that in the first experiment, all A's must be at the upper level. In this case, the values of π_1 and π_3 have to be at the top level, and the values of π_2 are

at the lower level. Of course, both these conditions are not feasible. In these cases, the proposed parameters, occurring simultaneously in several GV, leave at the basic level. This way, setting of the upper and lower levels is achieved through the proportional changes of other parameters included in the GV. It is the proportionality of changes of the remaining GV allows to objectively maintain the regularity in the relationship between the GV and the target function.

The planning matrix of the full factorial experiment (FFE) for this case is shown in Table 2.5. The symbols used in the planning matrix are:

A, B, C, D, M, N, K—the baseline parameters; $\Delta B'$, $\Delta C'$, $\Delta D'$, $\Delta M'$, $\Delta K'$, $\Delta N'$—the parameter increments to compensate for the necessary change of parameters in order to achieve the levels of the corresponding changes of the GV, i.e., additional increment;

ΔA, ΔB, ΔC, ΔD, ΔM, ΔK, ΔN—the parameter increments corresponding to changes of the GV, i.e., major increments. The implementation of this matrix and the corresponding processing of results will determine the regression equation of the GV.

2.3 Application of Group Method of Data Handling with Respect to Tribotechnical Problems

The method for creating the friction and wear mathematical models, using the theory of similarity, dimensions, and the mathematical planning of experiment, is progressive, since the transition to GV dramatically reduces the number of factors to be considered, reduces the time and labor to carry out the experimental studies, and provides reasonable enough values for output parameters.

Let us illustrate this by comparison. Suppose that we need to give a mathematical description of process with one objective function and 8 variable parameters. For the mathematical definition, in accordance with the theory of experimental planning, it is necessary to have $N = 2^8 = 256$ experiments at the FFE, and an average of two overlapping randomizations, and these are additional 512 experiments. Thus, the total number of required tests becomes 768. We assume that these variables are included in the three criteria of similarity. In this case, the mathematical description will require $N = 2^3 = 8$ experiments. Consider that the duplication has the total number of required experiments equal to 24. Thus, the number of experiments reduces by 32 times. The comparison shows a clear advantage of combining the two methods—the theory of similarity and the experimental planning. The advisability of such a synthesis is obvious, since it leads to the optimal use of the capabilities of each of the methods.

The comprehensive review of all the opportunities arising from the combination of methods of the theory of similarity and the statistical methods seems to us very important.

Table 2.5 The planning matrix of the full factorial experiment

#	π_1				π_2				π_3			
1	+	A	$B-\Delta B-\Delta B'$	$C-\Delta C-\Delta C'$	+	A	$D+\Delta D+\Delta D'$	$M+\Delta M+\Delta M'$	+	A	$N-\Delta N-\Delta N'$	$K-\Delta K-\Delta K'$
2	−	A	$B+\Delta B+\Delta B'$	$C+\Delta C+\Delta C'$	+	A	$D+\Delta D+\Delta D'$	$M+\Delta M+\Delta M'$	+	A	$N-\Delta N-\Delta N'$	$K-\Delta K-\Delta K'$
3	+	$A+\Delta A$	$B-\Delta B$	$C-\Delta C$	−	$A+\Delta A$	$D-\Delta D$	$M-\Delta M$	+	$A+\Delta A$	$N-\Delta N$	$K-\Delta K$
4	−	A	$B+\Delta B+\Delta B'$	$C+\Delta C+\Delta C'$	−	A	$D-\Delta D-\Delta D'$	$M-\Delta M-\Delta M'$	+	A	$N-\Delta N-\Delta N'$	$K-\Delta K-\Delta K'$
5	+	A	$B+\Delta B+\Delta B'$	$C+\Delta C+\Delta C'$	+	A	$D+\Delta D+\Delta D'$	$M+\Delta M+\Delta M'$	−	A	$N+\Delta N+\Delta N'$	$K+\Delta K+\Delta K'$
6	−	$A-\Delta A$	$B+\Delta B$	$C+\Delta C$	+	$A-\Delta A$	$D+\Delta D$	$M+\Delta M$	−	$A-\Delta A$	$N+\Delta N'$	$K+\Delta K$
7	+	A	$B+\Delta B-\Delta B'$	$C+\Delta C-\Delta C'$	−	A	$D-\Delta D-\Delta D'$	$M-\Delta M-\Delta M'$	−	A	$N+\Delta N+\Delta N'$	$K+\Delta K+\Delta K'$
8	−	A	$B+\Delta B+\Delta B'$	$C+\Delta C+\Delta C'$	−	A	$D-\Delta D-\Delta D'$	$M-\Delta M-\Delta M'$	−	A	$N+\Delta N+\Delta N'$	$K+\Delta K+\Delta K'$

2.3.1 Development of Mathematical Model with Initial Variables

The modern statistical methods of planning and analysis of experiments are increasingly used in the scientific research; with their help, we can significantly improve the efficiency of researches, requiring the considerable financial costs and long terms [7, 10, 29, 30]. The effect is especially significant in the study of complex multifactorial processes such as friction and wear processes [1]. The action of a large number of random factors usually leads to a fact that a proceeding of deviation does not always become "low," and they cannot be considered as corrections. The introduction of the various "factors of ignorance" reduces the quality of the calculations.

Most systems operate in accordance with the Pareto principle, which states that in terms of the system performance, there are only few important factors out of many. Indeed, in the most systems, the 20 % of factors define the 80 % of system, and the remaining 80 % of factors determine only 20 % of the system properties. Our task is to identify the significant factors [31]. To solve this problem, it is advisable to use the methods of group data handling (MGDH), a priori factor ranking, the rank correlation, the random balance, and others. The rational choice of an appropriate method is determined by the presence of a priori information about the tested process and the complexity of experiments.

At the present time to establish a connection between the input and output parameters, and to obtain the mathematical model that is adequate to the studied object, there are the widely used regression analysis and the method of group data handling (MGDH) [32]. We set n input variables $x_1, x_2, \ldots, x_n$ and output variable y. The search of the tribotechnical functional dependence $y = f(x_1, x_2, \ldots, x_n)$ is carried out in the class of polynomial functions, producing a sequential scan of the input variables and their various combinations in order to choose the most appropriate which will allow the best way to describe the experimental data. Two criteria determine the quality of description in MGDH, either the regularity criterion or criterion of a minimum offset [32].

We choose the selection criterion matching the requirements of desired model. The regularity is the main criterion, if the high accuracy is required from the model.

The model becomes more stable with respect to the initial experimental data when using the minimum offset criterion; in other words, by gradually increasing the complexity of model while changing the set of experimental data, the coefficients remained unchanged. The final mathematical model was presented as follows:

$$y = A_0 + \sum_{n=1}^{S} A_i Z_i,$$

where y—the output parameter; $A_0, A_1, \ldots, A_S$—the coefficients of mathematical model; Z_i—the generalized factor, a kind of GV, which are included in the test mode settings. The structure of the generalized factor is defined as follows:

$$Z_1 = \prod_{n=1}^{n} x_i^{k_{ij}}; \quad k_{ij} = 0, 1, 2.$$

The experiment is designed in accordance with the selected model and the study objectives. There are several ways of constructing the planning matrix of large dimension [33]. Here, we used a FFE. The planning and implementation of FFE consist of the following main steps: the selection of factors and levels and their variation; the encoding of factors; drafting up the EPM; the randomization of tests; and the implementation of the experiment plan.

There are literatures with a detail description on how to draft the EPM [34, 35]. In this work, we study the effect of sliding speed—V, loading—P, and braking work—W on the coefficient of friction during braking. After selecting variables and domain, there is a need to find a local area for the experiment. This procedure involves the choice of levels of the varying factors.

In order to start encoding, we initially choose the starting area of experiment by setting the upper and lower limits of change for each factor during the experiment. The upper level corresponds to $+1$, the lower level corresponds to -1, and the main is set at 0. It is easily done by using the formula that connects the values of factors in the coded scale (x_i) with ones in the natural scale (X_i):

$$x_i = \frac{X_i - X_{i_0}}{\Delta X_i}.$$

$$X_i - X_{i_0} = \Delta X_i x_i,$$

where $\Delta X_i = X_{i_{\max}} - X_{i_{\min}}/2$—the variation interval; X_{i_0}—the main level.

It should be noted that in the general case, the selection of the variation interval depends on the given problem.

We present the planning matrix and the test results of the experimental planing 2^3 of the friction material ФК-24А (for other materials the planning matrix is established in a similar way, see Table 2.6).

The three major classes of friction pad materials were tested (asbestos–resin, asbestos–rubber, metal–ceramic) pairing with steel 40ХН for the descending mode of the drilling tool in accordance with the drafted planning matrix. After processing the experimental data on the computer, the following mathematical model of the studied object is obtained, i.e., the equation relating the coefficient of friction f with predetermining factors:

for the friction material ФК-24А

Table 2.6 Planning matrix and the test results

Factors		v	P	W	f_e	F_c
Main level		3.5	355	7.5		
Upper level		4.2	430	9.5		
Lower level		2.8	280	5.5		
Variation level		0.7	75	2.0		
Code designation		x_1	x_2	x_3	y_e	y_c
	1	+1	+1	+1	0.26	0.301
	2	+1	+1	−1	0.28	0.312
	3	+1	−1	+1	0.30	0.297
	4	+1	−1	−1	0.29	0.309
	5	−1	+1	+1	0.34	0.332
	6	−1	+1	−1	0.33	0.339
	7	−1	−1	+1	0.31	0.320
	8	−1	−1	−1	0.34	0.328
	9	+R	0	0	0.35	0.300
	10	−R	0	0	0.37	0.314
	11	0	+R	0	0.36	0.319
	12	0	−R	0	0.32	0.312
	13	0	0	+R	0.28	0.300
	14	0	0	−R	0.29	0.315
	15	0	0	0	0.30	0.321

$$f_1 = 0.312 - 0.0308 \frac{v \cdot W^2}{P} + 0.0045 \frac{P}{v^4} + 4.785 \frac{v \cdot W}{P^2};$$

for the friction material Б—42

$$f_2 = 0.336 + 0.873 \frac{v^2}{P} + 0.000466 \frac{v^4 \cdot W}{P};$$

for the friction material МКБ—50

$$f_3 = 0.202 + 0.6017 \times 10^{-7} \cdot P^2 W + 0.92 \frac{1}{v \cdot W} + 27.596 \frac{1}{P}.$$

The indicator of successful synthesis of modeling of complex processes is the minimum depth of the basic selection criterion. All parameters of the calculated MGDH algorithms, as well as the structure of these algorithms, are chosen by selecting the number of options so as to obtain the deepest minimum. The modeling will not be considered complete if it cannot get the deepest minimum.

As shown in [32], the allowable minimum depends on the intensity of noise and it is 5–10 % for the usually occurring measuring accuracy of variables. The resulting models adequately reproduce the studied braking process, since the error of these equations according to the original sample is within 6–7 %, which is acceptable.

The resulting tribological functional dependences (the mathematical models) for various friction materials allow to reliably predict the behavior of the friction unit in the braking regime. The concept of a generalized factor is introduced, and its structure is formulated.

2.3.2 Development of Mathematical Model with Generalized Variables

Studying the friction and wear of various parts of machines, it is advisable to obtain a mathematical model, which is expressed as a tribotechnical functional relationship of the main regime, design, and operational parameters which determine the nature of the tested process. These dependencies can become main information that will be used by designers to create new designs of friction devices and their further operation.

However, the creation of mathematical models of friction and wear has a number of difficulties: the uncertainty in setting up the initial information; its probabilistic nature forces to conduct a large amount of experiments. In order to systematize the results of experiments, to determine the main characteristics of communication, to combine them into a general quantitative regularities it requires the experimental planning and the determination of minimum number of experiments. The mathematical model of process can be obtained using the modeling techniques and the statistical methods of experiment design.

During the braking process, a number of variables become a crucial factor [1]. With a large number of variables, it is extremely difficult and even practically impossible to bring the results into a specific system or to find the general quantitative regularities. Studying such a complex physical tasks, it is necessary to introduce a lot of dissimilar variables, and each of these quantities is considered as an independent variable.

Based on very general physical considerations, the multiplicity of relationships is not a specific property of the studied problems defined by their physical nature [11]. It is shown that the effect of individual factors, represented by the different values, should not be not considered individually, but as a complex, and that in fact it is necessary to consider not these individual values, but their combination defined for each process. It is known the method of constructing such populations—a method that allows the direct analysis of the problem formulation to find a connection between the individual values and their groups, and to combine them in the well-defined complexes of the specific form [11].

Thus, the new variables are inherently generalized and their application gives the whole analysis a generalized nature. The analysis prerequisite is the completeness of the initial information given by the parameter list, drawn up on the basis of the adopted process model by the researcher.

Since the studied process of friction is random, the task is, using the appropriate GV defining the friction and wear process in the braking units of the oil drilling equipment, to obtain the consolidate tribological functions for the qualitative and quantitative evaluations of the tested processes on the basis of the mathematical models.

The generalized equation obtained using the theory of dimensions for the braking process during the descent of drilling tool is presented in [17]. The explicit form of the generalized equation can be obtained by the statistical processing of the individual results of experiments.

Drawing up the plan and the experimental techniques, the following GV are selected to define the process:

the generalized thermal conductivity

$$\pi_\lambda = \pi_1 = \frac{\lambda_1 \cdot \lambda_2 \cdot \lambda_3 \cdot \vartheta_1^{\frac{3}{2}} \cdot \vartheta_2^{\frac{3}{2}}}{P^3 \cdot v^3 \cdot K_{\Gamma_1}^{-\frac{1}{2}} \cdot K_{\Gamma_2}^{-\frac{1}{2}}};$$

the generalized hardness

$$\pi_{HB} = \pi_2 = \frac{HB_1 \cdot HB_2 \cdot K_{\Gamma_1}^{\frac{2}{3}} \cdot K_{\Gamma_2}^{\frac{2}{3}}}{P^2};$$

the generalized braking work

$$\pi_w = \pi_3 = \frac{W_{\text{Т.П.}}}{P \cdot K_{\Gamma_1}^{\frac{1}{6}} \cdot K_{\Gamma_2}^{\frac{1}{6}}};$$

the generalized variable deceleration time

$$\pi_t = \pi_4 = \frac{v \cdot t}{K_{\Gamma_1}^{\frac{1}{6}} \cdot K_{\Gamma_2}^{\frac{1}{6}}}.$$

Here, π_1—the one of the main indicators of the material thermophysical properties; π_2—the hardness parameter, included in the molecular-mechanical model of friction, is the principal value; π_3 and π_4—the parameters defining the operation regime that have a great influence on the brake.

The experiment planning and methodology to identify the quantitative relations of the studied variables are described in detail in [17, 30]. Let us represent the planning matrix and the experimental results for the FFE type 2^4 of the friction

Table 2.7 The generalized mathematical model

Factors	π_1	π_2	π_3	π_4
Main level	2.5×10^3	16×10^6	3.3	11
Upper level	3×10^3	20×10^6	4.0	14
Lower level	2×10^3	12×10^6	2.0	8
Variation level	0.5×10^3	4×10^6	0.7	3
Code designation	x_1	x_2	x_3	x_4

material ΦK-24A (the planning matrix for other materials will be similar). The MGDH is explicitly employed to build the generalized tribotechnical functions.

In order to establish the relationship between the friction process and the GV, the test is conducted for the friction pad materials of three major classes (of asbestos resin, of asbestos, rubber, metal–ceramic) paired with the steel 40XH for the descending regime of the drilling tool in accordance with the planning matrix. The generalized mathematical model was adopted as in Sect. 2.3.1 (Table. 2.7).

After processing the experimental data on the computer the following mathematical model is obtained, i.e., the equation relating the coefficient of friction f with its predetermined GV:

for the friction material ΦK-24A

$$f_1 = 0.294 - 0.1287 \times 10^{-5} \pi_1 \cdot \pi_3 \cdot \pi_4 + 0.29 \times 10^{-9} \pi_2 \cdot \pi_3$$
$$+ 21.36 \frac{\pi_1 \cdot \pi_4}{\pi_2} + 0.86 \times 10^{-8} \frac{\pi_2^2 \cdot \pi_3^4}{\pi_2} + 0.01546 \frac{\pi_1 \cdot \pi_4}{\pi_2}$$
$$- 3.21817 \frac{\pi_2^2 \cdot \pi_3^3}{\pi_1^5 \cdot \pi_4^5} - 0.239 \frac{\pi_1^3 \cdot \pi_3^5 \cdot \pi_4^3}{\pi_3^3} + 0.4 \times 10^{-9} \pi_1^3 \cdot \pi_3;$$

for the friction material Б-42

$$f_2 = 0.413 - 0.135 \times 10^{-6} \frac{\pi_2}{\pi_3^2} - 0.163 \times 10^{-6} \pi_1 \cdot \pi_3 \cdot \pi_4 - 0.368 \times 10^{-8} \frac{\pi_2^3}{\pi_1^2 \cdot \pi_3^3 \cdot \pi_4^2}$$
$$- 0.321 \times 10^{-8} \frac{\pi_2^3}{\pi_1^2 \cdot \pi_3^8 \cdot \pi_4^2} + 0.367 \times 10^{-3} \frac{\pi_1^2 \cdot \pi_4}{\pi_2 \cdot \pi_3^3} + 11.138 \frac{\pi_2^2}{\pi_1^3 \cdot \pi_3^7 \cdot \pi_4^2}$$
$$+ 0.825 \times 10^{-7} \frac{\pi_1^6 \cdot \pi_4^2}{\pi_2^3 \cdot \pi_3^6} + 0.6693 \times 10^{-4} \frac{\pi_2}{\pi_1} + 0.189 \times 10^{-5} \frac{\pi_1^7 \cdot \pi_4}{\pi_2^4 \cdot \pi_3^3}$$
$$+ 0.4275 \times 10^{-8} \frac{\pi_2^2 \cdot \pi_3^3}{\pi_1^2};$$

for the friction material MKB-50

$$f_3 = 0.271 + 0.877 \times 10^{-8} \pi_1^2 \cdot \pi_4 + 3.99 \frac{1}{\pi_3^2 \cdot \pi_4} - 0.1676 \times 10^{-6} \frac{\pi_1^6}{\pi_3}$$
$$+ 17.79 \frac{\pi_1^1}{\pi_2 \cdot \pi_3^8 \cdot \pi_4^5} - 0.7426 \times 10^{-8} \frac{\pi_1^2 \cdot \pi_4}{\pi_3^2};$$

As shown in Sect. 2.3.1, the problem of modeling will not be considered solved if it does not get enough deep minimum, and only upon reaching it, the problem will be solved, with the practical measurement accuracy equal to 5–10 %. The resulting models adequately reproduce the studied friction process during braking, and according to the original sample, the error of these equations is within 3–5 %, which is acceptable.

The resulting generalized tribological functions (the mathematical models) for the different friction materials allow us to reliably predict the behavior of friction unit in the braking mode. They can also be used in the formulation of engineering calculations associated with the estimation of the friction and wear characteristics.

The foregoing also demonstrates the undoubted benefits of combining the methods of theory of similarity and the modeling methods with the experimental design. Of course, such synthesis will be beneficial and, as shown above, lead to the significant improvement of their individual application.

The results of obtained generalized description can be applied to all similar processes.

Literatures

1. E.D. Braun, Iu.A. Evdokimov, A.V. Chichinadze, Modelirovanie treniia i iznashivvaniia v mashinah (Mashinostroenie, Moscow, 1982), p. 191
2. A.M. Kuliev, Uproshchennyi podhod k opredeleniju raspredeleniia veroiatnostei kriteriev podobiia. Izv. AN SSSR, energetika i transport, № 2, 167–171 (1980)
3. I.M. Melamedov, *Fizicheskie osnovy nadezhnosti* (Energiia, Leningrad, 1970), p. 152
4. A.Kh. Mirzadzhanzade, S.A. Shirinzade, *Povyshenie effektivnosti i kachestva bureniia glubokikh skvazhin* (Nedra, Moscow, 1986), p. 278
5. L. Mitchell, C. Osgood, Prediction of the reliability of mechanisms from friction measurements. First European Tribology Congress. (Inst. Mech. Engrs, New York), pp. 63–70 (1975)
6. V.V. Bolotin, *Primenenie metodov teorii veroiatnostei i teorii nadezhnosti v raschetah sooruzhenii* (Stroiizdat, Moscow, 1971), p. 255
7. V.A. Venikov, G.V. Venikov, *Teoriia podobiia i modelirovaniia* (Moscow, Vysshaia shkola, 1984), p. 439
8. Kilbern, Trenie kak sluchainyi protsess. V kn.: Problemy treniia i smazki, **96**(2), 104–117 (1974)
9. V.N. Mastachenko, *Nadezhnost' modelirovaniia stroitel'nykh konstruktsii* (Moscow, Stroiizdat, 1974), p. 84
10. B.G. Keglin, Parametricheskaja nadezhnost' friktsionnykh ustroistv (Mashinostroenie, Moscow, 1981), p. 135
11. A.Kh. Janahmadov, *Fiziko-stokhasticheskoe tribomodelirovanie* (Baku, Elm, 1988), p. 152
12. V.A. Venikov, A.M. Kuliev, Veroiatnostnaia traktovka kriteriev podobiia. Izv. AN SSSR, energetika i transport, № 2, 26–35 (1974)
13. A.Kh. Janahmadov, A.M. Kuliev, V.I. Abdullaev, Analiz raspredelenii veroiatnostei kriteriev podobiia, primeniaemykh dlia issledovaniia protsessa treniia. Tezisy dokladov mezhdunarodnoi konferentsii: Trenie, iznos i smazochnye materialy, Tashkent **5**, 65–67 (1985)
14. E.S. Ventsel', Teorija veroiatnosteji (Nauka, Moscow, 1969), p. 576

15. Sbornik zadach po teorii verojatnostei, *matematicheskoi statistike i teorii sluchainykh funktsii* (Nauka, Moscow, 1970), p. 656

16. N.P. Buslenko, *Modelirovanie slozhnykh sistem* (Nauka, Moscow, 1969), p. 576

17. S.M. Mustafaev, A.Kh. Janahmadov, Issledovaniia protsessa vneshnego trenija v friktsionnykh uzlakh metodami teorii inzhenernogo eksperimenta. Izv. vuzov SSSR, Neft' i gaz, № 7, 85–88 (1975)

18. S.M. Ermakov, G.A. Mikhailov, *Statisticheskoe modelirovanie* (Nauka, Moscow, 1982), p. 296

19. I.M. Sobol', *Chislennye metody Monte Karlo* (Nauka, Moscow, 1973), p. 311

20. G. Kramer, *Matematicheskie metody statistiki. per. s angl.* (Mir, Moscow, 1975), p. 648

21. H. Weyl (1916) Über die Gleichverteilung von Zahlen mod Eins. Math. Annalen, **77**, №3, 313–352 (1916)

22. J.H. Halton, On the efficiency of certain quasirandom sequences of points in evaluating multi-dimensional integrals. Numer. Math. № 2, 84–90 (1960)

23. I.M. Sobol', *Mnogomernye kvadraturnye formuly i funktsii Haara* (Nauka, Moscow, 1969), p. 288

24. Iu.G. Polliak, Veroiatnostnoe modelirovanie na elektronnykh vychislitel'nykh mashinah (Sovetskoe radio, Moscow, 1971), p. 400

25. V.V. Stepanov, *Kurs differentsial'nykh uravnenii* (Gostekhizdat, Moscow-Leningrad, 1950)

26. I.G. Zhurbenko, *Analiz statsionarnykh i odnorodnykh sluchainykh sistem* (Izdatel'stvo Moskovskogo Universiteta, Moscow, 1997), p. 240

27. M.P. Aleksandrov, E.D. Braun, V.N. Fedoseev, Modelirovanie protsessa iznosa friktsionnykh par tormozov PTM po dolgovechnosti. Tezisy dokladov III-go mezhvedomstvennogo seminara: Trenie, iznos i metody ispytanii asbofriktsionnykh materialov. (TsNIITEneftehim, 1973)

28. G. Han, S. Sapiro, *Stasticheskie modeli v inzhenernykh zadachah* (Mir, Moscow, 1969)

29. Iu.A. Evdokimov, V. Kolesnikov, A.I. Teterin, Planirovanie i analiz eksperimentov pri reshenii zadach trenija i iznosa (Nauka, Moscow, 1980), p. 228

30. S.M. Mustafaev, A.Kh. Janahmadov, Nekotorye voprosy modelirovaniia protsessa trenija na statisticheskoi osnove. Izv. AN Azerb. SSR seriia fiziko-tekhnicheskikh i matematicheskikh nauk, № 3, 80– 83 (1977)

31. R. Shennon, Immitatsionnoe modelirovanie sistem – iskusstvo i nauka (Mir, Moscow, 1978), p. 418

32. A.G. Ivahnenko, *Induktivnyi metod samoorganizatsii modelei slozhnykh sistem* (Naukova dumka, Kiev, 1982), p. 296

33. V.V. Nalimov, T.I. Golikova, *Logicheskie osnovanija planirovaniia eksperimenta* (Moscow, Metallurgija, 1981), p. 152

34. V.V. Nalimov, N.A. Chernova, *Statisticheskie metody planirovaniia ekstremal'nykh eksperimntov* (Nauka, Moscow, 1965), p. 340

35. L.Ia. Ruzinov, *Statisticheskie metody optimizacii himicheskikh processov* (Khimiia, Moscow, 1972), p. 199

Chapter 3
Synergetic Model of Fracture and Mechanics of Fatigue Cracks During Friction

The difficulty with predicting the fatigue failure of metals and alloys is due to the fact that the fatigue resistance depends on several factors: the type and condition of loading, the stress state of node details, the asymmetry of loading cycle, the scale factor, temperatures, the structural state of material, the media influence, and the state of friction surface.

All this makes it very difficult to create a common synergetic model of the fracture mechanics and the mechanics of fatigue cracks upon the contact of solids. This is due to the introduction of new concepts, one of which relates to the self-organization of the friction process. The basic principle of self-organization is that the changes of external parameters or the method of loading cycles does not cause a hierarchy of structures that can be formed by the system, but implements the possible mechanism of destruction. Through time and space, the structures can be complicated and move from a less ordered to a more ordered process of self-organization.

The interpretation of the destruction phenomenon requires an involvement of specialists from various fields of science, such as physics, mechanics, chemistry, and design engineers—in the real world, the process of destruction is manifested itself in a very multifaceted way. This is linked with the variety of the elementary acts of destruction, the interpretation of which until recently dominated the model representations, which are based on the simple geometric figures proposed by Griffiths, Orovan, and others. However, it has become clear that the physics of destruction requires a further development of the basic ideas. In recent years, there have been attempts to use the nonlinear methods to develop the concept of broken bonds, the models are developed for the elementary carriers of destruction, there are methods of the theory of similarity and synergetics that are developed at the macroscopic level. The development of the latest general physical concepts of the theory of self-organization and the nonlinear phenomena have made it possible to further understand the nature of fracture mechanics in the interacting contact of solids.

3.1 Synergetic Analysis of Plastic Deformation and Fracture Using Bifurcation Doubling Model

Over the last fifty years, the solid strength science rapidly evolved into a new direction, based on the kinetic thermo-activation approach to the mechanisms and relationships of the plastic deformation (PD) and the fracture of real materials [1–3].

For a long time, the processes of PD were associated with the evolution of various types of the crystal defects, which interacted with each other and affected by the external fields, remained the independent structural formations specific to their properties (the geometric configuration, the distribution of the elastic fields, etc.) [4–6]. As part of this concept, PD seemed as a result of the ergodic behavior of the system defects, the trajectory of which was filling the space over time.

Due to primarily works of S.N. Zhurkov, a new approach is developed to understand the destruction—the kinetic approach. It is established [7–9] that the destruction is not a critical event but a process developing over time, and the decisive role in overcoming the potential barrier belongs to the thermal fluctuations, and the external loading only slightly reduces the height of the potential barrier and prevents the recombination of broken bonds.

The crack gets born and develops in the volume of materials which are prepared for the destruction in the first period—the period of accumulation of various defects and damages. Therefore, the problem of fracture mechanics which studies the kinetics of crack growth is to inextricably link with the development of evaluation method and account for the degree of damage (state) of a deformable element of body with the kinetics of crack growth.

The solids, constituting element of whole structure, during its operation undergo set of complex loading cycles varying in the level of frequency and duration. The multifactorial situation with the material impact during the fatigue crack involves a comprehensive synergetic analysis of process [10, 11].

The purpose of material self-organization and the kinetics of fatigue cracks are to save the ability to resist the external cyclic exposure with a minimum expenditure of energy on the creation of free surface per loading cycle.

The established by Ivanova [12], the discrete Δ-dependence on the kinetic diagrams of the fatigue crack growth (FCG), on the temperature diagrams of the yield strength, shows the implementation of the most simple bifurcation schemes in the metal under load—the period-doubling schemes of Feigenbaum [13, 14].

There are many systems of different nature (from hydrodynamics to electronics), undergoing a change at the control parameter hierarchy of the successive period doubling, when with the increase of excitation in the system of nonlinear oscillators along with the basis frequency appear the frequencies of 1/2, 1/4, 1/8, … of the basis. This phenomenon, known as a period doubling, is typical for the self-organizing systems [14]. This leaves the question on the physical conditions open, the conditions under which the mechanism of period doubling is possible.

In favor of the correctness of synergetic approaches to the analysis of FCG, i.e., a compliance with the requirements of self-organizing system that can serve the following reasons [15]:

1. the system—sample loading device is a dynamic open system;
2. the system consists of a large number of stochastically described subsystems (oscillators);
3. upon the excitation of crystal, the intensity of interaction between adjacent oscillators increases and the interaction becomes increasingly nonlinear.

The entropy decreases $(dS < 0)$ due to the pumping energy into the open non-linear system, which is a clear sign of the self-organization [16]. Moreover, far from the thermodynamic equilibrium, the behavior of nonlinear oscillators, which are under the influence of the harmonic external force, can be described by the equations known as Duffing [17]

$$\ddot{x}_i + \alpha \dot{x}_i + \beta x_i + \gamma x_i^3 = A_0 + A_1 \sin(\omega_0 t),$$

where α, β, γ—the crystal constants and A_0, A_1, ω_0—the parameters of the external periodic loading. The analysis of these equations shows that with an increase in the control parameter A_1, the sequential doubling of the period takes place [14].

In work [13], it is shown that the subharmonic half frequency, appearing after the bifurcation, is less dense than the fundamental. After a large number of bifurcations, the system behaves aperiodically, forming a continuous broadband spectrum.

As stated in [15], at least for the metals of cubic system, the frequency of Einstein (ω_E) and Debye (ω_D) is related by the relationship $\omega_E \sim \frac{\omega_D}{2}$. Now taking into account that the function of the phonon density of $F(\omega)$ has extremums in the vicinity ω_D and ω_E, and $F(\omega_D) > F(\omega_E)$, we can assume that broadband phonon spectrum of these metals is obtained with the fundamental frequency, for example ω_D, due to a large number of period-doubling bifurcations.

Thus, the implementation of the successive period-doubling mechanism in the system of nonlinear oscillators allows explaining the nature of discrete Δ-depending of V.S. Ivanova. It is particularly worth noting that the model within the period of doubling of Δ-dependence is not an approximation and it is accurate. The experimentally observed deviations are made through the experimental error and by blurring the frequency characteristic ω_*, which expresses the value of $\delta U = \text{const}$—a discrete decrease of the activation energy, the equivalent of phonon absorption:

$$\delta U = \hbar \omega_*,$$

where $\hbar$—the Planck's constant.

Depending on the temperature, there is distinction between the unsteady and steady creep, respectively, characterized by the extremely slow (approximately logarithmic) and by the linear increase of deformation over time. The first type of creep is shown at temperatures T, making less than half of the value of the melting

temperature T_m, and is characterized by falling of the strain rate to zero during the time of the constant loading. The second type is observed at temperatures $T > T_k$, where $T_k > 0.5T_m$, and it is characterized by the release of the strain rate as $t \to \infty$ at the final value of $K(\sigma) \neq 0$, where σ—the external loading. The consistent theory of transient creep is developed by Olemski [18–20]. He proved that in the case of very large values of the shear viscosity η, the chained process occurs forming a thermal cluster, with probability $P \sim \exp\left(-\frac{Q}{T}\right)$ (where Q—the thermodynamic potential (TP)) and the frustrons get together in pairs, and then with the same probability pairs form a quartet, etc., which seems obvious in the form of a multitier "Cayley tree." The super defects are formed by the coherent communication in the lower structural level of the tree. Since the tighter minimums are responsible for the TP dependence on the configuration coordinates of the initial defects rather than the super defects, the establishment of hierarchical subordination leads to the fractal structure distribution of TP in the configuration space. The probability density $w(u)$ of the chain process of the frustrons clustering, separated by the distance u in the ultrametric topology of the hierarchical structure, at the strong hierarchical subordination is expressed by the degree of dependence $w(u) \sim u^{-D}$, where $D\,(0 < D < 1)$—the fractal dimension of the potential relief, that determines the height Q of the TP values, which provides the slow logarithmic dependence for the probability $P(t)$ of lacking destruction at time t, i.e., it slows down the process of destruction. The mentioned critical slowing takes effect only at the initial period $t \ll \tau_{max}$, and when $t > \tau_{max}$, the relation becomes following $P(t) \sim \exp\left(-\frac{t}{\tau_{max}}\right)$ [21].

This phenomenon is consistent with the kinetic theory of damage [22, 23]. From a thermodynamic point of view, all elementary acts of the PD process and the fracture of real materials can be divided into two distinct groups with the different kinetic regularities. The first group of the elementary acts of the atomic and molecular rearrangements is associated with the origin and accumulation of various defects and damages at obstacles. These elementary acts control the strain hardening and the volumetric damage of material. The elementary acts of the second group are associated with the origin, movement, and disposal of various elementary defects at effluents. These microscopic processes control the quasi-viscous flow of materials and dynamic recovery (rest), and they are responsible for the transformation (conversion) of the irreversible deformation energy into the thermal energy, which is manifested itself in the form of the thermal effect of the PD.

Until recently, the methods of equilibrium statistical physics have been used in the study of the condensed medium. This is due to the assumption that the condensed medium, under the influence, represents the equilibrium or slightly non-equilibrium statistical system. However, there is a growing interest in phenomena such as the behavior of statistical system of atoms in the condensed state looses its usual applicability (the concept of phonons or the thermodynamic pictures of the phase transitions) or requires a fundamental review. This behavior is explained by the strong deviation of the atomic system from its equilibrium state, as it is the case in the core of defected lattice or areas of the plastic flow and fracture. The consistent pattern of the strongly non-equilibrium condensed medium requires

the use of techniques that allow us to represent properties such as the non-ergodicity of statistical ensemble, the emergence of hierarchical structures, the structural relaxation, the mutual influence of subsystem undergoing the phase transition, and the environment. The comprehensive study of the atomic state restructuring at a considerable distance from equilibrium is achieved based on the synergetic pattern representing the evolution of mutually agreed hydrodynamic modes parameterizing system [24]. It is shown that the thermodynamic potential corresponding to the different types of one-dimensional long-period structures has a fractal nature, so that the movement of the hierarchical tree determines the evolution of the system. The systems with a strongly pronounced hierarchy of one-dimensional long-period structures are particularly stable or slowly relax from one type to another. The presence of long-range one-dimensional long-stabilizing structures contributes to the growth of their period.

Considering the macroscopic picture of destruction, in accordance with the variety of manifestations of an ensemble of elementary carriers [25, 26], there are possible different scenarios for the evolution of the system. They are defined by two limiting regimes, the first of which corresponds to the usual picture of the formation and growth of a new phase—the elementary carriers' fluctuation combined into a hotbed of destruction, which grows by the gradual influx of the lattice defects. In the other limiting mode, the gradual union of destructors occurs—first the elementary carriers form the clusters, i.e., joining into superclusters until the formation of the main crack. This limiting mode is implemented in the process of fatigue failure. In this case, to describe the evolution of defects, it is convenient to use the concept of ultraparametric space with the hierarchical Cayley tree of the chain association of clusters [24].

The following is an analysis of the principles of synergy and fractal theory in the study of the evolutionary process of restructuring of the condensed state of the crystal structures under the intensive external influence, and the connections between the micro-kinetics of process with its tribological problems are established.

It is considered that the destruction is possible if the flow of energy at the crack tip W_i reaches a certain critical value [1], which implies the energy failure criterion

$$W_i \geq U_0, \tag{3.1}$$

where U_0—the maximum value of the density of the internal energy U.

Griffith's theory and the destruction as a critical event are built on the concepts of the classical mechanics, i.e., they require that the inequality (3.1) is to be held and does not take into account the time of development process.

Over the past 50 years (primarily through the works of S.N. Zhurkov), a new approach is developed for the destruction process—the kinetic and as shown by numerous experiments [2, 7, 27]

$$W_i = \gamma \cdot \sigma \ll U_0. \tag{3.2}$$

Thus, Zhurkov laid the foundations for a new approach in the process of destruction and experimentally proved the possibility of failure at $W_i < U_0$. But at the same time, which is quite natural from the kinetic approach, the time plays a fundamental role in destruction process along with the external load and temperature [2, 7, 8, 27]:

$$\tau = \tau_0 \cdot \exp\left(\frac{U_0 - \gamma\sigma}{k_0 T}\right), \tag{3.3}$$

here k_0—the Boltzmann constant, determined as a result of the experiments by Perrin. The Boltzmann constant is $k_0 = 1.38 \times 10^{-23}$ J/K, where K—the temperature in kelvin [28].

It is easy to see that the inequality (3.2) removes the contradiction of the catastrophic development of a fatigue crack in one or more cycles, but requires a review of the prevailing views on the process of fatigue failure. In particular, $W_i < U_0$ absorption spectrum of the energy supplied cannot be continuous [26].

On the other hand, over the past four decades V.S. Ivanova received and compiled the experimental data on the discrete phenomena of the kinetics of fatigue failure [29–31] that is unexplainable from the prospect of classical mechanics. The synergetic approach to these phenomena is considered in [32, 33]. The essence of this approach lies in the following considerations.

Let the fatigue crack, originated in the plate, develop along some axis $0x$. We partition the trajectory crack into the elementary segments Δx. At $T = \text{const}$, the first approximation of the growth for another crack is realized during Δx_{ij}

$$\tau_{ij} = \tau_0 \cdot \exp\left(-\frac{U_{ij}}{k_0 T}\right). \tag{3.4}$$

With an increase of fracture, the stress state at the top will increase and the potential barrier U_{ij}, according to [2], decreases by running through the series of values of the continuous spectrum. The crack growth rate in the ij–segment is

$$V_{ij} = \frac{\Delta x_{ij}}{\tau_{ij}} = \tau_0 \cdot \exp\left(-\frac{U_{ij}}{k_0 T}\right). \tag{3.5}$$

It was established experimentally [28, 34] that V_{ij} on the large plots of the trajectory remains constant (Fig. 3.1).

From [7], it follows that within the j area containing a large number of elementary segments, $U_{ij} = \text{const}$ and it changes abruptly at the transition to $(j+1)$-segment. This means that the values U_{ij} form the discrete spectrum.

The simplest example of the potential barrier is the barrier in one dimension, as shown in Fig. 3.2 [35]. The ordinate is the potential energy $U(x)$ as the function of particle in the coordinate x. At the point x_0, the potential energy has the maximum U_m. All space $-\infty < x < \infty$ are divided at this point into two areas: $x < x_0$ and $x > x_0$, where $U < U_m$.

Fig. 3.1 The scheme of the length, velocity, and acceleration of fatigue cycles in a discrete growth
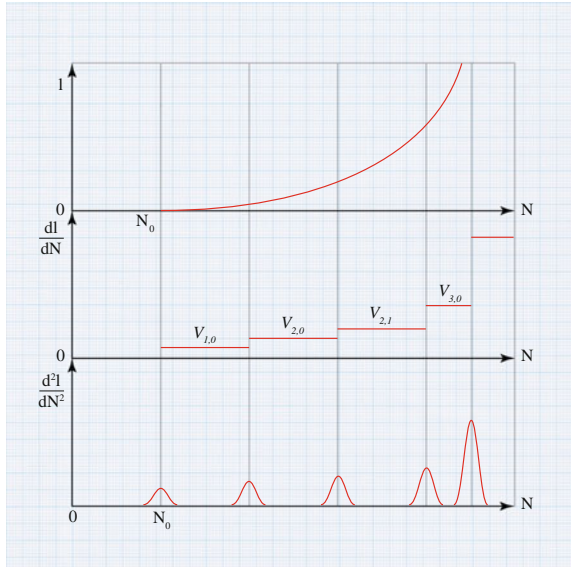
Fig. 3.2 The potential barrier in one dimension
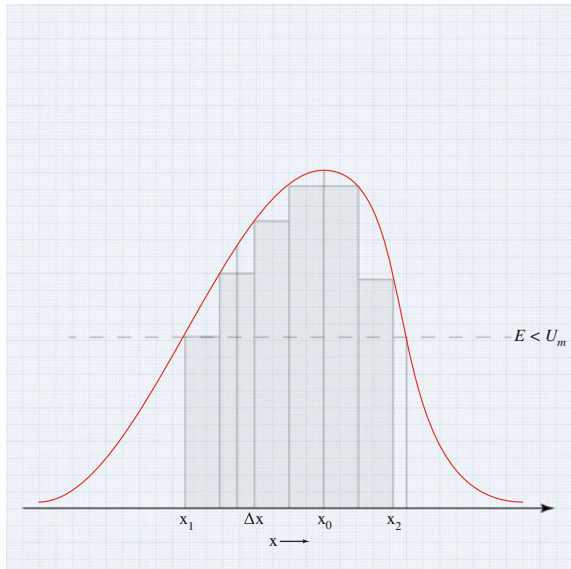
The meaning of "potential barrier" easily becomes clear if we consider the motion of particle in the field $U(x)$ on the basis of classical mechanics. The total energy E of the particle is equal to

$$E = \frac{p^2}{2\mu} + U(x), \tag{3.6}$$

where p—the particle momentum and μ—the particle mass. Solving (3.6) with respect to the momentum, we obtain

$$p(x) = \pm\sqrt{2\mu[E - U(x)]}. \tag{3.7}$$

The $\pm$ signs should be selected depending on the direction of the particle motion. If the particle energy E is greater than the "height" of the barrier U_m, and if the initial momentum is $p > 0$, then the particle will freely pass the barrier from left to right, or it will go in the opposite direction if the initial momentum is $p < 0$.

Let us assume that the particle moves from the left, with the total energy E less than U_m. Then, at some point x_1 the potential energy $U(x_1) = E$, $p(1) = 0$ the particle stops. All its energy will turn into the potential, and the movement will start in the reverse order: x_1 is a turning point. Therefore, when $E < U_m$, the particle moves from the left, passes through the region of the maximum capacity ($x = x_0$), and does not enter into the second region $x > x_0$. Similarly, if the particle moves from right to left, with $E < U_m$, it will not penetrate into the region after the second turning point x_2, where $U(x_2) = E$ (Fig. 3.2). Thus, the potential barrier is "opaque" partition for all particles with the energies less than U_m (on the contrary, it is "transparent" for the particles with energies $E > U_m$). This explains meaning behind the name "potential barrier."

Quite different phenomena occur near the potential barriers when it comes to the movement of microscopic particles in the microscopic field, which means the movements which cannot ignore the quantum effects. In this case, in contrast to the conclusions of classical mechanics, the particles with the energy E greater than the barrier height U_m are partially reflected from the barrier, and the particles with energy less than U_m are partially penetrated through the barrier. The phenomenon of the particles with energy $E < U_m$ passing through the potential barrier is called the _tunnel effect_. L.I. Mandelstam and M.A. Leontovich were first to consider this phenomenon in connection with the quantum theory of anharmonic oscillator.

The passing of micro-particles through the potential barriers seems a paradox at the first glance. This is due to the fact that the particle inside the potential barrier at the full energy less than the height of the barrier U_m should have the negative kinetic energy $K = \frac{p^2}{2\mu}$, because the total energy in the classical mechanics is the sum of the kinetic and potential energies (3.6). In the region where $U(x) > E$, $\frac{p^2}{2\mu} < 0$, it becomes meaningless, because the momentum p is the true value. Exactly these areas, as we know from the classical mechanics, are inaccessible for the particles. Meanwhile, according to the quantum mechanics, the particle can be detected in these "forbidden" regions. Thus, it appears as if the quantum mechanics leads to the conclusion that the kinetic energy of particle can be negative and the momentum of imaginary. This is called the paradox of "tunnel effect."

Actually, there is no paradox, and the conclusion itself is wrong. The truth is that the tunnel effect can only be viewed in terms of the quantum mechanics, since the transmittance D, defined by the formula [35]

$$D = D_0 \cdot \mathrm{e}^{-\frac{2}{\hbar} \int\limits_{x_1}^{x_2} \sqrt{2\mu[U(x) - E]}\mathrm{d}x}, \qquad (3.8)$$

when $\hbar \to 0$ tends to zero. Here, $\hbar = 1.054 \times 10^{-27}$erg s—the Planck's constant, and in the older literature, the Planck's constant is usually implied by the value (denoted by h), 2π times greater, i.e., $h = 1.054 \times 10^{-27}$erg s. The transition from the quantum to classical mechanics can be formally described as the passage to the limit $\hbar \to 0$ (just as the transition from the wave to geometrical optics corresponds with the transition of wavelength to the limit $\lambda \to 0$) [36].

The total energy of particle can be considered as the sum of kinetic and potential energies only on the basis of classical mechanics. The formula (3.6) implies that we know the magnitudes of both the kinetic K and the potential $U(x)$ energies. In other words, we simultaneously assign a certain value to the particle coordinates x and its momentum, which is contrary to the well-known principle of the quantum mechanics, the Heisenberg uncertainty principle. The division of total energy into the potential and kinetic in quantum mechanics does not make sense, so the paradox based on the idea that the full energy E is the sum of the kinetic (the pulse function) and potential energy (the coordinate function) energies is untenable.

Getting back to the kinetics of isothermal FCG, it should be noted that, according to the results of [31, 34], changing the speed of FCG is subject to the Δ-dependency of V.S. Ivanova [30]:

$$\frac{V_j}{V_{j+1}} = \Delta, \qquad (3.9)$$

where V_j—the FCG speed at the stress levels σ_j; Δ—the generic parameter (permanent failure), which is the average value of Δ_T characterizing the ratio of the critical stress values W_{cd} and W_{cv} for shear and pull at temperature T. Since in the interval of temperatures, from the room temperature and below, the value Δ_T weakly depends on the temperature, so the value Δ_T will be wise to determinate by calculating Δ_T at $T = 273$ K. Since for many alloys of the same basis, Δ_T is also weakly dependent on the chemical composition, for practical purposes, it is sufficient to calculate the average value Δ_T for the group of alloys.

As it follows from (3.5), under the isothermal conditions for the relation (3.9) to hold, it is sufficient that

$$U_{j+1} - U_j = \delta U = \text{const.} \qquad (3.10)$$

Similarly, for the relation

$$\frac{V_j}{V_{j+1}} = \Delta^{\frac{1}{2}} \tag{3.11}$$

it is sufficiently that

$$U_{j+1} - U_j = \frac{\delta U}{2^j}. \tag{3.12}$$

The value $\delta U = \text{const}$—the discrete decrease of the activation energy, which can be identified with the absorption of some phonon

$$\delta U = \hbar \cdot \omega_*, \tag{3.13}$$

where $\hbar$—the Planck's constant and ω_*—the characteristic frequency of phonon.

The phonons are the field quanta of sound waves in a macroscopic body. Theoretically, they are entered in exactly the same way as photons during the quantization of electromagnetic field [37].

Almost all concepts used in the application of photons, for example, the concept of wave–particle duality, are equally well suited to phonons. The thermal vibrations of atoms in crystals can be regarded as the thermal excitation of phonons, in analogy with the thermal excitation of photons that makes up the blackbody radiation.

At the finite temperatures, the atoms (ions) in the node of crystal lattice oscillate at the certain frequency (the translational and rotational movements are impossible), which are distributed throughout the crystal in the form of acoustic waves. With an increase in the temperature, they oscillate at the high frequency and simultaneously increase the intensity (amplitude) of already exciting oscillations. At the certain temperature $T = \theta$, all possible frequencies exist in the crystal. If we designate the highest frequency through $\omega_{\max}$, then that temperature is defined as

$$\theta = \hbar \frac{\omega_*}{k_0}, \tag{3.14}$$

where $k_0 = 1.38 \times 10^{-23}$ J/K $= 1.38 \times 10^{-16}$ erg/K—the Boltzmann's constant (K—the Kelvin temperature, $1J = 10^7$ erg), θ—the so-called Debye temperature.

At temperatures above Debye $T > \theta$, new frequencies do not form in the crystal, and only the amplitude of existing fluctuations grows.

Let us clarify the nature of the oscillations of atoms (ions) in node of crystal lattice sites. The oscillatory motion is either classical (the Newtonian mechanics) or quantum (the Schrödinger quantum mechanics) nature.

We define these movements from the classical or quantum perspectives. It is known that the movement s is referred to as classic when it is much greater than the Planck's constant $\hbar$:

$$s \gg \hbar, \tag{3.15}$$

where $s = M \cdot vx$—the oscillating motion, M—the mass of the vibrating atoms, v—the linear velocity, and s—the displacement from the equilibrium position. For simplicity, we take $x = A \cdot \cos \omega t$, and then $v \sim \dot{x} \sim \omega x$, where $x \sim \frac{v}{\omega}$, and hence

$$s \sim \frac{Mv^2}{\omega}. \tag{3.16}$$

If we consider that $Mv^2 \approx k_0 T$, we obtain

$$s \sim \frac{k_0 T}{\omega}. \tag{3.17}$$

If the condition (3.15) is rewritten for the highest frequency $\omega_{\max}$, then the condition for the classical vibration takes the form [38]

$$\frac{k_0 T}{\omega} \gg \hbar \quad \text{or} \quad k_0 T \gg \hbar \cdot \omega_{\max}, \tag{3.18}$$

Thus, the oscillatory motion of the lattice can be considered classic only at temperatures satisfying $T \gg \hbar \cdot \omega_{\max}/k_0$ or $T \gg \theta$, i.e., at temperatures above the Debye. At the low temperatures, $T \leq \theta$ that condition (3.18) does not hold, and the vibrational motion has the quantum nature.

The solids, which are built of the atoms forming the crystal lattice, are characterized in the quantum mechanics by the Hamiltonian $\widehat{H}$ [36], i.e., the operator corresponding to the classical mechanics $(\hbar \to 0)$ with the Hamiltonian function. The Hamiltonian $\widehat{H}$ can be approximated by the sum of terms, each of which represents a harmonic oscillator corresponding with the normal vibration of atoms. This approximation is plausible to the extent where we can neglect the enharmonic forces acting between the atoms causing the melt of the crystal lattice at the sufficiently high temperatures. In the classical theory, the normal vibration is the wave of deformations of lattice planes, i.e., the sound wave. In the quantum theory, the normal vibrations generate the quanta, called phonons.

From above, it follows that the quantum state of the crystal lattice is close to the main state and should be characterized by the number of available phonons with different impulses. Consequently, at the low temperatures, the solids can be considered as a volume containing the gas of non-interacting phonons.

Since the phonon is the quantum of harmonic oscillator, it has the specific frequency ω_i and the energy $\hbar\omega_i$. The lattice state, characterized by the presence of one phonon, corresponds to a sound wave, written in the form

$$\varepsilon \mathrm{e}^{i(kr-\omega t)}, \tag{3.19}$$

and the wave vector k has a value of $|k| = \omega/c$, where c—the speed of sound (for simplicity, it is assumed that c is independent of the polarization vector ε). The polarization vector is not necessarily perpendicular to the wave vector k. Thus, the polarization vector has three independent components corresponding to one of the longitudinal oscillations—the compression wave and two transverse vibrations—the shear waves. In the oscillated state, the harmonic oscillator can have any number of quanta—the phonons, and their total number is not constant.

The solids consisting of N atoms have $3N$ normal vibrations. Therefore, it should be $3N$ different phonons with the specific frequencies

$$\omega_1, \omega_2, \ldots, \omega_{3N}. \tag{3.20}$$

The values of these rates depend on the lattice properties. The Einstein model assumes that all frequencies are equal in the lattice model. The Debye model is the improvement of this model, only for the purpose to determine the frequency (3.20) we approximate the solids as the elastic continuum with the volume V. The frequencies (3.20) become $3N$ normal lower frequencies of such a system.

According to the Einstein's model, the total energy of the crystal consisting of N atoms can be represented as the total energy of $3N$ non-interacting harmonic oscillators with the same frequency ω_0 [38]:

$$E = 3N\varepsilon(\omega_0) = \frac{3N\hbar\omega_0}{e^{\frac{\hbar\omega_0}{k_0 T}} - 1} \tag{3.21}$$

taking into account the proposed Planck's quantum expression for the average energy of the harmonic oscillator with linear frequency ω:

$$\varepsilon = \frac{\hbar\omega}{e^{\frac{\hbar\omega_0}{k_0 T}} - 1}, \tag{3.22}$$

where k_0—the Boltzmann's constant.

At the high temperatures, when $k_0 T \gg \hbar\omega$, we have $e^{\hbar\omega/k_0 T} \approx 1 + \hbar\omega/k_0 T$ and from (3.22) follows the well-known classical expression for the harmonic linear oscillator $\varepsilon = k_0 T$.

From (3.21), it follows that the heat capacity $C_V = \left(\frac{\partial E}{\partial T}\right)_V$ is equal to

$$C_V = 3N\left(\frac{\hbar\omega_0}{k_0 T}\right)^2 \frac{e^{\frac{\hbar\omega_0}{k_0 T}}}{\left(e^{\frac{\hbar\omega_0}{k_0 T}} - 1\right)^2}. \tag{3.23}$$

We introduce the concept of the specific Einstein temperature $\theta_E = \hbar\omega_0/k_0 T$. Then, the expression (3.23) takes the form

$$C_V^E = 3N \left(\frac{\theta_E}{T}\right)^2 \frac{e^{\frac{\theta_E}{T}}}{\left(e^{\frac{\theta_E}{T}} - 1\right)^2}. \tag{3.24}$$

If the frequency is equal to $\omega_0 \approx 3 \times 10^{13}\,\mathrm{s}^{-1}$, then the Einstein temperature will be of the room temperature $\theta_E = 300\,\mathrm{K}$. At the high temperatures, $(T \gg \theta_E)$ from (3.24) there follows the well-known classical result for the solid specific heat $C_V = 3k_0 N = 3R$, where $R = 1.92\,\mathrm{kal/K\,mol}$ is the universal gas constant.

At the low temperatures, $(T \ll \theta_E)$, if we neglect unity in the denominator (3.24), then we obtain for the specific heat

$$C_V^E = 3N \left(\frac{\theta_E}{T}\right)^2 e^{\frac{\theta_E}{T}}, \quad T \ll \theta_E. \tag{3.25}$$

As it can be seen from (3.25) at the low temperatures $(T \ll \theta_E)$, the heat capacity is highly dependent on the temperature and at the extreme case $(T \to 0K)C_V^E$ it exponentially tends to zero. However, this dependence satisfies the known Nernst's principle (the different higher values of the system entropy S as well as the entropy difference should be equal to zero at the absolute zero), but this is consistent with the experiment only qualitatively. The numerous experiments show that at the absolute zero, the function $C_V(T)$ does not behave exponentially and has the form of $C_V(T) \sim T^3$.

This discrepancy between the theory and the experiment shows that despite the fact that Einstein's idea of the average energy for the quantum oscillator (3.22) is true, but the proposed model does not reflect the reality at the low temperatures.

In this situation, the Einstein model requires the improvement, and the Debye model provides that.

According to the Debye model, there is an elastic connection between the atoms (ions) in the nodes of crystal lattice; therefore, the oscillations with the frequency ω arising in any node are distributed throughout the crystal in the form of the elastic wave with the corresponding length λ. For each crystal, there is a specific relationship, obtained by the approximate continuum (when a one-dimensional crystal lattice (chain) is replaced by a continuous elastic string) [38]:

$$\omega(q) = \vartheta_0 \cdot q, \tag{3.26}$$

where ϑ_0—the elastic wave speed and q—the wave number, equal to $q = 2\pi/\lambda$.

Given that the crystal has a discrete, but a periodic structure and the wave vector and frequency vary in a finite interval $0 \leq q < q_{max}$ and $0 \leq \omega < \omega_{max}$, and they have a finite number of values in this range; Debye proposed the crystal model in the form of an ideal gas, consisting of $3N$ linear harmonic oscillators with the frequency

varying in the range $0 \leq \omega(q) < \omega_{\max}$. Specific for each rigid body, the Debye temperature (denoted θ_D) is defined by (3.14).

According to (3.14), the Debye temperature has the following physical meaning: θ_D—the temperature at which all possible frequencies acting ($\omega < \omega_{\max}$) in the crystal. Each solid has its own maximum frequency $\omega_{\max}$ and hence the Debye temperature. The value of the Debye temperature depends on the elastic properties of the crystal and more specifically on the speed of sound ϑ_0 in the crystal lattice and the lattice constant $a = V/N$ [15]. For the specific heat at the low temperatures, $(T \ll \theta_E)$, we obtain

$$C_V^D = \frac{12\pi^4}{5} k_0 N \left(\frac{T}{\theta_E}\right)^3, \quad T \ll \theta_D. \tag{3.27}$$

The Debye temperature θ_D, as the macroscopic parameter, defines the boundaries of the classical and quantum mechanics: at $T \gg \theta_D$, the oscillatory motion of atoms in the nodes of crystal lattice is a classic, and if $T \ll \theta_D$, it becomes quantum.

Referring back to the FCG model (3.9), we note that, as shown in [10, 15, 30, 31, 34], the full absorption spectrum is given by

$$W_{n,m} = \hbar\omega_* \left(n + \frac{m}{2^{n-1}}\right), \tag{3.28}$$

where $n \in N$ (N—the set of natural numbers) is the principal quantum number; $m \in N_n = \{1, 2, \ldots, 2^{n-1}\}$ is the sublevel quantum number. The full absorption spectrum (3.28) is shown in Fig. 3.2. The basic levels ($m = 0$) are plotted as the main lines, and sublevels ($m \neq 0$) are plotted as the thin lines.
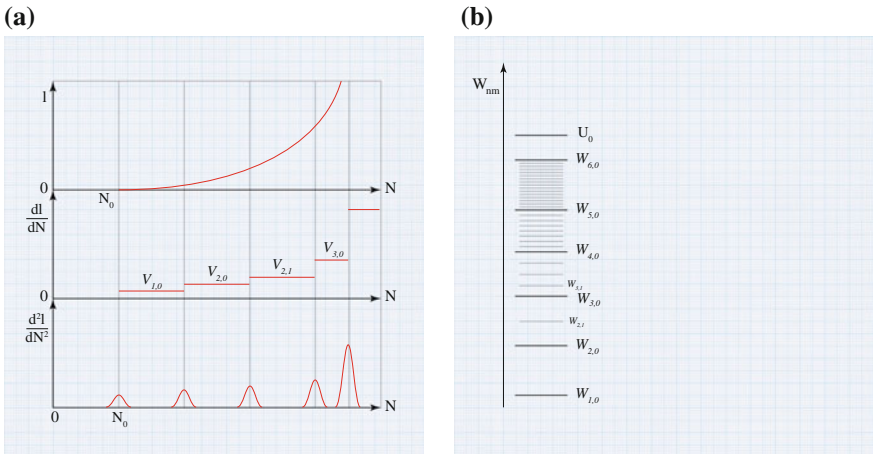
Fig. 3.3 **a** The dependence of length, velocity, and acceleration of fatigue crack on the number of cycles in a discrete growth (diagram). **b** The full absorption spectrum in the system of nonlinear oscillators following the Feigenbaum period-doubling bifurcation

From (3.28) and Fig. 3.3, it follows that with an increase of the principal quantum number n, the number of sublevels between the main levels increases in proportion equal to 2^{n-1}, which leads at large n to the degeneration of the discrete spectrum into the continuous, where the laws of the classical mechanics become valid. Obviously, as the critical threshold of breakage, we can take a critical event that satisfies the theory of Griffith, with the proviso that $W_{n,m}$ tends to U_0, remaining smaller.

Thus, the kinetic approach does not reject the theory of Griffith, and on the contrary, it actually contains it within as a limiting case for the high levels of loading.

As it can be seen from the curves (3.5) and (3.28),

$$V_{1,0} = C\,e^{\left(-\frac{U_0 - \hbar\omega_*}{k_0 T}\right)}; \quad V_{2,0} = C\,e^{\left(-\frac{U_0 - 2\hbar\omega_*}{k_0 T}\right)}; \ldots \tag{3.29}$$

then

$$V_{1,0}/V_{2,0} = V_{1,0}/V_{2,0} = \cdots = e^{\left(-\frac{U_0 - \hbar\omega_*}{k_0 T}\right)} = \Delta_T. \tag{3.30}$$

At $T = 300\,\mathrm{K}$, we have

$$\omega_* = -300\frac{k_0}{\hbar}\ln\Delta_{300}. \tag{3.31}$$

Using the well-known relation for the quantum statistics $\hbar\omega_* = k_0\theta_*$, valid for the specific $T = \theta_*$ [1], the expression (3.31) can be written in a more convenient form

$$\theta_* = -300\ln\Delta_{300}. \tag{3.32}$$

Moreover, in [30],

$$\Delta_{300} = \sqrt{GL_\mathrm{m}/EH_{300}}, \tag{3.33}$$

where E—the elastic modulus, G—the shear modulus, L_m—the latent heat of fusion, and H_{300}—the heat from the heating to $T = 300\,\mathrm{K}$ up to the melting temperature.

Table 3.1 shows the values θ_* for some metals, as well as their Einstein and Debye temperatures. The Einstein frequency ω_E is determined from the harmonic approximation

Table 3.1 The comparison of the specific temperatures with the Einstein and Debye temperatures for some metals

Metal	θ^*, K (15)	θ_D, K (16)	θ_E, K (17)	Metal	θ^*, K (15)	θ_D, K (16)	θ_E, K (17)
K	69	100	42	Ag	278	215	103
Na	125	150	78	Cu	268	315	158
Li	204	400	145	Ni	276	375	208
Fe	334	420	197	Au	282	–	76
Nb	306	275	115	Mg	245	318	137
Mo	313	380	193	Co	335	385	164
Ta	316	225	110	Y	352	256	92
W	302	310	156	Ti	340	380	144
Cr	335	460	217	Zr	307	250	104
V	334	390	165	Os	298	400	159
Pb	252	88	37	Zn	236	–	112
Al	224	394	195	–	–	–	–

$$\omega_E = \frac{\sqrt{r}}{a}\sqrt{\frac{E}{\rho}}, \tag{3.34}$$

and the Debye frequency from the equality

$$\omega_E = 2\pi\vartheta_0/a, \tag{3.35}$$

where a—the lattice constant, r—the number of atoms in the unit of volume a^3, ρ—the density, and ϑ_0—the speed of sound in the crystal. The calculations for the hexagonal lattice are carried out by the method of the equivalent cubic lattice.

The Debye temperature is calculated by the formula

$$\theta = \hbar \cdot \omega_{max}/k_0, \tag{3.36}$$

where k_0—the Boltzmann constant $\left(k_0 = 1.38 \times 10^{-16}\,\text{erg/K}\right)$ must only coincide with the experimentally determined at very low temperatures (below about 5 K—depending on the type of crystal). The available little differences between the two temperatures cannot be explained in the harmonic approximation, and it is due to anharmonicity [39].

At the temperatures $T > 10$ K, the results of the Debye theory and the experimental data can vary significantly. The true reason behind it lies in the fact that the Debye theory uses a simple dispersion function (3.34) and following from that the density function of frequency $g(\omega) \sim \omega^2$. Such a dispersion function is relevant when a simple crystal lattice (with a single atom or ion in the elementary cell) is replaced by the elastic wave and then only for wavelengths $\lambda > \pi \cdot a$, where a—the lattice constant [38]. For the real crystals, the dispersion function $\omega(q)$ and the

density function of frequency $g(\omega)$ are quite complicated due to the enharmonic interaction between the atoms.

It follows from (3.28) that in the absorption spectrum, along with the fundamental harmonic ω_*, there are the subharmonics $\omega_*/2^{n-1}$. This phenomenon is known as the period doubling, typical for the self-organizing systems [14].

In [17, 40], the different types of the elastic characteristics are viewed, as with the soft $(k > 0, \gamma < 0)$, hard $(k > 0, \gamma > 0)$, zero $(k = 0, \gamma > 0)$, and negative $(k < 0, \gamma > 0)$ linear stiffness. We note that by shifting the origin of the Duffing equation with $k < 0$ and $A_0 \neq 0$, it is reduced to the form

$$\ddot{y} + \alpha \dot{y} + ky + \beta y^2 + \gamma y^3 = B \cos \omega t, \qquad (3.37)$$

where $k > 0$, i.e., the equation of nonlinear oscillator with the asymmetric elastic characteristic and the symmetric external influence.

As with the soft and hard elastic characteristics, the chaotic oscillations exist for the sufficiently large amplitude of the external force in the frequency range ω, where the corresponding frequency response is ambiguous (the bistability region). As the numerical experiments show, these oscillations occur by the sequence of period-doubling bifurcations.

Transition $W_{1,0} \to W_{2,0}$ in Fig. 3.3 is equivalent to a decrease in the value of the potential barrier $\hbar\omega_*$, and the next transition $W_{2,0} \to W_{2,1}$ reduces the potential barrier for another value $\hbar\omega_*/2$, etc.

In the case of the isothermal FCG from (3.5) and (3.30), we obtain

$$\begin{aligned}
V_{1,0}/V_{2,0} &= \exp\left(-\hbar\omega_*/kT\right) = \Delta_T, \\
V_{3,0}/V_{2,1} &= \exp\left(-\hbar\omega_*/2kT\right) = \Delta_T^{1/2}, \\
V_{3,0}/V_{3,1} &= \exp\left(-\hbar\omega_*/4kT\right) = \Delta_T^{1/4}.
\end{aligned} \qquad (3.38)$$

From (3.38), it follows that the distribution process (the discrete growth) of fatigue crack is self-similar (scaling) in terms of Barenblat [41]. The scaling means that during the process of fatigue deformation, only the average size of defect changes (increases), but the shape of the defect distribution remains unchanged in terms of its size. In other words, the geometric pattern of defects at the later stage in the certain part of the sample (the size of which is much greater than the average distance between the defects) represents (in a statistical sense) an enlarged copy of the picture in the greater part of the sample at the earlier stage.

The hierarchy of the structural (scale) level of deformations is the base to find the relationship between the micro- and macro-parameters of the PD and fracture. Using the self-similarity function $\Delta_T^{1/m}$ $(m = 1, \frac{1}{2}, \frac{1}{4}, \ldots)$, we can set the fundamental relation between the parameters of the bifurcation controlling points (while maintaining the same type of the dissipative structures) and the returning points [42].

In addition to the considered ordering phenomena of the Δ-discreteness of the FCG, there are known other experiments, where the sharp macroscopic changes were observed, and in all cases, these changes were ordered by the Δ-dependence of Ivanova [30, 43, 44].

In [43], it was found that the voltage at the break points of the temperature dependences of the strength properties is ordered and follows the Δ-dependence of V.S. Ivanova. Most clearly, this ordering appears on the temperature dependences of the yield strength $\sigma_{0,2} = \sigma_0/\sigma_{f_2}$ where σ_0—the strength at $T \to 0K$ and σ_{f_2}—the theoretical mechanical strength. As an example, Fig. 3.4 shows the dependence of $\ln \sigma_{0,2}$ from $1/T$ for technical copper by the dotted line corresponding to the discrete levels j, varying according to

$$\frac{(\sigma_{0,2})_j}{(\sigma_{0,2})_{j_1}} = \Delta^{(1/2)^j}, \tag{3.39}$$

and the value of j increases at the low temperatures.

Thus, the appearance of the discrete Δ-dependence on the kinetic diagrams of the FCG, on the temperature diagrams of the yield strength and others, shows the formation of the self-organizing systems of the nonlinear oscillators in metals under loading, the most simple mechanism of bifurcation is Feigenbaum's mechanism of the period doubling. The cyclic loading is an optional condition, which leads to the macroscopic appearance of the self-organization process. The linearly increasing load leads to the same effect.

The transition of dynamic system from order to chaos, which is accompanied by the infinite sequence of the period-doubling bifurcations in accordance with the

Fig. 3.4 The nonlinear oscillator in the potential relief (the crack maximum speed)
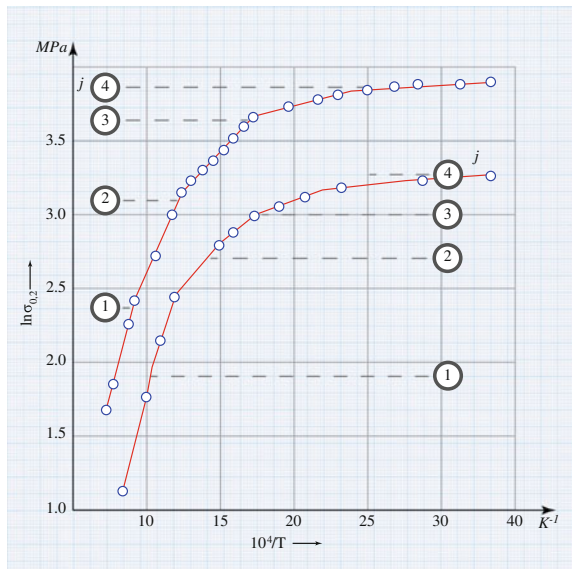
Feigenbaum law, is generally described as a one-dimensional point mapping with the smooth maximum at $x = 0$ for which the successor function can be written as [40]

$$f(x) = f - \mu |x|^z, \tag{3.40}$$

where $z > 1$; μ—the bifurcation parameter. Then, the generalized Feigenbaum law is [45]

$$\mu_\infty - \mu_n \sim \delta^{-n}, \quad n \to \infty, \tag{3.41}$$

where μ_n—the value of μ, when the nth period-doubling bifurcation takes place

$$\mu_\infty = \lim_{n \to \infty} \mu_n.$$

Here, δ—the constant depending on z (in the case of the quadratic mapping $z = 2$, $\delta = 4.6692\ldots$). Often the Feigenbaum law is written in the different form

$$\omega_n \sim (\mu_\infty - \mu_n)^\upsilon, \tag{3.42}$$

where $\omega_n = 2\pi / T_n = 2\pi (T \cdot 2^n)$ and $\upsilon = \ln 2 / \ln \delta = 0.4498\ldots$.

Thus, the function of parameter ω_n is similar to the corresponding functionality in the case of the phase transition of type II with the critical index υ. In contrast to the conventional phase transitions, so-called type I, the type II phase transition is called [37] the transition from one crystal modification into another, in which an arbitrarily small displacement of the atoms from their original symmetrical arrangement is sufficient that the symmetry of the crystal lattice immediately changes.

At $\mu_n \to \mu_\infty$, $d\omega / d(\mu_\infty - \mu_n) \sim \upsilon / (\mu_\infty - \mu_n)^{1-\upsilon} \to \infty$ on the other side of the transition, and at $\mu > \mu_\infty$, we take any positive Lyapunov exponent λ, or the topological entropy h, or the synchronization threshold B_n as the parameter of "disorder" [17]. Near μ_∞ for the positive Lyapunov exponent λ, the following power dependence holds:

$$\mu_\infty - \mu_n \sim \delta^{-n}, \quad n \to \infty, \tag{3.43}$$

where υ—the same critical exponent as in (3.42).

3.2 Application of Generalized Golden Ratios to Control Self-similarity and Stability Properties of Fractal Structure Distribution in Fatigue Cracks of Solids

In the recent past, the main efforts of researchers on the fracture mechanics of materials were aimed at establishing a link between their initial microstructure and properties, but it is currently established [10, 46–48] that the fracture resistance of metals and alloys is determined by the dynamic structure formed during the deformation, and it requires the analysis of deformable material as an open system exchanging the energy and matter with the environment. During the system evolution associated with the accumulation of the fatigue damage under the cyclic loading, the old structure gets destroyed and a new structure is formed. In this case, it is required to establish the research of the cooperative interaction of the static (the original) and dynamic (emerging under load) structures.

The formation of the actual microstructure of the crystalline solids is due to the phenomena that are far from the equilibrium and take place in the self-trapped, more non-equilibrium areas, existing even in the quasi-equilibrium condensed media. In accordance with the general regularities of the non-equilibrium system behavior [49], the deformed crystal should be viewed as the system in which during the deformation the dissipative structure occurs (like the Bernard cells) that can more effectively perform the macro-plastic flow in comparison with the motion of individual dislocations. Exactly, from this point of view, the phenomenon of fragmentation of deformable solids is now treated, and in the continuum mechanics, the presence of structural element deformation is taken into account [50, 51]. There is the hierarchy of its levels, defined as the initial structure of the medium, and the formation of dissipative structures is related to deformation defects [19, 20].

The dissipative structures, self-organizing in the open systems, are fractal [10, 46], which calls for combining the approaches of synergy and fractal theory in the studies of physical and mechanical natures of the material destruction. Synergetics has expanded the concept of structure, giving it the versatility, and the theory of fractals allowed introducing new quantitative structures in the form of fractal dimension [12, 30, 41, 52].

During the contact interaction in material through the merger of macroscopic damages, the micro-crack forms, and the stage of global destruction begins, which is based on the fact that the destruction process in time is controlled by the growth speed of such a crack from the ductile to brittle and then to the quasi-brittle fracture and when the body is divided into parts. The transition phenomenon of the deformable body from ductile to brittle is called the cold brittleness. It is associated with the transition from the controlled impact to the destruction of mesocluster instability (the ductile fracture) to the micro-cluster instability (the brittle fracture). This determines the change in type of the surface fracture, defined by the change of the fractal object and the fractal dimension of structure in the pre-fracture zone, and the spontaneous change in the fractal dimension depending on the transverse reduction [53].

Let us define the possibility of applying the fractal geometry approaches to studying the deformation process of pre-destruction and fracture (wear) of the metal materials, to controlling the critical points of the mechanical state, and to forecasting the fatigue damage upon the contact and friction of the rough surfaces based on the quantifying evaluation of the fractal dimension of the strain relief by the method of vertical sections (MBC) using the self-similar relationship of the perimeter to the square of the fractal closed profiles. The method of vertical sections [54] is especially useful for studying the profiles of fracture surfaces using the profilometer [55], which does not bring distortions into the object of study. According to [9, 56, 57], the reliable characterization of the crack surface roughness is obtained through the series of measurements of the profile length in two mutually perpendicular directions—up and down the crack front.

The synergetic approach to the analysis of the processes of plastic deformation (PD) and fracture, taking into account the collective effects and the self-organization of the dissipative structures, establishes the hierarchy structure (scaling) of the deformation levels, which are the basis for finding the connection between the micro- and macro-parameters of the PD and fracturing - from the prospects of the theory of fractals as the self-similar defects, and the fractal dimension as the characteristics of the object dynamic structure. However, the description of the self-similar growth of the dynamic objects requires the introduction of self-similar functions.

The periodic nature of the destruction on micro- and macro-levels can be described [30], using the function $\Delta^{1/m}$, where m changes exponentially ($m = 2, 4, 8, 16, \ldots$), corresponding with the cycle of self-organizing systems. Within one block of the intermediate asymptotic behavior, the transitions with the period doubling for the threshold values of the crack length l_1 have the form

$$
\begin{aligned}
&\text{I block:} \; l_1^{\mathrm{I}}/l_2^{\mathrm{I}} = l_2^{\mathrm{I}}/l_3^{\mathrm{I}} = \cdots = l_{i-1}^{\mathrm{I}}/l_i^{\mathrm{I}} = \Delta^{1/m}; \\
&\text{II block:} \; l_1^{\mathrm{II}}/l_2^{\mathrm{II}} = l_2^{\mathrm{II}}/l_3^{\mathrm{II}} = \cdots = l_{i-1}^{\mathrm{II}}/l_i^{\mathrm{II}} = \Delta^{1/m}
\end{aligned}
\tag{3.44}
$$

etc., for $m = 2, 4, 8, 16, \ldots \infty$. So in each block, the ratio is $l_{i-1}^{\mathrm{II}}/l_i^{\mathrm{II}} \to 1$ at $m \to \infty$. In general terms, this relationship can be written as [12]

$$
l_1^{\mathrm{I}}/l_1^{\mathrm{II}} = l_1^{\mathrm{II}}/l_1^{\mathrm{III}} = \cdots = \Delta^{M/m},
\tag{3.45}
$$

where M—the number of the intermediate asymptotic blocks ($M = 1, 2, 3, 4, \ldots$).

It is shown that the self-similarity function can set the fundamental connections between the parameters that control the bifurcation point (while maintaining the same type of the dissipative structures) and responding to these points [12, 53]. For instance, the self-similarity relation describes the alternation steps δ_i of the fatigue grooves

$$
\delta_i/\delta_{i+1} = \Delta^{1/m}, \quad m = 1, 2, 4, 8, 16, \ldots,
\tag{3.46}
$$

and the fractal cluster dimension at the self-similarity growth is expressed through the relationship

$$\left(r_0^j\right)_{i-1}/\left(r_0^j\right)_i = \Delta^{1/m}, \quad m = 2, 4, 8, 16, \ldots, \tag{3.47}$$

where $\left(r_0^j\right)_{i-1}$ and $\left(r_0^j\right)_i$—the previous and subsequent fractal cluster dimensions following the crack direction.

If we consider the constants of the crack growth rate and/or the steps of the fatigue grooves as the regularity of ordering the crack jumps under the loading cycle, it is possible to carry out their systematization through the "quantum" destruction and the universal constant of destruction Δ. As it will be shown below, Δ retain the constant value for each metal separately, and this is its versatility. The comparison of the identified levels of relations δ_i/δ_{i+1} for alternating steps of fatigue grooves shows [12] that they satisfy the values of $\Delta^{1/4}, \Delta^{1/8}, \Delta^{1/16}, \Delta^{1/32}$.

From (3.46), it follows that the theory of similarity [23, 41, 58–60] defines the propagation process (the discrete growth) of the fatigue crack as self-similar (scaling). According to the proposed hypothesis in [23], the process of the damage accumulation (in terms of the quantitative measurement of damage ω, first introduced by Kachanov and Rabotnov [61, 62]) under the cyclic deformation is self-similar.

The Eq. (3.47) defines the self-similarity property of the fractal clusters. It is formulated as follows [63]. If within the neighborhood of point, occupied by a cluster, we select the area of the relatively small volume, then the parts of cluster falling into her will be similar in the physical sense.

The most important feature of function $\Delta^{1/m}$ is the match of its value at $m = 2$ to the golden ratio Δ_p and at $m = 1$ to the value Δ_p^2. By definition [52], the set L is self-similar with the similarity coefficient $r(N)$ and the self-similarity dimension of D_s, if

$$r(N) = (1/N)^{1/D_s}, \tag{3.48}$$

where N—the number of fragments covering the initial set of L by its minimized copies. The segment can contain the segments $r(N) = (1/N)$, and the rectangle can contain the squares with sides $[r(N)]^2 = 1/N$ and the rectangular parallelepiped —$[r(N)]^3 = 1/N$.

To establish the connection between the numbers r, N, and D_s in [64, 65], we used the generalized golden ratio, which is the golden section—"golden mean" that follows the Fibonacci numbers [66]. A classic example of the golden ratio is the segment division with respect to the average proportionality, when the whole part relates to the most part, as the most relates to the smaller

$$\frac{a+b}{b} = \frac{b}{a}. \tag{3.49}$$

The analogue of the golden ratio (3.49) is the universal law of Feigenbaum and the Fibonacci sequence, which forms a geometric progression

$$a_n = a_1 q^{n-1}, \quad n = 1, 2, 3, \ldots, \tag{3.50}$$

whose members satisfy

$$a_n = a_{n-2} + a_{n-1}. \tag{3.51}$$

From (3.50) and (3.51), it follows that q is the root of the quadratic equation $q^2 = 1 + q$. This equation has two roots: $q_1 = 1.618$ and $q_2 = 0.618$ that match the golden ratio. In fact, assuming that $a + b = 1$ in (3.49), we find $b = 0.618$, $a = 0.382$ and $\frac{a+b}{b} = \frac{b}{a} = 1.618$.

It was promising to use the generalized golden p-proportions that express the general law of the golden ratio—the ratio of the whole part to its parts. The generalized golden p-proportion is called the positive root of the equation $x^{p+1} = x^p + 1$ providing the infinite number of proportional division of the interval at $p \to \infty$. For $p = 1, 2, 3, 4, \ldots$, the solution of this equation yields the following sequence of generalized golden p-proportions:

$$d_1 = 1.618 \to d_2 = 1.465 \to d_3 = 1.380 \to d_4 = 1.324 \cdots, \tag{3.52}$$

p—the golden ratio has the same properties as the 1st golden proportion: By subtracting the unit, it goes to the reciprocal of their pth level, i.e., $d_p - 1 = 1/d_p^p$. This means that sequence of the generalized golden p-proportions (3.52) corresponds to the following series $\Delta_p = 1/d_p^p$ of p-proportions:

$$\Delta_1 = 0.618 \to \Delta_2 \equiv 0.465 \to \Delta_3 \equiv 0.380 \to \Delta_4 = 0.324 \cdots \tag{3.53}$$

By indicating the scale factor $r(N)$ in (3.48) through λ_r, we represent this relation in the form

$$\lambda_r^{D_s} = 1/N. \tag{3.54}$$

If the line segment is divided into the segments with the length $\delta = 2^{-m}$, then $N = 2^m$ intervals will require to cover it, where m—the number of generations at the binary partition of interval.

For this case, the Eq. (3.54) takes the form

$$\lambda_r^{D_s} \cdot 2^m = 1. \tag{3.55}$$

This relationship implies that if one of the variables is constant ($m = $ const or $\lambda_r = $ const), the self-similarity dimension of the set D_s depends only on one parameter, namely on the scale factor λ_r when $m = $ const, and the number of generations m at $\lambda_r = $ const. The relationship between D_s and λ_r in the first case and between D_s and m in the second case, in accordance with Eq. (3.55), becomes

$$D_s = \frac{M_1}{\ln \lambda_r}, \tag{3.56a}$$

$$D_s = mM_2, \tag{3.56b}$$

at $M_1 = -m \ln 2$, $M_1 = -\ln 2 / \ln \lambda_r$. The formula (3.56a, b) can be obtained from the equation $D_s \cdot \ln \lambda_r = -m \ln 2$, which is equivalent to the ratio (3.55). There is inaccuracy in the corresponding formulas [53], where the "minus" sign was skipped in the expressions for M_1 and M_2, which should provide a positive value for D_s.

The relations (3.56a, b) meet both the condition of self-similarity [41] and the principle of subsidiarity in synergy [67]. In accordance with this principle, when the system reaches the critical state, its subsequent behavior is controlled by one (or more) variable, which is the parameter of order. The physical meaning of the parameter of order in this case is following. At iteration (the transition from one generation to the next one), the limit of the scale factor λ_r is reached, where we cannot differentiate the previous generation from the later. The new stable state at $D_s = $ const can be achieved only when the scale factor changes. The boundaries that define $D_s = $ const at $m = $ varia are the change of λ_r within $\Delta_p^2 \le \lambda_r \le \Delta_p$, where Δ_p is equal to one of the values of the generalized golden ratio (3.53).

The generalized golden ratio (3.53) permits to determine the interval of constancy of the self-similarity dimension set D_s at values of m, following the geometric progression: $m = 1, 2, 4, 8, \ldots$ within the interval $0 \le D_s \le 3$. This makes it possible to calculate on the basis of relation (3.55) range of values D_s and charge $m = 1, 2, 4, 8, \ldots$ for the golden ratio ([53], Table 9). The value of D_s^I (at $m = 1$) corresponds to the parameter of order Δ_p^2, defined by the expression (3.55) for $\lambda_r = \Delta_p^2$. This means that the sequence of golden ratios Δ_p^2 meets the following set of parameters of order:

$$0.382 \rightarrow 0.216 \rightarrow 0.144 \rightarrow 0.105\ldots, \tag{3.57}$$

derived from the squared terms of the series (3.53).

The feature of spectrum D_s at $\Delta_p = $ const is that the transition from one level to another is realized through the sequence of doubling D_s, i.e., D_s^{i+1}/D_s^i (at $i = $ I, II, III, IV or what is the same, $m = 1, 2, 4, 8, \ldots$).

Besides the spectrum D_s, the generalized golden ratios also control the stability of the cluster at the deformation of the solids. The fractal properties of the object cluster, appearing in the dynamic conditions, are attached at the bifurcation points to the dissipative structures. The stability criterion of the cluster at the deformation of solids is the condition [10]

$$W_d/W_v \le W_d^c/W_v^c, \tag{3.58}$$

where W_d, W_d^c—the density of distortion energy (the shape change) and its critical value; W_v, W_v^c—the density of dilation energy (the volume change) and its critical value. For the micro-clusters, W_d, W_d^c can be expressed in terms of strains in the form of

$$W_d = \frac{\tau^2}{2G}, \quad W_d^c = \frac{\tau_c^2}{2G}, \tag{3.59}$$

$$W_v = \frac{\sigma^2}{2E}, \quad W_v^c = \frac{\sigma_c^2}{2E}, \tag{3.60}$$

where G, E—the elastic and shear modulus (Young's modulus) of the intact material in the cluster; τ, τ_c—the shear stress and its critical value; σ, σ_c—the separation stress and its critical value.

The ratio τ_c/σ_c shows the critical state of cluster when it reaches instability. Considering such a cluster in terms of the percolation theory [68], we can talk about the formation at $\tau/\sigma = \tau_c/\sigma_c$ of the infinite cluster corresponding to the phase transition.

The critical dimensionless constants that control the stability of micro-clusters in a deformed solid body, as well as the critical exponents in the percolation theory (percolation), are interrelated. The relationship between them follows from (3.59) and (3.60) for W_d^c and W_v^c, from which it follows that

$$\frac{\tau_c}{\sigma_c} = \left(\frac{W_d^c}{W_v^c} \cdot \frac{G}{E} \right)^{1/2}. \tag{3.61}$$

From the energy analogue of melting and destruction [69], the equalities are following $W_d^c = L_m$ and $W_v^c = H_{T_s}$, where H_{T_s}—the internal energy density at the melting temperature T_s associated with the vibrations of the atoms. She determined, defined as

$$H_{T_s} = \int_{T_c}^{T_s} C_P(T) dT, \tag{3.62}$$

where T_s—the temperature below which the contribution of lattice of the atom vibrations into the energy can be neglected. Then, (3.61) can be written as:

$$\frac{\tau_c}{\sigma_c} = \left(\frac{L_m}{H_{T_s}} \cdot \frac{G}{E} \right)^{1/2}. \tag{3.63}$$

Denoting

$$\left(\frac{L_m}{H_{T_s}} \cdot \frac{G}{E} \right) = \Delta_T. \tag{3.64}$$

we obtain the condition for the realization of the micro-split (or the rotational stability) in the form

$$\frac{\tau_c}{\sigma_c} \geq \Delta_T^{1/2}.$$

The implementation of destruction through micro-shears with the accepted assumptions occurs at $W_d^c = W_v^c = L_m$, while taking into account the relation (3.61), we obtain

$$\frac{\tau_c}{\sigma_c} = \left(\frac{G}{E} \right)^{1/2}.$$

By designating G/E through Ω, the realization condition of the non-translational stability (arising when the critical shear stress τ_c is associated with the critical energy density W_d^c) can be expressed as

$$\frac{\tau_c}{\sigma_c} \geq \Omega^{1/2}.$$

Thus, to describe the energy state of the local areas of metal undergoing the critical PD at the micro-split, we can use the dimensionless ratio Δ_T introduced by Ivanova [70]. It combines the material elastic moduli (G and E) at the initial state, and the thermodynamic constants (L_m and H_{T_s}) that control the energy state of the metal local volumes away from the thermodynamic equilibrium and determine the critical conditions for the spontaneous outflow of entropy. The physical meaning behind the dimensionless parameter Δ_T is the ratio of the critical shear stress to pull within the temperature intervals, where $W_v^c = H_{T_s}$ is the energy characteristic to achieve the critical dilatation and $W_d^c = L_m$—the critical distortions [71].

With this in mind, the relation (3.64) can also be written as

$$\Delta_T = \left(\frac{G}{E} \right) \cdot \left(\frac{W_d^c}{W_v^c} \right). \tag{3.64'}$$

For many metals, $G/E \approx 0.4$ (since $\tan \varphi \approx 0.4$). Therefore, the ratio (3.64') can be represented as

$$\Delta_T = 0.4 \cdot \left(\frac{W_{\mathrm{d}}^{\mathrm{c}}}{W_{\mathrm{v}}^{\mathrm{c}}}\right).$$

From the above analysis, we can conclude that the parameter Δ_T for the given material is proportional to the energy ratio for the critical dilatations and distortion at the bifurcation point, characterizing the achievement of the critical level of the stored energy in the local volume, in which the small fluctuations can occur under the entropic forces to initiate the spontaneous process of the self-organization of the dissipative structures. At this point, the enthalpy becomes equal to the entropy. Since in the temperature range from the room temperature and below Δ_T does not depend on the temperature, the value of Δ_T is wise to determinate by calculating the value of Δ_T at 273 K. Since for many alloys of the same basis Δ_T also weakly depends on the chemical composition, it is suitable for the practical purposes to calculate the average value of Δ_T for the group alloys. These average values of Δ_T at the room temperature are denoted by Δ [71].

Then, (3.63) can be written as

$$\frac{\tau_{\mathrm{c}}}{\sigma_{\mathrm{c}}} = \Delta_T^{1/2}. \tag{3.65}$$

The relation (3.65) with (3.61) can be written as

$$\frac{W_{\mathrm{d}}^{\mathrm{c}}}{W_{\mathrm{v}}^{\mathrm{c}}} = \Delta \frac{E}{G}. \tag{3.66}$$

In [53], the formula corresponding to (3.66) is written incorrectly, on the right-hand side instead of G/E it should be E/G.

Taking into account the Poisson ratio in the expression,

$$\nu = \frac{E}{2G} - 1. \tag{3.67}$$

(3.66) can be written as

$$\frac{W_{\mathrm{d}}^{\mathrm{c}}}{W_{\mathrm{v}}^{\mathrm{c}}} = 2\Delta(1 + \nu). \tag{3.68}$$

Thus, the similarity constant of the micro-cluster instability is

$$\left(\frac{W_{\mathrm{d}}^{\mathrm{c}}}{W_{\mathrm{v}}^{\mathrm{c}}}\right)/2(1 + \nu) = \Delta. \tag{3.69}$$

The analysis of values Δ for the metals with the different crystallographic structure made it possible to separate the metals into three groups ([53], Table 12), in each of which the average (according to the group) Δ of the complex $\left(\frac{L_{\mathrm{m}}}{H_{T_{\mathrm{s}}}} \cdot \frac{G}{E}\right)$

matches with one of the values of the golden ratio series relationships (either $\Delta_p^2 = 0.216$, or $\Delta_p^2 = 0.144$ or $\Delta_p^2 = 0.105$). The value of Δ is separately constant for each metal: for the steel $\Delta = 0.11$; for the titanium alloys $\Delta = 0.12$; for the copper $\Delta = 0.17$; and for the aluminum alloys $\Delta = 0.22$.

It follows that the complex $\left(\frac{L_m}{H_{T_s}} \cdot \frac{G}{E} \right)$ for the metals and alloys is controlled by the golden ratio. Knowing Δ and H_{T_s}, we can forecast the critical value of the distortion energy density W_d^c according to the formula (3.64).

The mechanism of destruction has the significant effect on the fractal dimension of fracture; therefore, we should consider the changes in the fractal dimension when transferring from one scale into another, and in other words, the destruction should be considered as the multilevel multifractal process.

However, the actual materials and media often have the specific multilevel heterogeneity of their internal structure (state) and the defectiveness at the various hierarchical levels [72–75]. In this regard, along with the fluctuations of the micro- and macro-stress distributions on these irregularities, the practice of getting the specific properties for various materials based on the geometrically similar specimens showed that, along with the factors supporting the law of similarity, there is the significant deviation from it. Since this deviation is the consequence of the geometric dimensions of the deformable solid bodies, the reason causing it is called the scale factor and the phenomenon—the scale effect [76].

As it is shown in [41] for the continuously closed curve γ, having the properties of self-similarity and homogeneity, the power law holds

$$L_\eta = \lambda \cdot \eta^{1-D} \tag{3.70}$$

at the constant D (the Hausdorff dimension) along the curve; if $D > 1$, the curve becomes the fractal. Here, L_η—the length approximating this curve of the broken line composed of the segments with the constant length η. The _homogeneity_ property of the curve means that all parts of the curve between the neighboring vertices of the approximating polygonal with the units of length η generate the same number of segments in the approximating polygonal with the units of length $\xi < \eta$ and the _self-similarity_ property—the similarity of curve with its parts. So that the number of segments of the broken line with the length ξ placed between the adjacent vertices of the polygon with the unit length η depends only on the ratio η/ξ, but not on η and ξ separately.

However, the properties of self-similarity and homogeneity of the curve are not necessary for the continuous curve to be fractal, for that it is sufficient to have significantly weaker properties of its _local homogeneity_ and _local self-similarity_. This means that for any point on the curve, we can specify the small neighborhood Δ, where the curve has the following property. The principal term of the asymptotic representation of the number of vertices $N_{\xi\eta}$ of the approximating broken line with the length ξ between the two neighboring around Δ vertices of the polygon with the unit length η depends only on the ratio η/ξ with $\eta/\xi \to \infty$, i.e., for the fixed relation $\eta/\xi \gg 1$ there is a relationship

$$N_{\xi\eta} = f(\eta/\xi). \tag{3.71}$$

For the lengths of the approximating broken lines within the neighborhood of each point of the continuous curve, having the properties of local homogeneity and local self-similarity, a fair degree of asymptotic relation is valid [41]

$$L_{\xi} = \eta^D \cdot \xi^{1-D} + \cdots, \tag{3.72}$$

where the points denote the quantities comparatively small than the first member (here also gets the input from the extreme parts, which may not be whole). If everywhere on the curve $D > 1$, it means that the considered curve is fractal.

The length of the broken line that approximates the continuous curve between two of its points, spaced at a distance η, depends on two quantitative parameters: η and the link length of the broken line ξ. From the dimensional analysis, we obtain

$$L_{\eta} = \eta \cdot \Phi(\eta/\xi). \tag{3.73}$$

For the smooth (or partially smooth) curve at $\xi \to \infty$, i.e., at $\eta/\xi \to \infty$, the function Φ approaches the finite limit $\Phi(\infty)$. By definition, the value of

$$L_0 = \eta \cdot \Phi(\infty), \tag{3.74}$$

is the length of the segment of the smooth curve between two of its points, spaced at the distance η. Thus, for the smooth curves, there is *complete self-similarity in the parameter* η/ξ at $\eta/\xi \to \infty$.

For the fractal curves there are no the finite limits of the function $\Phi(\eta/\xi)$ at $\eta/\xi \to \infty$, it is infinite. However, from the above asymptotic representation (3.72) of L_{ξ}, it follows that at $\eta/\xi \to \infty$, the function $\Phi(\eta/\xi)$ has the exponential asymptotic representation

$$\Phi(\eta/\xi) \cong (\eta/\xi)^{D-1}, \tag{3.75}$$

i.e., there is the incomplete self-similarity on the parameter η/ξ at $\eta/\xi \to \infty$. Thus, moving from the geometric specimen to the actual physical objects, we can simply compare the fractal and the *incomplete self-similarity on the parameter*.

In the framework of the linear mechanics of fracture, it is permissible [77] to model the fractal cracks in the brittle materials based on the classical Griffith's criterion. It turns out that the stress intensity factor depends on the load, the average size of the crack, and its fractal dimension [42, 78]. This approach is based on the fact that the fracture or crack surfaces, emerging during the destruction of most brittle materials, are very irregular and characterized by irregularities of all different sizes such as peaks, jags, and rugs. Therefore, the real crack at friction is far from the idealized crack with smooth sides, which is considered in the linear mechanics of fracture. It has the "sawtooth" or "zigzag" type of structure at the different scales of consideration of the Koch curve [79].

In the case of the purely brittle fracture, there are such forces like the molecular cohesion forces. Therefore, the forces $G(s)$ are collectively called the *cohesive forces*.

Thus, we need to take into account the additional dimensional characteristics: the size of the crack head d, which is determined by the load and the material structure, and the characteristic of the cohesive forces G_0.

The analysis shows that for the large class of the practically important cases of the brittle and quasi-brittle fractures, the following hypothesis conjectures are valid [80]: (1) *the smallness of size* of the crack head d in comparison with the size of the crack $l(d/l \ll 1)$; (2) *the autonomy* of head, i.e., the similarity in the state of dynamic equilibrium (and hence in generating cohesive forces) for all cracks within material under the given environmental conditions. The maximum cohesive forces cause the dynamic equilibrium, so that the slightest increase in the load makes the crack to spread.

The autonomy of the crack head is due to the fact that the specific load applied to the body is σ_0 times much smaller than the cohesive forces $G_0(\sigma_0/G_0 \ll 1)$. Therefore, the theory of brittle (and quasi-brittle) destruction is intermediate asymptotic, and it turns out that not every significant permanents d and G_0 are separate: The only material constant, in addition to the constants of the theory of elasticity, is the *cohesive module* or the *crack resistance*:

$$K = \int\limits_{0}^{d} \frac{G(s)\mathrm{d}s}{\sqrt{s}}; \quad K \sim G_0\sqrt{d}. \tag{3.76}$$

The cohesive module has the dimension FL^{-32}. It characterizes the material resistance to the crack distribution and is the independent characteristic of the material strength properties. The values of cohesive module for some materials are the structural steel—$K \sim 2.5 \times 10^4 \, \text{kg/cm}^{3/2}$ and the duralumin—$K \sim 10^4 \, \text{kg/cm}^{3/2}$.

The cohesive module K, introduced in [80], should be distinguished from the material strength K_{IC} introduced at the same time by Irwin [81] and determined by the initial critical crack growth. The initial critical crack growth requires the instability of mobile equilibrium state. At the beginning of the crack spread, the unstable autonomous crack head may not enough have time to form. Hence, it explains the large scattering of K_{IC}.

The cohesive module (the crack resistance) is one of the crucial parameters in formulating the similarity laws of the brittle and quasi-brittle fracture. The appearance of one parameter $K \sim G_0\sqrt{d}$ instead of two d and G_0 is the typical manifestation of the incomplete self-similarity on the parameter G_0/σ_0 at $G_0/\sigma_0 \to \infty$.

There are three types of the loading parameters: the dimension stress σ, the tension (the force divided by the length) s, and the force S. The values of these parameters, corresponding to the destruction σ_{f}, s_{f}, S_{f} in the brittle or the quasi-brittle fracture of body of the predetermined shape, are defined by two dimensional parameters—the cohesive module K and the body dimension l.

The dimensional elastic constants are not part of the governing parameters, because when setting the loads, acting on the body, the stress field does not depend on them.

As it can be seen from the dimensional analysis, there is no similarity in defining the parameters at the brittle and quasi-brittle fracture, and therefore,

$$S_f = \text{const} \cdot Kl^{3/2}; \quad s_f = \text{const} \cdot Kl^{1/2}; \quad \sigma_f = \text{const} \cdot Kl^{-1/2}. \tag{3.77}$$

Therefore, the constants in (3.77) can be determined from the test on the geometrically similar model made of any material and fractured following the quasi-brittle mechanism. The only requirement for the design is the similarity of its geometrical model with the original, including the similarity of initial cracks.

If the PD of the material at the destruction is not concentrated near the crack, but occupies the significant part of structure (in this case, the destruction is unsuccessful called viscous), then there is a new dimension determining parameter, the yield strength σ_v. Consequently, there is the similarity parameter

$$I = \sigma_v \cdot \frac{\sqrt{l}}{K}, \tag{3.78}$$

which is called the parameter of Irwin because he [82] was the first to discover the decisive influence of parameter, equivalent to I, on the ductile fracture and the transition from the quasi-brittle fracture to the ductile.

Thus, to obtain the ductile fracture parameters, we have

$$S_f = \sigma_v l^2 \Phi_S(I); \quad s_f = \sigma_\gamma l \Phi_s(I); \quad \sigma_f = \sigma_\gamma l \Phi_\sigma(I). \tag{3.79}$$

3.3 Bifurcation Doubling Model (Feigenbaum Scheme) for Fatigue Crack Growth

As it was noted in Sect. 3.1, the analysis of the FCG from the prospects of synergetics allows to consider the system of "specimen-loading device" as the dynamic system consisting of the large number of nonlinear oscillators of Duffing (the oscillators with cubic nonlinearity), in which the transition from order to chaos is accompanied by the infinite sequence of the period-doubling bifurcations in accordance with the Feigenbaum law [22, 83, 84].

We shall note that the appearance of the period-doubling bifurcation is the threshold of synchronization, i.e., the beginning of the system complex behavior in time of leaving the region of synchronization [40]. Under the synchronization phenomenon, we refer to the periodic motion with a period multiplied by the period of the external force.

The main question of the theory of chaos comes down to how to determine its origin and predict the further course of the system evolution.

3.3.1 Universality of the Feigenbaum Theory to Describe
the Behavior of Nonlinear Systems

Feigenbaum began his studying of the nonlinear system behavior by analyzing the intervals between bifurcations (period doubling) in the orbit diagram for the quadratic function.

$$y = \lambda x(1 - x). \tag{3.80}$$

The dynamic system corresponding to this function is described by the quadratic mapping, called the *logistic mapping*

$$x_{n+1} = \lambda x_n(1 - x_n), \tag{3.81}$$

here x_n—the dynamic variable and λ—the parameter, which affects the dynamic property. The basic meaning of the analysis carried out by Feigenbaum lies in its versatility. He described the mechanism known as "*getting chaos via period doubling*" occurring not only at the iteration of the function $f(x) = \lambda x(1 - x)$, but also for the large class of the double-digit interval mapping within themselves, such as $x^2 + c$, with $\sin \pi x$ and $cx^2 \sin(\pi x)$, defined at the suitable intervals.

Appearing on the right-hand side of the Eq. (3.81), the function has the maximum at $x = 1/2$. If we count the variable from the point of extremum and assume that

$$X = \frac{x - \frac{1}{2}}{\frac{\lambda}{4} - \frac{1}{2}},$$
$$\mu = \lambda\left(\frac{\lambda}{4} - \frac{1}{2}\right), \tag{3.82}$$

in the new notation, we obtain

$$X_{n+1} = 1 - \mu X_n^2. \tag{3.83}$$

This presentation form of the logistic mapping is convenient for the theoretical analysis and will be further used in conjunction with the mapping

$$y_{n+1} = y_n^2 + c, \tag{3.84}$$

obtained from (3.83) after the substitution

$$X = \frac{1}{c} - y, \quad \mu = -c. \tag{3.85}$$

The simplest discrete dynamical system consists of the starting point x_0 and the iterated function f: x_0—the starting point, $x_1 = f(x_0)$, $x_2 = f(x_1) = f(f(x_0)), \ldots, x_n = f(x_{n-1}) = f(f \ldots (f(x_0))) = f^n(x_0)$, where $f^n(x_0)$

indicates nth iteration of the function $f(x)$ (rather than nth power of $f(x)$). Let $f(x)$ be the continuous function of the real variable $x \in X \subset R^1$, $R^1 = (-\infty; +\infty)$, mapping X in X, i.e., $f \in C(X,X)$. We shall consider the dynamical systems given by the mapping

$$x \to f(x), \tag{3.86}$$

when the phase space X is the interval on the line R^1, with limit or limitless.

If $x(t)$ is the solution of the equation

$$x(t+1) = f(x(t)), \tag{3.87}$$

$t \in Z^+$ (Z^+—the set of positive integers), then the graph of solution

$$\mathrm{gr}\, x(t) = \{(x,t) : x = x(t), t \in Z^+\} \tag{3.88}$$

is the countable set in the space $X \times Z^+$. The mapping

$$\{x \to f(x), t \to t+1\} \tag{3.89}$$

displays $\mathrm{gr}\, x(t)$ into itself. When designing graphics $\mathrm{gr}\, x(t)$ in the space X, we obtain the set

$$\{x \in X : x = x(t), t \in Z^+\} = \{f^t(x_0), t \in Z^+\}, f^0(x_0) = x_0.$$

This set is invariant under the mapping (3.86) and represents by itself passing through $x0$ the trajectory of the dynamical system $\{f^n\}$ or, for brevity, the trajectory of mapping (3.86). Thus, to solve the Eq. (3.87), it is equivalent to find the behavior of corresponding trajectory mapping (3.86).

The sequence $\{f^n(x_0)\}_{n=0}^{\infty}$ is also called the *orbital* of the initial point x_0. The fixed point of mapping f is defined as the point x satisfying $f(x) = x$. The fixed point x is called *attracting* if the point orbits within some neighborhood (possibly very small) converge to it. The fixed point x is called *repulsive* if the point orbits that sufficiently close to the point part away from it.

To investigate the fixed point x of mapping $f(x)$ on the stability, it is necessary to calculate the multiplier $\mu(x) = f'(x)$, showing the changes of the small perturbation for the cycle period.

If $|f'(x)| < 1$, then x is the attracting point, and if $|f'(x)| > 1$, then x is the repulsive point. In the case where $|f'(x)| = 1$, a certain conclusion can be drawn: The point x can be either attractive, or repulsive or neither one. The simplest behaviors have the *periodic orbits or cycles*. The point $x_0 \in X$ is called periodic of the period m, if $f^m(x_0) = x_0$ and $f^i(x_0) \neq x_0$ at $0 < i < m$. Each point $x_i = f^m(x_0)$, $i = 1, 2, \ldots, m-1$, is also periodic with the period m, and the points $x_0, x_1, \ldots, x_{m-1}$ form the periodic trajectory or the cycle of period m.

The following will be mainly used for the mapping, defining the dynamical system

$$x \to \lambda x(1 - x). \tag{3.90}$$

This mapping and other quadratic mapping, for example $x \to x^2 + c$ and $x \to 1 - c$, which are reduced to (3.90) after changing the coordinates, are most widely used. For $f(x) = \lambda x(1 - x)$, we have $f(0) = f(1) = 0$ and $\max f(x) = f(1/2) = \lambda/4$, and then, at $0 < \lambda \le 4$, the interval $x \in I$, $I = [0, 1]$ is mapped into itself. The graph $f(x)$ is the parabola with the peak at $x = 1/2$.

One of the main objects is the periodic points and formed by them the cycles. Naturally, two classes of cycles are distinguished among them: attracting and repulsive. The cycle $B = \{\beta_1, \ldots, \beta_m\}$ of mapping $X \to X$ is *attracting* if there is a neighborhood U of this cycle such that $fU \subset U$ and $\cap fU = B$. Hence, for each point $x \in X$, the trajectory $\{f^i(x)\}_{i=0}^{\infty}$ splits into the m sequences converging to the points $\beta_1, \ldots, \beta_m$, respectively.

The cycle B is repulsive, if there is a neighborhood U, such as each point of U/B departs U for a finite time, i.e., for each $x \in U/B$, there is n_x such as that $f^{n_x}(x) \notin U$.

The sufficient conditions distinguishing the attracting and repulsive cycles are well known, when f—the differentiable function [22, 85, 86]. The cycle B of the period m is attractive if the spectrum of the differential Df^m, calculated at one point of the cycle, lies within the unit circle, and it is repulsive if the spectrum lies outside the unit circle. In particular, if $X \subset R^1$, the spectrum consists of a single cycle multiplier

$$\mu(B) = \frac{\mathrm{d}}{\mathrm{d}x} f^m(x)\bigg|_{x \in B} = f'(\beta_1). \tag{3.91}$$

If $|\mu(B)| < 1$, then the cycle B is attracting, and if $|\mu(B)| > 1$, then the cycle B is repulsive.

When the dynamic system depends on the parameters, their change can lead to the various qualitative restructuring of the system, in particular the emergence of new periodic orbits, the conversion of the attracting cycles into the repulsive and vice versa, etc. In this case, we say that the bifurcations of periodic orbits take place in the dynamic system. Let us consider the emergence of the bifurcation for mapping (3.90).

1. $\underline{0 < \lambda \le 4}$. In this case, $I = [0, 1]$, there is only one fixed point $x = 0$, and it is attracting. Since $f(x) < x$ at $x \in I/\{0\}$, then

$$\bigcap_{n=0}^{\infty} f^n(I/\{0\}) = \{0\},$$

Whatever the point $x \in I/\{0\}$ is, there is $f^n \to 0$ at $n \to \infty$. Consequently, each trajectory $\{f^n(x)\}_{n=0}^{\infty}$ is attracted by the fixed point $x = 0$ (Fig. 3.5)

Fig. 3.5 The graph of the bifurcation occurrence (one fixed point, $x = 0$)
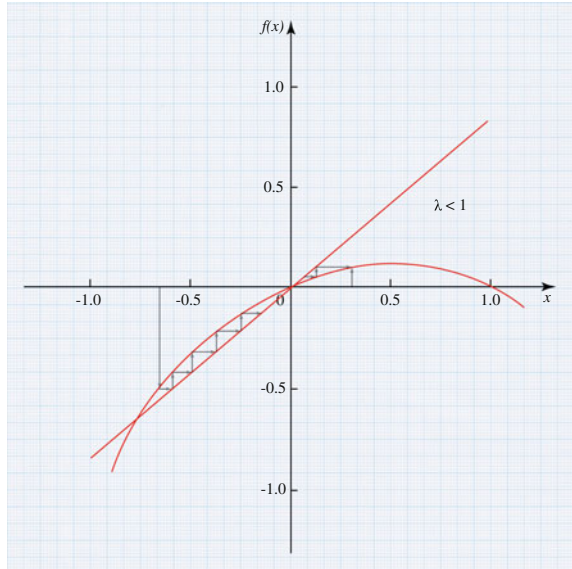
Fig. 3.6 The graph of the bifurcation occurrence $(x = \beta_1)$
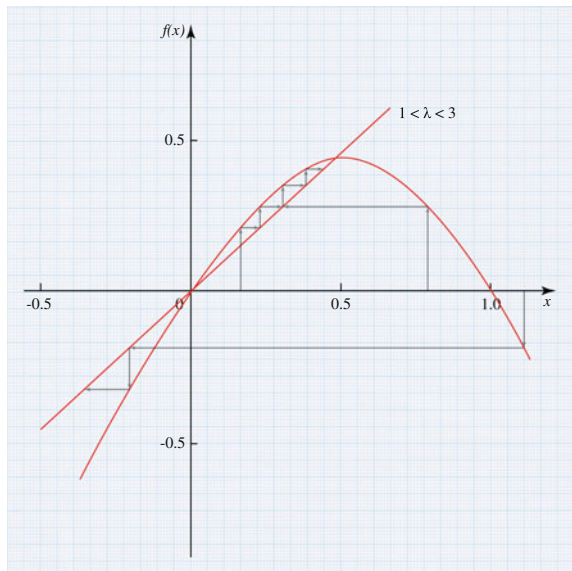
2. $\underline{1 < \lambda \leq 3}$. When $\lambda > 1$ besides the fixed point $X = 0$, another fixed point is formed $\beta_1 = 1 - 1/\lambda$ (Fig. 3.6). Since $f'(x) = \lambda(1 - 2x)$, the multiplier (3.91) can be written in the form $f'(\beta_1) = 2 - \lambda$, and hence, the fixed point $x = \beta_1$ at $1 < \lambda < 3$ is attractive. Whatever the point $x_0 \in (0, 1)$ is, there is $f^n(x_0) \to \beta_1$ at

$n \to \infty$. At $\lambda = 3$, the fixed point $x = \beta_1$ is still attractive, although $|\mu(\beta_1)| = 1$ (Fig. 3.6).

3. $3 < \lambda \le 1 + \sqrt{6}$. When the parameter λ passes through $\lambda_1 = 3$, there is a new bifurcation: The fixed point $x = \beta_1$ transforms from attracting into repulsive ($|\mu(\beta_1)| > 1$ for $\lambda > 3$), and it generates the attractive cycle of the period 2. The way the mapping (3.90) changes within the neighborhood of $x = \beta_1$ is shown in Fig. 3.7, and it shows the graph of the function $y = f(f(x))$, when the parameter λ passes through the value $\lambda_1 = 3$. The cycle of period 2 (Fig. 3.7) creates a point

$$\beta_1^{(1),(2)} = \frac{\lambda + 1 \pm \sqrt{\lambda^2 - 2\lambda - 3}}{2\lambda}. \tag{3.92}$$

The values $\beta_2^{(1)}$ and $\beta_2^{(2)}$ are defined as the roots of the equation $f^2(x) = x$ and are different from the roots of the equation $f(x) = x$ (from which we define the fixed points of the function $f(x)$). Thus, for $\beta_2^{(1)}$, $\beta_2^{(2)}$, we obtain the equation $\lambda^2 x^2 - \lambda(\lambda + 1)x + (\lambda + 1) = 0$, which gives (3.92). From (3.92), we see that there is the cycle of the period 2, where $\lambda^2 - 2\lambda - 3 > 0$, i.e., where $\lambda > 3$ or $\lambda < -1$, but we consider only the positive values for λ.

Figure 3.7 shows that the graph of $f^2(x)$ intersects the line $y = x$ in the triad of points $\left(\beta_2^{(1)}, \beta_1, \beta_2^{(2)} \right)$, where the point $x = \beta_1$ is repulsive, and points $x = \beta_2^{(1)}$ and $x = \beta_2^{(2)}$ are attracting.

Since

$$\mu\left(\left\{\beta_2^{(1)}, \beta_2^{(2)}\right\}\right) = f'\left(\beta_2^{(1)}\right) \cdot f'\left(\beta_2^{(2)}\right) = \lambda^2\left(1 - 2\beta_2^{(1)}\right)\left(1 - 2\beta_2^{(2)}\right)$$

$$= \lambda^2\left[1 - 2\left(\beta_2^{(1)} + \beta_2^{(2)}\right) + 4\beta_2^{(1)} \cdot \beta_2^{(2)}\right] = 4 + 2\lambda - \lambda^2,$$

then $\left|\mu\left(\left\{\beta_2^{(1)}, \beta_2^{(2)}\right\}\right)\right| < 1$ if $3 < \lambda \leq 1 + \sqrt{6} \approx 3.449$. At these values of λ, the cycle $S^2 = \left\{\beta_2^{(1)}, \beta_2^{(2)}\right\}$ of the period 2 is attracting and stable according to Lyapunov.

Whatever the point $x_0 \in (I \backslash \{0, 1\}) / \{f^{-n}(\beta_1)\}^{\infty}$ is, the trajectory of $f^n(x_0)$ is attracted by the cycles $\left\{\beta_2^{(1)}, \beta_2^{(2)}\right\}^{n=0}$, so that the sequence $\{f^{2n}(x_0)\}_{n=0}^{\infty}$ converges at the point of the cycle $\left\{\beta_2^{(2)}\right\}$, and the sequence $\{f^{2n+1}(x_0)\}_{n=0}^{\infty}$ converges at the point of the cycle $\left\{\beta_2^{(1)}\right\}$.

4. $\underline{1 + \sqrt{6} < \lambda < 3.569\ldots}$ While passing through $\lambda_2 = 1 + \sqrt{6} \approx 3.449$, next bifurcation takes place (Fig. 3.8): The cycle $\left\{\beta_2^{(1)}, \beta_2^{(2)}\right\}$ transforms from attracting into repulsive (at $\lambda > \sqrt{6}$, we have $\left|\beta_2^{(1)}, \beta_2^{(2)}\right| > 1$), and it generates the attracting stable cycle $\{S^4\}$ of the period 4: $x_{4n} \to \beta_4^{(1)}$, $x_{4n+1} \to \beta_4^{(2)}$, $x_{4n+2} \to \beta_4^{(3)}$, $x_{4n+3} \to \beta_4^{(4)}$ at $n \to \infty$, and $\beta_4^{(2)} = f\left(\beta_4^{(1)}\right)$, $\beta_4^{(3)} = f\left(\beta_4^{(2)}\right)$, $\beta_4^{(4)} = f\left(\beta_4^{(3)}\right)$, $\beta_4^{(1)} = f\left(\beta_4^{(4)}\right)$. If we keep increasing the parameter λ further, at

Fig. 3.8 The graph of generating new bifurcations
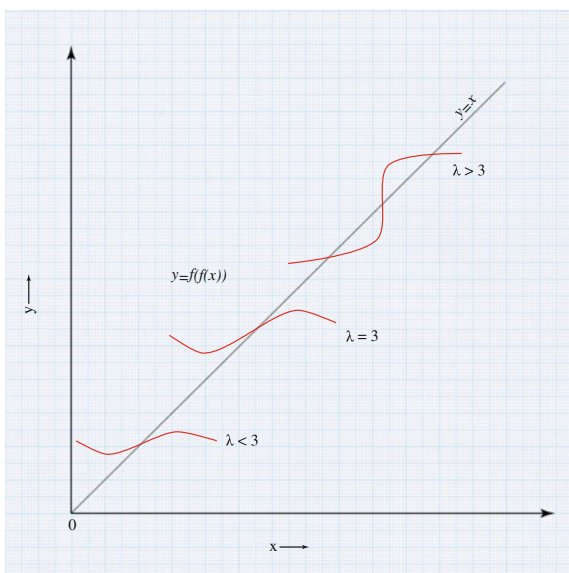
Table 3.2 Successive values of λ_n

#	The cycle type	λ_n (the values of λ when the cycles occur)
1	2-cycle	3.00
2	4-cycle	3.44948
3	8-cycle	3.54408
4	16-cycle	3.56872
5	32-cycle	3.5698912
∞	Aperiodic attractor	3.5699456

$\lambda_3 \approx 3.54$ the cycle S^4 of the period 4 also becomes repulsive, and from there, it generates the attracting cycle of the period 8 (it attracts all points of the interval *I*, with the exception of a countable set of points). The period doubling of the attracting cycles will continue, while the parameter λ keeps increasing until $\lambda = \lambda^* \sim 3.549$.

Here is the table of successive values of λ_n, where the bifurcation takes place (Table 3.2).

As is shown in Table 3.2, the sequence of the period-doubling bifurcation points converges to the certain limit, which in analogue with the theory of the phase transitions is also called *the critical point*.

The quality adjustments, occurring with cycles when the parameter λ increases, are convenient to present with the help of the bifurcation diagram (Fig. 3.9). This kind of diagram is called *the Feigenbaum tree*. The graph provides the visual representation on fragmenting the scale of the dynamic variable, and the presence of the *scaling* properties, i.e., *the scale invariance* when the same element of the image is repeated at the magnified scale.

Fig. 3.9 The bifurcation diagram (the Feigenbaum tree)
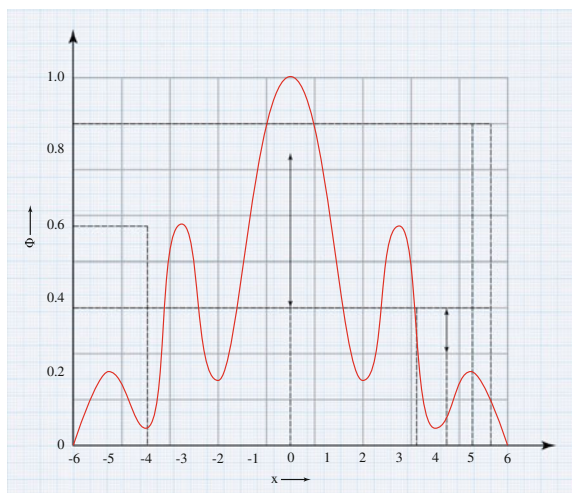
Here $\lambda_1, \lambda_2, \lambda_3, \ldots$—the values of the parameter λ, where the period doubling takes place; $\Lambda_1, \Lambda_2, \Lambda_3$—the values of parameter for which $x = 1/2$ is the element of the cycles S^2, S^4, S^8 etc., (such cycles are called the ultrastable).

The definition becomes clear from the inequality $|\mu(\beta)| < 1$. The bifurcation curves for $\beta_2^{(1)}$ and $\beta_2^{(2)}$ on the diagram spread as the branches of parabola (in accordance with the formula (3.92), it follows that for $\lambda \rightarrow \lambda_1 = 3\left|\beta_2^{(1)} - \beta_2^{(2)}\right| = 0(\sqrt{\lambda - \lambda_1})$, and the fixed point β_1 very slowly drifts at the same time: $\beta_1(\lambda) - \beta_1(\lambda_1) = 0(\lambda - \lambda_1)$. A similar situation occurs in the vicinity of the subsequent bifurcation values $\lambda_2, \lambda_3, \ldots$.

When the parameter λ passes through $\lambda_2 = 3.4498$, the function $f^3(x)$ intersects the line $y = x$ at seven points $\beta_3^{(1)}, \beta_2^{(1)}, \beta_3^{(2)}, \beta_1, \beta_3^{(2)}, \beta_2^{(2)}, \beta_3^{(3)}$. Where the points $\beta_2^{(1)}, \beta_1, \beta_2^{(2)}$ are repulsive, and the remaining four points are attracting, which at the next critical value of the parameter λ, equal to $\lambda_3 = 3.56872$, will become repulsive, etc. When $\lambda = \lambda_n$, corresponding to the appearance of the 2^n-cycle, the function f^{2n+1} crosses the line $y = x$ at $2^{n+1} - 1$ points, of which 2^n points will be attracting and the others are repulsive at $\lambda = \lambda_{n+1}$.

As it was noted by Feigenbaum, if we calculate the values of λ_n quite accurately and create relationships

$$\delta_n = \frac{\lambda_n - \lambda_{n-1}}{\lambda_{n+1} - \lambda_n}, \quad n = 1, 2, \ldots, \tag{3.93}$$

then $\delta_n \rightarrow \delta = 4.669162\ldots$ at $n \rightarrow \infty$, i.e., the cycle occurrence rate for the period doubling, with n increasing, is characterized by the single constant $\delta = 4.669162$, called *the Feigenbaum constant*.

The asymptotical (at large n) distance, separating the adjacent points of the attractor S^{2^n}, decreases between two successive period doublings by the constant factor. Besides, at each period doubling near $x = 1/2$, the attractor element moves from one side of the point $x = 1/2$ to the other. Let d_n be the algebraic distance from $x = 1/2$ to the nearest element of the attractor with the period 2^n at $\lambda < \lambda_n$. Then,

$$\lim_{n \rightarrow \infty} \frac{d_n}{d_{n+1}} = -\alpha, \tag{3.94}$$

where $\alpha = 2.502907875\ldots$.

Instead (3.81), we consider another set of mapping $x_{n+1} = f(x_{n+1}, \lambda)$ with the symmetric with respect to x functions f, having one maximum in the interval $[0, 1]$ and another close to the top of a quadratic parabola. In these mappings, there is also the infinite cascade of the period-doubling bifurcations when the parameter λ (particularly including the above logistic mappings (3.83) and (3.84)). It was found that in any such model, the numbers α and β are the same. Moreover, regardless of the type of function f, the limit is

$$\lim_{n\to\infty}(-\alpha)^n f^{2^n}\left(\frac{x-0.5}{(-\alpha^n)},\ \lambda_n\right) \tag{3.95}$$

and it will be the same. It is called *the universal function* $g_0(x)$.

It is sufficient that depending on one-parameter function $f(x,\lambda)$ to be a smooth function with a quadratic maximum (let it be the point $x=0$), it actually must be symmetric with respect to this point even far from it.

The existence of constants α, δ and the universal function $g_0(x)$ was discovered and explained by Feigenbaum in 1978. He proposed the functional equations defining α, δ, and $g_0(x)$. Because of the universality of numbers α, δ, the function $g_0(x)$, and other functions of this kind, this theory is called *theory of universality*.

The bifurcation diagram, or as it is also called *the orbit diagram* for the quadratic function (3.80), looks almost the same as for the quadratic function $y=x^2+c$. It is the graph in which the values are projected along the ordinate, and on each horizontal line $y=c$ we insert points attracting the periodic orbits of x^2+c.

We denote by $c_0, c_1, c_2, \ldots$ the bifurcation points on the orbit diagram, i.e., those points c_n, where the function $f(x)=x^2+c$ iteration replaces the attracting orbit of period 2^n with that attracting orbit of period 2^{n+1}. These points are listed in Table 3.3 [85].

At $c>1/4$, the mapping x^2+c has no real fixed points. At $3/4<c<1/4$, there is the attracting orbit of the period 1. At $-5/4<c<-3/4$, there is the attracting orbit of the period 2, which turns into the attracting orbit of period 4, when c passes through $-5/4$. This implies that $c_0=-3/4$ and $c_1=-5/4$. It becomes harder and harder to define these bifurcation points as n increases. Other values of c_0 up to $n=10$ inclusive are shown in Table 3.3.

Table 3.3 The bifurcation point c_n and the superattracting points c_n^* for the logistic mapping x^2+c

#	c_n	$\frac{c_n-c_{n-1}}{c_{n+1}-c_n}$	c_n^*	$\frac{c_n^*-c_{n-1}^*}{c_{n+1}^*-c_n^*}$
0	-0.75	$-$	0	$-$
1	-1.25	4.233738275	-1.0000000000000	3.21851142203809
2	-1.368989394	4.551506949	-1.31070264133683	4.38567759856834
3	-1.3940461566	4.645807493	-1.38154748443206	4.60094927653812
4	-1.3996312389	4.663938185	-1.39694535970456	4.65513049539190
5	-1.4008287424	4.668103672	-1.40025308121478	4.66611194782723
6	-1.4010852713	4.668966942	-1.40096196294484	4.66854858148123
7	-1.401140214699	4.669147462	-1.40111380493978	4.669060660577530
8	-1.401151982029	4.669199003	-1.40114632582695	4.66917155556749
9	-1.401154502237	4.66916224	-1.40115329084992	4.66919514619589
10	-1.401155041989	$-$	-1.40115478254662	$-$

Based on Table 3.3, we can make two important conclusions. The first one is that the bifurcation points c_n tend to the limit c_∞:

$$c_\infty = \lim_{n \to \infty} c_n = -1.401155. \tag{3.95}$$

The point c_∞ is called the Feigenbaum point. Within the interval $c = -1/4$ and c_∞, the period doubling occurs as $c \to c_\infty$. The other area, where $c > c_\infty$, is called the domain of chaos.

The second conclusion is that the ratio of the lengths of the successive intervals to the bifurcation points has the limit

$$\delta = \lim_{n \to \infty} \frac{c_n - c_{n-1}}{c_{n+1} - c_n} = 4.669162\ldots, \tag{3.96}$$

where $\delta = 4.669162\ldots$, is the Feigenbaum universal constant (3.93).

The constant δ is used to forecast the beginning of chaos, if we take into account that the interval between c_0 and c_∞ is approximately equal to

$$\frac{\delta}{\delta - 1}(c_1 - c_0).$$

As the numerical studies showed [51], the values of α and δ, defined by (3.95) and (3.96), do not depend on the particular form of the quadratic mapping. The main thing is that they are unimodal (have one extremum) and that extremum must be quadratic.

If near the maximum, which can be seen as located at $x = 0$, the successor function $f(x)$ is written in the form (see Sect. 3.1)

$$f(x) = 1 - \lambda|x|^z,$$

where $z > 1$, λ—the bifurcation parameter and then *the generalized Feigenbaum rule* can be written as [40]

$$\lambda_\infty - \lambda_n \, n \xrightarrow{\sim} \infty \, \delta^{-n},$$

Table 3.4 The parameters α and δ at different z values

z	δ	α	z	δ	α
1.0	2	∞	5.0	8.345	1.556
1.5	3.8004	3.8889	6.0	9.31	1.468
2.0	4.6692	2.5029	7.0	10.18	1.405
2.5	5.4127	2.1368	8.0	10.98	1.35
3.0	6.0847	1.9277	9.0	11.72	1.32
3.5	6.7053	1.7895	10.0	12.48	1.29
4.0	7.2851	1.6903	11.0	13.15	1.27

where λ_n—the value of parameter μ, at which there is the nth period-doubling bifurcation,

$$\mu_\infty = \lim_{n\to\infty} \mu_n,$$

δ—the constant depending on the exponent z in the expression for $f(z)$.

The parameters α and δ at different z values are shown in Table 3.4 [87].

The table shows that the value of δ monotonically increases with an increase of z. The value $\delta = 4.6692\ldots$, corresponding to $z = 2$, is commonly referred as the Feigenbaum constant. In the future, it is unless specifically stated, so under the symbol δ, we understand exactly that value.

The Feigenbaum rule can be written in another form [19]

$$\omega_{n\ n\to\infty}(\lambda_\infty - \lambda_n)^\nu,$$

where $\omega_n = 2\pi T_n$, $\qquad T_n = T \cdot 2^n$ $\qquad$ (T—the oscillation period), $\nu = \ln 2 / \ln \delta = 0.4498\ldots$.

The recorded in this form, the Feigenbaum rule is similar to the rule of change ω_n for the phase transition of type II with the critical exponent ν. Therefore, the constant υ is called *the critical index of transition* to the stochasticity through the sequence of the period-doubling bifurcations [88].

The process of broadening of the spectral lines of subharmonics exceeding the threshold is called universal [89]

$$\Delta\omega = c(\mu - \mu_u)^\beta,$$

where $\beta = 2.42$ for the chaotic display $x_{n+1} = \mu - x_n^2 = f(x_n, \mu)$, which is the one-parameter family of curves such as the inverted parabola with the quadratic maximum at $x_n = 0$.

Due to the broadening of the spectral lines according to the above dependences on the difference $(\mu - \mu_u)$ outside the critical region $(\mu > \mu_u)$ with an increase of the parameter μ, the strange attractor gradually "swells," continuously including into the area of stochasticity, the elements of 2^n-cycles ($n = \infty, \ldots, k, k - 1, \ldots, 0$). The versatility of broadening of the spectral lines naturally leads to the universality in the evolution of the integral power spectrum, which increases in the supercritical region according to the rule [90]:

$$S_I = \int\limits_{-\infty}^{+\infty} S(f)df = c(\mu - \mu^*)^\sigma, \quad \sigma \approx 1.525,$$

where $S(f) = |c(f)|^2$, $c(f)$—the amplitude of spectrum at the frequency f.

It should be noted that in the real physical systems, where there is the external noise, the bifurcation sequence might not be observed. The influence of noise on the Feigenbaum scenario of the transition to the chaos will be considered separately (Sect. 3.3).

It is quite difficult, if not impossible, to analytically determine the bifurcation points c_n for the particular function, such as $x^2 + c$. However, there is another way to determine them using points c_n^*, lying between each pair of the bifurcation points c_n and c_{n+1}, which have the superattracting orbit with the period 2^n (Table 3.3).

The point x_0, for which $f'(x_0) = 0$, is called the critical point of the function $f(x)$. For the value $c = c_n^*$, the critical point of $f_c(x)$, which determines the logistic mapping with the parameter c (e.g., for $f_c(x) = x^2 + c$, will satisfy the equation $f^{(n)}(x_0) = x_0$. It has been proven that the Feigenbaum constant δ is defined as

$$\delta = \lim_{n \to \infty} \frac{c_n^* - c_{n-1}^*}{c_{n+1}^* - c_n^*}. \tag{3.97}$$

The values of function c_n^* can be found numerically applying Newton's method to the function

$$\varphi(x_0) = f^{(2n-1)}(x_0) - x_0, \tag{3.98}$$

where x_0—the critical point of $f_c(x)$.

Finding the root of the equation $\varphi(x) = 0$ using Newton's method starts with the zero-order approximation $r^{(0)}$ and continues according to the formula

$$r^{(n)} = r^{(n-1)} - \frac{\varphi(r^{n-1})}{\varphi'(r^{n-1})}. \tag{3.99}$$

If $r^{(0)}$ is sufficiently close to the root, then $\lim r^{(0)} = r$. From (3.97), it follows that

$$c_n^* \approx c_{n-1}^* + \frac{c_{n-1}^* - c_{n-2}^*}{\delta}. \tag{3.100}$$

The suitable initial value $c_n^{*(0)}$ for $c_n (n \geq 2)$ can be obtained by substituting δ into δ_{n-1}^* in (3.100), where

$$\delta_n^* = \frac{c_{n-1}^* - c_{n-2}^*}{c_n^* - c_{n-1}^*}, \quad n = 2, 3 \ldots, \tag{3.101}$$

i.e.,

$$c_n^{*(0)} \approx c_{n-1}^* + \frac{\left(c_{n-1}^* - c_{n-2}^*\right)^2}{c_{n-2}^* - c_{n-3}^*}, \quad n = 2, 3. \ldots \tag{3.102}$$

In this case, there is a problem for the initial values $c_n^{*(0)}$ for $n = 2, 3$, which we solve by putting $\delta_1^* = \delta_2^* = 4$, while calculating $c_n^{*(0)}$ by the formula

$$c_{n-1}^{*(0)} \approx c_{n-1}^* + \frac{c_{n-1}^* - c_{n-2}^*}{4}, \quad n = 2, 3. \ldots \tag{3.103}$$

The values $f_c^{(2n-1)}(x_0)$ in (3.98) are calculated by the iteration of $x_k = f_c(x_{k-1})$, i.e., $f_c^{(2)}(x_0) = f_c(x_1)$, where $x_1 = f_c(x_0)$, $f_c^{(4)}(x_0) = f_c\left(f_c^{(3)}(x_0)\right) = f_c\left(f_c^2(x_1)\right) = f_c(f_c(f_c(x_1)))$.

The derivative $\varphi(c)$ is also computed by iterating. Let

$$z_k = \frac{\mathrm{d}}{\mathrm{d}c} f_c^{(k)}(x_0).$$

Then, in the case $f_c(x) = x^2 + c$, it gives

$$z_k = 2x_{k-1}z_{k-1} + 1, \tag{3.104}$$

and for $f_c(x) = cx(1 - x)$, we obtain

$$z_k = x_{k-1}(1 - x_{k-1}) + c(1 - 2x_{k-1}) \cdot z_{k-1}. \tag{3.105}$$

Found through Newton's method, the superattracting points c_n^* for the function $f_c(x) = x^2 + c$ can for $n > 10$ be equated to its bifurcation points c_n and thereby extend Table 3.2. From (3.82)–(3.85), we find $\lambda\left(\frac{\lambda}{4} - \frac{1}{2}\right) = -c$. Consequently, the bifurcation points λ_n for function $\lambda x(1 - x)$ are associated with the bifurcation points c_n of function $x^2 + c$ by the ratio

$$\lambda_n = 1 + \sqrt{1 - 4c_n}, \tag{3.106}$$

because we consider only positive values of λ.

Since d_n in (3.94) is the distance between $x = 1/2$ and the closest point of the element of the 2^n-cycle at $\lambda = \lambda_n$ and the closest element is the 2^{n-1}-iteration of the point $x = 1/2$ (this is so, because before the n-doubling cycle, providing the split, these points are the same), we have

$$d_n = f^{2^{n-1}}\left(\frac{1}{2}, \lambda_n\right)^{-1/2}. \tag{3.107}$$

For the subsequent, it is convenient to perform, as in (3.95), the translation of the coordinates $x = 1/2 \rightarrow x = 0$. After translation, the formula (3.107) takes the form

$$d_n = f^{2^{n-1}}(0, \lambda_n)^{-1/2}, \tag{3.108}$$

i.e., if the ratio (3.94) holds, the limit

$$\lim_{n \to \infty} (-\alpha)^n f^{2n}(0, \lambda_{n+1}) \tag{3.109}$$

must exist. In addition, there will be the limit function

$$g_0(x) = \lim_{n \to \infty} (-\alpha)^n f^{2n}\left(\frac{x}{-\alpha^n}, \lambda_{n+1}\right). \tag{3.110}$$

After the above translation of coordinates, the formula (3.95) can be written as

$$g_0(x) = \lim_{n \to \infty} (-\alpha)^n f^{2n}\left(\frac{x}{(-\alpha^n)}, \lambda_{n+1}\right). \tag{3.111}$$

In the theory of universality, we consider the space with mapping of the interval $[-1, 1]$ into itself, such that $f(x) \in c^2([-1, 1])$ and $x = 0$ is the maximum point $f(0) = 1$. For such mapping, summarizing the relations (3.110) and (3.111), we can define the family of versatile functions g_r:

$$g_r(x) = \lim_{n \to \infty} (-\alpha)^n f^{2n}\left(\frac{x}{(-\alpha^n)}, \lambda_{n+1}\right), \quad r = 0, 1, 2, 3, \ldots. \tag{3.112}$$

M. Feigenbaum explained the universal nature of the quantitative rules of transitions into chaos through the sequence of period-doubling bifurcations, and he also created *the theory of universality*. To analyze the mapping of the logistic parabola type, Feigenbaum applied the method of the *renormalization group* (RG), the content of which is as follows.

Let the critical point $\lambda = \lambda_u$ have the mapping

$$x_{n+1} = f(x_n),$$

where f—the arbitrary unimodal function with the quadratic extremum at the point $x_0 = 0$, where $f(x_0) = 1$; λ—the bifurcation parameter.

Applying this mapping twice, we obtain the mapping $x_{n+1} = f(f(x_n))$. We rescale the variable $x \rightarrow x/a_0$ so that the new mapping at the origin to be also normalized in unity, i.e., $a_0 = 1/f(f(0))$, and denote the new mapping as

$x_{n+1} = f_1(x_n) = a_0(f(x_n/a_0))$. Repeating this procedure many times, we obtain *the equation of renormalized group*

$$f_{i+1}(x) = \alpha_i f_i(f_i(x/a_i)),$$

where $a_i = 1/f_i(f_i(0))$. At the critical point μ_u due to the self-similarity, there are limits

$$\lim_{i\to\infty} f_i(x) = g(x), \ \lim_{i\to\infty} a_i = a.$$

The function $g(x)$ is the fixed point of the functional *equation of Feigenbaum–Cvitanovic*

$$\hat{T}g(x) = ag(g(x/a)) = g(x),$$

where $\hat{T}$—the doubling operator; $a = 1/g(g(0))$. For the critical point corresponding to the transition into chaos through the period doubling, the boundary conditions for the last equation will be $g(0) = 1$, $g'_x(0) = 0$. The function $g(x)$ is called *universal* because it does not depend on the particular shape of the original map and is determined only by the extremum. It provides the asymptotic form 2^k-fold the applied evolution operator at the critical point when $k \to \infty$. More specifically, the following relationship is valid for the asymptotic on k

$$f^2(x) = f(f(f(\ldots(x)\ldots))) \cong \frac{g(A_k x)}{A_k}, \quad A_k = \frac{1}{f^{2^k}(0)} \cong \mathrm{const} \cdot a^k.$$

The constant a, included in the equation of the fixed point, is also universal. Feigenbaum found the numerical solution for the equation $g(x)$ assuming the quadratic extremum and the specified boundary conditions, and it is of the form

$$g(x) = 1 - 1.5276330x^2 + 0.1048152x^4 + 0.0267057x^6 - 0.0035274x^8$$
$$+ 0.0000816x^{10} + 0.0000254x^{12} - 0.0000027x^{14}.$$

The Feigenbaum universal constant a_F is equal to $2.502907876. \ldots$.

If we introduce a small perturbation of the evolution operator $f(x_n)$, slightly deviating μ from the critical value, the doubling operator $\hat{T}$ and the function $g(x)$ are also perturbed. Linearizing the operator $\hat{T}$ at the point $g(x)$ with $\mu = \mu_u$, we obtain the operator $\hat{L}_g$, which determines the behavior of the perturbation, and the equation for the eigen functions of $h(x)$ and the eigenvalues of the linearized operator ρ:

$$\hat{L}_g h(x) \equiv a\left[g'^{\left(\frac{x}{a}\right)} \cdot h\left(\frac{x}{a}\right) + h\left(g\left(\frac{x}{a}\right)\right)\right] = \rho \cdot h(x).$$

The decisive role in the perturbation behavior plays the eigenvalues that are greater than ones in modulus. In the case of the quadratic extremum, there is one such value corresponding to the crucial component of perturbation and it defines the second *Feigenbaum universal constant* $\rho_1 = \delta = 4.6692016091. \ldots$.

Mapping with the non-quadratic extremum $(z \neq 2)$ is characterized by the different values of the universal constants α and δ (see Table 3.4). However, in the numerical and actual experiments conducted for the variety of flow systems (including the distributed systems) in accordance with the Feigenbaum scenario of chaos, the scale factor $a(a = -a)$ and the convergence rate of the bifurcation sequence δ within the experimental error were consistent with the values obtained on the basis of Feigenbaum's theory on the quadratic extremum [22]. Obviously, the typical mapping is generated by the evolution operator of the streaming system near the critical point and is close to the one-dimensional mapping with the quadratic extremum, where other cases are atypical.

The universality of Feigenbaum's scenario is also evident in the behavior of the spectral amplitudes of the subharmonics arising in each period doubling. To see this, we consider the logistic mapping for the cycle with period $N = 2^k$ at the critical point, and it corresponds to the sequence of values of the dynamic variable $x_0, x_1, x_2 \ldots, x_{N-1}$. The Fourier series expansion and the inverse transformation are defined by the expressions

$$x_n = \sum_{m=0}^{N-1} c_m \exp\left(\frac{2\pi j}{N}mn\right), \quad c_m = \frac{1}{N}\sum_{n=0}^{N-1} x_n \exp\left(-\frac{2\pi j}{N}mn\right) \quad \left(j = \sqrt{-1}\right).$$

The value of $f = m/N$ is the frequency of the mth component, and for the squared amplitude, we introduce the notation

$$S(f) = S\left(\frac{m}{N}\right) = |c_m|^2.$$

At the limited transition to the infinitely large period, we obtain the following approximations [91]:

$$S\left(\frac{f}{2}\right) \cong \left(\frac{1+a^2}{4a} + \frac{1}{2a^3}\cos \pi f\right)S(f),$$

$$S\left(\frac{1}{2} + \frac{f}{2}\right) \cong \left(\frac{1+a^2}{4a^4} - \frac{1}{2a^2}\cos \pi f\right)S(f),$$

where $a = -a$, $\alpha = 2.5029\ldots$—the first Feigenbaum universal constant. The spectral intensities at the frequencies $f = f_0 2^{-k}\left(f_0 = \frac{1}{2\pi T_0}, T_0\text{—the period}f(x)\right)$ are

obtained by the successive application of the above relationship between $S(\frac{f}{2})$ and $S(f)$. Since $f \to 0$ and $\cos \pi f \to 1$, the conversion factor of intensities is equal to

$$\rho = \left(1 + a^2\right) / 4a^4 + \frac{1}{2a^2}.$$

Therefore, $S(f_0 2^{-k}) \cong \rho^k \cdot S(f)$. We introduce $s(f) = S(f)/f^k$, where $k = \log_2 \rho = 6.19$. Then, we have $s(f \cdot 2^{-k}) \approx s(f)$. The constant ρ is slightly different from that empirically found value, which is explained by the approximations made in the derivation of the connection equations between $S(\frac{f}{2})$ and $S(f)$.

3.3.2 Bifurcation Doubling Process Forecasting

Let us define the local rescaling near the mth element of the 2^n-cycle, i.e., the distance between the mth iteration of the point $x = 0$ and next element of this cycle. If we denote this rescaling rule through the letter δ, then

$$\delta_n(m) = \frac{d_{n+1}(m)}{d_n(m)}, \tag{3.113}$$

Comparing α with the definition according to the formula (3.94), we note that $\delta_n(0) \approx (-\alpha)^{-1}$. It is easy to see that

$$d_n(m) = x_m - f^{2^{n-1}}(x_m, \lambda_n), \tag{3.114}$$

where x_m—the mth iteration of the point $x_0 = 0$. Taking into account the commutative property of iterations

$$f^n \circ f^m = f^m \circ f^n = f^{m+n}, \tag{3.115}$$

(3.114) it can be written as

$$d_n(m) = f^m(0, \lambda_n) - f^m\left(f^{2^{n-1}}(0, \lambda_n), \lambda_n\right). \tag{3.116}$$

Let $m = 2^{n-r}$, then

$$\begin{aligned}
d_n(2^{n-r}) &= f^{2^{n-r}}(0, \lambda_n) - f^{2^{n-r}}\left(f^{2^{n-1}}(0, \lambda_n), \lambda_n\right) \\
&= f^{2^{n-r}}\left(0, \lambda_{(n-r)+r}\right) - f^{2^{n-r}}\left(f^{2^{n-1}}(0, \lambda_n), \lambda_{(n-r)+r}\right).
\end{aligned} \tag{3.117}$$

For $r \ll n$ (but $r \gg 1$ for large n), using (3.112), we obtain

$$d_n(2^{n-r}) \approx (-\alpha)^{-(n-r)}\left[g_r(0) - g_r\left((-\alpha)^{n-r}f^{2^{n-1}}(0, \lambda_n)\right)\right]$$

or

$$d_n(2^{n-r}) \approx (-\alpha)^{-(n-r)}\left[g_r(0) - g_r\left((-\alpha)^{-r+1}g_1(0)\right)\right]. \tag{3.118}$$

It implies that

$$\delta(2^{n-r}) \approx \frac{g_{r+1}(0) - g_{r+1}((-\alpha)^{-r}g_1(0))}{g_r(0) - g_r\left((-\alpha)^{-r+1}g_1(0)\right)}. \tag{3.119}$$

Finally, we rescale the axis of iteration in such way that between all 2^{n+1} iterations, $f^1(0), f^1(0), \ldots, f^{2n+1}(0)$ were the unit interval. We denote the resulting axis through t, and then, the value of t in the mth element of the 2^n-cycle time is

$$t_n(m) = \frac{m}{2^n}. \tag{3.120}$$

In particular, we have

$$t_n(2^{n-r}) = 2^{-r}. \tag{3.121}$$

Naturally, to define δ along the t-axis, we do the following:

$$\delta(t_n(m)) \sim \delta_n(m)(\text{at } n \to \infty). \tag{3.122}$$

Approximating the 2^n-cycle, we need to calculate δ_n near $(2^{n-r_1} + 2^{n-r_2} + \cdots)$th iteration of the point $x = 0$, that is, in the element t of the 2^n-cycle, which is the rational number with the binary representation

$$t = 2^{-r_1} + 2^{-r_2} + \cdots,$$

where $r_1, r_2, \ldots$—the ranks of $t \in (0, 1)$, including the nonzero (single) values in the binary representation of its fractional part. By (3.115), we have

$$f^{2^{n-r_1} + 2^{n-r_2} + \cdots} = f^{2^{n-r_1}} \circ f^{2^{n-r_2}} \circ \cdots,$$

Therefore, the value of δ at such t can be obtained through the formulas (3.113) and (3.118) using the appropriate iterations of g_r. For example, at $t = 2^{-r_1} + 2^{-r_2} + \cdots + 2^{n-3}$, we have

$$\delta_n(2^{n-r_1} + 2^{n-r_2} + 2^{n-r_3}) = \frac{d_{n+1}(2^{n-r_1} + 2^{n-r_2} + 2^{n-r_3})}{d_n(2^{n-r_1} + 2^{n-r_2} + 2^{n-r_3})}, \qquad (3.123)$$

where

$$d_n(2^{n-r_1} + 2^{n-r_2} + 2^{n-r_3})$$
$$= (-\alpha)^{-(n-r_3)} \left[g_{r_3}\left((-\alpha)^{n-r_3}(-\alpha)^{-(n-r_2)} g_{r_2}\left((-\alpha)^{n-r_2}(-\alpha)^{-(n-r_1)} g_{r_1}(0) \right) \right) \right.$$
$$\left. - g_{r_3}\left((-\alpha)^{n-r_3}(-\alpha)^{-(n-r_2)} g_{r_2}\left((-\alpha)^{n-r_2}(-\alpha)^{-(n-r_1)} g_{r_1}((-\alpha)^{-r_1+1} g_1(0)) \right) \right) \right],$$
$$(3.124)$$

$$d_{n+1}(2^{n-r_1} + 2^{n-r_2} + 2^{n-r_3})$$
$$= (-\alpha)^{-(n-r_3)} \left[g_{r_3+1}\left((-\alpha)^{n-r_3}(-\alpha)^{-(n-r_2)} g_{r_2+1}\left((-\alpha)^{n-r_2}(-\alpha)^{-(n-r_1)} g_{r_1+1}(0) \right) \right) \right.$$
$$\left. - g_{r_3+1}\left((-\alpha)^{n-r_3}(-\alpha)^{-(n-r_2)} g_{r_2+1}\left((-\alpha)^{n-r_2}(-\alpha)^{-(n-r_1)} g_{r_1+1}((-\alpha)^{-r_1} g_1(0)) \right) \right) \right].$$
$$(3.125)$$

Summarizing the formulas (3.123)–(3.125), for any positive integer $j \geq 1$ and $t = 2^{-r_1} + 2^{-r_2} + \cdots + 2^{-r_j}$, we have [84]:

$$\delta(2^{-r_1} + 2^{-r_2} + \cdots + 2^{-r_j}) = \frac{d_{n+1}(2^{n-r_1} + 2^{n-r_2} + \cdots + 2^{n-r_j})}{d_n(2^{n-r_1} + 2^{n-r_2} + \cdots + 2^{n-r_j})}, \qquad (3.126)$$

where

$$d_n(2^{n-r_1} + 2^{n-r_2} + \cdots + 2^{n-r_j})$$
$$= (-\alpha)^{-(n-r_j)} \left[g_{r_j}\left((-\alpha)^{n-r_j}(-\alpha)^{-(n-r_{j-1})} g_{r_j-1}\left((-\alpha)^{n-r_{j-1}}(-\alpha)^{-(n-r_{j-2})} g_{r_j-2}(\ldots g_{r_1}(0)) \right) \right) \right.$$
$$- g_{r_j}\left((-\alpha)^{n-r_j}(-\alpha)^{-(n-r_{j-1})} g_{r_j-1}(-\alpha)^{n-r_j-1}(-\alpha)^{-(n-r_{j-2})} g_{r_j-2} \right.$$
$$\left. \left. \times \left(\ldots g_{r_2}(-\alpha)^{n-r_2}(-\alpha)^{-(n-r_1)} g_{r_1}(-\alpha)^{-r_1+1} g_1(0) \right) \ldots \right) \right],$$
$$(3.127)$$

$$d_{n+1}(2^{n-r_1} + 2^{n-r_2} + \cdots + 2^{n-r_{j-1}})$$
$$= (-\alpha)^{-(n-r_j)} \left[g_{r+1}\left((-\alpha)^{n-r_j}(-\alpha)^{-(n-r_{j-1})} g_{r_j-1}\left((-\alpha)^{n-r_j-1}(-\alpha)^{-(n-r_{j-2})} g_{r_j-2}(\ldots g_{r_1}(0)) \right) \right) \right.$$
$$- g_{r_{j+1}}\left((-\alpha)^{n-r_j}(-\alpha)^{-(n-r_{j-1})} g_{r_j-1}(-\alpha)^{n-r_j-1}(-\alpha)^{-(n-r_{j-2})} g_{r_j-2} \right.$$
$$\left. \left. \times \left(\ldots g_{r_2+1}(-\alpha)^{n-r_2}(-\alpha)^{-(n-r_1)} g_{r_1+1}(-\alpha)^{-r_1} g_1(0) \right) \ldots \right) \right].$$
$$(3.128)$$

There is one last moment in the calculation of δ. We know that $\delta(0) = -\alpha^{-1}$. Furthermore, $\delta_n(1) \approx \alpha$. But from (3.121), it follows that $t_n(1) = 2^{-n} \to 0$ as

$n \to \infty$. This implies that δ is discontinuous at $t = 0$; $\delta(0 - \varepsilon) = -\alpha^{-1}$ and $\delta(0 - \varepsilon) = \alpha^{-2}(\varepsilon \to +0)$. In fact, since x_{2n-r} is always very close to $x = 0$, each of these points is converted quadratically. Therefore, (3.126) actually defines $\delta(t - \varepsilon)$ for the rational t, whereas $\delta(t - \varepsilon)$ is obtained by replacing each g_r in the numerator and the denominator by its square g_r^2.

Thus, the function $\delta(t)$ can be calculated for any value of $t \in [0, 1]$. It is universal, because the procedure to calculate it depends only on the universal functions $g_r(x)$, defined by the formula (3.112) for all $f(x) \in C^2[-1, 1]$ with the quadratic maximum at $x = 0$. The function $\delta(t)$ is discontinuous at all rational points. However, the larger the number of elements in the binary expansion of the rational t, the smaller the gap δ becomes.

Further, since in the limit at $n \to \infty$ the finite number of iterations does not change the value of t, the function $\delta(t)$ must be *continuous* everywhere, except at the rational points. Despite its pathological structures, $\delta(t)$ has the following approximate representation (Fig. 3.10)

$$\delta(t) = \begin{cases} 1/\alpha & \text{at } 0 < t < 1/4, \\ 1/\alpha^2 & \text{at } 1/4 < t < 1/2. \end{cases} \tag{3.129}$$

It is easy to verify, using (3.114), that δ is periodic at t with the period 1. Besides

$$\delta(t + 1/2) = -\delta(t). \tag{3.130}$$

Therefore, only the interval $0 < t < 1/2$ is essential.

Fig. 3.10 The diagram of bifurcation process
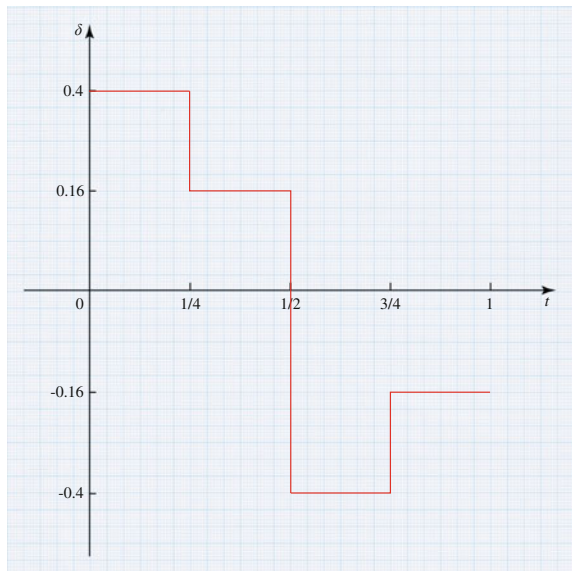
According to the theory of universality, the period doubling is universal for the above class of mapping $f(x)$, and for such a mapping, there exists the unique function $\delta(t)$, and its calculating method is described in detail above. Therefore, measuring the $x(t)$ at any particular cycle, we can completely predict the evolution of the system toward chaos.

Let $x_n(t)$—the T_n-periodic $(T_n = 2^n T_0,\ T_0 = 1)$ obtained after the 2^n iteration of the function $f(t; \mu_{n-1}) = 1 - \mu_{n-1} \cdot t^2$, defined by the quadratic mapping $f_\mu = 1 - \mu \cdot t^2,\ t \in [-1, 1],\ \mu \in [0, 2]$ (3.83). When $\mu = \mu_0 = 0.75$, the first period-doubling bifurcation occurs, and from the fixed point $\beta_1(0.75) = 2/3$, the cycle of the period 2 is born. The successive bifurcation values, corresponding to the emergence of cycles of the period 2^n, $n = 2, 3, 4, \ldots$, are equal to $\mu_1 = 1.25$, $\mu_2 = 1.3681\ldots$, $\mu_3 = 1.3940\ldots$ The sequence μ_n at $n \to \infty$ tends to $\mu = \mu_\infty = 1.40155\ldots$ such as that the mapping $f_{\mu_\infty} : [-1, 1] \to [-1, 1]$ has cycles with the periods of all powers of two and has no other periods.

The values of μ_n are associated with the bifurcation points c_n of mapping (3.84) by the ratio $\mu_n = -c_n$ (3.85) and they can be calculated for $n = 0$–10 according to Table 3.3. The ratio

$$\delta_n = \frac{\mu_n - \mu_{n-1}}{\mu_{n+1} - \mu_n}$$

takes values

$$\delta_1 = 4.23, \quad \delta_2 = 4.55, \quad \delta_3 = 4.65, \quad \delta_4 = 4.664, \quad \delta_5 = 4.668,$$
$$\delta_6 = 4.669, \ldots$$

The limit of the sequence δ_n at $n \to \infty$, as well as for the family $f_\lambda = \lambda x(1 - x)$ (3.80), is equal to $\delta = 4.6692\ldots$ Let the behavior of dynamic systems be described by the trajectory $x(t)$, with the quadratic maximum at t_0 and being symmetric with respect to the point $t = t_0$ within the local neighborhood of $t = t_0$. For identification of $x(t)$ as the quadratic function $f(t, \mu) = 1 - \mu t^2$, we select on the trajectory $x(t)$ the experimental points (t_i, x_i), $(i = 0, 1 \ldots N)$ (N—the even number), where $t_i = t_0 + i - N/2$, $x_i = x(t_i)$. After the translation $t = t_0 \to t = 0$, we obtain the experimental points (t_i, x_i), where already $t_i = i - N/2$. From these points, we construct the linear regression using OLS

$$x = at^2 + 1. \tag{3.131}$$

The function graph (3.131) is the parabola with vertex at (0.1) and with branches going down $(a < 0)$. OLS is the evaluation of parameter a:

$$\hat{a} = 2 \sum_{i=0}^{n} t_i^2 (x_i - 1) \bigg/ \sum_{i=0}^{n} t_i^2. \tag{3.132}$$

After the scaling transformation $t \rightarrow t/\alpha$, $\alpha = N/2$, we obtain the function

$$x = 1 - \mu t^2, \quad \mu = -\hat{a}/\alpha^2, \tag{3.133}$$

corresponding to the quadratic mapping (3.83) $X_{j+1} = 1 - \mu X_j^2$ and transforming the interval $[-1, 1]$ into itself. Where $t_i \rightarrow \frac{2}{N} \cdot t_i$, i.e., the abscissas $(-N/2, -N/2+1 \ldots 0, 1 \ldots N/2)$ of the trajectory $x(t)$ will pass through the points $(-1, -1+2/N \ldots 0.2/N \ldots 1)$. The mapping $X_{j+1} = 1 - \mu X_j^2$ by substitution, inverse to (3.82)

$$x = 1/2 + (\lambda/4 - 1/2)X, \quad \lambda = 1 + \sqrt{1 + 4\mu}, \tag{3.134}$$

leads to the mapping (3.81): $x_{j+1} = \lambda x_i(1 - x_i)$. We assume that the trajectory $x(t)$ of the system is described by the function $x(t) = \lambda t(1 - t)$, provided by the experimental points $(t_i, x_i)(i = 0, 1 \ldots N)$, where

$$\begin{aligned} t_i &= 1/2 + (\lambda/4 - 1/2)(-1 + i \cdot 2/N) \in [-1, 1], \\ x_i &= x(t_i) = \lambda t_i = (1 - t_i) \end{aligned} \tag{3.135}$$

and $x_n(t)$—the T_n-periodic function obtained after the 2^n iterations of the function $f(t, \lambda) = \lambda t(1 - t)$ from (3.135) and provided by the experimental points $(t_i, x_n(t_i))$, where t_i is defined in (3.135) and

$$x_n(t_i) = f^{2^n}(t_i, \lambda_{n-1}). \tag{3.136}$$

After replacing $\hat{t} = T_n/2(t + 1)$, the function $x_n(t)$ turns into the function $\hat{x}_n(\hat{t}_i)$, provided by the experimental points $(\hat{t}_i, \hat{x}_n(\hat{t}_i))$, where

$$\hat{t} = T_n/2(t + 1) \in [0, T_n] \quad (i = 0, 1 \ldots N). \tag{3.137}$$

Let us perform the linear interpolation of the function $\hat{x}_n(\hat{t}_i)$ on the interval $[0, T_n]$, i.e., we approximate $x_n(t)$ by a broken line in the plane (t, x) with nodes at the points $(\hat{t}_i, \hat{x}_n(\hat{t}_i))$. The function $\hat{x}_n(\hat{t}_i)$, defined on the whole interval $[0, T_n]$, will periodically continue at the period T_n through the whole real axis $-\infty < \hat{t} < \infty$. We denote the resulting periodic even function $\hat{x}_n(\hat{t}_i)$ with the period T_n for brevity by $x_n(t)$. Considering the distance between the points of the function $x_n(t)$ at times t and $t + (T_n/2)$, i.e., we define

$$d_n(t) = x_n(t) - x_n(t + T_n/2). \tag{3.138}$$

the analog of d_n values from (3.107). Since $\delta(t)$, by definition, is periodic with period 1, we have

$$d_{n+1}(t) \sim \delta(t + T_{n+1})d_n(t). \tag{3.139}$$

From (3.138), we have

$$d_{n+1}(t) = x_{n+1}(t) - x_{n+1}(t + T_{n+1}/2). \tag{3.140}$$

Since $x_{n+1}(t)$ is the periodic even function with the period T_{n+1}, its Fourier series contains only cosines:

$$x_{n+1}(t) \sim \frac{c_0}{2} + \sum_{k=1}^{\infty} c_k \cos \frac{k\pi t}{T_{n+1}}, \tag{3.141}$$

where

$$c_k = \frac{2}{T_{n+1} \int_0^{T_{n+1}} x_{n+1}(t)} \cdot \cos \frac{k\pi t}{T_{n+1}} \quad (k = 0, 1, 2\ldots). \tag{3.142}$$

From (3.140) taking into account (3.141), we obtain

$$d_{n+1}(t) = \sum_{k=1}^{\infty} (2 \sin k\pi/4) \cdot c_k \cdot \sin(k\pi(t + T_{n+1}/4)/T_{n+1}). \tag{3.143}$$

This means that the function $\hat{d}_{n+1}(t) = d_{n+1}(t - T_{n+1}/4)$ has the Fourier series made of sines

$$\hat{d}_{n+1}(t) \sim \sum_{k=1}^{\infty} b_k \sin(k\pi t/T_{n+1}) \tag{3.144}$$

with coefficients

$$b_k = \frac{2}{T_{n+1}} \int_0^{T_{n+1}} \hat{d}_{n+1}(t) \cdot \sin\left(\frac{k\pi t}{T_{n+1}}\right) dt. \tag{3.145}$$

Due to the partial differentiability of $x_{n+1}(t)$ and $d_{n+1}(t)$, the Fourier series of the functions converges to the functions themselves (Lipchitz's principle) at any point of t of the real axis t, and, therefore, in (3.144),

$$b_k = 2(\sin k\pi/4) \cdot c_k (k = 1, 2, 3, \ldots). \tag{3.146}$$

This implies that for all k non-multiple of 4 (i.e., $k \neq 4m$)

$$c_k = b_k \Big/ \left(\frac{2\sin k\pi}{4}\right) \quad (k = 1, 2, 3, \ldots). \tag{3.147}$$

To determine c_k at $k = 4m$, we use the equality

$$
\begin{aligned}
d_{n+1}(t + T_{n+1}/2) &= x_{n+1}(t + T_{n+1}/2) - x_{n-1}(t + T_{n+1}) \\
&= x_{n+1}(t + T_{n+1}/2) - x_{n+1}(t) = -d_{n+1}(t).
\end{aligned} \tag{3.148}
$$

By analogy with (3.143), the function $d_{n+1}(t + T_{n+1}/2)$ satisfies the relationship

$$d_{n+1}(t + T_{n+1}/2) = \sum_{k=1}^{\infty} (2\sin k\pi/4) \cdot c_k^* \sin\left(k\pi(t + \frac{T_{n+1}}{4})/T_{n+1}\right), \tag{3.149}$$

where c_k^*—the coefficients of Fourier series expansion on the cosine of the even function $x_{n+1}(t + T_{n+1}/2)$, i.e.,

$$x_{n+1}(t + T_{n+1}/2) = c_0^*/2 + \sum_{k=1}^{\infty} c_k^* \cos\left(\frac{k\pi t}{T_{n+1}}\right) \tag{3.150}$$

with the coefficients

$$c_k^* = \frac{2}{T_{n+1}} \int_0^{T_{n+1}} x_{n+1}\left(t + \frac{T_{n+1}}{2}\right) \cdot \cos\left(\frac{k\pi t}{T_{n+1}}\right) dt. \tag{3.151}$$

From (3.149), it follows that function $\hat{d}_{n+1}^*(t) = d_{n+1}(t + T_{n+1}/2 - T_{n+1}/4)$ is the Fourier series of sines

$$\hat{d}_{n+1}^*(t) = \sum_{k=1}^{\infty} b_k^* \sin(k\pi t/T_{n+1}) \tag{3.152}$$

with the coefficients

$$b_k^* = \frac{2}{T_{n+1}} \int_0^{T_{n+1}} \hat{d}_{n+1}^*(t) \cdot \sin\left(\frac{k\pi t}{T_{n+1}}\right) dt. \tag{3.153}$$

Wherein

$$b_k^* = 2\sin(k\pi/4) \cdot c_k^* \tag{3.154}$$

and due to (3.148)

$$b_k = -b_k^* \quad (k = 1, 2, 3, \ldots). \tag{3.155}$$

Consequently, for all k, non-multiple of 4:

$$c_k = -c_k^* \quad (k \neq 4m, \ k = 1, 2, 3, \ldots). \tag{3.156}$$

It is natural to assume that the Eq. (3.156) holds even at k being the multiples of 4, i.e.,

$$c_k = -c_k^* \quad (\forall k = 0, 1, 2, 3, \ldots) \tag{3.157}$$

so how

$$c_k - c_k^* = \frac{2}{T_{n+1}} \int_0^{T_{n+1}} \hat{a}_{n+1}^*(t) \cdot \cos\left(\frac{k\pi t}{T_{n+1}}\right) dt. \tag{3.158}$$

Substituting (3.144) into (3.158), and taking into account (3.157) for all $k \neq 4m$ $(m = 0, 1, 2, 3 \ldots)$, we obtain

$$
\begin{aligned}
c_{4m} = {} & 2 \sum_{k=1}^{\infty} b_{2p-1} \cos((2p - 1)\pi/4) \\
& \cdot \left[\frac{1}{(2p - 1 + 4m)\pi} + \frac{1}{(2p - 1 - 4m)\pi} \right].
\end{aligned}
\tag{3.159}
$$

However, according to the problem, only the function $x_n(t)$ is known, and therefore, to calculate the coefficients c_k based on the formulas (3.147) and (3.159), it is not possible yet.

Let us consider the function $\tilde{d}_{n+1}(t)$, being equal to the right-hand side of (3.139), i.e.,

$$\tilde{d}_{n+1}(t) = \delta(t/T_{n+1})d_n(t), \quad t \in [0, T_n], \tag{3.160}$$

where $\delta(t)$ according to (3.129) and (3.130) is the piecewise continuous function:

$$
\delta(t) = \begin{cases}
0.4 \ldots 0 < t < 1/4, \\
0.16 \ldots 1/4 < t < 1/2, \\
-0.4 \ldots 1/2 < t < 3/4, \\
-0.16 \ldots 3/4 < t < 1.
\end{cases}
\tag{3.161}
$$

We periodically extend the function $\tilde{d}_{n+1}(t)$ with the period T_{n+1} on the whole real axis t (again denoting the resulting function as $\tilde{d}_{n+1}(t)$).

The function $\hat{d}_{n+1}(t) = \tilde{d}_{n+1}(t - T_{n+1}/4)$ due to the asymptotic (for large n) equality $\tilde{d}_{n+1}(t) \sim d_{n+1}(t)$ and expansion (3.143) has the Fourier series on sines

$$\hat{d}_{n+1}(t) \sim \sum_{k=1}^{\infty} \tilde{b}_k \sin(k\pi t / T_{n+1}), \tag{3.162}$$

with the coefficients

$$\tilde{b}_k = \frac{2}{T_{n+1}} \int_0^{T_{n+1}} \hat{d}_{n+1}(t) \cdot \sin\left(\frac{k\pi t}{T_{n+1}}\right) dt. \tag{3.163}$$

Since $x_n(t)$ at $t \in [T_n, 2T_n]$ is the repetition of the broken line $x_n(t)$, $t \in [0, T_n]$ and $\delta(t/T_{n+1})$ is the piecewise constant, by (3.161) with the intervals of constancy

$$\Delta_j = \left[(j-1)\frac{T_{n+1}}{4}, j\frac{T_{n+1}}{4}\right]$$

$j = \overline{1.4}$, then

$$\tilde{b}_k = \frac{2}{T_{n+1}} \sum_{j=1}^{4} \int_{\Delta_j} y_{n+1;j,k}(t) dt, \tag{3.164}$$

where

$$y_{n+1;j,k}(t) = \begin{cases} 0.4 \cdot \hat{d}_{n+1}(t) \cdot \sin\left(\frac{k\pi t}{T_{n+1}}\right), & t \in \Delta_1, \\ 0.16 \cdot \hat{d}_{n+1}(t) \cdot \sin\left(\frac{k\pi t}{T_{n+1}}\right), & t \in \Delta_2, \\ -0.4 \cdot \hat{d}_{n+1}(t) \cdot \sin\left(\frac{k\pi t}{T_{n+1}}\right), & t \in \Delta_3, \\ -0.16 \cdot \hat{d}_{n+1}(t) \cdot \sin\left(\frac{k\pi t}{T_{n+1}}\right), & t \in \Delta_4. \end{cases} \tag{3.165}$$

To calculate the integrals in (3.164) over the interval Δ_j, it is convenient to use the trapezoidal rule. For this purpose, we divide each of the intervals Δ_j of the length T_{n+4} into $N_0 = 10^m$ equal parts $\Delta_{j,l} = \left[\underline{t}_{j,l}, \overline{t}_{j,l}\right] (l = 1 \ldots N_0)$ with the length $h = T_{n+1}/(4N_0)$. Then, according to the trapezoid formula, we will have

$$\int\limits_{\Delta_j} y_{n+1:j,k}(t)dt = \sum_{l=1}^{N_0} \int\limits_{\underline{t}_{j,l}}^{\overline{t}_{j,l}} y_{n+1:j,k}(t)dt$$

$$= \sum_{l=1}^{N_0} h \cdot \frac{y_{n+1:j,k}\left(\underline{t}_{j,l}\right) + y_{n+1:j,k}\left(\overline{t}_{j,l}\right)}{2}. \tag{3.166}$$

Substituting (3.166) into (3.164), we obtain

$$\tilde{b}_k = \frac{2}{T_{n+1}} \sum_{j=1}^{4} \sum_{l=1}^{N_0} h \cdot \frac{y_{n+1:j,k}\left(\underline{t}_{j,l}\right) + y_{n+1:j,k}\left(\overline{t}_{j,l}\right)}{2}. \tag{3.167}$$

Since the function $\hat{d}_{n+1}(t)$ is piecewise differentiable on $[-T_{n+1}, T_{n+1}]$ and at the end of this segment it has equal values, then

$$\left|\tilde{b}_k\right| < \varepsilon_k/k, \tag{3.168}$$

where $\varepsilon_k > 0$ and the sequence $\sum_{k=1}^{\infty} \varepsilon_k^2$ converges, and the Fourier series for $\tilde{d}_{n+1}(t)$ is uniform and absolute on the whole interval $[-T_{n+1}, T_{n+1}]$ and converges to the function $\tilde{d}_{k+1}(t)$, where the remainder of this series

$$r_s(t) = \tilde{d}_{k+1}(t) - \left(\tilde{a}_0/2 + \sum_{k=1}^{s} \tilde{a}_k \cos\left(k\pi t/T_{n+1}\right)\right)$$

is estimated as

$$|r_s(t)| < \frac{\eta_S}{s^{\frac{1}{2}}}, \tag{3.169}$$

where the infinitesimal η_S does not depend on t.

From (3.139), it follows that for large n, there is $\tilde{b}_k = b_k$, and consequently, the Fourier function coefficients of $x_{n+1}(t)$ with k, non-multiple of 4, will be determined by the formula

$$c_k = \frac{b_k}{2} \cdot \sin\left(\frac{k\pi}{4}\right) \quad (k = 1, 2, 3\ldots), \tag{3.170}$$

when $k = 4m$ $(m = 0, 1, 2, 3\ldots)$ from the expression (3.159), where b_{2p-1} is replaced by $\tilde{b}_{2p-1}$. The coefficients $\tilde{b}_{2p-1}$ are calculated by the formula (3.167) wherein $\hat{d}_{n+1}(t)$ is determined by $\tilde{d}_{k+1}(t)(t - T_{n+1}/4)$, and $\tilde{d}_n(t)$ is expressed in terms of $d_n(t)$ by the formula (3.160).

When calculating the function $x_{n+1}(t)$ by its Fourier series, it is enough to confine the sth partial sum of the series, i.e.,

$$x_{n+1}(t) \approx c_k/2 + \sum_{k=1}^{S} c_k \cdot \cos\left(k\pi t/T_{n+1}\right), \qquad (3.171)$$

where s is determined by the estimate of the remainder (3.169) for the specific forecast accuracy of the function $x_{n+1}(t)$. The more exact values of the coefficients c_k can be obtained if for the calculation $\delta(t)$ we use the formula (3.126), where $f(x, \lambda) = \lambda x(1-x)$, $d_n = f^{2n-1}(0, \lambda_n)$, and $\lambda_n = 1 + (1+4\mu_n)^{1/2}$ (see (3.85) and (3.106)). Thus, for computing the functions $g_r(x)$ in the formula (3.112), first we need to identify, using the above method, the mapping $X_{j+1} = 1 - \mu X_j^2$, and then mapping $x_{j+1} = f(x_j, \lambda) = \lambda x_j(1 - x_j)$ (see (3.134)).

The above approach to the prediction of the behavior of the 2^{n+1}-cycle of the dynamic system based on its behavior at the 2^n-cycle is implemented as the set of programs *FEIGENBAUM*.

After the infinite sequence of the doubling bifurcations, i.e., $\lambda = \lambda_\infty$ in the quadratic mapping (3.81), the period of cycle becomes infinite. In this case, the so-called Feigenbaum *attractor* appears in the logistic mapping, and it has the Cantor structure and the dimension $d_F = 0.548\ldots$. The logistic mapping with the Feigenbaum attractor is not yet chaotic. It has cycles of the period 2^m (and they are not stable) and does not have cycles of other periods.

When $\lambda > \lambda_\infty$, the more and more cycles will be born in the logistic mapping, including periods other than 2^m. Moreover, in this case, at the certain values of the parameter λ, it exhibits the chaotic properties. However, in the range $\lambda_\infty < \lambda < 4$, the chaotic behavior punctuated with the gaps of periodicity, where the dynamics is regular. For example, if $\lambda \simeq 3.74$ the steady cycle with the period five is observed in the logistic mapping, and at $\lambda = 1 + \sqrt{8} \simeq 3.83$, the cycle with period 3. Therefore, according to Sharkovski's theorem [92], this mapping has cycles of all periods.

3.3.3   *Analysis of the Noise Impact on the Feigenbaum Behavior*

The Feigenbaum scenario of chaos is well confirmed by the numerous studies. The sequences of the period-doubling bifurcations are found in many systems and mappings (e.g., [40, 86, 93]), including ones in the Lorenz system for the large values of r. A number of physical, chemical, and many other experiments also exhibit these bifurcation properties and some signs of universality.

However, despite the fact that for the systems described by the one-dimensional point mapping with the smooth maximum at $\lambda > \lambda_\infty$, there are always the stable

limit cycles [94], and the calculations show [95, 96] that due to the inevitable presence of small noise, these cycles, generally, do not appear near λ_∞, i.e., when the Lyapunov exponent λ_L satisfies the relationship

$$\lambda_L \sim (\lambda - \lambda_\infty)^\nu, \tag{3.172}$$

where ν—the same critical index that summarizes the Feigenbaum rule (see Sect. 3.3.1.). In the presence of the small external noise of intensity σ^2, the Lyapunov exponent λ_L can be positive for $\lambda = \lambda_u < \lambda_\infty$ [97, 98]. In [94], it is shown that for the quadratic mapping,

$$\lambda_\infty - \lambda_u \sim \sigma^2, \quad \text{where } \rho = \ln \delta / \ln(2\beta) = 0.8217\ldots,$$

$$\beta = \frac{\sqrt{2}\alpha^2}{\sqrt{1 + \alpha^2}} = 3.287\ldots,$$

where α and δ—the universal constants of Feigenbaum.

Thus, in the real experiments and the numerical calculations, where there are always physical noise or rounding errors, it is hard to observe the infinite sequence of period-doubling bifurcations. Instead, after the few doubling bifurcations, the movement once becomes chaotic.

In the study of transitions to chaos, under the context of the real physical systems the fundamental importance have the noise impact that destroys the fine details of the fractal structures in the phase space of parameters, the formation of which actually constitutes the essence of transition.

Initially, the idea of using the RG method for the analysis of the noise exposure at the chaos threshold was proposed in two papers published in 1981, in the same journal *Physical Review Letters* [99, 100] and it was related to the problem of transition to chaos through the sequence of the period-doubling bifurcations in the models with discrete time. A new universal constant was introduced, which shows how many times the amplitude of the noise impact on the system can be reduced being able to monitor the next level of the fractal structure associated with the period doubling.

Later, the similar approach was developed by the different authors with respect to other types of the universal behavior at the birth threshold of chaos and the strange non-chaotic attractor. The section of the site [98] contains the results of the analysis of the RG and illustrates the properties of the scaling similarity associated with the noise exposure for some of the known types of the critical behavior.

Below, there is the summary of the RG analysis of noise on the Feigenbaum type of behavior, described in detail in [101].

We consider the mapping

$$x_{n+1} = g_0(x_n) + kU_0(x_n)\xi_n, \qquad (3.173)$$

where $g_0(x)$—the quadratic mapping of kind $g_0(x) = 1 - \lambda_c x^2$ with the critical parameter $\lambda_c = 1.401155189092\ldots$; $U_0(x) = 1$; ξ_n—the sequence of statistically independent random variables with zero mean, variance σ^2, and the intensity k.

Applying the mapping (3.173) twice and assuming the noise intensity parameter k to be small, in the first order of smallness of this parameter, we obtain

$$x_{n+2} = g_0(g_0(x_n)) + k\left[g_0'(g_0(x_n))U_0(x_n)\xi_n + U_0(g_0(x_n))\xi_{n+1}\right].$$

Appearing in the square brackets, the expression will be interpreted as a new random variable, denoting it by $U_1(x)\xi_n'$. The factor $U_1(x)$ is chosen so that the value of ξ_n' has the same standard deviation σ, as ξ_n.

Since ξ_n and ξ_{n+1} are statistically independent, the medium-squared values of both terms of the sum are simply added. It follows that

$$U_1^2(x) = \alpha^2 \left[\left(g_0'(g_0(x))\right)^2 U_0^2(x) + U_1^2(g_0(x))\right].$$

Thus, the equation for the double iteration is reduced to the same form as the original

$$x_{n+2} = g_1(x_n) + kU_1(x_n)\xi_n,$$

but with new features

$$g_1(x) = \alpha g_0\left(g_0\left(x/\alpha\right)\right), \quad U_1(x) = \sqrt{\alpha^2 \left[\left(g_1'(g_0(x))\right)^2 U_0^2(x) + U_0^2(g_0(x))\right]}.$$

Applying the described procedure repeatedly, we obtain the sequence of functions g_k, U_k, satisfying the chain of recurrent functional equations

$$g_{k+1}(x) = \alpha g_k\left(g_k\left(x/\alpha\right)\right), U_{k+1}(x)$$
$$= \sqrt{\alpha^2 \left[\left(g_k'(g_k(x))\right)^2 U_k^2(x) + U_k^2(g_k(x))\right]}. \qquad (3.174)$$

According to the Feigenbaum theorem, the sequence g_k converges to the limit— the function $g(x)$, which is the fixed point of the functional equation of Feigenbaum–Tsvitanovich

$$g(x) = \alpha g\left(g\left(x/\alpha\right)\right).$$

So, by considering the behavior of the solution of the second equation in (3.174) for large k, g can be substituted instead of g_k. If we look for the solution in the form

Fig. 3.11 The universal mapping of function $g_0(x)$
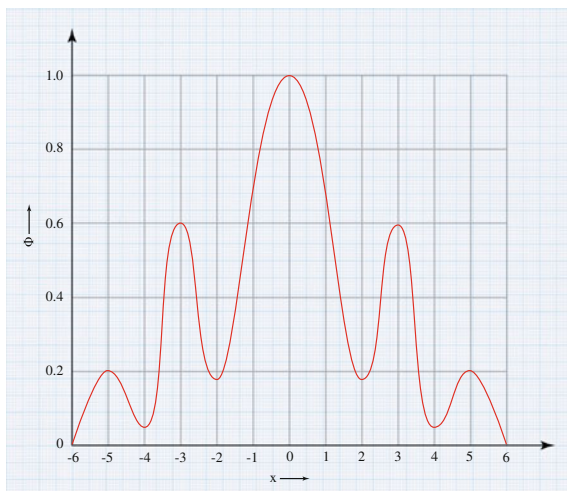
$$U_k(x) = \gamma^k \sqrt{\Phi(x)},$$

we come to the problem of the eigen functions and eigenvalues

$$\gamma^2 \Phi(x) = \alpha^2 \left[(g'(g(x)))^2 \Phi(x) + \Phi(g(x)) \right]. \tag{3.175}$$

This problem can be solved numerically if the function $g(x)$ and the constant α are known. For the quadratic mapping, $\alpha = 2.502907875$ and $g(x)$—the known function, the expression of which is found by Feigenbaum in the form of a polynomial (see Sect. 3.3.1).

The solution of (3.175) with the largest eigenvalue $\gamma = 6.619036513$ and the private function in the case of the quadratic mapping $g_0(x)$ is shown in Fig. 3.11.

The universal constant γ shows how many times the noise must be reduced, so we can watch a new level of the period doubling.

A more general formulation of the large-scale properties of similarity (scaling) is as follows.

Suppose that for some value of λ, close to the Feigenbaum critical point, and at the sufficiently low noise level k, there is some monitoring mode. At the deviation of the critical point of the parameter λ at $\delta = 4.6692\ldots$ times smaller and at the noise level k/γ, the statistically similar regime will be implemented with the characteristic timescale twice as large. In this case, the distribution of variable x near the extremum will be similar to the original with the characteristic scale of x at $\alpha = -2.5029\ldots$ less (with the reflection change of orientation x, which corresponds to minus). In the region of small deviations from the criticality and at the low noise level, the distribution, as it may be expected, is largely universal, i.e., it does not

depend on the distribution details and the correlation properties of the initial noise (as long as the correlation function decreases sufficiently quick).

3.4   Synergetics of the Restructuring of Crystal Structures with Condensed State Under the Influence of External Forces

The problem of describing the condensed atom state, exposed to the intense external action, is the most important task of the modern physics. Over the past decade, there have been significant achievements in this field. At the present time, we better understand the main features of the microscopic behavior of atoms at the structural phase transitions [45], as an example the ferroelectric transitions [102] and the martensitic transformation [103].

Until recently, while studying the condensed matter, we used the methods of the equilibrium statistical physics. This is due to an assumption that the influenced condensed matter represents by itself the equilibrium or slightly non-equilibrium statistical system. Recently, the interest is grown to the statistical system of atoms in the condensed state where the usual concepts (such as the concept of phonons or the thermodynamic pictures of the phase transitions) are inapplicable anymore or require the fundamental changes. Such behavior is explained by the strong deviation of the atomic system from equilibrium, as it is observed in the core of defects within lattice or the areas of plastic flow and fracture. The strongly non-equilibrium condensed state requires the use of techniques that allow us to represent such features as the non-ergodicity of statistical system, the emergence of hierarchical structures, the structural relaxation, the mutual influence of subsystem undergoing a phase transition, and the environment.

To address the specific problems of the theory of condensed state [104], it was proposed to use the potential relief, the distribution of which is given by the synergetic potential. The readjustment parameter of the ionic subsystem is determined by the correlation changes of the potential relief at the macroscopic distances. The collective perturbations, possessing the critical behavior, are reduced to the transverse acoustic branch phonons. At large distances, the collectiveness has the dissipative character due to the viscous flow and at small distances—the reactive character due to the elastic field. The full description is achieved by the mutually explained behavior of the ion subsystem and the collectiveness. Within the framework of the synergetic theory, it is achieved through the Lorenz system of equations for the temporary evolution of the lattice nodes, trapped in the readjusted potential relief, the shear deformation of the medium as a result of restructuring the conjugated stress field.

At the strong perturbations of crystal, the determinism nature of the ion subsystem becomes meaningless and the wave type of behavior is observed [105–107];

therefore, it is more useful to consider the readjusted single-particle potential of the perturbed crystal.

According to the modern concepts [108], at temperatures not exceeding Debye, the macroscopic large group of atoms is involved in two types of motion. The first one corresponds to the atom oscillations near the equilibrium state, which is compared to the branches of collective perturbations—phonons. With the full dispersion $\omega_{ph}^{(n)}\left(\vec{k}\right)$, where $n = 1, 2, 3$—the branch index, ω—the frequency, and $\vec{k}$—the wave vector, the phonons are reactively perturbed. They have the acoustic type at the hydrodynamic limit $k \to 0$

$$\omega_{ph}^{(n)}\left(\vec{k}\right) \approx C_n \cdot k, \qquad (3.176)$$

where $C_n = \sqrt{\lambda_n \rho}$—the sound wave velocity corresponding to the nth branch, ρ—the medium density, and λ_n—the corresponding modulus of elasticity (for the longitudinal waves λ_n—the compression modulus and λ_n—for the shear modulus). Most clearly, the perturbed phonons are expressed in the low-temperature region, where due to the uncertainty they do not disappear even at the absolute zero. The presence of some low-energy excitations, such as phonons, is inherent to the weakly condensed atoms corresponding with the conditions close to the equilibrium.

The Bose condensate of the static phonons, following $\omega_{ph}^{(n)} \to \infty$, is the carrier of the long-range elastic field [18]. The condensate of Bose or Bose–Einstein is the physical matter mainly comprised of *bosons*, cooled to a temperature that is less than millionth degree just above the absolute zero. At this strongly chilled medium, the sufficiently large number of atoms is in their lowest possible quantum states, and the quantum effects begin to appear at the macroscopic level. Based on Einstein's hypothesis, the cooling of atom—bosons (particles identical with the whole spinning) up to the very low temperatures will force them to move (or, in other words, to concentrate) at the lowest possible quantum state. As a result of such condensation, it will be the emergence of a new matter.

By increasing the temperature (or other energy sources influencing the atom system out of balance) in addition to increasing the number of phonons, we also observe the restructuring of dispersion, and the other type of movement—diffusion—becomes significant. The diffusion corresponding with the thermally activated atoms that jump through the potential barrier separating their equilibrium position has a purely imaginary dispersion

$$\omega_d = -iDk^2, \qquad (3.177)$$

where D—the coefficient of diffusion. Physically, this means that the diffusion is responsible for the redistribution of the relaxation processes of the concentration $c(\vec{r}, t)$, characterized by the relaxation time $\tau_d \equiv |\omega_d|^{-1} = \frac{1}{D}k^2$.

The coefficient of diffusion D increases exponentially as the temperature increases, leading to an increase in the imaginary frequency diffusion ω_d (reducing the diffusion time τ_d). However, since the maximum value of the coefficient of diffusion is bounded by $c \cdot a$, where c—the specific speed of sound and a—the interatomic distance, the condition $|\omega_d| \ll \omega_{ph}$ will always hold, meaning that the impact of diffusion on the movement of atoms in comparison with the phonon is negligent. Besides the provided strengthening of the diffusion mode, the increase in temperature also changes the phonon branches, defined by the viscous flow.

In the long-wavelength limit, the most well-identified longitudinal sound $\omega_l\left(\vec{k}\right) = c_l \cdot k$ (c_l—the velocity of longitudinal sound waves). As for the transverse acoustic $\omega_l\left(\vec{k}\right)$, in the hydrodynamic limit $\vec{k} \to 0$, it is a purely dissipative $\omega_l\left(\vec{k}\right) = -i/\tau_t$; $\tau_t = \eta/\mu$—the relaxation time, where μ—the shear modulus and η—the shear viscosity. In the language of quantum statistics, the elementary acts of such reconstruction are presented as the emission and absorption of the virtual excitations of atomic subsystem (relaxons) having the lifetime τ_t and localized in the size

$$\lambda = \frac{4\pi}{k_t} = 4\pi c_t \tau_t = 4\pi \frac{\eta}{\rho c_t} = \frac{4\pi\eta}{\sqrt{\mu\rho}}, \tag{3.178}$$

where $k_t = (c_t\tau_t)^{-1}$—the specific wave number, $c_t = \sqrt{\mu/\rho}$—the speed of propagation of the transverse sound waves, and ρ—the density of medium.

The transformation of the relaxation $\omega_t = -i/\tau_t$ into the phonon regime $\omega_l\left(\vec{k}\right) = c_l \cdot \overline{k}$ transitioning from the long-wave region $k < k_t/2$ to the short-wave region $k \gg k_t$ physically means that in the small area with the size $l \ll \lambda$, only the atom vibrations have effect, and when the size is $l > \lambda$, the relaxation effects become significant due to the restructuring of the atomic relief. Since the phonons are the carriers of the elastic field, and the relaxation is associated with the flow, the value λ can be described as the elastic field penetration depth into the viscoelastic medium. With an increase of the temperature and the loading up to the values T_m, σ_c, and the effects of the medium flow take place resulting in the screening of the elastic field. In this case, the dispersion of the transverse branches of phonon takes the form [104]:

$$w_t\left(\vec{k}\right) = \pm c_t k \sqrt{1 - k_t/2k} - \frac{i}{2\tau_t}, \tag{3.179}$$

where the specific values are given by

$$c_t = \sqrt{\mu/\rho}; \quad k_t = (c_t \cdot \tau_t)^{-1}; \quad \tau_t = \frac{\eta}{\mu}, \tag{3.180}$$

where μ—the shear modulus, ρ—the medium density, η—the dynamic shear viscosity, and τ_t—the decay time. If in the short-wave zone $k \gg k_t$ the dispersion (3.179) reduces to the usual acoustic type, then in the long-wave zone ($k < k_t/2$) the transverse phonons are rearranged in the dissipative regime $\omega_d = -\tau_t^{-1}$ corresponding to the medium flow. In the macroscopic view, this means a complete screening in the erosion of the elastic field at distances greater than the characteristic length λ, defined by (3.178). In the ideal elastic medium ($\eta = \infty$), the elastic field, as expected, is of long-range ($\lambda = \infty$), and with an increase of the temperature and the loading, the value $\lambda \sim \eta(T, \sigma)$ decreases to the finite values [107].

Thus, considering the restructuring of the collective behavior of atoms in the solids shows that there are characteristic scales of the spatial and temporal behaviors of the system, undergoing the non-equilibrium structural transformation: On the time axis, it is the macroscopic times τ_D (Debye time) and the macroscopic τ_t (the relaxation time of shear stresses), respectively, on the spatial axis—the distance a (interatomic) and λ_t (the localization area of the elastic field). Accordingly, the entire group of atoms of the solids can be divided into the atoms responsible for the transfer of the elastic field (unexcited) and the atoms supporting the processes of the viscoplastic flow (excited). As a result, the atomic states are characterized by the fraction of n atoms in the excited state.

The transition from the long-wave region $k < k_t/2$ into the short-wave region $k \gg k_t$ essentially means the movement from the phonon spectrum to the fracton. The fracton dimension, characterizing the spectrum of the natural oscillations of fractals, was introduced by Alexander and Orbach in 1982 [109] and defined by the formula

$$d_f = \frac{2D}{2 + \theta},$$

where D—the fractal dimension and $\theta > 0$—the anomalous diffusion parameter (in the case of an ordinary lattice $\theta = D$).

The fracton dimension (also called the spectral dimension [110]) acts as the space dimension in the low-frequency asymptotic density of the vibrational states. Indeed, for the density of ordinary phonons in the usual d-dimensional regular lattice from the last formula (based on $\theta = 0$), we obtain the well-known equality $d_f = d$.

In the case of the real fractal materials, there is the maximum scale ξ, limiting the region of the fractal behavior. At the scales exceeding ξ, and hence at the low frequencies not exceeding the certain crossover frequency $\omega_c(\xi)$, there is the usual phonon spectrum. At the higher frequencies, there is the transition (crossover) to the fractal spectrum [111]. The magnitude of the spectral dimension can be determined even for the more general case: for the non-isotropic elastic forces [112] and for the long-range interactions [113].

To explain the electrical and thermal conductivity of metals, we accept the following model: The conductive metal consists of the crystal lattice formed by the ions and electrons (*electron gas*), freely moving in the metal. The electron gas in

metals is not an ordinary classical quantum gas, following the Fermi–Dirac distribution. The emergence of the free electron gas in metals is not related to the temperature, and it is a purely quantum effect, i.e., the ionization of atoms (loss of electrons) of metal is not due to thermal motion, but due to the overlap of the wave functions of the valence electrons. The overlap of the wave functions leads to the generalization of the valence electrons, and they do not belong to any specific node of the crystal lattice and freely move between the nodes. For this reason, the metals have the free electron gas at any temperature, even at temperatures close to the absolute zero. Since the electron gas is the Fermi gas, using the thermodynamic properties of the Fermi gas, the specific heat of the electron gas C_V^{el} can be written in the two limiting cases:

$$C_V^{el} = \frac{3k_0 N}{2}; \quad T \gg T_0^{el}, \tag{3.181}$$

corresponding to the non-degenerate electron gas (the statistical properties of which are described by the Boltzmann distribution), and

$$C_V^{el} = \frac{\pi^2}{2} k_0 N \frac{k_0 T}{\mu_0^{el}} = \frac{\pi^2}{2} k_0 N \cdot \frac{T}{T_0^{el}}; \quad T \ll T_0^{el}, \tag{3.181}$$

corresponding to the strongly degenerate electron gas, called the quantum gas (the statistical properties of which are determined by the Fermi–Dirac or the Bose–Einstein distributions).

Here,

$$T_0^{el} = \frac{\mu_0^{el}}{k_0} = \frac{\hbar^2}{2mk_0} \left(\frac{6\pi^2}{g_0} n \right)^{2/3}$$

the degeneration temperature of the free electron gas in metals, N—the number of nodes in the metal lattice with volume V, $n = N/V$—the gas concentration, m—the electron effective mass in metal, and μ_0^{el}—the limit Fermi energy, $g_0 = 2$.

Setting ten external thermal perturbation leads, as we know, to the qualitative restructuring of the collective behavior of many systems [114]. In circumstances where the excitation system is so small that it has time to relax into the equilibrium state, to describe the behavior of the system it is enough to select a single hydrodynamic mode, the intensity of which is defined by the order parameter. The strong excitation can part away the system from the equilibrium state that it can cause its quality restructuring. In contrast to the thermodynamic, the description of the kinetic transformation requires the allocation of the several hydrodynamic modes and is based on, within the framework of the phenomenological approach, synergetics [14].

The description of readjustment of the monohydric states through the n excited atoms is insufficient to study the core of crystal defects and the carriers of brittle

fracture. As it is shown in [104], the main characteristic in determining the behavior of atoms in the condensed state far from equilibrium is the single-atom potential relief readjusting under the intense external influence.

For the correct definition of the potential relief, we consider the density distribution of atoms [24]

$$n(\vec{r}, t) = \sum_a \Omega_a \delta(\vec{r} - \vec{r}_a(t)), \qquad (3.182)$$

where the summation is taken over all atoms a, located at the points $\vec{r}_a(t)$ at time t, Ω_a—the volume of atom. Each distribution of atoms $n(\vec{r}, t)$ has the certain atomic system energy $E(t)$, and at each time t, the single-particle potential relief of atom, according to Landau's concept, is defined by

$$U(\vec{r}, t) = \frac{\delta E(t)}{\delta n(\vec{r}, t)}. \qquad (3.183)$$

From the known interaction potentials of the partial interaction V_i at each time t, it is possible to find the form of relief $U(\vec{r}, t)$, given by the distribution of atoms $n(\vec{r}, t)$, as the sum of infinite series:

$$U(\vec{r}, t) = V_1(r, t) + \int V_2(\vec{r}, \vec{r}') n(\vec{r}', t) d^2\vec{r}' t. \dots \qquad (3.184)$$

With further consideration of the macroscopic properties, everywhere we carry out the procedure of averaging the time t, responsible for the microscopic fluctuations in the distribution of atoms $n(\vec{r}, t)$. Following the ergodic hypothesis [115], for such averaging instead of one relief $U(\vec{r}, t)$, given by the macroscopically defined time t, the group of smoothed, according to the time, effective relief $\{U(\vec{r})\}$ is introduced. As the simple implementation, we can show the Gaussian group, characterized by the probability density

$$P\{U(\vec{r})\} \backsim \exp\left\{-W^{-2} \int |\delta U(\vec{r})|^2 d^3\vec{r}\right\}, \qquad (3.185)$$

where W—the parameter of relief variation around the mean

$$\langle U(\vec{r}) \rangle = \int U(\vec{r}) P\{U(\vec{r}) dU(\vec{r})\}, \qquad (3.186)$$

$\delta U(\vec{r}) = U(\vec{r}) - \langle U(\vec{r}) \rangle$—the relief variation. The Gaussian group is implemented at the chaotic, uncorrelated changing terrain. Indeed, using (3.185) for the correlator

$$S(\vec{r}, \vec{r}') = \langle \delta U(\vec{r}) \delta U(\vec{r}') \rangle, \tag{3.187}$$

we obtain $S(\vec{r}, \vec{r}') \backsim \delta(\vec{r} - \vec{r}')$ the so-called "white noise"; the angle brackets—the averaging over the distribution (3.185).

However, there are situations where the change of the potential relief in the different (even macroscopically distant) points flows coherently. A good example is the martensitic transformation, where the coherent displacement of the potential minimums $U(\vec{r})$ is self-consistently transferred through the elastic domain [22]. In this case, in the change $\delta U(\vec{r})$ of the potential reliefs, there are the long-range correlations, characterized by the parameter

$$|\Psi(\vec{r})|^2 = \lim_{|\vec{r}' - \vec{r}| \to \infty} S(\vec{r}, \vec{r}') / S(\vec{r}', \vec{r}'). \tag{3.188}$$

In the coherent restructuring of the potential relief the parameter Ψ, which generally can be a nonzero complex number; alternatively, when with the change of $\delta U(\vec{r})$ there are proximal correlations, we have $\Psi = 0$.

To determine the functional distribution of reliefs $P\{U(\vec{r})\}$, we assume that the reconstruction of the potential relief is carried out according to the Langevin equation

$$\delta \dot{u}(\vec{r}, t) = F(\delta u(\vec{r}, t)) + R(\vec{r}, t), \tag{3.189}$$

where the dot denotes the differentiation with respect to time t and $F(\delta u(\vec{r}, t))$ is the regular component of the external influence. In the linear approximation, it has the form

$$F(\delta u(\vec{r}, t)) = \gamma \delta u(\vec{r}, t), \tag{3.190}$$

where γ—the kinetic coefficient. The term $R(\vec{r}, t)$ describes the fluctuation contribution given by the correlator

$$\langle R(\vec{r}, t) R(\vec{r}, t') \rangle = \theta(\vec{r}) \delta(t - t'), \tag{3.191}$$

which is characterized by the intensity of $\theta(\vec{r})$. As a result, the density distribution $P\{U(\vec{r})\}$ is described by the Fokker–Planck equation [116]:

$$\dot{P}\{U(\vec{r})\} + \int \frac{\delta J\{U(\vec{r})\}}{\delta U(\vec{r})} dr = 0, \tag{3.192}$$

$$J\{U(\vec{r})\} \equiv F\{U(\vec{r})\} \cdot P\{U(\vec{r})\} - \int \theta(\vec{r}) \frac{\delta P\{U(\vec{r})\}}{\delta U(\vec{r})} d\vec{r}. \tag{3.193}$$

where the equality (3.192) is the equation of continuity in the space for the potentials $\{U(\vec{r})\}$, $J\{U(\vec{r})\}$—the corresponding flow, and the first component—the

drift and the second—the diffusion. In the stationary state, we have $\dot{P} = 0$, where for the closed stochastic system the condition $J = 0$ follows, which leads to the distribution

$$P\{U(\vec{r})\} \sim \exp\left\{-\frac{V\{U(\vec{r})\}}{\theta(\vec{r})}\right\}, \tag{3.194}$$

$$\frac{V\{U\}}{\theta} \equiv -\int\left(\frac{F\{U(\vec{r})\}}{\theta(\vec{r})}\right)\mathrm{d}U(\vec{r}). \tag{3.195}$$

We bring the linear approximation (3.190) to the time-dependent Gaussian distribution

$$P_t\{U(\vec{r})\} = N(\pi W_t)^{-\frac{1}{2}}\exp\left\{-\int\left[\frac{\delta U(\vec{r}) - U_t}{W_t}\right]^2\mathrm{d}\vec{r}\right\},$$

$$W_t^2 \equiv \frac{\theta}{\gamma}\left(1 - \mathrm{e}^{-2\gamma t}\right) + w\,\mathrm{e}^{-2\gamma t}, \quad U_t = u\,\mathrm{e}^{-2\gamma t}, \tag{3.196}$$

where N—the total number of atoms; u, w—the arbitrary constants. Such case is realized itself as the low impact on the atom system, when the characteristic variation of the relief is small enough ($\delta U \ll \langle U \rangle$). According to (3.196), at the relaxation time $t \gg \gamma^{-1}$, the distribution of relief is determined by the fluctuation $\delta U = \sqrt{\theta/\gamma}$ near the average potential $\langle U(\vec{r}, t)\rangle$. In general, the variation $\delta U(\vec{r})$ is

Fig. 3.12 The graph of the synergetic potential (*curve 1*) and the corresponding distribution of the atoms (*curve 2*), depending on the atom potential energy
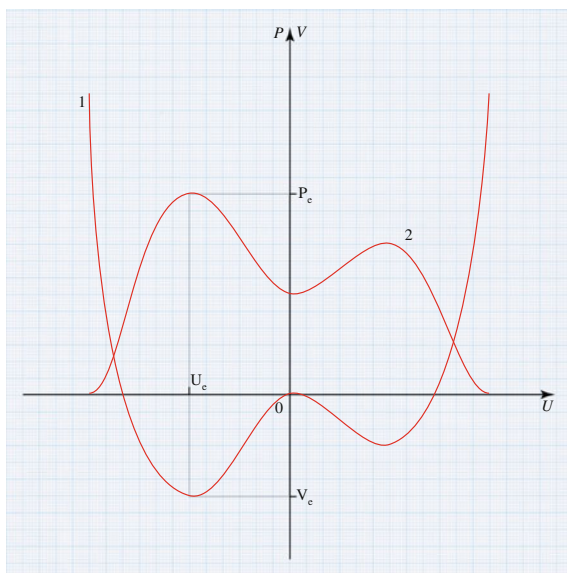
given by the distribution function (3.194), the form of which is determined by the synergy potential (3.195). The appropriate dependences are presented in Fig. 3.12, which demonstrate that the minimums of the synergistic potential V_e (curve 1) set the specified maximums of the probability P_e on curve 2.

The coherent distribution is also given by the same Eq. (3.194); however, the synergy potential is not reduced to the integral (3.195), but to some function of the order parameter. In the simplest way, this function is represented by the Landau expansion used in the theory of phase transitions. The macroscopic inhomogeneity can be taken into account by adding the gradient term, introduced by the Ginzburg–Landau theory. As a result, the synergistic potential takes the form [24]

$$V\{\Psi(\vec{r})\} = \int \left[\left(\frac{A}{2} \cdot |\Psi(\vec{r})|^2 + \frac{B}{4} |\Psi(\vec{r})|^4 \right) + \frac{\beta}{2} |\nabla\Psi(\vec{r})|^2 \right] d\vec{r}, \qquad (3.197)$$

where $A, B, \rho = \text{const}$ and the synergetic graph is reduced to the standard form of the phase transitions [117].

To describe the macroscopic behavior of the atom system, we can partition $U(\vec{r}, t)$ into two parts. The first one $U(\vec{r})$ changes at the macroscopic time intervals, much higher than Debye time τ_t. The second one $\tilde{u}(\vec{r}, t)$ quickly fluctuates during $t \ll \tau_t$. If at the weak excitation of the system $T, \sigma \ll T_m \cdot \sigma_c$ we can neglect these fluctuations, then at $T, \sigma \sim T_m \cdot \sigma_c$ we have $|U(\vec{r}, t)| \sim \tilde{u}(\vec{r}, t)$ and the deterministic description of the atom system loses its sense. Here, only the macroscopic view of values becomes possible, averaged over the time interval $\sim \tau_t$.

Within the provided scheme, the parameterization of viscoelastic medium is achieved by using the space–time dependences of the medium parameters $\psi(\vec{r}, t)$, which plays the role of the order parameter in the usual scheme of the phase transformations, and the elastic component of the medium flow velocity is $v(\vec{r}, t)$, representing the spatial components of the vector potential of the calibrating field coupled with the parameter ψ. Using the standard field-theoretical scheme for these dependencies in the stationary case, we obtain the system of equations [18]:

$$\left(\frac{\xi}{\lambda} \right)^2 \nabla^2 \psi = -\left(1 - v^2 \right) \psi + |\psi|^2 \psi, \qquad (3.198a)$$

$$\nabla^2 v = |\psi|^2 v, \qquad (3.198b)$$

where the values $\psi(\vec{r})$, $v(\vec{r})$ are referred to their maximum values, with $\psi(\vec{r}) = \Psi(\vec{r})/\Psi_0$, $\Psi_0 = \sqrt{-AB}$, where A and B—the coefficients from (3.197); the distances are measured in the units of length λ; ξ—the correlation length, indicating the scale of variation of $\psi(\vec{r})$ in space.

According to the earlier described qualitative picture, in the absence of restructuring of the medium ($\psi = 0$), the Eq. (3.198b) gives the trivial solution $v = 0$ corresponding with the perfect elasticity. In the restructured environment

Fig. 3.13 The radial
distribution of the potential
relief (**a**), the parameter of its
readjustment and the field
flow (**b**), and the model of
frustrons (**c**)
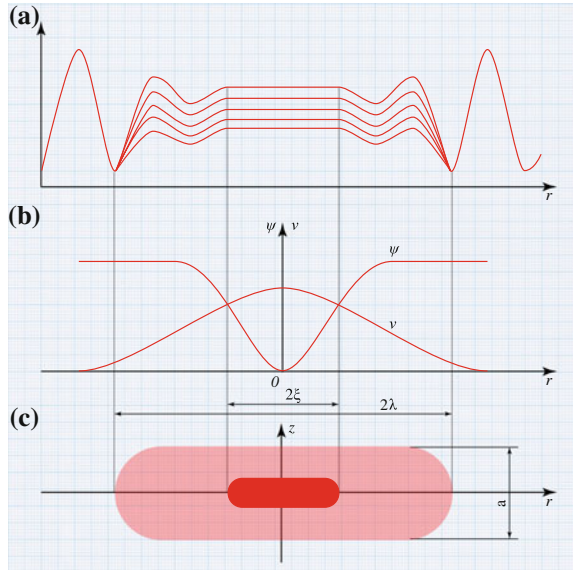
$(\psi \neq 0)$, the Eq. (3.198b) provides, as it should be, the dependence $v(\vec{r})$, exponentially decreasing at distances $\sim \lambda$.

The solution of the material Eq. (3.198a) is determined by $\chi = \lambda / \xi$. In the brittle materials, which are used by the most practical applications, the penetration depth of the elastic field λ is much greater than the correlation length ξ of restructuring the potential relief, and therefore, $\chi \gg 1$.

In the complete analogy with the superconductors of type 2 [118], we have the auto-localized solutions for the Eq. (3.198a, b) using the Gross–Pitaevskii solitons. It represents the axial formation with central gap of the parameter $\psi(\vec{r})$ within the radius $\sim \xi$ and the field of flow velocity $v(\vec{r})$, localized at much greater distances $\sim \lambda$ (Fig. 3.13a). Physically, this corresponds to the localized region with the radius $\sim \xi$, where the flatness of potential relief is caused by the violation of the interatomic bonds. The area is surrounded by the shell of plastic flow with the radius $\sim \lambda$ (Fig. 3.13b). In the crystal lattice, the Gross–Pitaevskii solitons correspond to the linear areas of violation of the crystal order, i.e., the disclinations—in the torsion field and the dislocations—in the shift field.

Since the decrease of the parameter $\psi(\vec{r})$ means the weakening of the interatomic bonds, and the region of the plastic flow is always localized near the origin of failure [15], it is normal to identify the found solution as the elementary carrier of brittle fracture. Bearing in mind the violation of the interatomic bonds, it is appropriate to call such formation as frustrons (originated from *English* for "frustration") [9].

For the materials that satisfy the condition $\chi \gg 1$, the region of the frustron existence corresponds to the external loads σ and included between the values

$$\sigma_{C_1} = 2^{-1/2} \ln \frac{\lambda}{\xi} \cdot \sigma_c, \quad \sigma_{C_2} = 2^{\frac{1}{2}} \frac{\lambda}{\xi} \cdot \sigma_c, \tag{3.199}$$

where σ_c—the critical value of σ (see, e.g., [23]).

At $\sigma \ll \sigma_{C_1}$, the frustrons are unstable, and if $\sigma > \sigma_{C_2}$, they merge to the homogeneous "phase," i.e., failure takes place.

As the elementary carriers of the brittle fracture, Zhurkov [119] proposed the dilaton model, which is the stable fluctuation region of the increased dilatation of lattice, realized through the anharmonicity of phonons.

The negative fluctuations of density, the dilatons, serve as the centers of the micro-crack formation. Due to the lower density, they become traps for the acoustic phonons. Under the favorable conditions, the nonlinear effects of the phonon absorption by the dilatons lead to the parametric energy pumping, to the thermal expansion, and to the disintegration of dilaton by forming the micro-cracks.

In the dilaton fracture model, the strength equation for solids can be represented as

$$\sigma_* = \frac{aE}{\Lambda}(\varepsilon_* - \varepsilon_d),$$

where Λ—the length of the phonon average free run, the size of atom; E—the elastic modulus; $\varepsilon_* \approx 0.2$—the tensile deformation of the interatomic bonds and $\varepsilon_d = \frac{\alpha T}{3} \ln \frac{\tau}{\tau_0}$—the critical strain when dilaton disintegrates forming micro-cracks; α—the linear thermal expansion coefficient; $\tau_0 \sim 10^{-13}$ s—the period of thermal atom vibrations; τ—the durability; and T—the absolute temperature. In this aspect, the structural imperfections affect the strength through the dependence of Λ on the atom impurity and the defects of deformed materials.

Because of the anharmonic effects, the crystalline dilaton is able to cumulate the energy from the environment. The phonon pumping occurs, and as a result, the dilaton deformation grows. Upon reaching the ultimate strain ε_*, the dilaton disintegrates, forming the embryonic cracks. The dilaton disintegration happens at a greater speed, determined by the lifetime of fluctuations, $\tau_d = \Lambda/s \approx (10^{-13} \div 10^{-13})\, s$ (s—the speed of sound). At such short durations, the cumulative process of the dilaton disintegration acquires the character of microburst, creating an empty space of the microscopic size inside the body. The collapse of the interatomic bonds within dilatons provides such an explosive mechanism, and it is accompanied by the sound, light, and electrical emissions usually observed during the destruction of solids. The energy required for such a violent microscopic processes is taken from the work performed by the external forces breaking the body.

During the explosion, the pressure drops on the dilaton boundary. As a result, the dilaton becomes not only the origin of the local failure, but also the point fluctuation

source of dislocations. Thus, the basic mechanisms of the destruction and the PD are interconnected and simultaneous.

However, the dilaton model cannot explain all the features of fracturing, because it neglects the presence of shear and the PD. The above provided model of the elementary carrier of strain in the form of frustrons, as it was proposed in [104], is free from this shortage.

As it is shown in [24], the restructuring of the potential relief $U(\vec{r})$ with the height $Q \propto \varepsilon_d$ (ε_d—the dilatation) under the pressure $p \propto \varepsilon_d$ leads to the kinetic transition into the non-equilibrium state at which the crystal flows like a liquid. In this case, besides the weakly excited atoms, oscillating near the nodes of lattice, there are the highly excited atoms, moving without activation over the Peierls fluctuation relief and providing the transfer though drift. Just as the collective excitement of phonons responds to the vibrations of weakly excited atoms, the movement of highly excited atoms can be compared with the collective regime associated with the drift. If phonons have the jet dispersion, then the mentioned regime responds to the central type of the structured factor, provided by the relaxation rule $\omega = i\upsilon k^2$, where υ—the kinetic viscosity and k—the wave number. Here, it would be appropriate to call such excitations as *relaxon*. Within the quasiparticle framework, the intensity of the drift flows is characterized by the density distribution of the Bose condensate of relaxons along with the wave vector $\vec{k}_0$ (in the microscopic homogeneous case, $\vec{k}_0 = 0$). In particular, the dilaton represents the localized area of condensate of size $\sim \lambda$, the formation of which is initiated by the dilatation fluctuations $|\Delta\varepsilon_d| > \varepsilon_c$,

$$\varepsilon_c \sim G^{-1}\frac{a}{\lambda}, \tag{3.200}$$

where G—the Grüneisen constant, a—the lattice parameter, and λ—the length of free run of the phonons emitted from dilaton and colliding outside of it.

Thus, the dilaton, representing the local area of the excited state, by itself cannot be the elementary carrier of destruction, because the shear component of the external stresses is reduced by the drift flows.

Under the influence of the external loading, when the difference between densities S_l of strongly and weakly excited states exceeds the critical value S_c, the stationary distribution of the Bose condensate of relaxons faces the soliton gaps, imposed over the uniform background. This means the local deterioration of the plastic properties, so these areas become the hubs of shear stresses determined by ξ and monotonically changing with the pressure p. The relaxon vacuum density is realized, if the interaction speed $v_- = |\Delta W_s|/\Delta t$ of the elastic energy outflow of shift $W_s \sim \mu a^3$ (μ—the shear modulus, the lattice parameter) is not less than the rate of inflow $v_+ = W_s \cdot \omega_D$ because of the external load (ω_D—Debye frequency). Assuming that for relaxons, ΔW_s is determined by the Grüneisen formula for phonons $\Delta\varepsilon_s = s \cdot (\Delta W_s/W_s)$, where ε_s—the shear strain component (s—the interaction parameter of relaxons defined by the Grüneisen constant G), and setting

the interval Δt by the frequency $\omega_{\mathrm{r}} = vk^2 < v\left(\frac{2\pi}{a}\right)^2$, we find the condition for the frustron stabilization [24]

$$\Delta\varepsilon_{\mathrm{s}} > \varepsilon_{\mathrm{f}}, \ \varepsilon_{\mathrm{f}} \sim k \equiv s \cdot Re, \quad Re \equiv \frac{a^2\omega_{\mathrm{D}}}{2\pi v}. \tag{3.201}$$

In contrast to the marginal dilatation ε_{c}, the boundary shear deformation ε_{f} is determined not only by the anharmonicity, but also by the plastic properties of the medium. By definition $|\Delta\varepsilon_{\mathrm{s}}| < 1$, and the effective Reynolds number Re satisfies $Re < s^{-1}$, corresponding to the laminar flow with relaxons. Physically, this condition means that the plastic flow does not wash away the elementary carriers of destruction in the materials with the kinematic viscosity v exceeding the critical value

$$v_{\mathrm{c}} = s \cdot a^2\omega_{\mathrm{D}}. \tag{3.202}$$

The condition (3.201) provides not only the frustron stabilization, but also the possibility of clustering. Formally, it is expressed as the positive value of the surface energy of such clusters, as the negative values correspond to the volume component. This allows us to consider the evolution in analogue with the birth of phase [118], where the role of atoms, limiting her formation, is performed by the frustron, merging into the cluster of destruction. Such mechanism is implemented in the brittle materials, where the kinematic viscosity exceeds the critical value (3.202). In the opposite case $v < v_{\mathrm{c}}$, the plastic flow washes away the cluster of

Fig. 3.14 The dependence of the free energy rate on the number of frustrons in the cluster: *1* the small loading $(g > 0)$; 2 the heavy loads $(g < 0)$. The *dashed lines* are obtained while neglecting the surface terms
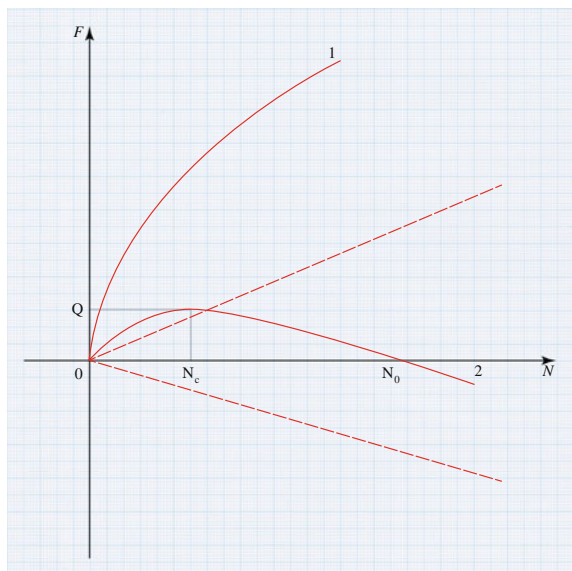
frustrons, and the destruction does not occur as long as the shear stresses exceed the tensile strength and the crack is formed in the material.

Such mechanism is implemented in the viscous materials, where it is impossible to unify not only frustrons into the cluster, but also their very formation.

To estimate the characteristic time of the destruction, we consider the group of elementary carriers of destruction (for brevity, we will only talk about the frustrons), which represents the non-equilibrium system. Provided by the formation of the cluster of frustrons, the rate of change of the free energy F as the function of the number $N \gg 1$ of frustrons is shown as the standard expression [117]

$$\dot{F} = gN + \sigma \cdot N^{\frac{2}{3}}, \tag{3.203}$$

where $g = g(p)$—the change of $\dot{F}$ by adding one frustron and $\sigma > 0$—the surface tension coefficient. At the low pressures, where $g(p) > 0$, the cluster formation is not possible as long as the condition $g(p) = 0$ is not fulfilled, which corresponds to the critical value p_c. With the pressure increasing up to values $p \geq p_c$, the dependence $\dot{F}(N)$ becomes non-monotonic, curve 2 in Fig. 3.14.

As a result of the fluctuation growth of the cluster, the number of frustrons exceeds the critical value $N_e = (2\sigma/(3|g|))^3$ that leads to the decrease in the dissipation rate of the free energy $\dot{F}$. The elastic field of such a supercritical cluster leads to the retraction of frustrons, until it reaches the limit $N_0 = (\sigma/|g|)^3$, exceeding which the cluster becomes the power generator $(\dot{F} < 0)$. This means the transition to the autocatalytic regime of the crack propagation, i.e., the destruction. Of course, the simple connection $N_e/N_0 = (2/3)^3$ between the number of frustrons at the critical and limiting sources of the destruction is the consequence of the model (3.203). Changing the shape of the cluster with its growth, the quantities g and σ depend on N, and in fact, that bond is much more complex. However, on the qualitatively level, the similar ratios reflect the main features of the evolution of the destruction source.

The full time t of transition into the autocatalytic regime consists of the incubation period τ_C, required for the fluctuation formation of the critical cluster, and the time τ_g, required for its growth up to the limit number of frustrons N_0. The last is determined by multiplying the difference $N_0 - N_c$ with the time

$$\tau_1 \sim \frac{T}{\sigma_{Cl} \cdot \varepsilon_c \cdot a} \cdot \frac{N_0}{D \cdot c},$$

necessary to retract one frustron in the supercritical cluster [120]:

$$\tau_g \sim (N_0 - N_c)\tau_1 \sim \frac{N_0^2}{D \cdot c} \cdot \frac{T}{\sigma_{Cl} \cdot \varepsilon_c \cdot a}. \tag{3.204}$$

Here, T—the temperature in the energy units, D—the effective diffusion coefficient of frustrons, $c \sim \exp\{\lambda^2 a(p - K \cdot \varepsilon_C)/T\}$—their equilibrium concentration,

σ_{Cl}—the characteristic value of the stress field, created by the clusters, and K—the modulus of the volumetric compression. The incubation period τ_C is determined by multiplying the time required to form one frustron $\tau_f \sim \omega_D^{-1}$ $\exp\{-\lambda^2 a(p - K\varepsilon_C)/T\}$ with the probability $\omega_c = N_c^{-1} \exp\{-Q \cdot \tau_1' N_c/T\}$ of the critical cluster, where $Q = gN_c/2$—the corresponding growth rate of the free energy and τ_1'—the time required to merge two frustrons with the order τ_1, where under σ_{Cl} it should be understood the field σ_1, created by one of them. As a result, the total time of transition into the autocatalytic regime takes the form [24]

$$\tau = \tau_0 \cdot \exp\left\{-\frac{\lambda^2 a}{T}\left(p - \frac{Ka}{G\lambda}\right)\right\}, \tag{3.205}$$

$$\tau_0 = (\omega_D N_c)^{-1} \cdot \exp\left\{-\frac{Q\tau_1 N_c}{T}\right\} + \frac{N_0^2 TG\lambda}{Da^2 \sigma_{Cl}}, \tag{3.206}$$

where G—the Grüneisen constant.

In the Eq. (3.205), the exponent part represents the probability of forming the frustron, recorded in the form of well-known Zhurkov's formula, in which the influence of the external environment is expressed through the exponential factor [47, 74]. To fulfill such condition, it is necessary that the supercritical growth of cluster acts as the major player, rather than its origin. Then, the second term dominates in the pre-exponential factor (3.206), which is weakly dependent on the state parameters T, σ. In the opposite case, when the main role is played by the cluster origin, the ratio

$$\tau_1 \propto c^{-1} = \exp\{-\lambda^2 a(p - K\varepsilon_c)/T\}$$

Fig. 3.15 The dependence of the relative wear resistance on the hardening energy of the surface layer
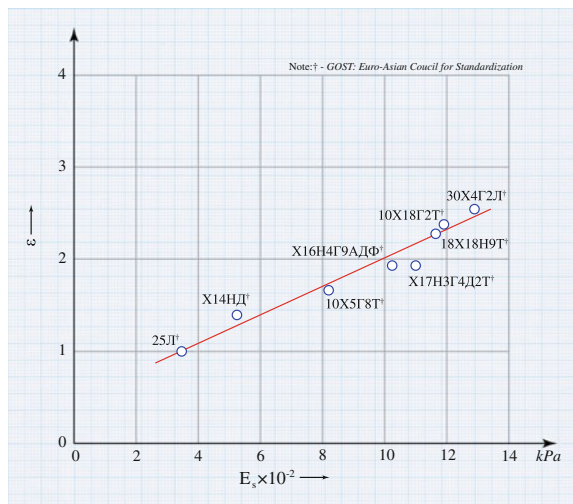
leads to the double exponential dependence $\tau_0(T, \sigma)$, much stronger than Zhurkov's exponent (3.205). Physically, this is due to the fact that Zhurkov's kinetic formula takes into account only the thermo-fluctuational formation of frustron in the stress concentrator field, played by the critical cluster.

Thus, the process of brittle fracture is defined by the formation and evolution of the group of the elementary carriers of destruction—frustrons. The latter are the mesoscopic areas of localization of the shear strain, surrounded by the superplastic shell. The mechanism of brittle fracture is provided by the clustered frustrons in the supercritical failure origin that requires the viscosity v exceeding the value in (3.202). In the viscous materials, where the opposite condition is realized, the destruction proceeds according to the dilaton mechanism [119, 121, 122], which is inherent in the heterogeneous materials, where the presence of the stress concentrators results in the tensile strength, the value of which is much lower than the theoretical limit [121].

The development of failure processes in time allows us to speak about the nature of fatigue wear. The value of the accumulated internal energy as a result of the deformation and hardening of the material surface layer can be the criterion of its durability.

The dependence of the relative wear resistance

$$\varepsilon = \left(\frac{E_s}{E_{cp}}\right)^{0.5}, \tag{3.207}$$

on the hardening energy of the surface layer E_s for the different steel grades (the steel grade 25Л is adopted as the standard) is shown in Fig. 3.15 [123], where $E_s = \left(H_\mu + H_\mu^{max}\right) \cdot \Delta H_\mu^{max}$; H_μ—the micro-hardness of the original surface; $\Delta H_\mu^{max} = H_\mu^{max} - H_\mu$—the maximum micro-hardness of the hardened surface layers.

Literatures

1. T. Ekobori, *Nauchnye osnovy prochnosti i razrusheniia materialov* (Naukova dumka, Kiev, 1978), p. 352
2. S.N. Zhurkov, B.N. Narzullaev, Vremennaia zavisimost' prochnosti tverdykh tel. ZhTF. **23** (10), 1677–1689 (1953)
3. V.M. Finkel', *Fizika razrusheniia* (Moscow, Metallurgiia, 1970), p. 376
4. Van Biurren, *Defekty v kristallakh* (Mir, Moscow, 1960)
5. D.zh. Khart, I. Lote, *Teoriia dislokatsii* (Atomizdat, Moscow, 1972)
6. G. Venkataraman, in *Proceedings of International School of Physics "Enrico Fermi". Course 82: Mechanical and Technical Behaviour of Metallic Materials*, 278 (1982)
7. S.N. Zhurkov, Problemy prochnosti tverdykh tel. Vestnik AN SSSR **11**, 78–82 (1957)
8. V.R. Regel', A.I. Slutsker, E.E. Tomashevskii, *Kineticheskaia priroda prochnosti tverdykh tel* (Nauka, Moscow, 1974), p. 560
9. V.V. Fedorov, *Kinetika povrezhdaemosti i razrusheniia tverdykh tel* (Tashkent, FAN, 1985), p. 167

10. V.S. Ivanova, *Sinergetika: Prochnost' i razrushenie metallicheskikh materialov* (Nauka, Moscow, 1992), p. 160
11. A.M. Pashaev, A.Kh. Janahmadov, O.A. Dyshin, Fraktal'naia razmernost' i ee sviaz' s mekhanicheskimi svoistvami metallov i splavov v usloviiakh predrazrusheniia. Vestnik Azerbaidzhanskoi Inzhenernoi Akademii **2**(2), 13–24 (2010)
12. V.S. Ivanova, A.A. Shaniavskii, *Kolichestvennaia fraktografiia. Ustalostnoe razrushenie* (Metallurgiia, Cheliabinsk, 1988), p. 400
13. M. Feigenbaum, Universal'nost' v povedenii nelineinykh sistem. UFN **141**(2), 343–374 (1983)
14. G. Khaken, *Sinergetika. Ierarkhiia neustoichivostei v samoorganizuiushchikhsia sistemakh i ustroistvakh* (Mir, Moscow, 1985), p. 423
15. I.G. Grabar, Diskretnye iavleniia v mekhanike razrusheniia s pozitsii sinergetiki. *V sb. Sinergetika i ustalostnoe razrushenie metallov*, ed. by V.S. Ivanovoi (Nauka, Moscow, 1989), pp. 191–199
16. Iu.L. Klimontovich, Entropiia i proizvodstvo entropii pri laminarnom i turbulentnom techenii. Pis'ma v ZhTF **10**(2), 80–85 (1984)
17. P.S. Landa, *Nelineinye kolebaniia i volny* (Moscow, LIBROKOM, 2010), p. 552
18. A.I. Olemskoi, I.I. Naumov, *Fraktal'naia kinetika ustalostnogo razrusheniia. v sb. Sinergetika i ustalostnoe razrushenie metallov* (Nauka, Moscow, 1989), p. 200–215
19. A.I. Olemskoi, I.A. Skliar, Evoliutsiia defektnoi struktury tverdogo tela v protsesse plasticheskoi deformatsii. UFN **162**(6), 29–79 (1992)
20. A.I. Olemskoi, Fraktal'naia kinetika polzuchesti tverdogo tela. Fizika tverdogo tela **30**(11), 3384–3394
21. R.G. Palmer, D.L. Stein, E. Abrahams et al., Models of hienraeheally constrained dynamics for glassy relaxation. Phys. Rev. Lett. **53**(10), 958–961 (1984)
22. V.S. Anishchenko (ed.), T.E. Vadivasova, V.V. Astakhov, *Nelineinaia dinamika khaoticheskikh i stokhasticheskikh sistem. Fundamental'nye osnovy i izbrannye problem* (Izd-vo un-ta, Saratov, 1999), p. 368
23. G.I. Barenblatt, L.R. Botvina, Metody podobiia v mekhanike i fizike razrusheniia. Fiz.-khim. mekhanika materialov **1**, 57–62 (1986)
24. A.I. Olemskoi, A.A. Katsnel'son, *Sinergetika kondensirovannoi sredy, izd. 2-e* (Editornaia URSS, Moscow, 2010), p. 336
25. V.I. Vladimirov, *Fizicheskaia priroda razrusheniia metallov* (Metallurgiia, Moscow, 1985)
26. V.S. Ivanova, *Razrushenie metallov* (Metallurgiia, Moscow, 1979)
27. R.L. Salganin, A.I. Slutsker, Kh Aidarov, Kvantovye osobennosti kinetiki razrusheniia tverdykh tel. DAN SSSR **274**(6), 1362–1366 (1984)
28. A.I. Kirilenko, *Diskretnye protsessy ustalostnogo razrusheniia aliuminievykh materialov D16ATV*. Avt. ref. diss. kand. tekhn. nauk. (Kiev, 1985), p. 18
29. V.S. Ivanova, Spektry energii aktivatsii elementarnykh protsessov atomnykh perestroek v metallakh. DAN SSSR **220**(3), 579–581 (1975)
30. V.S. Ivanova, V.F. Terent'ev, *Priroda ustalosti metallov* (Moscow, Metallurgiia, 1975), p. 455
31. A.A. Shaniavskii, S.A. Kunavin, Mekhanizm i diagramma diskretnogo rosta ustalostnoi treshchiny v aliuminievykh splavakh. Izv. AN SSSR. Metally **2**, 159–163 1984
32. A.M. Pashaev, AKh Dzhanakhmedov, O.A. Dyshin, Mekhanika razrusheniia tverdykh tel s pozitsii sinergetiki i fraktal'noi kinetiki. Vestnik Azerbaidzhanskoi Inzhenernoi Akademii **3** (2), 13–26 (2011)
33. A.Kh. Janahmadov, O.A. Dyshin, Synergetics and Fractal Dimensions in Tribology. J. Frict. Wear **32**(1), 61–71 (2011)
34. A.A. Shaniavskii, *Diagramma diskretnogo RUT v aliuminievykh splavakh*. Tez. plenar. dokl. VIII Vsesoiuzn. konf. po ustalosti metallov (IMET AN SSSR, Moscow, 1982), pp. 72–76
35. D.I. Blokhintsev, *Osnovy kvantovoi mekhaniki* (Moscow, Vysshaia shkola, 1961), p. 512
36. L.D. Landau, E.M. Lifshits, *Kvantovaia mekhanika* (Nauka, Moscow, 1972), p. 368
37. Ch. Kittel', *Vvedenie v fiziku tverdogo tela*, per. s angl. (Nauka, Moscow, 1978), p. 791

38. B.M. Askerov, *Termodinamika i statisticheskaia fizika* (Izd-vo Baki universiteti, Baku, 2007), p. 512
39. G. Leibfrid, V. Liudvig, *Teoriia angarmonicheskikh effektov v kristallakh*, per.s angl. (IIL, Moscow, 1963), p. 261
40. A. Nadai, *Plastichnost' i razrushenie tverdykh tel* (Moscow, Izd-vo inost. lit., 1954), p. 647
41. G.I. Barenblatt, *Podobie, avtomodel'nost', promezhutochnaia asimptotika* (St.Peterburg, 1982), p. 254
42. A.M. Pashaev, A.Sh. Mekhtiev, A.Kh. Janahmadov, O.A. Dyshin, Avtomodel'nost' i mekhanika razrusheniia. Vestnik Azerbaidzhanskoi Inzhenernoi Akademii **1**(1), 93–103 (2009)
43. V.A. Borisenko, V.P. Krashchenko, V.E. Statsenko, I.G. Grabar, *Iavlenie uporiadochennoi diskretnosti na temperaturnykh zavisimostiakh prochnostnykh kharakteristik tekhnicheskoi medi. Prochnost' materialov i konstruktsii pri nizkikh temperaturakh*. Tez.dok. II Vsesoiuz. Konf, IPP AN USSR, Kiev, 1986, p. 16
44. A.I. Radchenko, *Diskretno – veroiatnostnaia model' vyrabotki resursov detalei i elementov konstruktsii. Voprosy ekspluatatsionnoi dolgovechnosti i zhivuchesti konstruktsii letatel'nykh apparatov* (KNIGA, Kiev, 1982), p. 3–12
45. A. Brus, R. Kauli, *Strukturnye fazovye perekhody* (Mir, Moscow, 1984), p. 408
46. A.S. Balankin, *Sinergetika deformiruemogo tela* (Moscow, MO SSSR, 1991), p. 404
47. K. Dzhonson, *Mekhanika kontaktnogo vzaimodeistviia* (Mir, Moscow, 1989), p. 509
48. Kh. Chikhos, *Sistemnyi analiz v tribonike*, per. s angl. (Mir, Moscow, 1982), p. 236
49. U. Nikolis, I. Prigozhin, *Samoorganizatsiia v neravnovesnykh sistemakh* (Mir, Moscow, 1979), p. 300
50. V.E. Panin, V.A. Likhachev, Iu.V. Griniaev, *Strukturnye urovni deformatsii tverdykh tel* (Nauka, Novosibirsk, 1985), p. 163
51. V.E. Panin, Iu.V. Griniaev, V.I. Danilov i dr., *Strukturnye urovni plasticheskoi deformatsii i razrusheniia* (Nauka - Sib. otd-e, Novosibirsk, 1990), p. 255
52. B.B. Mandelbrot, *The Fractal Geometry of Nature* (W.H.Freeman and Co., New York, 1983), p. 360
53. V.S. Ivanova, A.S. Balankin, I.Zh. *Bunin i dr., Sinergetika i fraktaly v materialovedenii* (Nauka, Moscow, 1994), p. 383
54. E. Feder, *Fraktaly* (Mir, Moscow, 1991), p. 254
55. E.E. Underwood, K. Banerji, Mater. Sci. Eng. **80**(1), 1–14 (1986)
56. I.R. Kramer, Adv. Mech. Phys. Surfaces. **3**, 109–260 (1986)
57. Q.Y. Long, Li. Sugin, C.W. Lung, J. Phys. D. **24**(4), 602-607 (1991)
58. Avtomodel'nost' i fraktal'naia geometriia razrusheniia, Problemy prochnosti **1**, 3–7 (1988)
59. G.I. Barenblatt, L.R. Botvina, Avtomodel'nost' ustalostnogo razrusheniia. Nakoplenie povrezhdaemosti. Mekhanika tverdogo tela **4**, 161–165 (1983)
60. Ia.B. Zel'dovich, D.D. Sokolov, Fraktaly, podobie, promezhutochnaia asimptotika. Uspekhi fiz. Nauk **146**(3), 493–506 (1985)
61. L.M. Kachanov, *Osnovy mekhaniki razrusheniia* (Nauka, Moscow, 1974), p. 311
62. Iu.N. Rabotnov, *Polzuchest' elementov konstruktsii* (Nauka, Moscow, 1966), p. 752
63. B.M. Smirnov, *Fizika fraktal'nykh klasterov* (Nauka, Moscow, 1991), p. 136
64. V.S. Ivanova, *Aktual'nye problemy prochnosti* (Novgorod, 1994), p. 37
65. V.C. Ivanova, *Fracture and strength of solids* (Xian, 1994), p. 18
66. M.A. Vorob'ev, *Chisla Fibonachchi* (Nauka, Msocow, 1992), p. 192
67. G. Khaken, *Sinergetika* (Mir, Moscow, 1980)
68. I.M. Sokolov, Razmernosti i drugie geometricheskie kriticheskie pokazateli v teorii protekaniia. Uspekhi fizicheskikh nauk **150**(2), 221–255 (1986)
69. V.S. Ivanova, *Ustalostnoe razrushenie metallov* (Moscow, Metallurgiia, 1963), p. 271
70. V.S. Ivanova, *K raschetu fiziko-khimicheskikh konstant metallov, sviazannykh s prochnost'iu mezhatomnoi sviazi. Khimiia metallicheskikh splavov* (Nauka, Moscow, 1973), pp. 196–204
71. V.S. Ivanova, *Sinergetika razrusheniia i mekhanicheskie svoistva. V kn. Sinergetika i ustalostnoe razrushenie metallov* (Nauka, Moscow, 1989), pp. 6–29

72. A.F. Bulat, V.I. Dyrda, *Fraktaly v geomekhanike* (Kiev, Naukova dumka, 2005), p. 357
73. N.N. Davidenkov, *Nekotorye problemy mekhaniki materialov* (Gazetno-zhurn. izd-vo, Moscow, 1943), p. 152
74. N.N. Davidenkov, *Problema udara v metallovedenii* (Moscow, St.Peterburg, Izd-vo AN SSSR, 1938), p. 116
75. V.L. Kirpichev, O podobii pri uprugikh iavleniiakh. Zhurn. Russkogo khimicheskogo obshch-va i fizich. obshch-va. Chast' fizicheskaia **6**(otdel 1), vyp. **IX**, 152–155 (1874)
76. A.G. Ivanov, V.N. Mineev, O masshtabnykh effektakh pri razrushenii. Fizika goreniia i vzryva **15**(5), 70–95 (1979)
77. A.S. Balankin, A.L. Bugrimov, Fraktal'naia razmernost' treshchin, obrazuemykh pri khrupkom razrushenii model'nykh reshetok i tverdykh tel. Pis'ma v ZhTF **17**(7), 63–67 (1991)
78. A.M. Pashayev, A.Kh. Janahmadov, *Resrach of breaking mechanism of materials of heary loaded frictional systems*. Proc. European Conference of COST 532 action: Tribocience and Tribotechnology, Slovenia, vol. II, 1115–1121, June 12–15, 2007
79. A.B. Mosolov, Fraktal'naia Griffitsova treshchina. Zhurnal tekhnicheskoi fiziki **61**(7), 57–60 (1991)
80. G.I. Barenblatt, O ravnovesnykh treshchinakh, obrazuiushchikhsia pri khrupkom razrushenii. Prikladnaia matematika i mekhanika **23**(3), 434–444; **23**(4), 706–721; **23**(5), 893–900 (1959)
81. G.R. Irwin, J.A. Kies, H.L. Smith, Fracture strengths relative to onset and arrest of crack propagation. Proc. Am. Soc. Test. Mater. 640–657 (1959)
82. G.R. Irwin, Fracture mode transition for a crack traversing a plate. Trans. ASME D. **82**, 417–425 (1960)
83. M.J. Feigenbaum, Quantitative universality for a class of nonlinear transformations. J. Stat. Phys. **19**(1), 25–52 (1978)
84. M.J. Feigenbaum, Universal behavior in nonlinear system. Los Alamos Sci. **1**(1), 4–27 (1980)
85. R.M. Kronover, *Fraktaly i khaos v dinamicheskikh sistemakh*. *Osnovy teorii* (Postmarket, Moscow, 2000), p. 350
86. A.Iu. Loskutov, A.S. Mikhailov, *Osnovy teorii slozhnykh sistem* (Institut komp'iuternykh issledovanii, Moscow, Izhevsk, 2007) p. 620
87. B. Hu, J.J. Satija, A spectrum of universality classes in period doubling and period tripling. Phys. Lett. **98A**(4), 143–146 (1983)
88. V.S. Anishchenko, *Slozhnye kolebaniia v prostykh sistemakh. Mekhanizmy vozniknoveniia, struktura i svoistva dinamicheskogo khaosa v radiofizicheskikh sistemakh* (Nauka, Gl. red. fiz. mat. lit., Moscow, 1990), p. 312
89. A.S. Pikovskii, O povedenii spektra strannogo attraktora v kriticheskoi tochke. Izv. vuzov. Ser. «Radiofizika» , vol. 25(7), pp. 46–848 (1982)
90. B.A. Huberman, A.B. Zisook, Power spectra of strange attractors. Phys. Rev. Lett. **46**(10), 626–632 (1980)
91. S.P. Kuznetsov, *Dinamicheskii khaos (kurs lektsii). Uchebnoe posobie dlia vuzov* (Izd-vo fiz.-mat. Lit-ry, Moscow, 2006), p. 356
92. A.N. Sharkovskii, Iu.L. Maistrenko, E.Iu. Romanenko, *Raznostnye uravneniia i ikh prilozheniia* (Naukova dumka, Kiev, 1986), p. 280
93. A. Likhtenberg, M. Liberman, *Reguliarnaia i stokhasticheskaia dinamika*, per.s angl. (Mir, Moscow, 1984), p. 521
94. R.M. May, Simple mathematical models with very complicated dynamics. Nature **261**(6), 459–467 (1976)
95. B.A. Humerman, J. Rudnick, Scaling behavior of chaotic flows. Phys. Rev. Lett. **46**(3), 154–157 (1980)
96. C. Tresser, P. Coullet, Iterations d'endomirphismes et groupe de renormalization. C.R. Acad. Sci. Paris **287A**(7), 577–584 (1978)
97. J.P. Crutchfield, N.H. Packard, Symbolic dynamics of noisy chaos. Physica D **7D**(1–3), 201–223 (1983)
98. B. Shraiman, C.E. Wayne, P.C. Martin, Scaling theory for noisy period. doubling transitions to chaos. Phys. Rev. Lett. **46**(14), 935–939 (1981)

99. M. Khenon, *Dvumernoe otobrazhenie so strannym attraktorom, v sb. Strannye attraktory,* per. s angl. (Mir, Moscow, 1981), pp. 152–163

100. A.Kh. Janahmadov, A.M. Pashayev, M.G. Javadov, M.Y. Javadov, The Multifraktal analysis of the fatigue fracture under the process of friction. The 5th World tribology Congress, WTC 2013, September, 8–13, Torino, Italy. iD 821 (2013)

101. Reshetki sviazannykh otobrazhenii – Nauk – Saratovskaia gruppa teoreticheskoi nelineinoi dinamiki, http://www.sgtnd.narod.ru/science/cml/rus/main.htm

102. V.R. Vaks, *Vvedenie v mikroskopicheskuiu teoriiu segnetoelektrikov* (Nauka, Moscow, 1973), p. 328

103. G.V. Kurdiumov, ZhTF **18**, 999 (1948)

104. A.I. Olemskoi, V.A. Petrunin, Perestroika kondensirovannogo sostoianiia atomov v usloviiakh intensivnogo vneshnego vozdeistviia. Izvestiia vuzov. Fizika **1**, 82–121 (1987)

105. A.I. Olemskoi, V.E. Panin, V.A. Petrunin, Smeshannoe sostoianie i fizicheskaia mekhanika defektov v sil'no vozbuzhdennykh kristallakh. Izvestiia vuzov MV i SSO SSSR. Fizika **2**, 20–27 (1986)

106. A.I. Olemskoi, *Sinergetika slozhnykh sistem. Fenomenologiia i statisticheskaia teoriia* (KRASAND, Moscow, 2009), p. 348

107. V.E. Panin, Novoe v oblasti fiziki tverdogo tela. Izvestiia vuzov. Fizika **1**, 3–8

108. Dzh. Zaiman, *Printsipy teorii tverdogo tela* (Mir, Moscow, 1974), p. 591

109. V.M. Anisimov, M.I. Katsnel'son, A.I. Likhtenshtein, A.V. Trefilov, Vliianie pikov plotnosti sostoianii na strukturnuiu i magnitnuiu neustoichivost' splavov. Pis'ma v ZhETF **45**(6), 285–288 (1987)

110. I.M. Sokolov, *Sinergetika i ustalostnoe razrushenie metallov, sb. statei* (Nauka, Moscow, 1989), p. 246

111. V.V. Zosimov, L.M. Liamshev, Fraktaly v volnovykh protsessakh. Uspekhi fizicheskikh nauk **165**(4), 361–402 (1995)

112. J.R. Banavar, J.F. Willemsen, Ibidem, Ser., B, **30**, 6778 (1984)

113. A. Maritan, A. Stella, Padova prepint DFPD 17/85 (1985)

114. D.N. Zubarev, *Neravnovesnaia statisticheskaia mekhanika* (Nauka, Moscow, 1971), p. 591

115. P. Rezibua, M. De Lener, *Klassicheskaia kineticheskaia teoriia zhidkostei i gazov* (Mir, Moscow, 1980), p. 432

116. E.M. Lifshits, L.P. Pitaevskii, *Fizicheskaia kinetika* (Nauka, Moscow, 1979), p. 527

117. L.D. Landau, E.M. Lifshits, *Statisticheskaia fizika. Chast' I* (Nauka, Moscow, 1976), p. 584

118. E.M. Lifshits, L.P. Pitaevskii, *Staticheskaia fizika. Chast' I* (Nauka, Moscow, 1978), p. 448

119. S.N. Zhurkov, Dilatonnyi mekhanizm prochnosti tverdykh tel. Fizika tverdogo tela **25**(10), 3119–3123 (1983)

120. Ia.E. Geguzin, *Diffuzionnaia zona* (Nauka, Moscow, 1979), p. 343

121. O.A. Kaibyshev, *Sverkhplastichnost' promyshlennykh splavov* (Metallurgiia, Moscow, 1984)

122. V.A. Petrov, Dilatonnaia model' termofluktuatsionnogo zarozhdeniia treshchiny. Fizika tverdogo tela **25**(10), 3124–3127 (1983)

123. A.Kh. Dzhanakhmedov, *Neftianaia tribologiia* (Baku, Elm, 2003), p. 326

124. E.B. Vul, G. Sinai, K.M. Khanin, Universal'nost' Feigenbauma i termodinamicheskii formalizm. UFN, vol. 39; vol. 3(237), 3–37 (1984)

125. V.S. Ivanova, *Sinergetika. Prochnost' i razrushenie metallicheskikh materialov* (Nauka, Moscow, 1992), p. 160

126. V.I. Iveronova, A.A. Katsnel'son, *Blizhnii poriadok v tverdykh rastvorakh* (Nauka, Moscow), p. 1077

127. I.Ia. Korenblit, E.F. Shender, Izv. Vuzov. Fizika **10**, 23 (1984)

128. B.I. Neimark, P.S. Landa, *Stokhasticheskie i khaoticheskie kolebaniia* (Nauka, Moscow, 1987), p. 424

129. V.V. Fedorov, *Kinetika povrezhdaemosti i razrusheniia tverdykh tel* (Izd-vo "FAN" Uzbekskoi SSR, Tashkent, 1985), p. 168

130. S. Alekhander, C. Laerman, R. Orbach, H.M. Rosenberg, Phys. Rev. B. **28**, 4615 (1983)

Chapter 4
Fractal Kinetics of Fracture

4.1 The Concept of Fractal—Fractal Dimension

Fractals are called geometric objects: line, surface, spatial body having very jagged shape, and self-similarity. The founder of the theory of fractals, Mandelbrot [1], formed the term "fractal" from the Latin participle "fractus." The corresponding verb "frangere" translates as break or crush, i.e., to create fragments of irregular shape [2]. The self-similarity as the main property of fractal means that it is more or less uniformly arranged in the wide range of scales.

In mathematics, the fractal is the set of points whose Hausdorff-Besicovitch dimension (fractal dimension) exceeds the Euclidean topological dimension. The fractal dimension d characterizes any self-similar system, when the linear dimensions change f times, the fractal dimension (e.g., the "length" of loop or the "area" of surface) changes (at any f) f^d times. From the nature of the fractal dimension, we can see that it is not connected with the topology, but with the process of constructing the studying set [3].

Generally, the fractal objects are the set in the one-, two-, three-, etc. dimensional spaces, which all have certain specific properties, there is no a rigorous definition. We can only qualitatively indicate the typical features of fractal objects [4]:

- the existence of fine structure and "jaggedness" of arbitrarily small size parts;
- the object irregularity, not allowing them to be described within the framework of the traditional geometrical (Euclidean) or topological spaces;
- the regular or stochastic similarity of fractal parts with whole fractal—the self-similarity hierarchy of the object parts at the different scale levels;
- the manifestation through the simple recursive procedure or the algorithm, leading to the gradual refinement or the enlargement of details (see, e.g., the approach to build fractals based on the iterated function systems, proposed by Hutchinson [5] and improved by Barnsley [6]—the detail description is provided in [7]).

The objects with "sprawling," sparse or increasingly complex structure are considered as fractal, when the constituent patterns have the scaling invariance property, often arising from the chaotic processes. When observing such objects, it can be seen that with the growth they show the self-similarity property, repeated at the different scaling levels.

The self-similarity (auto-scaling) is the property when the set of points have the same geometrical structure through the different scaling levels.

The more rigorous physical definition is given in [8]: "Auto scaling is the special symmetry of physical system, based on fact that the changes in scale of the independent variables can be compensated by the similar transformations in other dynamic variables. The auto scaling results leads to the effective reduction in the number of independent variables." This terminology is also associated with others [9], such as the scale invariance (scaling)—the invariance property of equation describing some physical theory or some physical process, while changing all the distances and time intervals in exactly the same way. The scale invariance is sometimes referred to as self-similarity or likeness. The specialists of solids physics determine auto-scaling through the properties of similarity [10]: "Auto scaling is the similarity property of the system characteristics distribution at different time intervals."

The fractal dimension plays an important role in describing the fractal properties. Let us give the general definition of this measure. Let d be the normal dimension of the Euclidean space, where the fractal object is placed ($d = 1$—line, $d = 2$—plane, $d = 3$—ordinary three-dimensional space). Let us cover the entire object by the d—dimensional "balls" with the radius l. Suppose that we need to do no less than $N(l)$ balls. Then, at sufficiently small l, $N(l)$ changes with l according to the power rule

$$N(l) \sim 1/l^D, \tag{4.1}$$

then D is called the *Hausdorff-Besicovitch* dimension, or the fractal dimension of object.

Using the fractal dimension, Mandelbrot gave more rigorous definition of fractal. According to his definition, the fractal represents by itself an object, whose Hausdorff-Besicovitch dimension is greater than its surface topology (0 for points displacement, 1 for the curve, 2 for the surface, 3 for the volume, etc.).

The formula (4.1) can be rewritten in the form

$$D = -\lim_{l \to 0} \frac{\ln N(l)}{\ln l}. \tag{4.2}$$

This is the general definition of the fractal dimension D. In accordance with it, the value of D is the *local* characteristic of object. It is obvious that the same result could have been obtained for the fractal dimension if we used the fractal covering cubes (squares, if the fractal object is located on plane). Sometimes the covering is carried out by elements that make up the fractal. In this case, the simplified version of the formula (4.2) is used to determine the fractal dimension. Suppose that at

some stage of the fractal covering we have to use, as a minimum, $N(l)$ elements with specific size l, and at the other stage $N(l')$ element with specific size l'. Then the fractal dimension D can be calculated by the formula

$$D = -\frac{\ln\left(\frac{N(l)}{N(l')}\right)}{\ln\left(\frac{l}{l'}\right)}. \tag{4.3}$$

By fractals, we shall note not only self-similar, but also *self-affine* objects. The latter includes the geometric shapes, parts of which can be brought into the compliance with whole shape using the similarity transformations carried out in the different directions with the different coefficients of similarity. Further details on the self-affine and self-similar sets can be found in Mandelbrot's book [11] and in the articles by Voss [12, 13].

The fractal dimension of even simplest self-affine fractals is not uniquely determined [14, 15]. When analyzing the self-affine fractal curves, we should distinguish between the *local* fractal dimension, defined by the equation $D = 2 - H$ (H—the Hurst parameter), and the *global* fractal dimension [13, 15].

4.2 Fractals in Condensed Matter Physics

Until recently, the methods of equilibrium statistical physics were used to study the condensed medium. This is due to the assumption that the condensed medium under the influence, preserving it as such, represents the statistical system in equilibrium or slightly non-equilibrium.

Recently, there is a growing interest in the phenomenon, where the behavior of the statistical group of atoms in the condensed medium becomes such that the usual concepts (such as the concept of phonons or the thermodynamic phase transitions) lose their applicability or require fundamental changes [16]. This behavior is due to the strong deviation of the atomic system from equilibrium, e.g., in the core of lattice defects or the areas of plastic flow and failure. The strongly non-equilibrium-condensed medium requires the usage of techniques that allow us to represent such features as the non-ergodicity of statistical group, the emergence of hierarchical fractal structures, the structural relaxation, the mutual influence of subsystem undergoing the phase transition in the medium, etc.

In the strong excitation conditions, the system changes dramatically, fundamentally new structural states and associated degrees of freedom may appear particularly. Therefore, the initial state can no longer be used for the description of a highly excited crystalline lattice. Instead, the excited state itself must be considered as the initial state, and the transition into equilibrium must be seen as the continuous symmetry violation of that state with the condensation of corresponding Goldstone modes. Under this approach, the phonon condensation transforms the highly excited system into the balanced crystalline state forming the long-range

displacements, the condensation of concentrated excitations determines the long-range order of the atomic density, and the various configuration excitations define the short-range order, the amorphous state at quenching, etc. Essentially, all these phenomena correspond to the establishment of order in the system with the spontaneous asymmetry, and in each case the mentioned dynamic excitation determines the Goldstone mode [17].

In the highly excited state the crystal behaves nonlinearly, the mass transfer effects occur at the velocity many times exceeding the jumping diffusion with the possible plastic flow of the hydrodynamic character, generating the metastable structures and phase. It is absolutely clear that new ideas are required to describe the highly excited crystal since the perturbation theory for an ideal crystal is not applicable anymore.

For the first time, such representations were developed in [18]. This book justifies the position that under the strong excitation as the initial state we should take the maximum of the non-equilibrium thermodynamic potential (TP) for which the distribution function of atoms in space is significantly different from that of an ideal crystal. The new structural condition appears under the high excitation in the node space along with the original crystal structural conditions vacant or occupied by the highly excited atoms. New degrees of freedom get created in the crystal. The highly excited crystal essentially becomes the superposition of several structures, and the number of structural states in the system gets much higher than the number of atoms. Such crystal states are called the atom-vacant. They explain the nonlinear behavior of the highly excited crystal, the anomalous high velocities of mass transfer in it (the atoms in such conditions can move through the internodes), and the hydrodynamic flow. During the movement of the highly excited crystal, the intermediate structures associated with the possibility of localization of the highly excited atoms in new structural states can be created within it. In the final state, the intermediate structures are metastable, but they provide the additional channels of the energy dissipation through its creation process. The process is purely dissipative.

Of particular interest is the application of the theory of highly excited states in crystals to the plasticity and strength of solids. The principal disadvantage of existing theories of physics and the solids mechanics is in the analysis of plastic flow with respect to the original stable crystal, meanwhile neglecting the structural deformation levels. As it is shown in [19, 20], the plastic deformation should be considered through the behavior of inhomogeneous, highly non-equilibrium systems undergoing local structural changes, and achieving the equilibrium state by moving elements of new structures through the crystal within the fields of stress gradients. Rebuilding in relays between two adjacent structures, the deformable crystal can contain in the local volumes the plastic flow running like the dissipative process.

The creation of plastic shear is the local kinetic and structural transition and can occur only in the local area of crystal due to the entropy. The mentioned structural transformation is fundamentally different from the thermodynamic structural

transition, and it should be described on the basis of non-equilibrium thermodynamics [21].

It is fundamentally important that shear can only take place within one system of sliding planes, where is the loss of shear stability, at each point of deformable object. The simultaneous multiple sliding in one point is impossible that would mean the loss of shear stability of whole crystal. The shear data, being anisotropic, is always accompanied by the turn of material inside the structure deformation element (SDE) (grains, blocks, and cells of dislocation structure), where the turn of material in contrast to the crystallographic does not change the space orientation of crystal lattice [20]. This causes torque at the boundary to the SDE from the surrounding material. The rotary deformation modes drive the entire hierarchy of the structural levels of deformable material. The structural elements begin to move as whole, experiencing the translation and the crystallographic rotation. The field of the rotational moments provides the rotational modes of deformation, and within SED, the emergence of dislocations from their sliding planes and the formation of disoriented cellular dislocation substructure, the subsequent involvement of multiple sliding as the vortex of material turning of the crystallographic shears.

The organic relationships between shear and torque lead to the fact that the elementary act of the plastic deformation is not shift, but the translational–rotational vortex (TRV). With respect to the scaling factor, they can be micro-, meso-, and macro-vortices. The hierarchy of structure deformation levels creates its own hierarchy of vortices. At the plastic deformation, there may also occur meso-vortices associated with the formation of the mesoscopic dissipative structures. The vortex nature of deformation sets in motion the whole hierarchy of the structure deformation levels and ensures the organization of new channels of energy dissipation, more efficient than one caused by the motion of individual dislocations.

The toque deformation regimes at the different scale levels are significantly different from each other. Their evolution with an increase in the deformation degree is reflected in the changes of fractal dimension, which can be used in many theoretical and applied problems [22].

On the microscale level, only the multiple sliding can compensate the material turning of the crystal lattice. Therefore, in the continuum mechanics and the dislocation theory, the plastic flow is described as the superposition of shear on the 5–6 systems of sliding. The plastic deformation in such a description is purely translational process that is presented in the equations of mechanics by the components of the distortion tensor. The emergence of dislocations from their sliding planes due to the deformation of the disoriented dislocation structure is complicated because of the large splitting of dislocations and the short-range order. As a result, the creation of the adjacent planar clusters of opposite sign can only compensate the strong material turning (Fig. 4.1). Such a planar dislocation dipole is actually the volumetric meso-defects, the appearance of which is associated with the toque deformation. Its Hausdorff-Besicovitch fractal dimension is significantly greater than the topological dimension of a flat planar sliding.

The self-organization of single martensitic lamellae in the form of "chevrons" in the plastic deformation of the intervals with thermo-elastic martensitic
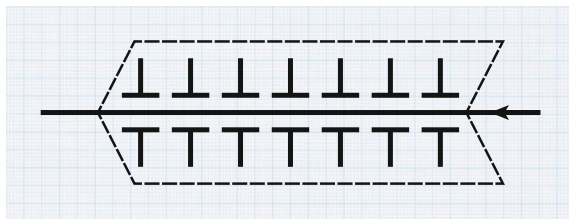
Fig. 4.1 The planar cluster of dislocations

transformation is even more exemplar (Fig. 4.2). The pairs of single lamellae with torques of different sign are linked in them. The martensitic lamella in the area of stress concentration is associated with the collective rotation of lattice in the specific direction and creates in the adjacent volume the field of torque moment of the opposite sign. The low shear resistance of the original austenite lattice reveals the zone of influence of the martensitic lamella in the form of conjugate lamella with the opposite sign of rotation. The matching pair of the martensitic lamellae has the Hausdorff-Besicovitch fractal dimension, significantly greater than the topological dimension of the planar martensitic.

   All varieties of meso-mechanisms deformation are due to the movement of the volumetric structure elements with the pronounced bending-torsion effects in the space. Experimentally, this is most clearly manifested itself in the high-temperature deformation, creeping, and alternating loading. During the active tension at the room temperature, the complex cross-sliding of dislocations and the small number of sliding contribute to the effects of bending-torsion. Naturally, the Hausdorff-Besicovitch fractal dimension in this case is very different from the topological dimension of planar dislocations.

   In general, by increasing the degree of deformation the role of large scale of structural levels, the large-scale structural elements included in TRV, continuously play a big role. Therefore, the fractal dimension of the deformable medium continuously increases. There is a good correlation between the curves of the plastic flow phases and the corresponding curves of the fractal dimension. This is explained by the inclusion of every new structural level into the deformation, which determines the involvement of a new energy dissipation channel, inevitably
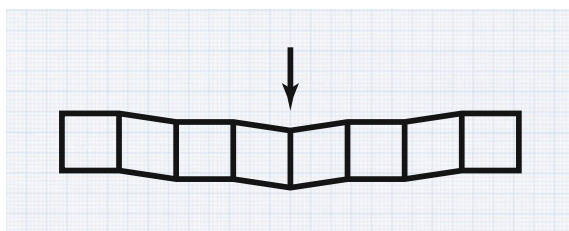
Fig. 4.2 The diagram of self-organization of single martensitic lamellae in the form of "chevron"

affecting the coefficient of hardening $\theta = d\sigma/d\varepsilon$ or the plastic flow rate at creeping [23]. Therefore, the study of the fractal dimension provides important information about the plastic flow involvement into the hierarchy of structural levels of deformation. Such information can be used to forecast the resource of loaded constructions.

The plastic deformation also occurs upon contacting of solids [24]. To describe this process, A.Kh. Janahmadov proposed a theory of thermo-mechanical wear [25] and investigated the tribological problems of the oil–gas equipment operation [26, 27]. The application of fractal analysis to diagnose the type of contact (elastic, elastic-plastic, and plastic) between solids under the external friction is considered in [28].

4.3   Fractal Properties of Hierarchical Structures of Potential Relief

Let the system state is determined by the parameter η. If the initial state is determined by the parameter η_i, then before you get to the final η_f system undergoes a chain of transitions between neighboring minimums of the free energy $U(\eta)$

$$\eta_i \rightarrow \eta_1 \rightarrow \eta_2 \rightarrow \cdots \rightarrow \eta_l \rightarrow \cdots \rightarrow \eta_f.$$

Each of the transitions is described by the probability $S_l(t)$ of transition from the l-th minimum to $(l+1)$-th. Its expression is given by the Arrhenius barrier height Q_l:

$$\tau_l = \eta_i e^{(Q_l/T)}, \tag{4.4}$$

where T—the temperature, τ_l—the relaxation time.

The characteristic feature of such a chain of transitions is that all of the barrier heights have the same order, due to the fact that the times $\Delta t = t_{l+1} - t_l$ required to overcome them are commensurable [29]. Therefore, during $t \gg n\tau_l$ the system with the probability $1 - S(t)$ overcomes n barriers with

$$S(t) = \prod_{l=1}^{n} S_l \tag{4.5}$$

where

$$S_l = e^{(-\Delta t_l/\eta_l)}, \quad \Delta t_n = t - t_n \tag{4.6}$$

is the Debye dependence of the probability of overcoming l-th barrier. When $n \gg 1$, we can ignore the spread Δt_l intervals, assuming $\Delta t_l = t/n$. Then (4.5) takes the Debye form (4.6)

$$S(t) = e^{(-t/\langle \tau \rangle)} \tag{4.7}$$

with the average relaxation time $\langle \tau \rangle$ given by the equation

$$\langle \tau \rangle^{-1} = \frac{1}{n} \sum_{l=1}^{n} \eta_l^{-1}. \tag{4.8}$$

Thus, the transition chain between the adjacent minimums of function $U(\eta)$ (the system metastable states) is reduced to the Debye relaxation with an average time $\langle \tau \rangle$. The sequential nature of process is reflected in the multiplicative elementary probabilities $S_l(t)$ and the additive inverse relaxation times. If, according to (4.4), the value of τ_l^{-1} is proportional to the probability of the thermal fluctuation overcoming the interphase barrier Q_l, then the given additive means the independence of fluctuations of microscopic quantities (e.g., energy phases).

If such a situation occurs at the macroscopic level, then the probabilities get added rather than the microscopic quantities τ_l^{-1}. This means that the set of parallel channels of relaxation operates independently. Each channel corresponds to the statistical ensemble α, realized with the probability w_α. The probability of transition between α and β channels has the form

$$S_{\alpha\beta}(t) = e^{(-t/\tau_{\alpha\beta})}, \quad \tau_{\alpha\beta} = \tau_0 e^{(Q_{\alpha\beta}/T)}. \tag{4.9}$$

The summary probability

$$S(t) = \sum_{\alpha,\beta} w_\alpha w_\beta S_{\alpha\beta}(t) \tag{4.10}$$

describes the relaxation provided by the full range of channels. Their parallel connection exists if the probabilities of the various channels

$$w_\alpha \propto e^{(-E_\alpha/T)}. \tag{4.11}$$

are comparable; E_α—the energy of α-channel. Such a situation requires the degeneration with respect to the energy levels

$$E_\alpha = \int U(\vec{r}) \rho_\alpha(\vec{r}) d\vec{r}, \tag{4.12}$$

where $\rho_\alpha(\vec{r})$—the distribution of structure units (e.g., atoms) in the α-channel relaxation; $U(\vec{r})$—the potential relief of system.

From the condition of commensurability of the energy E_α, it follows that various α channels should be compared with the minima of the potential relief $U(\vec{r})$, only slightly differing from each other. On the other hand, the presence of spectrum of relaxation times in (4.9) can only be achieved under the condition that the barriers

separating the different minimums α, β are significantly different in the height $Q_{\alpha\beta}$. These conditions can only be met if the hierarchical structure of the potential relief (Fig. 4.3a): on the large-scale minimums $U(\vec{r})$ the more fine are imposed, then on them even smaller, etc. At the end, we get the fractal dependence $U(\vec{r})$, strongly reminding the coastline.

From Fig. 4.3, it is seen that the statistical ensembles α, β may be combined into the clusters, each of which is characterized by the maximum height $Q_{\alpha\beta}$ of barrier separating this cluster from other clusters. On the other hand, since the ensembles α, β correspond to the nodes of Cayley tree (Fig. 4.3b), then it is possible to math them with α, β from the ultrametric space, separated by the distance $l_{\alpha\beta}$. Thus, the barrier height $Q_{\alpha\beta}$ and with them the relaxation times $\tau_{\alpha\beta}$ are the distance functions $l_{\alpha\beta}$ of the states in the ultrametric space. The parallel action of the different relaxation channels is only provided in the hierarchical subordination of the set of corresponding statistical ensembles. This situation occurs in the strongly non-equilibrium thermodynamic systems such as highly deformed material [20, 21, 30], the polytypic and martensitic structures [31, 32].

In a hierarchical system, the fastest processes run first corresponding to the barriers overcome with the minimum height $Q_{\alpha\beta}$. So the merger of the smallest statistical ensembles takes place, and the system moves to the higher hierarchical level of Cayley tree (Fig. 4.3b). Then, we overcome the barriers with even greater height $Q_{\alpha\beta}$, at the end we get a super clusters which merge into the larger system matching the following hierarchical level. Furthermore, this process can continue indefinitely. Its hierarchical nature is reflected in the fact that until the channels with the given relaxation time τ_l do not work, the parallel network of channels at next level will not switch on, having the relaxation time $\tau_{l+1} \gg \tau_l$. This hierarchical subordination is the cause of the critical deceleration of relaxation, which leads to
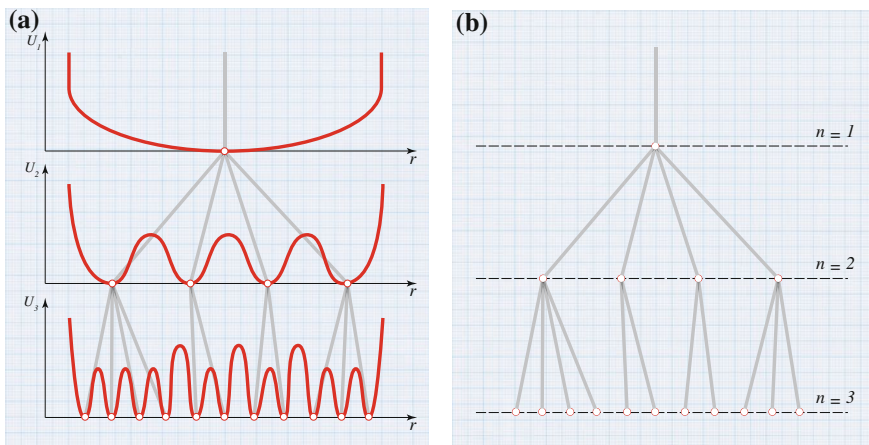
Fig. 4.3 a The type of potential relief on the different structural levels; **b** The corresponding hierarchical tree

the transformation of the Debye exponential in (4.9) into more slowly decreasing dependence.

The fractal nature of the hierarchical subordination system is manifested in the coordinate dependence of $U(r)$ potential energy of the system. This means that the set of clusters of statistical ensembles will also have the fractal properties, represented by the points in the ultrametric space. We note here to avoid further misunderstanding that the clusters of statistical ensembles in the ultrametric space do not necessarily correspond to the clusters of structural units in the r-space.

The Cayley tree is represented in Fig. 4.3b by the number of hierarchical levels $n = 3$ and branching $s = 4$. From the figure, it is shown that each node in the tree at any level $m(m \leq n)$ can be expressed by m numbers of a_l, where the index l runs from 0 to $m - 1$, and the numbers themselves a_l vary from 0 to $s - 1$. In other words, the coordinates of nodes of level m

$$\{a_l\}_m^s = a_0 a_1 \ldots a_l \ldots a_{m-1}, \quad a_l = 0, 1, \ldots, s - 1. \tag{4.13}$$

where m—the digit numbers in the s-array numeric system.

They define the space with ultrametric topology, the characteristic property of which is that its points can not form triangles with all the different parties [33]. This property observed at a given level m assuming that the distance l between any nodes of the Cayley tree is identified by the number of steps to the general order located at $m - l$ level. If two nodes are numbered by the set (4.13) of numbers a_l and b_l, then the distance between them depends on which number differs first from other. So, for the tree shown in Fig. 4.3b, the distance is equal to 2, if $a_0 \neq b_0$; and it is equal to 1 if $a_0 = b_0$, but $a_1 \neq b_1$. For an arbitrary combination of numbers m, s, the distance between these points is equal to $l = 1, \ldots, m$, if the following equalities hold $a_i = b_i$, $i = 0, 1, \ldots, m - l - 1$, but $a_{m-l} \neq b_{m-l}$. Here, m—the level of that numbers a and b, which is not higher than other number.

The ultrametric space concept is important because by reflecting the hierarchical structure of the system, it implements the so-called logarithmic metrics for the physically observable quantities. This means that in such a space the distance l is a linear function of the logarithm of the observed ρ. Since the manipulation with $\ln \rho$ is less convenient than with the linear dependence on l, then instead of the usual values on the axis ρ it is convenient to introduce the corresponding ultrametric space, characterized by the distance l, and conduct all the calculations in this space [33–35].

To determine the dependence $\rho(l)$, we represent the value ρ in s-array notation (4.13). This is done by the power series expansion

$$\rho(a - b) = (a_0 - b_0)s^m + (a_1 - b_1)s^{m-1} + \cdots + (a_{m-l} - b_{m-l})s^l \\ + \cdots + (a_{m-1} - b_{m-1})s + (a_m - b_m), \tag{4.14}$$

the first m coefficients are given by the m-valued numbers (4.13), and the latter determines the origin of ρ.

The beauty of expansion (4.14) is that at $s \gg 1$ only one term dominates in it. Indeed, if the distance between the points of the ultrametric space is equal to l, then the first $m - l$ terms containing the maximum power of the large number s are equal to 0, since by definition $a_i = b_i$ at $i = 0, 1, \ldots, m - l - 1$. The last l members of series include the degrees of s^k, $k = l - 1, l - 2, \ldots, 0$, the values of which are negligible in comparison with s^l. Thus, only one term $(a_{m-1} - b_{m-1})s^l \leq s^{l+1}$ remains, and with the logarithmic accuracy, the series (4.14) are reduced to the form

$$\ln \rho \approx (l+1) \ln s \approx l \cdot \ln s, \quad m, s, l \gg 1. \tag{4.15}$$

This equality represents the logarithmic metrics of the ultrametric space.

Everywhere above we meant the homogeneous Cayley tree, where the branching is the same at all nodes. Obviously, the corresponding ultrametric space has the dimension $D = 1$. Indeed, assuming that there is the similarity parameter $\xi = s^{-1}$, we obtain the elementary length $\ln s = \xi^n = s^{-n}$, and the formula $N_n = s^n$ for the number of nodes at the level n, takes the form (4.1), where $D = 1$.

It is easy to see that the fractional dimension $D < 1$ is obtained, only if, at each level n, and for part of nodes, the branching disappears. Such situation happens, for example, with the Fibonacci sequence. From the Cayley tree shown in Fig. 4.4, it is
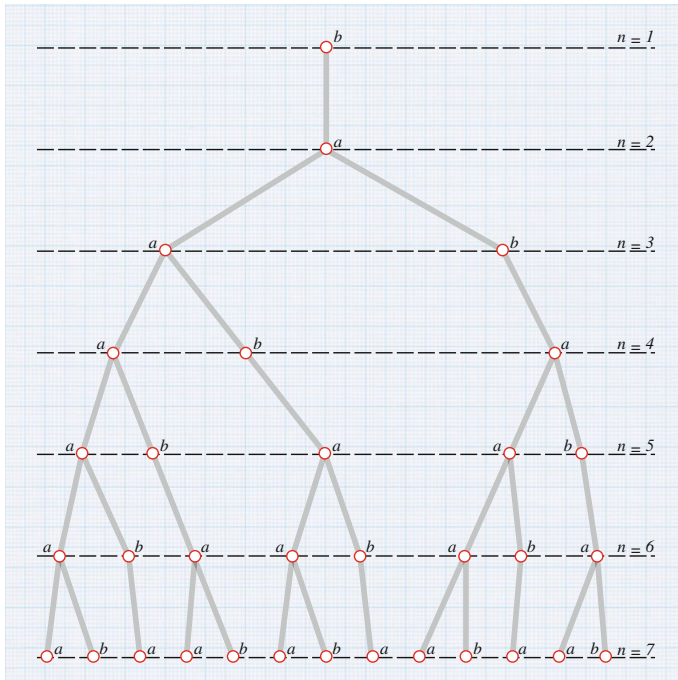
Fig. 4.4 The irregular Fibonacci tree with varying branches

evident that there is a non-periodic (but quite natural!) alternating nodes with branching $s = 1, 2. . ..$

Here, on each non-furcate node, there are double branching nodes, equaled to the so-called the golden mean $\tau = \left(\sqrt{5} + 1\right)/2 \approx 1.618$ [29]. It turns out that this leads to the reduction of ultrametric space dimension corresponding to the Fibonacci tree with a value $D = \ln \tau / \ln 2 \approx 0.694$. Generally, the equality is given as

$$D = \ln \rho / \ln s$$

where ρ—the number of furcate nodes $s = 2, 3. . .$ per one non-furcate node.

The above review refers to the rarefied ultrametric space, for which the fractal dimension D is less than the topological d. The reversed case is available, if not only the closest hierarchical level are connected, but also further away ones (Fig. 4.5).

In other words, the condition $D > d$ is realized for the non-Markov hierarchical systems with memory.
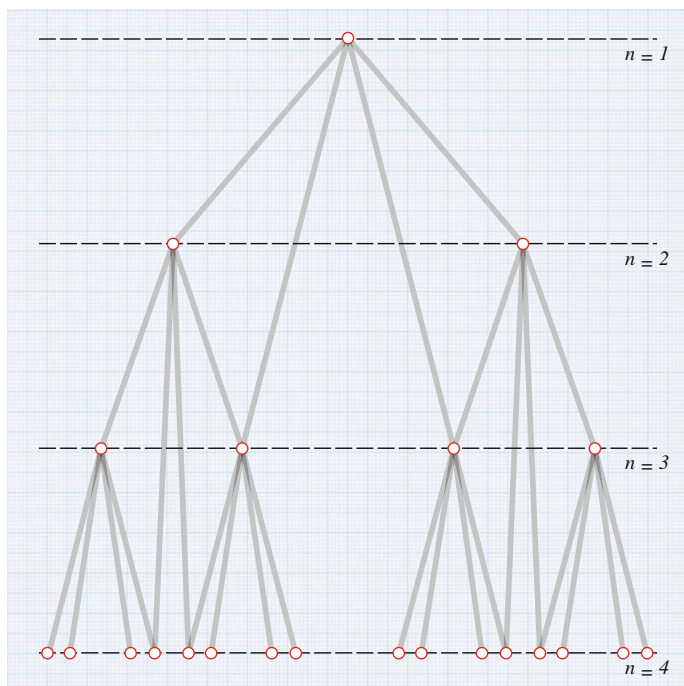
Fig. 4.5 The Cayley tree corresponding to the non-Markov scaling levels

4.4   Kinetics of Fracture from Positions of the Theory of Fractals

The numerous experimental data show that the cyclic loading applied at the first stage of destruction forms the highly dispersed grooved structure, distributed in accordance with the sample stress state [36]. If there is a stress concentrator (e.g., cut), then the growth of macro-cracks initiated by them happens at the expense of abrupt joining individual grooves, presented as the frustron clusters and other destruction carriers, grouped in accordance with the distribution of stress field.

In the homogeneous conditions, the grooves are formed in the larger particles, for which, in particular, the transition occurs from the micro-separations to the micro-shears. During its growth at this stage, the macro-crack instantly skips the entire volume of metal, which are formed by the given cellular structure. This forms the secondary cell structure on the background of already existing structures. This stage, which takes place in the certain range of the stress intensity factor $K \sim \sigma l^{1/2}$ (σ—the applied stress, l—the length of crack), grows into the macroscopic instability; as a result, there is a patching relief of fracture associated with the plastic deformation.

According to the data on acoustic emission, the process of fatigue failure is intermittent with the development of structural changes prior to the destruction, and the sample emits short impulses of varying intensity and frequency [36].

Moving to the interpretation of this data, we shall note firstly that there are two possible scenarios for the evolution of the group of elementary destruction carriers —frustrons, dislocations, etc. In materials with the kinematic viscosity v, exceeding the critical value, the brittle fracture mechanism is realized, and the crack growth leads to the qualitative change of the behavior of the group of elementary destruction carriers. Indeed, at the relatively low values of length l the coefficient of stress intensity is so small that the height of the activation barrier $Q \propto K^2 \propto l$, overcoming at the frustron grouping, is sufficient for the probability $P_N \sim e^{\{-QN/T\}}$ of fluctuation formation of the cluster, containing $N \gg 1$ frustrons. This process occurs when the limit of N_0 is achieved, and when the cluster becomes the energy generator and the crack moves into the autocatalytic propagation regime. This means the beginning of the brittle fracture.

By increasing the size of the crack l toward values at which the formation of cluster $N \gg 1$ becomes practically impossible, this mechanism is replaced by the chain-like process with the probability $P_1 \sim e^{\{-QN/T\}}$ of the frustrons pairing, then with the same probability the pairs of the same order form a quartet, and so on (Fig. 4.6).

The transition to such a process is due to the fact that at small l the clustering, consisting of N frustrons, leads to the multiplication of probabilities $P_1 \left(P_N = P_1^N \right)$, while the chain-like process is characterized by their superposition, giving much greater importance meaning to $P_N \sim N^{-2} P_{-1}$. This leads to the change of the kinetic process of destruction: If at time t the probability of absence of the fluctuation formation of N-cluster is characterized by the Debye dependence $P_1(t) \sim e^{\{-t/\tau_0\}}$
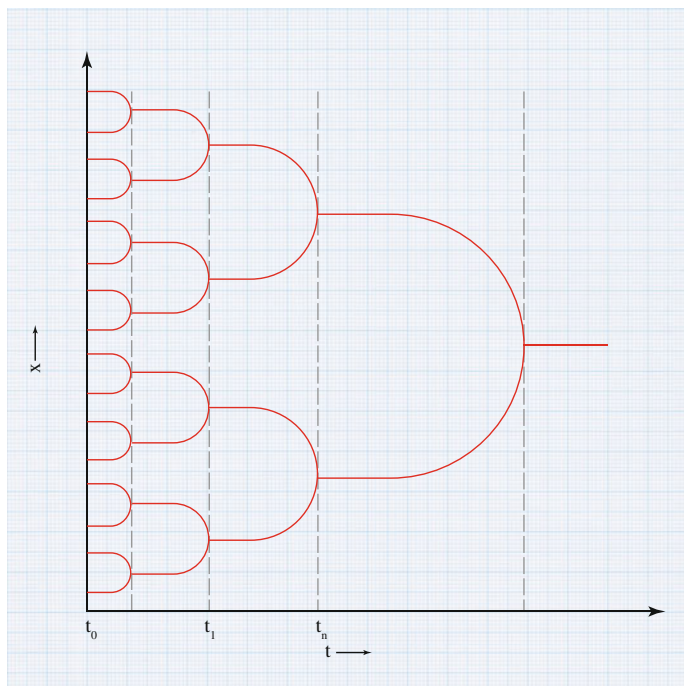
Fig. 4.6 The diagram of chain-like grouping of the destruction carriers

(where τ_0—the microscopic time), then for the commensurability of the equivalent formation time of the cluster $t_N = -\tau_0 \ln P_N \sim N\tau_0 \ln P_1^{-1}$ with the specific time for the chain-like process $\sim \tau_0/P_N$, the kinetics of latter is given by the dependence $P_N(t) \sim \tau_0/t$, which is quite different from the Debye ones. The application of the fractal theory allows us to obtain this result and its generalizations.

To quantify the evolution of the group of frustrons [37], the hypothetical coordinate x is introduced, the values of which correspond to the different frustron clusters at time t. As shown in Fig. 4.6, within the described framework, the grouping (doubling) of clusters occurs in the discrete points at time t_j, the intervals $\Delta t_j = t_j - t_{j-1}$ between them increase. Let the clusters in the interval Δt be characterized by the set of coordinates $\{x_j\}$. Then each elementary act of the pairwise merging of clusters is the inverse of the period-doubling process, described by the Feigenbaum quadratic function (3.90).

The consecutive values of μ_m, where the bifurcation takes place, are given in Table 3.2.

Corresponding to each μ_m, the values of d_m are calculated for $m = 1, \ldots, 10$ by the Eq. (3.108), and for $m \geq 6$ we take $\mu_m = \mu_\infty = 3.5699456$:

$$d_1 = 0.00035, \quad d_2 = 0.000287, \quad d_3 = 0.000226,$$
$$d_4 = 0.000901, \quad d_5 = 0.000359, \quad d_6 = 0.0009771, \tag{4.16}$$
$$d_7 = 0.02242, \quad d_8 = 0.035545, \quad d_9 = 0.090588, \quad d_{10} = 0.25.$$

The magnitude of $d_m(m = 1, 2, \ldots)$ will be used in Chap. 5 to determine the spectrums of generalized fractal dimensions of the multifractal set, formed by the pairwise merging of clusters of the solids micro-cracks.

In Sect. 3.3, the described qualitative transformation of the mapping dynamics (3.90), as the parameter μ changes, is a reflection of the scaling behavior of the system of clusters, shown in Fig. 4.6 as the hierarchical "Cayley tree." The nodes of the tree at each point of time t correspond to the clusters of microstructure. The merge of branches over time describes the union of these clusters in the process of the structure evolution.

From the mathematical point of view [33], the Cayley tree is a one-dimensional geometric image of the ultrametric space, where any three points can not have all three distances, differing from each other. Given that the distance between nodes corresponding to a specific time t is the number of steps to their common ancestor, see Fig. 4.6, it is easy to find the ultrametric space property.

Of course, the actual chain-like clustering process is not so simple, as it is shown in Fig. 4.6. In particular, there is a possibility of combining an arbitrary number of clusters (wherein the Cayley tree branching s is not equal to 2). Besides, the bifurcation point at the different branches of tree does not have to be bundled up for verticals $t'_n = \text{const}$, as it is shown in Fig. 4.6. Finally, the clustering process can happen in several Cayley trees, each of which has a certain probability. However, as it is shown in [38], it does not lead to the qualitative changes of picture, as it was discussed earlier based on the simplest example of a regular tree with $s = 2$.

According to the definition, the distance u in the ultrametric space is given by the smallest number of bifurcations in the Cayley tree, leading to the merger of the two points between which u is measured (from Fig. 4.6, it is clear that the magnitude of u is proportional to the number of steps n in the tree branches up to their coalescence). In the accepted framework, the chain clustering parameters, representing the ensemble of frustrons, become the functions of distance u. Thus, the elementary merging act of clusters is characterized by the Debye dependence

$$P_u(t) = \exp\left\{-\frac{t}{\tau(u)}\right\} \tag{4.17}$$

with the characteristic time

$$\tau(u) = \tau_0 \exp\left\{\frac{Q(u)}{T}\right\} \tag{4.18}$$

where τ_0—the microscopic time; $Q(u)$—the barrier height, separating the clusters, with the distance u between them, and; T—the temperature in energy units. Then,

assuming that the process of clustering distributed across the group of Cayley trees in accordance with the rule $p(u)$, $\int p(u)\mathrm{d}u = 1$ for the probability of absence of the fatigue failure at time t, we obtain

$$P(t) = \int\limits_0^\infty p(u)\exp\left\{-\frac{t}{\tau(u)}\right\}\mathrm{d}u. \qquad (4.19)$$

Taking the ultrametric space as homogeneous (i.e., the corresponding Cayley tree has a constant number of branches), the quantitative description of one-dimensional long-period structures (OLS), forming at an intermediate stage of restructuring of the original (short-period) crystal lattice, can be defined by the structuring factor (correlation factor) [39]:

$$S_k(t) = S_k \cdot \int p(u)\exp\left\{-\frac{t}{\tau(u)}\right\}\mathrm{d}u \qquad (4.20)$$

where k—the wave number, and S_k is expressed as follows:

$$S_k \equiv \sum_\alpha p_\alpha \cdot S_k^\alpha, \quad S_k^\alpha = \frac{1}{N_\alpha}\sum_{R_i-R_j} S_{ij}^\alpha e^{\left\{-ik\left(R_i-R_j\right)\right\}} \qquad (4.21)$$

Here, i and j—the layers index; R_i—the coordinate of the structure i-th layer; α—the hierarchy levels, each of which corresponds to the volume of the group of clusters $\{V_\alpha\}$ (in this case, the $(\alpha - 1)$-th group is equal to the subordinated, who, in turn to $(\alpha + 1)$-th, etc.); N_α—the number of layers at α level; p_α—the probability distribution of the group $\{V_\alpha\}$, $\sum p_\alpha = 1$; S_{ij}^α—the fluctuation correlation $\delta_{n_i}^\alpha(t) = n_i^\alpha(t) - \overline{n}^\alpha$, $n_i^\alpha(t)$—the number of nodes in the i-th layer at time t, $\overline{n}^\alpha$—the average number of nodes at α-level of the hierarchy.

To find the explicit form of the dependence $S_k(t)$ in (4.20), it is required to set distribution $p(u)$, $\tau(u)$ in the ultrametric space. Their definition is reduced to the microscopic problem within the phenomenological approach limited to the study of the possible types of $S_k(t)$ with acceptable majorants distributions $p(u)$, $\tau(u)$ [39]. At the fixed temperature T, the relaxation time is given by the height of the potential barrier $\Phi(u)$ according to the Arrhenius relation

$$\tau(u) = \tau_0\exp\left\{\frac{\Phi(u)}{T}\right\}, \qquad (4.22)$$

where $\tau_0 = \omega_D^{-1}$, ω_D—the Debye frequency. To evaluate the possible dependencies $\Phi(u)$, we base on the fact that for the large cluster sizes the value of the TP is proportional to their volume. Therefore, one step on the Cayley tree, corresponding to the single s cluster union, will increase TP s times. The distance u corresponds to l steps, and the change

$$\Delta\Phi \sim s^l = e^{\{l\ln s\}} = e^{\{\text{const } u\}},$$

Thus, in the thermodynamic limit, the strongest potential dependence $\Phi(u)$ and the heights of TP are realized in the ultrametric space. For small clusters and the presence of the long-range forces, the regular hierarchical relationship is broken, and TP increases much slower with an increase in volume. Accordingly, it should be expected that the dependence $\Phi(u)$ becomes weaker than the exponential.

We characterize the hierarchical object (the tree node) at level n with the intensity P_n, which for the stochastic system is reduced to the probability density and increases to the higher level $n-1$. This fact is expressed through the recurrence relationship

$$P_{n-1} = P_n + N_n^{-1} \cdot w(P_n) \tag{4.23}$$

where $w(P_n)$—the unknown function of the hierarchical relationship, N_n—the number of nodes at level n. For the simplest case of a regular tree, shown in Fig. 4.7a, and the inherent to the fractal objects, the power dependence is realized as

$$N_n = s^n, \tag{4.24}$$

where s—the tree furcation indicator (in Fig. 4.7a, and we have $s = 2$).
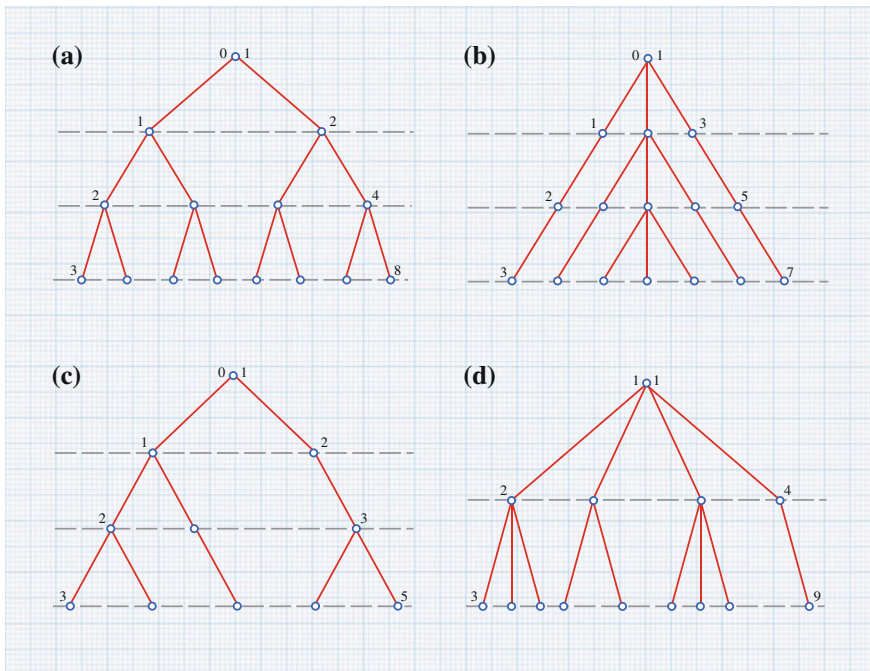
Fig. 4.7 The main types of hierarchical trees (the level number is listed to the *left*, and the node number is to the *right*): **a** the regular tree with $s = 2$; **b** the degenerate tree with $s = 3$; **c** the Fibonacci tree; **d** the irregular tree for $v = 1$, $a = 2$

For the degenerate tree, each level of which contains only one branching node (Fig. 4.7b), and we have the linear relationship

$$N_n = (s - 1)n + 1 \approx s \cdot n, \tag{4.25}$$

where the approximate equality corresponds to the case $s \gg 1$.

An interesting example is the Fibonacci tree shown in Fig. 4.7c. The number of nodes at n-th level $N_n = F(n+2)$ is determined by the Fibonacci number $F(n)$, which satisfies the equation

$$F(n+2) = F(n+1) + F(n) \quad \text{with } F(1) = F(2) = 1.$$

Its solution for $n \gg 1$ gives $F(n+2) \approx f \cdot \tau^n$, where $f = 1.17082$, $\tau = (\sqrt{5} + 1)/2 \approx 1.61803$—the golden section. As a result, the number of nodes in the Fibonacci tree is defined by

$$N_n = f \cdot \tau^n, \quad n \gg 1. \tag{4.26}$$

Finally, in general, the non-degenerate tree shown in Fig. 4.7d can be applied to the power approximation

$$N_n = v \cdot n^a, \quad v > 0. \tag{4.27}$$

For the regular tree, the intensity P and the power of hierarchical bonds w in the distance ζ from the ultrametric space have the following form [16]:

$$P = W^{-\frac{1}{1-D}}\left[(1 - u) + ue^{\zeta - \zeta_0}\right]^{\frac{1}{D}}, \quad u = \frac{DW^{\frac{1}{1-D}}}{\ln} s, \quad \zeta_0 n_0 \ln s, \tag{4.28}$$

$$w = \left[(1 - u) + ue^{\zeta - \zeta_0}\right]^{\Delta}, \quad \zeta \le \zeta_0, \tag{4.29}$$

where n_0—the total number of hierarchical levels; $W = w(1)$—the positive constant.

Equation (4.23) has the remarkable property of self-similarity, which is the main feature of the hierarchical systems. Indeed, assuming that the intensity $P_n \sim q^n$ is given by the similarity parameter $q < 1$ and the bonding function satisfies the homogeneity condition $w(pq) = q^\beta w(p)$, from (4.23), (4.24) for $n \gg 1$, when $P_{n-1} \sim P_n$, we get the usual bonding

$$\beta = 1 - D, \quad D \equiv \frac{\ln s}{\ln q^{-1}}, \tag{4.30}$$

between the index β of physical characteristic and the fractal dimension $D \le 1$ of the self-similar object rugged by coastline [29].

In equality (4.29) and further in text we assume that the function $w(\zeta)$ satisfies the condition $w(\zeta_0) = 1$. Thus, for the regular tree with increasing the distance ζ to the common ancestor of the dependence $P(\zeta)$, $w(\zeta)$ shows an exponential increase with the increments D^{-1} and Δ, respectively, where

$$\Delta = \frac{1-D}{D}, \tag{4.31}$$

According to (4.31), $\Delta = 0$ at $D = 1$, when the system obtains an ideal hierarchical bonding. Both of the decrements D^{-1} and Δ indefinitely increase at $D \to 0$.

From the comparison of Eqs. (4.24) and (4.26), it follows that when $n \gg 1$ the hierarchical system, represented by the Fibonacci tree (Fig. 4.7c), reduces to the regular tree (Fig. 4.7a) if the parameters s, W are replaced with τ, W/f, respectively. And the fractal dimension is $D = \ln \tau / \ln 2 \approx 0.6942$ [29].

For the degenerate tree, we have [16].

$$P = W^{-1/(1-D)}\left[1 - u\ln\left(1 + \frac{s-1}{\ln s}(\zeta - \zeta_0)\right)\right]^{1/D}, \quad u \equiv \frac{DW^{\frac{1}{1-D}}}{s-1}, \tag{4.32}$$

$$w = \left[1 - u\ln\left(1 + \frac{s-1}{\ln s}(\zeta - \zeta_0)\right)\right]^{\Delta}, \tag{4.33}$$

and for the irregular tree

$$P = w^{-1/(1-D)}\left[1 + u\left(1 - \frac{\zeta}{\zeta_0}\right)^{-(a-1)}\right]^{1/D}, \quad u \equiv \frac{DW^{\frac{1}{1-D}}n_0^{-(a-1)}}{v(a-1)}, \tag{4.34}$$

$$w = \left[1 + u\left(1 - \frac{\zeta}{\zeta_0}\right)^{-(a-1)}\right]^{\Delta}, \tag{4.35}$$

Thus, the transition from the regular to the degenerate tree leads to the replacement of exponential dependencies with the logarithmic ones, and in the case of the non-degenerate tree, the intensity and power of the hierarchical bonding exhibit the exponential behavior depending on the distance ζ. In all three cases (the regular, degenerate, and irregular trees), the studied characteristics of both hierarchical systems—the intensity P and the power of bonding w—gradually decrease with the distance ζ decreasing in the ultrametric space, which corresponds with the transition to the lower hierarchical level at the large values of n. The regular tree is especially underlined: The corresponding exponential behavior means the hierarchical bonding for the limited number, which is given as [16]:

$$k = (\Delta \ln s)^{-1} = D[(1 - D) \ln s]^{-1}, \tag{4.36}$$

In this sense, we can say that regular tree represents the weak hierarchical bonding.

In the transition to the irregular trees, which is most widely spread, the hierarchical bonding provides the subordination of all levels and damps exponentially. The slowest, logarithmic damping requires building of the degenerate hierarchy (Fig. 4.10b). It carries out by the single object at each level and meets the selection system. Both of these cases (the irregular and degenerate trees) inherent the strong hierarchical bonding, which is carried out between all levels, resulting in that the parameter Δ in (4.32) and (4.34) does not define the depth of bonding (4.31), but the damping rate. In particular, at the ideal hierarchical subordination $(D = l)$, we have $\Delta = 0$, and as in the regular system the hierarchical bonding $w(\zeta)$ does not damp. However, the intensity $P(\zeta)$ decreases with the indicator $D^{-1} = 1$.

Thus, at the given configuration of the hierarchical tree the fractal dimension D plays an important role, the value of which determines the strength of hierarchical relationship $w(\zeta)$. The fractal dimension in the pre-failure conditions is directly related to the mechanical properties, as well as the critical states of deformation of metals and alloys [40].

Above it is assumed that the power of the hierarchical relationship $w(\zeta)$ is characterized by the fixed value D, i.e., the hierarchical system is monofractal. However, in the non-stationary systems, the similarity parameter q varies with time, so in accordance with the second Eq. (4.40) the value of $D(q)$ also changes. In addition, for the complex systems the hierarchical bonding has the multifractal character, meaning that the spectrum of values $q \in (-\infty, +\infty)$ plays a significant role, based on which the binding force $w_q(\zeta)$ is distributed with the density $\rho(q)$. As a result, its total value is determined by the equality

$$w(\zeta) = \int_{-\infty}^{+\infty} w_q(\zeta)\rho(q)\mathrm{d}q, \tag{4.37}$$

where as the core $w_q(\zeta)$ the relationships (4.29), (4.33), (4.35) should be used with the variable fractal dimension $D(q)$. The following dependence is solution to the problem

$$\rho(q) = |D'(q_0)|^{-1}\delta(q - q_0), \tag{4.38}$$

where the stroke denotes the derivative, q_0—the root of the equation $D(q) = \text{const} \equiv D$, $\delta(\cdot)$—the Dirac function. Defining the dependencies $D(q)$, $\rho(q)$, which characterize the multifractal, is the separate problem.

It should be noted that these relationships define only the asymptotic behavior of the hierarchical system within the limit $1 \ll \zeta \leq \zeta_0$.

Considering that the distribution of the TP $\Phi(u)$ in the ultrametric space is determined by the strength of the hierarchical bonding, and taking into account that in the regular Cayley tree the hierarchical bonding varies exponentially and the transition to the irregular and degenerate trees leads to the weakening of this relationship down to the power and logarithmic, so let us approximate the dependence of $\Phi(u)$ in (4.22) as the logarithmic, power, and exponential functions

$$\Phi_l(u) = Q \ln \frac{u}{u_0}, \quad \Phi_p(u) = Q u^a, \quad \Phi_e(u) = Q e^{(u/u_0)} \tag{4.39}$$

(the indices l, p, e correspond to the words logarithmic, power, exponential), the constants Q, u_0, a are determined by the parameters of state, Q—the characteristic height of the barrier $\Phi(u)$.

In the Formula (4.19), the first of characteristics that define $P(t)$ (the probability density $p(u)$ at the distance u, affecting the clustering at the given ε) determines the nature of hierarchical subordination in the group of clusters. The minimal ones, frustrons, group the initial stage. This process requires overcoming the minimal barrier of the TP.

$$\Phi(u) \sim K^2 \sim (m\xi)^n \sim e^{\frac{u}{u_0}} = \text{const}$$

 (here, ξ—the coherent length).

Then, the number m of the merged clusters and the barrier height, overcome by the system during its evolution, increase. Moreover, the hierarchical subordination of the clustering process (the small ones fuse into the average ones, and then those into the large ones, etc.) is reflected in the fractal structure of the potential relief; in the configuration space of states, the dependence $\Phi(u)$ has the form of high and wide maximum, overcome by the system, on which the smaller are imposed and the latter, in turn, have even smaller, etc. During its evolution, the system of clusters passes through the lowest barriers initially, and then next in the height and so on as long as not overcome the tallest.

As for the function $p(u) \equiv p_\alpha$, being the part of correlation (4.20) and determining the distribution of states $\{V_\alpha\}$ in the ultrametric space, then it must be monotonic. Let us majorize its dependencies

$$p_s(u) = p^{-D}, \quad p_w(u) = \exp\left\{-\frac{u}{\varepsilon}\right\} \tag{4.40}$$

(the indices s and w correspond to the words strong and weak), where $D \in (0, 1)$—the fractal dimension, ε—the parameter that determines the depth of hierarchical bonding.

Substituting the dependences (4.22), (4.39), and (4.40) into (4.20), by the method of passage we find the asymptotes $t \to \infty$ for the correlation $S_k(t)$, shown in Table 4.1 from [16].

Table 4.1 The possible asymptotic behavior of the correlations $S_k(t)$ at $t \to \infty$

$S_k(t)$	$\Phi_l(u)$	$\Phi_p(u)$	$\Phi_e(u)$
$p_w(u)$	$e^{\{-t^\beta\}}, \beta = \left(1+\frac{Q}{T}\right)^{-1}$	$\exp\left\{-\left(\frac{T}{Q}\ln\frac{t}{\tau_0}\right)^{\frac{1}{a}}\right\}$	$\left(\frac{T}{Q}\ln\frac{t}{\tau_0}\right)^{-\frac{u_0}{a}}$
$p_s(u)$	$t^{-\gamma}, \gamma = \frac{(1+D)T}{Q}$	$\left(\frac{T}{Q}\ln\frac{t}{\tau_0}\right)^{-\frac{D}{a}}$	$\left[u_0\ln\left(\frac{T}{Q}\ln\frac{t}{\tau_0}\right)\right]^{-D}$

As the dependences $S_k(t)$ shown in Table 4.1, the critical process deceleration of the crystal structure restructure, corresponding to the transition from the rapidly damping exponential function to the smoothing power and logarithmic functions, realizes for any fractal relief in the case of the strongly pronounced hierarchical systems.

In the weakly hierarchical systems to ensure the critical deceleration, at least, the exponential increase of the relief height in the ultrametric space is required. However, it should be noted that the mentioned deceleration manifests itself only up to the certain moment τ_M, and at $t \gg \tau_M$ the Debye dependence takes place $S_k(t) \sim e^{\{t/\tau_M\}}$ [41]. The physical reason of such behavior is due to the fact that during the specified time the hierarchical bounding gets set at the distance u_M, given by the condition $p(u_M) = \tau_0/\tau_M$. This leads to overcoming the fractal relief height $\Phi_M \equiv \Phi(u_M)$. Consideration of (4.39), (4.40) and the dependencies $\Phi(u)$, $p(u)$ gives the expression of the maximum time of the structure restructuring τ_M, listed in Table 4.2 from [16].

First of all, we pay an attention to the increase of τ_M during the transition to less pronounced dependences $\Phi(u)$. The exponential growth of $\Phi(u)$ is responsible for the TP growth being proportional to the volume, and the transition to smoother dependences $\Phi(u)_p$ and $\Phi_l(u)$ is associated with the inhomogeneity and long-range fields. On the other hand, as the comparison of different rows in Table 4.2 is shown, the weakening of the hierarchical super-positioning leads to the increased dependence on external factors that determine the parameters Q, u_0, a of the fractal relief. Taking their dependence in its simplest form $Q \propto T - T_0$; T_0, u_0, $a = \text{const}$, it is not hard to notice that in the strongly hierarchical systems the dependent $\tau_M(T)$ takes the form of Vogel–Fulcher approximation [42] at the logarithmic distribution of relief $\Phi_l(u)$, and in the weakly hierarchical it is the power $\Phi_p(u)$. In the general case, there are possibilities for the power and logarithmic dependences.

From a physical point of view, the TP fractal distribution in the state space is defined, on the one hand, by the presence of volumetric and thermal effects of the

Table 4.2 The destruction time τ_M for the hierarchical structure

τ_M	$\Phi_l(u)$	$\Phi_p(u)$	$\Phi_e(u)$
$p_w(u)$	$\tau_0\left\{\frac{u_0}{\varepsilon}\exp\left(\frac{\Phi_M}{Q}\right)\right\}$	$\tau_0\exp\left\{\frac{1}{\varepsilon}\left(\frac{\Phi_M}{Q}\right)^{\frac{1}{a}}\right\}$	$\tau_0\left(\frac{\Phi_M}{Q}\right)^{\frac{u_0}{a}}$
$p_s(u)$	$\tau_0 u_0^D\exp\left\{\frac{D\Phi_M}{Q}\right\}$	$\tau_0\left(\frac{\Phi_M}{Q}\right)^{\frac{D}{a}}$	$\tau_0 u_0^D\left[\ln\left(\frac{\Phi_M}{Q}\right)\right]^D$

structure transformation, and on the other hand, by the smallness of the inhomogeneity energy. Indeed, under these conditions, the implementation of structural transformation in the minimal critical volume leads to an increase in the density of TP that is responsible for the minimum barrier. The smallness of the inhomogeneity energy causes a gradual growth of OLS clusters (one-dimensional long-period structures), for which it is more meaningful to grow not by shifting borders, as in the phase transitions of the first kind, but by correlating the clusters. This process leads to an increase in the volume and thermal effects, and hence, to the filling of deepest TP minimums.

As stated above, the slowly damping power distribution $p_s(u)$ of distances in the ultrametric space is realized in the systems with the strong hierarchical bonding, and exponential distribution $p_w(u)$ in the weak hierarchical systems. At the given level of probability $p_0 \leq 1$, it is expressed through the transformation of characteristic distance $u_0 \sim p_0^{-1/D}$ with the power distribution in comparison with the distance $u_w \sim \varepsilon |\ln p_\varepsilon|$ at the exponential. According to Table 4.1, the systems with the strong hierarchical bonding exhibit a slower kinetics than with the weak bonding. For them, in particular, it may cause substantial complete freezing of the process at all temperatures (in the case of the exponentially growing fractal relief height).

With regard to the restructuring of the crystal structure, this means that the stable long-period structures are implemented only in the strong hierarchical systems with an exponential increase of the relief height. It is easy to see that such conditions can be achieved through the presence of long-range forces. Indeed, if the value of s^u, where s—the branching of Cayley tree, is compared with the cluster size L/ξ, referred to the coherence length ξ, then for its formation the characteristic interaction radius must exceed the value $L = \xi s^{u_0} \sim \xi s^{-p_0^{-1/D}}$. As for the condition of the exponential growth of the relief height, it is obviously realized at the large sizes of clusters and when the thermodynamic limit is reached $\Phi(u) \propto L \propto e^{\{u \ln s\}}$.

If these conditions are not met, then over time there is one type of OLS restructuring in the other. To clarify their natures, we consider the distribution of the fractal relief heights corresponding to the set of structures that are solvable in this experiment. Let it be given by the sequence $\Phi_1 < \Phi_2 < \cdots < \Phi_n$. Then, in the microscopic time τ_0, long-period structure is a thermally formed, characterized by the greatest value of Φ_l, satisfying the condition $\Phi_l \leq T$. It will exist until the time $t_{l+1} = \tau_0 e^{\Phi_{l+1}/T}$ and until the thermo-fluctuational structure is formed, following the hierarchical series. As a result, the duration $\Delta t_l = t_{l+1} - t_l$ of the long-period structure existence is defined by

$$\frac{\Delta t_l}{t_l} = \exp\left\{\frac{\Phi_{l+1} - \Phi_l}{T}\right\} - 1 \tag{4.41}$$

The characteristic is that the value $\Delta t_l / t_l$ depends on the ratio of the temperature and nearest in the hierarchical series of the TP barriers.

When the ratio $\Phi_{l+1}/\Phi_l \approx 50$, $\Phi_l/T \sim 1$ in the first macroscopic level $(t_l \sim t_0 \sim 10^{-13}\,\text{s})$ we have the characteristic time Δt_l of the macrostructure stabilization in the order of several tenth of years [43].

The above picture of fatigue failure in the form of the sequence of elementary acts of merging clusters described in the ultrametric space with the dependence of $P_u(t)$ of type (4.17), with the characteristic time $\tau(u)$ of type (4.18) is reduced to the fractal kinetics of crystal structure readjustment, which takes into account the impact force of hierarchical relationship on the distribution of the TP $\Phi(u)$ in the ultrametric space. Thus, under the TP barrier height we should understand $Q(u)$. As a result, the substitution of relations (4.39) and (4.40) into (4.17) and (4.18) leads to the asymptotic behavior indicated in Table 4.1. It follows that at the power distribution $p_s(t)$, applicable to the high hierarchical systems, the logarithmic increase of relief $Q(u)$ gives the power dependence with the probability $P(t)$ (4.19), the power relief gives the slow logarithmic dependence. Accordingly, in the rapidly decreasing exponential distribution $p_w(u)$, corresponding to the weak hierarchical systems, we have the consistently stretched Kohlrausch exponential and the logarithmic damping of the probability $\overline{P}(t)$. Characteristically, in all cases the probability of failure $\overline{P}(t) \approx 1$ is implemented over time

$$t_d \sim \tau_0 \exp\left\{\frac{Q}{T}\right\} \qquad (4.42)$$

and it is reduced to the main result of the kinetic theory [44].

Thus, the hierarchical clustering of frustrons, flowing through the chain-like mechanism, leads to the significant slowdown of the destruction process. If the behavior of the system is determined by rapidly damping the Debye exponential, then the inclusion of the weak hierarchy [the exponential distribution $p_w(u)$] rebuilds it into the stretched Kohlrausch exponential, quasi-power, and logarithmic dependences [in accordance with the type (4.49) of the function $\Phi(u) = Q(u)$]; with the strong hierarchy, characterized by the power distribution $p_s(u)$, there is even the double logarithmic slowing, indicating the complete lack of destruction.

4.5   Relationship Analysis of the Fractal Dimension of Pre-fracture Dissipative Structures with Mechanical Properties and Critical States of Deformation of Metals and Alloys

The influence of solids surfaces on their strength and ductility has been the subject of a large number of studies over many decades. With development of the theory of dislocations, the view began to form that the primary dislocations in the loaded crystal arise on its surface. This idea was expressed in the middle of the last century

by Gilman based on a study of the deformed crystal of LiF with etching pits [45]. Further researches in this area support Gilman's idea [21, 46].

Whereas previously, the main efforts of researchers of fracture mechanics of materials were focused on the link between their initial microstructure and properties, then by now it was established [21, 46, 47] that the resistance to fracture of metals and alloys is determined by the dynamic structure forming in the deformation process, and it requires analysis of the deformable material as an open system, exchanging energy, and matter with the environment. During the evolution of system, due to the accumulation of fatigue damages under the cyclic loading, the old structure is destroyed and new one is created.

In this case, it is necessary to formulate the research of the cooperative interaction between the static (original) and the dynamic (emerging under load) structures.

Formation of the real microstructure of crystalline solids is due to phenomena far from equilibrium and takes place in the self-localized, non-equilibrium areas existing even in the quasi-equilibrium-condensed media. In accordance with the general laws of the non-equilibrium system behavior [45], the deformable crystal should be viewed as the system, where the dissipative structure formed during the deformation occurs (like the Bernard cells), capable of more effectively performing the macro-plastic flow in comparison with the individual dislocations. Exactly, from these positions the phenomenon of fragmentation of deformable solids is treated, and in continuum mechanics the structural elements of deformation are taken into account [21, 46]. In general, there is the hierarchy of its levels, defined as the initial structure of the medium, and the formation of dissipative structures related with the deformation defects [40, 47, 48].

The dissipative structures, self-organizing in the open systems, are fractal, which calls for the combined approach of synergy and fractal theory in the study of physical and mechanical nature of material fracture. Synergetics has expanded the concept of structure, giving it the flexibility and the fractal theory allowed to introduce new quantitative structures in the form of fractal dimension.

The synergetic approach to the tribological problems provides a solution to one of the most important tasks—to establish the bond between the fractal dimension of the dissipative zone of pre-fracture, and the mechanical properties and the critical states of deformation of metals and alloys [40].

The following is the solution to this problem.

For the dissipative structures, which include the structure of pre-destruction zone, the self-similarity dimension D_s is also the fractal dimension D. If we consider the destruction as the non-equilibrium phase transition in the bifurcation points, we should determine the fractal dimension of dissipative structures that control the free destruction. Near the bifurcation points, the dissipative structures are the dynamic set, having the property of universality and the scaling invariance, and the ability of self-similar growth. These same properties are also characteristic to the fractal structures. Therefore, it is natural to use the concept of fractals for the qualitative description of the dissipative structures of the pre-fracture zone, and establishing the bonds between its fractal dimension and the mechanical properties.

The self-similar growth of the fractal cluster crack is described by using the self-similarity in the form of:

$$\left(r_0^j\right)_{i-1}\Big/\left(r_0^j\right)_i = \Delta^{1/m}, \quad m = 2, 4, 8, 16, \ldots,$$

where $\left(r_0^j\right)_{i-1}$ and $\left(r_0^j\right)_i$—the preceding and subsequent sizes of the fractal clusters in the direction of crack motion; Δ—the universal constant of destruction.

Therefore, this growth can be represented as the blocks of the intermediate asymptotes in which the following sequence of threshold sizes of fractal clusters is observed [49]:

$$\text{I block: } r_{01}^{\text{I}}/r_{02}^{\text{I}} = r_{02}^{\text{I}}/r_{03}^{\text{I}} = \cdots = \left(r_{01}^{i-1}/r_{02}^{i}\right)^{\text{I}};$$
$$\text{II block: } r_{01}^{\text{II}}/r_{02}^{\text{II}} = r_{02}^{\text{II}}/r_{03}^{\text{II}} = \cdots = \left(r_{01}^{i-1}/r_{02}^{i}\right)^{\text{II}} \tag{4.43}$$

etc., so that during each iteration cycle

$$r_{01}^{\text{I}}/r_{01}^{\text{II}} = r_{01}^{\text{II}}/r_{01}^{\text{III}} = \cdots = r_{0j}^{N-1}/r_{0j}^{N} = \Delta. \tag{4.44}$$

This means that at each exit from the block of intermediate asymptotic sizes of the fractal cluster increases by an amount Δ^{-N}, where N—the number of iterations ($N = 1, 2, 3\ldots$). This allows us to use similar function $\Delta^{1/m}$ as $m \to \infty$ as a function of self-similarity in the ratio of Mandelbrot, presenting it in the form

$$\Delta^{D_s} = 1/i_r^c \tag{4.45}$$

Here, i_r^c is the scale factor, which takes into account the ratio of the maximum scale of observation to the minimum and characterizing the critical parameters of crack—its maximum increase $r_c^{\max}$ as a result of self-similar growth of micro-cracks with an initial length r_0^c. The value Δ in (4.44) is the universal constant, which is determined by the sequence of golden ratios $0.382 \to 0.216 \to 0.144 \to 0.105$ having the constant value for each metal.

The observation scale is the critical size of cluster, within which the density function of the deformation energy $(dW/dV)_c$ (W—the energy, V—the volume) has the constant value equal to W_c. Within r_0^c, the energy dissipation processes are associated with the non-equilibrium phase transitions of the crystalline phase in the quasi-amorphous and from the quasi-amorphous into the destructive at the same level of the density function of deformation energy W_c. The stability criterion of zone r_0^c is written as follows:

$$W_d/W_v \le W_d^c/W_v^c$$

where W_d, W_d^c—the density function of distortion energy (changes in shape) and its critical value; W_v, W_v^c—the density function of dilation energy (changes in volume) and its critical value.

Thus, the pre-fracture zone at the upper boundary of the crack growth following the rift mechanism (type I) under the conditions of plain deformation at $K_I = K_{Ic}$ (K_I—the stress intensity factor at the crack edge movement of type I and K_{Ic}—the critical value of factor K_I) can be characterized by two scaling parameters: the cluster size capable to the self-similar growth $\left(r_0^c\right)$ and the maximum size of the pre-fracture zone at auto-scaling $\left(r_c^{max}\right)$, which determines the scaling factor $i_r^c = r_c^{max}/r_0^c$. Then, (4.45) can be written as follows:

$$\Delta^{D_s} = r_0^c/r_c^{max} \tag{4.46}$$

Taking into account the expressions for r_0^c and r_c^{max}

$$r_0^c = [(1+v)(1-2v)/2\pi E] \cdot \left[K_{Ic}^2/W_c\right], \tag{4.47}$$

$$r_c^{max} = \left(K_{IR}^{max}/\sigma_T\right)^2 (1/2\pi) \tag{4.48}$$

formula (4.46) can be written as follows:

$$\Delta^{D_s} = \left[(1+v)(1-2v)/E\left(K_{IR}^{max}\right)^2\right] \cdot p_{**}, \tag{4.49}$$

where $p_{**} = \left(K_{Ic}\sigma_T\right)^2/W_c$; σ_T—the yield stress; K_{IR}^{max}—the dimensional constant that controls the borders of self-similarity at this scaling level. The values of constants K_{IR}^{max} for alloys based on iron, nickel, titanium, and aluminum are given in [50]; the values of K_{Ic} and W_c for different steel grades are given in [51].

From (4.49), we find

$$D_s = \ln\left\{\left[\frac{(1+v)(1-2v)}{E(K_{IR}^{max})^2}\right] \cdot p_{**}\right\} \Big/ \ln\Delta, \tag{4.50}$$

from where it follows that the self-similarity dimension of the fractal clusters in the pre-fracture crack zone (which is also the fractal dimension for the dissipative structure) depends on the elastic constants E, v and the invariant set of mechanical properties p_{**}.

Taking into account the maximum value of the effective Poisson's ratio, it is accepted [51] in (4.50) to limit the fractal dimension $D_s = 2.95$ and to discretely shift the dependence (4.50) to a new level $D_s - 1$ at $D_s > 2.95$. This shift corresponds to the expression (4.50), presented in the form of the following:

$$\Delta^{D_s+M} = \ln\left\{\left[\frac{(1+v)(1-2v)}{E(K_{IR}^{max})^2}\right] \cdot p_{**}\right\} \Big/ \ln\Delta \tag{4.51}$$

where $M = 0$ and $M = 1$ for the quasi-brittle and viscous rifting, respectively. The results of calculations using the formula (4.51) for the fractal dimension of the

pre-fracture zone according to the complex mechanical properties of various steel grades are given in [50, 51]. The existence of two values of the scaling factor $i_r^c = 985.4$ and $i_r^c = 985.8$ for the steel grading 16ГМЮ4 at $D_s = \text{const}$ and $\Delta K = K_{\text{IC}} = \text{const}$ is the reflection of the properties of synergistic systems—to express few balanced states in the transition through the critical point. In this case, at the same dissipative structure $(D_s = \text{const})$ the system during the transition "balance-instability-balance" chooses the optimal way of future energy dissipation mechanism, either by forming the free rift surfaces (the unstable fracture) or by doing the plastic deformation (the plastic instability). The first mechanism leads to the limitation of durability or to the reduction of the scaling factor [$M = 0$ in Eq. (4.51)], the second to an increase of durability ($M = 1$). This swaps to a new dissipative structure preserving the macro-stable system. The steels with the fractal dimension of dissipative structure corresponding to $M = 1$ have a greater margin of durability than the steels with $M = 0$, since the scaling factor determines the number of "quants" of emitted energy at the time of fracture instability.

As already mentioned, the maximum dimension D_{max} of the self-similar objects in the isolation should not exceed 2.95. This allows us to calculate the value of $1/i_r^c$, up to which the relation (4.45) is valid. Given the fact that for the steel $\Delta = 0.11$, for the titanium alloys $\Delta = 0.12$, and for the aluminum alloys $\Delta = 0.22$, we obtain 1.49×10^{-3}, 1.92×10^{-3}, and 1.19×10^{-2}, respectively. The analysis of experimental data from [50], obtained for the steels of different strength levels, shows that the dependence (4.45) in should be represented as follows:

$$\Delta^{D_s + M} = 1/i_r^c \qquad (4.45')$$

Fig. 4.8 The dependence of the fractal dimension on the scaling coefficient for steels with different strength levels: The continuous line is calculated; the points are experimental
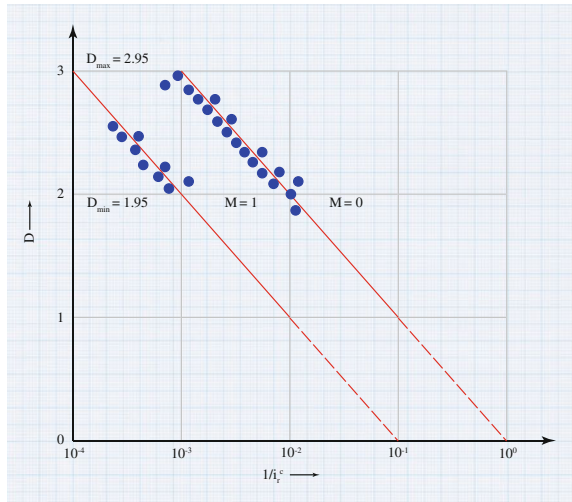
at $M = 1$ and $M = 0$. This means that in the transition from the dependence (4.45) to (4.45'), the straight line $D = \log\left(1/i_r^c\right)$ (Fig. 4.8) shifts at equal distance to the left by the value Δ.

The jolting of the fractal dimension D of the dissipative structure at $1/i_r^c = 1.49 \times 10^{-3}$ at the point Q in Fig. 4.11, corresponding to $D_{max} = 2.95$, is associated with the structural elastic-plastic transition in which $\Delta^{D_{max}} = \Delta^{D_{min} + 1}$, giving $D_{min} = 1.95$. Thus, at the rifting of type I, the fractal dimension of the grouped dissipative structure varies within the interval $1.95 \leq D \leq 2.95$. The value of D, complying the interval $0.95 \leq D \leq 1.95$, characterizes the fractal dimension of the dissipative structure in the form of an ensemble of crystallographic micro-cracks.

The connection in $\Delta K_I = K_{Iq}^{max}$, corresponding to the transition of the macro-cracks into the instability, is defined as [52]

$$K_{Iq}^{max} = K_{IR}^{max} \cdot \Delta^{-1/2}[(n_{max} - n)/(n_{max} - n_{min})]. \tag{4.52}$$

This allows us to calculate D using r_0^c, calculated through the relation:

$$r_{oc} = \left[\frac{(1 + v)(1 - 2v)\left(K_{IR}^{max}\right)^2}{2\pi E\Delta \cdot W_c}\right]\left[\frac{(n_{max} - n)}{(n_{max} - n_{min})}\right]^2. \tag{4.53}$$

Here, the parameter n is a characteristic associated with the dynamic structure that controls the destruction rate of the crack edge motion of the type I; the constant values of n_{max} and n_{min} for the alloys based on iron, nickel, titanium, and aluminum are given in [40].

On the other hand, at $K_I = K_{IC}$ the depth of zone h_A under the crack with the limiting density energy of deformation is associated with r_{oc} through relationship [53]

$$r_{oc} = 2h_A\left[\frac{(1 + v)(1 - 2v)}{2\pi(1 - v^2)}\right]. \tag{4.54}$$

So D can be determined either by K_{IC}, σ_T and W_c [the ratio (4.47)], or by σ_T, n and W_c [the ratio (4.53)], or by σ_T and h_A [the ratio (4.54)]. In [50], there is a comparison of the values of D, calculated on the r_{oc}, determined using (4.47) and (4.54). As shown in table, for many steel grades the discrepancies in obtained values for D only occur in the second decimal places.

However, quantifying the fractal dimension of the dissipative structure is not sufficient to describe the process energetics, as it is required by the bounds between the scaling factor, the fractal dimension, and the energy "quantum" necessary to develop the free destruction. To solve this problem, we use the concept of fractal energy by Williford [54], according to which the fractal energy is represented in the form:

$$E = k^1 \cdot \eta^D, \tag{4.55}$$

where k^1—the constant depending on the material properties; η—the scale observations.

Based on Rosenfeld [55], we express E through the ratio (4.55) in terms of energy per unit of crack length $E = G_{IC}/2$ for the maximum scale r_c^{max}, and for the minimum scale of observation r_{oc}—through $E = G_{OC}/2$, where the G_{OC}—the minimum energy required for the free destruction with rift. Then, on the basis of (4.55) we have

$$G_{IC} = k^l \cdot \left(r_c^{max}\right)^D, \quad G_{OC} = k^l \cdot (r_{oc})^D. \tag{4.56}$$

From (4.56), the following expression for the energy "quantum" of the free destruction with rift:

$$G_{OC} = G_{IC} \left(\frac{r_{oc}}{r_c^{max}}\right)^D. \tag{4.57}$$

Taking into account the expression that defines the critical velocity of energy emission value G_{IC} at the critical value of $K_I = K_{IC}$, required for the crack edge movement

$$G_{IC} = K_{IC}^2 \cdot \frac{(1 - v^2)}{E}, \tag{4.58}$$

from (4.57) with $K_I = K_{IC}$, we will have

Fig. 4.9 The relationship between the relative energy of free destruction and the fractal dimension of the dissipative structure during the rift for various strength level steels
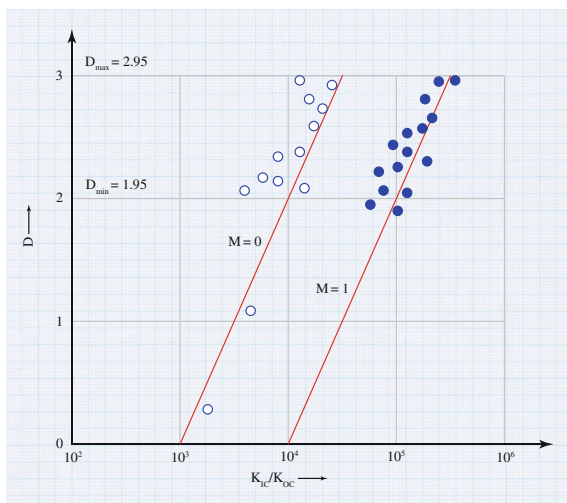
$$K_{\text{OC}}^2 = K_{\text{IC}}^2 \left(\frac{r_{oc}}{r_c^{\max}} \right)^D. \tag{4.59}$$

Thus, the relative "quantum" energy for the initial free self-similar crack growth and the scaling factor is related to each other (Fig. 4.9).

This allows using the fractal dimension to calculate the minimum energy G_{OC} for the micro-cracks self-similar growth. It is this energy that controls the beginning of crack growth near the threshold of kinetic diagrams of fatigue failure.

The above analysis implies the possibility of a sharp increase in the informativeness of experimental data with regard to the mechanical properties during transition to the fractal dimension analysis of the dissipative structures and the fractal energy. The presence of the single bonding between the scaling factor, the fractal dimension, and the relative energy of free destruction is the basis for development of methods to predict the behavior of materials in products using the indicators of dissipative properties in material.

As stated in [56], the fractal dimension D of the structural perturbation of three-dimensional crystal lattices is determined by the ratio of the longitudinal and shear stiffness:

$$2 \leq D \leq (E/G) = 2(1 + v) \leq 3. \tag{4.60}$$

Given the limits of Poisson's ratio v for solids ($v_{\max} = 0.475$ and $v_{\min} = 0.165$), established by Kuz'menko [57], the fractal dimension of dissipative structures implemented in the viscous rift must meet the interval

$$1.95 \leq D \leq 2.95. \tag{4.61}$$

As we know, the concentrated deformation precedes the viscous destruction of materials, which is absent in the quasi-brittle destruction. The critical parameter in both cases is the ultimate uniform deformation, the system in the form of deformable solids becomes unstable, and so the bi-furcation point is reached. At the transitions "balance-instability-balance," there are two possibilities: It is either destruction or plastic instability, accompanied by the transition into the concentrated strain (neck) (Fig. 4.10).

Therefore, the value of uniform deformation is not just a simple change of the geometrical shape and size, but also the changes in the state of deformable material. Since the transition from the uniform deformation to the concentrated is the unbalanced phase transition, so there must be a relationship between the parameters controlling this or the next point of instability.
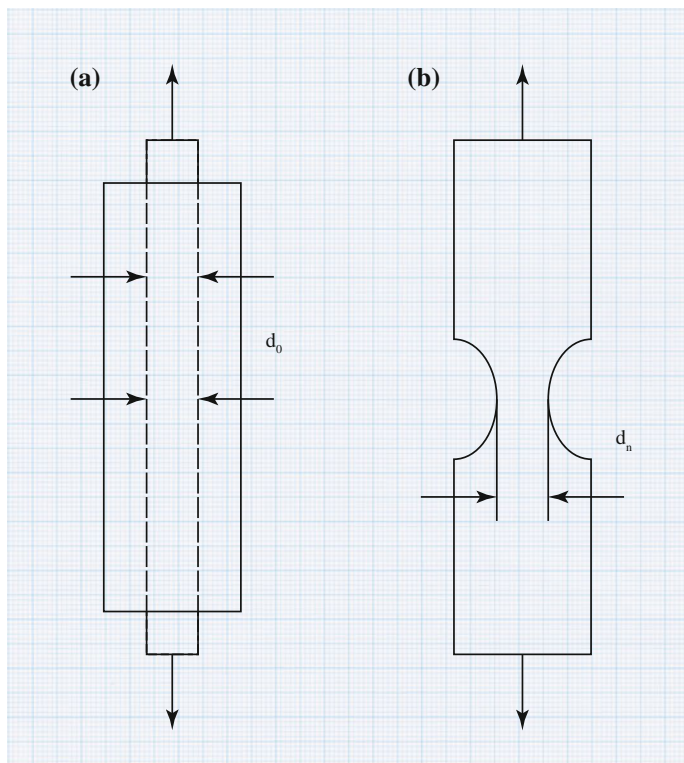
Fig. 4.10 Two types of instability deformable solids associated with the transition from the threshold to the destruction of uniform strain (**a**), or plastic instability (concentrated strain) (**b**)

Based on the data analysis of the steel samples on the mechanical tests for tensile in [58], the universal connection between mechanical properties is established:

$$1 - \psi = (1 - \psi_c)(1 - \psi_n), \tag{4.62}$$

$$\delta_n = 0.23\psi_n, \tag{4.63}$$

$$\delta_n = \frac{\psi_c}{1 - \psi_n}, \tag{4.64}$$

$$\delta = \delta_c + \delta_n, \tag{4.65}$$

where δ, δ_c and δ_n—the complete, uniform, and necking relative residual elongation, respectively; ψ, ψ_c and ψ_n—the complete, uniform, and necking relative residual, respectively.

Since the nature of destruction is determined by the type and the fractal dimension of the dissipative structures in the pre-fracture area, controlling the level of energy dissipation, then the ductile–brittle transition is the result of a spontaneous change of dissipative structures due to the non-equilibrium (phase) transition upon achieving the critical state of the lattice in the areas of accumulation excessive energy, that is already reshaping it cannot be compensated by the change in volume. This corresponds to the limit tensile strain at the meso-level [59], and it is equal to

$$\delta_c = \frac{1}{D},\qquad(4.66)$$

where $D = D_s$ is defined by (4.45).

Then, on the basis of (4.64) and (4.66), we have

$$D = \frac{1 - \psi_c}{\psi_c}.\qquad(4.67)$$

Taking into account the changes in the boundaries of D at the brittle fracturing $(1 \leq D \leq 2)$, we can set the thresholds ψ_c corresponding to $\psi_c = \psi_k^* = 0.50$ at $D = 1$, and $\psi_c = \psi_{k^2} = 0.50$ at $D = 1$.

At destruction controlled by the plastic instability $2 \leq D \leq 3$, $\psi_c = f(\psi)$. According to [59],

Fig. 4.11 The relationship between the normalized necking ψ_c/ψ in the uniform deformation area and the marginal transverse deformation for various yield stress
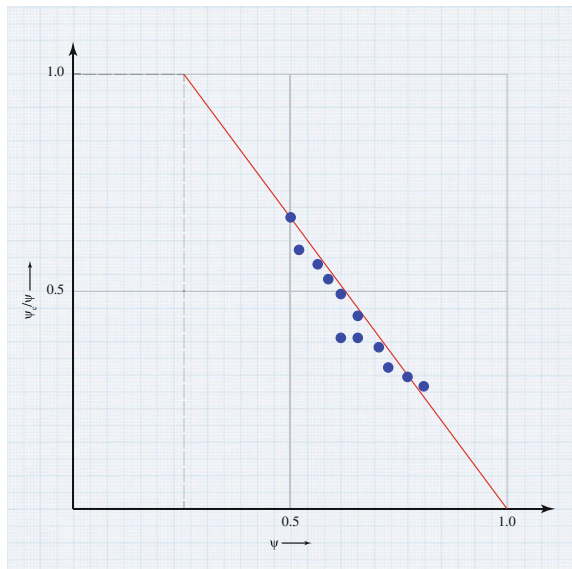
Table 4.3 Recorded transitions

Type of fracture	Fractal dimension	Threshold values ψ	Fractal object
Quasi-viscous	$D > 3$	$\psi_{k3} = 0.79$	Fractured volume
Viscous	$2 \leq D \leq 3$	$\psi_{k1} = 0.67 (D = 2)$; $\psi_{k3} = 0.79 (D = 3)$	Fracture surface
Viscous-brittle	$1.67 \leq D \leq 2$	$\psi_k^* = 0.50 (D = 1.67)$; $\psi_{k1} = 1.67 (D = 2)$	At $\psi = 0.5$, the transition from the fractal surface of fracture to the fractal front of crack
Quasi-brittle	$1 \leq D \leq 2$	$\psi_k^* = 0.50 (D = 1)$; $\psi_{k2} = 0.33 (D = 2)$	At $\psi = 0.5$, the transition from the fractal front of crack to the structure elements of fracture
Brittle	$D \leq 1$	$\psi \leq 0.33$	Structure elements at fracture

$$\frac{\psi_c}{\psi} = 1.5(1 - \psi). \tag{4.68}$$

This dependence on the upper boundary at $\psi_c/\psi = 1$ meets $\psi = 0.33$ and at the bottom—$\psi = 1$.

Figure 4.11 compares the dependence obtained by setting the boundary conditions with the experimental data. And they are in the perfect harmony.

The joint solution of Eqs. (4.67) and (4.68) gives

$$D = \left\{ \frac{1}{[1.5\psi(1 - \psi)]} \right\} - 1. \tag{4.69}$$

The Eq. (4.69) allows us to set the thresholds ψ at the neck fracture: $\psi = \psi_k^* = 0.50$ at $D = 1.67$, $\psi = \psi_{k1} = 0.67$ at $D = 2$, and $\psi = \psi_{k2} = 0.79$ at $D = 3$, and where ψ_{k3} corresponds with the transition into the quasi-viscous destruction, ψ_{k1}—to the ductile-brittle, and $\psi_k^* = 0.50$—to the quasi-brittle fracture. These transitions are recorded in Table 4.3 [51].

Figure 4.12 shows dependencies $D = f(\psi)$ by (4.69) in the change intervals $1 \leq D \leq 2$ (curve 1) and $1.67 \leq D \leq 3$ (curve 2). A comparison of the dependences (4.69) $D = f(\psi)$ and $D = f(1/i_r^c)$, resulted from (4.61), shows their agreement.

The phenomenon of deformed metal transition from the viscous condition into the brittle is called cold-brittleness. It is associated with the transition from the controlled impact on the destruction of instable meso-clusters (the ductile fracture) to the unstable micro-clusters (the brittle fracture). This determines the transformation of fractured surface, provided by the fractalness and the fractal dimension of structure in the pre-fracture zone, and the spontaneous change of the fractal dimension dependence on the lateral deformation (the transition from dependence (4.68) to (4.69) at $\psi_k^* = 0.50$). The transformation of fractal object is characterized
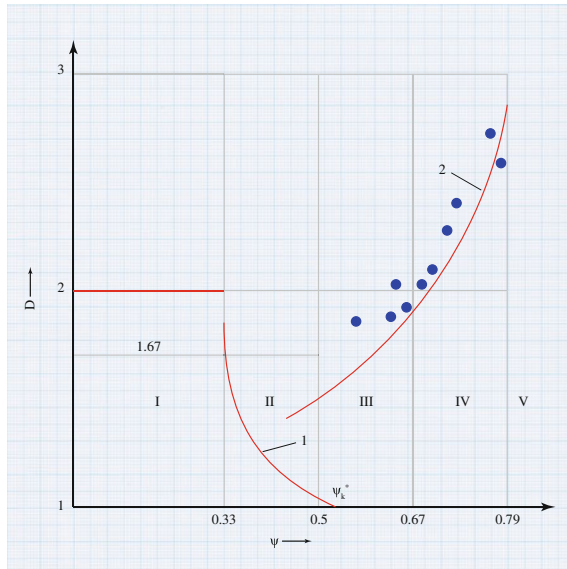
Fig. 4.12 The spontaneous change of dependence of the fractal dimension of structure in the pre-fracture zone D on the relative transverse deformation ψ and ψ_c. *I, II, IV, V* the areas of brittle, quasi-brittle, viscous, quasi-viscous and destruction; *III* the area of quasi-brittle transition; the points are values of D, calculated according to the formula $D = \ln(1/r_c)/\ln\Delta$, derived from (4.42)

by the transition at $\psi_k^* = 0.50$ for the fractal surface at $2 \leq D \leq 3$ to fractal front of crack at $1 \leq D \leq 2$.

Thus, the ductile–brittle transition meets all the properties of the critical points at $\psi = \psi_k^* = 0.50$. This allows us to use the ψ_k^* to determine the true transition temperature t_k^* based on the temperature dependence. In addition, knowing the threshold values $\psi = \psi_{k2}$, ψ_{k1} and ψ_{k3} matching, respectively, to 0.33; 0.67; and 0.79, allows the temperature dependence of $\psi = \psi(t)$, determined under the standard testing of smooth specimens in tension, and to establish t_{k1} and t_{k2} characterizing the transition from ductile to ductile–brittle, and from ductile–brittle from quasi-brittle fracture. The determination of transition temperature t_{k1} and t_{k2} is provided in accordance with ГОСТ 25.506-85.

Literatures

1. B.B. Mandelbrot, *Fractals: forme, chance and dimension* (Freeman, San Fracisko, 1977), p. 362
2. A.V. Korolenko, M.S. Maganova, A.V. Mesniankin, Innovatsionnye metody analiza stokhasticheskikh protsessov i struktur v optike. Fraktal'nye i mul'tifraktal'nye metody, veivlet-preobrazovaniia. Uchebnoe posobie (MGU im. M.V.Lomonosova, NII iadernoi fiziki im. D.V. Skobel'tsyna, Moscow, 2004), p. 82

3. B.F. Timofeev, Fraktal. Fizika tverdogo tela (Nauk. Dumka, Kiev, 1998), **2**, 460–461

4. A.F. Bulat, V.I. Dyrda, *Fraktaly v geomekhanike* (Nauk. Dumka, Kiev, 2005), p. 357

5. J.E. Hutchinson, Fractals and self similarity. Indiana Univ. Math. J. **30**(5), 713–747 (1981)

6. M. Barnsley, *Fractals everywhere* (Academic Press, Boston, 1988)

7. R.M. Kronover, Fraktaly i khaos v dinamicheskikh sistemakh. Osnovy teorii. per. s angl (Postmarket, Moscow, 2000), pp. 0–352

8. V.E. Rokotian, Avtomodel'nost'. Fizicheskaia entsiklopediia, vol. 1 (SE, Moscow, 1988), pp. 19–20

9. Iu.M. Maksenko, Masshtabnaia invariantnost' (skeiling). Fizicheskaia entsiklopediia, vol. 3 (BRE, Moscow, 1992), pp. 60–61

10. V.L. Vinetskii, Avtomodel'nost', Fizika tverdogo tela. Entsiklopedicheskii slovar', vol. 1 (Nauk. Dumka, Kiev, 1996), p. 16

11. B.B. Mandelbrot, *The fractal geometry of nature* (W.H. Frecman, New York, 1982)

12. R.F. Voss, Random fractal forgeries. in *Fundamental algorithms in computer graphics*, ed. by R.A. Earnshaw (Springer, Berlin, 1985), pp. 805–835

13. R.F. Voss, Random fractals. Characterization and measurement, in *Scalling phenomena disordered systems*, ed. by R. Pynn, A. Skjeltorp (Plenum Press, New York, 1985), pp. 1–11

14. E. Feder, Fraktaly, per. s angl (Mir, Moscow, 1991), p. 254

15. B.B. Mandelbrot, Self-affine fractal sets, in *Fractals in Physics*, ed. by L. Pietronero, E. Tosatti (North Holland, Amsterdam, 1986), pp. 3–28

16. A.I. Olemskoi, A.A. Katsnel'son, *Sinergetika kondensirovannoi sredy, Izd 2-e* (Editorial URSS, Moscow, 2010), p. 336

17. V.E. Egorushkin, V.E. Panin, E.V. Savushkin, Iu.A. Khon, Sil'novozbuzhdennye sostoianiia v kristallakh. Izv. vuzov. Fizika **1**, 9–33 (1987)

18. V.E. Panin, V.E. Egorushkin, Iu.A. Khon, T.F. Elsukova, Atomnovakansionnye sostoianiia v kristallakh. Izv. vuzov., Fizika, №12 (1982)

19. V.E. Panin, Iu.V. Griniaev, V.E. Egorushkin i dr. Spektr vozbuzhdennykh sostoianii i vikhrevoe mekhanicheskoe pole v deformiruemom kristalle. Izv. vuzov., Fizika, №1 (1987)

20. V.E. Panin, V.A. Likhachev, Iu.V. Griniaev, Strukturnye urovni deformatsii tverdykh tel (Nauka, Sib.otd-nie, Novosibirsk, 1985), p. 229

21. V.E. Panin, Iu.V. Griniaev, V.I. Danilov i dr. Strukturnye urovni plasticheskoi deformatsii i razrusheniia. (Nauka. Sib. Otd-nie, Novosibirsk, 1990), p. 255

22. V.E. Panin, V.E. Egorushkin, P.V. Makarov i dr., Fizicheskaia mezomekhanika i komp'iuternoe konstruirovanie materialov. V 2t. (Nauka. Sib. Izdat. firma RAN, Novosibirsk, 1995), p. 298

23. Iu.V. Grinaev, N.V. Chertova, Opisanie polzuchesti v ramkakh polevoi teorii defektov. Prikladnaia mekhanika i tekhnicheskaia fizika. **41**(3), 177–183 (2000)

24. Trenie, iznashivanie i smazka, Spravochnik v 2-kh kn., pod red. I.V.Krachel'skogo, V.V. Anisina (Mashinostroenie, Moscow, 1978), Kn. 1, p. 400

25. A.Kh. Janahmadov, *Termomekhanicheskaia teoriia iznosa* (Elm, Baku, 1997), p. 28

26. A.Kh. Janahmadov, *Neftianaia tribologiia* (Elm, Baku, 2003), p. 326

27. A.Kh. Janahmadov, *Tribotekhnicheskie problemy v neftegazovom oborudovanii* (Elm, Baku, 1998), p. 216

28. A.Kh. Janahmadov, M.Y. Javadov, O.A. Dyshin, Diagnosis of the contact interaction of solid bodies at friction using fractal analysis methods. J. Sci. Appl. Eng. Q. **04**, 5–16 (2014)

29. A.I. Olemskoi, A.Ia. Flat, Ispol'zovanie kontseptsii fraktala v fizike kondensirovannoi sredy. Usp. Fiz. Nauk., **163**(12), 1–50 (1993)

30. Sinergetika i ustalostnoe razrushenie metallov (Nauka, Moscow, 1980), p. 246

31. A.I. Olemskoi, E.A. Toropov, Teoriia nizkotemperaturnoi evoliutsii ortorombicheskoi fazy vysokotemperaturnykh sverkhprovodiashchikh oksidov. Fizika metallov. Metallovedenie, **7**, 32–40 (1991)

32. D. Adelman, C.P. Burmester, L.T. Wille, P.A. Stern, R. Gronsky, J. Phys. Condens. Matter **4**, 585 (1992)

33. R. Rammal, G. Toulouse, M.A. Virasova, Ultrametricity for physicists. Rev. Mod. Phys. **58**, 765, 788 (1986)

34. S.L. Ginzburg, *Neobratimye iavleniia v spinovykh steklakh* (Nauka, Moscow, 1989)

35. K. Binder, A.P. Jeung, Rev. Mod. Phys. **58**, 801 (1986)

36. V.S. Ivanova, V.F. Terent'ev, *Priroda ustalosti metallov* (Metallurgiia, Moscow, 1975), p. 456

37. A.I. Olemskoi, I.I. Naumov, Fraktal'naia kinetika ustalostnogo razrusheniia. V sb.: Sinergetika i ustalostnoe razrushenie metallov. (Nauka, Moscow, 1989), pp. 200–215

38. A.T. Ogielski, Phys. Rev. Let. **55**, 1634 (1986)

39. A.I. Olemskoi, Fraktal'naia kinetika perestroiki kristallicheskoi struktury. Fizika metallov. Metallovedenie, **68**(1), 56–65 (1989)

40. A.M. Pashaev, A.Kh. Janahmadov, O.A. Dyshin, Fraktal'naia razmernost' i ee sviaz' s mekhanicheskimi svoistvami metallov i splavov v usloviiakh predrazrusheniia. Vestnik Azerbaidzhanskoi Inzhenernoi Akademii **2**(2), 13–24 (2010)

41. R.G. Palmer, D.L. Stein, E. Abrahams et al., Models of hieracheally constrained dynamics for glassy relaxation. Phys. Rev. Let. **53**(10), 958–961 (1984)

42. V.V. Zosimov, L.M. Liamshev, Fraktaly v volnovykh protsessakh. Uspekhi fizicheskikh nauk **165**(4), 361–401 (1995)

43. A.Kh. Janahmadov, O.A. Dyshin, Synergetic and fractal dimensions in tribology. J. Friction Wear **32**(1), 61–71 (2011)

44. S.N. Zhurkov, Dilatonnyi mekhanizm prochnosti tverdykh tel. Fizika tverdogo tela **25**(10), 3119–3123 (1983)

45. Dzh. Gilman, V. Dzhonston, Vozniknovenie dislokatsii v kristallakh LiF pri nizkikh napriazheniiakh. Dislokatsii i mekhanicheskie svoistva kristallov. (Inostr. lit., Moscow, 1960), pp. 393–394

46. V.E. Panin, V.A. Likhachev, Iu.V. Griniaev, Strukturnye urovni deformatsii tverdykh tel (Nauka, Novosibirsk, 1985), p. 163

47. A.I. Olemskoi, I.A. Skliar, Evoliutsiia defektnoi struktury tverdogo tela v protsesse plasticheskoi deformatsii. Uspekhi fizicheskikh nauk **162**(6), 29–79 (1992)

48. U. Nikolis, I. Prigozhin, Samoorganizatsiia v neravnovesnykh sistemakh. (Mir, Moscow, 1979), p. 300

49. A.M. Pashaev, A.Sh. Mekhtiev, A.Kh. Janahmadov, O.A. Dyshin, Avtomodel'nost' i fraktal'naia mekhanika razrusheniia. Vestnik Azerbaidzhanskoi Inzhenernoi Akademii **1**(1), 93–103 (2009)

50. V.S. Ivanova, *Sinergetika: Prochnost' i razrushenie metallicheskikh materialov* (Nauka, Moscow, 1992), p. 160

51. V.S. Ivanova, A.S. Balankin, I.Zh. Bunin i dr. Sinergetika i fraktaly v materialovedenii (Nauka, Moscow, 1994), p. 383

52. V.S. Ivanova, Problemy prochnosti. **5**, 91–98 (1982)

53. V.S. Ivanova, S.A. Kunavin, Izv. AN SSSR. Metally **4**, 148–153 (1984)

54. R.E. Williford, Ser. Met. **22**(11), 1749–1754 (1988)

55. A.R. Rosenfeld, Ibid **21**(11), 1339–1361 (1987)

56. A.S. Balankin, A.A. Liubomudrov, I.T. Sevriukov, Zhurnal tekhnicheskoi fiziki. **59**(12), 102–104 (1989)

57. V.A. Kuz'menko, *Razvitie predstavlenii o protsesse deformirovaniia materialov* (UkrNIITI, Kiev, 1968), p. 47

58. O.D. Khlopotov, Metallovedenie i termicheskaia obrabotka materialov. №12, 12–14 (1974)

59. A.S. Balankin, V.S. Ivanova, V.P. Breusov, Dokl. AN SSSR. **322**(6), 1080–1085 (1992)

60. V.E. Panin, Iu.V. Griniaev, V.I. Danilov i dr. Strukturnye urovni plasticheskoi deformatsii i razrusheniia (Nauka, Sib.otd-e, Novosibirsk, 1990), p. 255

61. M. Feigenbaum, Universal'nost' v povedenii nelineinykh sistem. UFN **141**(2), 343–374 (1983)

62. V.A. Chernomorets, S.K. Gorbunov, Printsipy identifikatsii determinirovannoi osnovy v khaoticheskom povedenii sistem. Problemy uprvleniia i informatiki, №6, 24–33 (2005)

Chapter 5
Multifractal Analysis of Fatigue Failure

Various physical objects and signals even those with self-similarity very rarely can be described with only one value—the fractal dimension. That is why analyses based on the *multifractal* theory (inhomogeneous fractal objects) have received widespread. The multifractal provides vast new possibilities of fractal analysis for the complex stochastic processes. One fractal dimension is not enough to characterize the multifractal; it requires an infinite range of dimensions. The idea of multifractal analysis is to break down the studied sets with the complex statistics into the multiple homogeneous sets with distinct fractal dimensions [1, 2].

In 1983, Grassberg, Hentchel and Procaccia [3, 4] introduced a family of generalized dimensions D_q in the nonlinear dynamics, referred as *Rényi dimension* named after the Hungarian mathematician who proposed them earlier in a different context.

Using the abilities of multiscale analysis for the complex stochastic processes to identify their local singularities (singularities) based on the multifractal formalism, we research the mechanism of fatigue fracture as the process reversed to the process of the successive period-doubling bifurcations according to the Feigenbaum scheme.

5.1 Key Concepts of Multifractal Analysis—Generalized Fractal Dimensions

Let us give an overview of multifractal [5]. Consider the fractal object A, which occupies some limited area G of size L in the Euclidean space with dimension d. Suppose that at some stage of its construction, it represents the set of points $N \gg 1$ somehow distributed in this area. We assume that at the end $N \to \infty$.

The entire area G is divided into the cubic cells with sides $\varepsilon \ll L$ and volume ε^d. Next, we will be interested only in those cells that contain at least one point. Let the number of occupied cells i ranges $i = 1, 2 \ldots N(\varepsilon)$, where $N(\varepsilon)$—the total number of occupied cells, which is convergent and depends on the size of cell ε.

Let $n_i(\varepsilon)$—the number of points in cell with the cardinal number i, then

$$p_i(\varepsilon) = \lim_{N \to \infty} \frac{n_i(\varepsilon)}{N} \tag{5.1}$$

represents the probability that a randomly chosen point from the set A comes from the cell i. In other words, the probability p_i characterizes the relative cell density. From the normalization condition of probability, it follows that

$$\sum_{i=1}^{N(\varepsilon)} p_i(\varepsilon) = 1. \tag{5.2}$$

The generalized multifractal analysis is based on the so-called the partial function (the generalized partition function) $Z(q, \varepsilon)$, where the exponent q can take any value within the range $-\infty < q < +\infty$:

$$Z(q, \varepsilon) = \sum_{i=1}^{N(\varepsilon)} p_i^q(\varepsilon). \tag{5.3}$$

Characterizing the distribution of points in G, the spectrum of *generalized fractal dimensions* D_q (*Rényi dimensions*) is determined by the relation

$$D_q = \frac{\tau(q)}{q - 1}, \tag{5.4}$$

where the nonlinear function $\tau(q)$ (it is called the *scaling exponent* in the scientific literature) has the form

$$\tau(q) = \lim_{\varepsilon \to 0} \frac{\ln(Z(q, \varepsilon))}{\ln \varepsilon}. \tag{5.5}$$

If $D_q = D = \text{const}$, so it does not depend on q, then this set of points is a conventional (regular) fractal, characterized by only one value—the fractal dimension D. In contrast, if the function D_q somehow varies with q, this set of points is considered multifractals.

Thus, the multifractal is generally characterized by scaling exponent $\tau(q)$, which determines the behavior of the partition function $Z(q, \varepsilon)$ at $\varepsilon \to \infty$:

$$Z(q, \varepsilon) = \sum_{i=1}^{N(\varepsilon)} p_i^q(\varepsilon) \approx \varepsilon^{\tau(q)}. \tag{5.6}$$

In the case of the regular fractal, there are equal number of points in each cell

$$n_i = \frac{N}{N(\varepsilon)}. \tag{5.7}$$

so that the fractal is *homogeneous*. Then, the relative density of all cells, $p_i(\varepsilon) = 1/N(\varepsilon)$, is also the same, and the generalized partition function takes the form

$$Z(q, \varepsilon) = N^{1-q}(\varepsilon). \tag{5.8}$$

According to the definition of the fractal dimension D, the number of occupied cells at the sufficiently small ε behaves as the following

$$N(\varepsilon) = \varepsilon^{-D}. \tag{5.9}$$

Substituting this in (5.8) and comparing it with (5.6), we conclude that in the case of normal fractal the function

$$\tau(q) = (q - 1)D \tag{5.10}$$

is linear. Then, all $D_q = D$ and really do not depend on q. The fractals, where all the generalized fractal dimensions D_q coincide, are often referred by the term of monofractal.

It follows from (5.9) that the formula for the fractal dimension of monofractal is

$$D = -\lim_{\varepsilon \to 0} \frac{\log N(\varepsilon)}{\log \varepsilon}. \tag{5.11}$$

The quantity D, defined by the formula (5.11), is called *Minkowski dimension* of set A and denoted by $\dim_M(A)$. This dimension is related to the Hausdorff dimension (denoted by $\dim_H(A)$) in the inequality [6]

$$\dim_H(A) \le \dim_M(A). \tag{5.12}$$

In practice, we use the dimension $\dim_M(A)$ to construct the fractal dimension of monofractal (slightly inflated in comparison with $\dim_H(A)$), calculated on computer using the simple algorithms based on a point or cellular techniques [6]. The latter is also called the "box method" [7, 8].

At $q = 0$ from expression (5.3), it follows that

$$Z(0, \varepsilon) = N(\varepsilon). \tag{5.13}$$

On the other hand, according to the formulas (5.4) and (5.6)

$$Z(0, \varepsilon) \approx \varepsilon^{\tau(0)} = \varepsilon^{-D_0}.\tag{5.14}$$

Comparing these two equalities, we come to the relation $N(\varepsilon) \approx \varepsilon^{-D_0}$. This means that D_0 represents the ordinary dimension $\dim_M(A)$, which is also called the *volumetric dimension* [9].

At $q = 1$, due to the normalization of probability (5.2), the partition function is equal to

$$Z(1, \varepsilon) = 1,\tag{5.15}$$

then from (5.6) we find that $\tau(1) = 0$. Thus, the expression (5.4) at $q \to 1$ has the uncertainty $0/0$, and following L'Hospital's rule, we find that

$$\lim_{q \to 1} D_q = \lim_{q \to 1} \tau'(q).\tag{5.16}$$

Let us assume $Z(q, \varepsilon)$ in the form of obvious equality

$$Z(q, \varepsilon) = \sum_{i=1}^{N(\varepsilon)} p_i^q = \sum_{i=1}^{N(\varepsilon)} p_i e^{[(q-1)\ln p]}.$$

Now, expanding the exponential in the neighborhood of $q = 1$ and taking into account the normalization condition (5.2), we obtain

$$Z(q \to 1, \varepsilon) = \sum_{i=1}^{N(\varepsilon)} [p_i + (q-1)p_i \ln p_i] = 1 + (q-1) \sum_{i=1}^{N(\varepsilon)} p_i \ln p_i,$$

from which it follows that

$$\frac{\mathrm{d}}{\mathrm{d}q} Z(q, \varepsilon)|_{q=1} = \sum_{i=1}^{N(\varepsilon)} p_i \ln p_i.\tag{5.17}$$

Taking into account (5.15) and (5.17), we obtain

$$\frac{\mathrm{d}}{\mathrm{d}q}(\ln Z(q, \varepsilon))|_{q=1} = \frac{\frac{\mathrm{d}}{\mathrm{d}q} Z(q, \varepsilon)}{Z(q, \varepsilon)}\bigg|_{q=1} = \frac{\mathrm{d}}{\mathrm{d}q} Z(q, \varepsilon)\bigg|_{q=1} = \sum_{i=1}^{N(\varepsilon)} p_i \ln p_i.\tag{5.18}$$

Differentiating (5.5) at $q = 1$ taking into account (5.18) and substituting the expression found for $\tau'(1)$ into (5.16), we obtain

$$D_1 = \lim_{\varepsilon \to \infty} \sum_{i=1}^{N(\varepsilon)} p_i \frac{\ln p_i}{\ln \varepsilon}. \tag{5.19}$$

With accuracy up to the sign, the numerator in this equation is the entropy of a fractal set A

$$S(\varepsilon) = -\sum_{i=1}^{N(\varepsilon)} p_i \ln p_i.$$

Since the entropy is a measure of information required to determine the system at a position i, we may say that the value D_1 characterizes the information necessary to locate a point in some cell. Because of property, the magnitude D_1 is called the *informational dimension* [9].

At $q = 2$, the D_q is expressed as

$$D_2 = \lim_{\varepsilon \to 0} \frac{\ln \sum_{i=1}^{N(\varepsilon)} p_i^2}{\ln \varepsilon}. \tag{5.20}$$

The value D_2 is closely linked to the behavior of the so-called the correlation integral defined by the expression [10, 11]

$$I(\varepsilon) = \lim_{N \to \infty} \frac{1}{N^2} \sum_{n,m} \theta(\varepsilon - |\vec{r}_n - \vec{r}_m|). \tag{5.21}$$

The summation take place across pairs of all fractal points of the set A with the radius vectors $\vec{r}_n$ and $\vec{r}_m$; $\theta(x)$—the Heaviside (step) function, $\theta(x) = 1$ if $x \geq 0$, and $\theta(x) = 0$ if $x < 0$. The sum in (5.21) determines the number of pairs of points in n, m, for which the distance is less than ε. Since the quantity p_i^2 is the probability that two points will get into the same cell i of size ε, the distance between these two points will be less or equal to ε. Thus, with the accuracy of numerical coefficients, and taking into account the equality (5.20), we obtain

$$I(\varepsilon) \approx \sum_{i=1}^{N(\varepsilon)} p_i^2 \approx \varepsilon^{D_2}. \tag{5.22}$$

This shows that the generalized dimension D_2 determines the dependence of the correlation integral $I(\varepsilon)$ on ε within the limit $\varepsilon \to 0$. For this reason, D_2 is called the *correlation dimension*.

For any arbitrary exponent q, the generalized fractal dimension D_q always monotonically decreases (or remains constant in extreme cases) as q increases

$$D_q \geq D_{q'} \text{ at } q' > q. \tag{5.23}$$

The equality is valid, e.g., for a homogeneous fractal. The D_q reaches its maximum value of $D_{max} = D_{-\infty}$ at $q \to -\infty$, and the minimum value of $D_{min} = D_{+\infty}$ at $q \to +\infty$.

As it is already noted, one of the main characteristics of the multifractal is the dependence of the probability p_i on the size of cell ε. This dependence has exponential nature

$$p_i(\varepsilon) \approx \varepsilon^{\alpha_i} \tag{5.24}$$

where α_i is some exponent, generally different for various cells i (with respect to it, the terms "singularity component" and "singularity exponent" are widely used in the literature). The lower the value of α_i, the more singular is the measure.

It is known that for the regular (homogeneous) fractal, all exponents of α_i are the same and equal to the fractal dimension D. Then,

$$p_i = \frac{1}{N(\varepsilon)} \approx \varepsilon^D. \tag{5.25}$$

However, for such a complex object as the multifractal, due to its heterogeneity, the probability p_i of filling up the cells is generally not the same, and the exponent α_i is different for cells with different values. Fairly, the typical situation is when these values are continuously filling up a closed interval $[\alpha_{min}, \alpha_{max}]$, and

$$p_{min} \approx \varepsilon^{\alpha_{min}}, \text{ and } p_{max} \approx \varepsilon^{\alpha_{max}}. \tag{5.26}$$

It is easy to show that

$$\left.\frac{d\tau}{dq}\right|_{q \to +\infty} = D_{+\infty} = \alpha_{min}, \quad \left.\frac{d\tau}{dq}\right|_{q \to -\infty} = D_{-\infty} = \alpha_{max}. \tag{5.27}$$

So that the range of possible values α is defined by limits (at $q \to \pm\infty$) of the generalized fractal dimensions D_q.

Let us consider the nature of the probability distribution for the different values of α_i. Let $n(\alpha)d\alpha$ is the probability that α_i is within the range from α to $\alpha + d\alpha$. In other words, $n(\alpha)d\alpha$ represents the number of cells i with the same measure p_i, and α_i lying in this range. In case of monofractal, where all α_i are the same (and equal to the fractal dimension D), this number is obviously proportional to the total number of cells $N(\varepsilon) \approx \varepsilon^{-D}$, exponentially dependent on the size of cell ε. The fractal dimension D determines the exponent in this equation.

However, this is not the same for multifractal, so the different values α not just corresponds to the different values of the probability and D, but to the different (depending on α) values of $f(\alpha)$ in the exponent.

$$n(\alpha) \approx \varepsilon^{-f(\alpha)}. \tag{5.28}$$

Thus, the physical meaning of the function $f(\alpha)$ lies in the fact that it represents the volumetric dimension (denoted by d_c) of some homogeneous fractal subset A_α from the original set A, characterized by the equal probabilities of filling up the cells $p_i \approx \varepsilon^\alpha$. Since the fractal dimension of a subset is always less than or equal to the fractal dimension of the original set D_0, there is an important inequality for the function $f(\alpha)$

$$f(\alpha) \leq D_0. \tag{5.29}$$

So the set of different values of the function $f(\alpha)$ (at different α) represents the spectrum of the fractal dimensions of the homogeneous subsets A_α, derived from the original set A. This explains the term "multifractal." It can be understood as a kind of union of different homogeneous fractal subsets A_α, each of which has its own value of the fractal dimension $f(\alpha)$.

Since any subset owns only a fraction of the total number of cells $N(\varepsilon)$, derived from the original set A, the probability normalization condition (5.2), obviously, does not sum up only on this subset. The sum of these probabilities becomes less than one. Therefore, the probabilities p_i themselves with the same value of α_i are obviously less (or equal to in extreme cases) than the value $\varepsilon^{f(\alpha_i)}$, which is inversely proportional to the number of cells, covering the given subset (recall that in the case of monofractal $p_i \approx 1/N(\varepsilon)$). As a result, we arrive at the following important inequality for the function $f(\alpha)$. Specifically, for all values of α

$$f(\alpha) \leq \alpha. \tag{5.30}$$

As an example, the equality holds only for the completely homogeneous fractal, where $f(\alpha) = \alpha = D$.

Let us establish the connection between the function $f(\alpha)$ and the previously introduced function $\tau(q)$ (the scaling exponent). For that, we calculate the partition function $Z(q, \varepsilon)$. Substituting for the expression (5.3), the probabilities $p_i \approx \varepsilon^{\alpha_i}$ and moving from summation over i to integration over α with probability density function (5.28), we obtain

$$Z(q, \varepsilon) = \sum_{i=1}^{N(\varepsilon)} p_i^q \approx \int d\alpha n(\alpha) \varepsilon^{q\alpha} \approx \int d\alpha n(\alpha) \varepsilon^{q\alpha - f(\alpha)}. \tag{5.31}$$

Since ε is very small, according to the saddle-point method the values of α will have the greatest impact on the integral (5.31), corresponding to the minimum in the subintegrand. Thus, the relations follow

$$\frac{\mathrm{d}f}{\mathrm{d}\alpha}\bigg|_{\alpha=\alpha(q)} = q, \quad \frac{\mathrm{d}^2 f}{\mathrm{d}\alpha^2}\bigg|_{\alpha=\alpha(q)} < 0. \tag{5.32}$$

Comparing the first relation in (5.32) with (5.36), we conclude that

$$\tau(q) = q\alpha(q) - f(\alpha(q)). \tag{5.33}$$

Hence, with help of (5.4) we can find the function D_q:

$$D_q = \frac{1}{q-1}[q\alpha(q) - f(\alpha(q))]. \tag{5.34}$$

Thus, if the function of multifractal spectrum $f(\alpha)$ is known, then with help of (5.34) and the first ratio in (5.32), the function D_q can be determined. Conversely, knowing D_q, we can find the relationship $\alpha(q)$ using the equation

$$\alpha(q) = \frac{\mathrm{d}}{\mathrm{d}q}\big[(q-1)D_q\big], \tag{5.35}$$

and then find from (5.34) the dependence $f(\alpha(q))$. These two equations determine (in parametric form) the function $f(\alpha)$.

Formally, the transition from the variables $\{q, \tau(q)\}$ to $\{\alpha, f(\alpha)\}$, defined by the above relation, can be done using the Legendre transformation

$$\alpha = \frac{\mathrm{d}\tau}{\mathrm{d}q}, \quad f(\alpha) = q\frac{\mathrm{d}\tau}{\mathrm{d}q} - \tau. \tag{5.36}$$

Equations (5.36) determine the dependence $f(\alpha(q))$ in the parametric form. The inverse Legendre transformation is determined by formulas

$$q = \frac{\mathrm{d}f}{\mathrm{d}\alpha}, \quad \tau(q) = \alpha\frac{\mathrm{d}f}{\mathrm{d}\alpha} - f. \tag{5.37}$$

For the homogeneous fractal $D_q = D = \mathrm{const}$. Therefore, $\alpha = \mathrm{d}\tau/\mathrm{d}q = D$ and $f(\alpha) = q\alpha - \tau q = qD - D(q-1) = D$. In this case, the "graph" of function $f(\alpha)$ on the plane $(\alpha, f(a))$ consists of a single point (D, D).

5.2 Multifractal Nature of Micro-Cracks Merger

Numerous experimental data show [1] that during the cyclic loading at the first stage of destruction the highly disperse groove is formed, and it is distributed in accordance with a picture of the stress state of sample. If there is a stress concentrator (cut), then it initiates the growth of macro-cracks by the jumping union of

individual grooves, which are obviously the clusters of failure carriers, combined in accordance with the distribution of the stress field.

According to the data on acoustic emission, the process of fatigue failure is leaped by its nature with the development of structural changes, preceding destruction the sample emits short impulses of varying intensity and frequency [12].

There are two possible scenarios of evolution for the ensemble of elementary destruction carriers—frustrons (characterizing the break of atomic bonds), dislocations, etc. For not very high values of the shear viscosity η where the quasi-brittle fracture takes place, the height of the activation barrier Q_c, which the system has to overcome in order to join frustrons, is not very high due to the relative smallness of the characteristic values of the stress intensity $K_c \sim \sigma_c = \lambda^{1/2} \sim \eta^{1/2} \left(Q_c \sim K_c^2 \sim \eta \right)$. Therefore, with the feasible probability $P_N \sim \mathrm{e}^{(QN/T)}$ the fluctuation of cluster containing the large number of frustrons N becomes possible. This process is studied in [13] within the framework of non-equilibrium thermodynamics. It is shown that upon reaching a certain critical value the cluster of frustrons becomes an energy generator, which means a transition of crack into an athermal mode, i.e., the beginning of failure.

For the large values of η, when it becomes virtually impossible to form a dedicated cluster $N \gg 1$, the chain process becomes as the most probable for the formation of the athermal cluster: with the probability $P_1 \sim \mathrm{e}^{(-Q/T)}$ the frustrons pair, and then with the same probability, and form pairs again, etc. [14, 15].

The transition to such a process due to the fact that at small t the formation of a cluster consisting of N frustrons leads to multiplying the individual probabilities $P_1 \left(P_N = P_1^N \right)$, while the chained process is characterized by their superposition, giving much greater importance $P_N \sim N^{-2} \cdot P_1$. As a result, the kinetics of destruction varies critically [15]: if the probability of a lack of fluctuation of cluster formation at time t is characterized by the Debye dependence $P_1(t) \sim \mathrm{e}^{\{-t/\tau_0\}}$, where τ_0—the microscopic time, then time of its emergence

$$t_N \equiv -\tau_0 \ln P_n \sim N\tau_0 \ln P_1^{-1}$$

is comparable with the characteristic scale of the chain process $\sim \tau_0/P_N$, if we assume that kinetics of the latter is given by the dependence

$$P_N(t) \sim \tau_0/t \qquad (5.38)$$

quite different from the Debye one.

At step $\tilde{m}$ ($\tilde{m} \leq k$; k—the depth of hierarchical bounding of the elementary acts of the cluster union), the dependence of the barrier height $Q(u) = \Phi(u)$ on the distance $u = \tilde{m}$ between the nodes at levels $n = k$ and $n = k - \tilde{m}$ is presented by formula

$$Q(u) = Q\mathrm{e}^{\{u/u_0\}} \tag{5.39}$$

where Q—the Gibbs thermodynamic potential, expressed through the free energy F (Helmholtz potential), the pressure P and the volume V using the formula [16]

$$Q = F + P \cdot V. \tag{5.40}$$

Since Q—the height of the potential barrier before the beginning of chain mechanism in within one elementary act ($\tilde{m} = 1$) of cluster merging, the thermodynamic potential increases s times, from (5.39) we find

$$u_0 = 1/\ln s. \tag{5.41}$$

For the free energy of phonon gas, we have [17]

$$F = 3Nk_0T \ln\left(1 - \mathrm{e}^{-\theta/T}\right) - Nk_0D(\theta/T) \tag{5.42}$$

where θ—the Debye temperature; N—the number of elementary cells in the simple crystal lattice (in each unit cell is just one atom); $D(\theta/T)$—the Debye function

$$D(\theta/T) = 3\left(\frac{T}{\theta}\right)^3 \int\limits_0^{\theta/T} \frac{x^3\mathrm{d}x}{\mathrm{e}^x - 1}. \tag{5.43}$$

The Debye function has an asymptotic behavior:

$$\begin{aligned} D(\theta/T) &= \tfrac{\pi^4}{s}\left(\tfrac{T}{\theta}\right)^3, \quad T \ll \theta \text{ (for low temperatures)}; \\ D(\theta/T) &= 1 - \tfrac{3}{8}\left(\tfrac{\theta}{T}\right) + \tfrac{1}{20}\left(\tfrac{\theta}{T}\right)^2, \quad T \gg \theta \text{ (for high temperatures)}. \end{aligned} \tag{5.44}$$

The pressure P is expressed through

$$P = \frac{9}{8}\frac{Nk_0\theta}{V}\gamma_G\left[1 + \frac{8}{3}\frac{T}{\theta}D\left(\frac{\theta}{T}\right)\right], \tag{5.45}$$

where $k_0 = 1.38 \times 10^{-23}\,\mathrm{J/K} = 1.38 \times 10^{-16}\,\mathrm{erg/K}$—the Boltzmann constant (K—the temperature in Kelvin, $1\,\mathrm{J} = 10^{-7}\,\mathrm{erg}$), θ—the Debye temperature, γ_G—the Grüneisen parameter (for one-dimensional linear crystal γ_G is constant, and $\gamma_G \approx 1$, it does not depend on the temperature).

When considering the kinetics of fatigue crack growth according to V.S. Ivanova [18], one of the main problems is the finding of length change regions for crack, which contains the same micro-mechanism that controls the rate of crack growth, or only the micro-mechanism of normal separation, or only the mechanism of
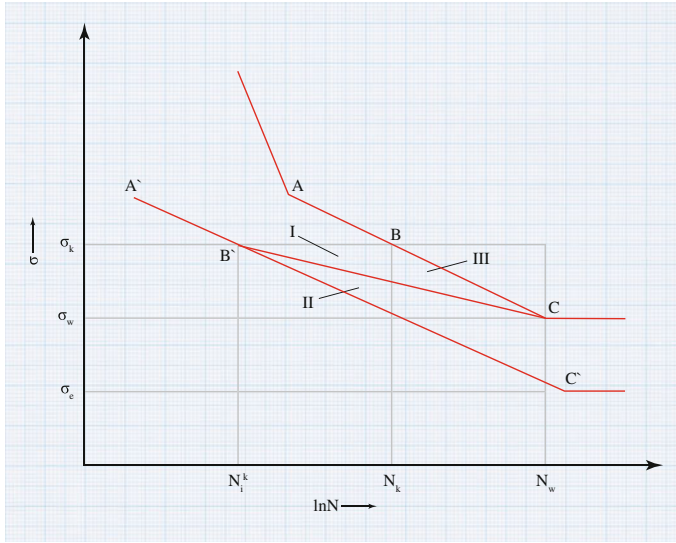
Fig. 5.1 The fatigue failure graph according to V.S. Ivanova

cross-micro-shear, or only mechanism of longitudinal micro-shear. In general, the fatigue process in accordance with the diagram of fatigue failure has several steps (Fig. 5.1) [19].

O.I. Romaniv in his works [20, 21] based on the analysis of experimental kinetic curves of the fatigue diagrams of structural materials showed that for the various stages of the fatigue micro-cracks the following growth rate is implemented: *I*—the phase of slow growth with the crack growth rate less than $10^{-6} - 5 \times 10^{-5}$ mm/cycle; *II*—the stage of stable growth with the speeds v, varying in the range of $10^{-6} - 5 \times 10^{-5} < v < 10^{-3}$ mm/cycle; *III*—the stage of accelerated growth or unstable with the speeds $v > 10^{-3}$ mm/cycle.

The diagrams of the temperature dependence of the structural strength $K_c - \sigma_{0,2}$ for various steels in logarithmic coordinates shows [21] the existence of the threshold K_c^* stress intensity factor (SIF), corresponding with the beginning of change of the destruction micro-mechanism from micro-split (quasi-split) to micro-viscous destruction, i.e., the transition from stage *II* to stage *III*. This conclusion is confirmed in [22, 23] by a more detailed analysis of the features of fatigue fracture of structural materials at the bifurcation points using the temperature dependences $K_c = f(t)$ as the linear fractional coordinates (Fig. 5.2)

$$\eta = \frac{K_{c_0}}{(K_c - K_{c_0})}, \quad \xi = \frac{T_0}{(T - T_0)},$$
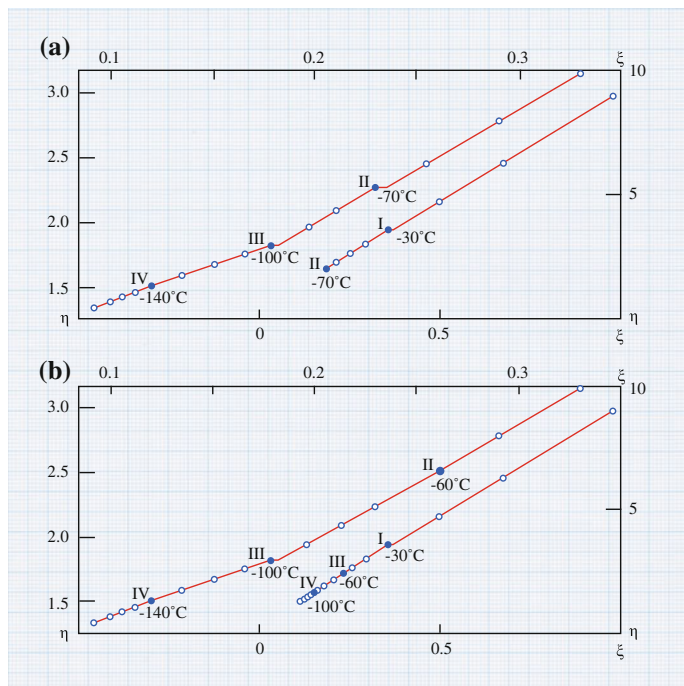
Fig. 5.2 The linear dependence $K_c = f(t)$ in the fractional linear coordinates for compact samples of steel 16Г2АФ with 70 mm thickness

where K_{c_0} and T_0 are, respectively, the values of the SIF and the experimental temperature at the end of dependence $K_c = f(t)$, and K_c and T are, respectively, the current values of the SIF and the experimental temperature.

The characteristic time of beginning of the chain unification of the crack clusters at the fatigue failure can be considered as the transition to the stage *III* or the transition time of the micro-band width into the zone of mixed destruction l_d.

The more complicated is the process of the material destruction at friction. In this case, the destruction is caused by the contact interaction accompanied by the joint action of the surface temperature and the temperature gradient, resulting in significant thermal stresses in material of the friction element. A.Kh. Dzhanahmedov [24, 25] proposed a theoretical model of the failure mechanism as a result of thermo-mechanical loading at friction. This model supports the hypothesis on the formation of the surface layer with a low dislocation density and the intense fracturing in the subsurface layers, which is consistent with experimental results. On the spot of the actual contact, the stress is proportional to the flash temperature and causes strong heating in the thin surface layers, which leads to the formation of burn marks, spots, and the thermal centers of micro-cracks. Therefore, we can assume that it is in the surface layer in the case of heat when exposed to the flash temperature T_{fla} the cracks are born, caused by thermal fatigue of material. The
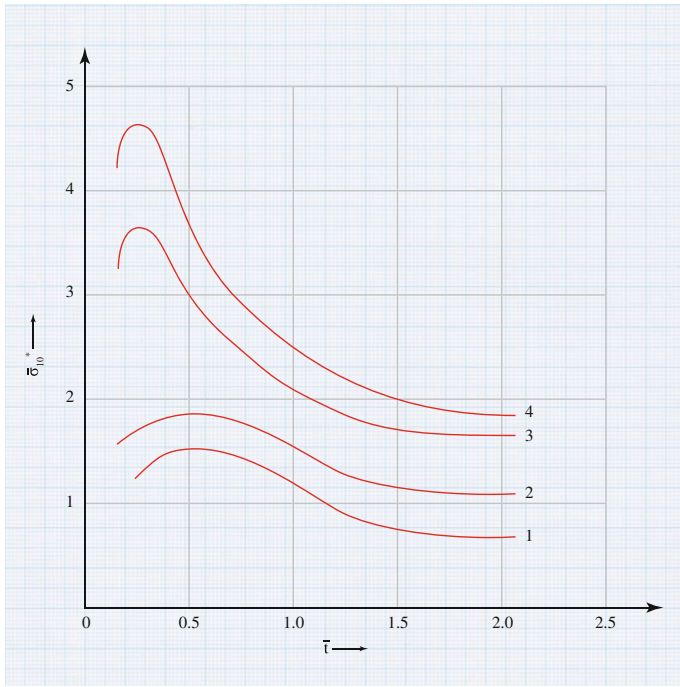
Fig. 5.3 The dependence of stress on deceleration time (both measureless) at the pulley cooling for various values of Biot: *1* Bi = 0.5; *2* 1.0; *3* 0.5; *4* ∞. x = 0

further development of the crack is a result of the cooling of the surface layer and occurrence of the gradient from the surface temperature T^*, when the thermal stresses in the surface layer reaches the highest value passing the maximum (Fig. 5.3).

The analyses of friction pairs wear show that under cyclic heating and cooling, the large impact on the emergence and development of cracks have as the multi-phase structure as the thermal properties of individual phases. A specific role in material destruction plays the distribution of cracks on the surface.

Since the flash temperature can quickly reach several hundred degrees, such a jump in temperature can lead to plasticity of material when the resistance to friction decreases. Since the actual contact spots interaction lasts $10^{-6} - 10^{-3}$ s, so the static strength of surface layer of the material of the friction pair is not important, but the properties of fatigue strength, given that the crystal lattice of the solid body reacts to impact after $10^{-8} - 10^{-5}$ s. Therefore, the restructuring of surface layer under the external heat loading occurs through setting the temperature field, and by the time the temperature becomes steady the surface layer is already under the influence of certain residual stresses (Fig. 5.4).

On Fig. 5.4 σ_z and σ_s are the surface tensions, caused by the gradient temperature and the flash temperature, respectively, at deceleration.
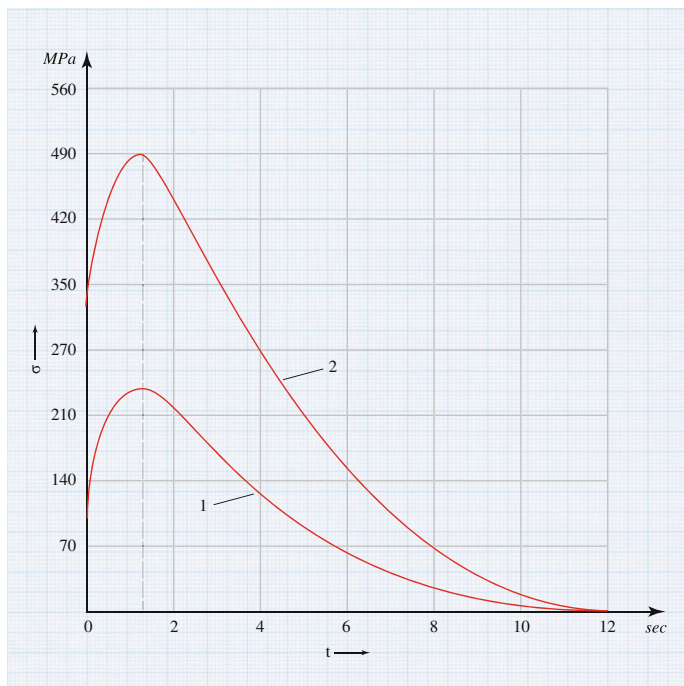
Fig. 5.4 Changes in the material surface tension of pulley caused by the temperature gradient and the flash temperature at braking: *1* σ_z; *2* σ_s

In view of the above, we can assume that the beginning of the chain process of the crack merging at friction (with accuracy up to 10^{-5} s) is the time t_{c_2} required to reach the flash temperature T_{fla}.

The elementary act of the crack cluster merging is characterized by the Debye dependence

$$P_u(t) = e^{\left\{-\frac{t}{\tau(u)}\right\}} \tag{5.46}$$

with the specific relaxation time

$$\tau(u) = \tau_0 e^{\left\{\frac{Q(u)}{T}\right\}}. \tag{5.47}$$

where $\tau_0 = 10^{-12}$ s—the microscopic time, $Q(u)$—the height of barrier separating the clusters, the distance between which is equal to u, and T—the temperature in energy units.

The formation of fractal set according to the Feigenbaum scenario, modeled on the quadratic mapping, is described by the bifurcation chains $m = k - \tilde{m}$, each of which divide the set into two. This process moves downwards along the

hierarchical branches of the regular Cayley tree with furcation $s = 2$, starting from the root at level $n = 0$. With each step of the mapping iteration, there is a movement from level on n nodes to level $n + 1$ on nodes, which fits into the general picture of the geometric description of arbitrary multifractal set [26]. It is formed as a result of $n \to \infty$ steps division of the original set N_n into i fractals with length $l_i \to 0 (i = 1 \ldots N_n)$.

With branching of the Cayley tree $s = 2$ under the fragment, we will understand the set of two nodes that share a common ancestor in the preceding level of tree. Then, after the nth step of division, we receive numerous fragments $N_n = \bigcup_{m=1}^{n} N_m$ where N_m consists of 2^{m-1} fragments and therefore, card $N_n = N_n = 2 + \cdots + 2^n = 2^{n+1} - 1$ (card—the sign of power in set). Clearly, $m = k - \tilde{m}$, as the process of pairwise division is inverse to the process of pairwise merging of clusters.

Let $\tau_{\tilde{m}}$—the time during which the hierarchical relationship is established at a distance $u = \tilde{m}$, given by the condition $p(\tilde{m}) = \tau_0 / \tau_{\tilde{m}}$. This leads to the overcoming the fractal relief with height $\Phi \leq \Phi_{\tilde{m}}$, bounded by $\Phi_{\tilde{m}} \equiv \Phi(\tilde{m})$. Then,

$$\tau_{\tilde{m}} = \tau_0 \left(\frac{\Phi_{\tilde{m}}}{Q} \right)^{\frac{u_0}{k}}. \tag{5.48}$$

Obviously, at $\tilde{m} = k \, \tau_{\tilde{m}}$ coincides with the expression for the time τ_M for the destruction of hierarchical structure from Table 4.2 the case $p_w(u)$ and $\Phi_e(u)$, i.e., the time of reaching the root of Cayley tree at level $n = 0$, starting from the tree nodes at level $n = k$. After simple transformations, taking into account the expression for $\Phi_e(u)$ from (Sect. 4.4), we find

$$\tau_{\tilde{m}} = \tau_0 \cdot e^{\tilde{m}/k} \tag{5.49}$$

Since the process of cluster merging is inverse to the process of fractal set formation according to the Feigenbaum scenario, considering formulas (5.39), (5.41), (5.46), and (5.47), the probability of achieving at time $\tau_{\tilde{m}}$ the nodes Cayley tree, at $u = \tilde{m}$ away from the most deepest level of nodes $n = k$ in the ultrametric space, moving upwards along the branches of tree, is equal to

$$P_{\tilde{m}}(\tau_{\tilde{m}}) = \exp \left\{ - \left(\frac{\tau_{\tilde{m}}}{\tau_0 e^{(Q(\tilde{m})/T)}} + \frac{\tilde{m}}{k} \right) \right\}, \tag{5.50}$$

where

$$Q(\tilde{m}) = Q e^{\{-\tilde{m} \ln s\}}. \tag{5.51}$$

As we already know, the simplest model to study the Feigenbaum scenario is the quadratic mapping

$$x_{n+1} = f(\mu, x_n) = \mu x_n (1 - x_n) \tag{5.52}$$

Let in mapping (5.52), the value μ_m of the parameter μ is chosen in such way so that when passing through these values, the super steady cycles of period 2^m are formed. The possibility of choosing such values of μ_m is shown earlier. Let us find out the distance (in the real physical space) d_m between the pair of elements of the super stable cycle of period 2^m, which includes the point $x_c = 1/2$ as the fixed point of 2^m (see equality 4.16 for d_m). We assume that the probabilities $P_{\tilde{m}} = P_{\tilde{m}}(\tau_{\tilde{m}})$ satisfy the relation

$$P_{\tilde{m}} = l_{\tilde{m}}^{\alpha} (\tilde{m} = 1 \ldots \tilde{m}_0; \tilde{m}_0 \leq k), \tag{5.53}$$

where $l_{\tilde{m}} = d_{\tilde{m}}$ and α—the scaling parameter.

From the sequence of pairs $\ln(P_{\tilde{m}}), \ln(l_{\tilde{m}})$ $(\tilde{m} = 1 \ldots \tilde{m}_0)$ using the method of least squares we find the parameter α.

As in the case with the monofractal, the original structure is the generating function with the parameter q:

$$M_n(q) = \sum_{\tilde{m}=1}^{n} N^{(\tilde{m})} P_{\tilde{m}}^q. \tag{5.54}$$

Assuming the scaling dependence

$$N^{(\tilde{m})} \propto l_{\tilde{m}}^{-\tau}, \tag{5.55}$$

where τ—the corresponding parameter, then substituting (5.53), (5.55) into (5.54), we obtain

$$M_n(q, \alpha, \tau) = \sum_{\tilde{m}=1}^{n} \left(\frac{P_{\tilde{m}}^q}{l_{\tilde{m}}^{\tau}} \right) = \sum_{\tilde{m}=1}^{n} l_{\tilde{m}}^{q\alpha - \tau}, \quad l_{\tilde{m}} \to 0 \text{ at } \tilde{m} \to \infty. \tag{5.56}$$

At fixed values of n among all fragments of the set N_n produced after the nth step of division, the value α is implemented for

$$N_n(\alpha) = l_n^{-f(\alpha)}, \tag{5.57}$$

fragments, where the function $f(\alpha)$ defines the dimension of the geometrical set (set of segments l_i), which realizes the allocation of measurement (5.56). Using (5.57), from (5.56) we obtain at given α:

$$M_n(q, \alpha, \tau) = l_n^{q\alpha - f(\alpha) - \tau}, \tag{5.58}$$

Considering the uniformity of values α, from the Eq. (5.58), we find

$$M_n(q, \tau) = \int\limits_{\alpha_{\min}}^{\alpha_{\max}} l_n^{q\alpha - f(\alpha) - \tau} \rho(\alpha) d\alpha, \qquad (5.59)$$

where the function $\rho(\alpha)$ describes the density distribution of the fragments l_n according to the parameter α. Evaluating the integral in (5.59) by the saddle-point method, and taking into account the equalities

$$\left.\frac{df}{d\alpha}\right|_{\alpha=\alpha(q)} = q, \quad \left.\frac{d^2 f}{d\alpha^2}\right|_{\alpha=\alpha(q)} < 0, \qquad (5.60)$$

we obtain an estimate

$$M_n(q, \tau) \approx l_n^{q\alpha(q) - f(\alpha(q)) - \tau}. \qquad (5.61)$$

By decreasing fragments $l_n \to \infty$, the measure (5.61) takes finite values, providing that the rate τ reduces to $\tau(q)$, defined by conditions

$$\tau(q) = q\alpha(q) - f(\alpha(q)), \qquad (5.62)$$

where the dependence $\alpha(q)$ is defined by (5.60). The generalized fractal dimension $D(q)$ of the multifractal set A, formed by the chain process of pairwise merging of frustron clusters with the geometric description in form of the Cayley tree, and using formula (5.62), is defined by the equality

$$D(q) = (q - 1)^{-1}(q\alpha(q) - f(\alpha(q))). \qquad (5.63)$$

From (5.62) and (5.63), it follows that

$$\alpha(q) = \frac{d}{dq}[(q - 1)D(q)], \qquad (5.64)$$

$$\tau(q) = (q - 1)D(q). \qquad (5.65)$$

The substitution of (5.65) into (5.64) leads to the relationship

$$\alpha(q) = \frac{d\tau(q)}{dq}. \qquad (5.66)$$

Let the solid body is subjected to the stress $\sigma = \sigma(t)$, $0 \le t \le \tau_M$. We introduce an auxiliary parameter

$$q = \frac{\sigma_c - \sigma}{\sigma_c}, \quad \sigma < \sigma_c, \tag{5.67}$$

where σ_c—the critical stress, defined by the theoretical critical strength of material.

At sufficiently large n from the condition

$$M_n(q, \alpha, \tau) = \sum_{\tilde{m}=1}^{n} l_{\tilde{m}}^{q\alpha-\tau} = 1 \tag{5.68}$$

we find the dependence $\tau(q)$ at fixed α. Now, using the relation (5.62)–(5.66) we find the dependence $D(q)$ and $f(\alpha)$.

The problem of failure at braking is investigated in [19, 24, 25]. According to the proposed by A.Kh. Janahmadov the thermo-mechanical theory of wear, the thermal stresses in elements of the friction pairs of brakes, are the consequence of thermal hit on the frictional surface [27]. The rapid rise of temperature on the frictional surface causes the thermal hit and all related significant stresses σ, and the structural changes of material in the surface layers of pair.

The sequence of values μ_m converges as the geometric progression, and starting from some $n = n_0$ the mapping (5.52) generates sequence

$$\begin{aligned}
x_{n_0+1} &= f(\mu_\infty, x_{n_0}), x_{n_0+2} = f(\mu_\infty, x_{n_0+1}), \ldots, x_{n_0+k} \\
&= f(\mu_\infty, x_{n_0+k-1}) \ldots
\end{aligned} \tag{5.69}$$

where $f(\mu_\infty, x) = \mu_\infty x(1-x)$. A countable set of discrete points $\{x_{n_0+1}\}k = (1, 2 \ldots)$ has the topological dimension of zero, and its fractal dimension is within interval $(0, 1)$ (here under the fractal dimension we mean the Minkowski dimension, since the Hausdorff dimension for any countable set of R^n is zero [6]). The higher $D(q)$, the closer to chaos is the process described by the sequence (5.69). Due to mutually reciprocity of processes (5.69) and chain process of cluster merging, the large values of a $D(q)$ indicate closeness of the hierarchical structure to destruction, i.e., the fatigue failure of material.

The probability analysis of durability curves under cyclic loading, and also the distribution of micro-cracks across the length, showed that the slope of curves controls the probability and the failure mechanism (cyclic, dynamic, and static). In other words, the rate of change of probability or the number of fragments in micro-cracks controls the kinetic process of destruction. Evaluation of this parameter allows us to link the statistical and physical characteristics of destruction, what cannot be done using the Weibull ratio to find the probability of failure.

Developed above multifractal formalism (see Sect. 5.1) can be expressed through thermodynamics [26].

Assuming that in (5.56),

$$P_{\tilde{m}} = \text{const} \equiv N_n^{-1}, \tag{5.70}$$

where N_n—the total number of fragments in set obtained by division after $n \to \infty$ steps. The condition $M_n(q, \tau) = 1$ yields

$$N_n^{-1} = \sum_{\tilde{m}} l_{\tilde{m}}^{-\tau}. \tag{5.71}$$

Let introduce the parameter of inverse temperature

$$\beta = -\tau \tag{5.72}$$

and the analog of partition (5.6):

$$Z = \sum_{\tilde{m}} l_{\tilde{m}}^{\beta} = \sum_{\tilde{m}} e^{-\beta \varepsilon_{\tilde{m}}}, \tag{5.73}$$

where the effective energy levels

$$\varepsilon_{\tilde{m}} = -\ln l_{\tilde{m}} \tag{5.74}$$

are set through the distribution of lengths $l_{\tilde{m}}$. The thermodynamic potential $g = g(\beta)$, corresponding to one of n iterations, has the form

$$g = -\frac{1}{n} \ln Z = -\frac{1}{n} \ln \sum_{\tilde{m}} l_{\tilde{m}}^{\beta}, \tag{5.75}$$

where g is measured in units of temperature β^{-1}. We also introduce the parameter μ according to the equation

$$N_n = \mu^n. \tag{5.76}$$

Then in view of (5.75), the condition (5.71) gives the expression

$$g = -g \ln \mu, \tag{5.77}$$

where the presence of logarithm indicates the entropic nature of the parameter μ.

We assume that all the elements of set at nth step of iteration have the same length

$$l_{\tilde{m}} = \xi^n, \tag{5.78}$$

determined by the scale

$$\xi = e^{-\lambda}, \tag{5.79}$$

the value of which is defined by the Lyapunov exponent λ. To clarify the meaning, we write the thermodynamic partition function (5.73) in the form

$$Z_n = N_n l_{\bar{m}}^{\beta} = \mu^n e^{-n\beta\lambda} = e^{[n(\ln \mu \sim \beta\lambda)]}, \tag{5.80}$$

which takes into account the equalities (5.76), (5.78), (5.79) and through l_n are denoted all equal to each other lengths of fragment at the nth step of division. Substituting (5.80) into (5.75), we obtain the expression for the specific free energy

$$g = \beta\lambda - \ln \mu, \tag{5.81}$$

It comes down to the usual definition of the free energy

$$G = E - TS,$$

if as the free energy G, we understand the value of $(n/\beta)g$, under the energy—the value of $E = n\lambda$ and introducing the entropy

$$S = ns, \quad s = \ln \mu, \tag{5.82}$$

Thus, thermodynamically the fractal set can be described by assuming the number of iterations $n \to \infty$ as the number of particles, the parameter β is the inverse temperature (with the opposite sign), the Lagrange multiplier λ—the specific entropy of E/n, and s—the entropy. Their values are determined by (5.72), (5.79), (5.82), and the energy spectrum $\varepsilon_{\bar{m}}$ is given by the distribution of segment lengths (5.74). Under this approach, β is the free parameter, and the equation of state determines the dependence $g(\beta)$. Using the thermodynamic identity

$$\lambda = \mathrm{d}g/\mathrm{d}\beta, \tag{5.83}$$

from the parameter β we can go to the conjugated field λ [28]. Then, equalities (5.81), (5.82) give the expression

$$s = \beta g'^{(\beta)} - g(\beta), \quad g' = \mathrm{d}g/\mathrm{d}\beta, \tag{5.84}$$

for entropy, the value of which is determined by the energy λ.

To establish the connection between the geometric and thermodynamic approaches, it is necessary to express the values τ, q, α, f, D, introduced in the multifractal analysis, through the parameters β, g. Determination of the first one τ is given through the identity (5.72). The expression for the second one

$$q = \left(1 - \frac{d \ln g(\beta)}{d \ln \beta}\right) \tag{5.85}$$

follows from (5.77), (5.82), and (5.84).

For α from Eq. (5.70) taking into account (5.76), (5.82), (5.78), and (5.79), it yields

$$P_n = l_n^{s/\lambda}.$$

Comparing this result with the definition (5.24), we come to the desired equality

$$\alpha = \beta - g(\beta)/g'(\beta), \tag{5.86}$$

which takes into account (5.83) and (5.84). Using the definitions (5.24) and (5.57), it is easy to note that the condition (5.70) means

$$\alpha = f, \tag{5.87}$$

so that equality (5.86) sets the value of f. On the other hand, substituting (5.87) into the definition (5.34), we find the last of the required geometric characteristics

$$D = f = \alpha = \beta - (g(\beta)/g'(\beta)), \tag{5.88}$$

considering (5.86).

Thus, the representation of the fatigue failure of material in the inverse form from the sequence of period-doubling bifurcation scheme of the Feigenbaum period to the chaos provides the calculation formula for the generalized fractal dimension of the multifractal structure formed by the chain process of pairwise merging clusters of frustrons and reveals the extent of destruction. The geometric characteristics of the multifractal structures have thermodynamic counterparts.

All of this poses the problem for further development of a new direction in physics of metals—the fractal materials.

5.3   Multifractal Singularity Spectrum of Time Series

Many signals recorded in field experiments embody the paramount multifractals, and for a number of practical problems, it is quite important to have the rigorous mathematical approach to analyze the complexity of processes of different nature. The simple, or *monofractal*, signals (i.e., $1/f$—noise and Wiener random process) are homogeneous in the sense that their scaling characteristics remain unchanged in any scale range. The spectrum of signals $S(f) \sim f^{-\beta}$ is unchanged over a wide frequency range, i.e., β has a constant value. The multifractal processes permit an expansion into zones with various local scaling properties [29]. Therefore, for the

quantitative description of such processes a large number of characteristics are required. Particularly, the spectrum of multifractal processes cannot be described by power law distribution with a single exponent β.

There were several attempts to extend multifractals into the functional dependencies (signals) [29, 30]. One of these attempts was made on the basis of structural features, which were often used by different researchers. The approach received the widespread use in studying problems of highly developed turbulence [29, 31].

The multifractal approach for signals can potentially characterize the broad class of processes that are more complex than the processes described by one number (singular values of the fractal dimension or the scaling characteristics describing, for example, the frequency dependence of the spectral power density).

Analysis of the irregular functions, as well as the analysis of fractal measures, is carried out in terms of "singularity spectrum." However, when considering the functional dependencies (of the irregular signals), there are changes in symbols. Instead of the spectrum $f(\alpha)$, the analogous function $D(h)$ is considered, the Holder exponent $h(x_0)$ characterizing the local singular behavior of g at point x_0

$$|g(x_0 + l) - g(x_0)| \sim l^{h(x_0)},$$

corresponds to α, and $D(h)$ is the subset dimension for the analyzed data, characterized by the local exponent h_0.

There are several ways to calculate the singularity spectrum. As in the case of fractal measures, the calculations are complicated due to the slow convergence, and by the fact there can be other singularities in the local neighborhood of point x_0 while considering the irregular behavior. The "imposing" multiple singularities will lead to the significant errors in calculation of the scaling characteristics and the unstable results in the algorithm of numerical analysis due to various parameters. To improve the reliability of $D(h)$ calculations, the statistical analysis is carried out based on structural or partial functions (see Sect. 5.3.1).

Multiextreme functions have singularities (irregularities), the scaling parameters of which cannot be described by monofractal with one scaling parameter. There can be transient (crossover) time series scales s_x, sharing modes with different scaling exponents.

In other cases, the scaling behavior of the time series is even more complicated and various terms of series may their own scaling parameters. Finally, the various scaling parameters may overlap with each other (i.e., to form various mixtures) in some fractal subsets of the time series. In this case, to get a full description of scaling behavior of series, a large number of scaling parameters is required, which makes the multifractal analysis important.

There are two distinct types of multifractality for the time series [32]: (1) multifractality caused by the wide probability distribution (the density function) of terms of the time series, such as the Levy distribution. In this case, the multifractality cannot be eliminated by mixing terms of series; (2) multifractality caused by the long-range correlations of small and large fluctuations. In this case, the probability density function values may correspond to the regular distributions with finite

moments, such as a Gaussian distribution. The appropriate mixed series will be non-multifractal scaling behavior, since all long-range correlations are suppressed as a result of the mixing procedure. The accidental mixing of the term positions is the easiest way to generate a surrogate data; however, there are more effective alternatives that will be discussed below. In both described types of multifractality, the mixed series will have weaker multifractality than the original series.

The multifractal analysis of time series can also detect the correlation of high order. The multifractal scaling can be observed, for example, in 3- or 4-point correlations differing from the standard 2-point correlation studied in the traditional autocorrelation analysis. In addition, the multifractal scaling is also observed in small and large fluctuations with different scaling behaviors. For example, the extreme events can be more or less correlated than the typical events.

The simplest type of the multifractal analysis is based on the standard multifractal formalism of partial functions, designed to study the multifractal properties of normalized and stationary measures [30, 33–35]. Unfortunately, this standard formalism did not provide correct results for the non-stationary time series due to the strong influence of trends and the impossibility of their normalization.

Currently, there are two basic approaches to estimate the singularity of the time series. The first method appeared earlier and is based on the analysis of chain of points of modulus maxima of continuous wavelet transformation. The method of "modulus maxima of wavelet transformation" (MMWT), proposed in the early 1990s by Muzy et al. [36, 37], has a number of significant advantages: the ability to analyze a wide class of singularities—not only the signals themselves, but also their derivatives, less errors in calculation of scaling characteristics, etc. The WTMM technique that can be successfully used in studies of inhomogeneous processes of different nature is based on the wavelet analysis [38, 39], called the mathematical "microscope" because of its ability to maintain a good resolution at different scales. The second approach is closer to the first technique based on the dependence of the standard deviation or variance from the sample length [40]. Most recently, *detrended fluctuation analysis* (DFA) was developed and widely applied to analyze fluctuations after eliminating scale-dependent trends [41, 42]. The comparative analysis of methods shows that DFA is more reliable and stable. At the same time, for the special types of self-similar signals, which may include the range of constant values (such as the famous "devil's staircase" constructed on the basis of a Cantor set), DFA becomes inapplicable and the wavelet transformation evaluation is more practical [40].

5.3.1 Standard Multifractal Formalism and Singularity Spectrum

In the general multifractal formalism, a normalized measure $\mu(t)$, $t \in [0, 1]$ is considered, and the probability of cell hitting in the neighborhood of point t with size (scale) $s \ll 1$ is determined by

$$\tilde{\mu}_s(t) = \int\limits_{t-\frac{s}{2}}^{t+\frac{s}{2}} \mu(t')\mathrm{d}t.$$

The multifractal approach is based on the partial function

$$Z_q(s) = \sum_{v=0}^{\frac{1}{s}-1} \tilde{\mu}_s^q \left[\left(v + \frac{1}{2} \right) s \right] \sim s^{\tau(q)} \text{ at } s \ll 1, \qquad (5.89)$$

where $\tau(q)$—the Rényi scaling parameter of and q—the material parameter can take both positive and negative values. Sometime, the exponent $\tau(q)$ has the negative sign (see, e.g., [33]). The object is called monofractal (or self-affine) if the Rényi scaling parameter $\tau(q)$ linearly depends on q; otherwise, it is called multifractals.

The generalized fractal dimension D_q is associated with $\tau(q)$ through the equation $D_q = \tau(q)/(q-1)$ (see Eq. (5.4)), so that the fractal dimension of carrier is equal to $D_0 = -\tau(0)$ and the correlation dimension is equal to $D_2 = -\tau(2)$.

In the time series with terms $\{x_i\}$, $i = 1 \ldots N$, there may also be negative numbers. Therefore, assuming $N_s = [N/s]$, where $[a]$—the whole part of number a, and

$$X(v, s) = \sum_{i=1}^{s} x_{vs+i} \text{ for } v = 0, 1, \ldots, N_s - 1,$$

we can determine [33, 34]

$$Z_q(s) = \sum_{v=0}^{N_s-1} |X(v, s)|^q \sim s^{\tau(q)} \text{ at } s > 1. \qquad (5.90)$$

For each segment $v = 0, 1, \ldots, N$, we compute *profile* of series (the integrated data)

$$Y_v(j) = \sum_{i=1}^{j} \left(x_{vs+i} - \langle x_{vs+i} \rangle_s \right) = \sum_{i=1}^{j} x_{vs+i} - \frac{j}{s} \sum_{i=1}^{s} x_{vs+i}. \qquad (5.91)$$

If the series has an average value $\langle x \rangle = 0$, then (5.91) takes form

$$Y_v(j) = \sum_{i=0}^{j} x_{vs+i} \qquad (5.92)$$

and the global profile, that is the cumulative sum has form

$$Y(j) = \sum_{i=0}^{j} x_i, \quad j = 0, 1, \ldots, N. \tag{5.93}$$

The method of fluctuation analysis (FA) discusses the profile fluctuations at the end of each segment $v = 0, 1, \ldots, N - 1$

$$F_{FA}^2(v, s) = [Y(vs) - Y((v+1)s)]^2 \tag{5.94}$$

and likewise for the segments $v = N_s, \ldots, 2N_s - 1$

$$F_{FA}^2(v, s) = [Y(N - (v - N_s)s) - Y(N - (v + 1 - N_s)s)]^2, \tag{5.95}$$

Averaging $F_{FA}^2(v, s)$ for all segments, we obtain the average fluctuation

$$F_2(s) = \left[\frac{1}{2N_s} \sum_{v}^{2N_s - 1} F_{FA}^2(v, s) \right]^{\frac{1}{2}} \sim s^{\alpha}. \tag{5.96}$$

For the uncorrelated values of x, $F_2(s)$ is Fick's diffusion and $F_2(s) \sim s^{1/2}$. In the case of long-range correlations in series $\{x_k\}$, when the correlation $C(s)$ changes according to the power law $C(s) \propto s^{-\gamma} (0 < \gamma < 1)$, $F_2(s)$ increases according to the power law.

$$F_2(s) \sim s^{\alpha} \text{ with } \alpha \approx H, \tag{5.97}$$

where the fluctuation exponent α coincides with the Hurst exponent H for the monofractal data, and it is linked with β and γ through equality

$$2\alpha = 1 + \beta = 2 - \gamma, \tag{5.98}$$

where β—the scaling parameter of the power spectrum $s(f) \sim f^{-\beta}$.

Substituting into (5.90) $Y(j)$ and $F_{FA}(v, s)$ from (5.93) and (5.94), respectively, we obtain

$$Z_q(s) = \sum_{v=0}^{N_s - 1} \left\{ [Y((v+1)s) - Y(vs)]^2 \right\}^{q/2} = \sum_{v=0}^{N_s - 1} F_{FA}^{q/2}(v, s). \tag{5.99}$$

Comparing (5.98) with (5.96), we see that the multifractal formalism can be regarded as the generalized version of the FA, where the exponent 2 is replaced by q. For example (using the summation of partial sums of the second order),

$$F_2(s) \sim \left[\frac{1}{N_s} Z_2(s) \right]^{\frac{1}{2}} \sim s^{[1+\tau(2)]/2} \Rightarrow 2\alpha = 1 + \tau(2) = 1 + D_2. \qquad (5.100)$$

It follows that all research methods of (mono) fractal properties of time series are based on the correlation dimension $D_2 = 2\alpha - 1 = \beta = 1 - \gamma$ (see Eq. (5.98)).

In addition, we can directly determine the generalized (multifractal) Hurst exponent $h(q)$, which characterizes the scaling behavior of q-moment of fluctuations [30, 35]

$$F_2(s) \sim \left[\frac{1}{N_s} Z_2(s) \right]^{\frac{1}{2}} \sim s^{[1+\tau(2)]/2} = s^{h(q)} \Rightarrow h(q) = \frac{1+\tau(q)}{q} \qquad (5.101)$$

with $h(q) = \alpha \approx H$.

Another characteristic of the multifractal time series is the singularity spectrum $f(\alpha)$, which is related with $\tau(q)$ by the Legendre transformation [33, 34]

$$\alpha = \frac{\mathrm{d}}{\mathrm{d}q} \tau(q) \text{ and } f(\alpha) = q\alpha - \tau(q). \qquad (5.102)$$

There α—the degree of singularity or the Hölder exponent, and $f(\alpha)$ is the dimension of subset series, characterized by the same α. From (5.101), we can obtain the relationship between α and $f(\alpha)$ with $h(q)$:

$$\alpha = h(q) + qh'^{(q)} \quad \text{and} \quad f(\alpha) = q[\alpha - h(q)] + 1.$$

There are also other versions of the multifractal analysis proposed by A.B. Chabroy and R.V. Jensen [43]. These versions do not require the Legendre transformation, they are based on following expressions to build the multifractal spectrum

$$\alpha(q) = \frac{\mathrm{d}\tau}{\mathrm{d}q} = \lim_{\varepsilon \to 0} \frac{\sum_i \mu_i(q) \ln p_i}{\ln \varepsilon},$$
$$f(q) = q\alpha(q) - \tau(q) = \lim_{\varepsilon \to 0} \frac{\sum_i \mu_i(q) \ln \mu_i(q)}{\ln \varepsilon}. \qquad (5.103)$$

There $\mu_i(q) = p_i^q / \sum_i p_i^q$ and p_i are probabilities that the studied set A hit the cell i of size ε of the hypothetically divided space to which the set A belongs to.

According to Eq. (5.103), we can construct an algorithmic function $f(\alpha) = f(q(\alpha))$, where $q(\alpha)$—the inverse function of $\alpha(q)$. Thus, the obtained singularity spectrum $f(\alpha)$ with a high degree of accuracy coincides with the same spectrum built on the basis of the standard procedure of multifractal formalism.

5.3.2 Wavelet Transform Modulus Maxima Method

As it follows from the name of method, the wavelet transform is the decomposition of signal on basis constructed from the soliton-like function (wavelet) with specific properties by means of scaling changes and transformation. Each of these functions characterizes a certain spatial or time frequency, and its location in physical space or time.

The continuous wavelet transform of function $g(x)$ is defined by the following formula

$$W(a,b) = \frac{1}{\sqrt{a}} \int\limits_{-\infty}^{+\infty} g(x)\psi\left(\frac{x-b}{a}\right) dx, \tag{5.104}$$

where a—the scale parameter, b—the coordinates in space or in moment of time, ψ—the soliton-like function (wavelet) with certain properties and constructed, for example, on derivatives of Gaussian function:

$$\psi^{(m)} = (-1)^m \frac{d^m}{dx^m}\left[e^{\left(-\frac{x^2}{2}\right)}\right], \tag{5.105}$$

Studying of local singularities of function $g(x)$ is usually considered at $m = 1$ ("WAVE" wavelet) or $m = 2$ ("MHAT" wavelet). The higher-order derivatives are rarely used. The choice of basis functions ψ is an important moment—we have to choose such a wavelet that allows us to see the information we need. The different functions can be interpreted as choosing microscope of right resolution; if the chosen resolution allows us to see the necessary details, then the wavelet is suitable for purpose. The subsequent choice of lenses does not provide anything new.

The Hölder exponent describes the singularity degree of function g. Its rigorous mathematical definition can be defined as follows [11]. Let us consider the case where the function g is differentiated n-times at point x_0, the $(n+1)$-th derivative does not exist. We can use Taylor expansion from x to n inclusive for function $g(x)$. The resulting series (the polynomial of degree n) is denoted by $P_n(x)$. The Hölder exponent at point x_0 is called the greatest value of h, when the following inequality holds

$$|g(x) - P_n(x - x_0)| \le C|x - x_0|^h. \tag{5.106}$$

The greater h, the more regular (more "smooth") is the function g. The integration of this function increases the value of h by 1, and the differentiation decreases. Suppose that the analyzed singular functions within the neighborhood $x = x_0$ can be represented in form of two terms

$$g(x) = P_n(x) + C|x - x_0|^{h(x_0)}, \tag{5.107}$$

i.e., as the sum of the regular component (the polynomial P_n) and some term that defines the irregular behavior and represented by a non-whole number $h(x_0)$. One of the features of wavelet transform, widely used to remove polynomial components from signal, is that wavelets with first m nil moments

$$\int\limits_{-\infty}^{+\infty} x^k \psi(x) \mathrm{d}z = 0 \ (k = 1, \ldots, m),$$

are the orthogonal polynomials with power m inclusive, and $m \geq n$:

$$\int\limits_{-\infty}^{+\infty} P_n(x)\psi(x)\mathrm{d}x = 0. \tag{5.108}$$

Therefore, the wavelet transform function $g(x)$ takes form

$$W(a, x_0) = Ca^{1/2} \int\limits_{-\infty}^{+\infty} \psi(x)|ax|^{h(x_0)}\mathrm{d}x.$$

In order to simplify the analysis in [44], it is suggested to slightly change the definition of wavelet transform, by multiplying the expression (5.104) with $1/\sqrt{a}$

$$W(a, x_0) = \frac{1}{a} \int\limits_{-\infty}^{+\infty} \psi\left(\frac{x - x_0}{a}\right)g(x)\mathrm{d}x. \tag{5.109}$$

In this case, at $a \to \infty$, there is a simple power law

$$W(a, x_0) \sim a^{h(x_0)}. \tag{5.110}$$

Thus, if the function $g(x)$ has a singularity at point $x = x_0$, then its local singular behavior is characterized by a power law of form (5.110). If this function is continuously differentiable up to order m at point x_0, then $a \to \infty$

$$W(a, x_0) \sim a^m.$$

In problems of studying the signal structure, the function $g(x)$ is analyzed more frequently, rather its derivatives. The signal is locally characterized by the dependence of the Hölder exponent on the signal point, and the Hölder exponent is easily calculated from the rate of decrease of wavelet coefficients with the scale a. The faster rates decrease at $a \to 0$, the more regular function at this point.
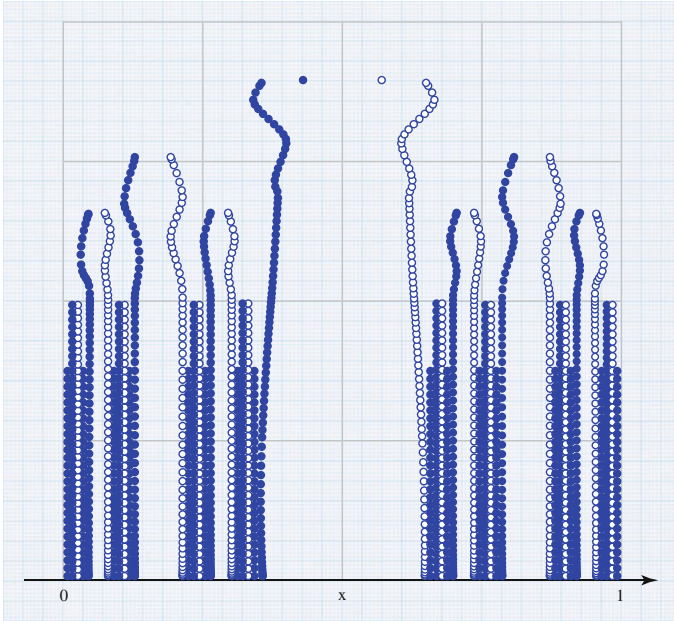
Fig. 5.5 The skeleton or the *lines* of local extreme surface coefficients $W(a,x)$: the local minimums (*open circles*) and maximums (*filled circles*)

Thus, the values of $W(a,x)$ in the neighborhood of the local feature may differ or abnormally decline at slow rate. Such behavior of wavelet coefficients permits the detailed analysis of structure of singularities.

The WTMM algorithm assumes studying of the irregular behavior of the function $g(x)$ through two stages. In the first stage, the wavelet transform is according to the formula (5.109). The result of wavelet transform can be interpreted as a surface in 3-dimensional space. The most important information is included in the "skeleton" or lines of local extreme surface coefficient $W(a,x)$, search of which is performed at each scale a (Fig. 5.5).

The type of information extracted from $g(x)$ determines the selection of basis function. The required condition is that the selected wavelet should not be less smooth than the analyzed signal. Selecting a parameter m (5.105), it should be noted that, increasing m allows ignoring the large-scale polynomial components (removing trend) and analyzing the small-scale variations of that function. On the other hand, the repeated differentiation leads to an increase in the number of lines of local extremums of wavelet coefficients and an emergence of a large number of additional lines terminating at small scale. Such lines are short to assess the degree of dependency of the form (5.110) and act as noises in the numerical analysis of singularities. The wavelet transform is arranged in a such way that $W(a,x_0)$ is a regular function even when $g(x)$ is irregular [45]. All information about $g(x)$, including its localization at x_0 and the indicator $h(x_0)$, is in the asymptotic behavior

of the coefficients of $W(a, x_0)$ at small a. If the coefficient diverge at small scales, then g has a singularity at x_0, and the Hölder exponent can be determined by presenting dependence (5.110) in the double-logarithmic scale and calculating the tangent of $\ln W(a, x_0)$ from $\ln a$. If the coefficients of $W(a, x_0)$ are close to zero within x_0 at small scales, then g is regular at this point. An important part of calculating the Hölder exponents is that the desired characteristics are theoretically independent from the basis functions of wavelet transform, which suggests that the analysis of local irregularities in some sense, is universal (although the wavelet decomposition on selected basis, of course, dependent).

Exposing the "skeleton" ends the first stage of the WTMM algorithm. The theoretical analysis of the highlighted lines of local extremums of local maximums of the wavelet transform modules allows us to calculate the Hölder exponent and analyze the singularity of function $g(x)$. However, this approach is inaccurate—an increase in scale affects on neighboring irregularities, leading to various errors.

In the multifractals theory, it is preferred to calculations based on statistical functions allowing to get more reliable estimates of the calculated characteristics. Therefore, the second stage of the WTMM is in construction of the function $Z(q, a)$, called statistical functions, according to the formula (compare with partial functions from (5.3)):

$$Z(q, a) = \sum_{l \in L(a)} |W(a, x_l(a))|^q, \tag{5.111}$$

where $L(a)$—the set of all possible lines (l) of local modulus maxima of wavelet coefficients existing at the scale a; $x_l(a)$ describes the location of maxima at that corresponding to the line l. In this case, the key moment is that the modulus of wavelet coefficients ensures the stability of method. Without it (including information about the phases) the method would not get a stable solution. Generally, the consideration of maxima can create problems in terms of stability of the method (it is better to use averages). However, the wavelet transform involves the computation of coefficients within the time-frequency framework that automatically provides averaging. The definition (5.111) is not suitable for negative q, because of situation when $W(a, x_l(a)) = 0$. Therefore, in practice, the different formula is used:

$$Z(q, a) = \sum_{l \in L(a)} \left(\sup_{a' \leq a} |W(a', x_l(a'))| \right)^q, \tag{5.112}$$

that is the maximum value of the modulus coefficients of wavelet—transform is selected along each line at the scale smaller than a predetermined value a. Usually, the following relationship is done

$$Z(q, a) \sim a^{\tau(q)}, \tag{5.113}$$

where the value of $\tau(q)$, defined for some q by calculating the slope between $\ln Z(q, a)$ and $\ln a$, is called the *scaling exponent*, in analogy with the case of singular measures. The variations of powers of q while constructing the partition functions (5.112) yield the linear dependence $\tau(q)$ for the monofractal objects $(H = \mathrm{d}\tau/\mathrm{d}q \neq \mathrm{const})$ and the nonlinear dependence $\tau(q) = gh - D(h)$ with a large number of Hölder exponents $h(q) = \mathrm{d}\tau/\mathrm{d}q \neq \mathrm{const}$ for the multifractals.

For some values of q, the scaling exponents $\tau(q)$ has a simple interpretation. Thus, there is a bond between $\tau(2)$ and the exponent β of the spectral power density function $S(f) \sim 1/f^{\beta}$

$$\beta = 2 + \tau(2).$$

Given the fact that the spectral power density function in turn is related to the correlation function through the Fourier transform, knowing β allows us to determine the deceleration rate of correlation $\psi(\tau) \sim \tau^{-\gamma}$, i.e., the index γ. The relationship between the main variables, considered within the WTMM algorithm framework, is determined by the Legendre transformation (compare (5.36) with $h = \alpha$ and $D(h) = f(\alpha)$):

$$\begin{cases} h = \frac{\mathrm{d}\tau}{\mathrm{d}q}, \\ D(h) = gh - \tau(q). \end{cases} \tag{5.114}$$

Unlike the structural function method based on wavelet transform, the multifractal analysis allows you to explore singularity for negative values of q. Statistical functions $Z(q, a)$ for $q < 0$ characterize the scaling features for the weak singularities (the small fluctuations), and at $q < 0$ for the strong singularities (the large fluctuations).

The wavelet transform method setting the foundation of WTMM is the best tool to study the self-similarity properties (in terms of wavelet coefficients that mean exponential behavior of higher moments while scaling). The method is well suited for solving physical problems, since it operates with features that already familiar to physicists. In particular, the singularity spectrum contains information, on the one hand, on the correlation properties of the analyzed process (which are among the basic properties in the theory of stochastic processes), and, on the other hand, on the degree of signal uniformity the quantitative measure of which is the width of the function $D(h)$ [46].

One feature of analyzing the local regularity of signal based on the coefficients of wavelet transform is that the calculation of the Hölder exponent is theoretically independent from the basic wavelet. In practice, however, this relationship is still obvious. The most well-known works used "WAVE" or "MHAT" as the basis functions (1st and 2nd derivatives of Gaussian function, respectively). If the derivatives of high order are used to analyze wavelet, the number of additional short lines of the local maximums $W(a, x_0)$ increases, resulting in oscillating "tails" of soliton-like functions $\psi(m)$. In this situation, it is necessary to find a compromise

between ignoring the polynomial components (trend), where it is desirable to increase the parameter m, and significant increase of number of short lines in local maximums, which complicate the skeleton and lead to the deviations from the power dependence in the small scales. In practice, it is recommend using a small m (usually, $m \leq 2$) for the multifractal analysis.

The wavelet transform multifractal analysis can be considered as a method of research of spectral-correlation properties of different processes, including non-stationary. It follows, in particular, from (5.108), that slow non-stationary (the polynomial trend) processes does not affect the result, if ψ is selected as the basis function with the first few moments as zero. Besides the non-stationary problem, WTMM can demonstrate another advantage over the classical spectral analysis based on the Fourier transform. Being an instrument of "local" studies of the structure of time functions, the multifractal analysis allows us to assess the correlation properties of random processes at relatively short signals.

One of the limitations of multifractal analysis is that it assesses the upper skirt of the real multifractal spectrum. This can lead to the erroneous interpretation of results of numerical analysis. Firstly, if the true singularity spectrum $D(h)$ is discrete, that is, h takes only a discrete set of values, the skirt will include "false" points while representing interpolation of the discrete spectrum $D(h)$. Second, the skirt does not identify the "internal" points not included into the upper skirt of the spectrum $D(h)$, if there is such (Fig. 5.6). The "bell" shape of spectrum of singularities can be obtained even in the case, where WTMM is used for the signal processing without multifractal properties. If the process is characterized by not a continuous spectrum $D(h)$, but by a small set of discrete Hölder components, then by obtaining the skirt similar to one shown in Fig. 5.6, in general, we cannot certainly say whether there is a singularity, characterized by h equal to, for example, 0.63 ± 0.005.

In order to avoid difficulties in interpreting the results, it is better not to analyze, finite, or infinite number of scaling characteristics, and consider WTMM as tool of numerical analysis, which allows to evaluate the range of the Hölder exponents (the degree of multifractality) and characterize the presence of various types of correlations in the non-stationary random processes. Thus, we are able to carry out a correlation analysis of the non-stationary signals of short duration and evaluate quantitatively the homogeneity of random process.

5.3.3 Multifractal Fluctuation Analysis

The time series analysis is the basis for development and verification of macroscopic models that allow in a consistent manner to represent the evolution of complex systems on the basis of microscopic data [47]. Such an analysis is reduced to the calculation of the correlation functions of the state vectors that represent the time series characterizing the system. Being traditionally the part of statistics, the time series analysis is based on the class of models of the harmonic oscillator that meet the
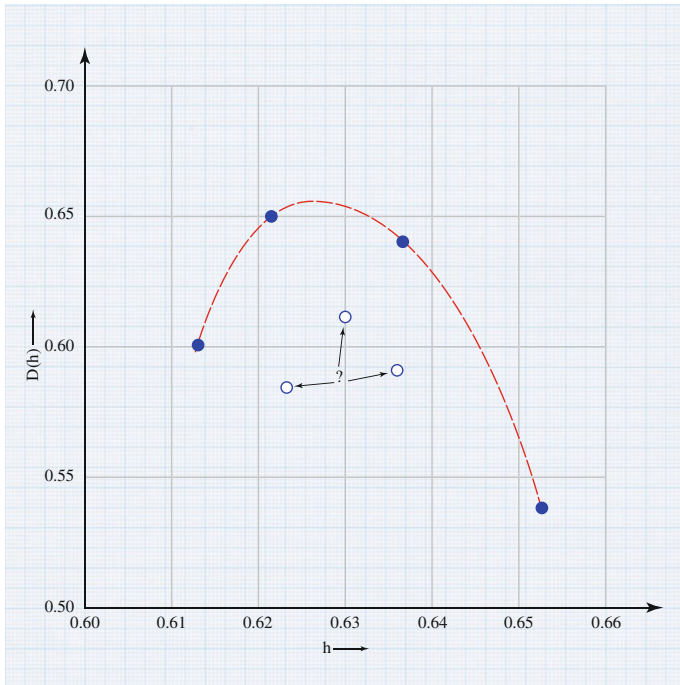
Fig. 5.6 The illustrations show the limitations of multifractal formalism. The *circles* represent the true multifractal spectrum, the *dotted line*—the result of applying the multifractal analysis. The inside circle (*white circle*) cannot be identified from WTMM

simplest case of a Gaussian random process [48]. However, in reality it turns out that the real time series matches the Levy flight than the Gaussian processes, which is its individual case [49]. The truncated Levy flight in high-volume processing of n converges to the Gaussian process, and the convergence is essentially controlled by the third moment of the dynamic variable $|x|$ [50]. The well-known feature of the Levy flight is their invariance under scale transformations [51], and therefore, the time series studies is the analysis of the self-similar stochastic processes, which are presented by the (multi) fractal sets [33]. The statistical description of the self-similar time series, based on the thermodynamic model [52], defines their global characteristics by determining the predictability of changes of a random variable. However, the local properties fall out of view, the understanding of which is achieved under the multifractal fluctuation analysis (MFFA), or as it is called multifractal detrended fluctuation analysis (MF-DFA) [41].

The multifractal fluctuation analysis (MF-DFA) method consists of five steps. The first three steps are substantially identical to the detrended fluctuation analysis (DFA) [53–58].

Consider the series $\{x_k\}$ with length N and a compact carrier. The carrier is defined as a set of values k, where $x_k \neq 0$. The carrier is considered compact if the

zero values of x_k represent only a small part of the series, assuming that corresponding values of k number is irrelevant.

Step 1. Define the "profile" of series

$$Y(i) \equiv \sum_{k=1}^{i} [x_k - \langle x \rangle], \quad i = 1, \ldots, N. \tag{5.115}$$

Subtracting the average value $\langle x \rangle$ is not compulsory, because it is leveled at detrending at the third step of algorithm.

Step 2. Let divide the profile $Y(i)$ into $N_s = [N/s]$ disjoint segments with equal lengths s. Since the length N is not a multiple of the time scale s, at the end of the profile after partition, there might remain a segment with length less than s. In order to evaluate this part of the series, we repeat the partition starting from the end of the series. Thus, we get $2N_s$ segments of the partition.

Step 3. We calculate the local trend for each of $2N_s$ segments applying least squares (OLS). Then, the variance of series is written as

$$F^2(v, s) \equiv \frac{1}{s} \sum_{i=1}^{s} \{Y[(v-1)s + i] - y_v(i)\}^2 \tag{5.116}$$

for segments $v = 1, \ldots, N_s$, going straight forward, and how

$$F^2(v, s) \equiv \frac{1}{s} \sum_{i=1}^{s} \{Y[N - (v - N_s)s + i] - y_v(i)\}^2 \tag{5.117}$$

for the inverse sequence $v = N_s + 1, \ldots, 2N_s$. Here, $y_v(i)$—the polynomial, approximates the series at segment v. We can use linear, quadratic, cubic, and higher-order polynomial, we call the appropriate procedure of approximation as DFA1, DFA2, DFA3, … [53, 54, 59].

Since such detrending of time series is equivalent to the subtraction of polynomial values from the profile, the DFA of different orders will have different qualities to exclude the trend from series. Comparison of results using DFA of different orders will help to assess the type of polynomial trend in the series [56, 57].

Step 4. Enter the deformed dispersion

$$F_q(s) \equiv \left\{ \frac{1}{2N_s} \sum_{v=1}^{2N_s} [F^2(v, s)]^{\frac{q}{2}} \right\}^{\frac{1}{q}}, \tag{5.118}$$

obtained by raising the expressions (5.116), (5.117) to the power of q and then averaging across all segments (the case $q = 0$ is considered separately in Step 5). In order to establish how moments $F_q(s)$ depends on the time

scale s at different values of q, we must repeat steps 2–4 for different values of s. Obviously, $F_q(s)$ will increase while increasing s. Of course, $F_q(s)$ is dependent on the order of m of the DFA procedures. Due to the construction, $F_q(s)$ is defined only for $s \geq m + 2$.

Step 5. Determine the dependence of the fluctuation function s on the change of scale by analyzing the points $\left(F_q(s), s\right)$ in the two-logarithmic coordinates. If the studied series is reduced to self-similar sets, exhibiting the long-range correlations, the fluctuation function $F_q(s)$ represents the power dependence

$$F_q(s) \sim s^{h(q)} \text{ at } s \gg 1 \tag{5.119}$$

with the generalized Hurst exponent $h(q)$, the value of which is determined by the parameter q. From the definitions (5.118) and (5.119), it follows that for $q = 2$ this parameter is reduced to the well known the Hurst parameter H [48]. For the time series that match the monofractal set, the fluctuation function $F^2(v, s)$ is the same for all segments of v, and the Hurst parameter $h(q) = H$ does not depend on the deformation parameter q. For the multifractal series when q is positive, the main contributions to the function $F_q(s)$ are made by the segments with the great deviation $F^2(v, s)$, and when q is negative, the segments with small variances are dominant. As a result, we can conclude that for negative values of q the generalized Hurst parameter $h(q)$ describes the segments exhibiting small fluctuations, and if positive—great.

For very large time scales $s > N/4$, the function $F_q(s)$ loses its statistical informativeness, due to a smallness of number $N_s < 4$ of segments used in the averaging. In addition, the systematic deviations from a scaling behavior (5.119) for the function $F_q(s)$ occur at very small time scales $s \approx 10$. Thus, carrying out this procedure assumes the exclusion, on the one hand, of the large segments of $(s > N/4)$, and on the other—small ones $(s < 10)$.

Since at $q = 0$, the Eq. (5.118) contains uncertainty and the ultimate expression should be used instead

$$F_0(s) \equiv \exp\left\{ \frac{1}{4N_s} \sum_{v=1}^{2N_s} \ln\left[F^2(v, s)\right] \right\}^{\frac{1}{q}} \sim s^{h(0)}. \tag{5.120}$$

We note that $h(0)$ cannot be determined for the time series with a fractal carrier, because in that case $h(q)$ diverges at $q \to 0$.

Typically, the large fluctuations are characterized by a smaller scaling parameter $h(q)$ for the multifractal series rather than small fluctuations. This is due to the following reasons.

For maximum scale $s = N$, the fluctuation function $F_q(s)$ does not depend on q, since the sum in (5.118) goes through only two identical segments ($N_s \equiv [N/s] = 1$). For very small scale $s \ll N$, the averaging procedure goes through several segments, and the average value of $F_q(s)$ will dominate $F_q(s)$ from the segments with small (large) fluctuations if < 0 ($q > 0$). Thus, for $s \ll N$, the values of $F_q(s)$ at $q < 0$ will be less than the value of $F_q(s)$ at $q > 0$, while when $s = N$ these two values are equal. Therefore, if we assume a uniform scaling behavior $F_q(s)$, following from (5.119), then the slope $h(q)$ of the function $F_q(s)$ with respect to s in the two-logarithmic coordinates at $q < 0$ is greater than at $q > 0$. Thus, $h(q)$ for $q < 0$ is greater than for $q > 0$.

However, the MF-DFA method can be used only in case of the *positive* generalized Hurst parameter $h(q)$ and becomes inapplicable for strictly uncorrelated signals when $h(q)$ is close to zero. In these cases, we should use a modified method (MF-DFA). The easiest way to analyze such data is the preliminary integration of the time series before MF-DFA. Therefore, we replace the *single* summation in (5.115), which describes the profile of the primary data x_k, by the *double* summation

$$\tilde{Y}(i) \equiv \sum_{k=1}^{i} [Y(k) - \langle Y \rangle]. \tag{5.121}$$

Following further the above procedure of MF-DFA, we obtain the generalized fluctuation function $\tilde{F}_q(s)$, describing the scaling law in the Eq. (5.119), but with a large parameter $\tilde{h}(q) = h(q) + 1$

$$\tilde{F}_q(s) \sim s^{\tilde{h}(q)} = s^{h(q)+1}. \tag{5.122}$$

Thus, the scaling behavior can be determined even when $h(q)$, which is less than zero (but greater than 1) for some values of q. Note that $\tilde{F}_q(s)/s$ corresponds to $F_q(s)$ in the Eq. (5.119). If we subtract the mean values at each step of summation in the Eq. (5.121), then the summation leads to the quadratic trend in the profile $\tilde{Y}(i)$. In this case, we have to use at least MF-DFA of the second order to eliminate these artificial trends.

The bond between MF-DFA and the standard multifractal analysis is set as following [42]. For the stationary normalized time series defining the measure with the compact carrier, the multifractal scaling parameters of $h(q)$, given by the Eq. (5.119), are directly connected, as it will be shown later, with the scaling parameter $\tau(q)$ (so-called the mass index), defined by the standard multifractal formalism based on partial functions (see Sect. 5.3.1).

Assuming that the series x_k with length N is fixed, positive and normalized sequence, i.e., $x_k \geq 0$ and

$$\sum_{k=1}^{N} x_k = 1.$$

Then, MF-DFA does not require the first 3 steps, because the studied does not have a trend. Thus, in this case, DFA may be replaced by the standard FA, which is identical to DFA, except for the simplified determination of the dispersion for each segment $v = 1, \ldots, N_s$ in Step 3 (see Eq. (5.117))

$$F_{FA}^2(v, s) \equiv [Y(vs) - Y((v-1)s)]^2. \tag{5.123}$$

Substituting (5.123) into (5.118) and using (5.119), we obtain

$$\left\{ \frac{1}{2N_s} \sum_{v=1}^{2N_s} |Y(vs) - Y((v-1)s)|^q \right\}^{\frac{1}{q}} \sim s^{h(q)}. \tag{5.124}$$

For simplicity, we assume that the length of series N multiple of scale s, we have $N_s = N/s$, and therefore,

$$\sum_{v=1}^{N/s} |Y(vs) - Y((v-1)s)|^q \sim s^{qh(q)-1}. \tag{5.125}$$

It is obviously that the difference $Y(vs) - Y((v-1)s)$ in (5.125) is the sum of x_k, within each segment v of size s. This amount is the probability $p_s(v)$ of entering into the cell (or box) in the standard multifractal formalism for the normalized series x_k:

$$p_s(v) \equiv \sum_{k=(v-1)s+1}^{vs} x_k = Y(vs) - Y((v-1)s). \tag{5.126}$$

The scaling parameter $\tau(q)$ is usually determined by the partial function $Z_q(s)$:

$$Z_q(s) \equiv \sum_{v=1}^{N/s} |p_s(v)|^q \sim s^{\tau(q)}, \tag{5.127}$$

where q—the real parameter, such as in MF-DFA. Sometimes, $\tau(q)$ is defined with the opposite sign (see [34]).

Taking into account (5.126), the Eq. (5.127) is equivalent to the Eq. (5.125), we find the relation between the two sets of scaling parameters

$$\tau(q) = qh(q) - 1. \tag{5.128}$$

So, the generalized Hurst parameter in the Eq. (5.119) for MF-DFA is directly related to the classic multifractal scaling parameter $\tau(q)$.

The results of application to the time series the methods of multifractal fluctuation analysis (MF-DFA) and the wavelet transform maxima modulus (WTMM) shows that MF-DFA has slightly greater sensitivity toward data [41, 42, 60]. In particular, MF-DFA has a slight advantage at the negative values of q and short series. In other cases, the results for both methods are approximately the same. The main advantage of MF-DFA, as compared to WTMM, is the simplicity of algorithm. However, MF-DFA is limited to the study of data with the one-dimensional carrier, while WTMM does not have such restriction. Both methods are generalized for the case of multidimensional data: MF-DFA [61] and WTMM [62].

5.3.4 Simple Multifractal Time Series Models

One of the simplest models of multifractal data, most commonly used in hydrology for example [63], is the multifractal cascade model [30, 33, 41]. In this model, the series $\{x_i\}$ of length $N = 2^{n_{\max}}$ are constructed recursively. The generation of $n = 0$ terms is constant in the series, i.e., $x_i = 1$ for all $i = 1\ldots N$.

The first half of the term is multiplied by a factor a, and the other half by b in the first step of cascade (the generation $n = 0$). This leads to $x_i = a$ for $i = 1, \ldots, N/2$, and $x_i = b$ to $i = N/2 + 1, \ldots, N$. The factors a and b lie between zero and one, $0 < a < b < 1$. For the model, it is not necessary that $b = 1 - a$, which is often used in the literature [33]. In the second step (the generation $n = 2$), the procedure from Step 1 is used toward two successive terms, which leads to $x_i = a^2$, for $i = 1, \ldots, N/4$, $x_i = ab$ for $i = N/4 + 1, \ldots, N/2$, $x_i = ba = ab$ for $i = N/2 + 1, \ldots, 3N/4$ and $x_i = b^2$ for $i = 3N/4 + 1, \ldots, N$. In the $(n+1)$-th step, the elements obtained at step n are divided into two sequences of equal length, the first half of x_i is multiplied by a, and the other half by b. For example, at the generation $n = 3$ we get series of 8 elements: $a^3, a^2b, a^2b, ab^2, a^2b, ab^2, ab^2, ab^3$. After the step $n_{\max}$, it reaches the final generation, all subsequence of which that will have length equal to 1 and they cannot be split any further split. The final elements can be written as

$$x_i = a^{n_{\max} - n(i-1)} \cdot b^{n(i-1)}. \tag{5.129}$$

where $n(i)$ is the number of units in the binary representation of i, such as $n(13) = 3$, because 13 corresponds to a binary number of 1101.

For the multiplicative cascade model, the formula for $\tau(q)$ can be established immediately [30, 33, 41]

$$\tau(q) = [-\ln(a^q + b^q) + q \ln(a + b)] / \ln 2 \tag{5.130}$$

or

$$h(q) = \frac{1}{q} - \frac{\ln(a^q + b^q)}{q \ln 2} + \frac{\ln(a+b)}{\ln 2}. \qquad (5.131)$$

Equation (5.131) follows from (5.128) and (5.130). In particular, when $a = p, b = 1 - p$ we obtain formula [41]

$$\tau(q) = -\frac{\ln(p^q + (1-p)^q)}{\ln 2}. \qquad (5.132)$$

$$h(q) = \frac{1}{q} - \frac{\ln(p^q + (1-p)^q)}{q \ln 2}. \qquad (5.133)$$

Equations (5.132) and (5.133) describe the binary Cantor multifractal [33], corresponding to it the binomial series is defined as

$$x_i = p^{n(i-1)} \cdot (1-p)^{n_{\max} - n(i-1)}. \qquad (5.134)$$

where $n(i)$—the number of units in the binary code of number i, and the parameter p determines the probability $0.5 < p < 1$. Obviously, such series will consist of $N = 2^{n_{\max}}$ members $x_i(i = 1, \ldots, N)$, the number of which is limited to the maximum rate $n_{\max}$.

The binomial series (5.134) is usually used to test MF-DFA (see, e.g., [64]). Generating it according to the definition (5.134), it is easy to find the multifractal characteristics of $\tau(q)$ and $h(q)$ using MF-DFA and compare them with the exact values from (5.132) and (5.133).

It is easy to see that the model (5.129) $h(1) = 1$ for all a and b. Thus, at $q = 1$ this model describes the process with the Hurst parameter $H = 1$, which is determined from the R/S method.

In order to generalize the multifractal cascade process so that $h(1)$ will take on any value we must be subtracted from $h(q)$ its difference $\Delta h = \ln(a+b)/\ln 2$ [65]. Constant difference Δh corresponds to the long-range correlations presented in the multiplicative cascade model. To get the process without difference Δh, we can rescale the power spectrum series. Therefore, we calculate the fast Fourier transformation (FFT) from the signal $\{x_i\}$ transforming the simple multiplicative cascade process into the frequency domain. Then, we multiply all the coefficients in the Fourier series by $f^{-\Delta h}$, where f—the frequency. Then, the slope β of the power spectrum $S(f) \sim f^{-\beta}$ to the axis f will shift from values $\beta = 2h(2) - 1 = [2\ln(a+b) - \ln(a^2 + b^2)]/\ln 2$ to the lower values $\beta' = 2[h(2) - \Delta h] - 1 = -\ln(a^2 + b^2)/\ln 2$. Finally, by inverse FFT we return the signal back into the time domain.

Let us consider another simple multifractal model—the so-called the bifractal model that is well suited for data modeling, multifractality of which is without doubt [66]. For the bifractal model, the exponents of Rényi is characterized by two different slopes α_1 and α_2:

$$\tau(q) = \begin{cases} q\alpha_1 - 1, & q \le q_x \\ q\alpha_2 + q_x(\alpha_1 - \alpha_2), & q > q_x \end{cases} \qquad (5.135)$$

or

$$\tau(q) = \begin{cases} q\alpha_1 + q_x(\alpha_2 - \alpha_1) - 1, & q > q_x \\ q\alpha_2 - 1, & q \le q_x \end{cases}. \qquad (5.136)$$

Using (5.101), we find that $h(q)$ is represented in the form of the plane stretching from $q = -\infty$ to q_x and breaks down into hyperboles at $q > q_x$:

$$h(q) = \begin{cases} \alpha_1, & q \le q_x \\ q_x(\alpha_1 - \alpha_2)\frac{1}{q} + \alpha_2, & q > q_x \end{cases} \qquad (5.137)$$

or vice versa

$$h(q) = \begin{cases} q_x(\alpha_2 - \alpha_1)\frac{1}{q} + \alpha_1, & q \le q_x \\ \alpha_2, & q > q_x \end{cases}. \qquad (5.138)$$

Both versions of the bifractal model depend on three parameters α_1, α_2, and q_x. The multifractal spectrum (the singularities spectrum) is generated at two points α_1 and α_2 and its width is equal to $\Delta\alpha = \alpha_1 - \alpha_2$.

Analysis of fractal and multifractal properties of time series is one of the promising areas of data analysis. This is due to the ability of fractal analysis to investigate the signals that from the standpoint of covariance and spectral theory are nothing more than noise or Brownian motion.

A further generalization of Brownian motion with constant the Hurst parameter H, $0 < N < 1$ assumes the dependence of the Hurst parameter on time. Mandelbrot was first to propose this generalization [67], and it is called the multifractal Brownian motion, which is described by the function $H(t)$ so-called the multifractal singularity spectrum. The singularity spectrum is the informative statistics characterizing the chaotic regime of fluctuations of observed value.

There are several methods of studying the multifractal characteristics of non-stationary signals. Among them there are two main ones: the wavelet transform modulus maxima (WTMM) method and the method of multifractal fluctuation analysis (MFFA or MF-DFA), which found a widespread usage at the moment. Both methods exclude the polynomial trends from the original time series, so that is why they have advantages over other methods, for example, comparing with the standard method based on the multifractal structural formalism based on the partial functions [33], or with the autocorrelation functions of high-order [30]. In the case of multidimensional data, MF-DFA method is generalized in [61], and the method WTMM in [62].

One of the promising directions of development of methods of multifractal analysis is the study of linear and especially nonlinear mutual correlative bonds

between multiple time series. It is also of great interest to improve the methods characterizing the cross-correlations and similar statistical relationships between several non-stationary time series. Most existing methods are applicable only to stationary series that are rare in real situations. In this regard, we shall note the recently received results [68] of using the fractal method to analyze the cross-correlation of non-stationary data.

It is noteworthy to study the time-dependent characteristics of large networks of signals. In such networks, nodes present the signals, while bonds (possibly of the certain direction) between each pair represent signals.

Finally, the practical use of fractal scaling parameters identified in time series is of greatest interest. Particular attention should be paid to developing of methods for forecasting time series and complex dynamical systems with an intention to adopt preventive measures to stop dangerous and emergency situations.

Literatures

1. S.V. Bozhokin, D.A. Parshin, Fraktaly i mul'tifraktaly (NITs "Reguliarnaia i khaoticheskaia dinamika", Izhevsk, 2001), p. 128
2. D. Harte, *Multifractals Theory and Applications* (Chapman & Hall/CRC, Boca Raton, 2001)
3. P. Grassberger, Generalized dimensions of strange attractors. Phys. Lett. A **97**, 227–230 (1983)
4. H.G.E. Hentschel, I. Procaccia, The infinite number of generalized dimensions of fractals and strange attractors. Phys. D **8**, 435–444 (1983)
5. P.V. Korolenko, M.S. Maganova, A.V. Mesniankin, Novatsionnye metody analiza stokhasticheskikh protsessov i struktur v optike. Fraktal'nye i mul'tifraktal'nye metody, veivlet preobrazovaniia. Uchebnoe posobie (MGU, NII iadernoi fiziki, Moscow, 2004), p. 82
6. R.M. Kronover, Fraktaly i khaos v dinamicheskikh sistemakh. Osnovy teorii (Postmarket, Moscow, 2000), p. 352
7. T.C. Halsey, M.H. Jensen, L.P. Kadanoff, I. Procaccia, B.I. Shraiman, Fractal measures and their singularities of strange sets. Phys. Rev. A **33**(2), 1141–1151 (1986)
8. A.B. Chhabra, R.V. Jensen, Direct determination of the $f(\alpha)$ singularity spectrum. Phys. Rev. Lett. **62**, 1327–1330 (1989)
9. T.S. Akhromeeva, S.P. Kurdiumov, G.G. Malinetskii, A.A. Samarskii, Nestatsionarnye struktury i diffuzionnyi khaos (Nauka, Gl. red. fiz.-mat. lit, Moscow, 1992), p. 544
10. G. Shuster, Determinirovannyi khaos. Vvedenie (Mir, Moscow, 1988), p. 240
11. A.N. Pavlov, Metody analiza slozhnykh signalov. Ucheb. posobie dlia stud. fiz. fak. (Nauchnaia kniga, Saratov, 2008), p. 120
12. V.S. Ivanova, *Razrushenie metallov* (Metallurgiia, Moscow, 1979), p. 168
13. A.I. Olemskoi, V.A. Petrunin, Perestroika kondensirovannogo sostoianiia atomov v usloviiakh intensivnogo vozdeistviia. Izv. vuzov. Fizika. (1), 82–121 (1989)
14. A.I. Olemskoi, I.I. Naumov, Fraktal'naia kinetika ustalostnogo razrusheniia. V kn. Sinergetika i ustalostnoe razrushenie metallov (Nauka, Moscow, 1989), pp. 200–214
15. A.I. Olemskoi, A.A. Katsnel'son, Sinergetika kondensirovannoi sredy. izd. 2-e. (Editorial URSS, Moscow, 2010), p. 336
16. Iu.B. Rumer, M.Sh. Ryvkin, Termodinamika, statisticheskaia fizika i kinetika (Izd.-vo Novosib. un-ta: Sib. univ. Izd.-vo, Novosibirsk, 2001), p. 608
17. B.M. Askerov, *Termodinamika i staticheskaia fizika* (Izd-vo Baky Universiteti, Baku, 2007), p. 512

18. V.S. Ivanova, V.F. Terent'ev, *Priroda ustalosti metallov* (Metallurgiia, Moscow, 1975), p. 455
19. A.Kh. Janahmadov, *Tribotekhnicheskie problemy v neftegazovom oborudovanii* (Elm, Baku, 1998), p. 216
20. O.N. Romaniv, *Viazkost' razrusheniia konstruktsionnykh stalei* (Metallurgiia, Moscow, 1979), p. 176
21. O.N. Romaniv, A.S. Krys'kiv, Ispol'zovanie kriteriev mekhaniki razrusheniia dlia otsenki khladnolomkosti stalei. Fiz.-khim. mekhanika materialov. (5), 40–51 (1981)
22. B.I. Medovar, L.I. Gladshtein, V.Ia. Saenko i dr. Viazkost' razrusheniia stali 16G2AF elektroshlakovogo pereplava. Probl. spets. Elektrometallurgii. (19), 32–35 (1983)
23. O.I. Shishorina, V.I. Burba, I.Zh. Bunin, Osobennosti protsessa ustalostnogo razrusheniia konstruktsionnykh materialov v tochkakh bifurkatsii. v sb. Sinergetika i ustalostnoe razrushenie materialov (Nauka, Moscow, 1989), pp. 215–224
24. A.Kh. Janahmadov, *Termomekhanicheskaia teoriia iznosa* (Elm, Baku, 1997), p. 28
25. A.Kh. Janahmadov, *Neftianaia tribologiia* (Elm, Baku, 2003), p. 326
26. A.I. Olemskoi, A.Ia. Flat, Ispol'zovanie kontseptsii fraktala v fizike kondensirovannoi sredy. Uspekhi fizich. nauk, Tom. 163(12), 1–50 (1993)
27. A.Kh. Janahmadov, O.A. Dyshin, Synergetics and fractal dimensions in tribology (reviews). J. Friction and Wear **2**(1), 61–71 (2011)
28. L.D. Landau, E.M. Lifshits, Statisticheskaia fizika. Ch. 1 (Nauka, Moscow, 1976)
29. U. Frish, G. Parisi, Turbulence and predictability in geophysical fluid dynamics and climate dynamics (Proceedings of the International School of Physics "Enrico Fermi", Cours 88, Eds M. Ghil, R. Benzi, G. Parisi) (Amsterdam, North Holland, 1985), p. 71
30. A.-L. Barabasi, T. Vicsek, Phys. Rev. A **44**, 2730 (1991)
31. Y. Gagne, E. Hopfinger, U. Frisch, *New trends in nonlinear dynamics and pattern*. Forming phenomena: The geometry of nonequilibrium, NATO AST Series, Ser. B, ed. by P. Coullet, P. Huerre. vol 237 (Plemon Press, New York, 1990), p. 315
32. J.W. Kantelhardt, Fractal and multifractal time series, arxiv: 0804.0747, v.1, April 04 (2008)
33. U.N. Feder, Fraktaly (Mir, Moscow, 1991)
34. H.O. Peitgen, H. Jürgens, D. Saupe, *Chaos and fractal* (Springer, Berlin, 2004)
35. E. Bacry, J. Delour, J.F. Muzy, Multifractal random walk. Phys. Rev. E **64**, 026103 (2001)
36. J.F. Muzy, E. Bacry, A. Arneodo, Phys. Rev. Lett. **67**, 3515 (1991)
37. J.F. Muzy, E. Bacry, A. Arneodo, Phys. Rev. E **47**, 875 (1993)
38. A. Grossman, J. Morlet, J. Siam, Math. Anal. **15**, 723 (1984)
39. S. Mallat, *A wavelet tour of signal processing* (Academic Press, San Diego, London, Boston, New York, Sydney, Tokyo, Toronto, 1998), p. 577
40. A.A. Liubushin, *Analiz dannykh sistem geofizicheskogo i ekologicheskogo monitoringa* (Nauka, Moscow, 2007), p. 228
41. J.W. Kantelhardt, S.A. Zschiegner, E. Konscienly-Bude, S. Havlin, A. Bunde, H.E. Stanley, Multifractal detrended fluctuation analysis of nonstationary time series. Phys. A **316**, 87–114 (2002)
42. J.W. Kantelhardt, D. Rybski, S.A. Zschienger, P. Braun, E. Koscienly-Bunde, V. Livina et al., Multifractality of river runoff and precipitation: comparison of fluctuation analysis and wavelet methods. Phys. A **330**, 240–245 (2003)
43. A.B. Chhabra, Ch. Meneveau, R.V. Jensen, K.R. Sreenivasan, Direct determination of the () singularity spectrum and its application to fully developed turbulence. Phys. Rev. A **40**(9), 40 (1989)
44. J.F. Muzy, E. Bacry, A. Arneodo, Int. J. Bifurcat. Chaos **4**, 245 (1993)
45. N.M. Astaf'eva, Veivlet-analiz, osnovy teorii i primery primeneniia. Uspekhi fizicheskikh nauk, Tom 166(11), 1145 (1996)
46. A.N. Pavlov, V.S. Anishchenko, Mul'tfraktal'nyi analiz slozhnykh signalov. Uspekhi fizicheskikh nauk, Tom **177**(8), 859–876 (2007)
47. G. Boffetta, M. Cencini, M. Falcioni, A. Vilpiani, Predictability, a way to characterize complexity. Phys. Rp. **356**, 367–474 (2002)

48. P.J. Brockwell, R.A. Davis, *Springer texts in statistics. Introduction to time series and forecasting* (Springer, New York, 1988)

49. R.N. Mantegna, Fast accurate algorithm for numerical simulation of levy stable stochastic processes. Phys. Rev. E **49**, 4677–4683 (1994)

50. M.F. Shlesinger, Comment on "stochastic process with ultraslow convergence to a Gaussian, The Truncated Levy Flight". Phys. Rev. Lett. **74**, 4959 (1995)

51. D. Sornette, *Critical phenomena in natural sciences* (Springer, New York, 2001)

52. A. Olemskoi, S. Kokhan, Effective temperature of self-similar time series, analytical and numerical developments. Phys. A **360**, 37–58 (2006)

53. C.-K. Peng, S.V. Buldyrev, S. Havlin, H.E. Stanley, A.L. Goldberger, Phys. Rev. E **49**, 1685 (1994)

54. S.M. Ossadnik, S.B. Buldgrev, A.L. Goldberger, S. Havlin, R.N. Mantegna, C.-K. Peng, M. Simons, H.E. Stanley, Biophys. J. **67**, 64 (1994)

55. D. Sornette, *Critical phenomena in natural Sciences* (Springer, New York, 2001)

56. A. Olemskoi, S. Kokhan, Effective temperature of self—similar time series, analytical and numerical development. Phys. A **360**, 37–58 (2006)

57. C.-K. Peng, S.V. Buldyrev, S. Havlin, H.E. Stanley, A.L. Goldberger, Phys. Rev. E **49**, 1685 (1994)

58. S.M. Ossadnik, S.B. Buldyrev, A.L. Goldberger, S. Havlin, R.N. Mantegna, C.-K. Peng, M. Simons, H.E. Stanley, Biophys. J. **67**, 64 (1994)

59. M.S. Taggu, V. Teverovsky, W. Willinger, Fractals **3**, 785 (1995)

60. J.W. Kantelhardt, E. Koscienly-Bunde, H.H.A. Rego, S. Havlin, A. Bunde, Phys. A **295**, 441 (2001)

61. K. Hu, P.Ch. Ivanov, Z. Chen, P. Carpena, H.E. Stanley, Phys. Rev. E **64**, 011114 (2001)

62. Z. Chen, P.Ch. Ivanov, K. Hu, H.E. Stanley, Phys. Rev. E **65**, 041107 (2002)

63. A. Bunde, S. Havlin, J.W. Kantelhardt, T. Penzel, J.-H. Peter, K. Voight, Phys. Rev. Lett. **85**, 3736 (2000)

64. P. Oswiecimka, J. Kwapien, S. Drozdz, Wavelet versus detrended fluctuation analysis of multifractal structures. Phys. Rev. E **74**, 016103 (2006)

65. G.-F. Gu, W.-X. Zhou, Detrended fluctuation analysis for fractal and multifractals in higher dimensions. Phys. Rev. E **74**, 061104 (2006)

66. A. Arneodo, B. Audit, N. Decoster, J.F. Muzy, C. Vaillant, Wavelet based multifractal formalism: application to DNA sequences, satellite images of the cloud structure, and stock market data, in *The science of disaster: climate disruptions, market crashes, and heart attacks*, ed. by A. Bunde, J. Kropp, H.J. Schellnhuber (Springer, Berlin, 2002)

67. I. Rodriguez-Iturbe, A. Rialdo, *Fractal river basins—change and self-organization* (Cambrige University Press, Cambrige, 1997)

68. A.I. Olemskoi, V.N. Borisiuk, I.A. Shuda, Mul'tifraktal'nyi analiz vremennykh riadov. Bisnik Sum DU, Seriia "Fizika, matematika, mekhanika", 2 (2008)

69. E. Koscielny-Bunde, J.W. Kantelhard, P. Braun, A. Bunde, S. Havlin, Long-term persistence and multifractality of river runoff records. J. Hydrol. **332**, 120 (2006)

70. J.W. Kantelhard, E. Koscielny-Bunde, D. Rybinski, P. Braun, A. Bunde, S. Havlin, Long-term persistence and multifractality of precipitation an river runoff records. J. Geophys. Res. (Atmosph.), 111, DO1106 (2006)

71. B.B. Mandelbrot, The Fractal Geometry of Nature (W.H.Freeman, 1983), p. 537

72. B. Podobnik, H.E. Stanley, Detrended cross—correlation analysis, a new method for analyzing two nonstationary time series. Phys. Rev. Lett. **100**, 084102 (2008)

Chapter 6
Fractal Analysis of Fatigue Failure of Kinematic Pair (Oil–Gas Xmas Tree Valve)

One of the most important types of oil field equipment is Xmas tree, designed to insulate the mouth of gushing oil and gas wells, as well as to regulate their operational modes.

Assuming that the most of the oil and gas exploitation are done using the fountain method, and then, the importance of fountain operational equipment at the mouth of well for the country's economy becomes more obvious [1].

A lot of research has been in this field. However, existing structures of equipment and extreme operational conditions linked with discovery of oil in most remote and harsh environment as onshore and offshore requires the implementation of new studies in wear resistance and reliability of mobile elements of the fountain Xmas trees.

The performance in this direction made researches and development works allowed the creation of variety of sizes Xmas trees operational under pressures 14, 21, 35, and 70 MPa, and with the well diameter 50, 65, 80, 100, and 150 mm. However, all these equipment have certain drawbacks.

In this regard, the creation of wellhead equipment that meets the modern requirements and international standards still has an important practical and scientific significance. And this goal requires an amount of work aimed at studying the existing structures of Xmas trees, an analysis of their operational performance and failures, and more accurate assessments and design of existing and newly developed wellheads.

The operational experience of Xmas trees under different conditions shows that the modern design of valves, the hermetical sealing of shutter (gate) which automatically supply a special grease to the sealing surface, have a sufficiently long lifetime. In this case, failures occur not only because of wear of the valve shutter (gate), but also due to running pair consisting of spindle and spindle nut.

6.1 Design Features and Operating Conditions of Flow Control Devices

Valves on the Xmas tree and wellhead equipment, in general, are divided into two groups:

- Flowing-type plug valves with sealing lubricants (KPPS/КППС);
- direct flow valves with single-plate (KhMS1/ХМС1) and double-plate (ZMAD/ ЗМАД) shutter (gate) with manual or automatic lubrication, with manual or pneumatic control.

The following coding is used for the specification of plug valves: KPPS/КППС —direct flow plug valve with lubrication; the first number—the nominal width, in mm, the second number—the working pressure, in MPa; KhL/ХЛ—the modification for cold climates. As an example, the direct flow plug valve, with lubrication, with nominal diameters 65 mm, designed for working pressure 14 MPa, for cold climates will be shown as KPPS-65×140KhL/КППС-65×140ХЛ.

The following coding is used for the specification of gate valves: ZM/ЗM—the valve with sealing gate "metal-on-metal"; S/C—or A/A—manually or automatically lubricated; 1 or D/Д—the single or double plated; B/Б—the flangeless valve body (if there is flange, then no letter is written); P/П—the pneumatic control; the first number—the nominal diameter, in m; the second number—the working pressure, in MPa; the corrosion resistance performance is similar to the Xmas tree. For example, the valve with sealing "metal-on-metal," with automatic lubrication, with double-plate gate, with nominal width 50 mm, designed for working pressure 70 MPa with up to 6 % H_2O and CO_2 is indicated ZMAD-50×700K2/ЗМАД-50×700K2 [2].

The plug valves with a pressure 14 MPa (Fig. 6.1) consist of a body and the overlapping channels separated by the conical plug when the wheel is rotated at 90°.

Fig. 6.1 The plug valve
KPPS-65kh14/КППС-65×14

The wheel regulates the gap between the plug and the body. The valve works only with lubrication. The lubricant seals the valve and the thread of spindle, makes the turn of plug easier, and also prevents corrosion of details. The lubricant is supplied through the channel in the spindle with the pressure screw t, and then through the check valve inside the body.

The valve (Table 6.1) is equipped with a special device to force the plug if it gets jammed [3].

The direct flow valves like ZMS1 (see Table 6.1) with forced lubrication, with manual control (Fig. 6.2a), and with nominal diameters of 65, 80, 100, and 150 mm, designed for working pressure 21, 35 MPa. The air-tightness of gate is provided a certain specific load on sealing components of gate and saddles. The preliminary

Table 6.1 Technical specifications of valves

Types of valves	Control	Dimensions			Total weight (asbl.), kg
		Length, L	Width, W	Height, H	
KPPS-65×14 (КППС-65×14)	Manual	350	205	420	53
KPPS-65×14KhL (КППС-65×14ХЛ)	Manual	350	205	420	53
ZM-65×21 (ЗМ-65×21)	Manual	350	320	650	64
ZMS-65×35 (ЗМС-65×35)	Manual	350	320	630	88
ZMS1-65×350 (ЗМС1-65×350)	Manual	350	320	630	88
ZMS-80×35 (ЗМС-80×35)	Manual	470	360	885	130
ZMS1-65×35K2 (ЗМС1-65×35К2)	Manual	390	320	715	127
ZMS1-65P×35K2 (ЗМС1-65П×35К2)	Pneumatic	390	400	1150	237
ZMS1-80×35K2 (ЗМС1-80×35К2)	Manual	470	360	915	160
ZMS1-80Px35K2 (ЗМС1-80П×35К2)	Pneumatic	470	400	118	265
ZMS1-100×21 (ЗМС1-100×21)	Manual	510	450	1120	218
ZMS1-100×21K2I (ЗМС1-100×21К2И)	Manual	510	450	1120	218
ZMS1-100P×21K2I (ЗМС1-100П×21К2И)	Pneumatic	510	450	1400	390
ZMS-100×35 (ЗМС-100×35)	Manual	550	450	930	287
ZMS-100×35K1 (ЗМС-100×35К1)	Manual	550	450	930	287
ZMS1-100×35K2 (ЗМС1-100×35К2)	Manual	550	450	930	300

Table 6.1 (continued)

Types of valves	Control	Dimensions			Total weight (asbl.), kg
		Length, L	Width, W	Height, H	
ZMS1-100P35K2 (3МС1-100П×35К2)	Pneumatic	550	450	1400	406
ZMSB-150×21 (3МСБ-150×21)	Manual	350	450	1485	353
ZMAD-50×70 (3МАД-50×70)	Manual	500	355	980	196
ZMADP-50×70 (3МАДП-50×70)	Pneumatic	500	355	1065	243
ZMAD-80×70 (3МАД-80×70)	Manual	650	500	1117	328
ZMADP-80×70 (3МАДП-80×70)	Pneumatic	650	500	1280	436
ZMAD-50×70K2 (3МАД-50×70K2)	Manual	500	355	980	196
ZMADP-50×70K2 (3МАДП-50×70K2)	Pneumatic	500	355	1065	243
ZMAD-80×70K2 (3МАД-80×70K2)	Manual	650	500	930	328
ZMADP-80×70K2 (3МАДП-80×70K2)	Pneumatic	650	500	1280	436
ZM-50×70 (3М-50×70)	Manual	500	355	890	156
ZMADP-50×70 (3МАДП-50×70)	Pneumatic	500	355	1065	203

specific load is created by disk springs. The lubrication LZ-162/ЛЗ-162 or "Armatol" provided through the discharge valve also helps to hermetically seal the gate. A metal gasket along with tightening screws air-tighten between the gap between the body and the lead. The regulating nuts align the passage between the openings of gate and body.

To facilitate the control of valve, the support of running nut is designed on the ball bearings, and valves with nominal diameters 80, 100, and 150 mm have a balancing rod.

The threads of spindle and running nut are separated and outside of the contact zone contact with environment, which improves their performance.

Sleeves act as sealants for spindle and rod. To improve the sealing ability, the lubricant is supplied through the discharge valve.

Currently, instead of valves ZMS1/3MC1 (see Fig. 6.2a), the more modernized versions of type ZM/3M and ZMS/3MC are produced [3].

The direct flow valves ZMAD/3МАД designed for pressure 70 MPa with automatic lubrication and manual control are shown in Fig. 6.2b.

The opening hole alignments are regulated with screws. The oiler provides lubrication of bearings.
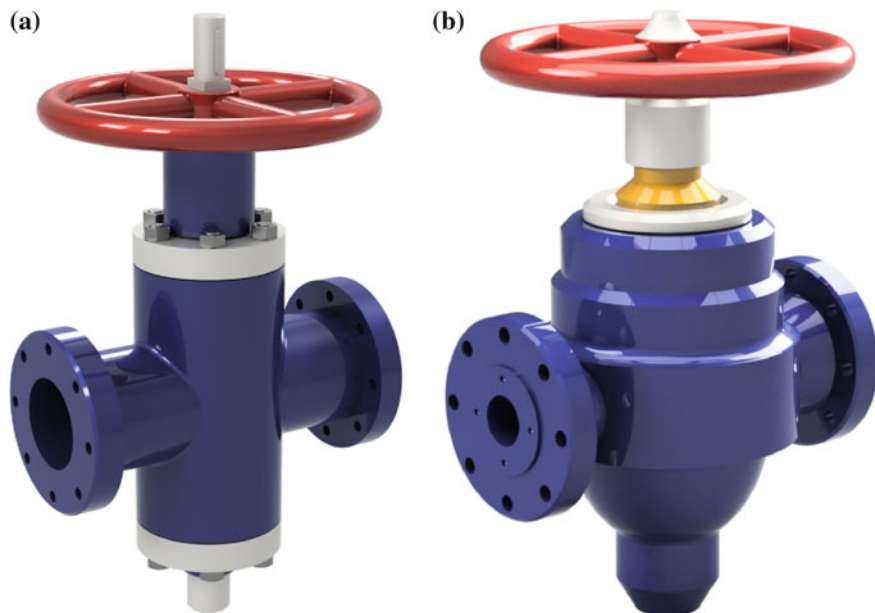
Fig. 6.2   The direct flow valves ZMS1/3MC1 (**a**) and ZMAD/ЗМАД (**b**) with manual control

The chevron-type sleeves help to lubricate spindle and balancing. To improve the sealing ability, the lubricant is supplied through a discharge valve.

The preliminary load on the sealing surfaces of units is created using six cylinder coil springs mounted between the dies.

The automatic supply of lubricant to the gate is an important feature of the valve; it is comprised of a cavity, pistons, and system of channels which lubricate the cavity with ring channel on the sealing surface of cheeks and discharge valves placed outside the body and designed for periodic injection of lubricant (every 10–15 cycles latches) into the cavity. The operating pressure of medium within the body is passed on the lubricant through pistons, which fills the cavity.

The valve ZMADP/ЗМАДП (see Table 6.1) with pneumatic control is significantly different of the one with manual control due to the presence driving part.

The driving part consists of pneumatic cylinder and backup manual control, to help control valve in case of failure of pneumatic system.

Controlling units are designed to manage the operational regimes of oil and gas wells through throttles that regulate the fluid flow by changing the area of opening channel.

The following coding is used for the specification of adjustable throttle where DR/ДР—the adjustable throttle; the first number—the nominal diameter, in mm; the second number—the working pressure, in MPa; the performance based on the corrosion resistance similar to the Xmas tree and valves. For example, the

Fig. 6.3 The regulated and unregulated throttle

adjustable throttle with nominal diameters 65 mm, with working pressure 35 MPa, for fluids containing up to 6 % CO_2, is written as DR-65×350K1/ДР-65×350K1.

The adjustable throttle (Fig. 6.3) designed for pressure 35 MPa, consists of body, wherein the fluid flow is diverted at right angle, housing with sleeves. A replaceable nozzle is inserted into the sleeve [3].

The internal parts of throttle are sealed with O-rings. The position of spindle is fixed with lock washer.

The technical specifications of adjustable throttle are given below.

Nominal diameter, mm—65,
Working pressure, MPa—35,
Dimensions, mm—343 × 320 × 605,
Assembled weight, kg—58.

The rotation of wheel translated into the movement of tip end, fastened to the end of the spindle with nut.

The opening and closing degree of throttle is determined by the index showing on the diameter of the cylindrical hole in mm, which is equivalent to the corresponding area of the annular section. As the nozzle of regular section, we assume

the unregulated throttle. For that, the assembly consisting of spindle, sleeve, nuts, and other items are replaced by gag.

To remove the body of nozzle, along with other accessories there is a disassembler.

6.2   Contact Interaction Between the Bolt and Nut. N.E. Zhukovsky Problem

The distribution of the axial forces between the threads could have been uniform if the thread was made high accuracy and the thread ductility was considerably higher ductility bolt and nut.

In reality, neither of conditions is plausible.

The influence of bolt ductility on the distribution of powers between the leads/pitches of thread can be shown from tightening the screw into a large detail, assuming it is not deformable. The force between each pair of contacting threads in screw and nut is proportional to the elastic movements of the threads according to Hooke's law. Meanwhile, the elastic displacements of thread along the length of nut are not identical. The thread displacements at the end of the nut vary from the displacements along the length of nut (the screwing length).

We graphically represent each pair of thread in the form of beams, clamped between the stem of bolt and the body of nut. Figure 6.4a shows the thread joint in the non-loading condition: threads, depicted as beams, are not deformed. Figure 6.4b shows the joint where the thread ductility is significantly higher than one the stem of screw and the body of nut: All threads have nearly the same displacement, and hence, they are equally loaded. The joint is shown in Fig. 6.4c; the screw stem ductility is almost the same as thread ductility, so the lower parts of thread receive more displacement than the upper ones [4].
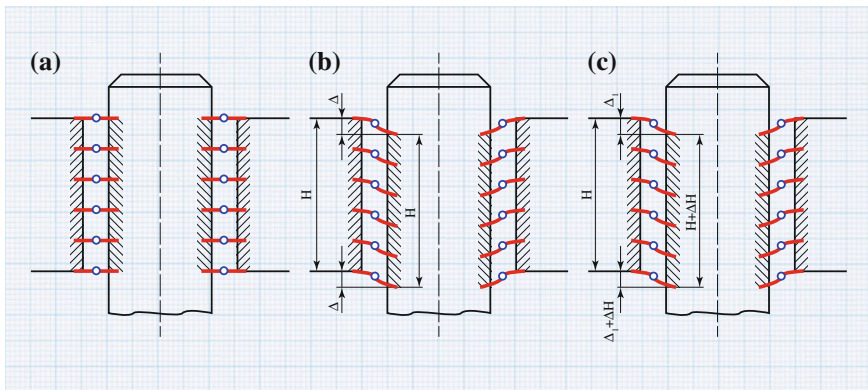
Fig. 6.4 The diagram of thread deformation at absolutely rigid nut

The uneven distribution of load along thread is complicated by the fact that the lead in the most extended part of the bolt is associated with thread located in the most compressed part of the nut.

The problem of the distribution of forces between the threads is statistically unsolvable.

The distribution of forces between the threads according to N.E. Zhukovsky for nut with ten threads is shown in Fig. 6.5. The first thread gets the most of the load, it is account for about 1/3 of the total force on the bolt, and the last tenth threads it is less than 1/100 of the total force. The deformations in the thread associated with profile errors, contact, and local plastic deformations somewhat reduce loading in the first thread down to 1/3–1/4 of the total force [5].

The force field in bolt and nut (Fig. 6.6) shows a quite clearly unequal distribution of forces between the threads. The direction of the field lines indicates the direction of the principal stresses, the density of force lines characterizes the intensity of stress.

With such a sharp uneven distribution of the load along the threads, a large increase in the height of nut becomes unnecessary because of the danger of sequential "chain" destruction of threads. The diagram of forces between the threads at ductile nut, working or tension, and rigid stem of bolt looks like the one on ordinary diagram.
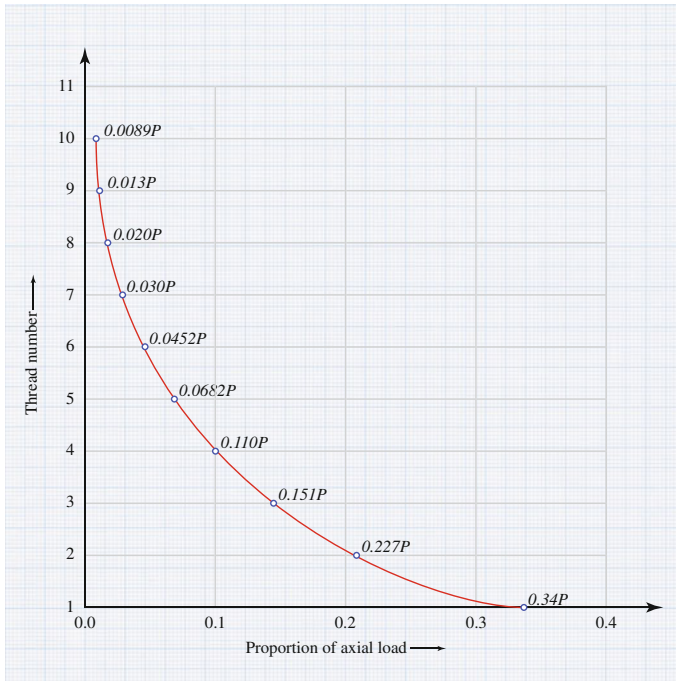
Fig. 6.5 The diagram of load distribution between the threads according to N.E. Zhukovsky

Fig. 6.6 The force field in
bolt and nut
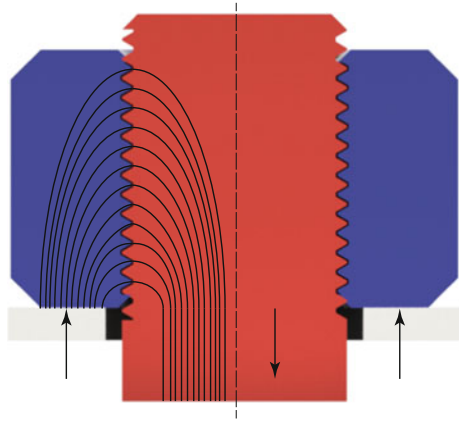
In the thread connection with nut, working for tension, and with normal ductility
of bolt and nut, the diagram of pressure distribution between the threads with
minimum in the middle portion of the length of screwing is obtained.

6.3   Load Distribution on Screw of Kinematic Pair

The Xmas tree is one of the most important equipment in the oil and gas field,
designed to seal the mouth of the gushing oil and gas wells, to regulate the oper-
ation [6].

The valve devices in Xmas trees are the direct flow type with gate, the tightness
of which is ensured by the close contact between the gate and the saddles. The gate
of valve is driven by rising spindle of the rotating lead nut.

The overall performance of valve is largely dependent on the running pair. In the
running pair of valve, the spindle is subjected to the tension and the nut is mainly to
compression [7].

Considering that the load acting on the spindle of valve repeatable variable, the
practice and results of research show that the weakest part is the initial threads from
the supporting end of the nut, where the screw gets stretched, and the nut gets
compressed.

This is due to the fact that the most of the load is concentrated in the first thread.
Further distribution of the load is uneven, and that unevenness of load distribution
between the threads is complicated by the local concentrations of stress in the pitch
of thread and by tensile forces and stresses in the threads. As a result, the stress in
the first thread exceeds the stress of the normal tensile forces. Therefore, there is an
intensive wear of the initial threads of the running pair and subsequent wear of
following ones. As a result, a gap is formed between the nut and the spindle, which
is connected with closing device, and it eventually contributes to the overall valve

depressurization, which is not acceptable. Therefore, the schematic design of spindle–nut plays an important role in terms of load distribution along the threads.

N.E. Zhukovsky was first to consider the distribution of loads along threads for the rectangular profile [5].

Let us try using all the parameters of thread, to consider the load distribution in diagrams: the spindle gets stretched, the nut gets compressed, and the spindle, just like and the nut, get stretched together [8].

Consider the distribution of load along threads when the spindle is stretched and the nut is compressed (Fig. 6.7).

When closing or opening the valve, the bend is formed on the thread due to the load. The sum of projections on axis of the first and second threads, respectively, is

$$f_1 = \left(\frac{0.44H}{2\pi rt} + \frac{0.38H}{2\pi r_1 t} \right) \frac{P}{g}; \qquad (6.1)$$

$$f_2 = \left(\frac{0.44H}{2\pi rt} + \frac{0.38H}{2\pi r_1 t} \right) \frac{P_1}{g}; \qquad (6.2)$$

Fig. 6.7 Estimating the distribution of load along threads when the spindle is stretched and nut is compressed
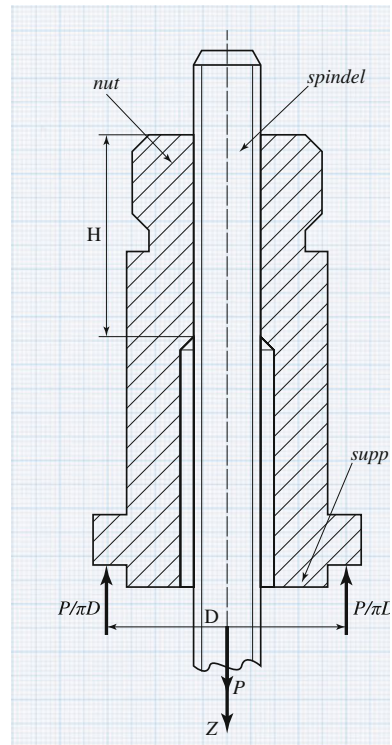
where P, P_1—the loading force along threads of the spindle and nut, the first and second threads, respectively; $2\pi rt$, $2\pi r_1 t$—the thread area for the spindle and nut, respectively, m^2; g—the coefficient of beveled threads under the pressure, N/m^2; H—the height of thread, m; t—the thread pitch, m; r, r_1—the radii of thread inner diameters of for the spindle and nut, respectively, m.

When nut moves, the tensile force is formed in the spindle, and the compressive force is formed in the nut. Let us denote this force through G.

The spindle elongation and the nut compression due to this force are

$$f_3 = \frac{Gt}{\pi r^2 E};\tag{6.3}$$

$$f_3 = \frac{Gt}{\pi(r_1^2 - r^2)E};\tag{6.4}$$

where E, E_1—the elasticity modules of materials for the spindle and nut.

The difference between (6.1) and (6.2) should be equal to the sum of (6.3) and (6.4)

$$P - P_1 = G\frac{2r_1 t^2 g(2r^2 - r_1^2)}{rE(Hr_1 + H_1 r)(r^2 - r_1^2)};\tag{6.5}$$

for the first and second threads, we can write

$$P_1 - P_2 = (G - P_1)\frac{2r_1 t^2 g(2r^2 - r_1^2)}{rE(Hr_1 + H_1 r)(r^2 - r_1^2)};\tag{6.6}$$

Solving together (6.5) and (6.6), we obtain the relationship between the forces on the three threads

$$P + P_2 = P_1\left(2 + \frac{2r_1 t^2 g(2r^2 - r_1^2)}{rE(Hr_1 + H_1 r)(r^2 - r_1^2)}\right);\tag{6.7}$$

After simple transformations (6.7), we obtain

$$\frac{P_1}{P} = \frac{1}{2 + F - \frac{P_2}{P_1}},\tag{6.8}$$

where $F = \frac{2r_1 t^2 g(2r^2 - r_1^2)}{rE(Hr_1 + H_1 r)(r^2 - r_1^2)}$; P_2—the load on the third thread.

Since the ratio of the acting forces on all threads is determined by such formulas, we can write

$$d = \frac{1}{2 + F - d}. \tag{6.9}$$

Solving the Eq. (6.9), we determine the root

$$d = \left(1 + \frac{F}{2}\right) - \left[\left(1 + \frac{F}{2}\right)^2 - 1\right]^{0.5}. \tag{6.10}$$

Equation (6.5) can be converted into

$$P - Pd = (R - P)F;$$

here

$$P = \frac{FR}{1 - d + F}. \tag{6.11}$$

This value can be determined from the sum of the infinitely decreasing geometric progression

$$R = \frac{P}{1 - d} \tag{6.12}$$

or

$$P = (1 - d)R, \tag{6.13}$$

where R—the gravity force of closing part of valve and d—the denominator of exponentially decreasing geometrical progression.

Taking into account (6.9), (6.11), and (6.12), they are identical.

Now consider the distribution of the loading forces along the thread, when the spindle and nut are stretched simultaneously (Fig. 6.8).

If the tensile force of the spindle is $G = R - P_1$, then we define the tensile force of nut.

Since $f_1 - f_2 = f_3 - f_4$, then

$$(P - P_1)\left(\frac{H}{2\pi rtg} + \frac{H_1}{2\pi r_1 tg_1}\right) = \frac{Rt}{\pi r^2 E} - \frac{(R - G)t}{\pi(r_1^2 - r^2)E}.$$

Hence,

$$P - P_1 = FG - \frac{\left[\pi RtE_1\left(r_1^2 - r^2\right) - \pi r^2 Et(R - G)\right]4t^2 gg_1 r_1 r}{r^2 EE_1\left(r_1^2 - r^2\right)(2\pi Hr_1 g_1 t + 2\pi H_1 rgt)}. \tag{6.14}$$

Fig. 6.8 Estimating the
distribution of load along
threads when the spindle and
nut are stretched
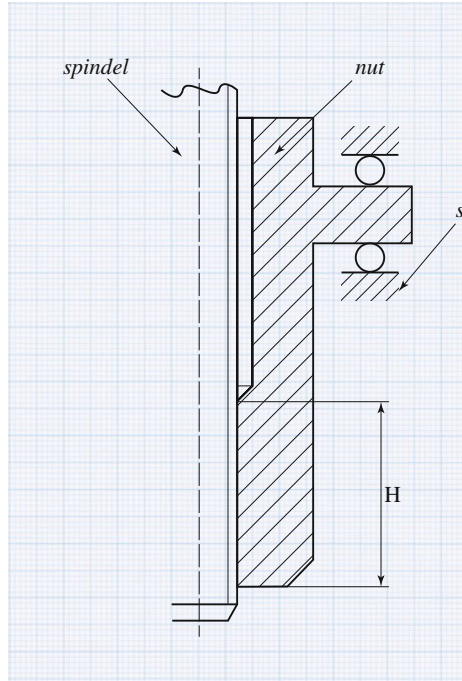
A similar ratio will be for the other threads

$$P - P_1 = F(G - P_1) - \frac{\left[\pi R t E_1 \left(r_1^2 - r^2\right) - \pi r^2 E t (R - G)\right] 4 t^2 g g_1 r_1 r}{r^2 E E_1 \left(r_1^2 - r^2\right)\left(2\pi H r_1 g_1 t + 2\pi H_1 r g t\right)}. \qquad (6.15)$$

Excluding G from (6.14) and (6.15), we obtain the connection between P, A, and P_2:

$$P + P_2 = P_1(2 + F). \qquad (6.16)$$

As we seen from (6.16), the pressure force on the threads decreases by geometrical progression; starting from the first thread and in the middle of the length it becomes close to zero. The denominator of this progression is determined by formula (6.10).

The relationship between P and R is determined from (6.14)

$$P = \frac{2G t^2 g}{(1 + d + F) H E r}. \qquad (6.17)$$

Similarly, we can determine what will be the loading force in the next thread

$$P = \frac{2G t^2 g_1}{(1 + d + F) H E_1 r_1}. \qquad (6.18)$$

If we form the sum of decreasing geometric progressions, which constitute the subsequent loading on the threads of nut at both ends, and equating them to R, we obtain

$$R(1 - d) = Q + Q_1. \tag{6.19}$$

Formulas (6.10), (6.17), and (6.18) lead us to the identity. Therefore, it can be concluded that the valves designed according to the load-sharing scheme on Fig. 6.8 will be more durable than the one designed according to the load-sharing scheme on Fig. 6.7.

Figure 6.9 shows the ratio between the distribution of load along threads and the loading force of threads of nuts for the structural diagrams (Figs. 6.7 and 6.8).

As we can see from Fig. 6.9, the distribution factor of loading along threads is advisable to select within the range from 0.5 to 0.985. When selecting lesser values for the distribution factor (Fig. 6.10), the first two threads take up most of the tensile force, which leads to the premature wear.

Figure 6.11 shows the graph of loading distribution along thread for valves design by AzINMASh.

As we can see from Fig. 6.8, the loading along threads on this design is 2 times less than the design on Fig. 6.7.
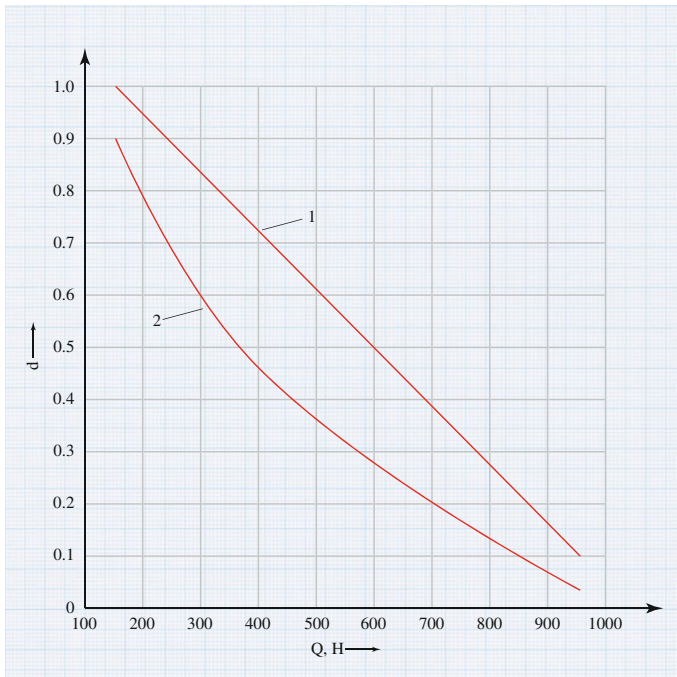
Fig. 6.9 The influence of loading factor distribution along threads on the loading distribution. *1* the diagram where "the nut is compressed, the spindle is stretched"; *2* the diagram where "the spindle and nut are both stretched"
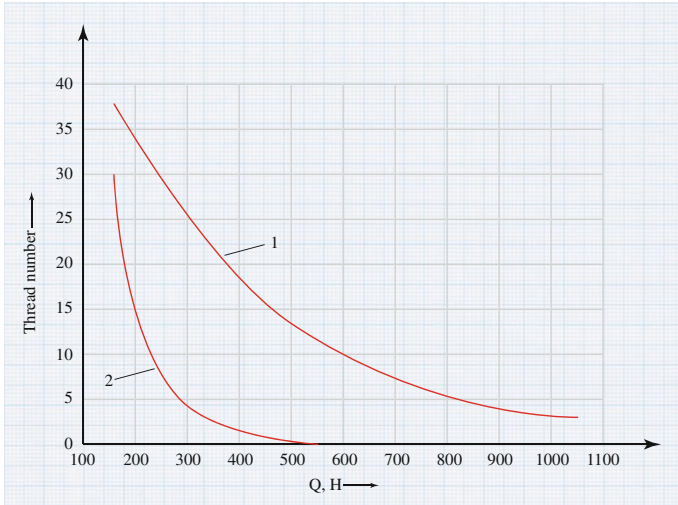
Fig. 6.10 The distribution of load along threads. The trapezoidal thread, the distribution factor of loading at $m = -d$, step $t = 6$ mm. _1_ the diagram where "the nut is compressed, the spindle is stretched"; _2_ the diagram where "the spindle and nut are both stretched"
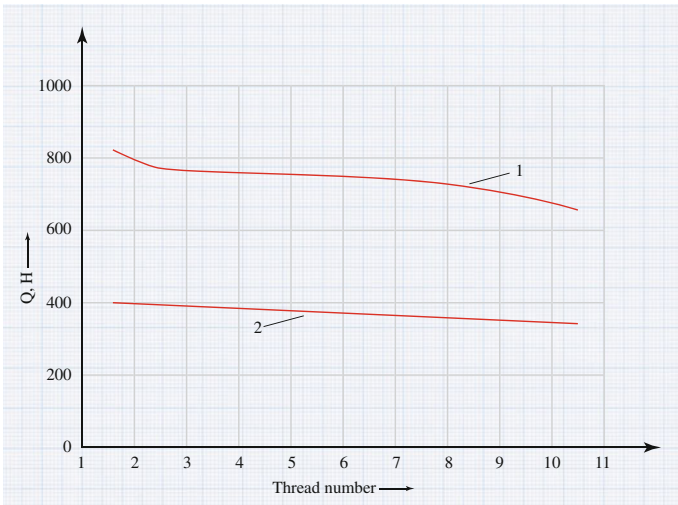
Fig. 6.11 The distribution of load along threads. The trapezoidal thread, the distribution factor of loading at $d = 0.984$, step $t = 6$ mm. _1_ the diagram where "the nut is compressed, the spindle is stretched"; _2_ the diagram where "the spindle and nut are both stretched"

6.4 Study of Wear of the Valve Kinematic Pair in the Elastic–Plastic Deformation Zone

Xmas trees are designed for sealing wellheads, to control and regulate their operation. The effectiveness of valves fixed on the fountain equipment depends largely on the performance of its individual units, including a running pair [9]. The complexity of this study is that on one side is a well-studied thread (the running pair); on the other hand, the deformed state of thread pair of Xmas valve complies with the well-known methods of calculation. The classical theory N.E. Zhukovsky does not provide the even distribution of axial forces along thread within the elastic range (Hooke's law).

However, the experience has shown [7] that the running pair of the direct flow valves has not only elastic, but also plastic deformations, and there is uneven wear along threads. From the theoretical curve of N.E. Zhukovsky, we can conclude that the maximum force occurs on the last thread. However, the pulsating effect of pressure acting on the spindle from the bottom gate creates an additional dynamic force on the thread [10], and the maximum loading starts along threads, due to this the plastic deformation is redistributed not only on the first thread, but also in the following threads and therefore, there is an effect of uneven wear.

This results in a radial displacement of points on the internal radius of thread of nut from the residual deformation, even after removing load [11].

Let us consider the problem of interaction of running pair, undergoing the elastic–plastic deformation in the polar coordinate system. For the argument purpose, we introduce the coefficient of transverse strain [12].

We define the stresses and strains, as well as the boundaries between the elastic and plastic zones at any time of deformation upon unloading. To this end, we introduce into the calculation the coefficient of transverse deformation on the thread of running nut.

To do this, first we write the equation of stress intensity [13]

$$\sigma_i = \frac{\sqrt{2}}{2} \sqrt{(\sigma_1 - \sigma_2)^2 + (\sigma_2 - \sigma_3)^2 + (\sigma_1 - \sigma_3)^2}, \qquad (6.20)$$

where A, σ_2, σ_3—the principal stresses.

The intensity of the deformation

$$\varepsilon_i = \frac{\sqrt{2}}{2(1 + \mu')} \sqrt{(\varepsilon_1 - \varepsilon_2)^2 + (\varepsilon_2 - \varepsilon_3)^2 + (\varepsilon_1 - \varepsilon_3)^2}, \qquad (6.21)$$

where μ'—the variable coefficient of the transverse strain; and ε_1, ε_2, and ε_3—the main strains.

It is known [13] that for the uniaxial strain

$$\sigma_2 = \sigma_3 = 0; \quad \sigma_1 = \sigma_x; \quad \varepsilon_1 = \varepsilon_2; \quad \varepsilon_2 = \varepsilon_3 = -\mu'\varepsilon_1.$$

If we take into account the parameters in (6.20) and (6.21), we obtain

$$\sigma_i = \sigma_x; \quad \varepsilon_i = \varepsilon_x.$$

It can also be written, according to [13]:

$$\frac{\varepsilon_1 - \ell}{\sigma_1 - \sigma} = \frac{\varepsilon_2 - \ell}{\sigma_2 - \sigma} = \frac{\varepsilon_3 - \ell}{\sigma_2 - \sigma} = \psi, \tag{6.22}$$

where ℓ—the average elongation $\ell = \frac{1}{3}\theta$; θ—the volumetric change.

$$\theta = \frac{1}{3}(\varepsilon_1 + \varepsilon_2 + \varepsilon_3), \tag{6.23}$$

$\psi = \frac{1}{2G}$—some stress function; G—the shear modulus. The average stress is determined in [14]

$$\sigma = \frac{1}{3}(\sigma_1 + \sigma_2 + \sigma_3). \tag{6.24}$$

From (6.20), (6.21) and (6.22), we obtain

$$\psi = \frac{1 + \mu'}{\sigma_i}\varepsilon_i. \tag{6.25}$$

Taking into account (6.25) in (6.22),

$$\varepsilon_1 - \ell = (1 + \mu')\frac{\varepsilon_i}{\sigma_i}(\sigma_1 - \sigma);$$
$$\varepsilon_2 - \ell = (1 + \mu')\frac{\varepsilon_i}{\sigma_i}(\sigma_2 - \sigma); \tag{6.26}$$
$$\varepsilon_3 - \ell = (1 + \mu')\frac{\varepsilon_i}{\sigma_i}(\sigma_3 - \sigma).$$

According to Hooke's law,

$$\theta = \frac{1 - 2\mu}{E}(\sigma_1 + \sigma_2 + \sigma_3).$$

where μ—the Poisson ratio and E—the modulus of elasticity of nut.
Then,

$$\ell = \frac{1}{3}\theta = \frac{1 - 2\mu}{E}\sigma. \tag{6.27}$$

From (6.26) and (6.27), we obtain

$$\varepsilon_1 = \left[\frac{1 - 2\mu}{E} - (1 + \mu')\frac{\varepsilon_i}{\sigma_i}\right]\sigma + (1 + \mu')\frac{\varepsilon_i}{\sigma_i}\sigma_1;$$

$$\varepsilon_2 = \left[\frac{1 - 2\mu}{E} - (1 + \mu')\frac{\varepsilon_i}{\sigma_i}\right]\sigma + (1 + \mu')\frac{\varepsilon_i}{\sigma_i}\sigma_2; \qquad (6.28)$$

$$\varepsilon_3 = \left[\frac{1 - 2\mu}{E} - (1 + \mu')\frac{\varepsilon_i}{\sigma_i}\right]\sigma + (1 + \mu')\frac{\varepsilon_i}{\sigma_i}\sigma_3.$$

From [13], it is known that $\mu' = \frac{1}{2} - \frac{1-2\mu}{E}\frac{\sigma_x}{\varepsilon_x}$, where σ_x, ε_x—the stress and elongation under the uniaxial deformation, and $\frac{\sigma_x}{\varepsilon_x} = \frac{\sigma_i}{\varepsilon_i}$. Then,

$$\mu' = \frac{1}{2} - \frac{1 - 2\mu}{2E}\frac{\sigma_i}{\varepsilon_i}. \qquad (6.29)$$

From (6.28) and (6.29), we have

$$\varepsilon_1 = \left[\frac{3}{2}\frac{\varepsilon_i}{\sigma_i} - \frac{1 - 2\mu}{2E}\right](\sigma_1 - \sigma) + \frac{1 - 2\mu}{E}\sigma;$$

$$\varepsilon_2 = \left[\frac{3}{2}\frac{\varepsilon_i}{\sigma_i} - \frac{1 - 2\mu}{2E}\right](\sigma_2 - \sigma) + \frac{1 - 2\mu}{E}\sigma; \qquad (6.30)$$

$$\varepsilon_3 = \left[\frac{3}{2}\frac{\varepsilon_i}{\sigma_i} - \frac{1 - 2\mu}{2E}\right](\sigma_3 - \sigma) + \frac{1 - 2\mu}{E}\sigma.$$

We proceed to the polar coordinates (Fig. 6.12) $\sigma_1 = \sigma_\theta$; $\sigma_2 = \sigma_r$, and we assume that the plane stress state is $\varepsilon_1 = \varepsilon_\theta$; $\varepsilon_2 = \varepsilon_r$ [13]

$$\sigma = \frac{1}{3}(\sigma_r + \sigma_\theta). \qquad (6.31)$$

Taking into account (6.31), we have

$$\varepsilon_r = \frac{\varepsilon_i}{\sigma_i}\left(\sigma_r - \frac{1}{2}\sigma_\theta\right) + \frac{1 - 2\mu}{E}\sigma_\theta;$$

$$\varepsilon_\theta = \frac{\varepsilon_i}{\sigma_i}\left(\sigma_\theta - \frac{1}{2}\sigma_r\right) + \frac{1 - 2\mu}{E}\sigma_r. \qquad (6.32)$$

For nut, i.e., any cylindrical bodies, the equilibrium equation [15] is

$$\frac{d\sigma_r}{dr} + \frac{\sigma_r - \sigma_\theta}{r} = 0 \qquad (6.33)$$

Fig. 6.12 The calculation diagram
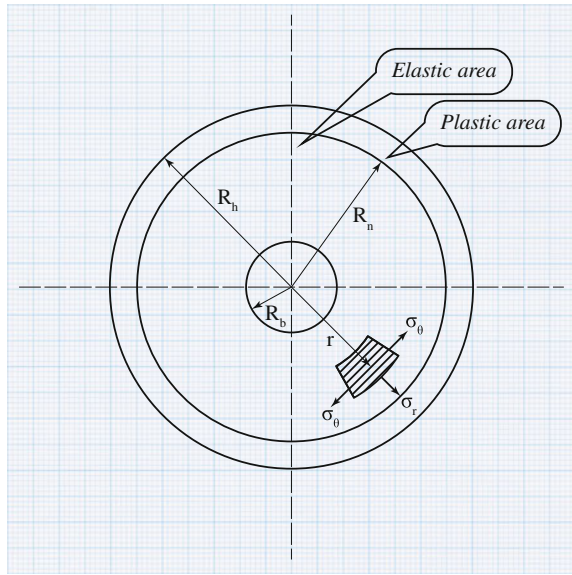
here

$$\sigma_r = \frac{1}{r}\frac{\mathrm{d}\varphi}{\mathrm{d}r};$$
$$\sigma_\theta = \frac{\mathrm{d}^2\varphi}{\mathrm{d}r^2}.$$

(6.34)

where $\varphi = \varphi(r)$—the stress function.

From (6.32) and (6.34), we get

$$\varepsilon_r = \frac{\varepsilon_i}{\sigma_i}\left[\frac{1}{r}\frac{\mathrm{d}\varphi}{\mathrm{d}r} - \frac{1}{2}\frac{\mathrm{d}^2\varphi}{\mathrm{d}r^2}\right] + \frac{1-2\mu}{E}\frac{\mathrm{d}^2\varphi}{\mathrm{d}r^2};$$
$$\varepsilon_\theta = \frac{\varepsilon_i}{\sigma_i}\left[\frac{\mathrm{d}^2\varphi}{\mathrm{d}r^2} - \frac{1}{2r}\frac{\mathrm{d}\varphi}{\mathrm{d}r}\right] + \frac{1-2\mu}{E}\frac{1}{r}\frac{\mathrm{d}\varphi}{\mathrm{d}r}.$$

(6.35)

We write the equation of deformation compatibility [15]

$$\frac{\mathrm{d}\varepsilon_\theta}{\mathrm{d}r} + \frac{\varepsilon_\theta - \varepsilon_r}{r} = 0$$

(6.36)

Then from (6.35) and (6.36), we get

$$\frac{\varepsilon_i}{\sigma_i}\frac{\mathrm{d}^2\varphi}{\mathrm{d}r^2} + \left[\frac{1}{r}\frac{\varepsilon_i}{\sigma_i} + \frac{\mathrm{d}}{\mathrm{d}r}\left(\frac{\varepsilon_i}{\sigma_i}\right)\right]\frac{\mathrm{d}^2\varphi}{\mathrm{d}r^2} - \left[\frac{1}{2r}\frac{\mathrm{d}}{\mathrm{d}r}\left(\frac{\varepsilon_i}{\sigma_i}\right) + \frac{1}{r^2}\frac{\varepsilon_i}{\sigma_i}\right]\frac{\mathrm{d}\varphi}{\mathrm{d}r} = 0.$$

(6.37)

If we accept that $\psi = d\varphi/dr$, then from (6.37) we have

$$\frac{\varepsilon_i}{\sigma_i}\frac{d\psi}{dr} + \left[\frac{1}{r}\frac{\varepsilon_i}{\sigma_i} + \frac{d}{dr}\left(\frac{\varepsilon_i}{\sigma_i}\right)\right]\frac{d\psi}{dr} - \left[\frac{1}{2r}\frac{d}{dr}\left(\frac{\varepsilon_i}{\sigma_i}\right) + \frac{1}{r^2}\frac{\varepsilon_i}{\sigma_i}\right]\psi = 0. \tag{6.38}$$

Then, Eq. (6.34) in terms of ψ can be written as

$$\begin{aligned} \sigma_r &= \frac{\psi}{r}; \\ \sigma_\theta &= \frac{d\psi}{dr}. \end{aligned} \tag{6.39}$$

Let us express σ_i and ε_i through ψ. From (6.20) and (6.34), we can write

$$\sigma_i = \sqrt{\left(\frac{\psi}{r}\right)^2 + \frac{d\psi}{dr} - \frac{\psi}{r}\frac{d\psi}{dr}}. \tag{6.40}$$

The characteristic Eq. (6.38) can be written as follows [13]

$$\frac{d^2\psi}{dr^2} + \frac{1}{r}\frac{d\psi}{dr} - \frac{\psi}{r} = 0. \tag{6.41}$$

We write the boundary conditions:

$$\sigma_r = -P \quad \text{at } r = R_B; \quad \sigma_r = 0 \quad \text{at } r = R_H. \tag{6.42}$$

Consistently, we solve the Eq. (6.38). If we assume that the volume of the nuts does not changed, then

$$\varepsilon_r + \varepsilon_\theta = 0 \tag{6.43}$$

or

$$\frac{dU}{r} + \frac{U}{r} = 0. \tag{6.44}$$

From (6.44), we get

$$U = \frac{A}{r}; \tag{6.45}$$

$$\varepsilon_r = -\frac{A}{r^2}; \quad \varepsilon_\theta = \frac{A}{r^2}. \tag{6.46}$$

At the constant volume of nuts, we can take $\mu' = 1/2$, and then from (6.46), we have

$$\varepsilon_i = \frac{2}{\sqrt{3}} \frac{A}{r^2}. \tag{6.47}$$

From (6.30), $(\varepsilon_z = 0;\ \sigma_z = \sigma)$

$$\sigma_\iota = \frac{1}{3}(\sigma_\iota + \sigma_\kappa + \sigma_\theta)$$

or

$$\sigma_\iota = \frac{1}{2}(\sigma_\kappa + \sigma_\theta). \tag{6.48}$$

Then from (6.20), we obtain

$$\sigma_i = \frac{\sqrt{3}}{2}(\sigma_\theta - \sigma_r). \tag{6.49}$$

At the plastic state for the nut element, we can write [13]

$$\varepsilon_i = \varepsilon_r + (\sigma_i - \sigma_r)E$$

or

$$\varepsilon_i = \sigma_r\left(1 - \frac{E_1}{E}\right) + E_1\varepsilon_i. \tag{6.50}$$

From (6.47), (6.49) and (6.50), we obtain

$$\sigma_\theta - \sigma_r = \frac{2}{\sqrt{3}}\sigma_T\left(1 - \frac{E_1}{E}\right) + \frac{4}{3}E_1\frac{A}{r^3}. \tag{6.51}$$

From (6.33) and (6.51), we obtain

$$\frac{d\sigma_r}{dr} = \frac{2}{\sqrt{3}}\sigma_T\left(1 - \frac{E_1}{E}\right)\frac{1}{r} + \frac{4}{3}E_1\frac{A}{r^3}. \tag{6.52}$$

From (6.49) and (6.52)

$$\sigma_r = \frac{2}{\sqrt{3}}\sigma_T\left(1 - \frac{E_1}{E}\right)\ln\frac{r}{R_B} - \frac{2}{3}E_1\frac{A}{r^3} + B. \tag{6.53}$$

$$\sigma_\theta = \frac{2}{\sqrt{3}}\sigma_T\left(1 - \frac{E_1}{E}\right)\left(1 + \ln\frac{r}{R_B}\right) + \frac{2}{3}E_1\frac{A}{r^3} + B. \tag{6.54}$$

The constants A and B are determined from the boundary conditions: $\sigma_r = -P$ at $r = R_B$, where P—the specific load on nut. When $r = R_b$ from (6.53), we obtain

$$-\frac{2}{3} E_1 \frac{A}{R_b^3} + B = -P. \tag{6.55}$$

Going from the field of elastic deformation to plastic, with $r = R_P$

$$\sigma_i = \frac{\sqrt{3}}{2} (\sigma_\theta - \sigma_r) = \sigma_T. \tag{6.56}$$

For the boundary of the elastic deformation of the nut thread at $r = R_P$, we apply the Lamé equation

$$\left.\begin{array}{l} \sigma_r = -P_{R_P} \\ \sigma_\theta = \frac{P_{R_G}\left(R_H^2 + R_P^2\right)}{R_H^2 - R_P^2} \end{array}\right\} \quad \text{at } r = R_P. \tag{6.57}$$

From (6.56) and (6.57), we obtain

$$\sigma_T = \frac{\sqrt{3}R_H^2}{R_H^2 - R_P^2} P_{R_P}.$$

From this expression,

$$-P_{R_P} = \frac{\sigma_T\left(R_H^2 - R_P^2\right)}{\sqrt{3}R_H^2}. \tag{6.58}$$

For the plastic region, according to (6.53)

$$\frac{2}{\sqrt{3}}\sigma_T\left(1 - \frac{E_1}{E}\right)\ln\frac{R_P}{R_b} - \frac{2}{3}E_1\frac{A}{r^2} + B = -\frac{\sigma_T\left(R_H^2 - R_P^2\right)}{\sqrt{3}R_H^2}. \tag{6.59}$$

From (6.58) and (6.59),

$$\frac{2}{\sqrt{3}}\sigma_T\left(1 - \frac{E_1}{E}\right)\ln\frac{R_P}{R_b} - \frac{2}{3}E_1\frac{A}{C^2} + B = -\frac{\sigma_T\left(R_H^2 - R_P^2\right)}{\sqrt{3}R_H^2}. \tag{6.60}$$

To determine the parameters A and B, we use the conditions of thread surface displacement:

For the elastic displacement,

$$U = \frac{1-\mu}{E} \frac{P_P R_P^2}{R_H^2 - R_P^2} r + \frac{1+\mu}{E} \frac{P_P R_H^2 R_P^2}{(R_H^2 - R_P^2)r} \tag{6.61}$$

For the plastic region, $U = A/r$. At $r = R_p$

$$\frac{A}{C} = \frac{1-\mu}{E} \frac{P_P R_P^2}{R_H^2 - R_P^2} R_P + \frac{1+\mu}{E} \frac{P_P R_H^2 R_P^2}{(R_H^2 - R_P^2)R_P}.$$

Hence,

$$A = \frac{P_{R_P} R_H^2 R_P^2}{E(R_H^2 - R_P^2)} \left[(1-\mu) \frac{R_P^2}{R_H^2} + (1+\mu) \right]. \tag{6.62}$$

From (6.58) and (6.62),

$$A = \frac{\sigma_T R_P^2}{\sqrt{3}E} \left[(1-\mu) \frac{R_P^2}{R_H^2} + (1+\mu) \right]. \tag{6.63}$$

From (6.59), we have

$$B = -\frac{\sigma_T}{\sqrt{3}} \left\{ \begin{array}{l} \left(1 - \frac{R_P^2}{R_H^2}\right) + 2\left(1 - \frac{E_1}{E}\right) \ln \frac{R_P}{R_B} \\ -\frac{2}{3}\frac{E_1}{E}\left[(1-\mu) \frac{R_P^2}{R_H^2} + (1+\mu) \right] \end{array} \right\}. \tag{6.64}$$

On the basis of Eqs. (6.53) and (6.54), the graphs are constructed for dependencies of the radial and tangential stresses from the radius of thread of running pairs (spindle–nut) for the following selected materials (Fig. 6.13): 1—the pair of steels 30KhMA/30XMA–40KhN/40XH (elasticity modulus $E = 2.15 \times 10^5$ MPa, yield strength $\sigma_T = 800$ MPa, and Poisson's ratio $\mu = 0.28$); 2—the pair of steel and bronze 30KhMA/30XMA–BrAMts9-2/БpAMц9-2 ($E = 1.15 \times 10^5$ MPa, $\sigma_T = 450$ MPa, $\mu = 0.32$); and 3—the pair of steel and brass 30KhMA/30XMA–LS-60/ЛC-60 ($E = 1 \times 10^5$ MPa, $\sigma_T = 350$ MPa, $\mu = 0.35$).

While selecting materials for the running pair, we base it on the fact that bronze BrAMts9-2/БpAMц9-2 and brass LS-60/ЛC-60 have sufficient resistance to wear and minimal friction coefficient.

As a result, the calculation established that all combinations of running pairs after reaching the thread radius 11.14 mm, at the tangential stress σ_T, operate in the elastic–plastic deformation.

The analysis of the influence of radial stresses shows that initially, the stress gradually increases and after reaching the thread radius 11.75 mm and the sign changes into the positive.

The statistical analysis and visual inspection of spindle shows that the areas of maximum wear is in the top of the thread.
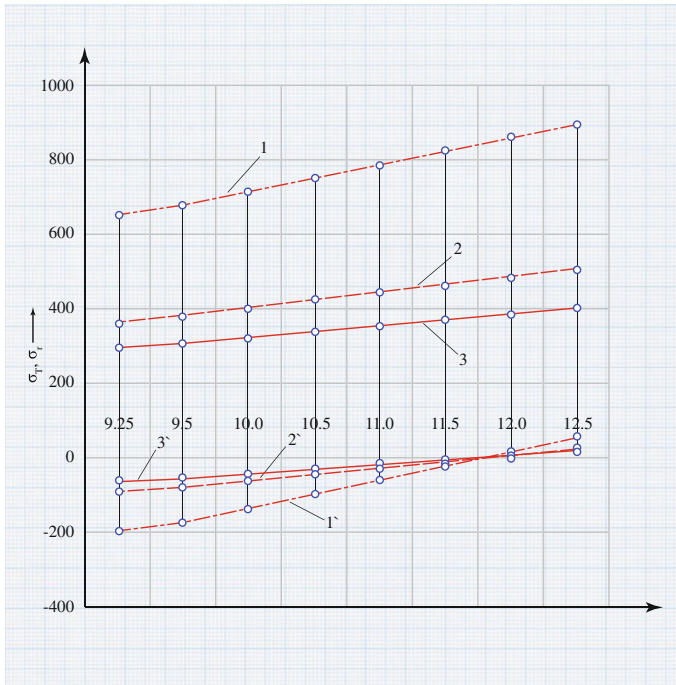
Fig. 6.13 The dependence of tangential (1, 2, 3) and radial (1′, 2′, 3′) stresses from the radius of thread of running pairs: *1* the pair of steels 30KhMA/30XMA–40KhN/40XH ($E = 2.15 \times 10^5$ MPa, $\sigma_T = 800$ MPa, $\mu = 0.28$); *2* the pair of steel and bronze 30KhMA/30XMA–BrAMts9-2/ БрАМц9-2 ($E = 1.15 \times 10^5$ MPa, $\sigma_T = 450$ MPa, $\mu = 0.32$); *3* the pair of steel and brass 30KhMA/30XMA–LS-60/ЛC-60 ($E = 1 \times 10^5$ MPa, $\sigma_T = 350$ MPa, $\mu = 0.35$)

The wear in the end of the thread is almost 2 times greater than the wear in the root of spindle thread (Fig. 6.14).

In our view, the summation of the tangential and radial stresses in the top of the thread confirms the satisfactory agreement between the analytical studies and experimental results.

The further analysis of the research results found that when the running pair is in the elastic–plastic deformation, it leads to the formation of scuffing on the surface.

The significant impact on scuffing has the presence of contact pressure in the area of considerable friction prior to a sharp increase in the friction coefficient.

The stress state at the friction process (movement of the running pair) and the elastic–plastic deformation may also occur in the local micro-volumes of material even at the relatively low nominal loads, since the actual stresses in them reach significant values.

The extension of the elastic–plastic deformation range occurs as a result of soaring number of individual contacts due to an increase of the normal load and the stress redistribution under the summary of tangential and radial stresses. Owing to the combined action of the radial and tangential stresses in the surface layer of the
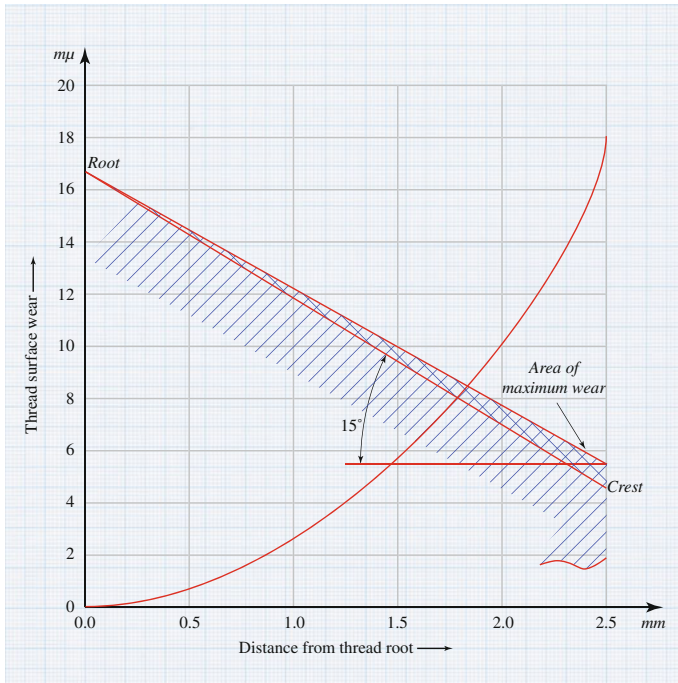
Fig. 6.14 The dependence of the thread surface wear from its radius

material in friction, the volumetric stress state is created in which, as shown by Grozin [16], even the high-strength materials exhibit sufficient ductility. In the surface layers, the shear stresses include the resistance stresses to the dislocation movements from the internal obstacles and from the surface layer.

The analysis of the research results and the calculations showed that the running pair made of steel 30KhMA/30XMA (spindle) and bronze BrAMts9-2/БрАМц9-2 (nut) increases the performance according to the criteria on resistance to scuffing and wear due to its low friction coefficient ($f = 0.106$).

6.5 Assessment of Tribological Characteristics of Kinematic Pair

The goal of this study develops the running pair of valves for Xmas tree with the critical operational parameters, so we studied the effect of various factors on the performance of running pair of valves with respect to the critical operating parameters and the necessary prerequisites for designing running pairs.

The peculiarities of design features and its operating conditions demand a number of specifications toward the material requirements for the details of running the pair.

The material of running pair of valve must have the sufficiently high mechanical properties, the resistance to general corrosion and hydrogen sulfide cracking, manufacturability, and durability, and the pair should provide a minimal friction coefficient.

The wear resistance for various types of surfaces is achieved by coating.

The presence of lubricant also increases the wear resistance of surfaces; in the absence of lubricant, the various surface hardening methods can be used.

When choosing the material for the running pair of valve of Xmas trees, designed to operated in the hostile environment, the necessary conditions are not only wear, but also resistance to corrosion.

The details of running pair operating in environments with H_2S and CO_2 are subject to the hydrogen sulfide cracking due to which the material must possess a sufficient resistance to the hydrogen sulfide stress cracking.

Given the above, we chose the low-alloy structural steel ZOKhMA/ЗОХMA, the high-alloy steel St40KhN/Cт40XH and non-ferrous metals (brass LS-60/ЛС-60, bronze BrAMts9-2/БpAMц9-2).

These materials are chosen due to the following specifications:

- St40KhN/Cт40XH has sufficient resistance to the hydrogen sulfide stress cracking, but subject to general corrosion in the highly aggressive environments;
- St30KhMA/Cт30XMA has a high resistance to cracking and the hydrogen sulfide and practically is not subjected to the general corrosion in H_2S and CO_2;
- BrAMts9-2/БpAMц9-2 and LS-60/ЛС-60 are characterized by sufficient durability and minimal friction coefficient.

The durability study of materials was in the special laboratory facility developed by AzINMASh [10].

In the first stage of the research, we determined the maximum contact load, which leads to the appearance of scuffing on the surface of friction samples.

The tests were conducted by gradually increasing the load. Each experiment was carried out with a new sample and in new portion of the experimental environment. Before next experiment, the samples got degreased with gasoline or acetone and dried out.

The scuff resistance of materials was evaluated by the critical contact pressure, the value of which was determined by the magnitude of the contact pressure prior to a sharp increase in the friction coefficient.

Samples were subjected to the metallographic analysis of friction zone.

As the scuffing analysis results show, the presence of environment in friction has a significant impact on the maximum contact pressure on the formation of scuff. For example, the presence of lubricant "Armatol-238" in friction the critical value of the contact pressure increases twice in comparison with the dry friction.

The thickness of metal coating plays a significant role on their resistance to scuffing. This is explained by the fact that for each coating there is an optimal thickness within which we can find the best properties (the tensile strength, the adhesion strength with the main metal).

The results showed to coat the surface with the pyrolytic chromium carbide; the most rational thickness is within 16 μm.

Given the impact of corrosion on metal surfaces, we explored its effect on resistance to scuffing. For this purpose, the samples were selected with the coated steel 30KhMA/30XMA "Coleman," which were initially treated in the following medium: the aqueous solution of 5 % NaCl, acidified with 0.5 % CH_3COOH and saturated with H_2S up to a concentration of 2500 mg/l. The exposure time of samples ranged from 24 to 624 h. The samples were tested on scuffing with the contact loading 50 and 125 MPa in the medium of mentioned sealing lubricant. During friction the maximum friction path was registered, which was taken from the sample before scuffing.

The analysis of results shows that the contact time of the metal with the sulfureted environment has a significant impact on its resistance to scuffing. The maximum decrease in resistance to scuffing of metal is observed in up to 324 h of exposing.

The metallographic examination of samples showed that the decline in resistance to scoring of metal is due to the softening of friction surface. This is a result of hydrogen penetration into the metal. The chemically nickel-plated samples experience higher micro-hardness of the nickel layer and the softening of base metal surface, which is also a reason of scuff reduction.

The friction coefficients of materials were determined through the 5-m friction path at the different contact pressures and environments.

The analysis of results show that during friction in the sealing lubricant, the friction coefficient for "Coleman" surfacing in comparison with dry friction is reduced by almost 4 times. The friction coefficient for "stellate" surfacing during friction in the sealing lubricant in comparison with dry friction is significantly reduced in only at the contact pressures above 25 MPa. At the contact loads of 50 MPa, the friction coefficients of sample pairs from St30KhMA/Ст30XMA and with the electrolysis nickeling in the sealing lubricant do not differ and are within 0.06–0.07. "Coleman" has the lowest coefficient of friction among tested samples in the sealing lubricant "Armatol-238."

Wear of samples were determined by the gravimetric method. The effect of the metal hardness on their durability was also investigated. For St30KhMA/Ст30XMA, it is found that with an increase of the alloy hardness its wear is reduced. The smallest surface wear is observed for "Coleman" at a hardness of 50–55HRC.

The impact on the sulfureted environment on wear of the non-ferrous metals was determined when it was paired with St30KhMA/Ст30XMA.

The pair was studied in the sealing lubricant "Armatol-238" at the contact pressure 50 MPa. Thus, the wear resistance of samples was determined with the prior exposure of sample to the hydrogen sulfide (324 h) and without impact. As the hydrogen sulfide environment, we chose NACE. We also studied the impact of hydrogen sulfide environment on the corrosion inhibitor "Visco-904NIK."

The results of experiment are shown in Table 6.2.

The metallographic analysis of samples showed that during first 500 cycles of experiment, the surface of samples from St30KhMA/Ст30XMA got smeared with bronze. The wear of pair is minimal.

Table 6.2 The results of experiment

Testing conditions	Pair details	Mass wear of sample, g 10^{-9} (with number of cycles)			
		500	1000	1500	2000
Without prior treatment in NACE	M	+0.1	+0.001	+0.001	+0.001
	S	20	4.9	9.9	2.3
With prior treatment in NACE (324 h)	M	+0.8	+1.55	–	–
	S	6.1	7.7	–	–
With prior treatment in NACE and inhibitor "Visco-904NIK"	M	+0.1	+0.001	+0.001	+0.001
	S	23	5.0	10	2.4

Note M—the moving sample, St30KhMA/Ст30ХМА; S—the stationary sample, BrAMts9-2/
БрАМц9-2; (+)—increase of sample weight

The samples treated in NACE have greater durability. The analysis revealed that this phenomenon is due to the emergence of a sulfide film made of bronze on the sample surface. The micro-hardness of sulfide film is greater than that of bronze. The wear resistance of samples after exposure to NACE with the corrosion inhibitor "Visco-904NIK" is virtually unchanged. The metallographic analysis of these samples showed the absence of friction on the surface of sulfide films.

Thus, the studies allowed establishing varying degrees of the hydrogen sulfide influence on the metal wear. So if the durability of steels and alloys decreases, then for the non-ferrous metals it conversely increases. The presence of corrosion inhibitor excludes the impact of sulfureted environment on the wear-resistant of steels, alloys, and non-ferrous metals.

Based on the results of laboratory tests, the full-scale details were manufactured. The spindle and nut were made from the listed materials and in the following combinations:

- St30KhMA + St40KhN (Ст30ХМА + Ст40ХН);
- St30KhMA + BrAMts9-2 (Ст30ХМА + БрАМц9-2);
- St30KhMA + LS-60 (Ст30ХМА + ЛС-60).

Tests were carried out on the actual parts of valve. This imitation of axial loading for pair with the minimum pressure was achieved by using the blind (without holes) saddles on both sides of the closing gate generating substantial friction.

The test pairs showed various performances.

For example, the running pair made of St30KhMA + St40KhN (Ст30ХМА + Ст40ХН) after 40 test cycles got completely destroyed. The research of friction surfaces of the pair displayed a complete destruction of the spindle thread and considerable wear of thread of nut (Fig. 6.15).

The second pair made of St30KhMA + LS-60 (Ст30ХМА + ЛС-60) for spindle and nut, respectively, got destroyed only 42 test cycle. The research of friction surfaces of the pair also showed considerable wear (Fig. 6.16).

The best results were obtained for the pair made of St30KhMA + BrAMts9-2 (Ст30ХМА + БрАМц9-2) for spindle and nut, respectively. This pair completely
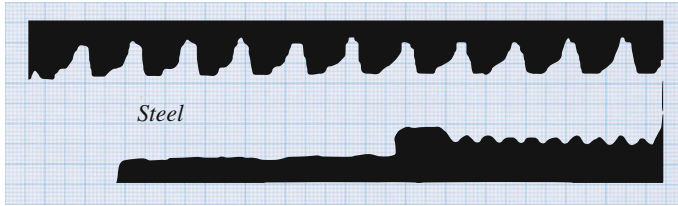
Fig. 6.15 Profilogram—the photograph of working surface of running pair St30KhMA + St40KhN (Ст30ХМА + Ст40ХН)
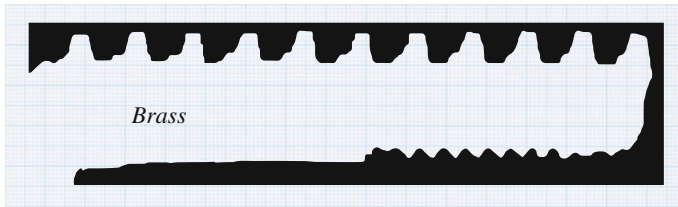
Fig. 6.16 Profilogram—the photograph of working surface of running pair St30KhMA + LS-60 (Ст30ХМА + ЛС-60)
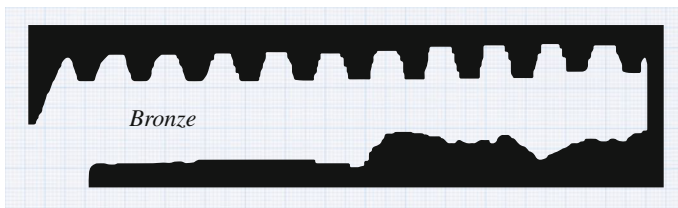
Fig. 6.17 Profilogram—the photograph of working surface of running pair St30KhMA + BrAMts9-2 (Ст30ХМА + БрАМц9-2)

preserved performance even after 1000 test cycles. The research of friction surfaces of the pair showed much lower wear (Fig. 6.17).

While testing the valves, the torqueses on the wheel were also determined (Table 6.3).

The analysis of test results (see Table 6.3) shows that the lowest torque is observed for the third pair, St30KhMA + BrAMts9-2 (Ст30ХМА + БрАМц9-2).

Based on these studies, we found that the running pair suitable to be used in environments with H_2S and CO_2 up to 25 % of total volume, and pressures up to 105 MPa are the ones made of St30KhMA + BrAMts9-2 (Ст30ХМА + БрАМц9-2) for spindle and nut, respectively.

To verify the findings of result, we study the fractal properties of profilograms for all three running pairs, as it is shown in Figs. 6.15, 6.16 and 6.17.

There are few fundamentally different definitions on geometrical dimension of object. The main ones are the Minkowski dimension (the term "box dimension" is

Table 6.3 The analysis of test result

#	Material (spindle + nut)	Friction medium	Torque, N m	Friction coefficient
1	St30KhMA + St40KhN (Ст30ХМА + Ст40ХН)	No lubrication	460–530	0.23
2	St30KhMA + St40KhN (Ст30ХМА + Ст40ХН)	Lubrication	280–300	0.11
3	St30KhMA + LS-60 (Ст30ХМА + ЛС-60)	Lubrication	160–170	0.08
4	St30KhMA + BrAMts9-2 (Ст30ХМА + БрАМц9-2)	Lubrication	110–130	0.06

used in English literature); the topological dimension and the Hausdorff dimension. The topological dimension of set is always expressed as an integer; this does not contradict to a notion that the curves are one-dimensional and the surfaces are two-dimensional. The Hausdorff dimension is at the heart of the fractal theory. In 1975, Mandelbrot [48] defined fractals as set, the Hausdorff dimension of which is strictly greater than the topological dimension. The Minkowski dimension can serve as an analog of the Hausdorff dimension, which is convenient in the practical applications. These dimensions are generally come with the similar values, but the algorithm for the Minkowski dimension is much more efficient. Generally,

$$\dim_M(A) \geq \dim_H(A),$$

where $\dim_M(A)$ and $\dim_H(A)$ are, respectively, the dimension of Minkowski and Hausdorff for the set A.

Hausdorff Dimension The well-known formula for the radius r of sphere volume in the Euclidean space of any (integer) number of dimensions d:

$$V_d = \gamma(d)r^d, \quad d = 1, 2, 3\dots \tag{6.65}$$

where $\gamma(d) = \frac{(\Gamma(1/2))^d}{\Gamma(1+d/2)}$.

In particular, at $d = 3$, we have $\Gamma(1/2) = \sqrt{\pi}, \Gamma\left(1 + \frac{3}{2}\right) = \frac{3}{2}\Gamma\left(\frac{3}{2}\right) = \frac{3}{2}\Gamma\left(1 + \frac{1}{2}\right) = \frac{3}{2} \cdot \frac{1}{2}\Gamma\left(\frac{1}{2}\right) = \frac{3}{4}\sqrt{\pi}$, so that $V_3 = \frac{(\sqrt{\pi})^3}{\frac{3}{4}\sqrt{\pi}}r^3 = \frac{4}{3}\pi r^3$.

The first step in constructing a theory of fractional dimension is to determine the *d-measure* of the ball with radius r in Euclidean n-dimensional R^n space, where d—any nonnegative real number. This is achieved by distributing the formula (6.65) for all real $d > 0$. For example, the ball volume (measure) in the 3/2-dimensional space is defined as

$$V_{3/2} = \gamma\left(\frac{3}{2}\right)r^{\frac{3}{2}} = \frac{\left(\Gamma\left(\frac{1}{2}\right)\right)^{\frac{3}{2}}}{\Gamma\left(1 + \frac{3}{4}\right)}r^{\frac{3}{2}} = \frac{\pi\sqrt{\pi}}{0.517}r^{\frac{3}{2}} = 1.934\pi\sqrt{\pi} \cdot r^{\frac{3}{2}}.$$

Note that the specific value of the coefficient $\gamma(d)$ in (6.65) does not play any role in the further reasoning and it can be considered a constant.

The next step is to transfer the concept of *d-measure* from the ball to an arbitrary set $A \subset R^n$. To do this, we consider a sequence of balls with radii $r_i < \varepsilon, i = 1, 2, 3 \ldots$, that cover A, and approximate *d-measure* of Hausdorff for set A with sum

$$\sum_{i=1}^{\infty} \gamma(d) r_i^d.$$

Further, the value is entered

$$S_{d,\varepsilon}(A) = \inf \sum_{i=1}^{\infty} \gamma(d) r_i^d, \tag{6.66}$$

where inf (precise low boundary) is sought over all coverings of the set A with r_i-balls and $r_i < \varepsilon$. The *d-measure outer dimensional* of the set A is defined as

$$S_d(A) = \lim_{\varepsilon \to 0} S_{d,\varepsilon}(A) \tag{6.67}$$

The following is true.

Theorem [49] *For any set $A \subset R^n$ there is a corresponding single number d, called the Hausdorff dimension of the set A, for which the*

$$e < d \Rightarrow S_e(A) = \infty,$$
$$e > d \Rightarrow S_e(A) = 0.$$

This number is denoted by $\dim_H(A)$*, and satisfies*

$$\dim_H(A) = \sup\{e : S_e(A) = \infty\} = \inf\{e : S_e(A) = \infty\}. \tag{6.68}$$

For the numerical implementation of the formula (6.68), it is necessary to introduce sets $\mathfrak{M}_1$, $\mathfrak{M}_2$, $\mathfrak{M}_3$ of sequences $\{e_k\}$, $\{\varepsilon_j\}$ and $\{r_i\}$, respectively, and first calculate in (6.66) at $d = e_k$, $\varepsilon = \varepsilon_j$, $e_k \in \mathfrak{M}_1$, $\varepsilon_j \in \mathfrak{M}_2$ *inf* for all $r_i < \varepsilon_j$, $r_i \in \mathfrak{M}_3$, then find the limit (6.67) at $d = e_k$, $\varepsilon = \varepsilon_j$, $\varepsilon_j \to 0$, and finally calculate the *sup* and *inf*, included in the right-hand side of (6.68). Obviously, such a procedure involves intensive computation and can lead to significant errors in the obtained results. Therefore, in practice instead of the Hausdorff dimension, the Minkowski dimension is used, which in most cases, as mentioned above, coincides with the first.

Minkowski Dimension The *d-measure* of the Minkowski dimension of the set A is approximated by combining the balls of fixed radius $r = \varepsilon$ and summing their volumes.

Let $N(\varepsilon)$ is the minimal number of balls with radius ε, necessary to cover the compact set A. Then, the *d-measure* of A, is denoted by $B_d(A)$, satisfies (approximately) the ratio

$$B_d(A) \propto N(\varepsilon)\varepsilon^d.$$

Assuming that $B_d(A) > 0$, for some $c > 0$ we have

$$N(\varepsilon) \approx \frac{c}{\varepsilon^d}. \tag{6.69}$$

Applying logarithm to the left and right sides, we get (approximately)

$$\log N(\varepsilon) = \log c - d \log \varepsilon, \tag{6.70}$$

where log means logarithm with base 2 that means

$$d = -\frac{\log N(\varepsilon)}{\log \varepsilon} + \frac{\log c}{\log \varepsilon}.$$

Since $\log \varepsilon \to -\infty$ at $\varepsilon \to 0$, the Minkowski dimension being $\dim_M(A)$ of A must satisfy the equality

$$\dim_M(A) = d = -\lim_{\varepsilon \to 0} \frac{\log N(\varepsilon)}{\log \varepsilon}, \tag{6.71}$$

If the limit exists, then the expression (6.71) determines the *Minkowski dimension* of the set A.

As it is proved in [49], to determine the Minkowski dimension instead of the balls in the Euclidean metrics (circles on the plane), you can use the cubes (squares on the plane).

The physical methods of calculating the fractal dimension are presented in [50]. The computer algorithms for computing the Minkowski dimension d are usually based on the ratio (6.70). The simplest way to calculate the Minkowski dimension of fractal A is to apply a cell method that is based on the following.

We divide the area of A, into the square cells (the two-dimensional case) of several sizes ε. Then, we calculate the number of cells $N(\varepsilon)$, necessary to cover A at fixed ε and substitute the obtained values into the ratio (6.70). The dependency graph of $\log N(\varepsilon)$ from $\log \varepsilon$—a straight line with slope d. Recall that $N(\varepsilon)$ denotes the minimal number of cells with side ε, necessary to cover the fractal. To determine the unknown parameters c and d (although the value of c is usually not important), we need to evaluate $N(\varepsilon)$ for several values of ε. With this purpose, for the sequence $\varepsilon_k (k = 1, \ldots, k_0)$ of values ε, we construct sequences $\{y_k\}$ and $\{x_k\}$, where $y_k = \log N(\varepsilon_k)$ and $x_k = \log \varepsilon_k$ and using the method of least squares (MLS), we calculate the regression coefficients

$$y = b + mx, \tag{6.72}$$

where $m = -d$, $b = \log c$. According to the MLS estimates for b and m, we evaluate

$$\hat{d} = -\hat{m}, \hat{c} = e^{\{\hat{b}\}}. \tag{6.73}$$

We show the use of the cell method for calculating the Minkowski dimension on the example of the working surface profilograms for spindle and nut as shown in Figs. 6.15, 6.16, and 6.17. Previously, these profilograms were processed on a computer using "Paint" software package to give them a kind of fine lines (skeleton). As a result, we get the graphics of profilograms as shown in Figs. 6.18, 6.19, and 6.20 and corresponding Figs. 6.15, 6.16, and 6.17. Then, using the "Get Data" software package on the monitor the meshes of different sizes L (instead of ε we use L) are applied and $\log L$ and $\log N(L)$ are computed. The dependency graphs of $\log N(L)$ from $\log L$ for curves from Figs. 6.18, 6.19, and 6.20, and corresponding linear regressions are shown in Figs. 6.21, 6.22, and 6.23.
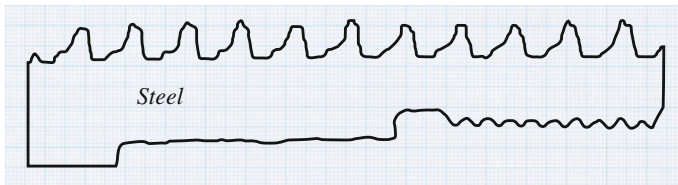
Fig. 6.18 The graph of profilogram from Fig. 6.15
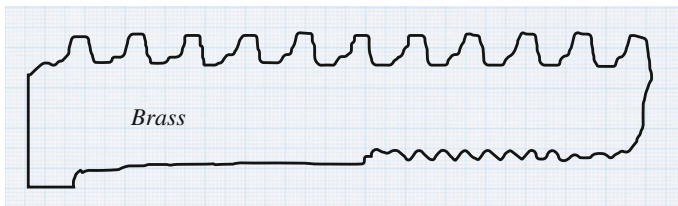
Fig. 6.19 The graph of profilograms from Fig. 6.16
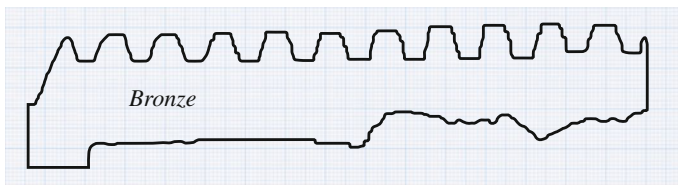
Fig. 6.20 The graph of profilograms from Fig. 6.17
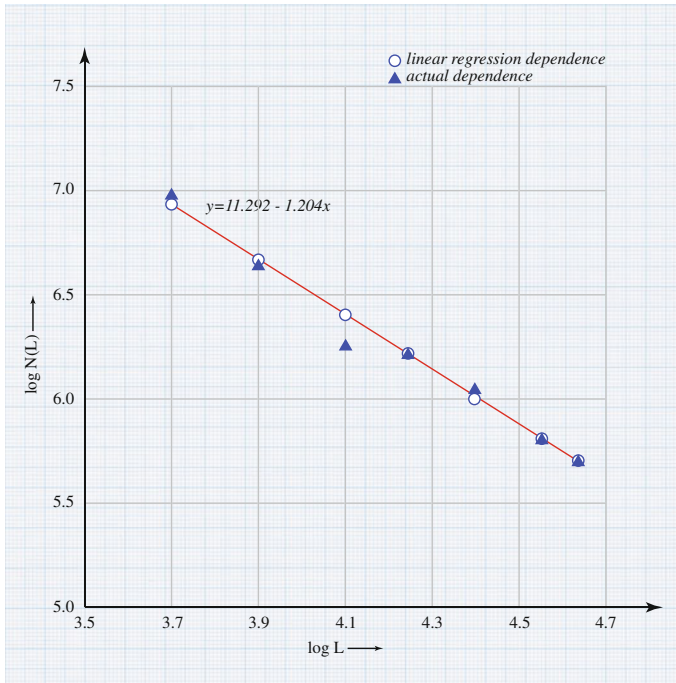
Fig. 6.21 The graph of dependence of $N(L)$ from L in the bi-logarithmic coordinates for the curve from Fig. 6.18

The results of calculation show that the fractal dimension d of the curves in Figs. 6.18, 6.19 and 6.20, respectively, are equal to 1.204, 1.195, and 1.154.

This means that the most regular (less chaotic and fractal) is the curve in Fig. 6.20 with $d = 1.154$, which confirms the findings previously obtained by experimental studies of torque and the friction coefficient for the considered running pairs (Table 6.3).

The field tests of Xmas trees show that the main cause of violating the original surface sealing in closing elements of valves is due to the presence of a significant amount of sand (NGDU "Azizbekovneft").

At the start of opening and at the end of closing, the sand grains get stuck in the minimal gap between the sealing surfaces of valve, with a further move they scuff the surface. The scratch crossing over the whole width creates some sort of grooves. The product of well running with high turbulence through the valve results in intense destruction of parts.

Considering that the opening and closing cycles are mainly repeated in replacement of supporting sleeves, then the durability of valves depends on wear resistance to the latter. This dependence is determined quantitatively with an increase in wear resistance of sleeves by 10 times, the average durability of valves increases on average by more than 3 times.
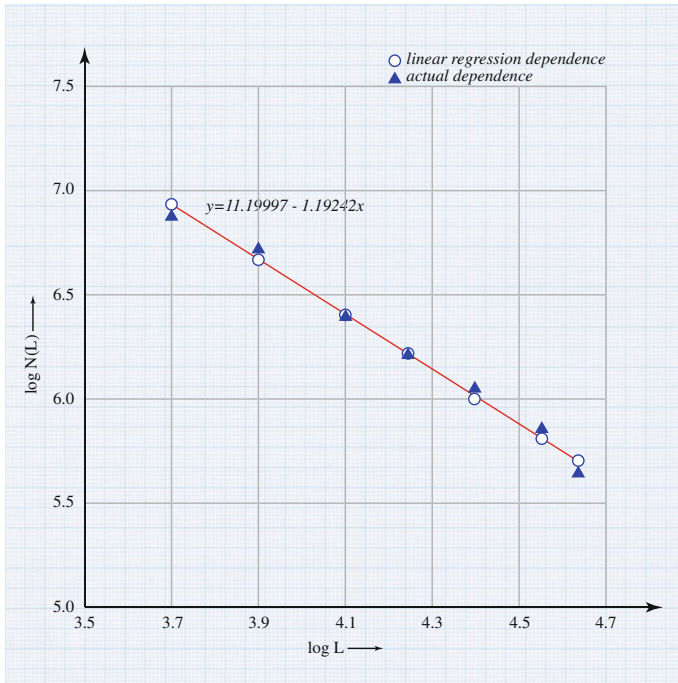
Fig. 6.22 The graph of dependence of $N(L)$ from L in the bi-logarithmic coordinates for the curve from Fig. 6.19

Operational conditions of wellhead equipment have their own specific features different from other machines and equipment:

- the same parts and components of valves, amounted at different parts of Xmas perform under different conditions;
- the faulty valves are removed from tree, repaired and installed on any other fittings that falls into the same category, but in completely different working environment;
- the wells being transferred into different operational regime, Xmas tree gets dismounted (even if it is still operational) and sent to workshop, for full maintenance.

During the operational period of Xmas tree, factors affecting their reliability can vary significantly.

The results of the statistical analysis from the operational data of 200 fountain wells show that the closing parts of valves fail as a result of the combined action of mechanical, corrosive-mechanical, abrasion, and other types of wear.

The wear resistance of valves substantially depends on the performance of disk springs of the direct flow valves.
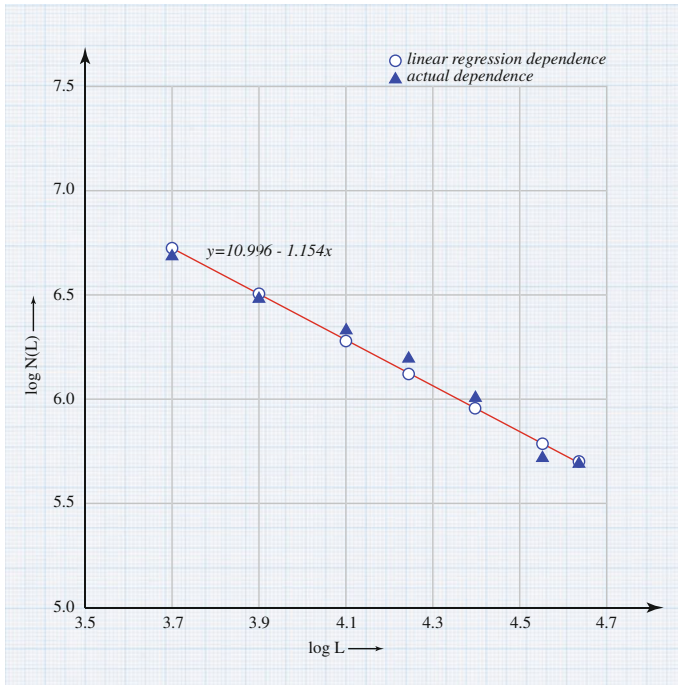
Fig. 6.23 The graph of dependence of $N(L)$ from L in the bi-logarithmic coordinates for the curve from Fig. 6.20

The special study was conducted to improve performance of the disk springs, and it helped to establish the main parameters of springs with regard to their properties and dimensions of closing parts.

To ensure the reliable sealing of valve at the initial stage of operation, it is required to have a specific pre-loading on the sealing surfaces of gate and saddle, obtained through the deformation of disk spring. The valve performance depends on the magnitude of that pre-deformation.

So to get stable characteristics of tribocoupling for gate–saddle it is necessary that the disk springs do not have a thickness deviation, i.e., the thickness of spring should have a close tolerance that should be kept in mind at the design stage.

Both in test and in operational conditions, the valves of Xmas tree were analyzed on the mechanism of wear in the contact surfaces of gate–saddle. Thus, it was established the basic criteria of mechanism failure of the friction surface of gate–saddle manufactured from the high-strength and anti-corrosive materials such as "stellate."

The most important of all the criteria of the mechanism of destruction of the contacting surfaces proved to be: the formation of colored spots on the mirror surface of gate–saddle; the increase in rate of spot size, and their localization in separate areas; the process of surface crystalline destruction in the area of localized spots; the appearance and nature of the uneven surface of gate seat [9].

6.6 Mechanics of Frictional Conical Surfaces of Xmas Tree Valves

In recent years of machine building, the manufactures cannot meet the growing demand in Xmas trees not only in quantity but also in quality and technical level.

The low durability and wear resistance of the gate valves primarily used as the closing devices led to the complication of the construction and weight of Xmas trees because of the valve duplication designed for the operating pressure significantly higher than the actual pressure of well, which in turn led to significant metal consumption and use material resources [7].

The analysis of these studies showed that the Xmas trees with the conical closing devices have the greatest prospects. AzINMASh successfully used these valves for active oil and gas wells, not only in our country, but also abroad.

However, one of the major drawbacks of the conical plug valves is the jamming in the body of valve and the high torque required to control valves.

Furthermore, under the impact of medium, the conical plug got pushed toward the inlet, whereby there is a sufficiently high specific load on the contact surface with the casing tube.

In this regard, we considered the problem to establish a specific relationship between the load generated between the working surfaces of plugs and the valve body and the contact pressure between the plug and the body due to the internal pressure, in the case of one-sided sealing valve, in other words for the valve operation in the mode of self-sealing given the physical and mechanical characteristics of material [17].

It should be noted that these issues are still not studied sufficiently.

To solve this problem, we write the equation of the relationship between the stress and strain assuming the condition $\sigma_3 = 0$; that is, the plane stress state [18] is

$$\left. \begin{array}{l} \sigma_1 = \frac{1}{1-\mu_{12}\mu_{21}} \cdot \frac{\sigma_{i1}}{e_{il}} \left(l_1 + \mu_{12} l_2 \right) \\ \sigma_2 = \frac{\mu_{12}}{\mu_{21}} \cdot \frac{1}{1-\mu_{12}\mu_{21}} \cdot \frac{\sigma_{i1}}{e_{il}} \left(l_2 + \mu_{21} l_1 \right) \end{array} \right\}, \tag{6.74}$$

where σ_1, σ_2, and σ_3—the principal stresses; μ_{12}, μ_{21}—the coefficient of transverse deformation; and e_{il}—the intensity of deformation.

$$l_1 = \ln \frac{r_0 S_0}{r S_\Phi}, \quad l_2 = \ln \frac{r}{r_0}. \tag{6.75}$$

where S_Φ—the effective (actual) conical area of plug; S_0—the nominal area; r_0—the small radius of the base; and r—the average radius of plug.

According to Kachanov [19], the intensity of deformation is determined by

$$e_{i1}^2 = \frac{1}{\mu_{21}(1 - \mu_{12}\mu_{21})}\left(\mu_{21}l_1^2 + 2\mu_{12}\mu_{21}l_1l_2 + \mu_{12}l_2^2\right). \tag{6.76}$$

Considering the hardening of material of contact surface of conical plug [18, 19],

$$\sigma_{i1} = ke_{i1}^n, \tag{6.77}$$

(where k—the constant characterizing the plasticity of material, $k = 0.5\sigma_T$), then Eq. (6.74) can be written as

$$\left.\begin{array}{l}\sigma_1 = \frac{k}{1-\mu_{12}\mu_{21}} \cdot e_{i1}^{n-1}(l_1 + \mu_{12}l_2) \\ \sigma_2 = \frac{\mu_{12}}{\mu_{21}}\frac{k}{1-\mu_{12}\mu_{21}} \cdot e_{i1}^{n-1}(l_2 + \mu_{21}l_1)\end{array}\right\}. \tag{6.78}$$

Taking into account (6.75)–(6.77), the Eq. (6.78) takes the following form:

$$\left.\begin{array}{l}\sigma_1 = \frac{k}{1-\mu_{12}\mu_{21}} \cdot A^{-m}\left(\ln\frac{r_0 S_0}{rS_\Phi} + \mu_{12}\ln\frac{r}{r_0}\right) \\ \sigma_2 = \frac{\mu_{12}}{\mu_{21}} \cdot \frac{k}{1-\mu_{12}\mu_{21}} \cdot A^{-m}\left(\ln\frac{r}{r_0} + \mu_{21}\ln\frac{r_0 S_0}{rS_\Phi}\right)\end{array}\right\}, \tag{6.79}$$

where

$$A = \frac{\left(\mu_{21}l_1^2 + 2\mu_{12}\mu_{21}l_1l_2 + \mu_{12}l_2^2\right)}{\mu_{21}(1 - \mu_{12}\mu_{21})}; \tag{6.80}$$

$$-m = \frac{n-1}{2}.$$

The specific load q can be defined as the following (see Fig. 6.19):

$$q = \frac{-T_2 \cos\alpha}{r}, \tag{6.81}$$

where T_2—the spherical unit force at the contact surface of the conical plug.

From the theory of shells [17, 19], we can write for T_2:

$$T_2 = \frac{kS_\Phi(l_2 + \mu_{21}l_1)}{y_0^m(1 - \mu_{12}\mu_{21})} \cdot \frac{\mu_{12}}{\mu_{21}}, \tag{6.82}$$

where y_0—the deformation function

$$y_0 = e_{1c}^2 + 2\mu_{12}e_{1c}e_{2c} + \bar{\mu}l_{2c}^2, \tag{6.83}$$

where e_{1c}, e_{2c}—the strain in the middle surface; and $\bar{\mu}$—the dimensionless coefficient of transverse deformation (Fig. 6.24).

Fig. 6.24 The design
diagram
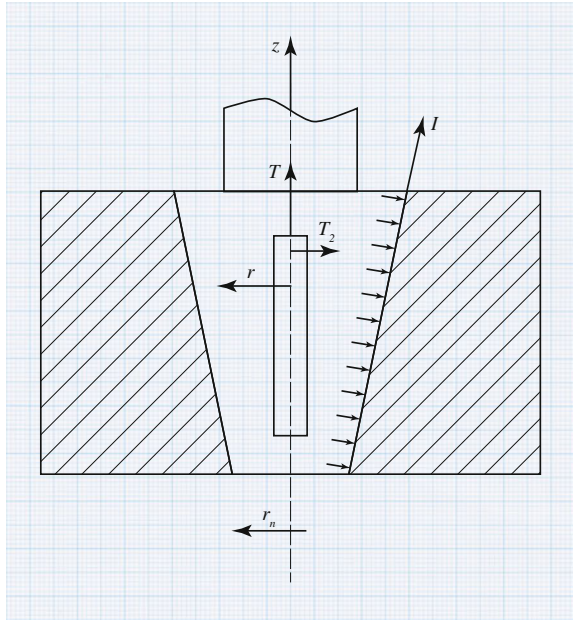
For constant volume [20],

$$e_{1c} + e_{2c} = 0. \tag{6.84}$$

With this arrangement, the equality (6.84) and assumption made on constancy of volume the middle of the surface

$$l_1 + l_2 = 0 \tag{6.85}$$

are performed with an accuracy to the first approximation.

Taking into account (6.84) and (6.85), the Eq. (6.81) takes the form

$$-q = \frac{S_\Phi k \mu_{12}}{r} [\mu_{21}(1 - \mu_{12}\mu_{21})]^{m-1}$$
$$\times (l_2 + \mu_{21}l_1)(\mu_{21}l_1^2 + 2\mu_{12}\mu_{21}l_1l_2 + \mu_{12}l_2^2)^{-m} \cos \alpha. \tag{6.86}$$

If Eq. (6.86) is expressed in terms of the original dimensions r_0 and S_0, then we obtain

$$-q = \frac{S_\Phi k \mu_{12}}{r} [\mu_{21}(1 - \mu_{12}\mu_{21})]^{m-1}$$
$$\times (\mu_{21}l_1^2 + 2\mu_{12}\mu_{21}l_1l_2 + \mu_{12}l_2^2)^{-m} e^{(-2l_2-l_1)} \cos \alpha. \tag{6.87}$$

The intensity of load required for the valve sealing mainly depends on the material and quality of sealing surfaces of friction, as well as the interaction force of sealing surfaces. We should take into account that the actual load intensity should not cause any significant plastic deformation or change the surface geometry of friction pair (plug–body).

The direction of action line of the friction force at the beginning of plug movement is important. In the case where the torque value reaches its maximum, the action line of the friction force coincides with the circle tangent lying on the contact surface. The friction force is determined as

$$F = -T_1 \cos \alpha, \tag{6.88}$$

where T_1—the meridian force that can be determined [21]

$$
T_1 = -Sk\mu_{21}^m (1 - \mu_{12}\mu_{21})^{m-1} \left(\ln \frac{r_0 S_0}{r S_\Phi} + \mu_{12} \ln \frac{r}{r_0} \right)
$$
$$
\times \left[\mu_{21} \left(\ln \frac{r_0 S_0}{r S_\Phi} \right)^2 + 2\mu_{12}\mu_{21} \left(\ln \frac{r}{r_0} \right) \left(\ln \frac{r_0 S_0}{r S_\Phi} \right) + \mu_{21} \left(\ln \frac{r}{r_0} \right)^2 \right]^{-m}. \tag{6.89}
$$

Taking into account (6.89) in (6.88), we obtain

$$
F = -S_0 k\mu_{21}^m (1 - \mu_{12}\mu_{21})^{m-1} \left(\ln \frac{r_0 S_0}{r S_\Phi} + \mu_{12} \ln \frac{r}{r_0} \right)
$$
$$
\times \left[\mu_{21} \left(\ln \frac{r_0 S_0}{r S_\Phi} \right)^2 + 2\mu_{12}\mu_{21} \left(\ln \frac{r}{r_0} \right) \left(\ln \frac{r_0 S_0}{r S_\Phi} \right) + \mu_{21} \left(\ln \frac{r}{r_0} \right)^2 \right]^{-m} \cos \alpha. \tag{6.90}
$$

We define the force with which the sealing surface is pressed against one another to allow the shutter to ensure reliable tightness.

It is necessary to maintain the necessary and sufficient condition which provides the tightness

$$F \geq \psi r f q, \tag{6.91}$$

where ψ—the coefficient of pressure transmission in contact; and f—the coefficient of friction metal-on-metal (plug–body).

These formulas enable us to characterize the causes and conditions of the phenomena of the plug–jamming plug in body. On the basis of the established friction laws on the conical surface, we define the conditions required to ensure a reliable sealing at the design stage and the recommendations that can correct and prevent jamming.

As an example of applying the above techniques, we consider the plug valve with the following elastic characteristics

$$\psi = 0.85; \quad k = 0.5 \cdot \sigma_T = 0.5 \cdot 800 = 400\,\text{MPa}; \quad m = 0.41;$$
$$\mu_{12} = \mu_{21} = 0.39; \quad f = 0.4; \quad d = 80\,\text{mm}; \quad D = 80\,\text{mm}; \quad \alpha = 17\text{--}23°.$$

The plug angle and the relative contact area varied.

Figure 6.25 shows the dependence of the friction force on the plug angle at various ratios of the contact area derived from the analytical solution of the Eq. (6.90), as well as on the basis of (6.91).

The analysis of Fig. 6.25 shows that for the considered conical plug, a real solution to the problem exists between the angles 17–23°, and the condition of inequality (6.91) holds for the relative values of the contact area 0.8. In order to establish the optimal value of the plug angle, we used dependence (Fig. 6.25) with the possible values of the relative contact area within 0.77–0.82 being equal to 0.8. It was found the optimal plug angle is in the intersection of lines, which is $\alpha = 19°$.
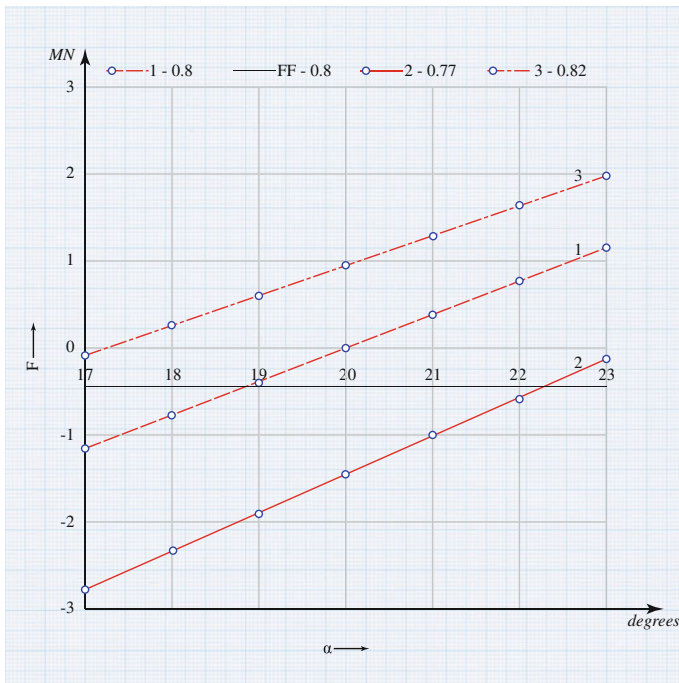
Fig. 6.25 The dependence of friction from plug angle at various ratios of the contact area

6.7 Fractal Dimension and Analysis of Fatigue Non-spreading Cracks of the Kinematic Pair of Valve

As it is known, the running pair is designed to move the gate while opening and closing valves. The running pair operating at variable load, the destruction (wear) often occurs as a result of fatigue cracks along the strain relief (or the cross section) of the spindle. Less common is the destruction due to the cyclic shear of threads as a result of the crack development curving these threads.

Fatigue cracks spread out from the pit, usually the first one, explained by the link of the threads and the load impact on threads joints [22, 23].

The aim of this study is to analyze the factors stopping the growth of fatigue non-spreading cracks along the running pair of valve taking into account the stress intensity factor (SIF) value range up to the threshold value along the strain relief.

As samples we used the carbon structural steels 45 and 40Kh/40X, which are often chosen as the primary material for spindles [24].

The experimental materials of study are presented by Azerbaijan Institute of Petroleum Engineering (AzINMASh), where the tests were carried out on the cylindrical samples with the metric thread M24 for bending with rotation.

The analysis of results on the cyclic fatigue shows that the surface non-spreading cracks are the most "acute" stress concentrators, and therefore, the maximum depth l_0 will serve as the criterion of maximum allowable sizes of crack-like defects in the given material. The conditions of fatigue cracks non-proliferation occur if the SIF amplitude values do not exceed the threshold value ΔK [25]. Let us write the expression for SIF as

$$\Delta K = \sigma_{-1}\sqrt{\pi l_0} = \sigma_{-1k}K_\sigma\sqrt{\pi l_0} = \Delta K_t, \tag{6.92}$$

where K_σ—the effective SIF; and σ_{-1k}–the sample endurance limit.

The Eq. (6.92) determines the estimated depth of the non-proliferative crack

$$l_0 = \frac{\Delta K_t^2}{\sigma_{-1k}^2 \cdot K_\sigma^2 \pi}. \tag{6.93}$$

According to the experimental data, a change in the strength of medium-carbon steels by varying the carbon content from 0.3 to 0.5 % and the annealing temperature in the range 500–700 °C have a little effect on the level of ΔK_t [26], which can be taken as being equal to 5.5 MPa m$^{1/2}$. Then, the relationship (6.93) implies that

$$l_0 = \frac{9.65}{\sigma_{-1}^2}. \tag{6.94}$$

The value of l_0 is the maximum size of non-proliferative cracks. Given that with an increase of the asymmetry coefficient, the values of loading cycles ΔK_t for the
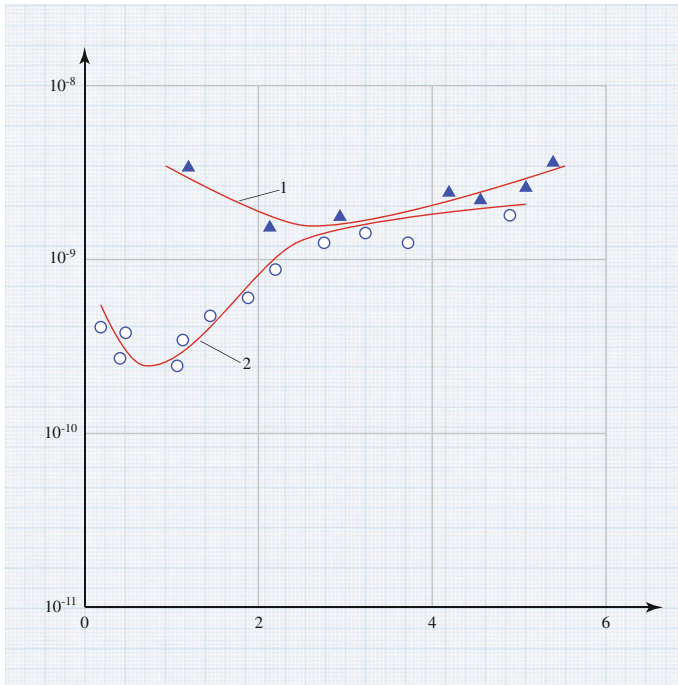
Fig. 6.26 The growth rate of near-threshold short cracks in thread, depending on the SIF range (*1* St40X/Cт40X, *2* St45/Cт45)

majority of steels begin to decrease [27] found from the formula (6.94) the values of l_0 can be considered as the maximum depth of non-proliferative cracks of medium-carbon steels.

The typical character of kinetics of the short crack near the SIF threshold [28] is shown in Fig. 6.26.

The obtained data in this study results suggest that the calculated and empirical values of l_0 coincide with 15 % accuracy. This confirms the validity of applying the linear mechanics of fracture for calculation of non-proliferative cracks.

Due to the discrete nature of the crack growth rate distribution, i.e., the discrete growth of level of nominal stresses with the discrete transition to the new values from the range of plastic deformation, the grooves of fatigue cracks at different levels of alternation of i follow the self-similarity relation [29]

$$\frac{\delta_i}{\delta_{i+1}} = \Delta^{1/m}. \tag{6.95}$$

Using the universal constant Δ according to (6.95), we control the ratio of the critical energy density distortions (change in shape) W_d^C and dilation (change in volume) W_γ^C. The value of Δ takes in average the value of $\bar{\Delta}$ for the group of metals, coinciding with the generalized golden ratios Δ_p^2.

It is also interesting to follow how the ratio W_d^C/W_γ^C behaves in the case of non-proliferative cracks.

Taking into account the phasic and multiscale properties of the fatigue crack growth, described by the kinetic diagram of fatigue fracture (KDFF) for the stage of subcritical fatigue crack growth, the relation is fulfilled

$$\frac{\mathrm{d}l}{\mathrm{d}N} = B\left(\frac{\Delta K}{\Lambda}\right)^{\eta}, \tag{6.96}$$

which can also serve as a key for understanding the mechanism of hindering the crack growth.

Taking into account the relationship between the fractal dimension of the deformation structures of metals and the critical points of the mechanical condition and the damage fatigue at the contact interaction and friction, we calculate the dimensions of the profile D', linked to the fractal dimension of the surface D_f, using the relationship [29]

$$D' = D_\mathrm{f} - 1.$$

We use the formula obtained by Mandelbrot

$$P(\delta) = C \cdot \delta^{1-D'}[S(\delta)]^{D'/2}, \tag{6.97}$$

where $P(\delta)$ and $S(\delta)$—the perimeter and area of the closed curve measured with the small scale δ. Hence, the ratio

$$\ln\left[\frac{P(\delta)}{\delta}\right] = \ln C + \frac{D'}{2}\ln\left[\frac{S(\delta)}{\delta^2}\right]. \tag{6.98}$$

Consequently, in the bi-logarithmic coordinates $\left(\ln\left[\frac{S(\delta)}{\delta^2}\right], \ln\left[\frac{P(\delta)}{\delta}\right]\right)$ the last equation represents a straight line with a slope $\tan\varphi = D'/2$, from which we find

$$P(\delta) = C \cdot \delta^{1-D'}[S(\delta)]^{D'/2}.$$

In this way, we can calculate D' and D_f having an image of the surface topography.

To apply the method of vertical sections (MVS), we must have the relief profiles along and across the crack obtained by the vertical sections of the relief surface. These profiles can be obtained using the profilometer that does not bring any distortions in the study.

Knowing the parameter of damage P and its dimension D', you can build the regression dependence of residual life N_resid from the variables D and D_f, where N_resid—the number of residual (until destruction) loading cycles, in %, D—the parameter of damage characterizing the surface saturation with traces of

micro-plastic deformation; D_f—the dimension, defined by the ratio of the cluster perimeter to its area cluster in the strain relief.

The ratio of perimeter to area of the crack cluster, proposed by Mandelbrot in (6.97), can be written as

$$\frac{P(\delta)}{\delta} = C\left(\frac{\sqrt{S(\delta)}}{\delta}\right)^D. \tag{6.99}$$

Taking the logarithm on both sides of (6.99), we obtain

$$\ln\left[\frac{P(\delta)}{\delta}\right] = \ln C + \frac{D}{2}\ln\left[\frac{S(\delta)}{\delta^2}\right]. \tag{6.100}$$

Here, δ—the size of squared cells (the side of square), which fully covers the shape bounded by the curve L.

$$y = \ln\left(\frac{P(\delta)}{\delta}\right), \quad x = \ln\left(\frac{S(\delta)}{\delta^2}\right),$$

$$\ln C = b_0, \quad \frac{D}{2} = b_1.$$

Equation (6.100) is the equation of line in plane (x, y)

$$y = b_0 + b_1 x. \tag{6.101}$$

Applying the method of least squares (MLS), we estimate b_1

$$b_1 = \frac{\sum_{i=1}^{n}(x_i - \bar{x})y_i}{\sum_{i=1}^{n}(x_i - \bar{x})^2} = \frac{\sum_{i=1}^{n}(x_i - \bar{x})(y_i - \bar{y})}{\sum_{i=1}^{n}(x_i - \bar{x})^2},$$

$$x_i = \ln\left\{\frac{S(\delta_i)}{(\delta_i)^2}\right\}, \quad y_i = \ln\left\{\frac{P(\delta_i)}{\delta_i}\right\}.$$

where

$$\bar{x} = \frac{1}{n}\sum_{i=1}^{n}x_i, \quad \bar{y} = \frac{1}{n}\sum_{i=1}^{n}y_i.$$

As δ_i we can take

$$\delta_i = 0.01 + (i - 1) \cdot 0.01 \quad (i = 1, \ldots, 100). \tag{6.102}$$

Defining b_1, we find that $D = 2b_1$ is the Hausdorff fractal dimension. Doing calculations by hand (or using calculator), we can get

$$\delta_i = 0.1 + (i - 1) \cdot 0.1 \quad (i = 1, \ldots, 10).$$

The curvature perimeter can be measured approximately as following, fit the broken line L' into the curve L, connect using line segments the intersection points of L with the square grid. The length $L' \approx L(\delta)$, and the area $S \approx S'(\delta)$ where $S'(\delta)$—the sum of the areas of squared cells lying entirely within the investigated shape.

Thus, the analysis of the evanescent fatigue cracks in the running pair of valve and the fractal dimension of strain relief showed that the main cause of the fatigue crack growth is the contacting interaction of the crack edges in the near-threshold destruction. The areas of "antinode" occur in the half-cycle loading of sample, along the front of crack, corresponding to the maximal opening of the fatigue crack edges, as well as the areas "relaxation," corresponding to the deformation of material without its fracturing. In "relaxation," that is, where the crack inhibits its development and becomes evanescent. The more the heterogeneous material along the front of developing crack, the greater the effects of micro-tunneling of fatigue crack.

The inhibition of cracks near the side surfaces of samples leads to the fact that beginning of the crack movement starts on the side surface occur at the significant length in its middle layers of material, and this effect should be considered when analyzing the evanescent cracks.

The analysis of experimental data of fatigue cracks tips at various asymmetries of cycle in the samples of aluminum alloy [30] shows that the direction of crack propagation at the certain intervals of length remains constant (Fig. 6.27) [31].
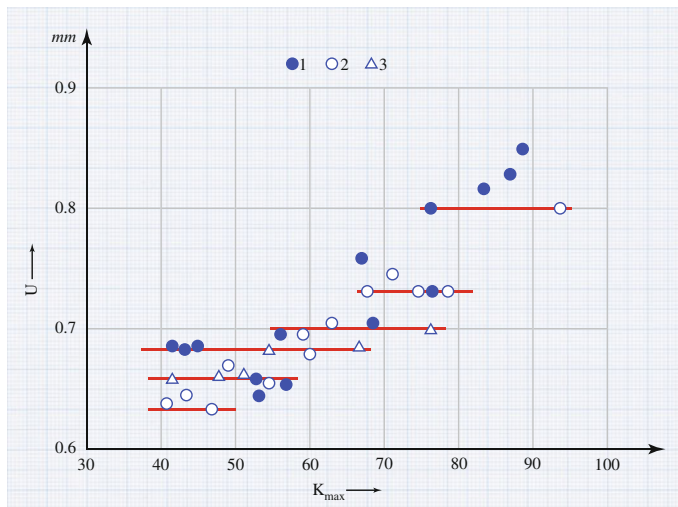
Fig. 6.27 The functionality of crack tip opening U in changing the coefficient of maximum cycle stress intensity factor K_{max} in the aluminum alloy AU4GI-T3 at $R = 0$, and values F_{max}, H: *1* 4.4; *2* 3.6; *3* 2.8

There is an alternation in opening of the crack tip. The opening of crack is proportional to its speed under the uniaxial loading of sample [32]. Therefore, the alternation of the crack growth rate is provided by the crack opening, which depends on the process of cracks tunneling and residual stresses, determined by the size of the plastic deformation zone.

The conditions of preserving its dimension by the plastic deformation zone through the development of fatigue crack can be determined by maintaining a constant range of plastic deformation in the low-cycle fatigue. Measuring the amplitude of plastic deformation while testing for the low-cycle fatigue with the constant strain rate shows [33] that there is a discrete growth increment in the level of nominal stresses with discrete transition to new range of values of plastic deformation.

Further, the deformation amplitude remains constant at a slight increase in the stress level, and then again, there is a discrete increase in stress and transition to new constant value of plastic deformation.

$$K_{\max}, \mathrm{MPa\, m}^{0.5}.$$

Crack is the system of self-collapsing zones that forms tunnels inside of which before reaching the critical stress state the conditions of crack formation do not change in the shock loading cycle, and during the extension of length, an increase of summary energy at the front of crack is compensated by the discrete transitions at discrete levels of metal stress state defining the alternation of crack jumps. The acceleration of crack growth takes place in one particular area of the crack front (the transition to a new level of alternation), while maintaining the alternation levels in neighboring areas of failing metal unchanged. This demonstrates the synergy of fatigue failure.

Thus, alternating the steps of fatigue grooves and fixing the values of crack growth rate in the experiment is the result of uneven distribution of energy along the crack front. The acceleration in crack development occurs alternately at the outer surface and in the middle layers along the sample thickness. The plastic deformation develops discretely in the local volumes of material determining the areas of plastic deformation. Through a number of cyclic loading, the measures of the plastic deformation zones are preserved, and upon reaching the critical conditions, the discrete increase of measures begins. Accordingly, the pace of fatigue grooves is unchanged in the specific length of the sample thickness, and after that, the pace changes discretely.

The analysis of causes of detail failure in the operation and the morphology of sample macro-pattern show that in some cases the products of fretting in form of oxides and spherical particles are formed in the individual zones of fracture. Scot and Mill were first to witness the spherical particles on the friction surface during the slide of retaliatory parts of free surfaces [34]. Subsequently, the similar particles were observed in the different friction conditions, including fretting corrosion [35].

Minakova and McEvily for the first time witnessed the mechanism of contact interaction of the contour lines of the fatigue crack in near the threshold area [36].

It was based on Otsuki's perception on the predominant role of the transverse shear K_{II} of material in near the threshold area. As shown in [36], with spanning of the stress intensity factor $\Delta K = 10 \, \mathrm{MPa \, m}^{0.5}$ the ratio of the maximum stress intensity factor $K_{\max}$ to the stress intensity factor of the crack opening K_0 becomes equal to $K_{\max}/K_0 \approx 0$, and at $\Delta K = 14 \, \mathrm{MPa \, m}^{1/2}$, it is equal to $K_{\max}/K_0 \approx 0.7$, that for the aluminum alloys correspond to the self-similarity relation $\Delta^{1/m} = \Delta^{1m}$ [37]. Reducing the crack opening in the loading cycle proves the idea of increasing role of the contact interaction of fatigue crack when the stress intensity factor approaches the threshold value ΔK_{th}.

Ritchie and Saresh [38] confirmed the inevitability of fretting occurrence with the crack growth due to the micro-roughness of fracture terrain formed under the joint actions of pulling and shear (scheme I + II). The geometric model of the crack closing was proposed based on these ideas [39], taking into account the fractures roughness and the specific interaction on the contour lines of cracks:

$$K_0 = K_{\max} \sqrt{2\gamma x/(1 + 2\gamma x)},$$

where x—the relative crack opening after releasing load; γ—the ratio between the height of roughness relief and the grain size.

The products of fretting in near the threshold values come as in the spherical as in the cylindrical forms (called "sausages"). In the factorgrams as shown in [40] the axis of cylindrical particles are oriented in the main direction of the fracture development and they matched to the particles identified in the breakage near the outer surface of sample where the stress state is close to plane tension.

Inclusions are one of the principal sources of anisotropy of the shifting level of the plastic deformation along the fracture contour. On the one hand they provide the greatest shifts of the plastic deformation with respect to the adjacent volumes of metal, and, on the other hand, they prevent the crack to passage through because they have a greater strength compare to the alloy matrix. Various researchers repeatedly noted the breaking actions of inclusions. By creating obstacles for the fracture development, they crushed the crack front and create conditions for its micro-tunneling.

In addition to the inclusions, the micro-tunneling of fatigue cracks is also provided by the energy redistribution along the crack front, expended on the plastic deformation and metal failure.

The spherical particles play a dual role in the growth of fatigue cracks. At the bridge, where they are located, these particles serve as an interim body intended to facilitate the mutual displacement of retaliatory parts of breakage. However, located deep inside the material, they have a limited movement and thereby, inhibit the crack opening. Therefore, during the formation of spherical particles at all stages of the crack growth, the crack opening cannot be characterized by the rate of fatigue crack growth. The formation of the spherical particles in the local areas of material is the highly energy-intensive process. An increase in area along the crack front,
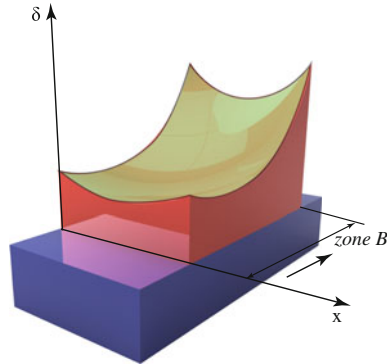
Fig. 6.28 The general functionality of the groove pace δ for the rectangular sample with height l and width x in the zone B. The arrow points the direction of crack growth

subjected to the formation of spherical particles, will mainly contribute to the absorption of the loading cycle energy inhibiting the crack development. Therefore, in terms of managing the failure process of material and searching for possible ways of distribution of the outside energy, it is necessary to create the special conditions, where in the crack developing plane the longitudinal movements of its contour assist in creating conditions for the emergence of spherical particles.

The pace of fatigue grooves δ has the crack length l, and the crack growth in the testing process is per cycle of loading, so in general, the value of $\Delta l/\Delta N$ and δ is related in following way (Fig. 6.28)

$$\Delta l/\Delta N = g_v \cdot \delta,$$

where g_v—the proportionality factor in 1/cycle. Comparing the paces of fatigue grooves with the growth of fatigue crack in loading cycle $\Delta l/\Delta N$ for various alloys, we illustrate following [41]

$$g_v = 1, \quad g_v = \text{const}, \quad g_v > 1, \quad g_v < 1.$$

The most paradoxical results are simultaneous comparison of the values δ and $\Delta l/\Delta N$ in the algorithmic testing the crack development along the sample side surface [42–44]. These tests are characterized by formation of the fatigue grooves in each loading cycle, and the crack development monitoring on sample's side surface shows no relationship between δ and $\Delta l/\Delta N$.

The repletion of stress along the crack front is due to the differences in the material stress state. The biggest displacement of plastic deformation in the middle of the sample leads to the fact that the crack get born and originally distributed in the middle layers of material. Any inhibition of the cracks growth near samples' side surfaces leads to the fact that the start of the crack movement along the side

surface occurs at a significant length in its middle layers. Depending on the inhomogeneity of material properties and the homogeneity of loading conditions of sample, the effect of crack macro-tunneling can be symmetrical or asymmetrical—the crack development on one surface of sample advancing faster than that of on another. The bending of crack as result of difference in the displacement of the plastic deformation can be permanent in the direction of its growth. In this case, the difference between the values of the pace of fatigue grooves and $\Delta l/\Delta N$ is characterized by $g_v = \text{const} \neq 1$.

However, in most cases the crack tunneling effect increases in the direction of its growth [45]. This situation corresponds with the change in differences between the values of δ and $\Delta l/\Delta N$. The latter situation is characteristic for the initial stage of the crack growth in the titanium alloys and steels. It means that after reaching the side surface of sample the crack front gets aligned and retains straightness over a substantial length. This is due to small differences of the deformation measures at the crack tip, on the surface and at its depth. At the initial stage of fracture $g_v < 1$, and then, $g_v = 1$. With an increase in the curvature of the crack front, the compared dependences in the function of the stress intensity coefficient overlap [45, 46]. However, this discrepancy, considering the spread of measured values of the fatigue grooves pace, is discounted, because in practice when calculating the period of the fatigue crack growth their rate can be characterized by the size of pace of the fatigue grooves with sufficient reliability.

It should be noted that the compliance of δ and $\Delta l/\Delta N$ has a great practical significance. The fact is that besides the micro-tunneling of fatigue crack there is a possible impact from the contact interaction of the fatigue crack contours, leading to the dissipation of the elastic strain energy. So the crack growth in the loading cycle will be determined by the action of a specific failure mechanism, not by how the large-scale process of the material destruction, which provides an averaged characteristic of migration of the entire front, differs from the micro-process of the material discontinuity.

Thus, the discrepancy between the macro- and micro-velocity of fatigue crack growth should not be attributed to the mechanism of the formation of grooves in the loading cycle, but to the terms of the plastic deformation flow and metal fracture along the crack front [47]. The greater the effects of macro- and micro-tunneling on cracks, as well as the formation of spherical particles, the more different, the rate of a crack growth at the same distance from the source of fracture in the middle layers and along the side surface of metal. Used in calculating the range of the stress intensity factor ΔK for crack length describes the averaging destruction of material on the considered crack length, which corresponds to an average growth rate of crack on the sample surface. Taking into account the effect of macro-tunneling of fatigue crack, the nomogram values of the pace of fatigue grooves, depending on the width and thickness of the sample, allow us to conduct an appropriate adjustment of length (Fig. 6.28), which is used to calculate the stress intensity factor in the construction of kinetic diagrams with respect to the specific point of the crack front.

6.8   Improving Durability of the Kinematic Pair of Valve

The above literature analysis on studying the valves and field observations of the available Xmas trees stocks at wells showed that the main criterion of the running pair performance is its wear resistance [30]. The load applied to the threads of pair is unevenly distributed, where first thread of nut (consisting of 10 threads), accounting for about 30 % of the total load.

The main reasons causing the wear of running pair are the contact pressure on the surfaces of friction pairs and operational environment. The impact of these parameters on the running pair performance is studied for the first time.

It is established that the major drawback of the modern valves is that nut gets compressed, as a result the loading on threads of spindle and nut increases, which leads to the degradation of the initial threads from the supporting flange of nut and further distribution of load between the threads gets exacerbated due to the concentration of local stresses in the gaps of threading from the tensile forces and load in threads. The voltage at the primary threads exceeds the normal operating tensile force.

As a result, there is an intensive wear of primary threaded and subsequent wear of following threads. This gives a rise of gap between the nut and the spindle, which contributes to the overall infringement of valve tightness.

The new design of valve allows the relatively even distribution of the load across threads, improve overall sealing for the long period, and increase the operational lifetime.

The main point of invention is that the thread starts at the lowest level of its support, and the lowest end of the nut is unsupported. Such arrangement provides that both the nut and spindle work only in tension, wherein the thread pitch is determined by the formula

$$t = \frac{\left(\frac{H}{\sigma} + \frac{H_1}{\sigma_1}\right)\left(\frac{1}{d} - 2 + d\right)}{\left(\frac{1}{\omega E} + \frac{1}{\omega_1 E_1}\right)g},$$

where σ and σ_1—the area of the main thread projections of spindle and nut, m^2; H and H_1—the height of the threads, m; ω and ω_1—the cross-sectional areas, m^2; E_1 and E—the modulus of elasticity, N/m^2; d—the coefficient of load distribution across threads; g—the factor of beveled threads due to pressure, N/m^2.

The coefficient of load distribution across threads is selected according to the criteria of wear resistance within the range $d = 0.5, \ldots, 0.985$.

The essential difference of the proposed technical solution is that the thread on the nut starts at a lower level of support nuts and the lower end of the nut is unsupported.

As a result of the mentioned above is that during the forward movement of the spindle, which is interconnected with the closing body, the uneven distribution of the load across threads is significantly reduced and wear is more even across all threads, which increases the service life of the valve. Fig. 6.29 shows the new proposed design for the valves.

Fig. 6.29 The new design
valve

6.9   Test Stand of the Kinematic Pair of Valve

In order to identify the causes of reduction of the running pair performance
(spindle–nut), the tests were conducted on three valves type ZMS/3MC in condi-
tions close to operating (i.e., the medium containing H_2S and CO_2 up to 6 % of
volume). Tests were carried out in AzINMASh measuring the torque required to
rotate the spindle and determining the force of friction on the running pair.

The basic premise of planning test bench chassis pair latches were as follows:

1. The probability of failure-free operation should be between 0.99 and 0.999, i.e.,
   $0.99 < P(t) \leq 0.999$;
2. The specified time t may be taken in accordance with the cycle of opening and
   closing of running pair and the amount of its revolutions. In the course of the
   valve operation, it should provide 500 revolutions (cycles of opening and
   closing). If the valve life span is equal to the Xmas tree life span (9 years), the
   revolution per each opening and closing should correspond to about seven days
   in time t;
3. Depending on wear and durability of the pair spindle–nut, the number of rev-
   olutions during the test can be taken from 200 to 250 in a stable loading regime;
4. After every 100 revolutions during the test, the thread wear on spindle and nut is
   measured;

5. Tests are carried out intermittently. Between each operation of 50 cycles, there should be brake at least for 18–20 h;
6. The axial force and gap in the thread of running pair are determined through calculations;
7. Each pair before tests must be subjected to the full checking for compliance with the parameters of the test samples and technical documentation parameters;
8. At periodic disassembly of the tested valves, the wear of working surfaces of thread for nut and spindle is determined, the dependence between the rate of wear and the loading number is estimated, the change in roughness of the working surfaces of the running pair is assessed;
9. The test results are periodically reviewed, and the conclusion is made on the continuation of tests.

The serial production valves manufactured in full compliance with the technical documentation were tested. The trapezoidal thread of nut matched the requirements of TR 24X4-LH-7H. The thread pitch, the surface roughness, and the gap between the nut and the spindle are given in Table 6.4.

The parameters of threads for the spindle and nut were measured with the required accuracy and their compliance with the drawing standards was established.

The inner sleeve of running nut is made of bronze and fixed with metric thread to the body of nut. The internal thread of sleeve is trapezoidal. The structure of running nut (made of two metals) is designed and the necessary strength at its various sections is established.

To rotate the sleeve inside the body of nut the threading joint sleeve–body is secured with wedges on both sides.

The parameters of metric thread of the inner sleeve of running nut were provided by the manufacture of engineering plant named after Sattarkhan.

When preparing the running pair of valve for testing, along with standard measuring devices and instruments (optimeter, micrometers, calipers, dial gauges, etc.), we developed a special tool to evaluate the gap in the running pair (Fig. 6.30).

Table 6.4 Dimensions of parts of running pair before test

Measured section of thread	Thread pitch, mm	Surface roughness of thread windings Ra, microns	Clearance between the threads of lead nut and spindle, mm	Additional information
Thread size of lead nut				
At entrance	5.0	6.4	0.02	Nut along with spindle
In middle	5.0	3.2	0.09	
At exit	5.0	12.5	0.06	
Thread size of spindle				
At entrance	4.95	3.5	0.02	Nut along with spindle
In middle	4.99	3.5	0.09	
At exit	4.98	6.3	0.06	
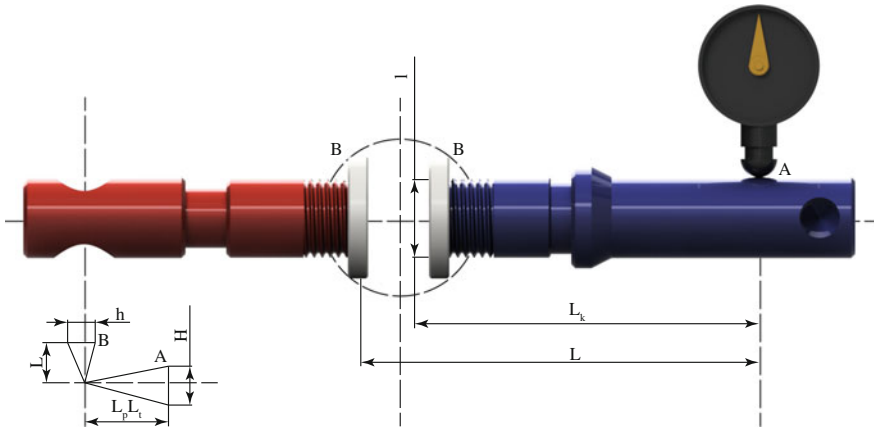
Fig. 6.30 The measurement of the movement of the cantilever end of the spindle at the fixed gate (with the combined nut) or the running nut

The displacement of the spindle cantilevered end is measured by the gauge of clock type with a scale division of 0.002 mm. The distance L_k from the point A - the point of the indicator, to the point B - the supports of thread of the nut (Fig. 6.30), was taken different to determine the measurement error.

The gap h according to the average diameter of the thread d_{avg}, marked with the letter l in the diagram (Fig. 6.30), is determined by the formula

$$h = \frac{Hl}{l},$$

where h—the gap in thread of the running pair, according to the average diameter of the thread, which characterizes the amount of wear on the measured portion of the spindle, resulting from the valve test; H—the movement of cantilevered end of the spindle at the point A; l—the distance between the reference point and the contact point on the measured part of the spindle, taken with certain allowance, equal to the average diameter of the thread d_{avg}; L—the distance between the support point of thread on the measurement part and the cantilevered end of the spindle in the contact point of the indicator tip with the spindle.

To obtain the numerical values of gap, that means the values of wear for various designs of the running pair, we substitute $Hl = d_{avg}$ and L, which are determined by measuring the details, and calculate the gap h according to the formula. The obtained value is quite reliable to assess wear on thread during exploitation or testing of valves.

The evaluation results of the running pair with 4 years of exploitation are important, for which we obtained the following values of h at the thread root corresponding to the open state of valve, and at the thread end corresponding to the close state.

At the thread root of spindle (the second thread from root)

$$h_k = \frac{H_k l}{L_k},$$

$H_k = 4.55\,\text{mm};\quad d_{\text{avg}} = l = 22.07\,\text{mm};\quad L_k = 195\,\text{mm};\quad h_k = 0.5149\,\text{mm}.$

As we can seen, the amount of wear in thread of the running pair for the given section is significant (reaches up to 0.5 mm), that is unacceptable for the normal operation of valve.

At the thread end of the spindle, the second thread from the end of the spindle

$H = 13.5\,\text{mm};\quad d_{\text{avg}} = l = 22.07\,\text{mm};\quad L = 275\,\text{mm};\quad h = 1.076\,\text{mm}.$

Comparing wear on the spindle thread at the root and end ($h_k = 0.5149$, and $h = 1.076$) we found that, depending on the gate path in opening and closing of valves and the magnitude of load acting on the thread, wear in threads varies within wide range. In this case, wear at the end of the thread is almost two times greater than the root (Fig. 6.14).

The gap assessment of thread of the running pair was also conducted after the resource testing, where the end of the thread was subjected to the testing. Therefore, one of the reasons of the significant gap in the thread end ($h = 1.0926\,\text{mm}$) rather in the root ($h_k = 0.5366\,\text{mm}$) is an intensive wear of that section. There could be another reason—the original difference in thicknesses of the threads due to bending in the spindle as manufacturing fault, which is not defined in these studies.

The survey and analysis of the thread wear for another type-size of the running pair and the valve design showed the following results:

In the thread root (the second thread from root)

$H_k = 1.22\,\text{mm};\quad d_{\text{avg}} = l = 22.9975\,\text{mm};\quad L_k = 100\,\text{mm};\quad h_k = 0.276\,\text{mm};$

in the end of the spindle thread (second thread from end),

$H = 1.6\,\text{mm}\; d_{\text{avg}} = l = 22.9975\,\text{mm};\quad L = 158\,\text{mm};\quad h = 0.296\,\text{mm}.$

In this case, the resource testing was conducted in the short period of time and at low loads. Therefore, the gaps in the root and end of the thread came out to be the same.

Besides, the running pair designs of tested valves had significant differences.

For testing purposes, we used the testing stand (unit) of the 1st Department of AzINMASh, created especially for this purpose. To test the running pair, every pair was visually inspected, the measurements collected and then the assembled valve was prepared for installation on the stand. This unit allows testing of the assembled valve (the pairs spindle–nut and gate–saddle) with the motional drive and under loading.

In this case, the axial force acting on the spindle is created by the medium pressure inside the valve and the friction force between the parts of gate (gate and saddle). The medium pressure also creates the mentioned force of friction.

Setting up the test unit is to bring into operation the motional drive and provide the required pressure inside the valve.

To create a uniform hydrostatic pressure of 35 MPa inside the valve, to the inlet flange of valve we attached the output of the plunger pump.

The efficiency of the running pair is evaluated in accordance with the following criteria:

- flexural strength of the nut threads;
- wear resistance of the contact surfaces of the nut threads;
- rigidness of the bronze sleeve with in the steel casing during testing;
- the gap between the threads of nut and spindle.

The first of these criteria was determined by calculation. The remaining three criteria defined and measured during the test. According to the prepared test–method, program within one working day of the pair was loaded with 50 cycles back and forth (which corresponds to the opening and closing of valve) and after every 50 cycles the overall condition, tightness, heating, noise of running pair were established, and a decrease in the pair performance was also estimated.

On the stand, the rotation (back and forth) and reverse rotation are transmitted through the driveshaft to the nut. The rotation of nut back and forth (left and right) drives the spindle back and forth (back and forth along the axis). In this case, the friction force is created on the spindle within the valve from the hydrostatic pressure of pump. The frictional force in turn creates the axial force and torque in the running pair. Influenced by this force for a certain time the spindle moves back and forth. Each cycle (1 rotation) consists of three stages—forward, stop, and backward.

To determine the duration of the rotation cycle and to reduce measurement errors, the measurements were taken three times: 1—the length of 1 revolution (cycle) is measured; 2–5 revolutions; 3—10 revolutions. Accordingly, $t_1 = 3$ min; $t_2 = 3.6$ min; $t_3 = 3.8$ min. Accepting: $t_{\text{avg}} = \frac{3 + 3.6 + 3.8}{3} = 3.5$ min.

The overall rotation of running pair is 3 min 30 s that corresponds to the time of opening and closing the valve. Within one day running, the pair makes 50 cycles (revolutions). All this time, the valve is pressurized on the test unit.

Since $t_{\text{avg}} = 3.5$ min, then the timing of 50 cycles is $T = 50 \times 3.5 = 175$ min. The observations show that during this time the valve lid heats up from 40 to 50 °C.

According to the program after every 100 revolutions, the following measurements were taken from the running pair:

1. For the running nut,

    - maximal diameter of thread;
    - thread pitch;
    - minimal diameter of thread;
    - thread surface roughness.

2. For spindle,

- maximal diameter of thread;
- thread pitch;
- minimal diameter of thread;
- thread surface roughness.

Results of the measurements of these parameters are given in the Table 6.5. To enable comparison, the table also shows the results of measurements of parts to test chassis pair. Note that despite the fact that the tested valve was examined every day and every 50 cycles, taking into account small differences in the parameters, the parts dimensions and the surface roughness were recorded after every 100 cycles (Table 4.2).

The thread roughness for the nut and spindle in the event of approximate equality of height of threads in the area of extensive wear reaches its maximum. However, in general that wear is negligible, the running pair performance is not reduced substantially.

Since for the test period, the sleeve size of thread of the nut and the outer diameter of thread of the spindle are unchanged, so they are not shown in Table 4.2.

It should be noted that the metallic gloss on the surface of the running pair varied during the tests. The shining gloss on the surface of bronze thread of the nut increased, while the shine on the threads of the spindle reduced. There were traces of corrosion on the threads of spindle.

Table 6.5   The results of measurements of running pair during the test

Number of full cycles (rotations) before measurement	Change in thread turn, mm	Surface roughness of thread turn Ra, mm	Clearance between the lead nut and spindle, mm	Additional information
Thread of lead nut				
0	0	12.5	0.020	Gap was measured while nut and spindle were together
100	0.003	3.5	0.025	
200	0.010	12.5	0.040	
300	0.015	1.6	0.035	
400	0.020	3.5	0.050	
500	0.035	6.3	0.060	
Thread of spindle				
0	0	6.3	0.02	Gap was measured while nut and spindle were together
100	0.005	12.5	0.025	
200	0.015	12.5	0.040	
300	0.025	10.0	0.035	
400	0.030	6.3	0.050	
500	0.050	3.5	0.060	

The presence of corrosion shows that the accelerated method has no impact on the test results. For testing the upgraded running pair, the act of test results was drafted, approved and submitted to the plant named after Sattarkhan.

The running nut along with spindle assembled in the valve were tested under pressure, the test showed that the operational conditions of these parts are matched with their design parameters.

The life span for the valve was established at from 9 to 10 years, providing 500 double strokes for the spindle. Within a year, the valve supposed to close and open 50 times in average (replacing nozzles or other processing operations). While testing, this number of cycles was carried out within a day. The service life with respect to the valve life cycling is approximately 365 times greater, and thus, corrosion was found; the tests shown that the accelerated test method has no impact on the results.

Thus, this study found that the increase of wear resistance of thread in the running pair can be achieved by improving the pair design; its wear resistance; the thread insulation reducing its contact with from its contact with the well products.

6.10 Choosing a Lubricant for the Direct Flow Valve of Xmas Tree

Reinforcing lubricant is designed for sealing and tightening the various types of valves: direct flow and plug valves of oil and gas wells, wellhead gas equipment fittings.

The general requirements for reinforcing lubricants can be summarized as following:

- provide a reliable sealing in the wide range of temperatures, matching the temperature and climatic conditions;
- separate the friction details with the high-strength film withstanding the heavy loads and preventing the contact surfaces from scuffing and wear;
- withstand the medium pressure and the contact load of the working in pair parts;
- provide a minimum torque, lightness, and fluidity of movement of the locking element, screwing and unscrewing of the thread connection;
- do not interact and not being soluble in the working environment;
- have high mechanical and chemical stability, the long life span and storage;
- do not cause corrosion of the contact surfaces, have high barrier properties protecting the contact surfaces from corrosion.

The shutoff valves of high-pressure lubrication should prevent leakage the gaps. The limiting pressure, at which the lubricants retain sealing properties without additives, ranges from 5 to 10 MPa [25]. At low pressures, the sealing ability is proportional to the shear strength and viscosity of lubricants. At high pressures (10–100 MPa), the rheological properties such as the oil type and the thickener

concentration do not affect the lubricant sealing ability. By decreasing the gap, the sealing of valve improves, but this increases the torque required to rotate the wheel of valve.

Developing and applying the lubricant "Armatol-238" to the direct flow valves, it is necessary to take into account the severe operating conditions. The lubricant must be leakproof at pressures of up to 100 MPa, operate in a range of temperatures from 50 to 120 °C, have a chemical stability, retain its rheological and physical and chemical properties in the aggressive working environment, particularly in hydrogen sulfide and carbon dioxide with 25 % of volume. At the time of the lubricant development, the domestic production did not have a lubricant fully matching all the necessary requirements.

Thus, the lubricant LZ-162/ЛC-162 unusable in the aggressive environments contains hydrogen sulfide and carbon dioxide, even at low temperatures. Where hydrogen sulfide and hydrogen sulfide gas are present, the lubricant LZ-162/ЛC-162 dramatically changes its physical, chemical, and rheological properties and becomes unsuitable for sealing the valve gate of Xmas trees. At temperatures 35 °C and below, which are often found in the northern regions (Siberia), the lubricant becomes solidified around the gate and body, and the valve partially or completely loses control.

The known domestic lubricants that are based on the soap, resistant to oil and hydrocarbon gas mixtures when tested in media containing carbon dioxide gases, but dramatically worsened their performance characteristics in hydrogen sulfide. These include the following lubricants:

SGP/СГП (based on the petroleum oil and a lithium–barium soap of synthetic fatty acids C_{17}–C_{20}, castor oil and asidola supplemented with lead powder) has a good sealing and low-temperature properties and is intended to provide sealing for the ball valves in pipelines of Far North;
AL-4/АЛ-4 (based on the petroleum oil and a lithium–zinc–lead soap of synthetic fatty acids C_{17}–C_{20}, castor oil, rosin acids, and oil acids with fillers such as graphite, alumina, and chrysotile asbestos of type M-5-65) is used to seal the pipe hangers and the wellhead casing heads of existing oil, gas, and general valves of anti-gushing manifolds equipment at pressures up to 70 MPa.

The narrow temperature range eliminates the use for the above purposes the sealing lubricants resistant to oil and natural gas, such as a lubricant for the gas valves obtained by the partial saponification of castor oil and calcium hydroxide petrol-resistant lubricant (GOST 7171-78) applied for sealing the gasoline pipe joints and thread connections, and obtained by thickening the resulting castor oil with zinc soap of resin acid.

Due to the lack of high sealing properties, the pump grease, which is the oxidized castor oil thickened with colloidal graphite of grade C-1, is not suitable as closing valves of Xmas tress operated in harsh and extreme conditions.

The domestic chemical-resistant lubricants designed for operation in hostile environments do not satisfy the high requirements of lubricants. The halocarbon lubricant (lubricant #8, 10, SKF/СКФ, EF/ЭФ), having the chemical resistance to

mineral acids, chlorine, hydrogen peroxide, and others are aggressive products, but are not suitable for high temperatures (above 100 °C). The hydrocarbon lubricant CIATIM-205/ЦИАТИМ-205 (GOST 8551-74) is designed to seal and prevent caking of contacting thread and sealing connections that come into contact with aggressive media, thickens at low temperatures (below −20 °C) and has a low upper temperature limit (50 °C).

Silicone Lubricants VNIINP-279/ВНИИН-279 (GOST 14296-78) and VNIINP-287/ВНИИН-287 (TU 38.101-83-76/ТУ 38.101-83-76) have chemical resistance, frost resistance, and low upper temperature range when they are used in corrosive environments (up to 50 °C).

Perfluoro-alkyl-polyether Lubricants SK-2-06/СК-2-06 (TU 6-02-786-73/ТУ 6-02-786-73), VNIINP-282/ВНИИНП-282 (TU 38.101274-78/ТУ 38.101-274-78), VNIINP-283/ВНИИНП-283, SCHIPS-02/ЩИПС-02 (TU 38.101-501-74/ТУ 38.101-501-74) meet the strict requirements of the lubrication for the locking devices of wellhead; however, these lubricants are expensive and rare and have insufficient sealing properties (no filler).

Testing the lubricant in media containing 25 % of hydrogen sulfide conducted on a special testing stand (unit) in AzINMASh—on autoclave unit for 720 h. The test conditions are as follows: the medium—an aqueous solution saturated with hydrogen sulfide up to 25 % of volume; the working pressure—13.0–15.0 MPa; and the fluid temperature—25–30 °C. After testing the lubricant, "Armatol-238" has not changed the original color and texture, as well as its quality indicators (Table 6.6).

While testing the reinforcing lubricants on the plane gate model in the unit under high pressure, the obtained results indicate higher sealing properties than its foreign analogues like lubricants of the company "McEvoy" (USA) (Fig. 6.31).

The low-temperature rheological properties of experimental samples of lubricants were evaluated according to standard procedures VNIIPKneftehim in comparison with "Armatol-238." Therefore, on the viscometer of constant flow the values of equivalent viscosity were determined at three shear rates and temperatures from 0 to 50 °C. The calculations on pumping resistance were done in accordance to the hydraulic resistance methodology with regards to the triple-constant

Table 6.6 The lubricant "Armatol-238" after treatment with hydrogen sulfide

Parameters	Initial lubricant	After testing in 25 % H_2S
Dropping point temperature, °C	180	185
Colloid stability of pressed oil, %	14.2	1.8
Water weight content, %	Absent	
Free organic acid content, mg KOH/g	15	15
Corrosive effect on metals	Hold	
Effective viscosity at 50 °C and velocity gradient 10 s^{-1}, Pa s	12.7	14.4
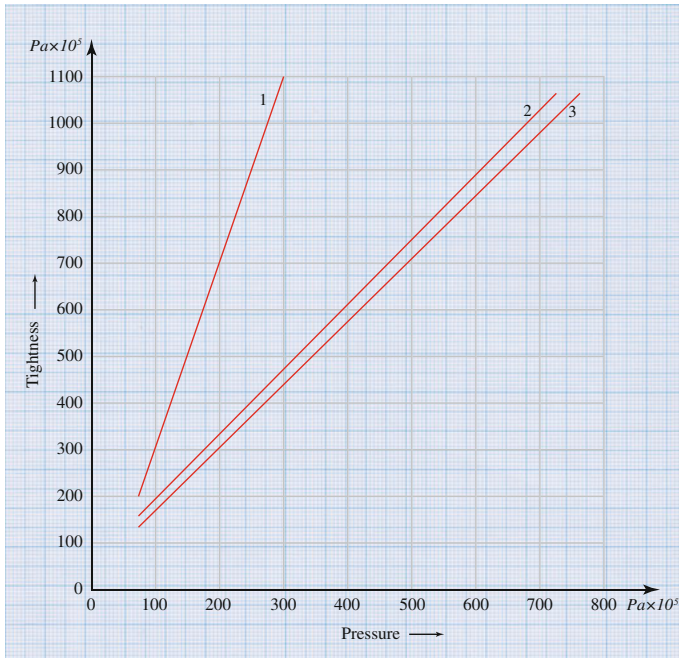
Fig. 6.31 The sealing capacities of reinforcing lubricants: *1* Armatol-238; *2* LZ-162/ЛC-162; *3* McEvoy

hydraulic rheological equation that is a generalization of the power law and the linear model for the viscose-plastic liquid of Shvedov-Bingham.

Omitting any specific calculations, we present the results of calculating hydraulic resistance for the pipe diameter of 20 mm and a length of 20 m when pumping lubricants at a flow rate of 0.05 l/min (Table 6.7) and graphically processing the data (Fig. 6.32). As seen from the data in this figure, the maximum pressure

Table 6.7 The pressure losses during the lubricant pumping
$(Q = 0.05 \, \text{l/min}, d = 0.02 \, \text{m}, l = 20 \, \text{m})$

Temperature, °C	$\Delta p \times 10^{-5}$, Pa
Armatol-238	
0	42
−10	83.2
−20	177.4
−30	411
−40	1033
Lubritol	
0	30
−10	30.5
−20	37.3
−30	50
−40	62
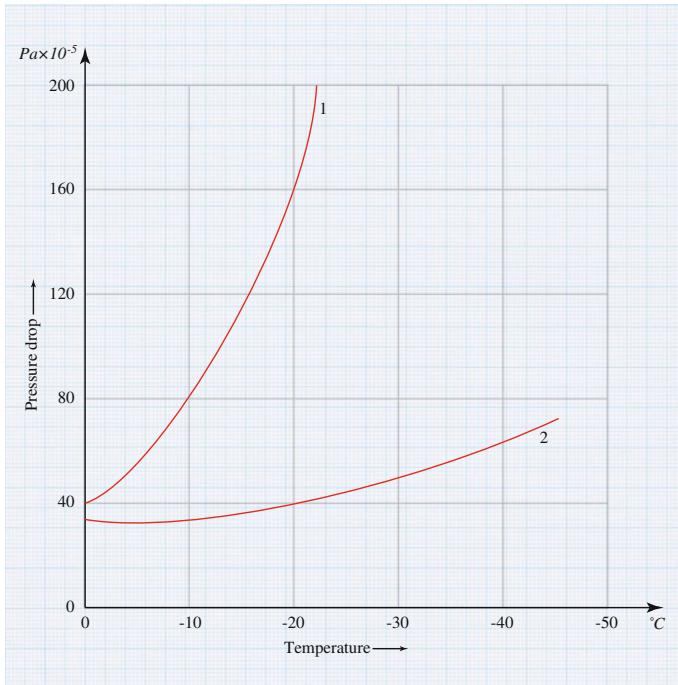
Fig. 6.32 The dependence of pressure drop from temperature: *1* Armatol-238; *2* Lubritol

corresponds to the pumping lubrication "Armatol-238," which seems being less useful at low temperatures. The minimum value of pumping pressure corresponds to lubritol lubricants.

The tribological characteristics of lubricants (Table 6.8) were evaluated on ChShM 3.2/ЧШМ 3.2 in accordance with GOST 9490-75 and the friction machine 2070 SMT-1/2070 СМТ-1 (the linear contact roller-on-roller for steel ShKh15/ШХ15 with diameter 40 mm, the sliding speed $0.314\,\mathrm{m\,s^{-1}}$, the load of $1000\,\mathrm{N}$, and the friction path $5600\,\mathrm{m}$).

Table 6.8 Tribotechnical characteristics of reinforcing lubricants

Parameters	Armatol-238	Lubritol
Quadra-ball machine		
Critical load, N	890	1600
Welding load, kN	5.3	5.6
Scuffing index	76	78
Wear scar diameter, mm for 1 h at load, N		
400	0.9	0.8
1000	1.9	1.2
Friction machine 2070 SMT-1		
Linear wear, mm	–	1.6

The testing on frost was done in AzINMASh on a specially designed "Programs and methods of laboratory tests to determine comparative viscosity properties of lubricants for lubricating sealing equipment at low temperatures." The special tools are filled with lubricant, loaded at positive and negative temperatures, and fixated the time of shifting in piston.

The viscosity properties of lubricants characterizing their frost resistance, depending on the test temperature, were estimated by the load applied to the piston and causing the start of the lubricant extrusion (shift point), and according to the lubricant extruded weight at a constant load, ensuring balanced extrusion, within 5 min.

The data analysis shows that libritol has the best viscosity properties at sub-zero temperatures. This lubrication at temperatures −40 °C requires a load 20 times less at the time of shift than "Armatol-238."

The analysis of the performed researches and the results of organized controlled by commercially available Xmas trees showed that along with the failure of valves because problem with sealing there is also not less common the loss of control of closing unit. The main reasons for loss of control are the spindle getting out connection with the gate, the failure of the nut thread, and salt deposits.

It is shown that in light of the general performance increase of valves of Xmas trees, especially working in the hostile environment (the presence of H_2S and CO_2 up to 6 % volume of reservoir fluid), the most promising direction is to increase the durability of the running pair in valves.

Research on the worn parts of running pairs of failed valves of Xmas trees provided new data on the characteristics of their work. Among the most important of which is an increased wear of the initial threads starting from suspension of nut (the first thread, consisting of 10 turns, accounts for about 50 % of the load). This is due to the uneven distribution of the workload across threads on running nut, which leads to the concentration of local stresses in the thread grooves from tensile forces. As a result, in the running pair, the gap between the nut and the spindle increases, which contributes to the overall depressurization of valve.

It is established that the uneven distribution of load across threads of running nut is connected with the adopted scheme of the threads deformation in spindle and nut under the applied load.

On this basis, we developed a method to solve the problem and to determine the rational distribution of the load on threads of the running pair. It is proved that for the distribution pattern of the applied load across thread, the preferred scheme is in which the spindle and nut got stretched under load.

It is shown that the load distribution coefficient across threads is advisable to select within the range from 0.5 to 0.985. By selecting small values of the load distribution coefficient, the first two threads take up the most of tensile force, which leads to a premature wear.

The values are defined for the load distribution coefficient across the thread of the running pair, which provides a more uniform distribution of the tensile force, which prevents the premature wear of the most highly loaded threads.

We solved the problem of the contact interaction of the running pairs (spindle–nut) subjected to the elastic–plastic deformation in the polar coordinate systems.

The analytical expressions for the determination of the tangential and radial stresses of elastic–plastic contact are obtained.

The boundaries of the transition from elastic to plastic deformations are found using the conditions of the surface displacement of the thread.

It was found that the production of the running pair from steel 30KhMA/30XMA (spindle) and bronze BrAMts9-2/БрАМц9-2 (nut) better preserves the performance and resistance to scuffing and wear through the low coefficient of friction ($f = 0.06$).

Based on the results of experimental and theoretical researches on the level of invention, we introduced a new design of valve, in which the uneven distribution of load cross threads of the running pair is substantially reduced, which can significantly increase the overall service life of the valve. In the proposed new structure, the threads on nut are twice less loaded than in the existing structure (Patent I 2001 0113, year 2001).

The conducted test results confirmed the validity of making structural changes in the performance of the running pair of the wellhead valves operating under the pressure 70 MPa by the criterion of durability.

On the basis of experimental studies and in the high-pressure testing unit, the gate is applied with armatol-238 which has higher sealing properties than its analogues.

Literatures

 1. G.V. Molchanov, A.G. Molchanov, *Mashiny i oborudovanie dlia dobychi nefti i gaza* (Nedra, Moscow, 1984), p. 464
 2. Neftegazopromyslovoe oborudovanie, *Katalog AzINMASha* (1991)
 3. E.I. Bukhalenko, *Neftepromyslovoe oborudovanie, Spravochnik, pod red* (Nedra, Moscow, 1990), p. 559
 4. I.A. Birger, G.B. Irsilevich, *Rez'bovye soedineniia* (Moscow, Mashinostroenie, 1973), p. 256
 5. N.E. Zhukovskii, *Polnoe sobranie sochinenii v 8-mi tomakh, Raspredelenie davlenii na narezkakh vinta i gaiki* (Moscow, Mashinostroenie, 1973), p. 256
 6. A.Kh. Janahmadov, Tribotekhnicheskie problemy pri ekspluatatsii neftepro-myslovogo oborudovaniia. Trenie i iznos, Tom **20**(32), 167–174 (1999)
 7. A.Kh. Janahmadov, B.M. Akhmedov, G.F. Mamedov, *Raschet i konstruirovanie fontannoi armatury* (Baku, Chashyogly, 1999), p. 236s
 8. A.Kh. Janahmadov, A.M. Mekhtiev, G.F. Mamedov, *Opredelenie raspredele-niia nagruzki po vitkam khodovoi gaiki zapornykh ustroistv fontannoi armatu-ry. Uchenye zapiski NII "Geotekhnologicheskie problemy nefti, gaza i khimiia'* (AGNA, Baku, 2000), pp. 105–113
 9. A.Kh. Janahmadov, *Tribotekhnicheskie problemy v neftegazovom oborudovanii* (Baku. 1998), p. 216
10. A.Kh. Janahmadov, R.D. Dzhabbarov, G.F. Mamedov, *Povyshenie iznosostoikosti detalei khodovoi pary zadvizhek fontannykh armature. Materialy mezh-dunar. Nauchno-prak. simpoz. Slaviantribo-4 'Tribologiia i tekhnologiia', Kniga 1*, Sankt-Peterburg, 1997

11. I.G. Goriacheva, M.I. Dobychin, *Kontaktnye zadachi v tribologii* (Moscow, Mashinostroenie, 1988), p. 250
12. A.Kh. Janahmadov, G.F. Mamedov, *Issledovanie uprugoplasticheskoi defor-matsii v rez'bovoi pare fontannoi zadvizhki. Uchenye zapiski NII "Geotekh-nicheskie problemy nefti, gaza i khimiia'* (Chashyogly, Baku, 2001), pp. 203–211
13. N.N. Malinin, *Prikladnaia teoriia plastichnosti* (Moscow, Mashinostroenie, 1968), p. 400
14. A.P. Gasanov, A.M. Aliev, A.Kh. Janahmadov, *Rabotosposobnost' friktsionnykh tormozov pod'emnykh ustanovok* (Baku, Chashyogly, 1999), p. 76
15. B.N. Zhelochkin, *Teoriia uprugosti* (Moscow, Gostoptekhizdat, 1957), p. 256
16. B.D. Grozin, *Iznos metallov* (Kiev, 1951), p. 252
17. A.Kh. Janahmadov, Mekhanika konicheskoi poverkhnosti treniia kranov fontan-nykh armature. Trenie i iznos, **3**(23), 300–303 (2002)
18. N.I. Bezukhov, *Osnovy teorii uprugosti plastichnosti i polzuchesti* (Moscow, Vysshaia shkola, 1968), p. 512
19. L.M. Kachanov, *Osnovy teorii plastichnosti* (Nauka, Moscow, 1969), p. 420
20. S.G. Babaev, *Nadezhnost' neftepromyslovogo oborudovaniia* (Nedra, Moscow, 1987), p. 264
21. M.M. Askerov, Raschet korpusa klin'evogo zakhvata dlia trub neftianogo sortamenta, Mashiny i neftianoe oborudovanie, VNIIOENG, №2, Moscow, 7–9 (1979)
22. A.Kh. Janahmadov, *Neftianaia tribologiia* (Baku, Elm, 2003), p. 326
23. A.Kh. Janahmadov, Analiz iznashivaniia khodovoi pary zadvizhki v usloviiakh uprugo-plasticheskogo deformirovaniia. Trenie i iznos, Tom **26**(5), 489–496 (2005)
24. G.F. Mamedov, Fraktal'naia razmernost' i analiz ustalostnykh nerasprostra-niaiushchikhsia treshchin na khodovoi pare zadvizhki. Vestnik Azerbaidzhanskoi In-zhenernoi Akademii, Tom **3**(3), 47–53 (2011)
25. A.A. Anonin, V.N. Kozlov, M.N. Georgiev, O nerasprostraniaiushchikhsia malykh treshchinakh pri tsiklicheskikh nagruzheniiakh. Fiziko-khimicheskaia mekhanika materialov **6**, 25–29 (1988)
26. O.N. Romaniv, Strukturnaia kontseptsiia porogov ustalosti konstruktsionnykh splavov. Fiziko-khimicheskaia mekhanika materialov **4**, 106–116 (1986)
27. L.R. Botvina, *Razrushenie: kinetika, mekhanizmy, obshchie zakonomernosti* (Nauka, Moscow, 2008), p. 334
28. S. Suresh, R.O. Ritcrie, Propagation of short fatigue cracks. Int. Met. Rev. **29**(6), 445–476 (1984)
29. A.M. Pashaev, A.M. Mekhtiev, A.Kh. Janahmadov, O.A. Dyshin, Avtomodel'nost' i fraktal'naia mekhanika razrusheniia. Vestnik Azerbaidzhanskoi Inzhenernoi Akademii **1**, 93–103 (2003)
30. M. Mostafa, M. Boivin, Mecanique Materiaux Electricite **399**, 15–30 (1983)
31. V.S. Ivanova, A.A. Shaniavskii, *Kolichestvennaia fraktografiia. Ustalostnoe razrushenie* (Metallurgiia' Cheliabin. Otd.-e, Cheliabinsk, 1988), p. 400
32. R.A. Meclintok, *Fatigue Mechanisms*, ASTM STP 415, ASTM, 168–182 (1967)
33. H. Mughrabi, F. Ackermann, K. Hezz, *Fatigue Mechanisms*, ASTM STP 675, ASTM, 69–105 (1979)
34. D. Scott, G.H. Mills, Wear **24**, 235–242 (1973)
35. J.F. Stower, E. Rabinowicz, J. Appl. Phys. **43**(5), 2485–2487 (1972)
36. K. Minakova, A.I. McEvily, Scr. Metall. **15**(6), 633–666 (1981)
37. V.S. Ivanova, *Advanced Fracture Research* (Pergamon Press, Oxford, 1984), vol. 3
38. R.O. Ritchie, S. Saresh, Metall. Trans. A. **13A**(5), 937–940 (1982)
39. S. Suresh, R.O. Ritchie, Metall. Trans. A. **13A**(9), 1627–1631 (1982)
40. M.A. Hicks, R.H. Teal, C.J. Beevers, Fatigue Engn. Mater. Struct. **6**(1), 51–65 (1983)
41. *Standartizatsiia fraktograficheskogo metoda otsenki skorosti ustalostnogo razrusheniia metallov* (Izd-vo standartov, Moscow, 1984), vol. 5, p. 95
42. E.I. Euw, R.W. Hertzberg, R. Roberts, ASTM STP 513, ASTM, Part 1, 230–243 (1972)
43. P.I.E. Forsyth, D.A. Ryder, Aircr. Eng. **32**(374), 96–102 (1960)

44. V.S. Ivanova, A.A. Shaniavskii, *Tsiklicheskaia viazkost' razrusheniia metallov i splavov* (Nauka, Moscow, 1981), pp. 168–193
45. P.I.C. Forsyth, Met. Tech. **5**(10), 351–357 (1978)
46. C. Bathias, R.M. Pelloux, Metall. Trans. A. **4A**, 1265–1273 (1973)
47. V.V. Panasiuk, O.P. Ostash, V.M. Kostiuk, FKhMM. Tom **21**(6), 3–10 (1985)
48. B.B. Mandelbrot, *Fractals: Form, Chance and Dimension* (Freeman, San Francisco, 1977)
49. R.M. Kronover, *Fraktaly i khaos v dinamicheskikh sistemakh. Osnovy teorii* (Postmarket, Moscow, 2000), p. 352
50. K. Tsillis, *Ob izmerenii fraktal'nykh razmernostei po fizicheskim svoistvam. v sb.statei "Fraktaly v fizike"* (Mir, Moscow, 1988)

Chapter 7
Fractal Fatigue Analysis of Valve Units of Sucker Rod Pumps

7.1 Design and Analysis of Operating Conditions of Valve Units

The valves are designed for periodic isolation of the bottom of the borehole pump occupied by already received fluid from the pump-compressor tubing (PCT), where this fluid flows. The valves are much more susceptible to wear than a sleeve-plunger pair. Therefore, most of the round-trip operations during the well operation are linked to the replacement of valve assemblies.

Among the various valves used in the sucker rod pumps (SRP), the most widely used are the ball valves, as they have the greatest performance.

Depending on the shape of saddle, the ball valves are divided into the valves with collar and the valves with a smooth outer surface. The latter are relatively small in size and used as discharge valves.

The sealed contact between the ball and saddle is provided by the inner edge of the upper surface of saddle, which has a chamfer. The main causes of wear of valve units are as follows:

- corrosive environment, which has a greater impact on valves made of carbon steel;
- abrasiveness related to the presence of sand in the produced fluid; causing the metal corrosion, it is particularly intense in valves with wider gap between the contacting surfaces;
- deformation of the saddle active surface, occurring when the ball hits the saddle;
- mechanical wear, explained by the friction between the ball and saddle, it depends on the relative hardness of materials.

The valve closing process is very complex. Any delay in the valve closing has adverse affects on the SRP filling coefficient, since the liquid flows from the discharge into the suction chamber.

This phenomenon is explained by the fact that the ball remains in a position of equilibrium on an inclined surface of the saddle cut and does not rolls down due to the ball roundness, because the ball does not move strictly along the geometric axis of the valve, but vertically deviates. Moreover, the upward flow is distributed unevenly in the valve cross section.

7.2   Analytical Dependencies for Assessing the Tightness of Valve Units

The sucker rod pumps play a significant role in the modern oil industry. The most of the wells, around 70 % of the existing oil wells, are operated using this method.

The design problems of the SRP elements that provide an increase in its durability and maintenance intervals depend on the hydrodynamic processes occurring in these elements. The valve unit plays a big in these elements, where the movement of fluid along with a ball, which serves as closing element of the valve. There are many experimental and theoretical studies dedicated to the analysis of the valve performance, as well as movement of the ball in upstream.

We consider based on the mathematical model of movement of fluid and ball in the sucker rod pump body and show the causes of premature wear of the valve saddle.

As it is known, in the incoming flow the ball, rising from a saddle chamfer, provides a rotational movement around the valve axis. After a certain lifting height of the ball, there is a violation of the axisymmetric vortex trail, thereby causing separation of a single vortex. At separation of the single vortex, there are changes in the circulation along the contour and the ball gets some momentum from the lifting force by shifting in the direction of the low pressure, formed in the vortex breaking spot. The ball displacement is accompanied by formation of eccentricity between the ball and the cell axis.

Determining the role of this eccentricity in a premature wear of saddle, we consider the speed of ball along with liquid (Fig. 7.1). To determine this function for the ball with mass m, moving in the liquid, we express the speed $\bar{V}$ of the ball in the fixed coordinate system through the velocity $\bar{V}_0$ of the translational motion of the liquid and the speed $\bar{V}_1$ of the moving ball in the coordinate system moving along with the liquid

$$\bar{V} = \bar{V}_0 + \bar{V}_1. \tag{7.1}$$

Fig. 7.1 The diagram of
calculation model
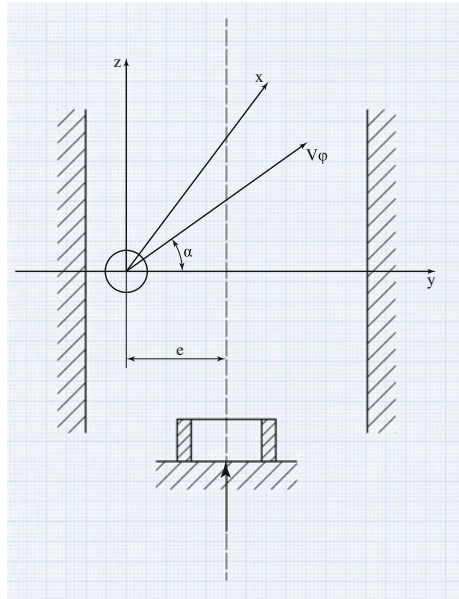
The Lagrange function for the ball with mass m, which moves with the liquid, has the form

$$\Delta E = \frac{m\bar{V}^2}{2} - U_p. \tag{7.2}$$

Substituting (7.1) in (7.2), we obtain

$$\Delta E = \frac{m\bar{V}_0^2}{2} + m\bar{V}_0\bar{V}_1 + \frac{m\bar{V}_1^2}{2} - U_p, \tag{7.3}$$

where U_p—the liquid potential energy, the term $m\bar{V}_0^2/2$ is the derivative $\bar{V}_0$ on time and it can be omitted.

Appearing in (7.3), the velocity $\bar{V}_1$ is the derivative of the radius vector $\bar{r}$ of the ball over time in the coordinate system associated with the liquid that means

$$m_0\bar{V}_0\bar{V}_1 = \frac{d}{dt}(m\bar{V}_0\bar{r}) + m\bar{r}\bar{V}_0. \tag{7.4}$$

Solving together the Eqs. (7.2) and (7.4), and taking into account (7.2) from (7.4), we get

$$\Delta E = \frac{m\bar{V}_1^2}{2} + m\bar{r}\bar{a} - U_p, \tag{7.5}$$

where $\bar{a} = \dot{\bar{V}}_0$—the acceleration of the liquid translational motion. The speed $\bar{V}_1$ is a sum up of the rotational speed of the ball together along with the liquid and the velocity $\bar{V}$, i.e.,

$$\bar{V}_1 = \bar{V} + \bar{\omega}\bar{r}, \tag{7.6}$$

where $\bar{\omega}$—the angular velocity of the liquid. Substituting this in (7.5) with the assumption that $a = 0$, $U_p = 0$, $\omega = \text{const}$, we get

$$\Delta E = \frac{m\bar{V}^2}{2} + m\bar{V}\bar{\omega}\bar{r} - \frac{m}{2}(\bar{\omega}\bar{r})^2. \tag{7.7}$$

Substituting the total differential of the function (7.7) for each of the three components, respectively, in the three Lagrange equations, we get

$$\frac{\mathrm{d}}{\mathrm{d}t}\frac{\partial\omega}{\partial\bar{V}} = m\dot{\bar{V}} + m\bar{\omega}\bar{V} - m\dot{\bar{\omega}}\dot{\bar{r}};$$

$$\frac{\partial\Delta E}{\partial\bar{r}} = m\bar{V}\bar{\omega} + m\bar{r}\bar{\omega}^2 - \frac{\partial U_p}{\partial\bar{r}};$$

$$\delta_r E = m\bar{V}\bar{\omega}\bar{r}\delta + m\bar{\omega}^2\delta\bar{r}^2 - \frac{\partial U_p}{\partial\bar{r}}\delta\bar{r} = \left(m\bar{V}\bar{\omega} + \bar{r}\bar{\omega}^2 - \frac{\partial U_p}{\partial\bar{r}}\right)\delta\bar{r}. \tag{7.8}$$

From which we can determine the Lagrange equation

$$\frac{\mathrm{d}}{\mathrm{d}t}\left(\frac{\partial\Delta E}{\partial\bar{V}}\right) = \frac{\partial\Delta E}{\partial\bar{r}}. \tag{7.9}$$

as

$$m\dot{\bar{V}} = 2m\bar{V}\bar{\omega} + \bar{\omega}^2 r - \frac{\partial U_p}{\partial\bar{r}} + m\bar{r}\bar{\omega}. \tag{7.10}$$

The potential energy in the gravity field is

$$U_p = g\bar{r}\,\bar{m}, \tag{7.11}$$

where $\bar{g}$—the vector of acceleration of gravity force, which is a component of the z-axis, and equal to g.

Solving together the Eqs. (7.10) and (7.11), given the smallness of values of terms containing the square of the angular velocity, and neglecting them, we write the equation of motion in the form of

$$\dot{\bar{V}} = 2\bar{V}\bar{\omega} - g. \tag{7.12}$$

Solving (7.12) by the method of successive approximations, that is, assuming that $\bar{V} = \bar{V}_2 + \bar{V}_3$, where $\bar{V}_2$ is the solution of $\dot{\bar{V}}_2 = -\bar{g}$, we get

$$\bar{V}_2 = -\bar{g}t + \bar{V}_H, \qquad (7.13)$$

where $\bar{V}_H$—the initial rate of the ball rise. Substituting $\bar{V}_2$ into the original equation, we define the derivative of $\bar{V}_3$:

$$\dot{\bar{V}}_3 = 2\bar{V}_2\bar{\omega} = -2t\bar{g}\bar{\omega} + 2\bar{V}_H\bar{\omega}$$

from whence

$$\bar{V}_3 = -t^2\bar{g}\bar{\omega} + 2t\bar{V}_0\bar{\omega}. \qquad (7.14)$$

Then, $\bar{V} = \bar{V}_2 + \bar{V}_3 = \bar{V}_H - \bar{g}t - t^2\bar{g}\bar{\omega} + 2t\bar{V}_H\bar{\omega}$. Integrating again, we find

$$\bar{r} = h + \bar{V}_H t - \frac{\bar{g}t}{2} - \frac{t^3}{3}\bar{g}\bar{\omega} + t^2\bar{V}_H\bar{\omega}. \qquad (7.15)$$

where h—the height of the ball lifting under which the latter begins to rotate (the ball can rise higher anymore due to limitations).

Upon reaching the height h, the ball will have the following coordinates

$$z = h - \frac{gt^2}{2};$$

$$x = \frac{t^3}{3}g\omega; \qquad (7.16)$$

$$y = \frac{t^3}{3}g\omega;$$

If we choose the x-axis perpendicular to the rotating axis of the ball, the angle between the rotation axis and the y-axis is α. Then, the projections of ω on the axis x, y, z, respectively, are

$$0;\ \omega\cos\alpha;\ \omega\sin\alpha.$$

Since the total rise of the ball within the time $t = \sqrt{2h/g}$, the deviation of the ball on the y-axis is equal to

$$e = y = \frac{1}{3}\left(\frac{2h}{g}\right)^{\frac{3}{2}} g\omega\cos\alpha. \qquad (7.17)$$

It is known that to provide a passage for the fluid with minimal resistance through the gap between the ball and saddle, it should be raised to the height

$$h = \frac{1}{4}d,$$

and for normal sealing of the valve, the diameter of chamfer is selected as following

$$d = (0.75, \ldots, 0.8)d_{\mathrm{b}}.$$

where d—the diameter of the saddle chamfer. Hence, we can determine the height of the ball

$$h = 0.2d_{\mathrm{b}}. \tag{7.18}$$

taking into account Eq. (7.18), the Eq. (7.17) takes the form

$$e = \frac{1}{3}\left(\frac{0.2d_{\mathrm{b}}}{g}\right)^{\frac{3}{2}}. \tag{7.19}$$

Thus, the focus is made on a model determining the angular velocity of the ball together along with the liquid. As the liquid flowing around the ball gets both translational and angular velocity, consider the relationship between the size of the ball, and these speeds.

The resistance strength of the incompressible fluid flowing around the ball is determined according to the Stokes formula and has a value

$$T = 6\pi\mu r_{\mathrm{b}}U, \tag{7.20}$$

as taking into account the dimensionless resistance coefficient, the same force is equal to

$$F = \frac{1}{2}\rho U^2 C_0 \pi r_{\mathrm{b}}^2. \tag{7.21}$$

Solving together the Eqs. (7.20) and (7.21), we determine the total translational velocity of the liquid and ball

$$U = \frac{12V}{C_0 r_{\mathrm{b}}}, \tag{7.22}$$

where μ and v—the dynamic and kinematic viscosities of the liquid, respectively; ρ—the liquid density; r_{b}—the ball radius; and C_0—the drag coefficient.

Since the flow around the ball is the circulative and caused by the single vorticity, the axis of which coincides with the axis of coordinates and it moves forward along with the liquid, and then, the flow in the whole region is potential and the

circulation is same at any distance from the vortex axis. The current line in this case would be a circle, the velocity is tangential to the circle, and its radial component is zero, i.e.,

$$U = \frac{\Gamma}{2\pi r}. \tag{7.23}$$

From the theory of vortices, we known that the circulation of vortex at the finite dimensions is determined by the following formula:

$$\Gamma = \pi r^2 \Omega, \tag{7.24}$$

where r—the radius of the circle current line and Ω—the whirlwind. Since the angular velocity

$$\omega = \frac{1}{2}\Omega, \tag{7.25}$$

then simultaneously solving (7.20) (7.23) (7.24), and (7.25), we can define the angular velocity

$$\omega = \frac{12v}{C_0 r r_b}. \tag{7.26}$$

Since the radial liquid motion is limited by the cell inner diameter, we can write $r = r_k$, where r_k—the cell inner radius. The Eq. (7.26) takes a form

$$\omega = \frac{12v}{C_0 r_k r_b}. \tag{7.27}$$

The Eq. (7.19) with (7.27) will have a form:

$$e = \frac{2}{3}\left(\frac{0.4d_b}{g}\right)^{\frac{3}{2}} g \frac{12v}{C_0 r_k r_b} \cos \alpha. \tag{7.28}$$

The Eq. (7.28) shows that for large and small valves, the eccentricity "e" has a scale effect, i.e., due to friction between the ball and fluid for the small balls, the greater the "e" the smaller the ball itself.

Multiplier standing before $\cos \alpha$ shows that the angular velocity for the small balls is larger than for the large balls. This is apparently due to the fact that the kinematic viscosity of liquid is proportional to the angular velocity. The growth of the latter, hence, increases the deviation of the ball from an ordinate of the fixed coordinate system.

From the above, it follows that in wells where there are high-viscosity oil, the use of small valves is undesirable not only due to the difficult pumping, but also

because of the relatively large magnitude of the eccentricity "*e*" that would result in premature wear of the valve saddle.

To prevent a premature wear of the valve saddle from unilateral hydrodynamic shock, it is necessary to create a protective device that helps to achieve a uniform seating of the ball in the saddle.

7.3 Wear and Its Determination in Valve Units

The operational conditions of valves in the sucker rod pumps are important for studying wear and leakage through the worn area. Despite the large number of theoretical and experimental works on this problem, there are not many works that correctly describes the behavior of wear and leakage. In most of the carried out experimental works, the researchers try to determine the relative durability of pumps.

Let us provide the results of experimental studies on level of wear and fluid leakage through the worn valve area of SRP [22].

Experiments to determine areas of wear and leakage were conducted on a specially designed testing unit, as shown in Fig. 7.2. The valve unit is installed in the quick assembling unit 12 and the working fluid pumped into the tank 16 flowing then through the valve 7 into the tank 10 for the hydraulic fluid. The vessels are monitored by the pressure gauges 8 and 9, and the level of liquid in the vessel by the Klinger glass, besides with the valves 4 and 6 are closed, after filling the tank 10 the valve 7 is closed. To supply the compressed air, the command is given from the control unit 17 to open the electro-valves 2 and 3 and the containers management unit.

The thermometer 11 controls the temperature of the liquid in the tank 10. The created pleasure in the tank 10 will squeeze the liquid through the valve gap into the measuring tank 15. When the control panel is on, the measurements are taken from the stopwatch 18, the pressure gauge 9, the thermometer 11. As soon as the measurements are taken, the commands are given from the control panel 17 to close the above-mentioned closing devices, and the valves 4 and 6 are open for replacing the working liquid with other physical–chemical properties.

The testing unit provides the following tasks: conducting experiments on liquids with different physical properties; measuring the volumetric flow rate of leakage; and measuring drainage time.

The unit has two operating lines: one to pump the working fluid, and another to drain out when the task is accomplished. The liquid supply—the displacement by supplying the liquid from tanks with compressed gas.

The gas reduction is a two-stage process, which provides highly stable pressure supply for a long time. The measurement of the leakage average rate during spilling in continuous operation is carried out by the weight method. The valve assembly is mounted in the quick assembling unit at the lower part of the supply line. The electronic measuring system enables the measurement of drainage time.
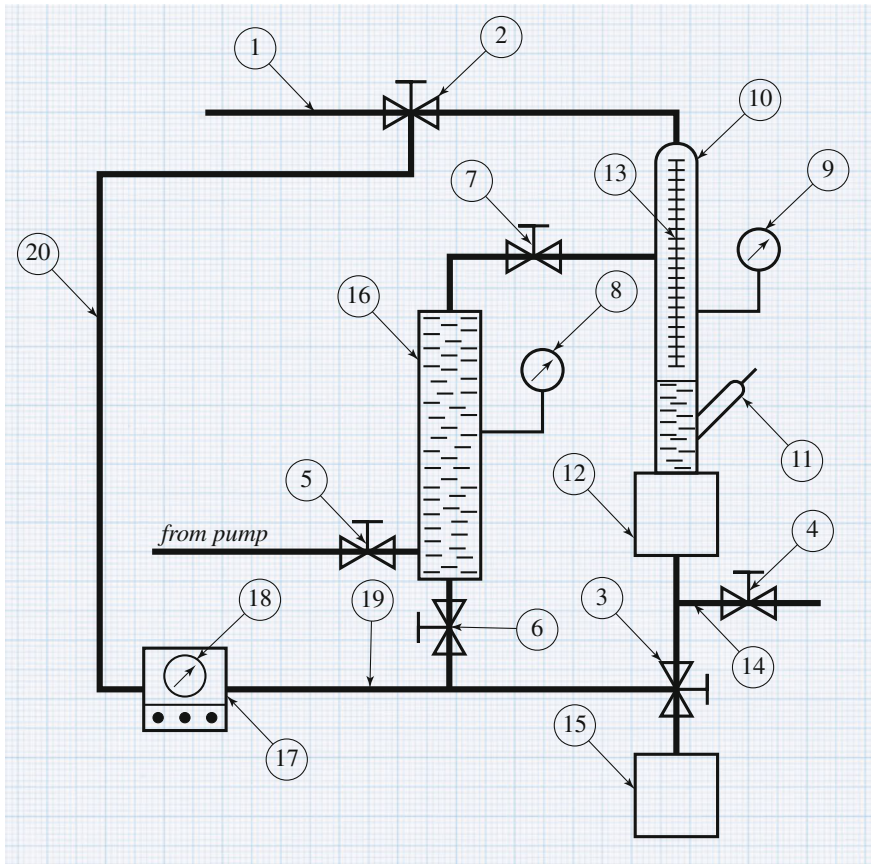
Fig. 7.2 The diagram of experimental unit: *1* gas supply line; *2, 3* locking device with electric control; *4, 5, 6, 7* valves; *8, 9* pressure gauges; *10* tank for the hydraulic fluid; *11* thermometer; *12* quick assembling unit with the tested valve; *13* the Klinger glass; *14* discharge line; *15* measuring tank; *16* tank for supplying liquid; *17* control panel; *18* timer; *19, 20* electrical communication lines

The volumetric flow rate is determined by formula:

$$Q = \frac{G}{\gamma \cdot t}$$

where *G*—the weight of liquid collected in the measuring tank for the time *t*; γ—the specific gravity of liquid.

We investigated the suction valves of the sucker rod pumps with diameters of 32, 43, and 56 mm. The valves were chosen in the field workshops from the unsuitable for further use valves due to wear of saddles. The number of valves with

43 and 56 mm was 435 units, and the valves with 32 mm—367 units, which provides the accuracy to the experiment.

The research was conducted on valves with the oil mixtures of the dynamic viscosity coefficient $\mu = 0.01425$ kg s/m^2, the volumetric specific gravity of the liquid $\gamma = 0.86$ kg/m^3.

Since the measuring leakage rate is very small, so it is required the measuring tool of high precision to eliminate random measurement errors. The random measurement errors could be:

1. liquid loss through evaporation when draining and liquid remains on the walls of measuring tank. The plastic bags were used as measuring tank, weighed with accuracy to 0.1 g. Bags must be thoroughly dried after use;
2. errors caused by weighing inaccuracy, not exceeding 0.2 g. For weighing the exemplary scale with weights of class III type 0.3—20, and weights of class I type 1–20. Drainage time must be selected in such way that the amount of liquid was not weighed less than 800 g;
3. error in determining the drainage time must be negligent, 0.2 s.

With an exclusion of systematic measurement errors, which is not provided in this work, the maximum measurement error of the average flow rate was 0.05 %, and the maximum summary error was 0.1 %.

Processing the results of observations based on the theoretical assumptions, the consumption rate was defined by function depending on the height of the liquid column H_Π, m; the specific volumetric weight of liquid γ; kg/m^3; the coefficient of flow dynamic viscosity μ; kg s/m^2; the length of destruction of the saddle parts l, m; and the area of destruction of the saddle parts F, m^2.

The main functional relationship

$$Q = H_\Pi \gamma f(\mu, l, F), \tag{7.29}$$

is determined from the research results carried out under the above procedure. Because the measurements were taken according to the parameters γ, μ, and l, then in a first approximation through the linear regression the function has been defined as

$$Q = K \cdot H_\Pi \cdot \gamma. \tag{7.30}$$

The coefficient K is determined from the following formula:

$$K = \frac{\sum_{i=1}^{N} H_{\Pi_i} \cdot \gamma \sum_{i=1}^{N} Q_i - N \sum_{i=1}^{N} H_{\Pi_i} \cdot \gamma \cdot Q_i}{\left(\sum_{i=1}^{N} H_{\Pi_i}\right)^2 - N \sum_{i=1}^{N} \gamma^2 \cdot H_{\Pi_i}^2}. \tag{7.31}$$

As a result, the dependence of the first approximation in the form

$$Q = 0.2036 \times 10^{-3} \gamma \cdot H_\Pi. \tag{7.32}$$

At further calculations of the experimental data, the results were processed in terms of the actual physical destruction of the saddle surfaces.

For this purpose, based on the destruction, the local failure chart was built, which was used to determine the levels of saddle destruction.

Assuming that the function $f(\mu, Q, F)$ from Eq. (7.29) is the local measure of the total area, which is sealed by the ball, the coefficient K from the Eq. (7.30) must be expressed in terms of the gap area, the shape of which is unknown, and the flow through these gaps must certainly satisfy the Poiseuille flow of liquid, as it is supported by the results of research.

To establish the final model of leakage through the gap, we consider the flow through the capillary tube based on the Poiseuille law, which is fully described by the following relationship:

$$Q = \frac{\pi \Delta P d^4}{128 \mu l},$$
(7.33)

where ΔP—the pressure drop, μ—the coefficient of liquid dynamic viscosity, l—the tube length, and d—the capillary diameter.

If the numerator and denominator of the Eq. (7.33) is multiplied by $\pi/16$, after some transformations we have

$$Q = \frac{F_1^2 \Delta P}{25.12 \mu l} = k_1 \frac{F_1^2 \Delta P}{\mu l_1},$$
(7.34)

where F_1—the capillary cross-sectional area and $k_1 = 0.47 \times 10^{-1}$—the coefficient of channel shape.

Processing the results of observations (these methods are not provided in this book), we obtain the following relationship

$$K = \frac{0.0154 \frac{\pi^2 d^4}{16}}{\mu e},$$
(7.35)

where d—the diameter of a working facet of saddle.

The length of the destroyed part of the saddle was taken as 2.5 mm according to the experimental results on failed saddles taken from wells for the pump size 32, 43, and 56 mm. From Eq. (7.35), it is obvious that the maximum summary area of the gap, as a result of destruction, is 0.0154 part of a squared area of the valve saddle that means, the required area can be calculated as following

$$F = \sqrt{0.0154 \frac{\pi^2 d^2}{16}}.$$
(7.36)

Summarizing the results of research, the leakage flow through the gap formed by the destruction of saddle can be determined by formula:

$$Q = 0.95 \times 10^{-2} \frac{d^4 \gamma H_\Pi}{\mu l}. \tag{7.37}$$

where 0.95×10^{-2} is the coefficient of channel shape. Comparing (7.34) and (7.37) shows that in overall they differ by the coefficient of channel shape.

By the finding through the method of local criterion the relationship between the diameter of chamfer and the area of wear, we can analyze the process of physical destruction from the dynamic impact. For this purpose, there is a need to study the reaction of the saddles of above sizes to the pure dynamic impact. This experiment made it possible to determine the parameters of failure without taking into account the solid particles hitting between the saddle and ball, the impact of gas and corrosive materials on the process of destruction.

This experiment was conducted using a hydraulic hammer. Studies using this method have shown that the destruction of the saddle is accompanied by the plastic deformation. However, there are three kinds of failure: plastic, shear, and mixture of two. The last two types of failure are observed in the saddle with the flow part being reinforced with a hard alloy.

Summarizing the results on defining the leakage through the SRP valves of all sizes, we can write the following relationship

$$Q_{\text{total}} = \frac{1}{2}\eta(D_0 + D_k)h\left\{\frac{2g[P_3 + (L_{\text{ck}}6 - 2H_n)\gamma]}{10\gamma}\right\}^{\frac{1}{2}} + 0.95 \times 10^{-2}\frac{d^4}{\mu c}\gamma A_n. \tag{7.38}$$

The data on wear of saddles retrieved from wells and destructed using the hydraulic hammer are shown in Table 7.1.

The statistical data collected in the oil and gas fields number 1, 2, 3, 4 at NGDU "Binagadineft" with intermaintenance period due to the destruction of SRP saddles are shown in Table 7.2.

By applying the method of logarithmic regression, the dependence for the average number of operational days of the pump in the well by the formula

$$T = -4.71I \cdot n \cdot F. \tag{7.39}$$

where T—the number of operational days of pump before wear of saddles and F—the total area of gap from the destruction of saddles. The calculated data for the formula (7.36) is shown below in Table 7.3.

Table 7.1 The data on wear of saddles using the hydraulic hammer

Pump dimensions, mm	Saddle extracted from wells, m²	Saddle destroyed with hydrohammer, m²
32	0.526×10^{-4}	0.537×10^{-4}
43	0.842×10^{-4}	0.848×10^{-4}
56	0.1885×10^{-3}	0.1902×10^{-3}

Table 7.2 The statistical data collected in the oil and gas fields number 1, 2, 3, 4

Field number	Well number	Pump size, mm	Average number of days of pump operation for period 1991–93, days
1	2	3	4
First	1247	32	45
Second	986		45.02
Third	344		44.8
	362		45.3
	1933		45.1
Third	926	43	43.1
	279		42.6
	296		42.9
	356		43
Fourth	2602		43.4
Third	1932	56	39.7
	1942		40.2
	2745		40.1
	2447		39.8

Table 7.3 The calculated data

Pump dimension, mm	Average number of days in well
32	44.6
43	44.42
56	38.8

According to the research results, we can conclude that the loading rate of ball has a significant impact on the type of fracture. We can say that stress is defining parameter of the destruction by shear. This is due to the fact that in the hard alloys, the fracture resistance coefficient at the dynamic pressures is lower than at the static pressures. Where in the valves, the saddles are made of a relatively soft material so at the static pressures as well as dynamic pressures the plastic fracture occurs, so the dynamic coefficient exceeds static one.

From the foregoing, it is obvious there is important to improve the life span of valves by offloading dynamic impact on the ball by the opening of the discharge valve.

7.4   Fluid Leakage and Its Determination in Valve Units

As it is known, one of the factors that significantly affect the pumps is the fluid leakage in the valve units.

The fluid leakage in the valve consists of two forming components: the first one is formed due to delay in closing of the suction and discharge valves, the second one is formed due to wear and tear of the valve saddle. The amount of leakage for the sucker rod pumps essentially depends on the dynamic properties of the flowing liquid, determining the delay in time of the ball setting on the saddle.

The literature on studying the SRP valves only has a general idea with regard to the fluid leakage in the valve units. At the same time designing and exploiting SRP in the absence of concrete dependences on the constructive parameters and the operational depth does not allow to predict and prevent premature wear of the valve saddle.

In order to determine the fluid leakage in the valve units of the sucker rod pumps, consider the following functional dependence

$$Q = f(\eta, h, \Delta p, D),$$

where Q—the liquid loss through the gap between the saddle and ball; η—the coefficient of fluid leakage; h—the height caused by the delay in landing the ball on saddle of valve; Δp—the pressure drop across the valve; D—the chamfer diameter of saddle.

Based on the theoretical analysis of the hydrodynamic flow in the pump valves, it is revealed that wear depends on the ball movement inside the body.

In the deep-well pumps, the initial ball velocity is relatively large, and together with the rotational effect of ball around the valve body axis, arising after lifting the ball, the transient processes can significantly affect the movement at the time ball landing (sealing) in his saddle.

In order to find the impact of the above-listed parameters on the valve tightness, we established based on prior theoretical analysis that the liquid flow through the gap between the saddle and ball in the transient processes could be represented by the following formula

$$Q = \frac{\pi}{2} \eta (D_0 + D_k) H \sqrt{\frac{2g\Delta p}{\gamma}},$$

where h—the maximum lifting height of the ball: D_k and D_0—the ball section diameter, included between the perpendicular dropped from the ball center on the facet diameter of the valve saddle at the current h and full H lift.

As the testing pumps we used SRP with a diameter of 43 and 32 mm. The experiment was conducted to find the flow coefficient by studying 50 valves. The experiment had following steps: while the ball landing on the saddle, its position gets recorded every 0.1 mm and the liquid leakage get measured. As a criterion to find the coefficient of liquid loss, we used the ratio of the lifting height of the ball (fixed lift height of the ball) to the diameter of the valve facet. The experiment was conducted on petroleum products with dynamic viscosity of $\mu = 1.095 - 5.73$Pa s.

From this it follows that the coefficient of pump filling at higher viscosities is greater than for lower viscosities.

Comparing the data, it showed that the discharge coefficient at the low viscosities is greater than higher ones.

The experimental data were investigated through by regression analysis according to

$$\eta = b_0 \left(\frac{h}{D}\right)^{b_1};$$

$$b_1 = \frac{\sum_{i=1}^{N} \ln\left(\frac{h}{D}\right)_i \sum_{i=1}^{N} \ln(\eta)_i - N \sum_{i=1}^{N} \ln\left(\frac{h}{D}\right)_i \sum_{i=1}^{N} \ln \eta_i}{\sum_{i=1}^{N} \ln\left(\frac{h}{D}\right)_1^2 - N \sum_{i=0}^{N} \ln\left(\frac{h}{D}\right)_1^2};$$

$$b_0 = \exp\left[\frac{1}{N}\left(\sum_{i=1}^{N} \ln \eta_i - b_1 \sum_{i=1}^{N} \ln\left(\frac{h}{D}\right)_i\right)\right],$$

where N—the number of observations; η—the discharge coefficient, obtained through observations.

After proper processing of the experimental data for the above pumps, we determined that the coefficients of liquid loss could be expressed through relationship

$$\eta_{\mathrm{p}} = 0.2608 \left(\frac{h}{D}\right)^{-1.4286}. \tag{7.40}$$

The data obtained during the study and calculated from formula (7.40) are shown below:

h/D	0.1	0.12	0.14	0.16	0.18	0.22	0.25	0.3	0.36	0.42
η	6.8	5.25	4.2	3.47	2.9	2.2	1.84	1.4	1.09	0.87
η_{p}	7.0	5.4	4.3	3.5	3.02	2.2	1.89	1.42	1.0	6.9

The height of the ball delay landing on the saddle was obtained experimentally. The height of ball delay landing on the saddle, and the delay times were found with sufficient accuracy using the thermocouple and an electronic stopwatch.

The pump inlet pressure can be determined by the formula

$$P_{\mathrm{in}} = \frac{(H_{\Pi} - H_{\mathrm{g}})\gamma}{10}, \tag{7.41}$$

which H_Π—the depth of pump suspension; H_g—the dynamic level of liquid

$$H_g = L_{well} - \frac{10P_3}{g},\qquad(7.42)$$

where L_{well}—the well depth; P_3—the pressure inside the well. Solving the Eqs. (7.41) and (7.42), we obtain

$$P_{in} = P_3 - \frac{L_{well}\gamma}{10} + \frac{H_\Pi\gamma}{10}.\qquad(7.43)$$

After some simple transformations of Eq. (7.38) with (7.43) in mind, we have

$$Q = \frac{k}{2}\eta(D_0 - D_k)h \cdot \left\{\frac{2g[P_3 + (L_{well} - 2H_\Pi)\gamma]}{10\gamma}\right\}.\qquad(7.44)$$

D_0 and D_k are determined constructively.

At known parameters of well, pumped liquid, and valve, the formula (7.44) permits to determine the leakage during the ball delay landing on saddle.

The leakage due to wear of saddle is subject of another research and therefore is not considered in this book.

As a result of research into the causes of unstable operation of valves developed and tested in field conditions the new design of valve assemblies is proposed, positive results were obtained.

7.5   Recommendation for Improving the Wear Resistance of Valve Units

To increase the wear resistance of the valve its components get a considerable hardness, but the hardness of the ball surface must be much greater that saddle hardness since the operability of pair is primarily determined by how during operation ball retains its original shape and surface condition. Even small changes in the ball shape and the surface smoothness can lead to loss of the valve tightness and cause liquid loss. This is certainly not true for the saddle, the saddle facet can greatly change in the shape and size during the process, and yet the valve will still successfully retain its service ability, without leakage.

In new design valve, the deviation of ball from the strict spherical shape should not exceed 1–4 micrometers for the different sizes of valves. Otherwise, we cannot place the ball on the saddle. To improve the performance of valves offered, E.V. Kostychenko offered the valve with a deeper and broader facet that really showed a significantly higher efficiency in comparison with the conventional valves. However, the Kostychenko valve had disadvantages like delays in closing down and large hydraulic resistances. The first circumstance caused the need for a second

ball, preventing an arbitrary movement of the main ball, thus preventing delay in landing on a saddle.

Obviously, the valve performance depends on the pumping rate: at the same pumping rate, the greater the number of strokes, the greater the wear inside the valve. So long stroke-pumping regimes are more favorable to the valves.

The presence of free gas in the pumped fluid increases wear of the valve.

Corrosive wear in the modern valves is almost completely eliminated, since both the ball and saddle are made of high-chromium steel, and the saddle can also be made from the oil-resistant rubber.

A significant impact on the valve operation has their abrasive wear, especially with free gas in the pumped liquid. The presence of sand in the pumped fluid often leads to failure due to corrosion, primarily in saddle. The primary cause of wear is slight distortions in tightness of the valve. Under the considerable pressure (after the ball lands on the saddle), the liquid containing abrasive particles with high-velocity flows through the gap between the ball and saddle and quickly (sometimes within a few hours) disrupts the valve functionality. However, if the valve is completely sealed, the pump can deliver the liquid with a high content of sand for a long time, which is observed in reality.

The design of the suction and discharge valves is of great importance for the work of sucker rod pumps, as they play an important role in providing the volumetric efficiency. The properties of the pumped liquid and the operating conditions will vary greatly, therefore, to increase the efficiency of the valves during the design we should take into account the following factors—the viscosity and specific gravity of the pumped fluid, its corrosive and abrasive properties, and inlet and outlet pressures. These factors influence the area, the gap between the ball and saddle during lift, the landing area and the construction properties of materials.

Floating ball with the fixed lift height is probably the most effective element os SRP. Their service life is considered long, due to a continuous rotation of the ball wear does not concentrated in any of the critical points, if we ignore the occurrence of eccentricity between the axis of the ball and saddle during lifting and rotation of the latter. With such landing of the ball on the saddle, the saddle gets deformed unilaterally, which decreases the valve reliability. It becomes practically impossible to prevent wear of the saddle by changing its material or design.

Obviously, some of the challenges facing the SRP designers now and will confront them in the future will be resolved only then when we develop a new high-strength and wear-resistant materials for the valve components. However, success in developing the valve units will greatly depend on the degree of protection of the saddles and designing a more detailed mathematical analysis to create a protective device which will prevent premature wear and to ensure a reliable operation of the valve assembly.

At the beginning of suction, the ball movement in the body is such that when the ball gets separated from the saddle its rotation begins to intensify around its own axis and about the axis of the saddle with a further deviation toward the periphery of the flow. This produces an eccentricity between the axis of the ball and saddle.

The above process is confirmed by mathematical analysis of the movement of the ball and the liquid in the upstream as well as a pilot study using tachometer photodevices.

The experimental results showed that there is a problem in studying the ball movement and the liquid flow at the downstream. Since at the end of the compression, the liquid, which place the ball on the saddle, can cause a hydrodynamic shock of the ball and if it reaches the ball while it deviated from the central axis of the saddle, the ball may not sit in the center of saddle, so that it can cause a one-sided wear. In addition, such a hydrodynamic shock for a brittle material, than a hard alloy, can have an adverse impact, so the saddle made of brittle materials will not wear plastically, but shearing.

Experimental studies confirmed the validity of the above assumptions. In this regard, it is proposed a protective device to reduce the hydrodynamic impact of the liquid on the ball in the shape of parabolic cage. The experimental study of the downstream valve assembly showed that the parabolic cage, by extending the flow significantly, reduces the effect of hydrodynamic impact from the liquid, with the ball evenly sitting on the saddle under its own weight causing only a moderate plastic wear of the saddle, which increases the service life of the valve.

The design of the parabolic cage prevented the deterioration of facets of the saddles by associated gas, which is available in conventional valves.

The proposed valve unit for the sucker rod pumps with the parabolic cage allows increasing a turnaround time of the pump by 1.6 times.

7.6 Fractal Dimension Analysis of Cumulative Crack Area of Valve Fracture

SRP installations play an important role in the modern oil industry. 70 % of the existing stocks on oil wells are equipped with these settings. They are used in wells with flow rates up to 50 m^3 per day and with an average depth of 1000–1500 m.

The valve unit is the core element of pump; it provides flow of the liquid and acts as sealing device. Operating modes of the SRP valve assemblies is one of the important tasks in the study of wear and destruction. Therefore, issues related to the determination of the amount of leakage from the sealing and pressure losses (hydraulic resistance) are of paramount importance. Despite the large number of theoretical and experimental work on this issue (see Bibliography of recent years [1, 2] and earlier work in [3]), the ones, which correctly describe the degree of wear and tear, are very small. The carried out experimental works determined the relative wear and durability of SRP. The most general results of experimental studies on the degree of wear and leakage of the SRP valves are given in [4].

The aim of this study is to analyze the degree of wear of sucker rod pump valves, depending on the fractal dimension of the destruction surface and the total area of gap formed by the destruction of valve [5].

7.6.1   Measurement and Fractal Structure Analysis of the Rough Surfaces

The surfaces of machine parts and equipment are never absolutely smooth; they are always uneven, depending on the structure of the material and the nature of processing and operational areas due to uneven wear of the rubbing bodies during the operation [6].

Deviations from the regular geometric shape are divided into macro-deviation, waviness, and roughness. The micro-deviations are made of singular, not regularly repeating deviations from the nominal surface shape (convex, concave, taper, etc.). The waviness is made of the set of periodic, recurring, and similar the size ups and downs forming the unevenness with a distance much larger than the surface roughness. The waveform is often close to the sine wave. The distance between the vertices of irregularities (wave pitch) is in the range 0.25–300 microns, and the height 0.03–500 microns.

By surface roughness, we understand the set of irregularities with a relatively small pitch, considered within the area whose length is equal to the base length. The basic length is the length of the conditional surface area, selected to determine the roughness and allows ignoring the irregularities having a larger pitch. The pace unevenness depends on the processing and varies 0.001–8 mm, and the height 0.03–300 microns.

Surface roughness can be measured by analyzing the surface height or profiles [7].

In the first approach, we measure the surface height z at different points along a certain direction of x. Having a large number of measurements on all available surface areas, we can calculate the surface roughness by determining the dependence $\sigma^2 = \langle z^2(x) \rangle$. Here, the angle brackets denote the averaging over a series of measurements of the surface topography. The reference point is vertically chosen so that $\langle z(x) \rangle = 0$.

An important measure of the statistical properties of the correlation function of the surface is determined by a number of heights for stationary $\{z_n\}_0^N$, $z_n > 0$, by relationship

$$C(m) = \frac{1}{N} \sum_{n=0}^{N} z_{n+m} z_n.$$
(7.45)

The Fourier transform of the covariance function $C(m)$ gives the power spectrum $G(f)$ of the random variable Z, defined by a number $\{z_n\}$:

$$G(f) = \frac{1}{2N} \sum_{m=-N}^{N} e^{-i2\pi mf} C(m), \quad i = \sqrt{-1}.$$
(7.46)

Taking into account Euler's formula $e^{\pm ix} = \cos x \pm i \sin x$, given the parity function $C(m)$, we obtain

$$G(f) = \frac{1}{N} \sum_{m=0}^{N} \cos 2\pi mf \cdot C(m), \tag{7.47}$$

Sayles and Thomas [8] suggested that the power spectrum of the surface height has scaling properties and has the form

$$G(f) = \frac{k}{f^2}, \tag{7.48}$$

The spatial frequency f is related to the wavelength λ of surface irregularities by the equation $f = 1/\lambda$. The physical systems have a finite length L_{max} and accordingly the minimum spatial frequency $f_{min} = 1/L_{max}$. Assuming (7.48) the variance of the random variable Z is

$$\sigma^2 = \langle z^2(x) \rangle = \int\limits_{f_{min}}^{\infty} G(f) \mathrm{d}f = \frac{k}{f_{min}}, \tag{7.49}$$

i.e., $\sigma^2 = kL_0$, $L = 1/f_{min}$ and the dispersion increases with the size of the surface, as it is expected for Gaussian random processes. The approximation of the observed spectral density by dependence (7.48) determines k and the normalization takes the form $G\left(\frac{1}{\lambda}\right)k = \lambda^2$.

Berry and Hannay [9] noticed that statistically isotropic surface, not allocated to any scale and the level of which is well defined, but non-differentiable, can really have the spectrum of fractal type

$$G(f) = \frac{k}{f^\alpha} = kf^{-2H-1}. \tag{7.50}$$

As shown by Mandelbrot [10], the rate of H is equal to the fractal co-dimension and is expressed as following by the fractal dimension of the surface D

$$D = 3 - H. \tag{7.51}$$

For Brownian surfaces that means in the case of the conventional Gaussian statistics, we obtain (7.48), since for such surfaces, the Hurst exponent H is 0.5 and $D = 2.5$. For surfaces obtained from the generalized Brownian motion, introduced by Mandelbrot and called the Fractal Brownian motion (FBD), the value of α in (7.50), providing the best approximation of the power spectrum, is in the range of $1.07, \ldots, 3.03$ that corresponds to the values of the fractal dimension $D = 7 - \alpha/2$ from 2 to 3. In response to the [9], Sayles and Thomas [11] conducted a new approximation of their data and histograms of the spectral parameter estimates α,

which received α values are grouped around the Gaussian value α, but distributed to the permissible range of 1–3. This result is quite reasonable, since used in [9], the experimental data were obtained from various sources (from the surfaces of ball bearings from the airfield runways) and it is unlikely that a completely different test surfaces have the same statistics.

Another approach to the measurement of surface roughness is based on the analysis of the profiles offered by Mandelbrot et al. [12] in studying the fractal structure of a rough and irregular surfaces formed by break of the metal body. They studied the breaks of samples of the martensitic steel grade 300. These breaks first nickel-plated and then polished parallel to the fault plane. As a result, the "islands" of steel surrounded by a nickel were formed, with further polishing of the island kept growing and eventually merged with each other. The length of "contour," or the perimeter L, and the area A of the islands were measured with a "measuring standard" of length $\delta = 1.5625$ mm.

Mandelbrot previously showed that for the islands, the contour outlines of which are similar satisfy the following relationship for the perimeter and area

$$L(\delta) = C\delta^{(1-D)}[A(\delta)]^{\frac{D}{2}}. \tag{7.52}$$

These relationships for any measuring standard of the length δ, small enough to satisfactorily measure the smallest of islands, are the basis of a practical definition of the fractal dimension of the outlines. In fact, we can write (7.52) in the form

$$\frac{L(\delta)}{\delta} = C\left(\frac{\sqrt{A(\delta)}}{\delta}\right)^D, \tag{7.53}$$

After taking the logarithm of both sides of (7.53), we obtain the bi-logarithmic coordinates $y = \ln(L(\delta)/\delta)$ and $x = \ln(A(\delta)/\delta^2)$ equation of the line

$$y = \ln C + \frac{D}{2}x \tag{7.54}$$

with slope $\tan \varphi = D/2$. How do we find $D = 2 \tan \varphi$. The coefficients of Eq. (7.54) are defined by a standard MLS (method of least squares) from the measured values (y, x) at different sufficiently small δ.

The fractal fracture surfaces should be characterized by the different laws of similarity in the fault plane and across it. Therefore, the surface of fracture may be, in the best case, self-similar with the local fractal dimension (valid for scales, smaller than a certain critical).

By definition [13], the set S is self-similar with respect to the sequence of N of the diagonal affine transformations α_n, if the equality holds

$$S = U_{n=1}^N \alpha_n S, \tag{7.55}$$

and $\alpha_n S \cap \alpha_m S = \emptyset$ at $n \ni m$. That means S is divided into N parts (no two of them do not intersect) each of which is obtained from one of the affine transformation sequences.

Under the diagonal, we understand [13] an affine transformation, acting in the E-dimensional affine space A^E, which is defined by specifying a fixed point with coordinates $x_m = \varphi_m$ and a set of transformation coefficients $r_m (0 < m < E + 1)$, and acts according to the rule

$$x_m \rightarrow \varphi_m + r_m (x_m - \varphi_m). \tag{7.56}$$

The coefficients r_m may not be positive, and not all of them need to be equal, as in this case the transformation degenerates into a similarity transformation (homothety).

The simplest of self-similar surfaces proposed by Mandelbrot [10] as the model of the earth surface—the fractional Brownian surface $B_H(x, y)$ of type FBM with coordinate type (x, y), located in the isotropic plane. All the properties of the surface depends on a single parameter H and its Hausdorff–Besicovitch dimension $D_{HB} = 3 - H$. The vertical cross sections of this surface have both local and global (valid for scales larger than the critical) properties. The horizontal sections are the outlines of all islands, considered together. They are self-similar and have only one dimension, which is also the local dimension of the vertical sections.

The intersection of self-similar fracture surface of the metal body with the horizontal plane gives outlines that are self-similar and have a fractal dimension $D' = D - 1$ [14, 15]. Therefore, we can use the relation (7.52) for definition of the fractal dimension D' and $D = D' + 1$.

In [12] by approximating the dependence (7.52) the estimate $D' = 1.28$ is obtained, from which it follows that in a prominent range of scales investigated by authors the fracture surface has the fractal dimension $D = 2.28$. Approximately, the same value of the fractal dimension $D = 3 - H = 2.26$ was found with the help of (7.50) of the power spectrum of heights z of the fracture surface.

Thus, both sets of the approaches to evaluate the surface roughness give almost the identical (up to two decimal places) values for the surface fractal dimension.

7.6.2 Durability Modeling of Submersible Pumps Depending on Fractal Dimension of Surface Breakage and Cumulative Crack Area of Valve Fracture

In the monograph [1], the results of experimental studies are provided on the degree of wear and leakage of fluid through the wear area of the SRP valves.

The valve assembly studies were conducted on the oil mixtures with the coefficient of dynamic viscosity $\mu = 0.01425 \, \text{kg s/m}^2$ and the specific gravity of the liquid $\gamma = 0.86 \, \text{kg/m}^2$.

Fig. 7.3 The sucker rod pump valve with a gap from the saddle destruction

Fig. 7.4 The fractured surface of the sucker rod pump valve
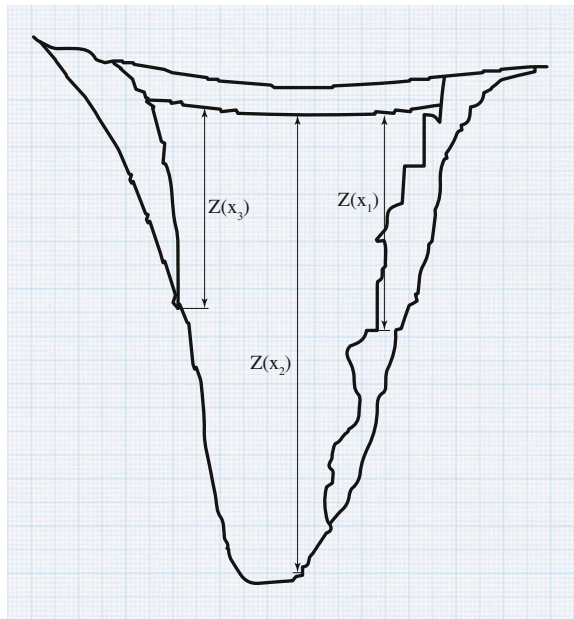
Figure 7.3 shows a photograph of the sucker rod pump valve with a fracture in saddle; and on Fig. 7.4, there is a schematic drawing of the fractured surface.

Let $\alpha = 2H + 1$ and write the formula (7.50) in the form

$$G(f) = kf^{-\alpha},$$

where after taking the logarithm, we obtain

$$\ln G(f) = \ln k - \alpha \ln f.$$

In the notation $y = \ln G(f)$, $x = \ln f$, $b = \ln k$, $m = -\alpha$ the last expression is written in the form of linear regression model

$$y = b + mx. \tag{7.57}$$

We divide the frequency range $[0, 0.05]$ into equal segments of length 0.05 and denote their right ends via $f_i(i = 1, \ldots, N)$ (N—the total number of segments of the partition). For a given sample $\{y_i, x_i\}$ $i = \overline{1, N}$, $y_i = \ln G(f_i)$, and $x_i = \ln f_i$ we calculate the coefficients b, of model m (7.63) by MLS (the method of least squares). For this purpose, we used a computer program called EXEL LINEAR. From the coefficient t, we find $\alpha = -m$, and then from the formulas $H = (\alpha - 1)/2$ and $D = 3 - H$, we determine the fractal dimension D.

The results of calculation show that the surface fracture is characterized by the fractal dimension $D = 2.45$, significantly different from the topological dimension $D_T = 2$. Since the surface fractal dimension must satisfy the inequality $2 < D < 3$, the value $D = 2.45$ means that the valve resource is exhausted almost by half.

The results can be used for plotting

$$T = f(D, F), \tag{7.58}$$

where T—the number of operational days of the pump before wear of saddle, F—the total area of the gap from the destruction of saddles, D—the fractal dimension of the surface fracture. The dependence for $T = f(F)$ was obtained earlier in [1] (Fig. 7.5).

Fig. 7.5 The logarithmic scale of the frequency range 0–0.05
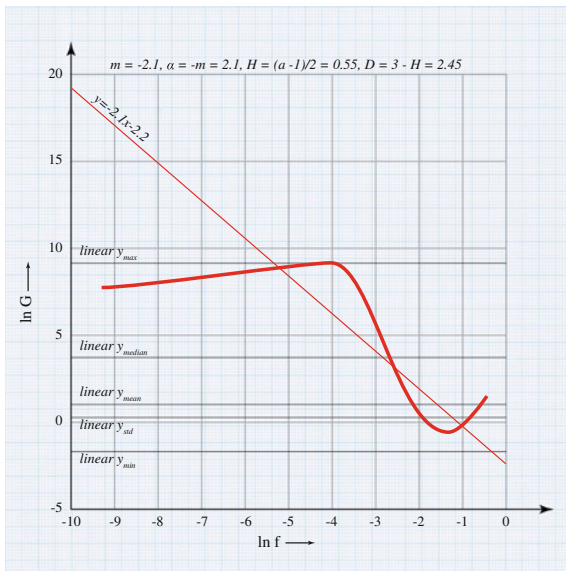
7.7   Kinetics of Damage at Contact Fatigue of Parts of Submersible Pump

The action of cyclic stresses promotes the phenomenon of material fatigue; it already appears at relatively low stresses defined by the gradual accumulation of damage. Fatigue damage upon the contact interaction of solids is the result of repeated deformation of the surface layers, essential for the normal operation friction pairs, and reduced to fracturing and loosening [16]. One of the forms of appearing of the contact fatigue of the valve parts of submersible pump is wear by friction [2].

We consider the process of fatigue wear from the position of the kinetic theory of the damage accumulation [17, 18]. According to L.M. Kachanov [17], the damage is described by a scalar $1 \geq \psi \geq 0$, which can be interpreted as the material continuity. In the absence of damage, ($\psi = 1$) during fatigue wear, the damage of surface layers of the material increases with an increase in loading time t. Therefore, a change in the continuity ψ of the surface layers can be described by the kinetic equation, according to the ideas of statistical physics, and it has a form

$$\frac{\mathrm{d}\psi}{\mathrm{d}t} = F(\psi, \ldots), \tag{7.59}$$

here the function F depends on ψ and other variables that are essential for the wear process. These variables are, in particular, the strain tensor, time, and also parameters arising from friction and characterizing the orientation at the hardening of the surface layer of material on the valve saddle.

Accounting all the selected variables is a very complex task and requires a detailed analysis of the experimental data. At the same time, it is significant [18] that the functions and parameters included in the equation of the form (7.59) could be determined by relatively simple experiments.

Figure 7.6 schematically shows the typical kinetic curves of destruction $k = f(t)$ with the parameter $P_i = \text{const}$, defining the test conditions (load rate, temperature, etc.). It can be seen that the fracture curves are similar until it reaches a certain critical value P_c. When $P_i = P_c$, the steady phase disappears on the kinetic curves of destruction, and they become close to a straight line [18].

Many dependencies, as kinetic as parametric, are shown in Fig. 7.6 to describe the deformation and failure characteristics similar to the curves. These curves are creeping, stretching, wear, and also curve of internal friction and damageness of material, etc. The initial stage I on the kinetic curves of destruction may be absent. This is most likely due to the fact that the registration of extremely thin failure curves may be absent. This is mainly explained by lack of registration tools for such thin lines, than the registration of processes at the stages II and III. However, other functionalities do hold. Stage II, when the parameter P_i changes in a fairly wide range, is reduced to zero. Near the values P_c, the dependence of durability on the parameter P increases, and its spread increases.

Fig. 7.6 Typical time
dependences of the
deformation characteristics K
and failure at different values
of P_i, determining the loading
conditions (diagram): *I, II, III*
—the stages of the formation
of defect
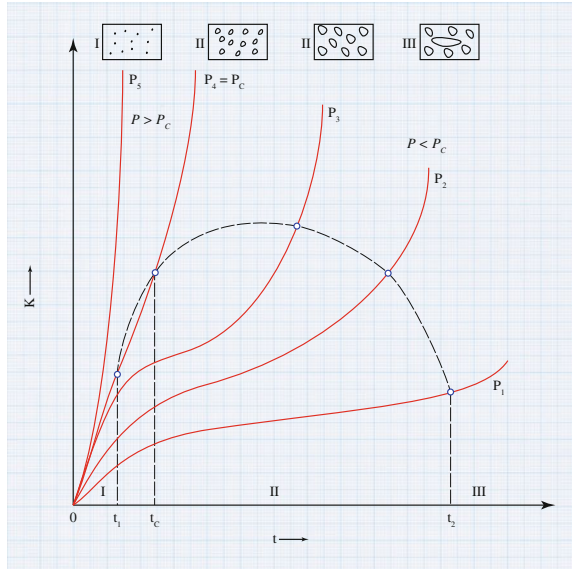
In [19], as a result of X-ray analysis of structural changes of the friction surfaces, it is established that an important role in the process of fatigue wears belongs to the residual strain in the surface layer of material. Therefore, we consider here a simple the kinetic Eq. (7.59), assuming the surface temperature and friction parameters unchanged as the temperature in the wellbore, wherein the pump is installed, is about $150\,^\circ$C. In addition, we agree that the material aging (and other similar events) does not occur over time. Then, the time does not explicitly enter into the right-hand side of the Eq. (7.59).

Let us take as the basic parameters determining the degree of fatigue damage, the intensity of the residual deformation ε_T in the surface layer with external friction for loading time t^*, corresponding to one cycle of loading and loading time t.

Then, the rate of decreasing the continuity ψ, which characterizes the formation of defects, their growth, as well as changes in the properties of the surface layers of the solid body due to wear, can be represented as a power dependence

$$\frac{\mathrm{d}\psi}{\mathrm{d}t} = -A\left(\frac{\varepsilon_T}{\psi}\right)^n, \tag{7.60}$$

where $A > 0$—the coefficient and $n \geq 0$—the rate of fracture. These dependence should be interpreted only as a convenient approximation, but not as a physical law. The rate of decrease of the material continuity can be described by other dependencies [17]. Note also that the differential equation of the type (7.60) can pass through its finite-difference analogue [18].

At the initial state in the absence of damage in the valve saddle ($\varepsilon_T = 0$ and $\psi = 1$) at the time of the destruction of the surface layer in the fatigue wear, the continuity reaches its critical value ψ_c, and at $t = t_c$:

$$\psi_c^{n+1} = 1 - (n+1)A \int_0^{t_c} \varepsilon_t^n dt. \tag{7.61}$$

On the other hand, ψ can be determined by extending the Eq. (7.61) in case of failure (breakage) of the surface layer in the outer friction after a single loading during time t^*

$$\psi_c^{n+1} = 1 - (n+1)A\varepsilon_t^n t^*, \tag{7.62}$$

where ε_c—the critical intensity of material deformation of the valve saddle in friction.

Equating the relationships (7.61) and (7.62), we obtain the equation of fatigue wear in friction

$$\int_0^{t_c} \varepsilon_t^n dt = \varepsilon_t^n t^*. \tag{7.63}$$

Taking the independence of the intensity of deformation ε_T from the number of loading cycles $N = t/t^*$, we obtain the equation $\varepsilon_T \cdot N_c^{1/n}$, which is structurally identical to the experimentally established equation of friction fatigue, such as steel 45 [19] $\varepsilon_T \cdot N_c^{0.4} = 0.06$, where $N_c = t_c/t^*$—the critical number of loading cycles corresponding to the destruction (damage) of the surface layer. Generally speaking, adopting the independence of the variables ε_T from the number of loading cycles is strictly valid only for the cyclically stabilizing material. For the cyclically hardening and softening materials, the strain intensity ε_T varies with the number of loading cycles (an account of this change can be made in accordance with the existing guidelines [19]). Apparently, the phenomenon of hardening and softening of materials during friction can be explained by their different durability, as well as improving the durability of material after finishing it with anti-friction non-abrasive processing.

The dependence of durability on values of the cyclic deformation is used in the range less than the number of cycles $(1, \ldots, 5)10^3$. The dependence of durability on values of the cyclic elastic–plastic deformation is used throughout the range of low-cycle range of numbers of loading cycles.

We now consider the laws of accumulation of damage during fatigue wear. To this end, we rewrite the damage (7.60) as following:

$$\left[\frac{\mathrm{d}\psi^{n+1}}{\mathrm{d}t}\right] = -A(n+1)\varepsilon_t^n. \tag{7.64}$$

From (7.61) at $\varepsilon_T = \mathrm{const}$, we obtain an expression for the critical time corresponding to the destruction of the surface layer in friction, which is converted to the form

$$\left[\frac{\mathrm{d}\psi^{n+1}}{\mathrm{d}t}\right] = \frac{-\left(1 - \psi_\mathrm{c}^{n+1}\right)}{t_\mathrm{c}}. \tag{7.65}$$

From (7.65), it follows the principle of linear summation of damage in integral form with the fatigue wear in case of sliding friction

$$\int_0^{N_\mathrm{c}} \frac{\mathrm{d}N}{N_\mathrm{c}} = 1. \tag{7.66}$$

It takes into account the connection between the loading time and the number of loading cycles.

The resulting functionalities of the kinetics damages and fatigue wear confirm the general analytical relationships describing the destruction of materials at the ordinary fatigue and friction. Consequently, the conventional equation of fatigue should be legitimately used to assess the durability and service life span of the valve saddle of submersible pump.

7.8 Contact Interaction Diagnosis of Solids at Friction Using Fractal Analysis

Quality, reliability, and durability of developed structures depend to a great extent on the processes taking place during the contact interaction between solids in external friction and resulting in wear of the machine parts and devices with the surface roughness and waviness caused by the parameter of pre-technological treatment, as well as friction and wear. The contact is discrete, and the friction area is just nominal. The interaction of surfaces at friction occurs on the actual contact area; therefore, at the calculation of friction and wear, we must have parameters characterizing the geometry and the physical and mechanical properties of the contact. The photomicrographic characteristics of surface are based on a number of parallel transverse profilograms taken from the investigated surface under study [20].

The soviet scientist I.V. Kragelski proposed to explain the force interaction of solids with external friction using the molecular-mechanical theory of friction [21]. Abroad, it is often referred to as the adhesion–deformation theory of friction

[22, 23]. According to this theory, the introduction of more stringent macro-roughness into the surface of the less hard counter in the actual contact areas is due to the differences in the mechanical properties, their heterogeneity in some parts of the bodies [16], and the geometric shapes in contacting areas [24]. Therefore, when one body relatively slides against another one, the deformation of embedded irregularities of less rigid surface layer takes place. The resistance to deformation of the surface layers in sliding (the so-called deformation or mechanical component of the friction force) can be calculated from the mechanical properties of the surface layers, the geometric shapes of micro-asperities, and the stress in the contact area using the main provisions of continuum mechanics.

In addition to the deformation of the surface layers under external friction in the contiguous close enough (10.7 cm) sections, there are notable intermolecular interactions. As a result of these interactions, the resistances to slipping occurs, it is often called the molecular component of the friction force. Very often, especially abroad, this component of the friction force is called an adhesion, which is inaccurate, since adhesion is the attraction, while the intermolecular interactions are characterized by the presence of the forces of attraction and repulsion [25].

In reference [25], the contact interactions of solids are differentiated into the following types: elastic (unsaturated and saturated), elastic–plastic, and plastic (unsaturated and saturated), and the formulas are provided for the dependencies of contour pressure and the magnitude of embedment of surface roughness.

The fractal dimension is a meta-characteristic of the complex systems instability. The best application of the fractal theory is in the field of modern material science to solve the problem of obtaining materials with desired properties [26, 27]. The theory of fractals is combined with the limited representation of structures. We can say that the theory of fractals is the basis for a quantitative description of dissipative structures formed under conditions far from equilibrium. This approach allowed identifying in the science of materials the main direction—the materials fractal, which was proposed and developed at the Institute of Metallurgy and Materials Science (ИМЕТ РАН) [26, 28]. It becomes possible to establish links between the composition, structure, and fractal properties of material, which is very important in studying the processes of surface formation. Analysis of hidden patterns and finding the fundamental parameters affecting the nature of the system dynamics allows in terms of the fractal geometry to characterize some important features and characteristics of its evolution [29, 30].

In this book, to change the values of the fractal dimension of curve of the supporting surface of contacting solids we set thresholds that separate from each other different types of contact and are characterized by the transition from one type of contact into another.

Having established such a classification of zones of uniform contact, it is not difficult to carry out the diagnosis of the contact type, i.e., the state of the contacting surfaces of any two studied solids. It is sufficient to calculate the power spectrum profilograms of their contact and from the known scaling relations [31, 32]

connecting the power spectrum with the fractal dimension, to find the fractal dimension of profilograms and compare them with the threshold values of the fractal dimensions of the supporting surface curve.

7.8.1 Emergence of Fractal Structures Through the Evolution of Complex Systems

In accordance with the general laws of non-equilibrium systems behavior [33], the deformable crystal should be viewed as a system in which the deformation occurs in the dissipative structure (similar to Benard cells), which is a transition from the individual defects, especially dislocations, to their groups and more complex entities. On this way, there is a growing role of collective effects in the defect structure, which is the highest manifestation of the dislocation (or vacancy–dislocation–disclination) ensemble. The substructure type, i.e., the structure and properties of the dislocation ensemble, largely irrespective of the way in which the substructure was created, defines many factors of the plastic deformation and strain hardening. It is from these positions the phenomenons of fragmentation of deformable solids are now treated, and in continuum mechanics it takes into account the strain structural elements. In general, there is a hierarchy of its levels, defined as the initial structure of the medium and the formation of dissipative structures related to the deformation defects [34, 35].

We assume that the density function φ of a number of abnormal (having the deformation defects) elements I of the less rigid body (hereinafter, referred to as the system), consisting of a large number of elements N, upon contact of two solids at the current time is described by the Fokker-Planck-Kolmogorov (FSP) from [29]

$$\frac{\partial \varphi'}{\partial t} = -\frac{\partial (A_1 \varphi)}{\partial I} + 0.5 \frac{\partial^2 (B\varphi)}{\partial I^2}, \qquad (7.67)$$

corresponding the Langrage equation

$$\frac{\partial I}{\partial t} = A_1(I) + F(t). \qquad (7.68)$$

with the right side additively consists of $A_1(I)$ and the fluctuating force $F(t)$ of white noise. If ΔI is the change of the number of abnormalities for a small time interval, the coefficients of diffusion (B_1) and drift (A_1) are defined as the corresponding average.

Assuming the statistical stationary, the existence of many degrees of freedom and the multifactorial process of the system functioning for interacting two solids, we can expect from it the self-similarity properties, the scale invariance, and

incomplete self-affinity [36]. The essence of these properties is in a constant ratio of the relative changes in the density distribution and the number of anomalies

$$[\partial\varphi/\varphi]/[\partial I/I] = \alpha_1. \tag{7.69}$$

The term of scale invariance—the fairly rigid limitation, among the most popular distributions only the Pareto distribution satisfies it. A more general assumption is

$$[\partial\varphi/\varphi]/[\partial I/I] = \alpha_1 f(I), \tag{7.70}$$

where $f(I)$ is some function of I. This condition is satisfied by such distributions as exponential, gamma, Erlang, and χ^2-distribution.

If the coefficients $A_1(I)$ and $B_1(I)$ of the FPK equation (7.67) are twice differentiable on functions of I, it brings to a linear equation of the form [29]

$$\frac{\partial\varphi}{\partial t} = \alpha_1 \cdot \varphi, \tag{7.71}$$

where α_1 is some function of I.

It is known [31] that in a significant number of applications of the FPK equation reduces to the divergence form

$$\frac{\partial\varphi}{\partial t} = 0.5\frac{\partial^2(B\varphi)}{\partial I^2}, \tag{7.72}$$

which is associated with the performance of equality $0.5(\partial B_1/\partial I) = A_1$ in the original FPK equation, following from the principle of detailed balance. As it is shown in [29], and this is quite common variant the FPK equation comes to the form (7.71) under the same conditions of self-affinity.

The process of changing the number of anomaly elements in the system is random, and its evolution, obviously, can also be described by the equation FPK in the space of anomalies I just not with respect to the distribution functions of the latter, as before, but with respect to the distribution of the proportion of anomaly elements of the system n/N (assuming that the total number of elements of the system N is sufficiently large). Assumptions on the statistical stationary, availability of many degrees of freedom and multifactorial process of operation of the large system of N elements are appropriate in this space too. Therefore, we can expect the appearance here of self-similarity, the scale invariance, and the incomplete self-affinity [36]. Consequently, by analogy with (7.71), the equation FPK for the ratio n/N looks like

$$\frac{\partial n}{\partial t} = \alpha_2 \cdot n, \tag{7.73}$$

here at the initial time $n = n_0$.

Combining this equation with (7.71), it is easy to obtain the dependence for the probability corresponding to a small interval $(n, n + dn)$, in the form of a fractal

$$\varphi = cn^{-d}, \tag{7.74}$$

where $d > 0$.

The fractal (7.74) indicates the scale invariance in the (n, φ). The Eq. (7.73) structures the system, turning it into a different space of a different (fractal) dimension. This is important in order to clarify the creation mechanism of the fractal structures, as well as for understanding the subsequent studies. Moreover, (7.74) shows that fractals as a dynamic chaos can be generated by a relatively simple systems. Where in analogy with the theory of chaos in the movement of nonlinear dynamic systems [37], it should be expected that the large classes of nonlinear phenomena show as the close qualitative behavior as the universal quantitative laws of the fractal geometry.

The parameter d in (7.74) is usually called the fractal dimension. The fractal dimension belongs to the generalized characteristics of set, reflecting its basic properties transmitted by model. The fractal-structured sets are characteristic to the systems having the stochastic regimes and complex temporary ordering. The fractal dimensions, in some cases, allow allocating the order parameters and synthesizing a hierarchy of simplified models. Knowing the dimension allows us to judge about the system behavior. Therefore, the parameter d can be interpreted as an integral characteristic of system [33, 37].

The fractal invariance on the scale is similar to the theory of deterministic chaos, a link with which for the behavior of complex systems is not difficult to imagine. The chaotic behavior has similar patterns in the variations of the different time-scales, like fractals at different spatial scales (in this case the space of anomalies).

7.8.2 Dependence of Contour Pressure on Roughness at Elastic and Plastic Contacts

The spherical model of rough surface is widely used as the calculation method for the solids interaction during friction [38, 39]. In the area of embedment, where the conditions of external friction stand the use of the spherical model of the elementary uneven surface results in the following [40]: (1) FPK provides an error of no more than 10 % in finding the actual contact area; (2) determining the mean normal stress for the plastic deformation in the zones of contact an error does not exceed 4 %, and for the coefficient of friction—3–7 %.

Considering that during the contact of the solids the embodiment of more rigid areas into less rigid, and thus, the deformation of the rigid areas is negligible, we can regard one of the bodies as absolutely rigid. The mutual influence of the individual strain sources in the calculation of force interaction can be ignored, since

the elastic deformation in the contact zones is small, and in the plastic it encounters at $\varepsilon \approx 0.5$, in the area where the usual friction units do not work.

The force interaction of solids at the external friction significantly depends on the form of deformations in the contact areas and the degree of the contact saturation. In areas of the actual contact of the friction bodies, there can generally be elastic, elastic–plastic, and plastic deformations. The most widespread deformation is elastic–plastic. For the calculation purposes, we can assume that there are only elastic (which is true for the contour pressures $p_c \le 10$ MPa on the surfaces treated for the 10th grade of roughness or higher) or plastic deformations (the surface treated for 8th grade of roughness or the contour pressures $p_c \le 10$ MPa) in the contact zones. There are 14 grades of the surface roughness, according to GOST 2789-59 and they are given in [20].

The elastic contact occurs when the maximum stress at the most embedded roughness is less than the Brinell hardness (HB) of a less rigid element of friction, it corresponds to the embodiment value of

$$\frac{h}{r} \le 2.4\left(1 - \mu^2\right)^2 \left(\frac{HB}{E}\right), \tag{7.75}$$

The surface roughness is defined by

$$\Delta = \frac{R_{max}}{rb^{1/\nu}}, \tag{7.76}$$

R_{max}—the largest radius of the spherical indentation of a rigid element into a less rigid. The constants b and ν define the curve of the supporting surface in the relative coordinates [20]

$$\eta_s = b\varepsilon^\gamma, \tag{7.77}$$

where η_s—the relative cross-sectional area of material and ε—the relative convergence $(\varepsilon = h/H_{max})$.

Given the relationship between the convergence h and the contour pressure p_c [25]

$$h = \frac{R_{max}}{b^{1/\nu}}\left(\frac{2P_c}{HB}\right),$$

we obtain the following dependence on the embodiment value of h/r of p_c:

$$\frac{h}{r} = \Delta \cdot \left(\frac{2p_c}{HB}\right)^{\frac{1}{\nu}}, \tag{7.78}$$

from here it follows

$$p_c = HB \cdot \frac{\left(\frac{h}{r}\right)^{\nu}}{2\Delta^{\nu}}. \tag{7.79}$$

From (7.75) to (7.78), it follows that the elastic contact occurs when the inequality holds

$$\frac{p_c}{HB} \leq \frac{1}{2}\left(\frac{2.4}{\Delta}\right)^{\nu}\left[\frac{HB}{E}\left(1 - \mu^2\right)\right]^{2\nu}. \tag{7.80}$$

For the most widespread in machine building, the mechanical roughness $(\nu = 2, b = 2)$ (7.79) is written in the form

$$\frac{p_c}{HB} \leq \frac{2.88}{\Delta^2}\left[\frac{HB}{E}\left(1 - \mu^2\right)\right]^4. \tag{7.81}$$

Changing the ratio p_c/HB, in which the elastic deformation pass into the elastoplastic depending on the surface roughness of Δ for the different ratios of HB/E, is shown in Fig. 7.7 [25].

The plastic contact occurs when the average normal stresses in the contact zones of asperities reach the hardness values by Brinell of the deformable material. It will be observed at embodiment

$$\frac{h}{r} \geq 5.4\left(1 - \mu^2\right)^2\left(\frac{HB}{E}\right)^2. \tag{7.82}$$

Fig. 7.7 The dependence p_c on Δ: 1 $HB/E = 0.01$, $\mu = 0.3$; 2 $HB/E = 0.05$; $\mu = 0.5$; 3 $HB/E = 0.1$, $\mu = 0.5$
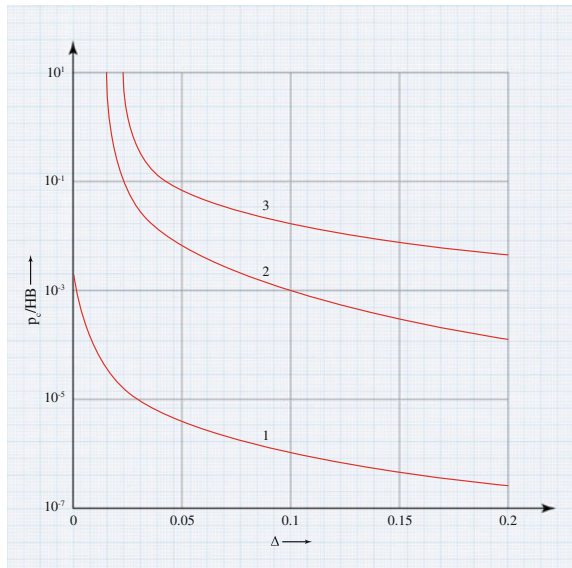
Using the formula (7.78), taking into account the relation (7.82), we obtain the contour pressure, resulting in the plastic contact

$$p_c \geq \frac{5.4^v}{2\Delta^v} \cdot \frac{HB^{2v+1}(1-\mu^2)^{2v}}{E^{2v}}. \tag{7.83}$$

For the most widespread surface roughness used in machine building $(v = 2, b = 2)$

$$p_c \geq 14.58 \cdot \frac{1}{\Delta^2} \frac{HB^5(1-\mu^2)^4}{E^4}. \tag{7.84}$$

Using (7.83), taking into account the relation (7.79), we find that for the plastic contact the inequality

$$\frac{p_c}{HB} \geq \frac{1}{2}\left[\frac{5.4}{2\Delta}\left(\frac{HB}{E}\right)^2(1-\mu^2)^2\right]^4. \tag{7.85}$$

Changes for p_c/HB depending on Δ for the different ratios $HB(1-\mu^2)/E$ are shown in Fig. 7.8.

As we can see, there is the plastic contact at relatively low values of the contour pressure for surfaces treated below the 8th grade of roughness. With an increase of the surface finish, the contour pressure leading to the plastic deformation in the contact area significantly increases reaching higher values for the 10th grade of roughness and higher.

Fig. 7.8 The dependence p_c on Δ: *1 HB/E* = 0.1, $\mu = 0.5$; *2 HB/E* = 0.05; $\mu = 0.5$; *3 HB/E* = 0.01, $\mu = 0.3$
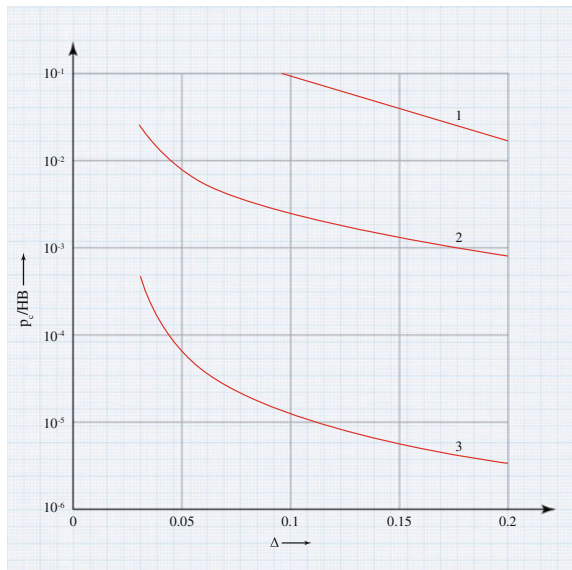
Due to the distribution of roughness according to their heights, some of them with embodiment greater than defined by the formula (7.75) plastically deform the countermaterial, roughness with the minimal embodiment defined by the formula (7.82), deform the material elastically, and their embodiment varies within the range

$$2.4\left(1-\mu^2\right)^2 \cdot \left(\frac{HB}{E}\right)^2 \leq \frac{h}{r} \leq 5.4\left(1-\mu^2\right)^2 \cdot \left(\frac{HB}{E}\right)^2, \qquad (7.86)$$

deforming the material elastic–plastically. Introducing limits (7.75) and (7.82), and taking into account the relation (7.79), we correspond the variation of the contour pressure

$$\frac{1}{2}\left[\frac{2.4}{\Delta}\left(\frac{HB}{E}\left(1-\mu^2\right)\right)^2\right]^{\nu} \leq \frac{p_c}{HB} \leq \frac{1}{2}\left[\frac{5.4}{\Delta}\left(\frac{HB}{E}\left(1-\mu^2\right)\right)^2\right]^{\nu}. \qquad (7.87)$$

Thus, there is no an ideal plastic contact of two solids with a surface roughness. However, the calculations show [25] that for surfaces below the 9th grade of roughness during the plastic contact the contribution of irregularities deforming elastic and elastic–plastic materials and force interaction of solids is negligible in comparison with the contribution of irregularities deforming the material plastically. The 10th grade of roughness usually works in the contact areas of the elastic and elastic–plastic deformations. Therefore, in the first approximation, we can assume that after reaching the contour pressures defined by the formula (7.85), there is an ideal plastic contact between solids.

Thus, the occurrence of the elastic–plastic contact is characterized by the dependence

$$\frac{p_c}{HB} = \frac{1}{2}\left[\frac{2.4}{\Delta}\left(\frac{HB}{E}\left(1-\mu^2\right)\right)^2\right]^{\nu} \qquad (7.88)$$

and the occurrence of the plastic contact is characterized by the dependence

$$\frac{p_c}{HB} = \frac{1}{2}\left[\frac{5.4}{\Delta}\left(\frac{HB}{E}\left(1-\mu^2\right)\right)^2\right]^{\nu}. \qquad (7.89)$$

7.8.3 Calculation of Fractal Dimension on Supporting Surface Curve at Threshold Values of Injection

For the spherical model of the rough surface, we have $H_{max} = R_{max}$ and the relative convergence of contacting solids is represented by the formula [20].

$$\varepsilon = h/R_{\max}. \tag{7.90}$$

Then, taking into account (7.76) and (7.79), we find

$$\varepsilon = \left(\frac{2}{b}\right)^{\frac{1}{v}} \left(\frac{\rho_c}{HB}\right)^{\frac{1}{v}}. \tag{7.91}$$

Then, the curve of supporting surface takes the following form

$$\eta_s = 2 \cdot \frac{p_c}{HB}. \tag{7.92}$$

From (7.92), it follows that the fractal dimension (the Hausdorff dimension) of curve $\eta_s(\Delta)$ is equal to the fractal dimension of curve $\frac{p_c}{HB}(\Delta)$, where Δ—the surface roughness. Since the graphics of curves $\frac{p_c}{HB}(\Delta)$, shown in Figs. 7.7 and 7.8, are shown in different scales on the axis $\frac{p_c}{HB}$, it is convenient not to calculate the fractal dimension of the graphs of functions (7.88) and (7.89) themselves, corresponding to the threshold values of embodiment (defined by the left and right sides of the bilateral inequality (7.91)), but the graphs of their inverse functions $\Delta\left(\frac{p_c}{HB}\right)$. The latter, in the notation $x = \frac{p_c}{HB}$ and $y = \Delta$, respectively, are written in the form

$$y = \frac{x^{1/v}}{2.4\left[\frac{HB}{E}\left(1 - \mu^2\right)\frac{1}{2}\right]^{2/v}} \tag{7.93}$$

and

$$y = \frac{x^{1/v}}{5.4\left[\frac{HB}{E}\left(1 - \mu^2\right)\frac{1}{2}\right]^{2/v}} \tag{7.94}$$

The results of the analysis for the stable slip bands (SSB), formed under the cyclic loading, lead to the conclusion [26] that macro-bands topography is irregular due to the superposition of the intrusion–extrusion process in the formation of protrusions. Changes by the dislocations of substructure cause the stabilization of protrusion heights with an increase in the number of loading cycles. The height of protrusions in the SSB is linked to the width of macro-bands with a weak linear dependence [46]. Therefore, the surface of macro-bands is a rough surface, the size of the irregularities that slowly decreases with a decrease in the projected area of roughness [47]. We can therefore assume that the surface of macro-bands is self-similar and under the certain conditions a stochastic process of the SSB formation is a curve of the fractal dimension.

The provided views in Sect. 7.6.1 with regard to the fractal properties of the fracture surfaces suggest that the rough surface by contacting the metal bodies in the process of friction also becomes self-similar.

Table 7.4 The fractal dimensions of curved bearing surfaces (d)

	$\mu = 0.3, HB/E = 0.01$	$\mu = 0.5, HB/E = 0.05$	$\mu = 0.3, HB/E = 0.1$
Elastic → elastic–plastic	1.0035836	1.0054545	1.0064359
Elastic–plastic → plastic	1.0002506	1.0006126	

For the self-affine curves, which are the curves of supporting surface (7.93) and (7.94) for various combinations of parameters μ and HB/E ($m = 0.3$, $HB/E = 0.01$; $m = 0.5$, $HB/E = 0.05$ and $m = 0.5$, $HB/E = 0.1$), the fractal dimensions for transient contacts (from elastic to elastic–plastic and from elastic–plastic to plastic contact) are listed in Table 7.4. The Minkowski dimension is taken as the calculation method for the fractal dimension of the curves of supporting surfaces [43].

7.8.4 Calculation of Power Spectrum of Roughness Profile and Contact Regime Diagnosis of Metal Bodies

In practice, various average roughness characteristics (R_a, R_q, etc.) are used to describe the surface roughness; the algorithms determine their typical values and these regulated values are listed in national and international standards [48]. However, this approach cannot be considered satisfactory, since it cannot obtain a clear functional relationship between the average surface roughness characteristics and functional properties of these surfaces. This fact is connected ultimately with poorness of specified averaging as such, since the same average values can correspond to the fundamentally different (and including functionally) types of roughness.

The development of computer technology and its widespread implementation in practice made it possible to implement a quite different approach. Under this approach, the roughness profiles are regarded as the implementation of a random process (field), and their analysis involved instruments such as correlation functions, structure functions, spectrum analysis, and wavelet analysis [49].

In work [50], the power spectrum of the profile roughness, as suggested in [31, 32], is used as the characteristic of the surface roughness. This characteristic is thinner than conventionally used mentioned above the simple average roughness characteristics, and yet macroscopic.

The fractal profile of roughness has the following property: At different levels of magnification, it looks in a similar manner, namely the statistical properties of surface are the scale invariant. Naturally, for the real surface this feature exists in a limited range of the scale (or the spatial frequency). The connection between the power spectrum and the fractal properties of the roughness profile is expressed through the scaling relationship [31, 32]

$$S(\omega) \sim \frac{C}{\omega^{5-2D}}, \quad \omega \to 0 \tag{7.95}$$

where C—the constant that depends on the amplitude of the surface roughness and D—the fractal dimension of profile $1 < D < 2$.

The Eq. (7.95) is not new and it follows as a consequence of the formulas (7.50)–(7.51) with the equality $D' = D - 1$. Let $\alpha = 5 - 2D$.

After taking the logarithm (7.95) and applying the OLS to the linear regression

$$y = ax + b, \tag{7.96}$$

where $y = \ln S(\omega)$, $x = \omega$, $a = -\alpha$, and $b = \ln C$; with the OLS estimation of the coefficient a, we find $\hat{\alpha} = -\hat{a}$ and the assessment $\hat{D}$ of the parameter D

$$\hat{D} = 5 - \hat{\alpha}/2, \tag{7.97}$$

With the help of Table 7.4, it is easy to diagnose the type of contact for a given profilogram (the roughness profile).

The construction algorithm consists of the following steps:

1. Assuming the observations $\{V(t_k)\}$ $(k = 1, \ldots, N)$ for the profilograms $V(t)$, we build its power spectrum $S(\omega)$, equal to the Fourier transformation of the autocorrelation function.
2. Based on the sequence of frequencies close to zero, that is, the sequence $\{\omega_k\}$ $(k = 1, \ldots, k_1; \; k_1 > 10, k_1 \ll N)$, we build regression

$$y = ax + b \, (b \neq 0),$$

with coefficients $a = -\alpha$, where α—the constant of the scaling ratio $S(\omega) = C \cdot \omega^{-\alpha}$.
By the method of least squares (OLS), we find the estimate $\bar{\alpha}$ of parameter a and, accordingly, an assessment

$$\hat{\alpha} = -a,$$

3. We calculate the estimate $\hat{D}$ for the fractal dimension of the profilogram D, using the relationship $\alpha = 5 - 2D$

$$\hat{D} = 5 - \hat{\alpha}/2,$$

4. From the values of the parameters μ and HB/E, we define the appropriate column in Table 7.4 with the threshold parameters D_u for various contact regimes.
5. Select the row in which the estimate value of $\hat{D}$ is closest to D_u, thereby defining the type of transient contact.
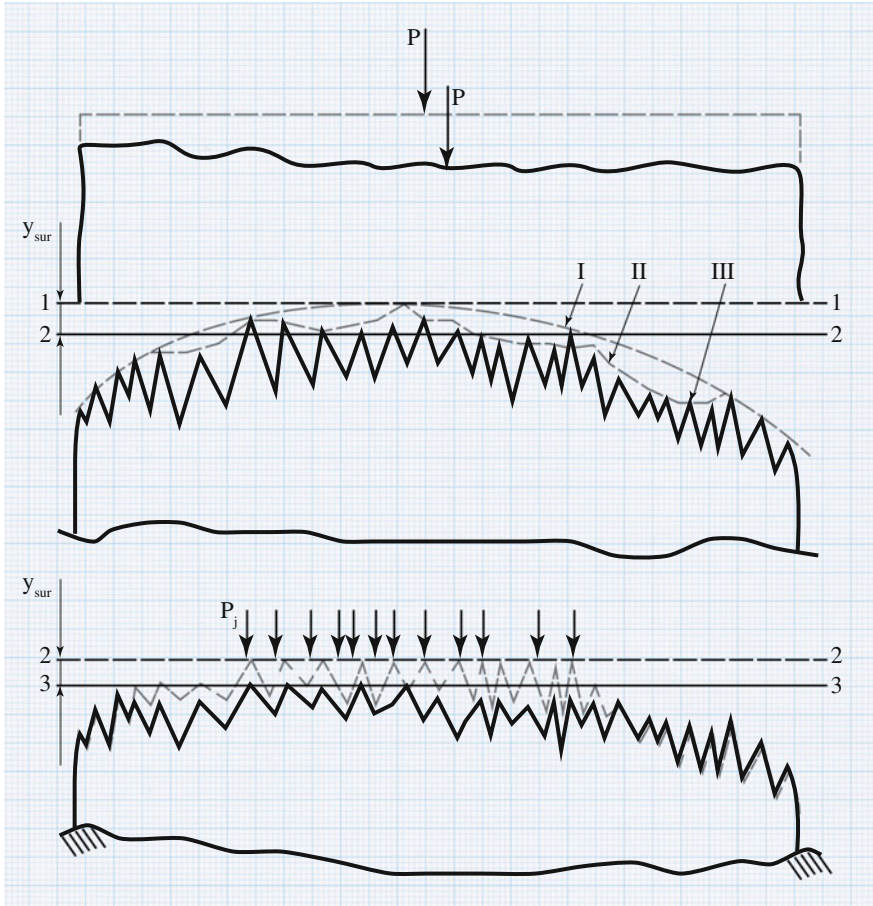
Fig. 7.9 The original diagram for the calculation of normal contact displacement: 1-1 starting position of the adjacent surface; 2-2 positions of the adjacent surface with respect to the plastic deformation of the protrusions; 3-3 the final position of the adjacent surfaces (*I* the profile of macro-deviation; *II* the profile of waviness; and *III* the profile of roughness)

Example Let roughness profile (profilogram) $V(t)$ is set with the image on Fig. 7.9, we construct the power spectrum $S'(\omega)$ of the signal $V(t)$.

The formula (7.97) is used to calculate the fractal dimension D of roughness profile as shown in Fig. 7.9 and the schemes of the normal contact movement for contacting surfaces of the parts.

The graph of the power spectrum of the profilograms in the bi-logarithmic coordinates is shown in Fig. 7.10.

The fractal dimension of profilograms calculated using the formula (7.97) is equal to 1.0029. Since the profilogram on Fig. 7.9 corresponds to $\mu = 0.5$ and

Fig. 7.10 The power
spectrum of the profilograms
in the bi-logarithmic
coordinates
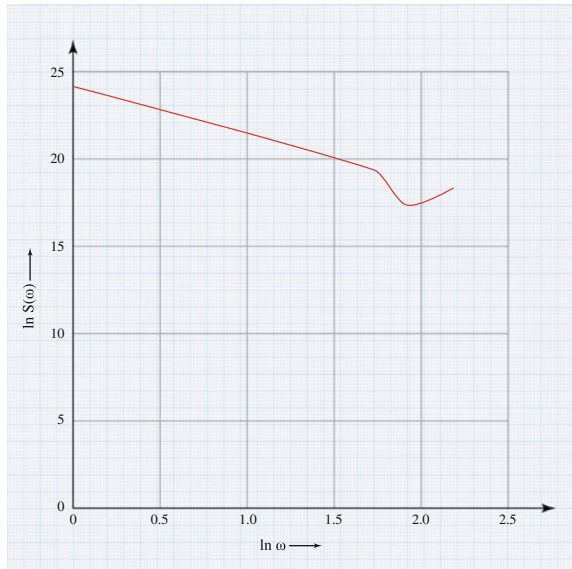
$HB/E = 0.05$, in accordance with the 3rd column of Table 7.4, we find that the study corresponds to the profile of the roughness of elastic–plastic contact regime.

The existing connection of the power spectrum with fractal characteristics is particularly important for the fracture surfaces of metals, having in many cases, the fractal nature.

Resulting in additional quantitative tools—the fractal dimension of the curves of supporting surfaces and the profilograms, we can apply in the fractographic studies as a new method of fractal material science.

On the basis of determining the fractal dimension of the curves of supporting surfaces with the property of self-affinity for the transient contacts, we established the range of fractal dimensions with the threshold values for the three types of contacts: elastic, elastic–plastic, and plastic.

For the studied rough surface of the metal contact interaction on the calculation formula that uses the connection of the power spectrum of profilograms with the spatial frequencies in the region of small values, we calculate the fractal dimension of profile, and based on the scale of fractal dimensions of the curves of supporting surfaces, we diagnose the form of contact. It creates a database of the power spectrum of the rough surface at the initial state after various kinds of deformations. The power spectrum of roughness measured for particular loading of friction units is compared with the data of the power spectrum of rough surfaces, and the results of the comparison reveals the type of contact of the tested tribocoupling.

Literatures

1. A.Kh. Dzhanahmedov, *Tribotekhnicheskie problemy v neftegazovom oborudovanii* (Baku, Elm, 1998), p. 216
2. A.Kh. Janahmadov, *Neftianaia tribologiia* (Baku, Elm, 2003), p. 326
3. A.N. Adonin, *Voprosy gidravliki i rabotosposobnosti glubinnogo nasosa* (Aznefteizdat, Baku, 1955), p. 192
4. A.Kh. Janahmadov, L.A. Akbarova, A.M. Mekhtiev, Issledovanie stepeni iznosa v klapannykh uzlakh skvazhinnogo shtangovogo nasosa. Uchenye zapiski AzGNA, 35–45 (1994)
5. M. Alesai, Analiz fraktal'noi razmernosti ploshchadi povrezhdeniia klapannykh uzlov shtangovyh skvazhinnykh nasosov. Vestnik Azerbaidzhanskoi Inzhenernoi Akademii, Tom **8**(3), 37–45 (2011)
6. N.B. Demkin, *Kontaktirovanie sherohovatykh poverhnostei* (Nauka, Moscow, 1976), p. 227
7. E. Feder, *Fraktaly, per. s angl* (Mir, Moscow, 1991), p. 254
8. R.S. Sayles, T.R. Thomas, Surface topography as a nonstationary random process. Natura **271**, 431–434 (1978)
9. M. Berry, J. Hannay, Topography of random surfaces. Nature **273**, 573 (1978)
10. B.B. Mandelbrot, *The fractal geometry of nature* (W.H. Freeman, New-York, 1982)
11. R.S. Sayles, T.R. Thomas, Reply to tomopgraphy of random surfaces by M.V. Berry and J.H. Hanny. Nature **273**, 573 (1978)
12. B.B. Mandelbrot, D.E. Passoja, A.J. Paullay, Fractal character of fracture surfaces of metals. Nature **308**, 721–722 (1984)
13. B.B. Mandelbrot, *Samoafinnye fraktal'nye mnozhestva, v kn. Fraktaly v fizike* (Mir, Moscow, 1988), p. 9–47
14. B.B. Mandelbrot, Self-affine fractals and fractal dimension. Phys. Scr. **32**, 257–266 (1985)
15. R.F. Voss, Random fractals, Characterization and measurement, Scaling Phenomena, in *Disordered Systems*, ed. by R. Pynn, A. Skjeltorp (Plenum Press, New-York, 1985), pp. 1–11
16. A.V. Chichinadze, E.L. Braun, N.A. Bushe, *Osnovy tribologii* (Mashinostroenie, Moscow, 2001), p. 664
17. L.M. Kachanov, *Osnovy mekhaniki razrushenija* (Nauka, Moscow, 1974), p. 312
18. L.R. Botvina, *Razrushenie. Kinetika, mekhanizmy, obshchie zakonomernosti* (Nauka, Moscow, 2008), p. 334
19. K.V. Frolov, *Metody sovershenstvovaniia mashin i sovremennye problemy mashinovedeniia* (Moscow, Mashinostroenie, 1984), p. 224
20. N.V. Demkin, *Kontaktirovanie sherohovatykh poverkhnostei* (Nauka, Moscow, 1970), p. 227
21. I.V. Kragel'skii, M.N. Dobychin, V.S. Kombalov, *Osnovy raschetov na trenie i iznos* (Moscow, Mashinostroenie, 1977), p. 526
22. H. Chikhos, *Sistemnyi analiz v tribonike, per. s angl* (Mir, Moscow, 1982), p. 236
23. K. Dzhonson, *Mekhanika kontaktnogo vzaimodeistviia, per. s angl* (Mir, Moscow, 1989), p. 509
24. A.Kh. Janahmadov, *Fiziko-stokhasticheskoe tribomodelirovanie* (Elm, Baku, 1988), p. 152
25. I.V. Kragel'skogo, V.V. Alisina, *Trenie, iznashivanie i smazka. Spravočnik, v 2-h kn., pod red* (Mašinostroenie, Moscow, 1978), kn. 1-ia, p. 400
26. V.S. Ivanova, A.S. Balankin, I.Zh. Bunin, A.A. Oksogaev, *Sinergetika i fraktaly v materialovedenii* (Nauka, Moscow, 1994), p. 383
27. V.S. Ivanova, V.U. Novikov, Nelineinyi mir. Tom **2**(3), 197–202 (2004)
28. A.I. Olemskoi, I.I. Naumov, *Fraktal'naia kinetika ustalostnogo razrusheniia, v sb. Sinergetika i ustalostnoe razrushenie* (Nauka, Moscow, 1989), p. 200–214
29. I.K. Kohanenko, Fraktaly v otsenke evoliutsii slozhnykh sistem. Avtomatika i telemekhanika **8**, 54–62 (2002)
30. Standart ISO 4287:1998, *Geometricheskie kharakteristiki izdelii. Struktura poverhnosti - profil'nyi metod. Terminy, opredeleniia i parametry struktury* (Moscow, 1999), p. 252

31. B. Person, O. Albohr et al. On the nature of surface roughness with application to contact mechanics, sealing, rubber friction and adhesion. J. Phys. Condens. Matter **17** (2005)
32. A. Majumdar, B. Bhushan, Characterization and modeling of surface roughness and contact mechanics. in *Handbook of Micro and Nanotribology*, Chapter 4, (1999)
33. G. Nikolis, I. Prigozhin, *Samoorganizatsiia v neravnovesnykh sistemakh* (Mir, Moscow, 1979), p. 300
34. V.E. Panin, V.A. Likhachev, V. Grinaev, *Strukturnye urovni deformatsii tverdykh tel* (Nauka, Novosibirsk, 1995), p. 163
35. V.E. Panin, V. Grinaev, V.I. Danilov, *Strukturnye urovni plasticheskoi deformatsii i razrusheniia* (Nauka Sib. otd-nie, Novosibirsk, 1990), p. 255
36. A.Kh. Janahmadov, O.A. Dyshin, Synergetics and Fractal Dimensions in Tribology. J. Frict. Wear **32**(1), 80–95 (2011)
37. A.Kh. Janahmadov, A.M. Pashaev, M.G. Javadov, M.Y. Javadov, *The multifraktal analysis of the fatigue fracture under the process of friction, 5th World tribology Congress, WTC 2013*, September, 8–13, Torino, Italy, id 821 (2013)
38. I.V. Kragel'skii, *Trenie i iznos* (Mashgiz, Moscow, 1968), p. 480
39. N. Drozdov, E.G. Iudin, A.I. Belov, *Prikladnaia tribologiia* (Eko-Press, Moscow, 2010), p. 604
40. A.Kh. Janahmadov, M.Y. Javadov, O.A. Dyshin, Diagnosis of the contact interaction of solid bodies at friction using fractal analysis methods. J. Sci. Appl. Eng. Q. **04**, 5–16 (2014)
41. B. Mandelbrot, *Fractals, Form, Chance and Dimension* (Freeman, San-Francisco, 1977)
42. T.S. Akhromeeva, S.P. Kurdiumov, G.G. Malinetskii, A.A. Samarskii, *Nestatsionarnye struktury i diffuzionnyi khaos* (Nauka, Moscow, 1992), p. 544
43. R.M. Kronover, *Fraktaly i khaos v dinamicheskikh sistemakh. Osnovy teorii, per. s angl* (Postmarket, Moscow, 2000), p. 350
44. A.M. Pashaev, A.Sh. Mekhtiev, A.Kh. Janahmadov, O.A. Dyshin, Avtomodel'nost' i fraktal'naia mekhanika razrusheniia. Vestnik Azerbaidzhanskoi Inzhenernoi akademii, Tom **1** (1), 93–103 (2009)
45. M. Berry, J. Hannay, Topography of random surface. Nature **273**, 573 (1978)
46. J. Polac, K. Obetlik, Strength metals and alloys, in *Proceedings of VIII International Conference, Tamper*, 22–26 Aug., ICSMA 8 Oxford etc., vol. 2, pp. 761–766 (1988)
47. B. Zel'dovich, D.D. Sokolov, Uspekhi fiz. nauk., Tom **146**(3), 493–506 (1985)
48. D. Vaitkhauz, *Metrologiia poverkhnostei. Printsipy, promyshlennye metody i pribory* (Intellekt, Dolgoprudnyi, 2009)
49. X. Jiang, P.J. Scott, D.J. Whitehouse, L. Blunt, Paradigm shifts in surface metrology. Part I. Historical Philosophy. Part II. The current shift. in *Proceedings of the Royal Society of London A: Mathematical, Physical and Engineering Sciences*, vol. 463 (2007)
50. A. Fedotov, Spektr moshchnosti kak kharakteristika sherokhovatosti poverkhnosti. Fotonika **6**, 18–21 (2010)

Chapter 8
Flicker Noise Spectroscopy (FNS) of Dynamics Signals and Its Application in Wear of Oil-Field Compressor Units (OFCU)

8.1 Analysis of Technical Manufacturing Characteristics of Operating Oil-Field Compressor Units

The implementation of the new energy policy in Azerbaijan is impossible without scientific–technical progress at all levels of the energy complex, which is improving the energy efficiency and ensuring the environmental acceptability of energy facilities.

The stock of compressor equipment is extensive, and the number of units reaches more than 500 pieces with various capacities from 4 to 25 MW. A significant part of stock is manufactured before 1970. This leads to an increase in operating costs and above all the maintenance cost associated with repairing of the aggregates.

The diagnosing of compressor operating modes is associated with the management control to provide a continuous performance at the programmed level, determining conditions when to turn off from the optimal conditions, studying the factors that affect on the equipment load, OFCU performance evaluation characterizing mainly economy, efficiency, reliability, and so on. At the deep analysis of theory and practice of the compressor equipment operational regimes, we can build a strategy for improving the maintenance work, the selection of optimal operational–maintenance cycles, and the determination of residual resources that can be used to improve the design or redevelopment.

The SOCAR gas pipeline system has been in operation for a long time, in order to maintain the technical condition of the pipeline equipment, and more maintenance (repair) hours and resources are required. The repair mainly supports the technical condition of the equipment.

To prevent failures of the pipeline equipment, accompanied by accidents, we need to maintain the technical and energy levels. The repair hardware resources are assigned according to the specifications by its manufacture, and its further development and adjustment can be done during operation.

For example, in case of the forced emergency stop, followed by failures, accidents, and downtime, the repair resources get corrected. To adjust these resources, we employ various accident statistics and the diagnosis methods. There are established methods of diagnosis: diagnostic inspection and diagnostics, based on the analysis of operational modes of the pipeline equipment.

In the event of significant maintenance, the equipment must be under the great attention to control operating modes and conditions. Along with the standard diagnosis methods in recent years, specialized diagnostic techniques, such as flicker noise spectroscopy (FNS), get well spread. The FNS requires technical–economic justification and analysis of failure.

There is a lack of necessary statistical data in oil fields which can be used to judge how the costs of the pipeline facility-specific equipment is associated with the organization and analysis of failures, reduction of the overall production cost, and the number of failures, including failures followed.

Currently, the much attention is directed toward the technical diagnostics of compressor equipment in oil and gas industry and in pipelines particularly.

The main purpose of the FNS diagnosis method is to determine and analyze the technical conditions of the compressor equipment so that to develop sound programs and strategies for repairing, restoration, modernization, and reconstruction of parts and equipment in general.

According to Table 8.1, each factor influencing the reliability, quality is evaluated four levels. Thus, the factors affecting the reliability of the equipment shall be considered as linguistic variables.

Grade values are as follows: *I-1*—not harsh; *I-2*—a little harsh; *I-3*—severe; *I-4*—very severe; *II-1*—very good; *II-2*—good; *II-3*—the average; *II-4*—poor; *III-1*—very good; *III-2*—good; *III-3*—poor; and *III-4*—very bad.

Using the data in Table 8.1, we can represent a qualitative assessment of the reliability of the equipment on the basis of expert assessments. Along with this, it is also possible to apply the quantitative evaluation of the reliability of the equipment as a whole, using a point system. For this purpose, it is proposed to use the data presented in Table 8.2.

The technical inspection of the equipment was carried on expert assessments of all the above factors characterizing the reliability of the equipment as a whole. The result of this survey found that conditions are assessed as severe—0.60. The equipment conditions, taking into account the state-of-the-art developments and manufacturing, are estimated as an average—0.65. The service level, taking into account the number of found defects, not eliminated since the last overhaul, is estimated as bad—0.60.

Table 8.1 The equipment reliability under operating conditions

Factor I grades				Factor II grades				Factor III grades			
1	2	3	4	1	2	3	4	1	2	3	4

Table 8.2 Quantitative evaluations of factors affecting the reliability of the equipment as a whole under operating conditions

Factors determining the process conditions				
Process conditions	Mild	Moderate	Severe	Harsh
	0.9–1	0.7–0.9	0.4–0.7	<0.40
Factors determining the condition of changes in the technical condition of the equipment				
Equipment conditions	Excellent	Good	Average	Poor
	0.9–1	0.7–0.9	0.4–0.7	<0.40
Factors determining the level of maintenance and repair				
Service conditions	Excellent	Good	Average	Poor
	0.9–1	0.7–0.9	0.4–0.7	<0.40

Thus, the reliability of the inspected unit as a whole is as follows:

$$H_{tot} = H_{con} \cdot H_{tec} \cdot H_{tes} = 0.60 \cdot 0.65 \cdot 0.60 = 0.234.$$

The technical inspection was done on the same unit at the compressor station after the next major overhaul; it was established that process conditions have not changed, the technical condition of it is at the same level, and the service level has improved, which is reflected particularly in the elimination of a number of previously existing faults and possibly to evaluate the service level with a good estimate—0.90.

Thus, the reliability of the resurveyed unit becomes equal to

$$H_{tot} = 0.60 \cdot 0.65 \cdot 0.90 = 0.351,$$

At the same time, the quality of the equipment in operation is affected not only by its technical condition, but also the amount of reserved capacity. The poor technical condition affects the efficiency of equipment and the value of its working power. These examples show the results of operational ranking and quality indicators of a large group of compressor equipment in the overseas and domestic gas transportation systems for many years on the operational parameters from the data on the compressors performances.

8.2 Flicker Noise Spectroscopy—A New Approach to Solving the Problem of Extracting Information from Complex Dynamic Signals

The problem of extracting information from the chaotic signals has been relevant at all times, if under information we understand a new knowledge required to solve practical problems. Tasks varied from simple self-preservation in this world to understanding the universe at all spatial and temporal levels of its organization.

Today, the problem of establishing the content of chaotic signals (produced by open nonlinear dissipative systems, including natural and experimentally obtained time series, spatial mappings, energy series) is formed specifically. You have to understand what kind of useful information is contained in the measured signals and how to extract the information in the required amount for the solution of practical problems.

The complexity of the problem is that the signals produced by the real open systems enclosed to determine from the studied signals the full information about signals, such as Shannon using an image "bits," and it is basically impossible, as extraction and further processing of any signal gets "digitized" and a set of "sample rates" is a priori limited. Moreover, the signals are measured at some finite time intervals and are unsteady in varying degrees: Input at the statistical averaging over some time interval, the signal characteristics depend on the choice of the interval on the time axis. These circumstances do not allow full use of many of the developed mathematical methods for analyzing complex signals (Fourier analysis, Takens' theorem on the topology of the strange attractor, and others).

The general difficulty of these and other theoretical approaches to the analysis of signals produced by open systems, in order to obtain on their basis an adequate information about the studied system, is linked to the need to allocate in this analysis the contribution of "resonance" components. The number of functionally important "resonances" in the real signals can reach several hundreds. At the same time due to the relationships realized in vivo in the resonance system, and the influence of external factors of different types, including casual produced by the open systems, the signals are non-stationary. All these factors "masked" a purely random signal components without allowing uniquely define the parameters of "chaos." Such a variety of dynamic factors cannot be considered within the model framework.

Sometimes, in order to highlight the parameters of chaos in the complex processes, fractal and multifractal analyses are applied. However, the applications of these approaches in order to find the relevant parameters (in the theory of fractals—the Hearst constants and the indicators of flicker noise dependences, in particular) and the "resonance" components are also generally not allocated. In addition, we should pay attention to one fundamental limitation inherent in such approaches—the postulation of scaling self-similarity of the studied signals at every conceivable scale. This is clearly not case for the real signals: The features of scaling self-similarity are usually manifested itself at the best in 1.5–2 levels of changes in studied dynamic variable.

A number of practical problems associated with the analysis of complex signals are successfully solved using wavelet analysis. Nevertheless, only the qualitative conclusions on the state of the tested processes can be made on basis of the wavelet analysis. And it is not just the absence of physical sense in the used wavelet coefficients (they reflect purely "mathematical" properties of signal by isolating the intervals with the sharpest changes), but also the difficulties associated with the adequate and sufficient parameterization of the obtained wavelet maps. It is important to emphasize that success in applying the wavelet analysis for the specific

range of practical problems (in particular, the problems of compression and packaging of information, as well as being "decoration" of different images) should be considered as additional [along with the concept of self-organized criticality (SOC)] arguments in favor of information the significance of irregularities in the signal.

Problems of analysis of the real natural objects are associated primarily with the uncertainty of the complete information contained in the structure of each of these systems at all levels of its spatial organization, and in the complex, usually chaotic behavior of dynamical variables $V(t)$, usually measured on finite time intervals T. The task is complicated by the fact that investigated the dynamics of real systems, along with random components inevitably present a wide and rebuilt during the evolution of the spectrum of "resonance" constitute defining features of the structural organization of systems or side impact factors (considered open systems whose evolution generally not stationary!).

It was found that internal sources of these features of the dynamics of complex systems, including power laws, reflect the existence of extended in space and prolonged in time ("infinite"—for flicker noise) correlations in the studied systems with the external chaotic evolution or formed in the course of its structures associated with the implementation of such systems in the *complex* ("multiparticle," nonlinear) *interactions*, the inevitable *dissipative processes* and the manifestation of *inertia*.

That achievement of the nonlinear sciences, supported by numerous computer calculations of the evolution of modeling systems and the dynamics of the formation of complex structures, gives I. Prigozhin and I. Stengers a reason to write about the potential readiness of science to start "A New Dialogue with Nature" [1], although the development on the basis of the theory of cellular automata the concept of "self-organized criticality" (SOC) [2] did not allowed to advance in solving the practical problems of the parameterization of the dynamics of real processes and structures to predict catastrophic changes in the evolution of complex systems. The problem actually lies in how to establish and organize the initial information contained in the time series $V(t)$, measured the dynamic variables, or the "spatial" series $h(x)$, or "maps" obtained from the study of structures, and how to use the input and output information to address specific problems.

Currently, the most developed approach to the analysis of the dynamics of the complex systems is the nonlinear time series analysis—a methodology based on the theory of deterministic chaos [3]. According to [4], the effects of nonlinear relationships in the dissipative system with only three degrees of freedom can already give rise to the chaotic regime with an insensitive dependence of the system evolution to the choice of the initial conditions at the asymptotic attraction of trajectories in the phase space for a certain set—a strange attractor.

The strange attractor itself is characterized by the fractional dimension and has a zero volume in this phase space of integral dimension, though its domain of attraction is a finite (or even infinite) volume. It is necessary to emphasize the fundamental difference between the systems with friction (dissipative) and the systems without friction (conservative or Hamiltonian).

It is the presence of internal friction (in the broadest sense) implies the existence of the attractor as the asymptotic (at $t \to \infty$) limit, which does not directly affect the initial conditions: the trajectory, corresponding to different initial conditions outside the attractor, by evolving "settles" down on the attractor.

The chaotic processes in the deterministic nonlinear dissipative systems are one of the fundamental problems of the modern science. In such systems, the cause of generation of complex oscillatory processes, which may not be different with respect to the physical characteristics from the truly random, is not in a large number of degrees of freedom, and not in the presence of fluctuations, as previously thought, but in the exponential instability of modes, generating a sensitive dependence on the accuracy of initial state of the system.

Studying the real evolutionary processes in natural science requires an expansion and generalization of the classical notion of a dynamical system (DS). More general notion of DS should include the impact of fluctuations and provide the possibility to use as evolution equations of statistical theory. From a physical point of view, we can talk about dynamic systems even if we cannot write the equations of DS, although experimentally there is a process in changing the state of a physical system through time. It is assumed that there is a continuous or discrete operator, approximately describing its evolution (in time and/or space). Under the noise, we can understood the internal or external fluctuations or the impact of a large number of factors that have little effect on the behavior of the system and therefore not taken into account when setting the state. Then, the minimum number of independent coordinates sufficient to describe the state of the system, in a given approach, may be called its dimension. Such systems are called the "real dynamic systems" (RDSs) [5].

Let us clarify the concept of "chaos." The classic phenomenon of Brownian motion of particle gives us a clear idea of the physical chaos as an unpredictable, random process. Thus, if we speak about the chaos, we mean that the time variation of the state of the system is a random (it cannot be clearly predicted) and non-reproducible (the process cannot be repeated) [6].

At first glance, the concepts of "determinism" and "chaos" seem to be the opposite in terms of meaning. The determinism is associated with a unique full predictability and reproducibility, where chaos—with complete unpredictability and irreproducibility. The possible modes of deterministic chaos in nonlinear systems with energy dissipation can be illustrated by the well-known three-dimensional dynamic system called the *modified generator with inertial nonlinearity* [7]

$$
\begin{aligned}
\dot{x} &= mx + y - xz, \\
\dot{y} &= -x, \\
\dot{z} &= -gz + gl(x) \cdot x^2, \quad I(x) = \begin{cases} 1, & x > 0, \\ 0, & x \le 0. \end{cases}
\end{aligned}
\tag{8.1}
$$

Let us consider the solution of (8.1) for the control parameters $m = 1.5$ and $g = 0.2$ for the initial conditions near the equilibrium state of the system at the

origin of coordinates. Indeed, here the main principle of determinism works: The future is uniquely determined by the initial state.

However, the evolution of the system over time is complex and aperiodic. Outwardly, it is no different from random, but with a more detailed analysis a significant difference is revealed between this process and random: This process is reproducible! Indeed, by repeating the initial state once again, due to the determinism, a computer again reproduces the same path regardless of its complexity. So this aperiodic process is not chaotic according to the definition on chaos given above. Yes, it is complicated, like a random, yet a deterministic process implements the phenomenon of deterministic chaos.

In practice, it is quite often not possible to measure the time dependence of all coordinates of the system state. A typical situation when only one of the characterizing the process variables is available for the measurement, one of the coordinates of the system state is $a(t)$. The dependence of variable describing the system state by some independent variable, which is often either time or spatial coordinates, is called a realization of the (observed) system. The time-dependent realization discretized with some step Δt, called a one-dimensional time series $a(i\Delta t) = a_i, i = 1 \ldots N$. The reconstruction of the dynamic system is actually a restoration of the modeling system on the experimental time series a_i.

Until 1980, it was thought that to describe nonlinear DS in terms of the phase space, it is necessary to know the time dependences of all state coordinates. In 1980, the paper was [8], in which it was noted that the phase portrait of the dynamical system could be restored to the scalar time series a_i, as if for the missing coordinates of the state vector the same series is used, taken with some delay.

In 1981, the paper [9] appeared, which proved a theorem (now known as Takens's theorem), claiming that the one-dimensional realization $a(t)$ of the dynamic system has an attractor A, owned by the smooth M-dimensional set, and the delay method can obtain the n-dimensional reconstruction A_R of the original attractor as the set of vectors $\vec{x}(t)$ in R^n

$$\vec{x}(t) = \Lambda_n[a(t)] = (a(t), a(t+\tau)), \ldots, a(t+(n-1)\tau) = (x_1, x_2, \ldots, x_n). \quad (8.2)$$

Here, n satisfies the condition of Mans theorem [10]

$$n \geq 2M + 1. \quad (8.3)$$

According to the Takens' theorem, the mapping $\Lambda_n: A \to A_R$ is a smooth and reversible on A_R for almost any delay τ (if $N \to \infty$). The number n is called the dimension of attachment.

This theorem is proved under conditions that the investigated dynamic system is autonomous, not noise, and the time series is measured exactly and within an infinite time interval, i.e., it is not formally applicable to real dynamic systems (e.g., for systems with noise) and the real experimental conditions (any time series can be measured in a finite time interval and with a finite precision). Despite this, since the beginning, it is used by the experimenters to restore the phase portraits and

evaluation on its basis different characteristics of the DS attractors. Only in 1997, Stark et al. [11] proved a theorem, which gave a spread for Takens' theorem on systems under the external influences and the system noise.

The emergence of Takens' theorem opened opportunities for solving the problems on predicting the system behavior [12–14], calculating the metric [15, 16] and dynamic [17, 18] characteristics of attractors. In 1987, the works were published independently [19, 20], which proposed a method for recovery of the DS equations on its one-dimensional implementation (the global reconstruction method).

It should be noted that the Takens' theorem does not imply that the vectors $\vec{x}(t)$ of (8.2) *always* allow us to study the properties of a dynamic system for time series. Such research is only possible *as a rule*, of which there are always exceptions (see [21]). In the literature, we can find a lot of advice and ways to select a delay τ and embedding dimension n, for example, [22–24]. However, neither one of them cannot be fully relied upon. It was found that there are not many experimental time series, for which the apparatus of nonlinear dynamics could be effectively used. In the simplest cases, the model (e.g., signals from the relatively simple electronic circuits, chaotic oscillations in some lasers, separate, specially organized experiments in fluid dynamics, and a few relatively simple signals in physiology) and the methods of nonlinear dynamics usually work, but for some arbitrary a particular pilot, time series results are often unintelligible.

It follows that some hope in solving complex natural parameterization signals can be associated with the development of general phenomenological approach, not focused on the modeling of processes and do not use artificial hypothesis.

We must have methods for processing complex signals that identify quantitative changes in the study of complex systems; for establishing the relationship between the individual subsystems of such systems; and for predicting the approach of danger (catastrophic) event.

In this context, it is of considerable interest method of FNS, as a general phenomenological approach to the analysis of the different nature of chaotic signals [25].

8.3   Essence of Flicker Noise Spectroscopy

The emergence of the flicker noise in a complex dynamic system is associated with the effect of intermittency, which is a change with respect to the long sections of laminar or the regular time behavior characteristics of the non-equilibrium dynamic system patches of the chaotic bursts and surges. The effect of intermittency, i.e., succession of the two above-mentioned conditions, is a paradigm of "self-organized criticality" (SOC).

A basic way to extract information from complex signals in FNS method uses the correlation function. For the classification of the information contained in the correlation function, it is proposed to analyze the function itself is not, and some of its transformation ("projection"), such as the power spectrum $S(f)$ (f—frequency),

the time difference ("transitional structure function"), and the second order $\Phi^{(2)}(\tau)$. The dependences characterized by the difference in momentum, are exclusively formed by the irregular jumps, and the splashes and the jumps of dynamic variable contribute to the formation of the power spectrum. The recovered by this way the informational "passport data" of systems have the meaning of time correlation and the characteristics of the "memory" loss (correlations) in these time correlations —for irregularities such as "bursts" and "jumps." In some cases, along with the "passport parameters" to enter conveniently "passport patterns"—the specific information "cliché," formed on the basis of the power spectrum and transient difference moments of analyzed chaotic series. The relevant characteristics for the irregularities of the "gaps" are extracted from the power spectrum and difference "moments" that are based on "quasi-derivative" original signal.

Due to the system inertia, each abrupt change in value of the dynamic variable may be accompanied by the dynamic bursts—a sharp short-term increase $V(t)$ with a relaxation attenuation values on a subsequent "laminar" section, leading to discontinuities of related to "laminar" sections. The adoption of the irregularities of dynamic variables as an information basis of the FNS methodology allows not only in the most general phenomenological form to classify all contained in a chaotic series information, but also to discernibly extract the necessary part.

Traditionally, the existing opinion about the identity of the information provided in $S(f)$ and $\Phi^{(2)}(\tau)$ is valid only for sufficiently "smooth" functions, what the real signals $V(t)b$ are not. The FNS methodology, focused on giving information entity to the sequences of irregularities, hidden in the real signals, permits the above information seeming inconsistency and "disengages" information contained in the dependences $S(f)$ and $\Phi^{(2)}(\tau)$, distinguishable features—the various types of irregularities, "color information." Thus, the averaging interval T acts as the "active" parameter and its variation allow, in particular, identifying some of the factors characterizing the real non-stationary processes.

The work [25] convincingly proves the legibility of information differences of functions $S(f)$ and $\Phi^{(2)}(\tau)$. This indicates a well-known result of the monograph by Schuster [3], which was considered a stationary chaotic signal with intermittency: the fields of slightly varying "laminar" phases punctuated by sharp chaotic "comb-bursts." Such a signal is approximated in [3] δ-function of Dirac in the areas of "combs" and obtain a sequence of δ-functions with typical time intervals T_0 between adjacent δ-functions on macroscopic time intervals $[-T/2, T/2]$ $(T_0 \ll T)$, and the power spectrum $S(f)$ was calculated. It is shown [3] that this artificially created signal in the low-frequency region of the spectrum at $f \ll \frac{1}{2}\pi T_0$ can generate the flicker noise dependencies $S(f) \sim f^{-n}$ $(n \approx 1)$ that means to be informatively significant. It was therefore a hasty conclusion was made that for this signal model, the function $S(f)$ is only the informative indicator.

However, if in addition to the power spectrum $S(f)$ of the sequence of δ-functions we consider the transient difference moments of order p

$$\Phi^{(p)}(\tau) = \langle |V(t) - V(t+\tau)|^p \rangle, \quad (p = 2, 3 \ldots), \tag{8.4}$$

in particular, at $p = 2$

$$\Phi^{(2)}(\tau) \le (V(t) - V(t+\tau))^2 \ge 2(\psi(\tau) - \psi(0)),$$

(the angle brackets denote averaging over time), it is easy to make sure that all values $\Phi^{(p)}(\tau)$ are zero, since the set of moments ("domain"), which is defined by a sequence of δ-functions, has a value of zero [26]. It is also easy to verify the validity of this conclusion using as δ-functions one of the known approximations (e.g., Gaussian with variance σ^2), and then passing the limit $\sigma \to \infty$. The function $\Phi^{(p)}(\tau)$ for the given level of the hierarchy becomes different from zero, if the sequence of irregularities in addition to δ-functions shows θ-Heaviside function. In other words, the information contents of dependencies $\Phi^{(2)}(\tau)$ and $S(f)$ for the considered by Schuster a modeling signal are different.

The FNS methodology used in the logic of introducing "*various signs*," details of which can be recovered in different ways from the dependencies $S(f)$ and $\Phi^{(2)}(\tau)$, $p \ge 2$, calculated on the basis of experimentally measured random series (and because of this forms the basis of empirical knowledge of the system), fully complies with the basic principles of "abstract theory of information" [27].

8.4 Flicker Noise and Self-similar Criticality

The name of the FNS method uses the term "flicker noise." For a long time, almost 75 years, the low-frequency flicker noise (or $1/f$-noise) was considered one of the mysteries of nature. Johnson discovered the flicker noise (a name suggested by Schottky [28]) in the mid-twenties of the last century [29] while studying the thermionic emission current. The peculiarity of this noise is that its power spectral density (PSD) increases with a decrease of frequency f by law, close to $1/f$.

There are many researches about the flicker noise (see, e.g., [30, 31]). Variety of metals, semi-metals, semiconductors, gases, liquids, electrolytes, radio-electronic devices, uniform and non-uniform conductor at high and low temperature, the film and contacts, animate and inanimate objects, and so on were subjected to studies. As a result of the research, it became clear that the flicker noise—an extremely common phenomenon— is the characteristic of many electrical, magnetic, electromagnetic, acoustic, sonar, hydro-physical, astrophysical, and other processes. In the low-frequency dependence of PSD, the flicker noise frequency obeys $1/f^\beta$, where β is the form factor of the spectrum (in connection with which the noise is sometimes called $1/f^\beta$-noise).

The flicker noise can be focused not just about zero frequency, but, for example, about the natural frequency of the oscillating circuit [32].

An interest to the flicker noise is caused by the fact that its dispersion, which is often independent of the observation time [30, 33], leads to the restriction of accuracy. It was found [30, 34] that the dispersion of quartz resonators is connected with Q by ratio $124 \ln 2Q^{-4.3}$ (the empirical formula).

Studies have shown that in some cases, the flicker noise is close to the Gaussian distribution. Sometimes (but not always), it is possible to consider a flicker noise as a stationary process.

There is still no common understanding of what is the source of flicker noise. Apparently, $1/f^\beta$-noises are caused by many different factors. According to some researchers in solids, the flicker noise has the thermodynamic equilibrium nature. However, an essential role, for example, is the presence of electrical noise and movement of defects in conductors (the idea expressed by Schottky). There are equilibrium and non-equilibrium flicker noises. PSD of first is usually described by law close to $1/f$, and second$-1/f^\beta$, where the spectral power $\beta > 2$ [31].

It is noted [32] that the flicker noise can have a fractal property—the property of statistical self-similarity.

In general, under the flicker noise we understand the process PSD of which is adequately described by a power function with an exponent $\beta > 0$.

The electrical $1/f^\beta$-noise is the most thoroughly experimentally studied: The dependence of the spectral density from the frequency $1/f^\beta$ is traced to the frequencies of the order 10^{-7} Hz, and almost always the value of β is in the range from 0.8 to 1.2 [35].

The system $1/f$ can be represented by a set of elements, in each of which there is a gradual accumulation of energy, bringing an element to an unstable state. At some point under the external influence, the element condition can change dramatically and the stored energy is released ("discharge"), after which a new cycle of accumulation discharge starts. Thus, the external exposure can lead to the self-organization, and as a result, a non-equilibrium system goes into an ordered state.

Like all phase transitions, the self-organization process requires an intensive external influence. In recent years, however, we found many systems in which self-organization occurs spontaneously. The most striking manifestation of this behavior, known as the SOC, is earthquakes and avalanches. In addition, the SOC regime expresses itself at the flow of bulk material on an inclined surface (the sand pile model), the natural selection in biological systems, the forest fires, and the fluid flow in porous media. The essential feature of SOC is discontinuous nature of the process corresponding to the regime of intermittency: The most of time the dissipation prevents a spontaneous accumulation of energy storage, and the system is in a precritical condition; the uncompensated pumping of energy can occur spontaneously, which leads to the self-organization; then for a short time δ the discharge of stored energy occurs, which is referred to as an avalanche of size s [36]. The elements of system with the SOC regime are in the "wind-up" non-equilibrium state, and besides some of them come close to the critical point, beyond which there is a "discharge."

These elements are so weak that any push can cause a premature discharge. The avalanche can be triggered by any shake-up, gust of wind, sharp sound, etc. If the entire system is experiencing a push, then all elements on way to the critical point (so-called active elements) respond to it, and in a short time, the release of energy occurs, significantly surpassing the usual.

The open systems, consisting of a large number of simple components, capable of cooperative interaction, spontaneously develop in a way that comes to the state of SOC and have complex dynamics. The basic requirements for the system to function in the SOC regime are next [37]:

1. the system must consist of a large number of elements capable of interacting with its neighbors;
2. the storing of its current state is essential for each element; and
3. the constant supply of energy to the system is important, while all the local interactions occur for far less time than the time between two disturbances caused from outside.

The solution to the problem of assessing the possibilities of the phenomenon of SOC in the concrete structures is generally difficult due to a poor knowledge, and often lack of the formal procedures binding the model systems or their parameters with the phenomenon of the flicker noise, which is, as it is clear from the foregoing, described by the physical level of SOC. Finding the solution is facilitated by the results of Shuster [3], Zaslavski and Sagdeev [38], Zaslavskogo et al. [39], Akhromeeva et al. [40], Klimontovich [41] on the theory of intermittency of weak chaos. This theory explains the appearance of flicker noise. Its essence lies in the formal description of the appearance of the chaos (in the stochastic sea [38]) for some values of the control parameters islands (windows) regular behavior. The system condition, characterized by a random alternation of the long regular phases and the relatively short random bursts, usually called the attractor type of noise cycle [42]. G. Shuster phenomenon is called intermittency, linking it with the flicker noise. On the basis of numerical experiments in [3], the values of the control character (r) to display Feigenbaum are as follows [43]:

$$x_{n+1} = rx(1 - x_n), \tag{8.5}$$

from which there may be the flicker noise. This value r should be slightly larger the threshold value $r_\infty = 3.5699456\ldots$. The low-frequency power spectrum divergence of the mapping characteristic of the flicker noise appears after exceeding r_∞ because the boxes (islands) of regularity (the area of intermittency) randomly appear [3, 38]. In the range $r_\infty < r < 4$, which for the M. Feygenbaum display of natural area is called a weak chaos, the regular structures of cycle 3 appears (the stable oscillations of period 3), interrupted by chaos.

In [3], the solution of the emergence of SOC, or the flicker noise is associated with the determination of the values of the fractal dimension (the Hausdorff dimension) process described by one-dimensional mapping of the form $x_{n+f} = f(x_n)$ (which is a particular type of the M. Feygenbaum mapping), in which the

power spectrum display at a frequency $f \to 0$ has the power dependence $1/f^{\beta}$ $(\beta > 0)$. It is assumed that the mapping for $0 < x < x^*$ has the regular and for $x > x^*$ has the arbitrary decisions; here, x^* defines a border region that the return of mapping from the area $x > x^*$ to $0 < x < x^*$ comes with a nonzero probability. Then for $f \to 0$

$$S(f) \sim \begin{cases} f^{-(3-d_H)} & \text{at } 2 < d_H < 3; \\ f^{-(d_H-1)} & \text{at } 1.5 < d_H < 2; \\ \dfrac{|\ln f|^2}{f^{0.5}} & \text{at } d_H = 1.5; \\ f^{-(5-3d_H)} & \text{at } 1 < d_H < 1.5; \\ f^{d_H-1} & \text{at } 0 < d_H < 1. \end{cases} \qquad (8.6)$$

where d_H is the Hausdorff dimension.

This relationship is consistent with the physical concepts [37] that the large islands of the regularity generating low frequencies occur with less probability than the larger fractal dimension. For that it follows that, if under the flicker noise we only understand the type of noise $1/f^{\beta}$ when $\beta > 0$, it corresponds to the fractal dimension in the range of

$$2 < d_H < 3, 1.5 < d_H < 2, 1 < d_H < 1.5, 0 < d_H < 1.$$

Consequently, the systems with such dimension are expected to have a self-organized critical phenomenon. Therefore, the asymptotic (as $t \to 0$) relation (8.6) can be used as a criterion for the instability of complex systems.

The work [44] shows the possibility of applying the criterion (8.6) to the evaluation of the geo-ecosystems instability on the example with the pollution of the Caspian Sea by petroleum hydrocarbons.

In [45], we consider a system of N elements, each of which has a frequency of discharges f_i (e.g., for the avalanche frequency it is a slope of ith element). The values of f_i range from f_1 to f_N and with the equal intervals f_i between the values. The discharge energy of ith element is denoted by E_i. Let the energy accumulation rate through all elements is the same, then $E_i = a/f_i$, where a is the constant. If the discharges occur independently, and the intervals between them are random, the system generates $1/f$-noise. A required condition that the considered $1/f$-system has a high sensitivity to the higher influences is a quite large number of active elements. In the semiconductor, they correspond to defects in the crystal structure, which are mainly localized near the surface. The biggest impact the surface phenomena have on the performance of the alloyed bipolar and metal-oxide-semiconductor field-effect transistors (MOSFETs). It is no accident that it is in the operators of noise on the basis of such semiconductor devices observed effects associated with the remote human influence and the cosmic rhythms. In similar devices with other types of semiconductors (the planar transistors, the field-effect transistors with $p-n$ junction, the zeners), the similar effects were not observed. Apparently, this is due to not large enough value of N in these devices.

Thus, considering even the simplest system of independent energy "accumulators" generating $1/f$-noise, we find its high sensitivity to the external influences at sufficiently large number of active elements. Obviously, the real $1/f$-systems are much more complex: They manifest nonlinearity, a large number of conditions, the element interaction, and the chain and avalanche processes. A variety of interesting phenomena occurring in the non-equilibrium systems ("active media") are studied by the non-equilibrium thermodynamics [1, 46, 47]. The most important are the emergence of ordered structures (e.g., auto-waves), as well as processes such as predator–prey and "wandering around a strange attractor." A theoretical analysis of the last two processes shows that they lead to strong fluctuations of system parameters that are easy to adapt to the rhythms of external influences (even very weak). As an example of such adjustment are the fluctuations in the number of lynx and hares with the 11-year cycle of solar activity [46].

The identification of nonlinear relationships in the studied systems, responsible for the fluctuation dynamics ("deterministic chaos") as well as the establishment of specific "resonance", can be the basis for further modeling of the dynamics of complex systems or structures. Thus, there is a complex of open issues related to the representation of dynamics in accordance with the Trieste theory by von Weizsäcker [48]. According to this theory, the fact of the phenomenon actualization is due to the irreversibility of transitions into a new state system. Thus, the idea of evolution must include the realized discrete sequences of irreversible "steps–events" or the intervals "now," mating with Locke's "moments." The irreversibility is introduced a priori a fixation of defined jump—the change in evolving system. The key concept of this evolution is the interval bounded by two "events, moments," and not moments of times along the continuous time axis, as it is the case in traditional science.

8.5   Conceptual Foundations of Flicker Noise Spectroscopy

According to the conceptual FNS framework [25] suggests that the most common form of the evolution of a dynamic variable $V(t)$ for the ith space–time level is presented in the form of intermittency, when not all the intervals on the time axis are informatively equivalent. Such dynamic, as it was mentioned above, is characterized by (Fig. 8.1) relatively weak variable changes on the relatively extended time intervals—the "laminar phases" with typical durations T_0^i and the sharp interruptions of this evolution, the jumpy changes in the dynamic variable in the short intervals with duration $\tau_0^t (\tau_0^t \ll T_0^i)$.

Due to the system inertia, each such a jumpy change of the dynamic variable may be accompanied by the dynamic bursts—the sharp short-term increase $V_i(t)$ with the relaxation attenuation up to the values on a subsequent "laminar" section, leading to the discontinuation of the related adjacent "laminar" sections. The magnitude and duration of these bursts are specific to each system, causing a contribution to the corresponding power spectrum. Such jumps and breaks are
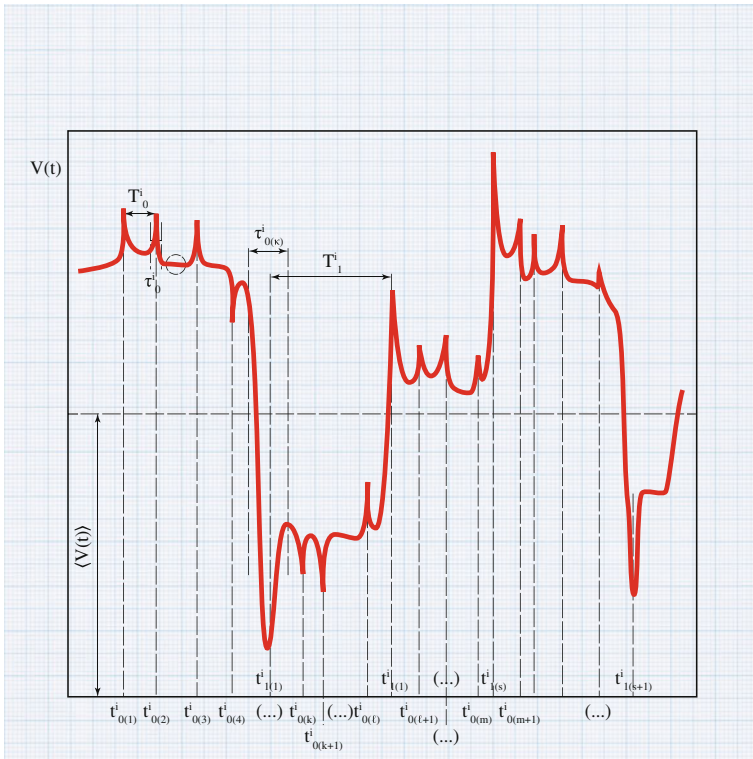
Fig. 8.1 The diagram of evolutionary dynamics of the complex system corresponding to the change of dynamic variable at the same level of spatial time hierarchy

provisionally allocated [25] to the *first type of jumps* and breaks of derivatives, assuming that the variable $V_i(t)$ can be characterized by sharp, at intervals τ_1^i jumpy changes of the "laminar" background, as shown in Fig. 8.1. For the typical time intervals between such sharp jumps (they conditionally belong to the *second type of jumps*), the designation T_1^i is introduced (assumed that $\tau_1^i \ll T_1^i$). In addition, it is assumed that all the basic information about the evolutionary process for the *i*th hierarchical level is contained only in the jumps of the first and second type. All these irregularities are considered as the main and only "markers" of the evolutionary process.

At the same time, the intervals between selected δ-intervals (intervals τ_0^t and τ_1^t) are considered as informative, containing sequences smaller δ-intervals of informatively important for the smaller levels of the hierarchical organization system. Such allocation of the smaller informatively significant intervals should be continued. Inside of each input *i*th level in the hierarchy of sequences of δ-intervals, there are dynamical variables of system, in general, that are bound by the information relations of various types, carrying information about the system dynamics.

The term intermittency came into use in the context of dynamic after French researchers Pomo and Manneville who published their work in 1980 [49]. In
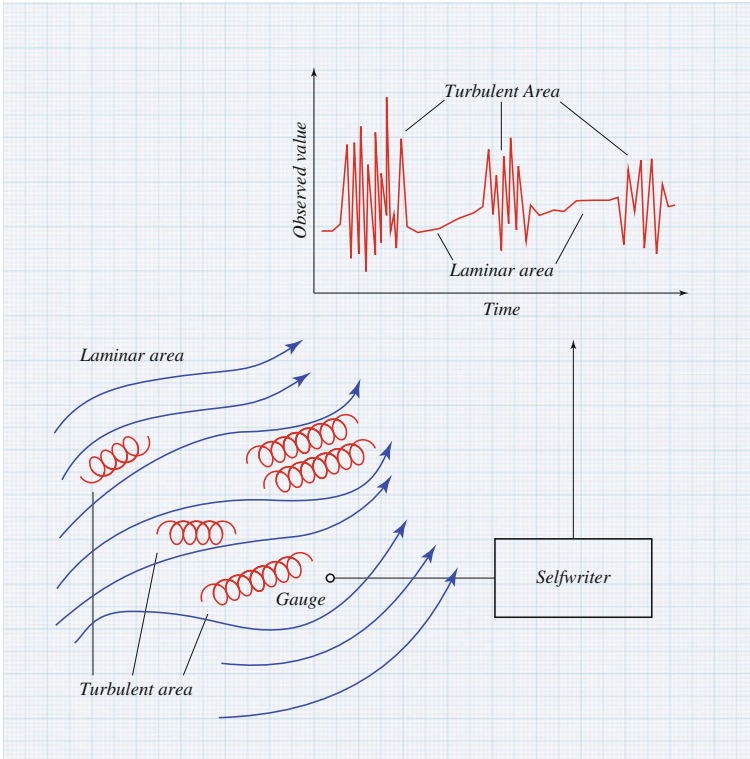
Fig. 8.2 The intermittent turbulence in the hydrodynamic flow

hydrodynamics, it has long been known as "intermittent turbulence," when current in a specific range is smooth and laminar, but they alternate with the areas of irregular, turbulent regimes. Due to the turbulent areas move, change a shape, appear and disappear, the intermittent nature of the relationship is also observed values from time to time at a fixed point in space (Fig. 8.2).

Pomo and Manneville indicated a number of possible situations where there may be intermittency in the dynamical systems (including those with a relatively small dimension of the phase space) and outlined the classification by introducing three types of intermittency. In particular, for the intermittency of type *I* and *III*, renormalization group analysis was developed, similar to the Feigenbaum theory [50].

The convenience of introducing the power spectrum $S(f)$—the Fourier transform of the autocorrelation function $\psi(t) = \langle V(t)V(t+\tau)\rangle$ (for the stationary signal $S(f)$ it coincides with the cosine Fourier transform $S_c(f)$), is that this dependence present the most clear specifics for the analyzed signals—a set of m peaks, characterizing the position f_{oi}, the half-widths γ_i and the partial weights $A(i = 1...m)$. These frequencies manifest themselves in the graph $S(f)$ in the double logarithmic coordinates (Fig. 8.3c) in the form of called "scallops" because of their apparent continuity and correspond to the resonances characteristic of the evolutionary
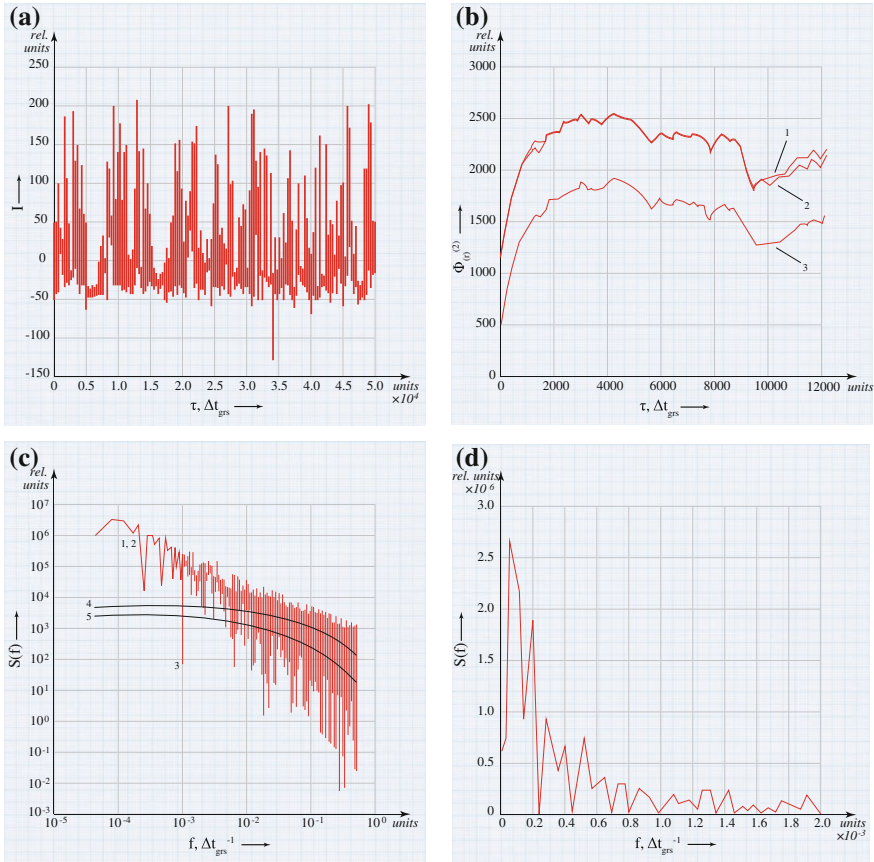
Fig. 8.3 The dynamics of binary X-ray system GRS 1915 + 105 from January 1, 1996, to December 31, 2005: **a** and **b** the structure functions $\Phi^2(\tau)$ of the signal: *1* the "experimental" relationship; *2* the calculated dependence, determined by specific frequencies and contribution of "irregular-jumps" at $\sigma = 1.79$ relative units; $H_1 = 0.14$; $T_1 = 14\Delta t_{grs}$; *3* the contribution of specific frequencies; **c** the power spectrum of $S(f)$ signal in the double logarithmic scale: *1* the "experimental" dependency; *2* the calculated dependence, determined by specific frequencies and contribution of "irregularities-jumps" and "irregularities-bursts"; *3* the contribution of specific frequencies; *4* the contribution of "irregularities-bursts" at $S_s(0) = 3866$ relative units; $n = 1.43$; $T_0 = 14\Delta t_{grs}$; *5* the contribution of "irregularities-jumps"; **d** the low-frequency part of the power spectrum (100 frequency) of the signal

dynamics of the systems reviewed under conditions of external influences, the frequency spectrum of which may also contain a set of characteristic frequencies. Therefore, the spectrum $S(f)$ may contain the interference frequencies, resulting in the addition of the resonant components of different nature. During the evolution of open systems, the summary of these resonant frequencies and interference can be reconstructed.

In the future, all the specific frequencies that appear in the oscillatory nature of the investigated dynamic variable $V(t)$, without regard to the genesis of such frequencies, latched in the dependences $S(t)$, for the sake of convenience, we shall define as "resonance."

Figure 8.3 illustrates the dynamics of the X-ray binary system GRS 1915 + 105, located in the constellation of Aquila and is a star donor, which revolves around a rapidly rotating massive compact object—a black hole. The numeral 3 in Fig. 8.3 denotes the total power spectrum $S(t)$ in the bi-logarithmic coordinates, which reflects the contribution of specific frequencies with a pronounced "comb" in the frequency range (0.005, 1).

8.6 Assessment of Irregularities-Bursts and Catastrophic Changes in the State of Oil-Field Compressor Units

8.6.1 Formulation of the Problem and Solution Method

For the analysis of the individual elements of oil-field compressor units (OFCUs), we selected the bearing of the piston compressor. We considered the output of inductive counter of the bearing particle when testing the oil from the piston compressors. While testing the samples N1 using the inductive particle counter in the laboratory, we recorded the Babbitt wear particle with a size 200–1000 mkm. The typical recorded signal at the output of the counter is shown in Fig. 8.4. The registered pulse corresponds to the non-ferromagnetic metal particles (Babbitt particles) of 500 and 30 μm.

Fig. 8.4 The output signal of the inductive particle counter of the bearing when testing the oil for the piston compressors (the sample *N*1 is selected before the bearing failure)
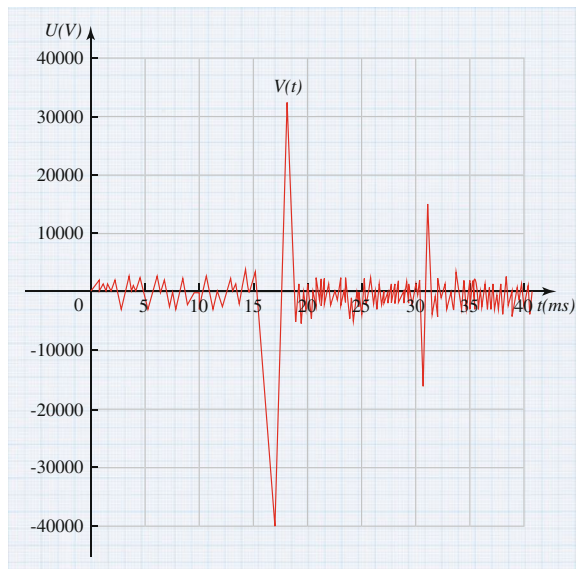
The inductive counter can reliably detect the initial moment of failure of the bearing pad and ensure the timely adoption of measures to prevent the catastrophic deterioration of the equipment.

The aim of studying is to assess the type of irregularities of type bursts and disastrous wear during operation of the tested OFCU equipment. We will use the FNS, which is used to estimate the parameters of the singular component of the power spectrum of the signal and find significant changes in the dimensionless parameters of unsteadiness providing an indication of the approaching moments of a catastrophic deterioration of the equipment.

The FNS is a common phenomenological (non-model) approach to the analysis of chaotic signals of the different nature [25]. The essence of the FNS approach is to give an informative significance to correlations, which are implemented in the signals of irregular sequences—bursts, jumps, breaks of the derivatives of various orders—as the carrier of changes in information taking place in each space–time level of the hierarchical organization of the studied dynamical system.

8.6.2 Parameterization of Singular Component of Signal Power Spectrum

For the signal $V(t)$, defined on the interval $[0, T]$ with the discrete steps Δt at points $t_k = k \cdot \Delta t$ $(k = 1 \ldots N)$, $N = [T/\Delta t]$, we calculate its average value

$$\langle V(t) \rangle = \frac{1}{N} \sum_{k=1}^{N} V(t_k). \tag{8.7}$$

Further, we believe that the signal $V(t)$ is stationary and

$$\langle V(t) \rangle = 0. \tag{8.8}$$

The power spectrum of the signal $S(t)$ is defined as the Fourier transform of the autocorrelation function. When calculating the power spectrum $S(t)$, the autocorrelation function is as follows:

$$\psi(\tau) = \langle V(t)V(t+\tau) \rangle \tag{8.9}$$

and the moment difference of the second order is as follows:

$$\Phi^{(2)}(\tau) = \left\langle |V(t) - V(t+\tau)|^2 \right\rangle \tag{8.10}$$

we assume that

$$f \leq f^* (f^* = f_{\max}, f_{\max} = 1/\Delta t, \tau \leq \tau^* (\tau^* = T/4)), \tag{8.11}$$

where f is the frequency and τ is the time delay setting.

For the stationary signal $S(f) = S_c(f)$, where $S_c(f)$ is the cosine of Fourier transform of the autocorrelation function.

In the discrete case, the "experimental" power spectrum $S_c(f)$ is calculated by the method of trapeze

$$S_c(f) = \frac{1}{\Delta t} S_c(q), \tag{8.12}$$

$$
\begin{aligned}
S_c(q) = \psi(0) + \psi\left(\frac{M}{2}\right)(-1)^q \\
+ 2 \sum_{m=1}^{\frac{M}{2}-1} \psi(m) \cos\left(\frac{2\pi q m}{M}\right) \quad (q = 0, 1\ldots, M-1),
\end{aligned}
\tag{8.13}
$$

$$q = f \cdot T_M, \quad T_M < T, \quad T_M = M \cdot \frac{T}{N} = M \cdot \Delta t, \tag{8.14}$$

$$f = \frac{q}{T_M} = \frac{q}{M\Delta t} = \frac{q/M}{\Delta t}. \tag{8.15}$$

$M = \left[\frac{T_M}{T} \cdot N\right]$ is an even number of points on the frequency axis.

For any $m = [\tau/\Delta t]$ and $N = [T/\Delta t]$, the "experimental" autocorrelator is calculated by the formula

$$\psi(m_\tau) = \frac{1}{N - m_\tau} \sum_{k=1}^{N-m_\tau} V(k)V(k + m_\tau)(m_\tau = 0, 1, \ldots, M-1). \tag{8.16}$$

The number M must satisfy the relation

$$\frac{4}{3} \leq M \leq N. \tag{8.17}$$

The power spectrum $S(f)$ is the nonnegative even function of f with period 2π [51]. From a parity and frequency, it follows that the core domain of $S(f)$ can, if necessary, take the interval $[0, \pi]$.

Note. Essentially, the formula (8.13) is a quadrature formula of trapezoid to calculate the cosine of continuous type—the Fourier transform of the autocorrelation function $\psi(\tau)$ and coincides with the Blackman–Tukey method (the correlation function method) to calculate the power spectrum density $S_c(f)$ without smoothing the autocorrelation function using the window filter [52]. In order to increase the speed of calculation $S_c(f)$, we can use the known methods of finding the fast Fourier transform (FFT). However, at a small number of lags, the FFT may not be beneficial. In addition, when using the FFT, it may happen that the desired step frequency is unattainable.

Fig. 8.5 The experimental power spectrum of $S(f)$
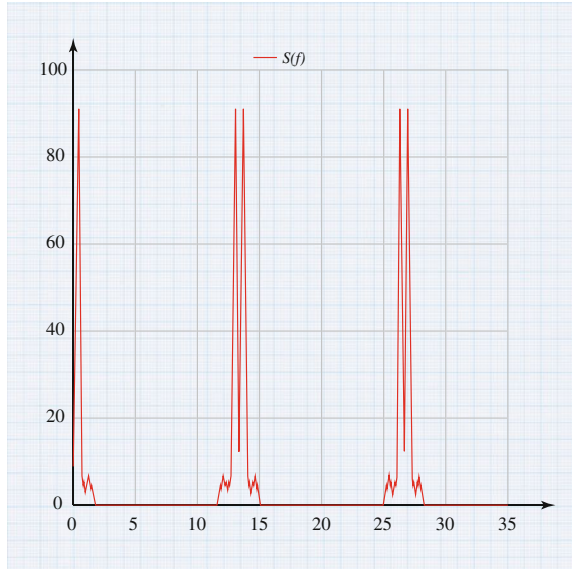
For the considered signal $V(f)$ in Fig. 8.4, the experimental spectrum $S(f)$ is shown in Fig. 8.5.

We denote by $V_R(t)$ and $V_F(t)$, respectively, the low- and high-frequency components of the signal. The isolation of high-frequency component is based on the "relaxation" procedure [53] constructed by analogy with the solution of the diffusion equation with the diffusion coefficient χ

$$\frac{\partial V}{\partial \tau} = \chi \frac{\partial^2 V}{\partial t^2}, \tag{8.18}$$

and it is represented as the difference equation

$$\frac{V_k^{j+1} - V_k^j}{A\tau} = \chi \frac{V_{k+1}^j + V_{k-1}^j - 2V_k^j}{(\Delta t)^2}. \tag{8.19}$$

corresponding to the simple difference scheme for numerical solutions.

From (8.19) we obtain

$$V_k^{j+1} = V_k^j + \frac{\chi \cdot \Delta \tau}{(\Delta t)^2} \left(V_{k+1}^j + V_{k-1}^j - 2V_k^j \right). \tag{8.20}$$

Introducing the notation $\omega = \frac{\chi \cdot \Delta \tau}{(\Delta t)^2}$, we rewrite the last equation in the form:

$$V_k^{j+1} = \omega V_{k+1}^j + \omega V_{k-1}^j + (1 - 2\omega)V_k^j. \tag{8.21}$$

From the theory of stability for difference schemes [54], it is known that the difference scheme is absolutely stable at $\omega < 1/2$. To use the Eq. (8.21) as a smoothing procedure, we must set the boundary conditions. In this case, these terms are defined as follows.

Let smoothing is carried out for a series of length M points. Then on each step of the smoothing iteration, the extreme values are calculated at $k = 1$ and $k = M$ as follows:

$$V_1^{j+1} = (1 - 2\omega)V_1^j + 2\omega V_2^j, \quad V_M^{j+1} = (1 - 2\omega)V_M^j + 2\omega V_{M-1}^j. \qquad (8.22)$$

The iteration of these equations, i.e., calculating the new values of the signal V_k^{j+1} at $j + 1$th "relaxation" step through values V_k^j (at $j = 0$ we taken the signal $V(t)$ itself), provides the low-frequency component V_R. Subtracting it from the original signal, we receive the high-frequency component V_F.

In fact, the above procedure of smoothing corresponds to the consecutive reduction of the gradients of local variable "concentrations" with the mutual convergence points in each of the considered triples $\left(V_{k+1}^{j+1}, V_k^{j+1}, V_{k-1}^{j+1} \right)$. Splitting the original signal $V(t)$ into two components $V_R(t)$ and $V_F(t)$ allows counting the functional dependencies $S(t)$ and $\Phi^{(2)}(\tau)$, introduced above for each of the three functions $V_J(t)$ ($J = R, F$ or G), and the index G is used for calculations with the initial signal $V(t)$, where R and F are the regular and chaotic signal components.

The described version of the "diffusion" smoothing is initially focused on minimizing the "high-frequency" information in the "low-frequency" $V_R(t)$ part of the signal, and vice versa—the minimization of "low-frequency" information in the "high-frequency" part of the $V_F(t)$ signal. This conclusion follows from the diffusive nature of the "relaxation," in which the maximum speed is realized by generating entropy [55, 56] and the relationship between entropy and information [57, 58]. In the latter case, we talk about the Fischer information as the quantitative measure of heterogeneity of the density distribution of the analyzed dataset.

We construct the image $S(f)$ in the bi-logarithmic scale $(\log S(f); \log f)$ (Fig. 8.6). If for some f we have $S(f) < 0$, then instead of $S(f)$ we consider $|S(f)|$.

The following asymptotic representation is valid

$$S(f) \rightarrow \begin{cases} 1/f^n, & \text{if } f \gg f_0, \\ S(0), & \text{if } f \ll f_0. \end{cases} \qquad (8.23)$$

The symbols "$\gg$" and "$\ll$" mean, respectively, "much more" and "much less." Here,

$$f = \frac{1}{2}\pi T_0, \qquad (8.24)$$

T_0 is the parameter defining some specific time within which the relationship of measured dynamic variable $V(t)$ is realized; the dimensionless parameter

Fig. 8.6 The asymptotic behavior of the power spectrum $S(f)$ at the high and low frequencies
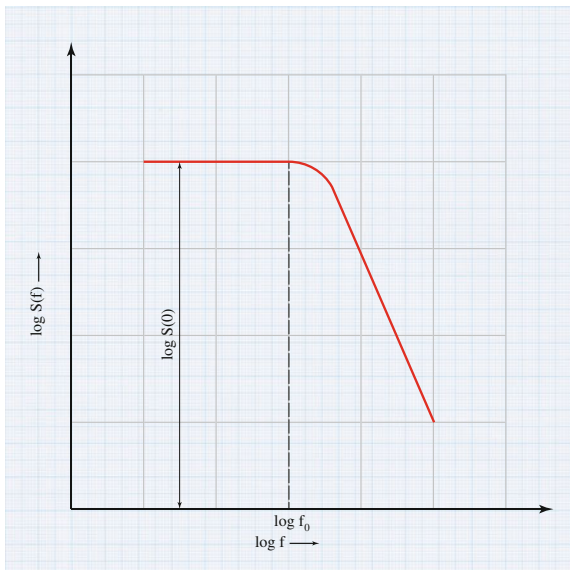
n effectively determines how this relationship is lost by decreasing the frequency to the value f_0. From Fig. 8.6, it is clear that f_0 is approximately equal to the frequency f_0^*, from which $S(t)$ ceases to stabilize around some constant $S(0)$.

The singular component $S_S(t)$ of the experimental spectrum $S(t)$ is calculated according to formulas (8.12) and (8.13) by replacing $\psi(t)$ in the autocorrelator $\psi_S(t)$, calculated by the formula [25]

$$\psi_S(m_\tau) = \frac{1}{N - m_\tau} \sum_{k=1}^{N-m_\tau} [V_S(k)V_S(k+m_\tau) + V_R(k)V_S(k+m_\tau) \\ + V_S(k)V_R(k+m_\tau)], \quad (m_\tau = 0, 1, \ldots, M-1). \tag{8.25}$$

The graphic of the singular component $S_S(t)$ of the power spectrum $S(t)$ for the considered signal is shown in Fig. 8.7. Figure 8.8 shows simultaneously graphs for $S(t)$ and $S_S(t)$, which in this case is little different from each other, because of its regular part of the signal $V(t)$, which is not powerful enough (have a small amplitude) (Fig. 8.4).

In the low-frequency limit $2\pi fT_0$ for the singular component $S_S(t)$, it is convenient to use an interpolation formula [25]

$$S_S(t) \approx \frac{S_S(0)}{1 + (2\pi fT_0)^{n_0}}. \tag{8.26}$$

As an approximate parameter $S_S(0)$ in the low-frequency region of the function graph $S(t)$ (or $|S(t)|$), preceding the frequency range in which there are significant

Fig. 8.7 The graphic of the singular component $S_S(t)$ of the power spectrum
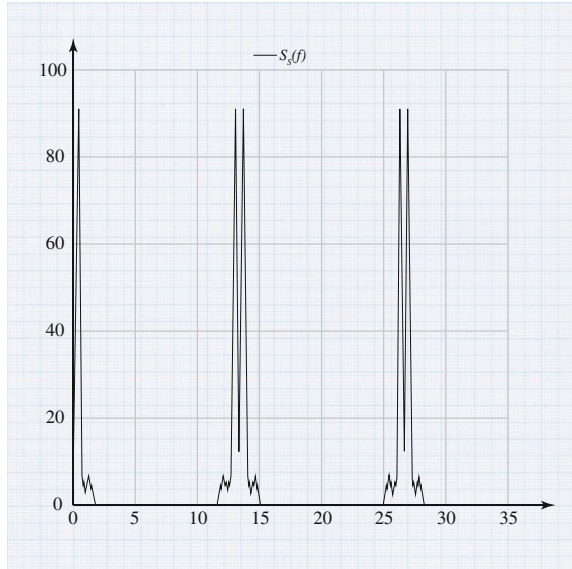
Fig. 8.8 The graphs of $S_S(t)$ and $S(t)$
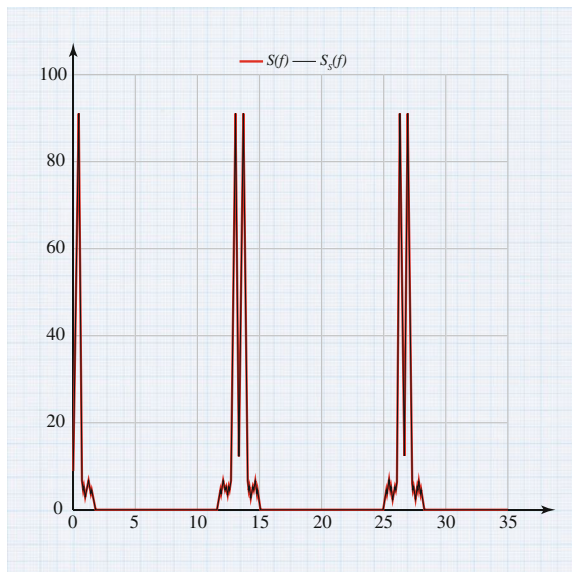
changes of this dependence revealed by the representation of $S(t)$ (or $|S(t)|$) in the bi-logarithmic scale, we select some value $S^*(0)$, which gives meaning to the parameter $S_S(0)$ in the interpolation expression (8.26) [57]. We assume that $S_S(f) < S_S^*(0)$ in $2\pi f T_0 < 1$.

The parameters T_0 and n_0 in the interpolation dependence (8.26) for the contribution of irregular bursts in $S(t)$ (or $|S(t)|$) are determined from the matching conditions (using the least squares method) of the spectrum $S_S(t)$ on the right-hand side of formula (8.26).

To do this, we use the following algorithm.

Algorithm 8.1 We introduce $S_S^*(0)$, $\text{RSS}_1^* = 10^{10}$, $\lambda = 0$.

1. Assuming $S_S(0) := S_S^*(0)$, we estimate T_0 and n_0. Consider the regression

$$y = ax + b, \tag{8.27}$$

where $y = \ln\left(\frac{S_S(0)}{S_S(f)}\right)$, $x = \ln(2\pi f)$, $a = n_0$, $b = n_0 \ln T_0$. According to OLS estimates $\hat{a}$, $\hat{b}$, we find $n_0 = \hat{a}$, $\hat{T}_0 = \exp\left\{\frac{\hat{b}}{\hat{a}}\right\}$.

2. We calculate from the regression (8.27)

$$\text{RSS}_1^{(1)} = \sum_{m=0}^{M-1} \left[y - \left(\hat{a}x_m + \hat{b}\right)\right]^2,$$

where y_m and x_m correspond to frequencies $f_m = \frac{m}{M\Delta t}$. If $\text{RSS}_1^{(1)} < \text{RSS}_1^*$, then $\text{RSS}_1^* := \text{RSS}_1^{(1)}$, $n_0^* := \hat{n}_0$, $T_0^* := \hat{T}_0$.

3. Assuming $S_S(0) := S_S^*(0)$, $n_0^* := \hat{n}_0$, we estimate T_0. Consider the regression

$$y = ax + b, \quad (b = 0), \tag{8.28}$$

where $y = \left(\frac{S_S(0)}{S_S(f)} - 1\right)^{\frac{1}{n_0}}$, $x = 2\pi f$, $a = T_0$. According to OLS estimation, we find $\hat{T}_0 = \hat{a}$.

4. We calculate for the regression (8.28)

$$\text{RSS}_1^{(2)} = \sum_{m=0}^{M-1} [y_m - \hat{a}x_m]^2.$$

If $\text{RSS}_1^{(2)} < \text{RSS}_1^*$, then $\text{RSS}_1^* := \text{RSS}_1^{(2)}$, $T_0^* := T_0$.

5. Assuming $S_S(0) := S_S^*(0)$, $T_0 := T_0^*$, we evaluate n_0. Consider the regression

$$y = ax + b, \quad (b = 0). \tag{8.29}$$

where $y = \left(\frac{S_S(0)}{S_S(f)} - 1\right)$, $x = \ln(2\pi f T_0)$, $a = n_0$. According to OLS estimation $\hat{a}$, we find $\hat{n}_0 = \hat{a}$.

6. We calculate for the regression (8.29)

$$\text{RSS}_1^{(3)} = \sum_{m=0}^{M-1} [y_m - \hat{a}x_m]^2.$$

If $\text{RSS}_1^{(3)} < \text{RSS}_1^*$, then $\text{RSS}_1^* := \text{RSS}_1^{(3)}$, $n_0 := \hat{n}_0$.

7. Assuming $T_0 := T_0^*$, $n_0 := \hat{n}_0$, we estimate $S_S(0)$. Consider the regression

$$y = ax + b \quad (b = 0), \tag{8.30}$$

where $y = S_S(f)$, $x = \frac{1}{1 + (2\pi f T_0)^{n_0}}$, $a = S_S(0)$. According to OLS estimation $\hat{a}$, we find $\hat{S}_S(0) = \hat{a}$.

8. We calculate for the regression (8.30)

$$\text{RSS}_1^{(4)} = \sum_{m=0}^{M-1} [y - \hat{a}x_m]^2.$$

If $\left(\text{RSS}_1^{(4)} < \text{RSS}_1^*\right) \bigwedge \left(\hat{S}_S(0) \geq S_S^*(0)\right)$, then $\text{RSS}_1^* := \text{RSS}_1^{(4)}$, $S_S^*(0) := \hat{S}_S(0)$, $\lambda := \lambda + 1$.

9. If $\lambda < 10$, then go to step 1.
10. Print $S_S^*(0)$, T_0^*, n_0^*, RSS_1^*.
11. END

Thus, the formula (8.26) can be written as follows:

$$S_S(t) \approx \frac{S_S^*(0)}{1 + \left(2\pi f T_0^*\right)^{n_0^*}}. \tag{8.31}$$

As a result, from the Algorithm 8.1 at the initial approximation $S_S(0) = S_S^*(0)$, the following parameters $S_S(0)$, T_0, n_0 are obtained:

$$S_S^*(0) = 15; \quad T_0^* = 0.051; \quad n_0^* = 3.429. \tag{8.32}$$

8.6.3   Precursor Calculation of System Catastrophic States

To identify the effects of unsteadiness in the investigated process, we study the dynamics of changes in functions $S_S(f)$ and $\Phi^{(p)}(\tau)$ with a sequential shift of the tested interval $[t_k, t_k + T]$, where $k = 0, 1, 2, 3 \ldots$ and $t_k = k\Delta T$ along the entire length T_{tot} of the available experimental data $t_k + T < T_{\text{tot}}$.

The phenomenon of the precursor of catastrophic events is naturally associated with the most drastic changes in dependency of the power spectrum $S(f)$ and the difference between the moments of p-order

$$\Phi^{(p)}(\tau) = \langle |V(t) - V(t + \tau)| \rangle. \tag{8.33}$$

when approaching the upper limit of the time interval the averaging t_k to the moment t_c of the catastrophic event, when the system is rearranged at all possible spatial scales. It is clear that to speak of "precursor" only in the event that the development time "harbinger" t_k spaced from the moment t_c not less than the interval ΔT, i.e., $\Delta T_{\text{sn}} = t_c - t_k$ when performing inequality $\Delta T_{\text{sn}} \leq T_{\text{tot}}$.

Within the FNS framework in the non-stationary dynamics, as opposed to the stationary case, the information about the system evolution extracted from the analysis of the dynamics at different levels of the hierarchy (at the different frequencies of discretization of the measured signal, in particular) may be different. This means that in a non-stationary system, the system evolution is characterized by a set of specific times T_{sn} of structural rearrangements for the appropriate set of spatial organization of the system and the problem of forecasting in general becomes multiparameter, oriented to search for at least some variables, "precursors" of a catastrophic event, separated in time scale. Each of these "precursors" can be detected in the analysis of time series of dynamic variables with the set of certain period averaging T, not exceeding the duration of detectable value T_{sn}.

We consider "forerunners" based on the moment difference $\Phi^{(p)}(\tau)$ and the power spectrum $S_J(f)$, calculated on the basis of the high- and low-frequencies component $V_J(f)$, where $J = R$, F, or G (R—the regular and F—the chaotic components; G—the entire signal $V(t)$). At the same time, we note that dependencies $\Phi_J^{(p)}(\tau)$ are reliably calculated only for the range $[0, \alpha T]$ of the argument τ being less than half of the averaging interval T, so that $\alpha < 0.5$. When calculating dependencies $S_J(f)$ for the boundaries of the frequency range, $[f_{\min}, f_{\max}]$ will choose: $f_{\min} = 1/(2\pi T)$ and $f_{\max} = (1/4)(1/t_{\min})$, where $t_{\min}$ is the time interval between adjacent values of the measured dynamic variables.

As the "precursors" of catastrophic events, we consider spikes of the indicators of unsteadiness $c_J(t_{k+1})$ and $D_J(t_{k+1})$ determined by the dimensionless ratios, created on the basis of the moment difference $\Phi^{(2)}(\tau)$ and the power spectra $S_J(f)$ [53, 58]. In the discrete case, the precursor $c_J(t_{k+1})$ is defined by

$$c_J(t_{k+1}) = 2 \cdot \frac{Q_{k+1}^J - Q_k^J}{Q_{k+1}^J + Q_k^J} \bigg/ \frac{\Delta T}{T}, \tag{8.34}$$

$$
\begin{aligned}
Q_k^J &= \frac{1}{N_1} \sum_{n_\tau=1}^{N_1} \left[\Phi_J^{(p)}(n_\tau) \right]_k \\
&= \frac{1}{N_1} \sum_{n_\tau=1}^{N_1} \frac{1}{N - n_\tau} \sum_{m=[1+kb]}^{[N-n_\tau+kb]} |V_J(m) - V_J(m+n_\tau)|^p .
\end{aligned}
\tag{8.35}
$$

Here

$$\mathrm{b} = [\Delta T / \Delta t], \quad N = [\alpha N].$$

The precursor $D_J(t_{k+1})$ in a continuous form is written as follows:

$$D_J(t_{k+1}) = 2 \cdot \frac{\left[\int_{f_{\min}}^{f_{\max}} S_J(f) \mathrm{d}f \right]_{(k+1)\Delta T}^{T+(k+1)\Delta T} - \left[\int_{f_{\min}}^{f_{\max}} S_J(f) \mathrm{d}f \right]_{k\Delta T}^{T+k\Delta T}}{\left[\int_{f_{\min}}^{f_{\max}} S_J(f) \mathrm{d}f \right]_{(k+1)\Delta T}^{T+(k+1)\Delta T} + \left[\int_{f_{\min}}^{f_{\max}} S_J(f) \mathrm{d}f \right]_{k\Delta T}^{T+k\Delta T}} \bigg/ \frac{\Delta T}{T}. \tag{8.36}$$

The lower and upper designations in brackets (8.36) show the boundaries of the time intervals in which the power spectrums are calculated corresponding to the component $V_J(f)$.

The precursors $c_J(t_{k+1})$ and $D_J(t_{k+1})$ are "non-stationary measure" of the analyzed process when moving averaging interval T on the time axis by the amount Δt, particularly, when approaching the upper boundary averaging of the time interval t_k to the time t_c of a catastrophic event.

To calculate the integrals in (8.36), we used a quadrature formula for trapeze

$$\int_a^b f(x)\mathrm{d}x = h\left(\frac{f(a)}{2} + f(a+h) + f(a+2h) \right) + \cdots + f(b-h) + \frac{f(b)}{2}.$$

The graphs of precursors $c_G(t_{k+1})$ and $D_G(t_{k+1})$ are shown in Figs. 8.9 and 8.10, respectively.

From Fig. 8.9, it is clear that $c_G(t_{k+1})$ varies significantly at $t = 10$, heralding a cataclysmic event after $t = 10$. In fact, as it is shown in Fig. 8.4, at $t = 17$ in the dynamic signal $V(t)$, the irregular spike (release) appears. So, in spite of the insensitivity of precursors $D_G(t_{k+1})$ to this release, the precursor $c_G(t_{k+1})$ proved to be more sensitive and predicted a critical condition, what happened when $t_c = 17$ at moment t_k, satisfying the required ratio $t_c - t_k = \Delta T$ (taken into account $\Delta T = 1$, i.e., shift of the window by unit with length T).

Fig. 8.9 The graph of precursor
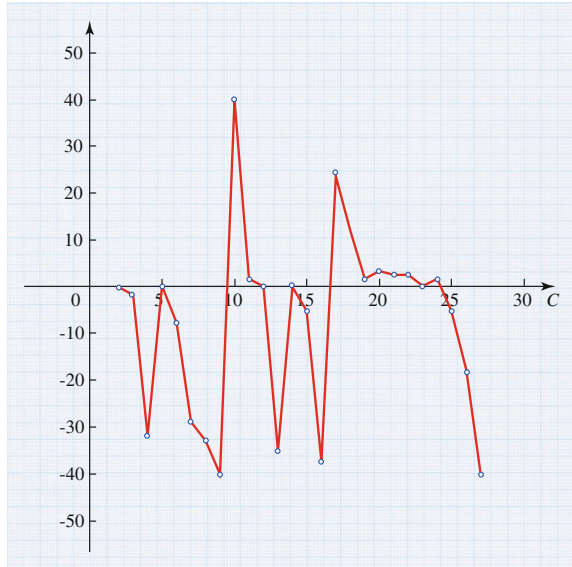
Fig. 8.10 The graph of precursor D_G
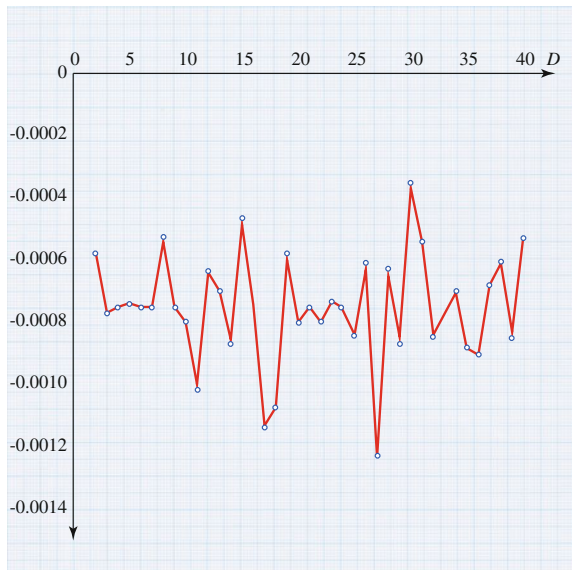
8.7 Parameterization of Signal Regular Component

Defining the parameters of the chaotic signal given within the limited range T is based on the method of the FNS [25], taking into account the contribution of the "resonant components" into the autocorrelation function

$$\psi(\tau) = \langle |V(t)V(t+\tau)| \rangle, \tag{8.37}$$

consequently, in the cosine transform

$$S_{c}(f) = \int\limits_{-T/2}^{T/2} \psi(\tau) \cos(2\pi f\tau) \mathrm{d}\tau \tag{8.38}$$

and the moment difference of the second order

$$\Phi^{(2)}(\tau) = \left\langle \left| V(t) - V(t+\tau)^2 \right| \right\rangle. \tag{8.39}$$

where $V(t)$ is a stationary signal ($\langle V(t) \rangle = 0$), $\langle \cdot \rangle$—the symbol averaging.

Designed in [58], the parameterization method of the signal is based on the fact that the input "irregularity bursts" and "irregularity-jumps" contribute to the different spectral regions according to $S(f)$. In fact, the first step of the irregularity parameterization made in the previous section is to allocate "wavelet" (singular), the most "high-frequency" (the so-called flicker noise tail) component of the signal irregularities in the spectral dependence $S(f)$.

On the basis of the remaining (after the deduction of "wavelet" contribution) spectral dependence, we can now determine the structure function $\Phi^{(2)}(\tau)$, a contribution from the "jump" and slowly changing in its background "resonance" components. The next steps are to parameterize the "higher frequency" (of the remaining) "jumy" (regular) component using the method of least squares.

It must be borne in mind that in the solution of the signal parameterization, problems are associated with the limited averaging interval T. For this reason, in particular, the "experimental" (built on the basis of the observed signal $V(t)$) dependent $S(f)$ in some frequency intervals may be negative. Therefore, along with $S(f)$ in such cases we introduce $|S(f)|$.

The parameterization procedure of the regular part of the signal is presented below in the following sequence of operations.

Algorithm 8.2

1. From the "experimental" spectrum $S(f)$ pin out the singular component $S_S(f)$, calculated by the interpolation formula (8.31) (the result is denoted by $S_{rR}(f)$):

$$S_{rR}(f) = S(f) - S_S(f). \tag{8.40}$$

Here

$$S_S(f) = \frac{S_S(0)}{(1 + 2\pi f T_0)^{n_0}}. \tag{8.41}$$

The parameters $S_S(0)$, T_0, and n_0 in this formula have been identified earlier.

The resulting difference represents the contribution of "resonance" components $S_r(f)$ and "irregularity-jumps" $S_R(f)$ in the general dependence $S(f)$. If in some frequency ranges will be that $S_{rR}(f) < 0$, we assume that

$$S_{rR}(f) := S_{rR}(f).$$

2. Take the inverse cosine Fourier transform of $S_{rR}(f)$:

$$\psi_{rS}(\tau) = 2 \int_0^{f_{max}} S_{rR}(f)\cos(2\pi f\tau)\mathrm{d}f \quad (\tau \le \tau^* = T/4), \qquad (8.42)$$

$$\tau = k\cdot\Delta\tau(k=1,\ldots,k_0), \quad \Delta\tau = \frac{T/4}{k_0}, \quad k = 500, \quad f_{max} = \frac{1}{4\Delta t}.$$

Let

$$a = 0, \quad b = f_{max}, \quad h = f_{max}/n, \quad n = 100,$$

$$S_{rR}(f)\cos(2\pi f\tau) = g(f,\tau)$$

and apply the trapezoidal rule

$$\int_a^b g(f,\tau)\mathrm{d}f = h\left(\frac{g(a,\tau)}{2} + g(a+h,\tau) + g(a+2h,\tau)\right)$$

$$+ \cdots + g(b-h,\tau) + \frac{g(b,\tau)}{2},$$

3. Compute

$$\Phi_{rR}^{(2)} = 2[\psi_{rR}(0) - \psi_{rR}(\tau)], \quad \tau = k\cdot\Delta\tau(k=1,\ldots,k_0).$$

4. Let

$$\Phi_r^{(2)}(\tau) = \Phi_{rR}^{(2)}(\tau).$$

5. Denote

$$\tilde{\Phi}^{(2)}(\tau) = \Phi_r^{(2)}(\tau) + \tilde{\Phi}_R^{(2)}(\tau).$$

where $\tilde{\Phi}_R^{(2)}(\tau)$ is given by the interpolation formula

$$\tilde{\Phi}_R^{(2)}(\tau) = \begin{cases} 2\sigma_1^2 \cdot \frac{1}{\Gamma^2(H_1+1)} \left(\frac{\tau}{T_1}\right)^{2H_1}, & \tau \ll T_1 \quad (1) \\ 2\sigma_1^2 \cdot \left[1 - \Gamma^{-1}(H_1)\left(\frac{\tau}{T_1}\right)^{H_1-1} e^{(-\tau/T_1)}\right], & \tau \gg T_1 \quad (2) \end{cases} \tag{8.43}$$

Note. The expressions (8.43_1) and (8.43_2) are used to describe the relations (8.39) obtained on the basis of the experimental time series $V(t)$ in the case of the stationary evolution. It identifies the parameters H_1, T_1, and σ_1, which can be considered as one of the sets of "passport" characteristics of the considered stationary process, along with a set of characteristics $S_S(0)$, T_0, and n_0, obtained earlier for the singular component $S_S(f)$ of the power spectrum $S(f)$. We note here that the parameter H_1 is the Hearst constant, which characterize the rate of "forgetting" the magnitude by the dynamic variable at times, less than the correlation time, and is usually introduced to describe dependencies $\Phi^{(2)}(\tau)$ at small τ (see (8.46)). However, the parameter H_1 in (8.43) is somewhat different to the Hurst parameter.

Since $S(f)$ and $\Phi^{(2)}(\tau)$ are determined by the autocorrelation function $\psi(\tau)$, it would be possible to believe that the relevant parameters T_1 and T_0, H_1, and n are connected, and the number of independent parameters, input through analysis of $\Phi^{(2)}(\tau)$ and $S(f)$, should decrease. However, the experience shows that for the time series $V(t)$, corresponding to the evolution of the real processes, the expected ratios

$$T_1 = T_0, \quad 2H + 1 = n$$

do not hold. It should be noted that the second of these relationships expresses the famous image of the "fractal self-similarity" of the evolutionary processes. The principal difference of the FNS method from the fractal analysis is that the latter has a significant limitation—the postulating of scale self-similarity (scaling) at every conceivable scale. In the case of the real signals, it is clearly not the case: The features of a large-scale self-similarity, as it follows from [25, Chap. 3] results, are usually appear at best in a half to two orders of the changes in the studied dynamic variable.

The above-mentioned mismatch of the information parameters included in dependencies $S(f)$ and $\Phi^{(2)}(\tau)$ can be attributed either to the "unsteadiness" of real processes $V(t)$, or to the limited interval T, which provides the average. This raises the question: Which of the dependences $S(f)$ and $\Phi^{(2)}(\tau)$ should be considered as a base for an adequate parameterization of the real processes, which, of course, are defined in the final time intervals T and may be "non-stationary." Until recently, the question remained open, and the analysis of a variety of chaotic signals relied mainly on $S(f)$, rather than on $\Phi^{(2)}(\tau)$.

The solution of this problem was possible within the FNS framework based on the generalization of the concept of the information contained in the complex signals of different nature. The information contained under the FNS in $S(f)$ and

$\Phi^{(2)}(\tau)$ varies, so to determine the appropriate structure of the parameters, in an amount sufficient to solve specific problems, it is necessary to analyze the both dependences.

6. Compare the function $\tilde{\Phi}_R^{(2)}(\tau)$ with function

$$\Phi_R^{(2)}(\tau) = \Phi^{(2)}(\tau) - \Phi_r^{(2)}(\tau), \qquad (8.44)$$

where $\Phi^{(2)}(\tau)$ is the "experimental" structure function (8.39), calculated by the autocorrelation

$$\psi(m_\tau) = \frac{1}{N - m_\tau} \sum_{k=1}^{N-m} \tau V(k)V(k+m_\tau), \quad m_\tau = [\tau/\Delta t]. \qquad (8.45)$$

A preliminary assessment of T_1^* of the parameter T_1 can be obtained using the asymptotic representation of the structure function $\Phi^{(2)}(\tau)$ (Fig. 8.11).

$$\Phi^{(2)}(\tau) = \begin{cases} \tau^{2H_1}, & \text{if } \tau \ll T_1 \\ 2\sigma^2, & \text{if } \tau \ll T_1 \end{cases} \quad \sigma^2 = \langle V^2 \rangle - \langle V^2 \rangle. \qquad (8.46)$$

As T_1^* value, we take τ for small delays for which $\Phi^{(2)}(\tau)$ takes the maximum value of $\Phi^{(2)}(\tau) \approx 2\sigma^2$.

Fig. 8.11 The graph of $\Phi^{(2)}(\tau)$ in the bi-logarithmic coordinates
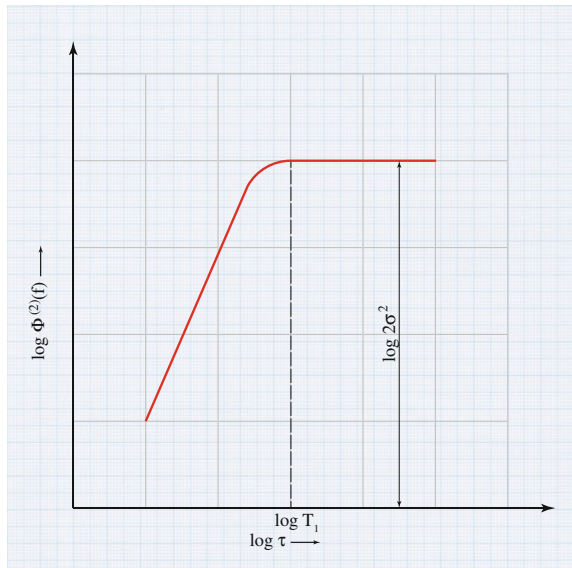
We introduce thresholds

$$\text{RSS}_1^* = \text{RSS}_2^* = 10^{10}.$$

6.1. We define $T_1 = T_1^*$ and estimate the parameter σ_1. To this end, we regress

$$\text{RSS}_1^* = \text{RSS}_2^* = 10^{10}. \tag{8.47}$$

where

$$y = \ln\left\{\Phi^{(2)}(\tau) - \Phi_r^{(2)}(\tau)\right\}, \quad x = \ln\left\{\frac{\tau}{T_1}\right\},$$

$$a = 2H_1, \quad b = 2\ln\frac{\sigma_1}{\Gamma(H_1 + 1)}.$$

the OLS estimation of $\hat{a}$ and $\hat{b}$ is obtained from the sequence $\{\tau_k\}$ $(k = 1, \ldots, k_1; k_1 \ll k_0)$ using the representation (8.43). According to the $\hat{a}$ and $\hat{b}$, we find

$$\widehat{H}_1 = \frac{\hat{a}}{2}, \quad \hat{\sigma} = e^{\frac{\hat{b}}{2}} \cdot \Gamma\left(\widehat{H}_1 + 1\right).$$

Compute

$$\text{RSS}^{(1)} = \sum_{k=1}^{k_1}\left[y_k - (\hat{a}x_k + b)^2\right].$$

(y_k and x_k correspond to τ_k).
If $\text{RSS}^{(1)} \geq \text{RSS}_1^*$, then go to line 6.2. Otherwise, we assume

$$\text{RSS}_1^* = \text{RSS}^{(1)}, \sigma_1^* = \hat{\sigma}_1, H_1^* = \widehat{H}_1.$$

6.2. By setting $\sigma_1 = \sigma_1^*$, we evaluate H_1 and T_1 at $\tau \ll T_1$. Build a regression

$$y = ax + b \quad (b \neq 0), \tag{8.48}$$

$$a = 2H_1, \quad b = -\ln\Gamma^2(H_1 + 1) - 2H_1\ln T_1,$$

$$y = \ln\left\{\frac{\Phi^{(2)}(\tau) - \Phi_r^{(2)}(\tau)}{2\sigma_1^2}\right\}, \quad x = \ln\tau.$$

The OLS estimation of $\hat{a}$ and $\hat{b}$ is obtained from the sequence $\{\tau_k\}$ $(k = 1, \ldots, k_1; k_1 \ll k_0)$. Compute

$$\widehat{H}_1 = \frac{\hat{a}}{2}, \quad T_1 = \left\{\Gamma^2(H_1+1)\right\}^{-\frac{1}{2\widehat{H}_1}} \cdot \exp\left\{-\frac{b}{2\widehat{H}_1}\right\},$$

$$\mathrm{RSS}^{(2)} = \sum_{k=1}^{k_1} \left[y_k - (\hat{a}x_k + b)^2\right].$$

If $\mathrm{RSS}^{(2)} \geq \mathrm{RSS}_1^*$, then go to line 6.3. Otherwise, we assume

$$\mathrm{RSS}_1^* = \mathrm{RSS}^{(2)}, \sigma_1^* = \hat{\sigma}_1, H_1^* = \widehat{H}_1.$$

6.3. By setting $\sigma_1 = \sigma_1^*$ and $H_1 = H_1^*$, we evaluate T_1 at $\tau \ll T_1$. Build a regression

$$y = ax + b \quad (b = 0), \tag{8.49}$$

where

$$y = \left(\frac{\Phi^{(2)}(\tau) - \Phi_r^{(2)}(\tau)}{2\sigma_1^2/\Gamma^2(H_1+1)}\right)^{\frac{1}{2H_1}}, \quad x = \tau, \quad a = \frac{1}{T_1}.$$

The OLS estimation of $\hat{a}$ is obtained from the sequence $\{\tau_k\}$ $(k = 1\ldots k_1; k_1 \ll k_0)$. We compute $\widehat{T}_1 = 1/\hat{a}$.

6.4. Compute

$$\mathrm{RSS}^{(3)} = \sum_{k=1}^{k_1} [y_k - \hat{a}x_k]^2.$$

If $\mathrm{RSS}^{(3)} \geq \mathrm{RSS}_1^*$, then go to line 6.5. Otherwise, we believe

$$\mathrm{RSS}_1^* = \mathrm{RSS}^{(3)}, T_1^* = \widehat{T}_1.$$

6.5. Print $\sigma_1^{(1)} = \sigma_1^*$ and $H_1^{(1)} = H_1^*$, we evaluate $T_1^{(1)} = T_1^*$

6.6. By setting $H_1 = H_1^*$ and $T_1 = T_1^*$, we evaluate σ_1 at $\tau \gg T_1$. Build a regression

$$y = ax + b \quad (b = 0), \tag{8.50}$$

where

$$y = \Phi^{(2)}(\tau) - \Phi_r^{(2)}(\tau), \quad x = \left[1 - \Gamma^{-1}(H_1)\left(\frac{\tau}{T_1}\right)^{H_1-1} \exp\left\{-\frac{\tau}{T_1}\right\}\right]^2,$$

$$a = 2\sigma_1^2.$$

We compute the OLS estimate of a according to the sequence $\{\tau_k\}(k = 1, \ldots, k_1; k_1 \ll k_0 k_1 \approx 20$. We compute $\sigma_1 = a_2$ and find

$$\text{RSS}^{(4)} = \sum_{k=1}^{k_1} [y_k - \hat{a}x_k]^2.$$

If $\text{RSS}^{(4)} \geq \text{RSS}_1^*$, then go to line 6.7. Otherwise, we believe $\text{RSS}_2^* = \text{RSS}^{(4)}, \sigma_1^* = \hat{\sigma}_1$ and go to line 6.7

Note. The value of $\Gamma(x)$ can be calculated by using the package $\Gamma(x)$ (x—any complex number) in MATHCAD

$$\Gamma(x) = \frac{\Gamma(x+1)}{x} = \frac{\Gamma(x+1)}{x(x+1)} = \cdots = \frac{\Gamma(x+n)}{x(x+1)\dots(x+n-1)} \qquad (8.51)$$

and evaluate $\Gamma(x+n)$ for a sufficiently large n, using the asymptotic representation of the gamma function at $|z| \to \infty$, $\pi - \alpha < \arg(z) < \pi + \alpha$ (α is some arbitrarily small positive number) [59].

$$\Gamma(z) = \exp\left\{\left(z - \frac{1}{2}\right)\ln z - z + \frac{1}{2}\ln 2\pi\right\}[1 + O(z^{-1})]. \qquad (8.52)$$

6.7. We assume that

$$\exp\left(-\frac{\tau}{T_1}\right) \approx \left(\frac{\tau}{T_1}\right)^{-\alpha} \qquad \tau \gg T_1, (\alpha > 0) \qquad (8.53)$$

where α is the parameter to be determined.

By setting $\sigma_1 = \sigma_1^*$ and $H_1 = H_1^*$, we evaluate T_1 and σ_1. Imagine equality is as follows:

$$\Phi^{(2)}(\tau) - \Phi_r^{(2)}(\tau) = 2\sigma_1^2\left[1 - \Gamma^{-1}(H_1)\left(\frac{\tau}{T_1}\right)^{H_1 - 1 - \alpha}\right]^2$$

in the form of

$$\Gamma(H_1)\left(1 - \sqrt{\frac{\Phi^{(2)}(\tau) - \Phi_r^{(2)}(\tau)}{2\sigma_1^2}}\right) = \left(\frac{\tau}{T_1}\right)^{H_1 - 1 - \alpha}.$$

After taking the logarithm, we obtain

$$\ln\left[\Gamma(H_1)\left(1 - \sqrt{\frac{\Phi^{(2)}(\tau) - \Phi_r^{(2)}(\tau)}{2\sigma_1^2}}\right)\right]$$
$$= -(H_1 - 1 - \alpha)\ln T_1 + (H_1 - 1 - \alpha)\ln \tau.$$

Denote

$$y = \ln\left[\Gamma(H_1)\left(1 - \sqrt{\frac{\Phi^{(2)}(\tau) - \Phi_r^{(2)}(\tau)}{2\sigma_1^2}}\right)\right], \quad x = \ln\tau,$$

$$a = H_1 - 1 - \alpha, \quad b = -(H_1 - 1 - \alpha)\ln T_1,$$

We estimate the coefficients a and b of the regression

$$y = ax + b \quad (b \neq 0), \tag{8.54}$$

According to the OLS estimates $\hat{a}$ and $\hat{b}$, we find

$$\hat{\alpha} = \hat{a} - H_1 - 1, \quad \hat{T}_1 = \exp\left\{-\frac{\hat{b}}{H_1 - 1 - \alpha}\right\},$$

We compute

$$\mathrm{RSS}^{(5)} = \sum_{k=1}^{k_1} [y_k - (\hat{a}x_k + b)]^2, \quad \tau_k = T - k.$$

If $\mathrm{RSS}^{(5)} \geq \mathrm{RSS}_2^*$, then go to 6.8. Otherwise, we believe

$$\mathrm{RSS}_2^* = \mathrm{RSS}^{(5)}, \quad \alpha^* = \hat{\alpha}, \quad T_1^* = T_1.$$

6.8. By setting $\sigma_1 = \sigma_1^*$ and $T_1 = T_1^*$, we find H_1 and α.
We have

$$1 - \sqrt{\frac{\Phi^{(2)}(\tau) - \Phi_r^{(2)}(\tau)}{2\sigma_1^2}} = \Gamma^{-1}(H_1)\left(\frac{\tau}{T_1}\right)^{H_1 - 1 - \alpha}.$$

After taking the logarithm, we obtain

$$\ln\left[1 - \sqrt{\frac{\Phi^{(2)}(\tau) - \Phi_r^{(2)}(\tau)}{2\sigma_1^2}}\right] = -\ln[\Gamma(H_1)] + (H_1 - 1 - \alpha)\ln\left(\frac{\tau}{T_1}\right).$$

Build a regression

$$y = ax + b \quad (b \neq 0), \tag{8.55}$$

where

$$y = \ln\left[1 - \sqrt{\frac{\Phi^{(2)}(\tau) - \Phi_r^{(2)}(\tau)}{2\sigma_1^2}}\right], \quad x = \ln T_1,$$

$$a = H_1 - 1 - \alpha, \quad b = -\ln[\Gamma(H_1)],$$

According to the OLS estimates $\hat{a}$ and $\hat{b}$, we find $\hat{b}$ from the equation

$$\Gamma\left(\widehat{H}_1\right) = \exp\{-\hat{b}\}n, \tag{8.56}$$

and

$$\hat{a} = H_1 - 1 - \hat{\alpha}, \tag{8.57}$$

We compute

$$\mathrm{RSS}^{(6)} = \sum_{k=1}^{k_1}[y_k - (\hat{a}x_k + b)]^2, \quad \tau_k = T - k.$$

If $\mathrm{RSS}^{(6)} \geq \mathrm{RSS}_2^*$, then go to 6.9. Otherwise, we believe

$$\mathrm{RSS}_2^* = \mathrm{RSS}^{(6)}, \quad \alpha^* = \hat{\alpha}, \quad H_1^* = \widehat{H}_1.$$

6.9. Print $\sigma_1^{(2)} = \sigma_1^*$ and $H_1^{(2)} = H_1^*$, we evaluate $T_1^{(2)} = T_1^*$.
6.10. END

Note. For the solution of (8.56), we proceed as following. Let $x = \widehat{H}_1$ and $z = x + n$. Let $n = 100$, and we introduce the function as follows:

$$Q(x) = \frac{\Gamma(x+n)}{x(x+1)\ldots(x+n-1)}. \tag{8.58}$$

The condition is $0 < \widehat{H}_1 < 1$. With the step of discreteness $\Delta x = 10^{-2}$, we iterate in (8.58) the values $x_k = k \cdot \Delta x$ $(k = 1, \ldots, k_0)$, where $x_{k_0} < 1$ and $x_{k_0+1} < 1$.

When $k = 1, \ldots, k_0$, we compare the left-hand and right-hand sides of the expression (8.58).

At a given accuracy of calculation of the quantity H_1 (e.g., $\varepsilon = 10^{-1}$) for the H_1, we will take the first value x_k, in which

$$\left|Q\left(\widehat{H}_1\right) - \Gamma\left(\widehat{H}_1\right)\right| < \varepsilon. \tag{8.59}$$

Table 8.3 The parameters of structural features for small and large delays

Parameters	(1)	(2)
H_1	0.2816	0.7613
σ_1	36.16424	3.91
T_1	10	3.817288

If (8.59) does not hold for any value $x_k(k = 1, \ldots, k_0)$, we believe that $\Delta x := \Delta x/2$ and repeat the comparison (8.59), going over the values $x_k = k \cdot \Delta x$ in (8.58) with a new step Δx.

Thus, we get the values $\sigma_1^{(1)}, H_1^{(1)}, T_1^{(1)}$ and $\sigma_1^{(2)}, H_1^{(2)}, T_1^{(2)}$ of parameters σ_1, H_1, T_1, respectively, for small $\tau(\tau \ll T_1)$ and large $\tau(\tau \gg T_1)$ and the value of α, which is true in the asymptotic representation (8.53).

The results of calculation of values $\sigma_1^{(1)}, H_1^{(1)}, T_1^{(1)}$ and $\sigma_1^{(2)}, H_1^{(2)}, T_1^{(2)}$ of parameters σ_1, H_1, T_1 are shown in Table 8.3.

The asymptotic representations (8.43) can now be written as follows:

$$
\tilde{\Phi}_R^{(2)}(\tau) = \begin{cases} 2\left(\sigma_1^{(1)}\right)^2 \cdot \dfrac{1}{\Gamma^2\left(H_1^{(1)} + 1\right)} \left(\dfrac{\tau}{T_1^{(1)}}\right)^{2H_1^{(1)}}, & \text{if } \tau \ll T_1^* \quad (1); \\[4mm] 2\left(\sigma_1^{(2)}\right)^2 \cdot \left[1 - \Gamma^{-1}\left(H_1^{(2)}\right)\left(\dfrac{\tau}{T_1^{(2)}}\right)^{H_1^{(2)}-1-\alpha}\right]^2, & \text{if } \tau \gg T_1^* \quad (2). \end{cases}
$$

$$(8.60)$$

To get the parameterization for $\tilde{\Phi}_R^{(2)}(\tau)$ on the entire range of the delay, we apply the method of matching asymptotic expansions described below in Sect. 8.8.

8.8 Joining Asymptotic Representations of the Structure Function $\tilde{\Phi}_R^{(2)}(\tau)$

According to (8.60), the structure function $\tilde{\Phi}_R^{(2)}(\tau)$ has two asymptotic representations: for small τ, it is $\tau \ll T_1$ and described by the branch (8.60$_1$), and for large $\tau \gg T_1$ by the branch (8.60$_2$). In Sect. 8.7, we obtained parameters $\sigma_1^{(1)}, H_1^{(1)}, T_1^{(1)}$ for the first node, and the parameters $\sigma_1^{(2)}, H_1^{(2)}, T_1^{(2)}$ for the second node.

In order to parameterize the function $\tilde{\Phi}_R^{(2)}(\tau)$ throughout the considered interval of the delay τ, we should apply the method of merging (stitching) asymptotic (8.60$_1$) and (8.60$_2$) [60, 61].

Building a single solution is not a trivial task, which can be summarized as follows: We know the behavior of $f(x)$ in the zones *I* and *III* (in this case, the gaps $0 \le \tau \le \tau_1$ ($\tau_1 \ll T_1$) and $\tau_2 \le \tau \le T_1 - 1$ ($\tau_2 \ll T_1$)), we need to finish it in the

intermediate zone II $\tau_1 \leq \tau \leq \tau_2$. For this purpose, we can use the two-point Padé approximant [62]. Let

$$f(\varepsilon) = \sum_{n=0}^{\infty} c_n \varepsilon^n \quad \text{at} \quad \varepsilon \to 0, \tag{8.61}$$

$$f(\varepsilon) = \sum_{n=0}^{\infty} c_{-n} \varepsilon^n \quad \text{at} \quad \varepsilon \to \infty. \tag{8.62}$$

Then, the two-point Padé approximant has the form [63, 64]

$$f(\varepsilon) = \frac{\sum_{j=0}^{m} \alpha_j \varepsilon^j}{\sum_{j=0}^{n} \beta_j \varepsilon^j}, \tag{8.63}$$

where the numerator and denominator are selected from the conditions of decomposition of expression (8.63) at $\varepsilon \to 0$ and $\varepsilon \to \infty$ and they must coincide with the expressions (8.61) and (8.62), respectively.

Note that the Padé approximant has the remarkable property of auto-correction [65]. The essence is in following to determine the numerator and denominator of the Padé approximant, and it is necessary to solve a system of linear algebraic equations. This operation is mathematically incorrect, i.e., when solving large systems of linear algebraic equations, and we get the answer with a great inaccuracy. However, it appears that the error in determining the numerator and denominator cancel out, and the fraction of Padé gives an answer with a high accuracy, while the numerator and denominator are very inaccurate.

The series of the form (8.61) and (8.62) were first introduced by Poincare in the "New methods of celestial mechanics" [66] and are, in general, the divergent series, which converge at some finite $n = n_0$ and $\varepsilon \to \varepsilon_0$. Such series are called the asymptotic series, in contrast with the conventional series converging at $\varepsilon = \varepsilon_0$ and $n \to \infty$. The series (8.61) is asymptotic if there is n_0 such as that for the function $f_{n_0} = c_0 + c_1\varepsilon + \cdots + c_{n_0}\varepsilon^{n_0}$ and it holds the limit equality

$$\lim_{\varepsilon \to 0}(f - f_{n_0})\varepsilon^{-n_0} = 0,$$

The development of asymptotic mathematics led to the following experimental result: The summation of asymptotic series to the smallest term ensures the exponential accuracy [67]. In other words, the error in determining the value of the function f over the interval of its asymptotic series takes up the least-largest term, is as small as the exponent of a certain order, i.e., as $e^{-(1/\varepsilon)^k}$ for some integer k. It was established experimentally also [60] that the smallest term is usually obtained when $n = a(1/\varepsilon)^k$, where a positive number a is determined by the task.

Let $\tau_0 > 0$ is a small number $\tau_0 \ll T_1^{(1)}$ (in calculation we assume $\tau_0 = 0.1$). Let $\tau/T_1^{(1)} = x$, $\tau_0/T_1^{(1)} = x_0$, and $x - x_0 = \varepsilon$. The expansion of the function (8.60$_1$) with respect to ε and accuracy up to $O(\varepsilon^5)$ can be written as follows:

$$f_1(\varepsilon) = c_0 + c_1\varepsilon + c_2\varepsilon^2 + c_3\varepsilon^3 + c_4\varepsilon^4, \quad (\varepsilon \to 0) \tag{8.64}$$

with coefficients

$$c_k = \frac{1}{k!}\frac{\mathrm{d}}{\mathrm{d}\tau^k}\tilde{\Phi}_R^{(2)}(\tau)\bigg|_{\tau=\tau_0} \quad (k = 0, 1, 2),$$

where $\tilde{\Phi}_R^{(2)}(\tau)$ is given by expression (8.60$_1$). By calculating it, we obtain

$$c_0 = \frac{2\left(\sigma_1^{(1)}\right)^2}{\Gamma^2\left(H_1^{(1)} + 1\right)}\left(\frac{\tau}{T_1^{(1)}}\right)^{2H_1^{(1)}}$$

$$c_k = \frac{2\left(\sigma_1^{(1)}\right)^2}{\Gamma^2\left(H_1^{(1)} + 1\right)} \cdot \frac{1}{k!}\left(2H_1^{(1)}\right)\left(2H_1^{(1)} - 1\right) \tag{8.65}$$

$$\dots\left(2H_1^{(1)} - k + 1\right)\left(\frac{\tau_0}{T_1^{(1)}}\right)^{2H_1^{(1)} - k}, \quad (k = 1, 2\dots).$$

By setting $m = n = 2$, we write the Padé approximant for $f_1(\varepsilon)$ in the form

$$f(\varepsilon) = \frac{\alpha_0 + \alpha_1\varepsilon + \alpha_2\varepsilon^2}{\beta_0 + \beta_1\varepsilon + \beta_2\varepsilon^2}. \tag{8.66}$$

Using the known representation for infinitesimal x

$$\frac{1}{1-x} = 1 + x + x^2 + \dots,$$

we get with an accuracy up to $O(\varepsilon^2)$ the following expansion for $f(\varepsilon)$ in powers of ε

$$f(\varepsilon) = \left(\alpha_0 + \alpha_1\varepsilon + \alpha_2\varepsilon^2\right) \cdot \frac{1}{\beta_0}\left[1 - \left(\frac{\beta_1}{\beta_0}\varepsilon + \frac{\beta_2}{\beta_0}\varepsilon^2\right)\right]. \tag{8.67}$$

By equating in (8.64) and (8.67), the coefficients of the powers of ε^0, ε^1, and ε^2, we obtain a system of nonlinear equations

$$\left.\begin{array}{l} \dfrac{\alpha_0}{\beta_0} = c_0; \\[2mm] \dfrac{\alpha_1}{\beta_0} - \dfrac{\alpha_0}{\beta_0} \cdot \dfrac{\beta_1}{\beta_0} = c_1; \\[2mm] \dfrac{\alpha_2}{\beta_0} - \dfrac{\alpha_0}{\beta_0} \cdot \dfrac{\beta_2}{\beta_0} - \dfrac{\alpha_1}{\beta_0} \cdot \dfrac{\beta_1}{\beta_0} = c_2. \end{array}\right\}, \tag{8.68}$$

We assume that the signal $V(t)$ is defined on the sufficiently large interval $[0, T]$ and

$$\tau_0 \gg T_1^{(2)}, \quad \tau_0 \ll T$$

e.g., $\tau = \left(T_1^{(2)} + T\right)/2$. Then, in the notation $\tau/T_1^{(2)} = x$ and $\tau_0/T_1^{(2)} = x_0$, the limiting transition $\tau \to T$ means that $x - x_0 = \varepsilon \to \infty$.

The expansion of the function (8.60_2) with respect to ε and an accuracy up to $O\!\left(\varepsilon^{-5}\right)$ can be written as follows:

$$f_2\!\left(\varepsilon^{-1}\right) = \bar{c}_0 + c_{-1}\varepsilon + c_2\varepsilon^{-2} + c_3\varepsilon^{-3} + c_4\varepsilon^{-4}, \quad (\varepsilon \to \infty). \tag{8.69}$$

The coefficients of the expansion (8.69) are given by

$$\bar{c}_0 = \tilde{\Phi}_R^{(2)}(\tau_0), \quad c_{-k} = \left.\frac{d^k}{dx^k}\Phi_R^{(2)}(\tau)\right|_{\tau=\tau_0}, \quad (k = 1, 2 \ldots)$$

where $\tilde{\Phi}_R^{(2)}(\tau)$ is defined by (8.60_2) and $\tau_0 = \left(T_1^{(2)} + T\right)/2$.

Given the asymptotic representation (8.53), the coefficients $\bar{c}_0$ and c_{-k} $(k = 1 \ldots 4)$ can be written as follows:

$$\bar{c}_0 = 2\left(\sigma_1^{(2)}\right)^2 \left[1 - \Gamma^{-1}\!\left(H_1^{(2)}\right)\left(\frac{\tau_0}{T_1^{(2)}}\right)^{H_1^{(2)}-1-\alpha}\right]^2 ;$$

$$c_{-1} = -4\left(\sigma_1^{(2)}\right)^2 \left[1 - \Gamma^{-1}\!\left(H_1^{(2)}\right)\left(\frac{\tau_0}{T_1^{(2)}}\right)^{H_1^{(2)}-1-\alpha}\right]$$
$$\cdot \left[\Gamma^{-1}\!\left(H_1^{(2)}\right)\frac{H_1^{(2)}-1-\alpha}{T_1^{(2)}}\left(\frac{\tau_0}{T_1^{(2)}}\right)^{H_1^{(2)}-2-\alpha}\right] ;$$

$$c_{-2} = 4\left(\sigma_1^{(2)}\right)^2 \left\{\left[\Gamma^{-1}\!\left(H_1^{(2)}\right)\frac{H_1^{(2)}-1-\alpha}{T_1^{(2)}}\left(\frac{\tau_0}{T_1^{(2)}}\right)^{H_1^{(2)}-2-\alpha}\right]\right.$$
$$- \left[1 - \Gamma^{-1}\!\left(H_1^{(2)}\right)\left(\frac{\tau_0}{T_1^{(2)}}\right)^{H_1^{(2)}-1-\alpha}\right]$$
$$\left.\cdot \left[\Gamma^{-1}\!\left(H_1^{(2)}\right)\frac{\left(H_1^{(2)}-1-\alpha\right)\left(H_1^{(2)}-2-\alpha\right)}{\left(T_1^{(2)}\right)^2}\left(\frac{\tau_0}{T_1^{(2)}}\right)^{H_1^{(2)}-3-\alpha}\right]\right\} ;$$

$$c_{-3} = 4\left(\sigma_1^{(2)}\right)^2 \left\{ 3 \left[\Gamma^{-1}\left(H_1^{(2)}\right) \frac{H_1^{(2)} - 1 - \alpha}{T_1^{(2)}} \left(\frac{\tau_0}{T_1^{(2)}}\right)^{H_1^{(2)} - 2 - \alpha} \right] \right.$$

$$\cdot \left[\Gamma^{-1}\left(H_1^{(2)}\right) \frac{\left(H_1^{(2)} - 1 - \alpha\right)\left(H_1^{(2)} - 2 - \alpha\right)}{\left(T_1^{(2)}\right)^2} \left(\frac{\tau_0}{T_1^{(2)}}\right)^{H_1^{(2)} - 3 - \alpha} \right]$$

$$- \left[1 - \Gamma^{-1}\left(H_1^{(2)}\right)\left(\frac{\tau_0}{T_1^{(2)}}\right)^{H_1^{(2)} - 1 - \alpha} \right]$$

$$\left. \cdot \left[\Gamma^{-1}\left(H_1^{(2)}\right) \frac{\left(H_1^{(2)} - 1 - \alpha\right)\left(H_1^{(2)} - 2 - \alpha\right)\left(H_1^{(2)} - 3 - \alpha\right)}{\left(T_1^{(2)}\right)^3} \left(\frac{\tau_0}{T_1^{(2)}}\right)^{H_1^{(2)} - 4 - \alpha} \right] \right\};$$

$$c_{-4} = 4\left(\sigma_1^{(2)}\right)^2 \left\{ 3 \left[\Gamma^{-1}\left(H_1^{(2)}\right) \frac{\left(H_1^{(2)} - 1 - \alpha\right)\left(H_1^{(2)} - 2 - \alpha\right)}{\left(T_1^{(2)}\right)^2} \left(\frac{\tau_0}{T_1^{(2)}}\right)^{H_1^{(2)} - 3 - \alpha} \right] \right.$$

$$+ 3 \left[\Gamma^{-1}\left(H_1^{(2)}\right) \frac{H_1^{(2)} - 1 - \alpha}{T_1^{(2)}} \left(\frac{\tau_0}{T_1^{(2)}}\right)^{H_1^{(2)} - 2 - \alpha} \right]$$

$$\cdot \left[\Gamma^{-1}\left(H_1^{(2)}\right) \frac{\left(H_1^{(2)} - 1 - \alpha\right)\left(H_1^{(2)} - 2 - \alpha\right)\left(H_1^{(2)} - 3 - \alpha\right)}{\left(T_1^{(2)}\right)^3} \left(\frac{\tau_0}{T_1^{(2)}}\right)^{H_1^{(2)} - 4 - \alpha} \right]$$

$$- \left[1 - \Gamma^{-1}\left(H_1^{(2)}\right)\left(\frac{\tau_0}{T_1^{(2)}}\right)^{H_1^{(2)} - 1 - \alpha} \right]$$

$$\left. \cdot \left[\Gamma^{-1}\left(H_1^{(2)}\right) \frac{\left(H_1^{(2)} - 1 - \alpha\right)\left(H_1^{(2)} - 2 - \alpha\right)\left(H_1^{(2)} - 3 - \alpha\right)\left(H_1^{(2)} - 4 - \alpha\right)}{\left(T_1^{(2)}\right)^4} \left(\frac{\tau_0}{T_1^{(2)}}\right)^{H_1^{(2)} - 5 - \alpha} \right] \right\}.$$

The Padé approximant for $f_2(\varepsilon^{-1})$ is obtained from (8.64) by dividing the numerator and denominator on ε^2

$$f\left(\varepsilon^{-1}\right) = \frac{\alpha_2 + \alpha_1 \varepsilon^{-1} + \alpha_0 \varepsilon^{-2}}{\beta_2 + \beta_1 \varepsilon^{-1} + \beta_2 \varepsilon^{-2}}. \tag{8.71}$$

With accuracy up to $O(\varepsilon^{-3})$, we obtain the following expansion of the function (8.71) in powers of ε^{-1}:

$$f\left(\varepsilon^{-1}\right) = \left(\alpha_2 + \alpha_1 \varepsilon^{-1} + \alpha_2 \varepsilon^{-2}\right) \cdot \frac{1}{\beta_2} \left[1 - \left(\frac{\beta_1}{\beta_2} \varepsilon^{-1} + \frac{\beta_0}{\beta_2} \varepsilon^{-2}\right) \right], \tag{8.72}$$

By equating the coefficients in (8.69) and (8.72) at the powers $\left(\varepsilon^{-1}\right)^0$, ε^{-1} and ε^{-2}, we obtain a system of equations:

$$
\begin{cases}
\dfrac{\alpha_2}{\beta_2} = \bar{c}_0; \\[2ex]
\dfrac{\alpha_1}{\beta_2} - \dfrac{\alpha_2}{\beta_2} \cdot \dfrac{\beta_1}{\beta_2} = c_{-1}; \\[2ex]
\dfrac{\alpha_0}{\beta_2} - \dfrac{\alpha_1}{\beta_2} \cdot \dfrac{\beta_1}{\beta_2} - \dfrac{\alpha_2}{\beta_2} \cdot \dfrac{\beta_0}{\beta_2} = c_{-2}.
\end{cases}
\tag{8.73}
$$

So we have a system of 6 nonlinear Eqs. (8.68) and (8.73) with respect to 6 unknowns $(\alpha_0, \alpha_1, \alpha_2, \beta_0, \beta_1, \beta_2)$.

The initial approximation for the unknown unknowns will be chosen as following.

Comparison of the coefficients ε^3 and ε^4 in (8.64) and (8.67) gives a system of equations:

$$
\left.
\begin{array}{l}
\beta_2 c_1 + \beta_1 c_2 + \beta_0 c_3 = 0 \\
\beta_2 c_2 + \beta_1 c_3 + \beta_0 c_4 = 0
\end{array}
\right\},
\tag{8.74}
$$

which in matrix form is written as follows:

$$
\begin{pmatrix} c_1 & c_2 \\ c_2 & c_3 \end{pmatrix}
\begin{pmatrix} \beta_2 \\ \beta_1 \end{pmatrix}
= -\beta_0 \begin{pmatrix} c_3 \\ c_4 \end{pmatrix}.
\tag{8.75}
$$

The entire set of coefficients $(\alpha_0, \alpha_1, \alpha_2, \beta_0, \beta_1, \beta_2)$ is determined up to a common factor for certainty we can say $\beta_0 = 1$. Then, the system of Eq. (8.75) has a solution

$$
\beta_1 = \frac{c_1 c_4 - c_2 c_3}{c_2^2 - c_1 c_3}, \quad
\beta_2 = \frac{c_3^2 - c_2 c_4}{c_2^2 - c_1 c_3}.
\tag{8.76}
$$

and from (8.68), we find

$$
\alpha_0 = c_0, \quad \alpha_1 = c_1 + \beta_1 c_0, \quad \alpha_2 = c_2 + \beta_1 c_1 + (\beta_1 + \beta_2)c_0.
\tag{8.77}
$$

Comparison of the coefficients ε^{-3} and ε^{-4} in (8.69) and (8.72) gives a system of equations

$$
\left.
\begin{array}{l}
\beta_0 c_{-1} + \beta_1 c_{-2} + \beta_2 c_{-3} = 0 \\
\beta_0 c_{-2} + \beta_1 c_{-3} + \beta_2 c_{-4} = 0
\end{array}
\right\}.
\tag{8.78}
$$

or in matrix form

$$
\begin{pmatrix} c_{-3} & c_{-2} \\ c_{-4} & c_{-3} \end{pmatrix}
\begin{pmatrix} \beta_2 \\ \beta_1 \end{pmatrix}
= -\beta_0 \begin{pmatrix} c_{-1} \\ c_{-2} \end{pmatrix}.
$$

Assuming $\beta_0 = 1$, we obtain a solution

$$\beta_1 = \frac{c_{-2}c_{-1} - c_{-2}^2}{c_{-3}^2 - c_{-2}c_{-4}}, \quad \beta_2 = \frac{c_{-4}c_{-2} - c_{-3}c_{-1}}{c_{-3}^2 - c_{-2}c_{-4}}. \tag{8.79}$$

and from (8.73), we find

$$\begin{aligned}
\alpha_2 &= \bar{c}_0 \cdot \beta_2; \\
\alpha_1 &= c_{-1} \cdot \beta_2 + \bar{c}_0 \cdot \beta_1; \\
\alpha_0 &= c_{-2} + c_{-1} \cdot \beta_1 + \bar{c}_0 \left(1 + \frac{\beta_1}{\beta_2}\right).
\end{aligned} \tag{8.80}$$

Solution of the system of nonlinear Eqs. (8.68) and (8.73) is obtained by the commands "Given" and "Find" in MATHCAD asking as initial approximations $\beta_0 = 1$, and the remaining unknowns are determined either from (8.76), (8.77) or (8.79), (8.80).

The results of calculation for the coefficients $(\alpha_0, \alpha_1, \alpha_2, \beta_0, \beta_1, \beta_2)$ are shown in Table 8.4. Figures 8.12 and 8.13 show the graphs of the structure function $\Phi_R^{(2)}(\tau)$, respectively, for small $(\tau \ll T_1)$ and large $(\tau \gg T_1)$ delays τ, and Fig. 8.14 shows the graph of the corresponding matching asymptotic expansions.

Table 8.4 Coefficients of the splice function

Coefficients	0	1	2
α	205.698	1.253×10^4	1.964×10^5
β	1	-50	833.333

Fig. 8.12 The graph of the structure function for small delays
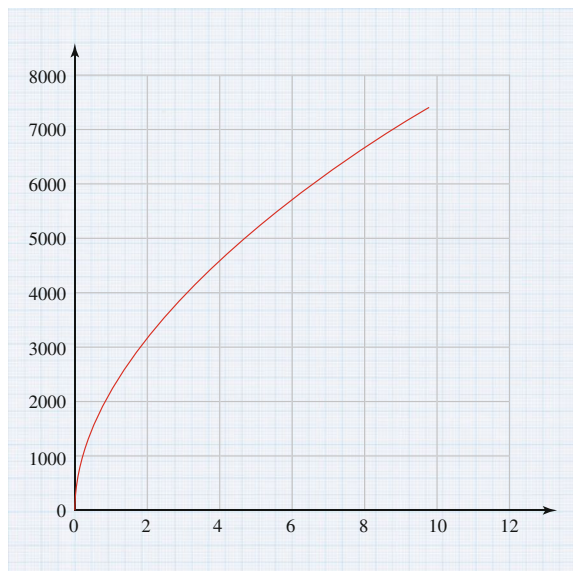
Fig. 8.13 The graph of the
structure function for large
delays
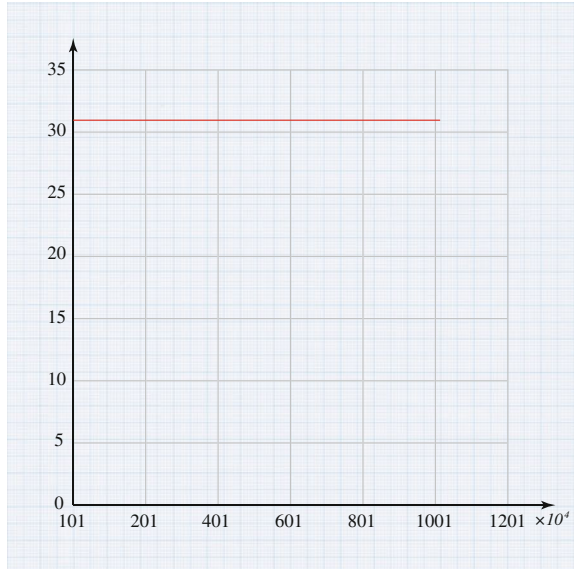
Fig. 8.14 The splicing of
asymptotic expansions for the
structure function
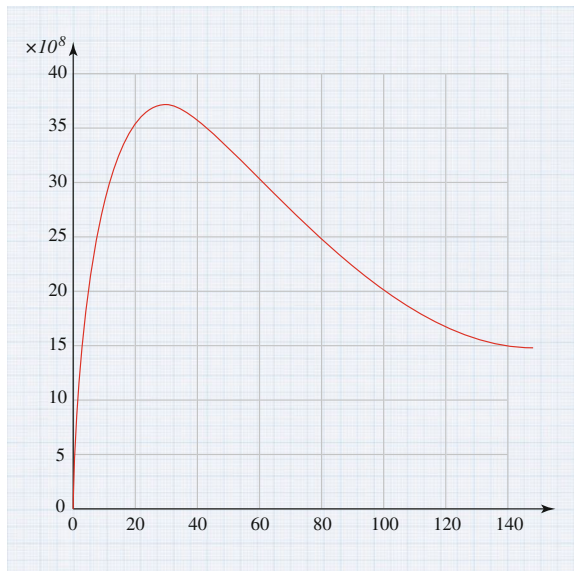
Adoption of irregularities of dynamic variables as a data carrier allows not only
in the most general form of the phenomenological to classify all information
contained in a chaotic series, but also to discernibly extract the necessary part of it.
At the same time, the analyzed object may reveal different qualities and charac-
teristics in the distinguished different levels of the object organization. All detected

"passport information" naturally generates a single information unit (a set of parameters, dimensional and dimensionless), defined as "information of dynamic differences" (IDDs), which is the multivariable generalization of Kolmogorov's K-entropy—the rate of losing information that in the theory of deterministic chaos is introduced as a scalar.

The need to "go beyond" the scope of the orthodox statistical physics is due to the inability to solve problems based on her information extraction from complex, including natural, signals.

It is an unorthodox approach, by rejecting the image of the ideal "thermostat," and the view of the evolutionary dynamics as a series of "steps–events" in the Weizsäcker evolutionary scheme, originally irreversible at every level of evolution, can solve this fundamental and important in terms of "expert knowledge" problem. Therefore, we actually question the currently approved method by introducing into the equation the dynamic time as a continuously changing variable.

Literatures

1. I. Prigozhin, I. Stengers, *Poriadok iz khaosa. Novyi dialog cheloveka s prirodoi, per. s angl.* (Editornaia URSS, Moscow, 2000), p. 310
2. R. Vak, *How Nature Works. The Science of Self-organized Criticality* (Oxford University Press, Oxford, 1997), p. 212
3. G. Shuster, *Determinirovannyi khaos. Vvedenie, per. s angl.* (Mir, Moscow, 1988), p. 240
4. P. Berzhe, I. Pomo, K. Vidal', *Poriadok v khaose. O deterministskom podkhode k turbulentnosti*, per. s fran (Mir, Moscow, 1991), p. 368
5. V.S. Anishchenko, T.E. Vadivasova, V.V. Astakhov, *Nelineinaia dinamika khaoticheskikh i stokhasticheskikh sistem. Fundamental'nye osnovy i izbrannye problem, pod red. V.S. Anishchenko* (Izd-vo Sarat. Un-ta, Saratov 1999), p. 368
6. Iu.L. Klimontovich, *Turbulentnoe dvizhenie, struktura khaosa. Novyi podkhod k stokhasticheskoi teorii otkrytykh system* (Nauka, Moscow, 1990)
7. V.S. Anishchenko, *Slozhnye kolebaniia v prostykh sistemakh. Mekhanizmy vozniknoveniia, struktura i svoistva dinamicheskogo khaosa v radiofizicheskikh sistemakh* (Nauka, Moscow, 1990), p. 312
8. N.H. Packard, J.P. Crutchfield, J.D. Farmer, R.S. Shaw, Geometry from a time series. Phys. Rev. Lett. **45**, 712–715 (1980)
9. F. Takens, in *Detecting Strange Attractors in Turbulence, Dynamical System and Turbulence*, ed. by D. Rang, L.S. Young, Lectures Notes in Math., vol. 898 (Springer, Berlin, 1980), pp. 366–381
10. R. Mane, in *On the Dimension of the Compact Invariant Sets of Certain Nonlinear Maps, Dynamical Systems and Turbulence*, ed. by D. Rang, L.S. Yong. Lecture Notes in Math., vol. 898 (Springer, Berlin, 1980), p. 230
11. J. Stark, D.S. Broomhead, M.E. Davies, Huke Takens embedding theorems for forced and stochastic systems, Nonlinear Analysis, Theory, Methods and Applications, in *Proceedings of 2nd Congress of Nonlinear Analysis*, vol. 30(8) (Elsevier Science Ltd., Amsterdam, 1997), pp. 5303–5314
12. J.D. Farmer, J.J. Sidorowich, Predicting chaotic time series. Phys. Rev. Lett. **59**(8), 845–848 (1987)
13. M. Casdagli, Nonlinear prediction of chaotic time series. Phys. D **35**, 335–356 (1989)

14. H.D.I. Abarbanel, R. Brown, J.B. Kadtke, Prediction in chaotic nonlinear systems—Methods for time series with broadband Fourier spectra. Phys. Rev. A **41**(4), 1782–1807 (1990)
15. P. Grassberger, I. Procaccia, Characterization of strange attractors. Phys. Rev. Lett. **50**, 346–349 (1983)
16. P. Grassberger, I. Procaccia, Measuring the strangeness of strange attractors. Phys. D. **9**, 189–208 (1983)
17. A. Wolf, J.B. Swift, H.L. Swinney, J.A. Vastano, Determining Lyapunov exponents from a time series. Phys. D. **16**, 285–317 (1985)
18. J.P. Eckmann, S.O. Kamphorst, D. Ruelle, D. Gilberto, Lyapunov exponents from a time series. Phys. Rev. A **34**, 4971–4979 (1986)
19. J. Cremers, A. Hübler, Construction of differential equations from experimental data. Z. Naturforschung A. **42**, 797–802 (1987)
20. J.P. Crutchfield, B.S. McNamara, Equations of motion from a data series. Complex Syst. **1**, 417–452 (1987)
21. G.G. Malinetskii, A.B. Potapov, *Sovremennye problemy nelineinoi dinamiki* (Moscow, Editornal URSS, 2000), p. 336
22. A.M. Fraser, Reconstructing attractors from scalar time series: a comparison of singular systems and redundancy criteria. Phys. D **34**, 391 (1989)
23. J.F. Gibson, J.D. Farmer, M. Casdagli, S. Eubank, An analytic approach to practical state space reconstruction. Phys. D **57**, 1 (1992)
24. M.B. Kennel, S. Isabelle, Method to distinguish possible chaos from colored noise and to determine embedding parameters. Phys. Rev. A **46**, 3111 (1992)
25. S.F. Timashev, *Flikker-shumovaia spektroskopiia, informatsiia v khaoticheskikh signalakh* (Moscow, FIZMFTLIT, 2007), p. 248
26. V.S. Vladimirov, *Uravneniia matematicheskoi fiziki* (Nauka, Moscow, 1967), p. 136
27. H. Lure, *Time and Information. Time, Temporality, Now, Experiencing Time and Concept of Time in an Interdisciplinary Perspective*, ed. by H. Atmanspacher, E. Ruhnau (Springer, Berlin, 1997), pp. 81–89
28. W. Shottky, Phys. Rev. **28**, 74 (1926)
29. J.B. Johnson, Phys. Rev. **26**, 71 (1925)
30. Sh.M. Kogan, Nizkochastotnyi tokovyi shum so spektrom tipa $1/f$ v tverdykh telakh, Uspekhi fizich. nauk., Tom 145, №2, 285–325 (1985)
31. G.P. Zhigal'skii, Neravnovesnyi $1/f^{\gamma}$ – shum v provodiashchikh plenkakh i kontaktakh, Uspekhi fizich. nauk, Tom 173, №5, 465–490 (2003)
32. Iu.L. Klimontovich, *Vvedenie v fiziku otkrytykh system* (Ianus-K., Moscow, 2002), p. 284
33. R.F.C. Vesset, Experimental Gravitation, *Proceedings of International School of Physics "Enrico Fermi", Coorse 56* (Academic Press, New-York, 1974), p. 111
34. J.J. Gagnepain, J. Uebersfeld, *Proceedings of Symposium on 1/f Fluctuations,* Tokyo, ed. by T. Musha (1977), p. 173
35. G.N. Bochkov, E. Kuzovlev Iu, Novoe v issledovaniiakh $1/f$ –shuma, Uspekhi fizich. nauk, Tom 141, №1, 151–176 (1983)
36. A.I. Olemskoi, A.I. Katskel'son, *Sinergetika kondensirovannoi sredy, izd. 2-e* (Editorial URSS, Moscow, 2010), p. 336
37. A.R. Brazhe, *Fraktal'nyi i veivlet – analiz elektricheskoi aktivnosti nervnykh kletok. Dis. na soisk. uch. step. kand. biolog. nauk* (MGU, Moscow, 1998)
38. G.M. Zaslavskii, R.Z. Sagdeev, *Vvedenie v nelineinuiu fiziku* (Nauka, Moscow, 1988)
39. G. Zaslavskogo i dr, *Slabyi khaos i kvazireguliarnye struktury, pod. red.* (Nauka, Moscow, 1991)
40. T.S. Akhromeeva, S.P. Kurdiumov, G.G. Malinetskii i dr, *Nestatsionarnye struktury i diffuzionnyi khaos* (Nauka, Moscow, 1992)
41. Iu.Ia. Klimontovich, *Statisticheskaia teoriia otkrytykh system* (GOO "Ianus", Moscow, 1995)
42. G.G. Malinetskii, *Vvedenie v nelineinuiu dinamiku* (Editorial URSS, Moscow, 2000)
43. M.J. Feigenboum, The universal metric properties of nonlinear transformations. J. Stat. Phys. **21**(6), 669–706 (1979)

44. A.Kh. Janahmadov, O.A. Dyshin, N.Z. Askerova, Fraktal'nyi podkhod k prognozirovaniiu sostoianiia samoorganizovannoi kritichnosti prirodnykh system. Vestnik Azerbaidzhanskoi Inzhenernoi Akademii, Tom **4**(3), 97–106 (2012)

45. A.G. Parkhomov, Nizkochastotnyi shum – universal'nyi detektor slabykh vozdeistvii, Parapsikhologiia i psikhofizika, №5, 59–65 (1992)

46. A.I. Osipov, *Samoorganizatsiia i khaos, ser. "Fizika'*, №7 (Znanie, Moscow, 1986)

47. L.A. Shelepin, *Vdali ot ravnovesiia, ser. "Fizika'*, №8, (Znanie, Moscow, 1987)

48. C.F. von Weizsäcker, *Time—Empirical Mathematics—Quantum Theory, Time, Temporality, Now, Experiencing Time and Concept of Time in an Interdisciplinary Perspective*, ed. by H. Atmanspacher, E. Ruhnau (Springer, Berlin, 1997), p. 91–104

49. Y. Pomeau, P. Manneville, Intermittent transition to turbulence in dissipative dynamical system. Commun. Math. Phys. **74**, 189 (1980)

50. S.V. Kuznetsov, *Dinamicheskii khaos (kurs lektsii), Ucheb. posobie dlia vuzov, 2-e izd. pererab. i dop.* (Izd.-vo Fiz.-mat. Lit.-ry, Moscow, 2006), p. 356

51. D. Brillindzher, *Vremennye riady. Obrabotka dannykh i teoriia, per. s angl.* (Mir, Moscow, 1980), p. 536

52. R. Otnes, L. Enokson, *Prikladnoi analiz vremennykh riadov. Osnovnye metody, per. s angl.* (Mir, Moscow, 1982), p. 428

53. S.F. Timashev, G.V. Vstovskii, Flikker – shumovaia spektroskopiia v analize khaoticheskikh vremennykh riadov dinamicheskikh peremennykh i problema otnosheniia "signal-shum". Elektrokhimiia, Tom **39**(2), 156–169 (2003)

54. A.A. Samarskii, A.V. Gulin, *Ustoichivost' raznostnykh skhem* (Nauka, Moscow, 1973), p. 415

55. B.B. Kadomtsev, *Dinamika i informatsiia* (Moscow, Red. zh.-la Uspekhi fizicheskikh nauk, 1997), p. 401

56. E.P. Ageev, *Neravnovesnaia termodinamika v voprosakh i otvetakh (MGU* (Moscow, Khimicheskii f.-t, 1999), p. 114

57. G.V. Vstovskii, *Elementy informatsionnoi fiziki* (Moscow, MGPU, 2002), p. 258

58. S.F. Timashev, Yu.S. Polyakov, Review of flicker noise spectroscopy in electrochemistry. Fluctuation and Noise Letters **7**(2), R15–R47 (2007)

59. D.S. Kuznetsov, *Spetsial'nye funktsii, 2-e izdanie* (Moscow, Vysshaia shkola, 1965), p. 272

60. I.V. Andrianov, R.G. Barantsev, L.I. Manevich, *Asimptoticheskaia matematika i sinergetika: put' k tselostnoi prostote* (Moscow, Editorial URSS, 2004), p. 304

61. M. Van Daik, *Metody vozmushchenii v mekhanike zhidkosti, per. s angl.* (Mir, Moscow, 1967), p. 310

62. J. Eizek, E.J. Weniger, P. Bracken, V. Spirko, Effective characteristic polynomials and two-point Pad'e approximation as summation techniques for the strongly perturbation expansions of the ground state energies of anharmonic oscillators. Phys. Rev. E **53**, 2915–2939 (1996)

63. Dzh. Beiker (jr.), P.Greivs-Morris, Approksimatsii Pade, per. s angl. (Mir, Moscow, 1986), p. 502

64. D. Shanks, Nonlinear transforms of divergent and slow convergent sequences. J. Math. Phys. **34**, 1–42 (1995)

65. G.L. Litvinov, *Priblizhennoe postroenie ratsional'nykh approksimatsii i effekt avtokorreliatsii pogreshnosti* (Pushchino, Matem. Modelirovanie, 1990), pp. 99–141

66. A. Puankare, *Novye metody nebesnoi mekhaniki, izbrannye trudy, Tom 1(2)* (Nauka, Moscow, 1971), pp. 329–744

67. Zh.-P. Ramis, *Raskhodiashchiesia riady i asimptoticheskaia teoriia* (Moscow, Izhevsk Inst-t komp'iut. issled., 2002), p. 80